

# Heartbeat Stars and the Ringing of Tidal Pulsations

by

Kelly Hambleton

A thesis submitted in partial fulfilment for the requirements for the degree of  
Doctor of Philosophy at the University of Central Lancashire

August 2016



## Abstract

With the advent of high precision photometry from satellites such as the *Kepler* satellite, a whole new collection of interesting astronomical features and objects has been revealed: heartbeat stars are prime example of this. Heartbeat stars are eccentric ellipsoidal variables that undergo strong tidal interactions at periastron, when the stars are close to each other. These interactions induce the deformation of the stars, which causes a change in the cross-sectional area and temperature variations over the stellar surface. In the precise *Kepler* data, these changes cause a notable variation in the light curve in the form of a tidal pulse. In this work I present novel modelling tools produced specifically to model heartbeat stars. These include the BAYES-TODCOR software, which generates radial velocities and fundamental stellar parameters from spectra using a combination of EMCEE and TODCOR; and software created for modelling heartbeat stars, which is a combination of PHOEBE, EMCEE and my own codes. One of the features added to the PHOEBE modelling software is the ability to model tidally induced pulsations simultaneously with the binary star features, enabling a complete and accurate heartbeat star model to be determined. Tidally induced pulsations are stellar oscillations driven by the tidal force of the companion star. Approximately 20% of our sample of 173 *Kepler* heartbeat stars show prominent tidally induced pulsations, which present in the light curve as oscillations at precise multiples of the orbital frequency. In this work I present a selection of heartbeat stars, modelled with the aforementioned codes. The majority of these show tidally induced pulsations. Additional features include rapid apsidal motion, tidally resonant modes, solar-like oscillations and tidally influenced pressure modes. I also applied my codes to a binary star presenting a strong case of frequency modulation, the Doppler shift of the stellar pulsation frequencies as the pulsating star moves towards and away from the observer. Combined, these objects form the majority of heartbeat stars that have been studied in detail in the literature today.



## Dedication

This thesis is dedicated to my husband and soul mate, Andrej, who has been my rock and my inspiration throughout my PhD studies. For all your time, energy and love, I thank you from the bottom of my heart.



## Acknowledgements

Firstly I would like to thank my adviser, Don Kurtz, for bestowing upon me his vast knowledge of stars, astronomy and life in general. For his contagious enthusiasm, continuous support, patience, motivation and immense knowledge, I am extremely grateful. Thanks to him, this PhD was a perfect combination of excitement, hard work and success. For all his guidance and friendship, I am eternally thankful.

I would like to thank the JHI for offering me a PhD position and for the continued support of the department. As an undergraduate of the JHI I grew to know many of the members very well and am extremely grateful for the family-like community that I enjoyed for many years.

To Gordon and Jerry the panel members on my PhD committee: thank you for taking the time to read my thesis and for all your suggestions, comments and wisdom.

I would like to acknowledge the NASA Science Mission directorate, for the funding of the *Kepler* satellite. The launch of the *Kepler* satellite coincided perfectly with my post-graduate studies, providing me with a plethora of exciting data to analyse. For this I am very grateful.

I would like to thank the STFC for providing me with financial support throughout my PhD studies. I would further like to thank the STFC for selecting my application for the long term attachment grant. My time at Villanova University was successful on many levels, for which I am eternally thankful.

To Villanova University Astronomy Department, for taking me under your wing during the final years of my PhD. For offering me an office space and a home-away-from-home. The opportunity you provided enriched my education and my life, and for this I am extremely grateful.

I would like to thank my fellow office mates and PhD friends from around the globe. For all the discussions, lunches, chats, late-night venting sessions and even the odd night out, I am sincerely grateful. I am extremely grateful to you all for your friendship and support, and hope we can all continue to be friends in the future.

Finally, I would like to thank all of my family, both old and new. For making time for me, supporting me and loving me throughout my education and throughout my life. For dealing with all my travelling and time away from home. For being welcoming with open arms every time I return. For being there for me when I needed it the most and for simply being there. For all these things and for all of you, I am forever grateful. Thank you!

# Contents

<b>1</b>	<b>Introduction</b>	<b>1</b>
1.1	<i>Heartbeat</i> Stars . . . . .	4
1.2	Asteroseismology . . . . .	10
1.2.1	Pressure Modes . . . . .	11
1.2.2	Gravity Modes . . . . .	12
1.2.3	Delta Scuti Stars . . . . .	17
1.2.4	Gamma Doradus Stars . . . . .	20
1.2.5	Hybrid $\gamma$ Dor– $\delta$ Sct . . . . .	20
1.2.6	Solar-Like Oscillators . . . . .	23
1.2.7	Red Giants . . . . .	27
1.3	Binary Stars . . . . .	30
1.3.1	Binary Star Modelling . . . . .	32
1.3.2	Doppler Boosting . . . . .	35
1.3.3	Apsidal Motion . . . . .	36
1.3.4	Frequency Modulation . . . . .	39
1.4	Conclusion . . . . .	41

<b>2</b>	<b>The Bayesian Approach to Radial Velocity Determination</b>	<b>43</b>
2.1	Markov Chain Monte Carlo Techniques . . . . .	44
2.2	TODCOR . . . . .	48
2.3	Bayes' Todcor . . . . .	51
2.3.1	Parameters . . . . .	52
2.3.2	The Software in a Nutshell . . . . .	52
2.3.3	Posteriors, Distributions and Results . . . . .	55
2.4	The Application . . . . .	56
2.4.1	Creation and Application of Synthetic Data . . . . .	59
2.4.2	Comparison of Uncertainties . . . . .	71
2.4.3	Spectral Reduction . . . . .	73
2.4.4	Application to Observed Data . . . . .	76
2.5	Conclusion . . . . .	79
<b>3</b>	<b>The Heartbeat Phenomenon</b>	<b>82</b>
3.1	Tidally Induced Pulsations . . . . .	85
3.1.1	Resonance Locking . . . . .	91
3.2	The Bayesian Approach . . . . .	94
3.3	Additional Functions for Generating Heartbeat Star Models . . . . .	98
3.3.1	The Implementation of Tidally Induced Pulsations . . . . .	101
3.3.2	Doppler Boosting . . . . .	103
3.3.3	Phase Shift . . . . .	107
3.3.4	Passband luminosity . . . . .	110

3.3.5	The Stellar Equipotential . . . . .	111
3.3.6	The Critical Potential . . . . .	116
3.3.7	The $\log g$ Constraint . . . . .	119
3.3.8	The Spin-to-Orbital Rotation Frequency . . . . .	120
3.4	Conclusion . . . . .	122
<b>4</b>	<b>KIC 8164262</b>	<b>124</b>
<b>5</b>	<b>KIC 3749404</b>	<b>137</b>
<b>6</b>	<b>KIC 5006817</b>	<b>152</b>
<b>7</b>	<b>KIC 4544587</b>	<b>172</b>
<b>8</b>	<b>KIC 8569819</b>	<b>190</b>
<b>9</b>	<b>Conclusions and Future Work</b>	<b>202</b>
9.1	Conclusion . . . . .	202
9.2	Future Work . . . . .	211
<b>A</b>	<b>The BayesTodcor Software: the <math>\chi^2</math> version and the <i>CCR</i> version</b>	<b>214</b>
A.1	The $\chi^2$ version . . . . .	214
A.2	The <i>CCR</i> version . . . . .	231
<b>B</b>	<b>The heartbeat Star Modelling Software</b>	<b>246</b>
	<b>Bibliography</b>	<b>263</b>



# List of Tables

- 2.1 Parameters of the *example1* synthetic data and corresponding results for the BAYES-TODCOR program using the CCR function and  $\chi^2$ . Alpha denotes the flux ratio. The one sigma uncertainties are given in parentheses. The value highlighted in blue does not agree with the predefined parameter to  $1\sigma$ , but agrees within  $2\sigma$ . . . . . 63
  
- 2.2 The radial velocities for the *example1* synthetic data and corresponding results for the BAYES-TODCOR program using the CCR function and  $\chi^2$ . RV1 and RV2 denote the primary and secondary components, respectively. The one sigma uncertainties are given in parentheses. The values highlighted in blue agree with the predefined parameters to  $2\sigma$ , and those highlighted in red do not agree within  $2\sigma$ . . . . . 65
  
- 2.3 Parameters of the *example2* synthetic data and corresponding results for the BAYES-TODCOR program using the CCR function and  $\chi^2$ . The one sigma uncertainties are given in parentheses. The values highlighted in blue agree with the predefined parameters to  $2\sigma$  precision, and those highlighted in red do not agree within  $2\sigma$ . . . . . 68
  
- 2.4 The radial velocities for the *example2* synthetic data and corresponding results for the BAYES-TODCOR program using the CCR function and  $\chi^2$ . RV1 and RV2 denote the primary and secondary components, respectively. The one sigma uncertainties are given in parentheses. The values highlighted in blue agree with the predefined parameters to  $2\sigma$  precision, and those highlighted in red do not agree within  $2\sigma$ . . . . . 70

2.5	<p>A comparison of the radial velocity uncertainties between TODCOR and the <math>\chi^2</math> BAYES-TODCOR software for <i>example2</i>. RV1 and RV2 denote the primary and secondary components, respectively. The uncertainty for the primary component is only marginally increased. However, it is anticipated that the difference will be more significant for real objects, where the likelihood function and observed data are less similar. In some cases, the TODCOR uncertainty is greater than the BAYES-TODCOR uncertainty (highlighted in red). This is a consequence of combining Gaussian distributions with similar parameters. The secondary component displays larger differences, which can be attributed to the low contribution of light from the secondary component. . . . .</p>	72
2.6	<p>Parameters and radial velocities of for KIC 8164262 generated using the BAYES-TODCOR <math>\chi^2</math> software for the fix metallicity of <math>[Fe/H] = 0.5</math>. When using the <math>\log g</math> value from the run with free metallicity, the model would not fit the data as the amplitude of the periastron brightening was too large. The one sigma uncertainties are given in parentheses. . . . .</p>	77

# List of Figures

1.1	A theoretical Hertzsprung-Russell diagram depicting the main sequence, blue and red giants, super giants, and white dwarfs. Adopted from LCOGT.net (Las Cumbres Observatory Global Telescope Network). . . . .	2
1.2	Depicted are the observed <i>Kepler</i> time series (top panel) and phased (bottom panel) light curves of KOI-54, the iconic heartbeat star. The large variation is caused by the tidal deformation and heating at periastron and the smaller variations are tidally induced pulsations that occur at precise multiples of the orbital period (see §1.1). Adopted from Welsh et al. (2011). . . . .	3
1.3	The time series (left panel) and phased light curve (right panel) of the Quarter 9 <i>Kepler</i> data of KIC 5034333. The large variation at phase 0.0 is the periastron variation caused by tidal deformation and heating, and the smaller variations are a combination of naturally occurring and tidally induced pulsations (where only the tidally induced pulsations are visible in the phased data). Note that this system is not eclipsing; the strong dip in the light curve is geometrical in origin. See Fig. 1.4 below. . . . .	5

- 1.4 A grid of light curves generated using the static term of the analytical tide theory of Kumar, Ao & Quataert (1995). The light curves show the variation in the shape of the periastron brightening as a function of argument of periastron, inclination and eccentricity where red denotes  $e = 0.6$  and blue denotes  $e = 0.4$ . It can be clearly seen that for higher inclination angles the dip in the light curve is small compared to lower inclinations, whilst the duration of the periastron brightening (with respect to the orbital period) decreases as the eccentricity increases. Finally, the argument of periastron has a large impact on the asymmetry and morphology of the light curve. Adopted from Thompson et al. (2012). . . . . 7
- 1.5 Depicted are the stellar rotational periods from heartbeat stars with spots, against the calculated values of the pseudo-synchronous rotational periods. The observed rotational periods were extracted from Fourier transforms where harmonics indicative of spots were present. KOI-54 is represented by the cyan point, KIC 8164262 (see Chapter 4) by the yellow point and KIC 3547874 by the magenta point. Adopted from (Zimmerman et al., 2016) . . . . . 9
- 1.6 MW . . . . . 11
- 1.7 Propagation diagram for the  $M = 2.35 M_{\odot}$ ,  $R = 2.34 R_{\odot}$  stellar model, showing the value of  $N$ , the Brunt-Väisälä frequency (solid black line), and the Lamb frequency,  $S_l$  (dashed black line), in units of  $(GM/R^3)^{1/2}$ . These theoretical values were obtained by modelling the dominant frequencies present in the KOI-54 (the horizontal red lines). These are (from top) the dynamical frequency of the star,  $(GM/R^3)^{1/2}$ ; the highest frequency mode observed ( $\sigma_{\alpha} = 91\Omega$ ); the lowest frequency mode observed ( $\sigma_{\alpha} = 22.42\Omega$ ); and the orbital angular frequency,  $\Omega$ . The  $y$ -axis on the right-hand side displays the corresponding periods, in units of hours. From Fuller & Lai (2012). . . . . 13
- 1.8 Buoyancy frequency,  $N$  (straight line), and Lamb frequency,  $S_l$  (dashed line with labels for incremental values of  $l$ ), shown as a function of fractional radius for a model of the Sun. The solid horizontal lines indicate regions where a g mode of  $\nu = 100\mu\text{Hz}$  and a p mode of degree 20 and  $\nu = 2000\mu\text{Hz}$  would be trapped. . . . 14

- 1.9 A pulsational H-R diagram. Delta Sct stars can be found on the intersection between the main sequence (dashed line from the top left region tending towards the bottom right) and the instability strip (encompassed by two, almost vertical long-dashed lines), and the  $\gamma$  Dor stars slightly below them in a region outside the instability strip. From Aerts, Christensen-Dalsgaard & Kurtz (2010). . . . . 16
- 1.10 Large separation-mean density relation for 7 binary systems. A linear fit to the points is depicted, solid line, as well as the solar-like scaling relation (Tassoul, 1980), dashed line, and the theoretical scaling relation for non-rotating models of  $\delta$  Sct stars (Suárez et al., 2014), dashed-dotted line. The different coloured symbols denote the stellar rotation rates where  $\Omega_K$  is the Keplerian break-up rotation rate. Figure adopted from García Hernández et al. (2015). . . . . 19
- 1.11 Period echelle diagram, plotted twice for clarity for KIC 9244992. Symbol sizes indicate mode amplitudes and symbol shapes indicate different values of azimuthal order  $m$ . Adopted from Bedding et al. (2014). . . . . 22
- 1.12 Period spacings of  $l = 1$  modes for twelve *Kepler*  $\gamma$  Dor stars. For each star, symbol shapes indicate different values of azimuthal degree  $m$ . Adopted from Bedding et al. (2014). . . . . 23
- 1.13 Echelle diagrams of three *Kepler* stars (*Kepler* input catalogue number indicated above). The  $l = 0$  modes are indicated by the filled red circles;  $l = 1$  by the open blue circles and  $l = 2$  by the small black points.  $l = 3$  modes are rarely seen from space as the light integrated over the surface does not significantly change, except in the presence of a strong filter such as limb darkening. Figure adopted from Chaplin et al. (2010). . . . . 24

- 1.14 Depicted is a C-D diagram, which shows the relationship between the evolutionary state of stars, and their corresponding large and small separations. In this diagram, the ZAMS (zero age main sequence) is the top dashed line, where dashed lines denote stellar isochrones. The lower most dashed line represents an isochrone for stars of 12 Gyr. The most evolved stars are at the bottom left of the diagram. The evolutionary tracks for different mass objects (with approximately solar metallicity) are over plotted with solid lines, ranging from 0.7–2.0  $M_{\odot}$  (blue) and greater than 2.0  $M_{\odot}$  (grey). Observations are from CoRoT (orange circles), *Kepler* (red triangles) and ground based observations (purple diamonds). The grey circles at the bottom left depict the red giants from the Huber et al. (2010) study of *Kepler* red giants. The Sun is depicted with its usual symbol. Caption and figure adopted from White et al. (2011). . . . . 26
- 1.15 The large separation in period space of mixed modes vs. the large frequency separation from p modes for  $\sim 400$  red giants. Two distinct groups can clearly be seen: The helium-core-burning stars (red diamonds and orange squares) and the hydrogen-shell-burning stars (blue circles). The solid lines show average observable period spacings for models of hydrogen-shell-burning giants on the red giant branch as they evolve from right to left. The black stars show theoretical period spacings calculated in the same way, for four models of helium core-burning stars that are midway through that phase (core helium fraction 50%). Caption and figure adopted from Bedding et al. (2011). . . . . 28
- 1.16 Contributions to the total rotational splitting. Partial integrals of normalized rotation kernels, illustrating the contribution from different regions to the rotational splitting for pressure-dominated modes ( $\nu_4, \nu_5$ ; solid lines) and gravity-dominated modes ( $\nu_1, \nu_2, \nu_3$ ; dashed lines), as a function of the mass-fraction for KIC 8366239. The left-most vertical line represents the boundary of the helium burning core and the vertical line at  $m/M \sim 0.2$  represents the end of the hydrogen burning shell and beginning of the convective envelope. Adopted from Beck et al. (2012). . . . . 30

1.17 Examples of the ultra-high photometric precision and uninterrupted observing mode of *Kepler*. The left panels depict 5-d segments of characteristic *Kepler* light curves in time domain and the right panels show the corresponding phased light curves using all of the Quarter 1 data. Red dots correspond to mid-exposure times of *Kepler*'s 30-min cadence. Top to bottom: a detached eclipsing binary KIC 5513861 ( $P = 1.51012$  d); a semi-detached eclipsing binary KIC 8074045 ( $P = 0.53638$  d); and an over-contact eclipsing binary KIC 3127873 ( $P = 0.67146$  d). 32

1.18 Depicted is a PHOEBE 2.0 model of a “Ferrari” orbiting a UFO generated through analytical descriptions of a car and a UFO. The surface is rasterized using a series of triangles. The green triangles are visible, the blue are partially visible and the red are not visible to the observer. . . . . 35

1.19 The effect of the periastron value,  $\omega$ , on the shape of the periastron brightening for one full cycle of the orbit around the centre of mass. The peaks change both their position in phase *and* their shape drastically as a function of  $\omega$ . The model used in this demonstration is of KIC 3749404, a *Kepler* heartbeat star that exhibits one of the largest periastron advance rates ( $\sim 1^\circ/\text{yr}$ ; Hambleton et al. 2016, in prep.). Depicted in the inset is the light curve variation over 4.5-yr (slightly longer than the the length of the extended *Kepler* mission). . . . . 38

2.1 The contours of an example of a non-isotropic distribution in phase space, described by Eqn. 2.3. . . . . 46

2.2 A contour plot of the two dimensional correlation function. The dashed lines pass through the maximum and indicates the velocity shift of the primary and secondary components. Figure adapted from Zucker & Mazeh (1994). . . . . 49

- 2.3 The  $\ln p$  as a function of iteration for the  $\chi^2$  version of the BAYES-TODCOR software (when applied to synthetic data), where each colour represents a different chain. As the  $\chi^2$  statistic is not normalised, the value should tend to  $0.5n$ , where  $n$  is the number of data points. This plot is used as a first gauge to determine if the model has converged. From consideration of this plot alone, it appears the burn-in time was approximately  $\sim 100$  iterations, as the probability does not change after this point. . . . . 56
- 2.4 Depicted are the posteriors generated using the BAYES-TODCOR program with synthetic data. Lower left sub-plots: two dimensional cross-sections of the posterior probability distribution functions for the effective temperatures  $T_{\text{eff}1}$  and  $T_{\text{eff}2}$ ;  $\log g_1$  and  $\log g_2$ ; the metallicity of both components, *metal*; the stellar rotational velocities  $v_{\text{rot}1}$  and  $v_{\text{rot}2}$ ; and the light ratio, *alpha*. The crosses show the  $1\sigma$  (red) and  $2\sigma$  (green) uncertainties, and are centred on the minima. Diagonal sub-plots from top left to bottom right: histograms displaying the probability distribution of each individual parameter. Upper right sub-plots: the correlations for the two-dimensional cross-sections mirrored in the diagonal line where 1 is direct correlation and -1 is a direct anti-correlation. The values above the plot give the mean value and one sigma uncertainty for each parameter, based on the fitted Gaussians. . . . . 57
- 2.5 Depicted are the normal distributions for the TODCOR mean and average uncertainty (black dashed line) and the combined means and uncertainties determined using the BAYES-TODCOR software (blue line) for KIC 8164262 (see Chapter 4). The red line depicts the weighted mean determined using the BAYES-TODCOR software. . . . . 58
- 2.6 A segment of the synthetic observations of *example1* before noise has been added (black line), with Gaussian noise where  $\sigma = 0.04\text{\AA}$  and with noise added (blue line) and subsequent instrumental broadening (red line). A dispersion of  $0.04\text{\AA}$  was applied for the instrumental broadening, mimicking the broadening of the spectrograph on the Kitt Peak 4-m Mayall telescope. . . . . 60

- 2.7 The light and radial velocity curve of the *example1* model binary, built to test the BAYES-TODCOR software. The top panel depicts the light curve generated by PHOEBE (red line) and the bottom panel depicts the synthetic radial velocity curves for the primary (blue line) and secondary (pink line) components. The equally spaced radial velocity points depict the phases that synthetic observations were made. Note, synthetic observations were not built during times of eclipse. . . . . 62
- 2.8 The synthetic “observed” and computed radial velocities for the CCR (left panel) and  $\chi^2$  (right panel) versions of the TODCOR software for *example1*. Top panels: the TODCOR computed radial velocity points of the primary (red) and secondary (blue) components. The synthetic “observed” data are denoted by black points and are joined by black lines (the black lines do not represent a model). Lower panels: The residuals of the computed data and their associated one sigma uncertainties. . . . . 62
- 2.9 A small region of the *example1* synthetic spectral data created for testing (blue). The  $\chi^2$  version of the BAYES-TODCOR best-fit model and one sigma uncertainty (red envelope) are over plotted. The black line depicts the synthetic data without noise. It can be seen that the red envelope almost completely encompasses the black line, showing that this region essentially lies within the one sigma range. . . . . 63

- 2.10 The spectral parameter posterior distributions created using the CCR version of the BAYES-TODCOR software for *example1*. Lower left sub-plots: two dimensional cross-sections of the posterior probability distribution functions for the effective temperatures  $T_{\text{eff}1}$  and  $T_{\text{eff}2}$ ;  $\log g_1$  and  $\log g_2$ ; the metallicity of both components, *metal*; the stellar rotational velocities  $v_{\text{rot}1}$  and  $v_{\text{rot}2}$ ; and the light ratio, *alpha*. The crosses show the  $1\sigma$  (red) and  $2\sigma$  (green) uncertainties, and are centred on the minima. Diagonal sub-plots from top left to bottom right: histograms displaying the probability distribution of each individual parameter. Upper right sub-plots: the correlations for the two-dimensional cross-sections mirrored in the diagonal line where 1 is direct correlation and -1 is a direct anti-correlation. The values above the plot give the mean value and one sigma uncertainty for each parameter, based on the fitted Gaussians. . . . . 64
- 2.11 The light and radial velocity curve of the *example2* model binary, built to test the BAYES-TODCOR software. The top panel depicts the light curve generated by PHOEBE (red line) and the bottom panel depicts the synthetic radial velocity curves for the primary (blue line) and secondary (pink line) components. The equally spaced radial velocity points depict the phases at which synthetic observations were made. . . . . 67
- 2.12 The synthetic “observed” and computed radial velocities for the CCR (left panel) and  $\chi^2$  (right panel) versions of the TODCOR software for *example2*. Top panels: the TODCOR computed radial velocity points of the primary (red) and secondary (blue) components. The synthetic “observed” data are denoted by black points and are joined by black lines. Lower panels: The residuals of the computed data and their associated one sigma uncertainties. As expected due to its low light contribution, the secondary component’s radial velocities have not been accurately reproduced. . . . 67

- 2.13 A small region of the *example2* synthetic spectrum created for testing (blue). The BAYES-TODCOR best-fit model (red line) and one sigma uncertainty (red envelope, not visible due to small uncertainties) are overplotted. The synthetic data without noise (black line) can barely be seen as black line is completely encompassed by the red envelope, showing that this region completely lies within the one sigma errors. The results from the  $\chi^2$  version of the software were used to create this plot. . . . . 68
- 2.14 The spectral parameter posterior distributions created using the CCR version of the BAYES-TODCOR software for *example2*. Lower left sub-plots: two dimensional cross-sections of the posterior probability distribution functions for the effective temperatures  $T_{\text{eff}1}$  and  $T_{\text{eff}2}$ ;  $\log g_1$  and  $\log g_2$ ; the metallicity of both components, *metal*; the stellar rotational velocities  $v_{\text{rot}1}$  and  $v_{\text{rot}2}$ ; and the light ratio, *alpha*. The crosses show the  $1\sigma$  (red) and  $2\sigma$  (green) uncertainties, and are centred on the minima. Diagonal sub-plots from top left to bottom right: histograms displaying the probability distribution of each individual parameter. Upper right sub-plots: the correlations for the two-dimensional cross-sections mirrored in the diagonal line where 1 is direct correlation and -1 is a direct anti-correlation. The values above the plot give the mean value and one sigma uncertainty for each parameter, based on the fitted Gaussian distributions. As expected, due to the low light contribution of the secondary component, the Gaussian distributions do not fit the histograms for the secondary component parameters. . . . . 69
- 2.15 An IRAF image of the apertures for KIC 8164262 on night 12. The x-axis is in pixels and the y-axis is in photon counts. The cross hairs and boxes above each aperture are adjusted to select the appropriate centre and width of each aperture. . . . . 74
- 2.16 Depicted is an IRAF image of the binned photons along one aperture and the polynomial fit (trace) to those photons for a comparison lamp. The points at the ends are excluded to improve the fit. . . . . 75

- 2.17 Depicted are the observed spectral data of KIC 8164262 (blue), and the fit to the data using BAYES-TODCOR (red). The thickness of the line denotes the one sigma uncertainty. It can be seen that there is a large discrepancy in the depths of the lines, which has been attributed to the use of TODCOR's cross correlation function as the fitting parameter. . . . . 77
- 2.18 Depicted are the posteriors generated using the BAYES-TODCOR program with the two observed spectra of KIC 8164262. I elected to fix the metallicity to  $[Fe/H] = 0.5$  through consideration of the spectra by eye. Lower left sub-plots: two dimensional cross-sections of the posterior probability distribution functions for the primary effective temperature,  $T_{\text{eff}1}$ ; the primary surface gravity,  $\log g_1$ ; the primary stellar rotational velocity  $v_{\text{rot}1}$ ; and  $\alpha$ , the light ratio. The crosses show the  $1\sigma$  (red) and  $2\sigma$  (green) uncertainties, and are centred on the minima. Diagonal sub plots from top left to bottom right: histograms displaying the probability distribution of each individual parameter. Upper right sub-plots: the correlations for the two-dimensional cross-sections mirrored in the diagonal line where 1 is direct correlation and -1 is a direct anti-correlation. The values above the plot give the mean value and one sigma uncertainty for each parameter, based on the fitted Gaussians. . . . . 78
- 2.19 Depicted are the distributions of radial velocities of the primary component for the first observed spectrum (left) and second observed spectrum (right) of KIC 8164262. The distributions contain the spread due to the uncertainty in the radial velocity shift and uncertainty in the template spectrum for 100 iterations of BAYES-TODCOR. The dashed red line denotes the mean radial velocity in each case. . . . . 79
- 3.1 An image of a tidally distorted star in a binary system. Due to the gravitational force of the companion, the morphology of the star has become distorted and prolate with the point facing the companion. Although exaggerated in this image, this is one of the two primary effects that give heartbeat star light curves their characteristic shape. Adapted from <http://astro.matf.bg.ac.rs/> (the University of Belgrade) . . . . . 82

- 3.2 A schematic diagram of a heartbeat star orbit depicting the stars at two phases: periastron and a random phase away from periastron. At periastron, due to the gravitational forces of their companions, *star 1* and *star 2* become tidally distorted into a tear drop shape. As heartbeat stars are highly eccentric ( $e = \sim 0.3\text{--}0.9$ ), the tidal distortions are significantly stronger during a small part of the orbit and for the remaining orbit the stars are essentially spherical. . . . . 83
- 3.3 A selection of heartbeat stars from the *Kepler* sample. Depicted are the time series (left panel) and phase folded data (right panel). The phase folded data clearly show the pulsations that are integer multiples of the orbital frequency: tidally induced pulsations. KIC 8112039 is KOI-54. . . . 84
- 3.4 A histogram of heartbeat stars as a function of temperature. The red bars mark the red giants with  $\log g \leq 3.3$  and the blue bars mark the main sequence stars. The  $\log g$  values were taken from the *Kepler* Input Catalog. 85
- 3.5 The times series (left panel) and phased light curve (right panel) of the Quarter 5 *Kepler* data of KIC 3965556. The non-coherent nature of the light curve is due to the presence of spots on one of the stellar components. 86
- 3.6 Upper panel: A phased light curve (black points) of KIC 8164262, a heartbeat star with a single high amplitude pulsation. The model is overlaid in red and comprises of the binary features and highest amplitude pulsation. The periastron variation, centred on zero, has a similar amplitude to the highest amplitude pulsation. Lower panel: the residuals of the binary model fit to the phased data (black points). Only a fraction of the orbit is shown for clarity. . . . . 87
- 3.7 Fourier transform of the *Kepler* light curve of KIC 8164262. The data are from Q 1–Q 16. The prominent frequency is the 229<sup>th</sup> harmonic of the orbital frequency. Upon prewhitening of this frequency, the features due to the binary orbit are visible. . . . . 87

- 3.8 A Fourier transform of KIC 3749404 (purple); with the binary model removed (green); and with the binary model and the oscillations below  $0.5 \text{ d}^{-1}$  removed to an amplitude of 1 ppm (blue). The blue Fourier transform depicts the tidally induced pulsations. The sub-plot depicts the window function of each oscillation peak. . . . . 89
- 3.9 Depicted are the identified modes (black stars) of KOI-54 and the model predictions for the average expected amplitude (lower solid line) for forced modes as a function of frequency, the upper bound for tidally excited modes (upper dashed line). The modes present outside the solid line are believed to be travelling waves. The red regions show the model predictions for prograde resonantly locked modes. It can be seen that the 90<sup>th</sup> and 91<sup>st</sup> harmonics are just touching the red region. Figure provided by J. Fuller; private communication. . . . . 92
- 3.10 Depicted are the identified modes (black stars) of KIC 8164262 and the model predictions for the average expected amplitude (lower solid line) for tidally excited modes as a function of frequency, the upper bound for tidally excited modes (upper dashed line). The two lowest frequency points (black stars) depicted are not orbital harmonics, but are the signature of rotation from spots. The red and blue regions show the model predictions for prograde and retrograde resonantly locked modes, respectively. It can be seen that the highest amplitude harmonic is overlaying the red region. Figure provided by J. Fuller; private communication. . . . . 93
- 3.11 The probability as a function of iteration for the model of KIC 8164262, where each colour represents a different chain. This plot is used as a first gauge to determine if the model has converged. From consideration of this plot alone, we can see that the model has not converged as the likelihood value is still rapidly decreasing, as shown in the insert. Furthermore, as we have used the  $\chi^2$  test, we would expect the probability to equal  $-0.5N$  at the time of convergence, which is  $\sim 1000$ . This plot consequently indicates that the number of iterations required to obtain convergence for this model is large, or alternatively, that the uncertainties are underestimated. . . . . 97

- 3.12 Depicted are the posteriors generated using the PHOEBE code combined with MCMC for KIC 8164262. Lower left sub-plots: two dimensional cross-sections of the posterior probability distribution functions for the inclination,  $incl$  ( $^\circ$ ); argument of periastron,  $\omega$  (rad); eccentricity,  $ecc$ ; mass ratio; semi-major axis,  $sma$ ; systemic velocity,  $vga$  ( $\text{km s}^{-1}$ ); primary and secondary radii ( $R_\odot$ ); and the amplitude ( $\mu\text{mag}$ ) and phase (rad) of the primary pulsation. The crosses show the  $1\sigma$  (red) and  $2\sigma$  (green) uncertainties, and are centred on the minima. Diagonal sub-plots from top left to bottom right: histograms displaying the probability distribution of each individual parameter. Upper right sub-plots: the correlations for the two-dimensional cross-sections mirrored in the diagonal line where 1 is direct correlation and -1 is a direct anti-correlation. The values above the plot give the mean value and one sigma uncertainty for each parameter, based on the fitted Gaussians. . . . . 99
- 3.13 Upper panel: a model for KIC 8164262 (black line) with one sigma uncertainty envelope (red) and phased *Kepler* data with per-point uncertainties (blue points). I selected an initial model before full convergence was obtained, as the one sigma envelope is larger during this stage and thus more easily visible. Lower panel: the residuals of the fit to the data. . . . . 100
- 3.14 Top panel: examples of one (blue) five (red) and three higher frequency (green) sine curves with frequencies that are multiples of the orbital frequency. Bottom panel: the curves from the top panel multiplied with an example heartbeat star model. The colours correspond to the curves in the top panel and the black curve represents the light curve model with no pulsations. . . . . 102

- 3.15 Top panel: heartbeat star light curve with (red) and without (black) Doppler boosting. Middle panel: the Doppler boosting signal (red) that has been applied to the light curve in the top panel. Lower panel: the primary star's radial velocity curve. Only the primary component's radial velocity curve is displayed as the light from the secondary is less than 2%, thus the contribution of the secondary component to the Doppler boosting is insignificant. . . . . 105
- 3.16 Top panel: heartbeat star light curve of two identical components with (red) and without (black) Doppler boosting. Middle panel: the Doppler boosting signal (red) that has been applied to the light curve in the top panel. Lower panel: The radial velocities of the primary and secondary components (blue and green dashed lines), and summed radial velocities of the primary and secondary component (black line) . The identical nature of the primary and secondary components causes the total motion of the two components to be zero and consequently I expect Doppler boosting to have zero contribution to the light curve, as found. . . . . 106
- 3.17 A graphical representation of the true anomaly  $v$ , eccentric anomaly  $E$  and the mean anomaly  $M$ . The star is at point  $P$  on the orbit, travelling in a counter-clockwise direction around the focal point  $S$ . Point  $Q$  is the vertical projection of the star's position on the auxiliary circle. The angle  $ROS$  is proportional to the time elapsed since the star's passage through periastron. . . . . 107
- 3.18 Left panel: the computed values of the mean anomaly at superior conjunction as a function of eccentricity and argument of periastron. Right panel: the computed values of the phase of superior conjunction as a function of eccentricity and argument of periastron. . . . . 109

- 3.19 Depicted are 9 binary star models with eccentricities between  $ecc = 0.82 - 0.88$  and phase of periastron between  $\omega = 1.0 - 2.0$ . The phase of each model has been calculated by considering the shift of the phase of superior conjunction. If the phase shift of the dip in the periastron variation moved precisely as the phase of superior conjunction, all models would be precisely aligned at zero phase. However, this is not the case and so we are not able to utilize this method for determining the phase shift of heartbeat stars. . . . . 110
- 3.20 The stellar potential as a function of radius for the primary (upper panels) and secondary (lower panels) components. From left to right, the panels depict how varying the eccentricity, mass ratio and spin-to-orbital period affect the relationship between the potential and the stellar radius. In these diagrams the eccentricity, mass ratio and spin-to-orbital period are fixed to 0.5, 0.5 and 1.0 respectively, when they are not a plotted variable. The semi-major axis was set to  $sma = 100 R_{\odot}$  for all plots. . . . . 115
- 3.21 A schematic diagram of a circular binary star with the two stars,  $M_1$  and  $M_2$ , the center of mass and the five Lagrangian points clearly marked. Adapted from Prša (2005). . . . . 116
- 3.22 The critical potentials of the primary (blue line) and secondary (red line) components at L1 as a function of eccentricity, mass ratio and spin-to-orbital period for  $sma = 100 R_{\odot}$ . When not acting as the independent variable, the parameters  $e$ ,  $q$  and  $F$  are set to 0.5, 0.5 and 1.0 respectively. 118
- 9.1 Upper panel: Best-fit PHOEBE model without pulsations (green line) and including 7 pulsations (black line), and the phased *Kepler* light curve (blue points) of KIC 3749404. The red envelope depicts the  $1\sigma$  spread of the final 128 models determined using MCMC for the model with 7 pulsations. Lower panel: the residuals (blue points) of the best-fit model. The uncertainties are depicted on the residual points, although they are not visible on the scale provided. . . . . 205

9.2	Upper panel: A magnified region of the best-fit light curve model (red line) to the phased <i>Kepler</i> data of KIC 8164262 (black), focused on the ellipsoidal variation. one sigma uncertainties are displayed on the data points. Lower panel: The corresponding residuals of the best-fit model. . . . .	206
9.3	Theoretical PHOEBE model without beaming (red line) and observed light curve (black points) of the phased (94.82 d), binned <i>Kepler</i> long cadence data of Quarters 0–12 for KIC 5006817. Lower panel: the residuals of the best-fit model. The dashed and solid lines are centred on the times of superior and inferior conjunction respectively. Our analysis showed that the long term Doppler boosting component was not present in the data. We expect that this is a consequence of the <i>Kepler</i> processing pipeline and our own detrending. . . . .	208
9.4	An echelle diagram of the p-mode frequencies modulo the orbital frequency using the short cadence <i>Kepler</i> data of Quarters 7 and 8 for KIC 4544587. The points are coloured in terms of their amplitude in units of relative flux $\times 10^{-3}$ (see the key at the right of the figure). The filled circles are the identified p-mode values and the open circles represent further frequencies with amplitudes in the region $0.02 - 0.04 \times 10^{-3}$ relative flux units, which are below our predefined confidence limit of $3\sigma$ . The uncertainty in the frequencies is smaller than the points, thus not depicted. A high pass filter was applied to the g-mode region prior to the identification of the p modes to remove any possible window pattern. . . . .	209
9.5	Upper panel: theoretical PHOEBE model (red line) and observed <i>Kepler</i> light curve (black points) for KIC 8569819. The width of the line depicts the spread of the final 1048 models determined using MCMC. Lower panel: the residuals (black points) of the best-fit model. The per-point uncertainty in the model is displayed as error bars. . . . .	210
9.6	The <i>Kepler</i> long-cadence time series (left) and phased light curve (right) of KIC 5034333 for Quarter 9. The phased data clearly depict the presence of tidally driven modes as the pulsations are commensurate with the orbital period. This object does not appear to have any eclipses, although the shape of the light curve is rich in information about the fundamental parameters due to the tidal distortions of the stellar components and as such will be an ideal object to model. . . . .	212

# Chapter 1

## Introduction

Stars form the building blocks of our visible Universe. Fig. 1.1 depicts a Hertzsprung-Russell diagram displaying a wide variety of stars, from those beginning their lives on the main sequence to white dwarfs at the end of their lives. Not only are the evolutionary states of these objects different, but also their temperatures ( $2\,500\text{ K} < T_{eff} \lesssim 30\,000\text{ K}$ ), sizes ( $0.1 R_{\odot} \lesssim R < 1500 R_{\odot}$ ), masses ( $0.08 M_{\odot} \leq M \lesssim 120 M_{\odot}$ ), luminosities (up to  $\sim 8 \times 10^6 L_{\odot}$ ) and metallicities ( $-4.9 \lesssim [Fe/H] \lesssim 0.44$ ) leading to a wide assortment of stars with vastly different structures. These structural differences lead to an exceedingly diverse population of stars, including those with spots and flares, stars with magnetic fields (up to  $\sim 10^6$  Gauss) and a wide variety of stellar pulsations. Further adding to the stellar diversity, not depicted on the Hertzsprung-Russell diagram, is the multiplicity of stars. The majority of stars are multiples and often interact with their companions, further adding to the complexity of stellar objects.

Alongside its primary mission, the study of planets, the original *Kepler* mission (2009 May–2013 May), with its impressive photometry and unparalleled detail, observed a wide range of stellar objects. Attributes such as a stable platform that enabled extended observations, and a precision as good as a few parts per million made the *Kepler* observations quintessential for the advancement of stellar astrophysics.

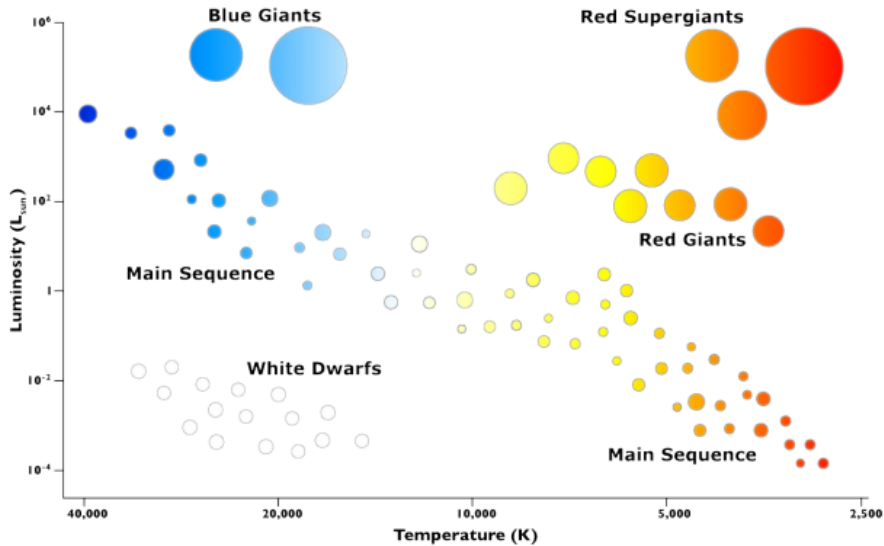


Figure 1.1: A theoretical Hertzsprung-Russell diagram depicting the main sequence, blue and red giants, super giants, and white dwarfs. Adopted from LCOGT.net (Las Cumbres Observatory Global Telescope Network).

Throughout its mission, *Kepler* has not only discovered 1033 planets, a significant portion of the 1890 confirmed planets (<http://exoplanetarchive.ipac.caltech.edu>); but also enabled the study of interesting binary stars, such as KIC 4150611, a quintuple system (Shibahashi & Kurtz 2012; Prša et al. in prep.); detected circumbinary planets (Welsh et al., 2012; Haghighipour, Orosz & Welsh, 2014); and determined, through eclipse timing variations, that between 15 and 20 per cent of binary stars are in fact triple systems (Conroy et al., 2014; Orosz, 2015).

*Kepler* is in a heliocentric, Earth-trailing orbit of 372.5 d. Four times an orbit, during the original mission, *Kepler* would perform a spacecraft roll (to keep the solar panels pointed at the Sun) and send the data to Earth. Each downloaded,  $\sim 90$  d segment of *Kepler* data is referred to as a Quarter of data. As the data were downloaded regularly, this provided enough bandwidth to keep a small percentage ( $\sim 0.3\%$ ) of the total number of targets as short cadence (SC) data (58.89 s), which comprises 9 co-added nominal 6.02-s exposures. The majority of data; however, were co-added 270 times to produce the standard, long cadence data of  $\sim 30$  min. The  $\sim 1$  min short cadence data allow for detailed photometric analysis of high frequency pulsations, such as white dwarf pulsations ( $\sim 1$  min) and the solar-like oscillations of main

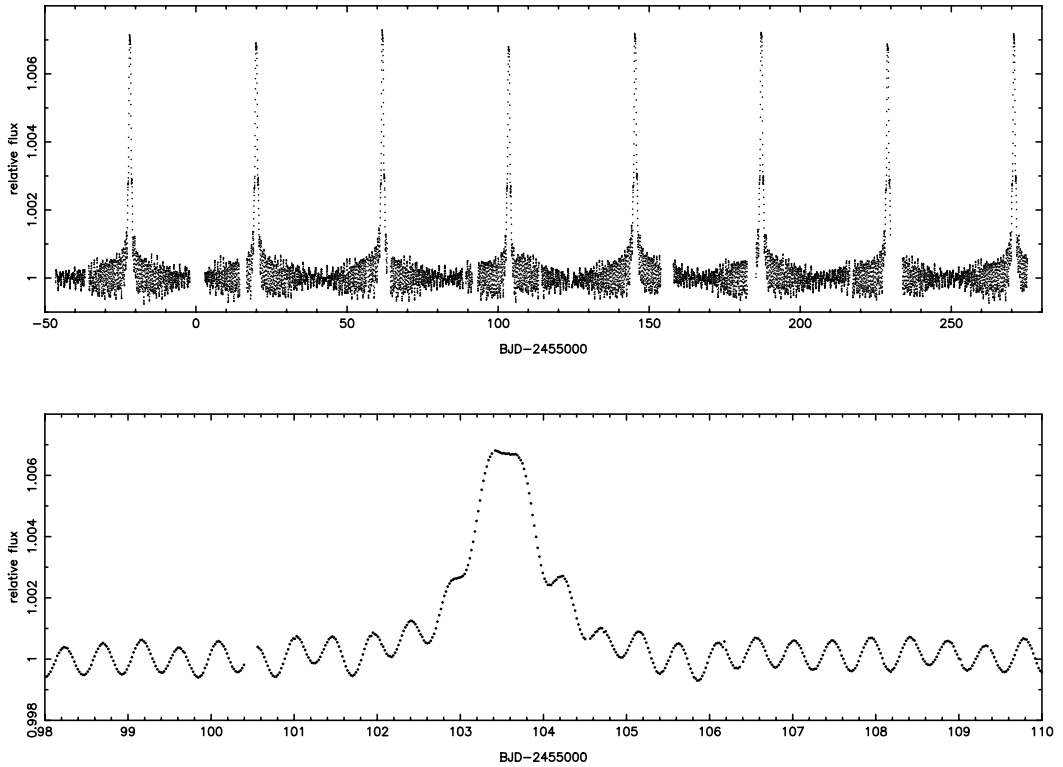


Figure 1.2: Depicted are the observed *Kepler* time series (top panel) and phased (bottom panel) light curves of KOI-54, the iconic heartbeat star. The large variation is caused by the tidal deformation and heating at periastron and the smaller variations are tidally induced pulsations that occur at precise multiples of the orbital period (see §1.1). Adopted from Welsh et al. (2011).

sequence stars ( $\sim 5$  min) providing a broad complement of stellar pulsators for the study of stellar structure and the determination of fundamental stellar parameters using asteroseismology. The recent advances in this field are detailed in §1.2.

Since the advent of the *Kepler* satellite, a plethora of new physical phenomena has been unveiled by the new level of detail that was obtained with this revolutionary instrument. One interesting phenomenon, which had only been theorised prior to *Kepler*, is the heartbeat phenomenon. A heartbeat star is an eccentric ( $e \gtrsim 0.3$ ) ellipsoidal variable that displays a prominent variation in the light curve at periastron due to tidal effects and heating.

When the light curve of the first, iconic heartbeat star, KOI-54 (Fig. 1.2), was discovered, the initial reaction was that the light curve had been inverted – magnitudes and fluxes had been confused. Once that hypothesis was dismissed, the next thought was that it was a star interacting with a black hole. This was also wrong. Finally,

detailed analysis determined that KOI-54 is a system of two A stars orbiting each other in a highly eccentric ( $e = 0.834$ ) orbit in an object we now classify as a heartbeat star.

One of the prominent physical attributes of KOI-54, and many heartbeat stars, is its tidally induced pulsations – pulsations induced by the varying gravitational interaction between the stellar components (see §1.1). As the focus of this thesis is to extend the work on heartbeat stars and tidally induced pulsations, I begin by introducing heartbeat stars, which are discussed in more detail in Chapter 3. Next I discuss asteroseismology with particular reference to the types of pulsators commonly found in heartbeat stars (§1.2). I end by discussing binary stars, the facilitators of tides, with a focus on binary star modelling (§1.3), which forms the basis of many of the projects included in this work.

## 1.1 *Heartbeat Stars*

*Heartbeat* stars, the basis of this work, are eccentric ( $e \gtrsim 0.3$ ) ellipsoidal variables, identifiable by a characteristic periastron variation in their light curves (*e.g.* see Fig. 1.3). The name heartbeat star was given to these objects as their light curves resemble the output of a electrocardiogram. As with ellipsoidal variations, the periastron variation is a consequence of heating and gravitational interactions between the stellar components, which cause deformation and temperature variations across the star. However, due to the eccentric nature of the orbits of these objects, the gravitational interactions occur over a small fraction of the total period, resulting in a variation in the light curve that is preceded and followed by quiescence, during which time the stars are barely interacting and the light curve is flat (with the exception of spots and stellar pulsations).

At present (2016 March), the number of known heartbeat star systems is 183.

Of these, eight were observed using OGLE <sup>1</sup> (Nicholls & Wood, 2012); one by CoRoT<sup>2</sup> (Hareter et al., 2014); one by MOST<sup>3</sup>, which was followed up using the CHARA<sup>4</sup> array (Richardson et al., 2016); and 173 by *Kepler* (Thompson et al., 2012; Beck et al., 2014; Schmid et al., 2015; Smullen & Kobulnicky, 2015; Kirk et al., 2016). The list of *Kepler* heartbeat stars, which I have vetted personally, is held at <http://keplerebs.villanova.edu>. The list is comprised of heartbeat stars identified by the *Kepler* Eclipsing Binary Working Group, Planet Hunters, the *Heartbeat Star* team (of which I am a member), the *Kepler* science office and several by individuals. The *Kepler* mission has clearly observed a significant fraction of the currently known heartbeat stars, which is why the data from the *Kepler* mission forms the majority of the data analysed in this work.

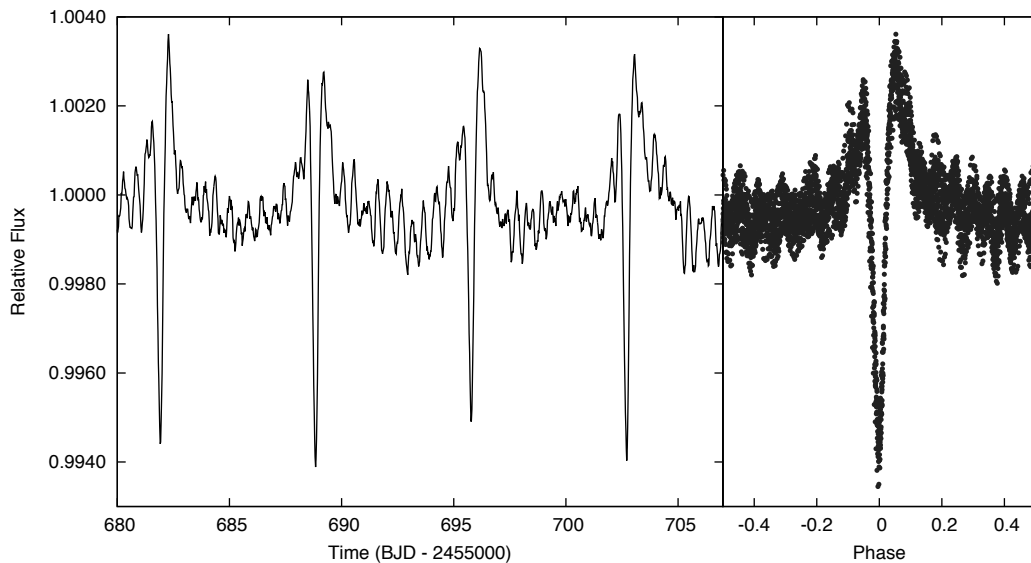


Figure 1.3: The time series (left panel) and phased light curve (right panel) of the Quarter 9 *Kepler* data of KIC 5034333. The large variation at phase 0.0 is the periastron variation caused by tidal deformation and heating, and the smaller variations are a combination of naturally occurring and tidally induced pulsations (where only the tidally induced pulsations are visible in the phased data). Note that this system is not eclipsing; the strong dip in the light curve is geometrical in origin. See Fig. 1.4 below.

A subset of the heartbeat stars in our *Kepler* sample,  $\sim 20\%$  of the total sample,

<sup>1</sup><http://ogle.astrouw.edu.pl/>

<sup>2</sup><http://sci.esa.int/corot>

<sup>3</sup>[http://astro-canada.ca/\\_en/a2118.php](http://astro-canada.ca/_en/a2118.php)

<sup>4</sup><http://www.chara.gsu.edu/array.php>

show tidally induced pulsations. Tidally induced pulsations were first discussed by Cowling (1941) as pulsations created by the varying gravitational force of the stellar companion as it moves around the binary star orbit. Tidally induced pulsations occur when the eigenfrequency of a star is close to a multiple of the orbital frequency. Consequently, the signature of a tidally induced pulsation is a pulsation at a precise multiple of the orbital frequency.

In 1995, Kumar, Ao & Quataert (1995) theorised that two terms would describe compact objects in highly-eccentric ellipsoidal-variable configurations: the static term, relating to the periastron or ellipsoidal variation; and the oscillatory term, which describes tidally induced pulsations. If the ratio of the periastron passage time to the mode period is high (Kumar, Ao & Quataert (1995) suggest greater than 5), then the oscillatory term can be ignored and the resulting light curve depicts the static term only. Light curves generated by the static term only can be seen in Fig. 1.4. While Kumar's work was focused on the theory of binary neutron stars, I have found it applicable to main sequence and red giant stars in heartbeat star systems.

## **Tidal Interactions**

Our current sample of 173 heartbeat stars identified in the *Kepler* data primarily contains stars of spectral type A–G, suggesting that there is a dearth of these objects with temperatures less than 5200 K. Due to the observational bias of *Kepler* towards G-type stars (Borucki et al., 2010), there is also a more subtle deficiency of G stars in our sample, with temperatures less than 6000 K. As the transition between convective and radiative outer envelopes occurs at approximately this temperature (Aerts, Christensen-Dalsgaard & Kurtz, 2010) and the time required for circularisation is shorter for stars with convective outer envelopes (Torres, Andersen & Giménez, 2010), it is possible that the lack of low mass stars in our sample is a direct consequence of the relationship between stellar structure and tidal evolution.

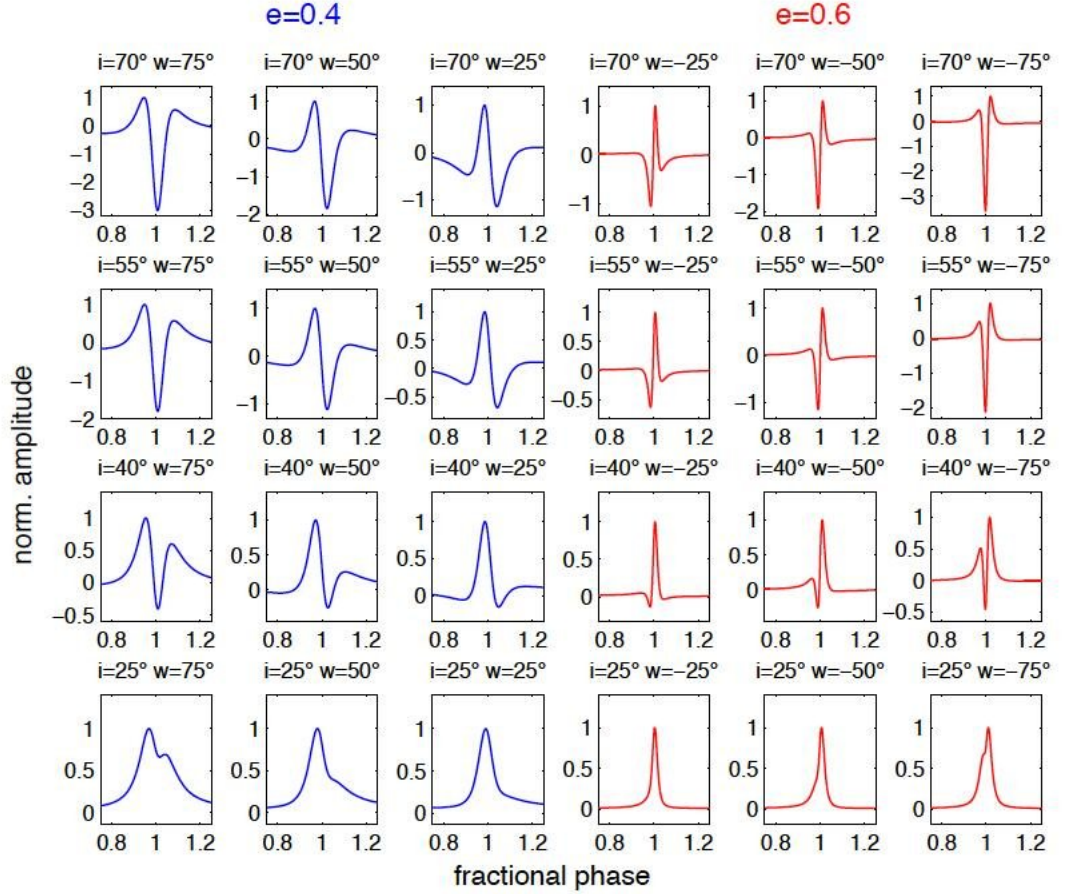


Figure 1.4: A grid of light curves generated using the static term of the analytical tide theory of Kumar, Ao & Quataert (1995). The light curves show the variation in the shape of the periastron brightening as a function of argument of periastron, inclination and eccentricity where red denotes  $e=0.6$  and blue denotes  $e=0.4$ . It can be clearly seen that for higher inclination angles the dip in the light curve is small compared to lower inclinations, whilst the duration of the periastron brightening (with respect to the orbital period) decreases as the eccentricity increases. Finally, the argument of periastron has a large impact on the asymmetry and morphology of the light curve. Adopted from Thompson et al. (2012).

In late-type stars, turbulent viscosity in the convective envelope provides the required torque to enable synchronization. Zahn (1975) predicted that tidally induced pulsations would provide the required torque, through radiative damping, to enable the synchronisation of early-type stars in close binaries. This was recently confirmed by Khaliullin & Khaliullina (2010). As early stars have radiative envelopes, Zahn (1975) suggested that a dissipative process, such as the radiative damping of tidally induced pulsations, may alter the symmetry of the mass configuration, relative to the potential, enough to synchronize close binary stars.

Based on the work of Darwin (1879), who considered the effects of lunar tides on the Earth, Alexander (1973) conducted further research into the effect of tides on binary orbital evolution, including circularisation times, although unlike Darwin, Alexander considered the effects of tides on both objects. Hut (1980, 1981) extended this work to include pseudo-synchronous rotational angular velocity,  $\Omega_{ps}$ , the synchronization of the rotational period of the stellar components with the instantaneous rotational period at periastron. He also considered the equilibrium rotation for eccentric orbits:

$$\frac{\Omega_{ps}}{n} = \sqrt{\frac{1+e}{(1-e)^3}} \quad (1.1)$$

expressed in terms of the mean motion,  $n$ . Pseudo-synchronous rotation tends to  $\Omega_{ps} = 0.825n_p$  (where  $n_p$  is the angular velocity at periastron) as  $e \rightarrow 1$ . Fig. 1.5 depicts the observed rotation period against the calculated pseudo-synchronous rotation period for a selection of heartbeat stars where rotation is determined from spot rotation. As anticipated, the majority of points lie on or above the one-to-one line, which suggests that angular momentum is being transferred from the rotation of the stars to the binary star orbit, as predicted by theory. Those that lie under the one-to-one line are rotating slower than their pseudo-synchronous rotation which may be suggestive of a third component in the system.

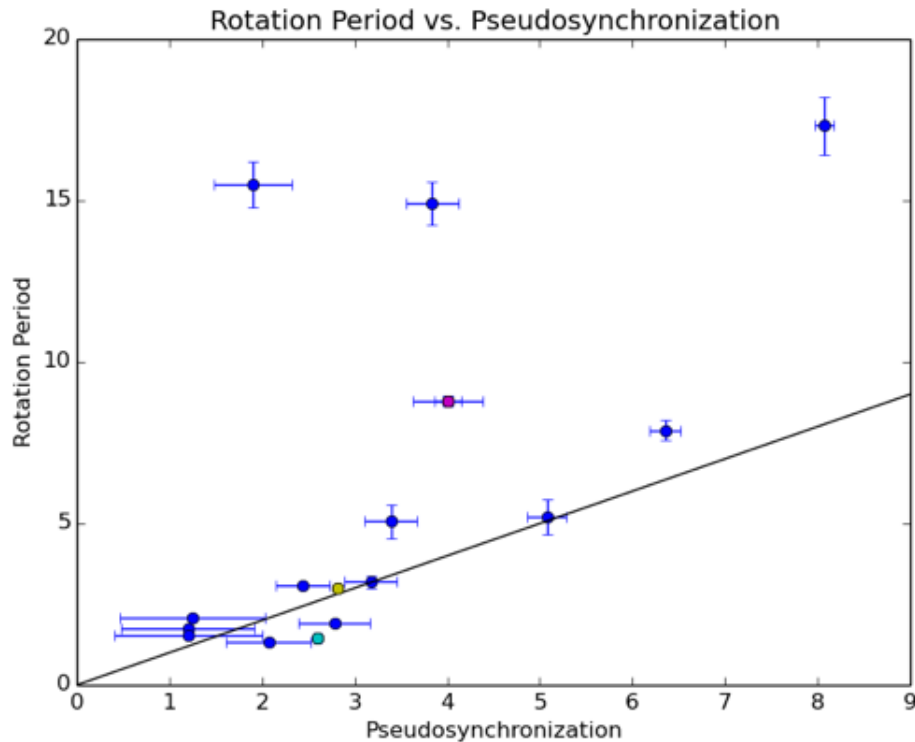


Figure 1.5: Depicted are the stellar rotational periods from heartbeat stars with spots, against the calculated values of the pseudo-synchronous rotational periods. The observed rotational periods were extracted from Fourier transforms where harmonics indicative of spots were present. KOI-54 is represented by the cyan point, KIC 8164262 (see Chapter 4) by the yellow point and KIC 3547874 by the magenta point. Adopted from (Zimmerman et al., 2016)

### Asteroseismology of Heartbeat Stars

A subset of heartbeat stars,  $\sim 40\%$ , lie within the  $\delta$  Sct and  $\gamma$  Dor temperature ranges, and thus should also pulsate intrinsically. A further 15% of heartbeat stars contain a red giant component and consequently should pulsate with easily detectable solar-like oscillations (with frequencies visible in the more common 30-min-cadence *Kepler* data). In §1.2 I discuss a selection of asteroseismic effects. These fall under two categories: those that can provide additional information to that determined through binary modelling, for example the internal rotation rate can be determined through the examination of p-mode multiplets (Kurtz et al., 2014); and those that provide fundamental parameters that can aid the modelling process, *i.e.* the mass and radius of a solar-like oscillator can be determined through asteroseismology (Beck et al.,

2014). Interestingly, in some cases, the tidal interactions of the binary have been found to inhibit solar-like oscillations completely, *i.e.* (Derekas et al., 2011). However, in all cases, asteroseismology provides insights into physics that otherwise would remain a mystery.

## 1.2 Asteroseismology

Asteroseismology is the study of stellar pulsations analogous to seismology, the study of earthquakes. The majority of stars pulsate in pressure modes (p modes), gravity modes (g modes) or a combination of both, depending on their structure. Through the study of these modes, we are able to determine information about the interiors of stars across the Hertzsprung-Russell diagram. For the specific case of heartbeat stars, asteroseismology can often provide additional information to light curve modelling and in some cases provide key information that enables a unique heartbeat star model to be determined (see Chapter 6).

The study of asteroseismology is the study of waves - their amplitudes, phases and frequencies, and their relations to one-another. As a wave propagates through the stellar interior, its frequency and amplitude depend on the stellar structure, differential rotation rate, age, density distribution and the transition regions within the star. By applying a Fourier transform to the light curve of a pulsating star, we can measure its frequencies, phases and amplitudes and commonly extract the aforementioned information, enabling the analysis of the stellar interior. Fig. 1.6 depicts the propagation of pressure modes and gravity modes within the Sun, and demonstrates how different modes probe different regions of the stellar interior for this specific case.

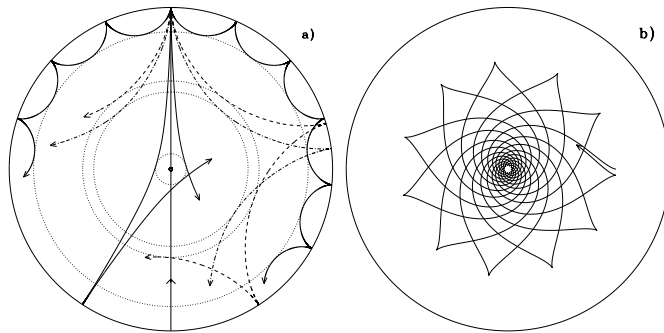


Figure 1.6: *Left panel (a)*: A ray diagram to demonstrate the propagation of p mode sound waves through the solar interior. The line passing through the centre is indicative of a radial mode and lines of decreasing depth demonstrate the behaviour of modes with increasing  $l$  values where  $l$  is the degree of the mode. *Right panel (b)*: A ray diagram to demonstrate the propagation of g mode sound waves through the solar interior. Due to the convective outer layer of the Sun, the g modes do not emerge to the surface; this is not true of  $\delta$ Sct stars where the outer envelope is radiative. Adopted from Cunha et al. (2007).

### 1.2.1 Pressure Modes

Pressure modes, also known as acoustic or sound waves, are longitudinal waves with the primary restoring force of pressure. The presence of pressure modes in heartbeat stars enable detailed pulsational modelling to be performed, which can aid in deciphering from which star the pulsations are propagating (*e.g.* see Chapter 7). Pressure modes act primarily on particles in the vertical sense with respect to the direction of the wave motion and are able to penetrate both convective and radiative stellar interiors. As a sound wave (with velocity  $c_s$ ) propagates from the surface of the star inwards, it passes across a positive temperature gradient and, consequently, into a higher temperature environment. The temperature gradient within the star causes the refraction of the wave and eventually the wave returns to the stellar surface. As each pressure mode of a given degree penetrates to a different depth, if a star is pulsating in multiple modes, we can probe different radial layers of the star (also known as acoustic cavities). Through assumptions of the chemical composition of the stellar interior, we can then map the density gradient of a star:

$$\rho = \frac{\Gamma_1 p}{c_s^2}, \quad (1.2)$$

where  $\Gamma_1$  is the adiabatic exponent,  $p$  is pressure and  $\rho$  is density. Assuming the star is an ideal gas, the temperature variations of the star can also be mapped through the use of asteroseismology:

$$T = \frac{c_s^2 \mu m_u}{\Gamma_1 k_B}, \quad (1.3)$$

here  $k_B$  is Boltzmann's constant,  $T$  is the temperature,  $\mu$  is the mean molecular weight and  $m_u$  is the atomic mass unit.

Within a star, the wavelength of a p mode must be greater than  $4\pi H_\rho$ , where  $H_\rho$  is the density scale height (the height at which the density decreases by a factor of  $e$ ); if not, the general density profile of the star will dominate and the p-mode perturbations will not be visible. This also determines the boundary of the acoustic cavity where p modes are refracted back towards the surface at various turning points dependent on the direction of propagation and the density distribution within the star. Consequently, the higher degree modes are concentrated closer to the surface. As these modes have a higher number of surface reflections (which can be seen in the left panel of Fig. 1.6) they have a larger horizontal component:

$$k_h^2 = l(l+1)/r^2, \quad (1.4)$$

where  $r$  is the radial position in the star and  $k_h$  is the horizontal component of the wave vector, also known as the wave number.

## 1.2.2 Gravity Modes

All confirmed tidally induced pulsations are g modes, but unlike p modes, g modes only propagate in radiative regions as they are dynamically unstable towards convection. Consequently, the Brunt-Väisälä frequency ( $N$ ), which is the frequency at

which a fluid element will oscillate in a statically stable environment, creates an upper limit for the frequency of gravity waves. Moreover, the Brunt-Väisälä frequency also creates a boundary beyond which no g modes can propagate and where g modes are reflected. Any frequencies greater than the Brunt-Väisälä frequency are predominantly restored by pressure and those less than the Brunt-Väisälä frequency are restored by buoyancy. Fig. 1.7 shows the propagation region of g modes in KOI-54, the iconic heartbeat star. As a result of this, g modes are ideal for probing the conditions near the core in higher-mass main-sequence stars, where the core is convective (thus the modes reflected) and the envelope is predominantly radiative (where the modes are able to travel).

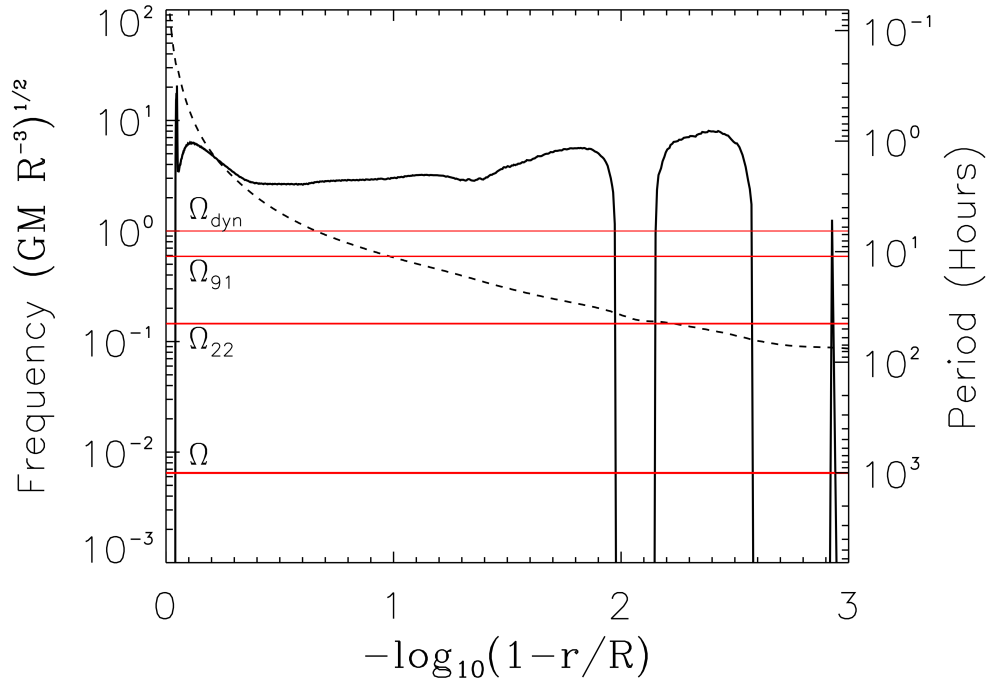


Figure 1.7: Propagation diagram for the  $M = 2.35 M_{\odot}$ ,  $R = 2.34 R_{\odot}$  stellar model, showing the value of  $N$ , the Brunt-Väisälä frequency (solid black line), and the Lamb frequency,  $S_l$  (dashed black line), in units of  $(GM/R^3)^{1/2}$ . These theoretical values were obtained by modelling the dominant frequencies present in the KOI-54 (the horizontal red lines). These are (from top) the dynamical frequency of the star,  $(GM/R^3)^{1/2}$ ; the highest frequency mode observed ( $\sigma_{\alpha} = 91\Omega$ ); the lowest frequency mode observed ( $\sigma_{\alpha} = 22.42\Omega$ ); and the orbital angular frequency,  $\Omega$ . The  $y$ -axis on the right-hand side displays the corresponding periods, in units of hours. From Fuller & Lai (2012).

Buoyancy is the restoring force of gravity modes, which have primarily horizontal

motions. Consequently, higher frequency g modes have larger transverse components:

$$\omega^2 = N^2 \cos^2 \theta \quad (1.5)$$

where  $\omega$  is the frequency of the mode and  $\theta$  is the angle of propagation with respect to the horizontal plane. Moreover, unlike p modes, there are no radial g modes as the frequency of the mode is related to the propagation angle of the wave. This can be seen in Eqn 1.5, which shows that if the angle of propagation is  $90^\circ$  (a purely radial mode) the frequency of the mode becomes zero.

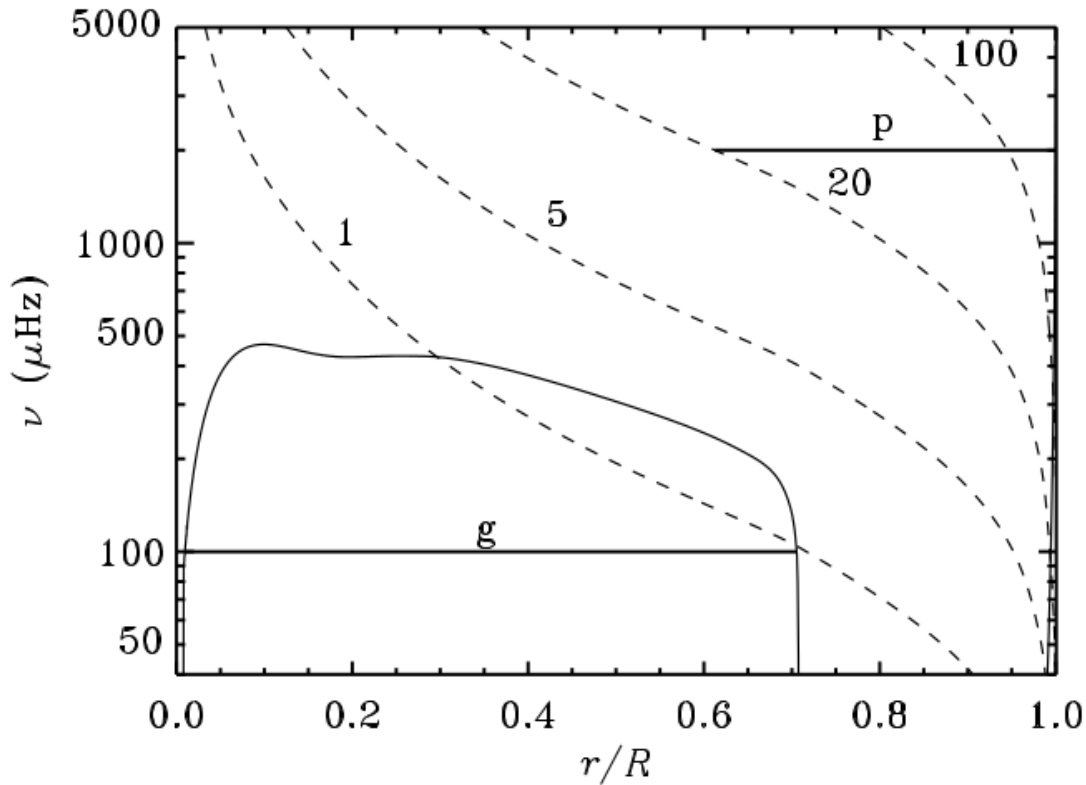


Figure 1.8: Buoyancy frequency,  $N$  (straight line), and Lamb frequency,  $S_l$  (dashed line with labels for incremental values of  $l$ ), shown as a function of fractional radius for a model of the Sun. The solid horizontal lines indicate regions where a g mode of  $\nu = 100 \mu\text{Hz}$  and a p mode of degree 20 and  $\nu = 2000 \mu\text{Hz}$  would be trapped.

A property of g modes is that the degree of the mode is inversely related to the frequency, which can be derived from the following equation (Aerts, Christensen-

Dalgaard & Kurtz, 2010):

$$K_s(r) = \frac{\omega^2}{c^2} \left( \frac{N^2}{\omega^2} - 1 \right) \left( \frac{S_l^2}{\omega^2} - 1 \right); \quad (1.6)$$

here,  $r$  is the radial position in the star, the subscript,  $l$ , denotes the degree of the mode and  $K_s$  is a constant related to the change of the radial component of displacement  $\xi_r$  as a function of radius:

$$\frac{d^2 \xi_r}{dr^2} = -K_s(r) \xi_r, \quad (1.7)$$

$S_l$  is the Lamb frequency (Lamb, 1909) or the characteristic acoustic frequency, which is the inverse of the time needed to travel one horizontal wavelength through the stellar medium:

$$S_l^2 = \frac{l(l+1)c_s^2}{r^2}, \quad (1.8)$$

which tends to infinity at the centre of the star and towards zero at the surface (see Fig. 1.8 for an example of how the Lamb frequency behaves as a function of stellar depth). Above the Lamb frequency, modes are restored by pressure and below it they are restored by buoyancy. For high order g modes we can assume that  $\omega \ll S_l$ , giving:

$$K_s(r) \simeq \frac{1}{\omega^2} (N^2 - \omega^2) \frac{l(l+1)}{r^2}. \quad (1.9)$$

From the above equation it can be seen that, as  $\omega$  decreases (for given values of  $K_s$  and Brunt-Väisälä frequency,  $N$ ) the degree of the mode  $l$  increases.

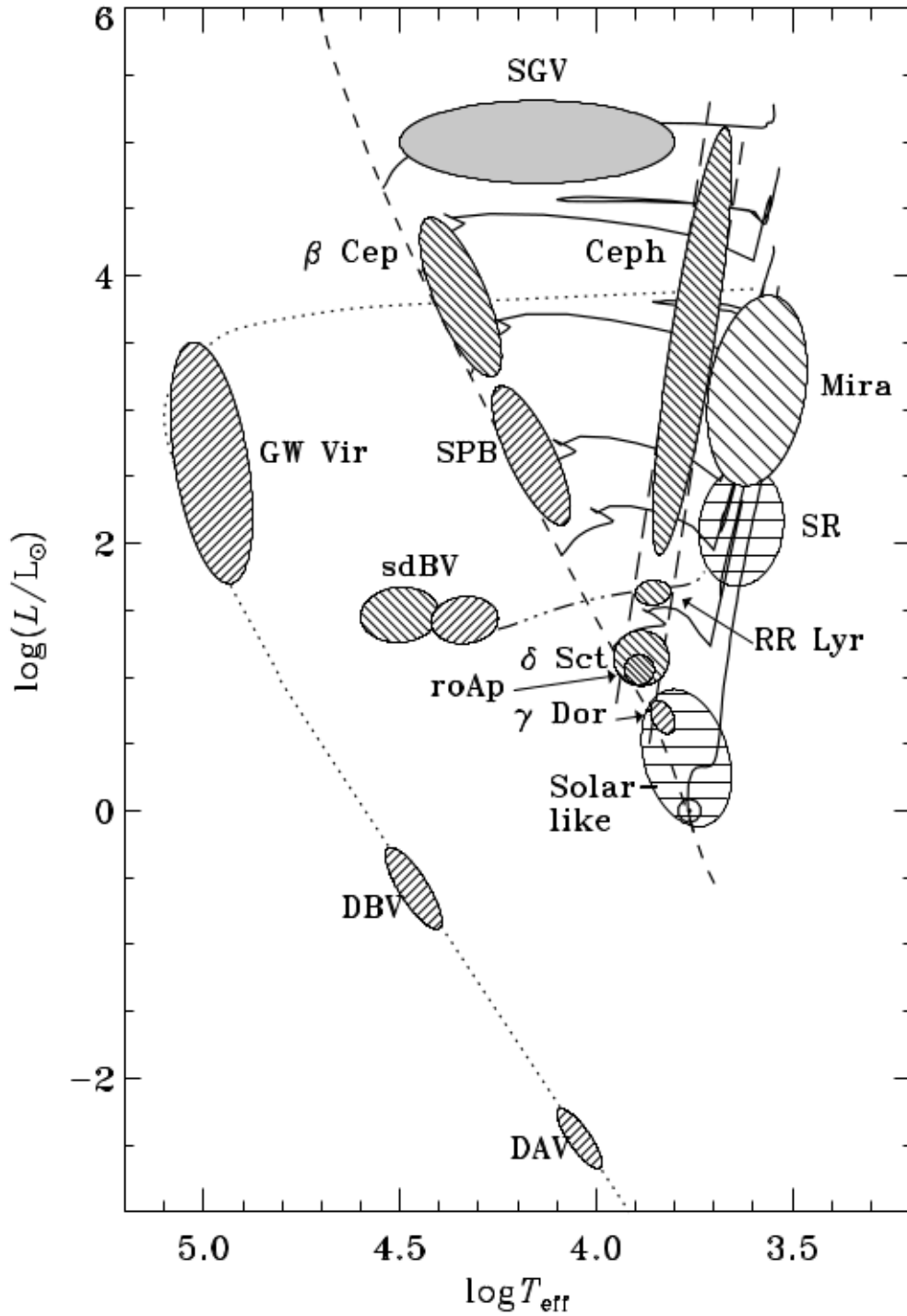


Figure 1.9: A pulsational H-R diagram. Delta Sct stars can be found on the intersection between the main sequence (dashed line from the top left region tending towards the bottom right) and the instability strip (encompassed by two, almost vertical long-dashed lines), and the  $\gamma$  Dor stars slightly below them in a region outside the instability strip. From Aerts, Christensen-Dalsgaard & Kurtz (2010).

### 1.2.3 Delta Scuti Stars

Approximately 40% of the known *Kepler* heartbeat stars have temperatures within the  $\delta$  Sct range. Delta Scuti stars are a class of variable stars that lie on the classical instability strip of the Hertzsprung-Russell diagram (see Fig. 1.9). Their temperatures range from  $6300 \text{ K} < T_{\text{eff}} < 8900 \text{ K}$  (Buzasi et al., 2005), with a luminosity range of  $0.6 < L/L_{\odot} < 2.0$ . Importantly, they have masses from  $1.5 < M/M_{\odot} < 2.5$ , meaning that  $\delta$  Sct stars include the mass range where, as you travel up the main sequence to hotter stars, the central radiative core becomes convective and the outer convective envelope becomes radiative (Aerts, Christensen-Dalsgaard & Kurtz, 2010).

Delta Scuti stars pulsate in p modes, with their dominant frequencies between  $5 \text{ d}^{-1}$  and  $50 \text{ d}^{-1}$  (Grigahcène et al., 2010b). Hotter  $\delta$  Sct stars, that are towards the blue edge of the instability strip, tend to pulsate in higher frequency modes, whereas the cooler  $\delta$  Sct stars tend to pulsate in lower overtone, lower frequency modes. Their primary pulsation mechanism is the  $\kappa$ -mechanism, although they also pulsate through the  $\Gamma$ -mechanism and one  $\delta$  Sct star, which was originally thought to pulsate with stochastically driven modes (Antoci et al., 2011), is now theorised to pulsate with coherent modes attributed to perturbations of the turbulent pressure in the hydrogen ionization zone (Antoci et al., 2014).

The  $\kappa$ -mechanism describes the trapping of heat in the partial ionisation zones of the star and works in a similar way to a heat engine. The opacity of the ionisation layers trap the heat which increases the temperature of the ionisation zone. This causes the star to swell until the ionisation layer becomes fully ionised and the heat is released. As the star cools, it also contracts and the ions return to their original state of ionisation. The process then repeats causing stable pulsations. The  $\Gamma$ -mechanism enhances the effect of the  $\kappa$ -mechanism because the large temperature gradient between the partially ionised zone and the surrounding volume causes heat to flow into the cooler ionisation zone, causing further ionisation.

Due to the structure of  $\delta$  Sct stars, they pulsate in low-order (radial overtone) modes, which means they do not pulsate in the asymptotic regime. However, frequency spacings akin to the large frequency separation (see § 1.2.6) were first identified by Handler, Kanaan & Montgomery (1997); Breger et al. (1999). In 2008, Breger, Lenz & Pamyatnykh (2008) presented all the frequency differences of FG Vir in a histogram, and were able to identify preferred differences, which they attributed to the spacing between radial modes. Following this work, García Hernández et al. (2009) identified the large separation in HD 174936 to be  $52 \mu\text{Hz}$ , consistent with their models. In 2013, García Hernández et al. (2013) identified a second  $\delta$  Sct pulsator, HD 174966, with equally split modes. Furthermore, this time they were able to rule out the possibility that the spacing was due to rotation, as with a  $v \sin i$  of  $126.1 \text{ km s}^{-1}$ , the maximum rotational splittings would be  $\sim 27 \mu\text{Hz}$ . Using the method of Reese, Lignières & Rieutord (2008), who showed that for rapid rotators, the large separation is proportional to the square-root of the mean density of the star, they were also able to transform their large separation value,  $\Delta\nu = 64 \mu\text{Hz}$ , into a stellar density,  $\bar{\rho} = 0.54 \pm 0.3 \text{ kg cm}^{-3}$ , which again agreed with their models.

To further test the possibility of extracting fundamental parameters from  $\delta$  Sct stars using asteroseismology, García Hernández et al. (2015) selected 7 binary  $\delta$  Sct stars from the literature to search for frequency separations. Using echelle diagrams, the large frequency separation was identified in each case. Fig. 1.10 depicts  $\log \bar{\rho}/\bar{\rho}_{\odot}$  vs.  $\Delta\nu/\Delta\nu_{\odot}$  where the densities are derived from the binary-determined radii and masses (relative to the Sun for comparison with solar like oscillations). The very strong linear trend shows that the large separation is related to density and furthermore, is essentially independent of metallicity and rotation. This is a very compelling argument for the relation between the frequency spacings and density of  $\delta$  Sct stars. However, one object, KIC 4544587 (discussed in detail in Chapter 7), was shown to have frequency spacings relating to the orbital frequency ( $0.456810 \pm 1 \times 10^{-6} \text{ d}^{-1}$ ), which (to the provided precision) is 14 times the suggested frequency for the large separation ( $74 \pm 1 \mu\text{Hz}$  or  $6.39 \text{ d}^{-1}$ ) making the result for this object questionable.

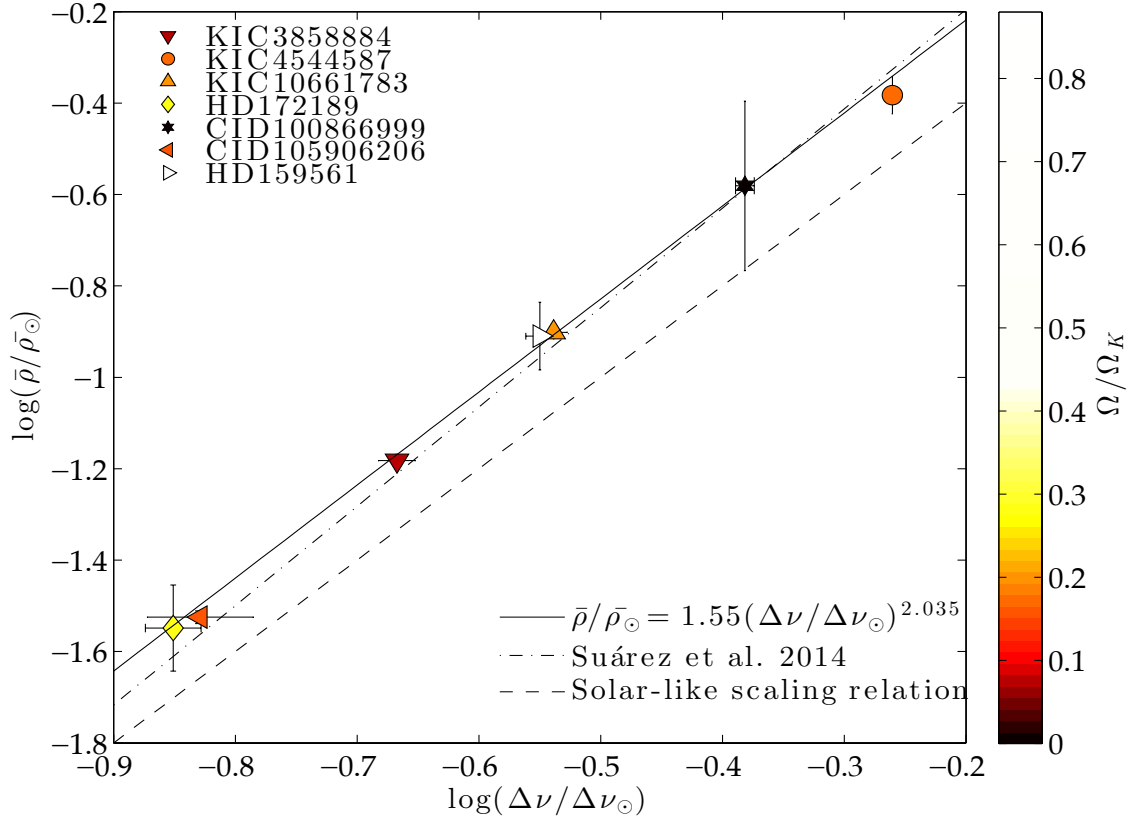


Figure 1.10: Large separation-mean density relation for 7 binary systems. A linear fit to the points is depicted, solid line, as well as the solar-like scaling relation (Tassoul, 1980), dashed line, and the theoretical scaling relation for non-rotating models of  $\delta$  Sct stars (Suárez et al., 2014), dashed-dotted line. The different coloured symbols denote the stellar rotation rates where  $\Omega_K$  is the Keplerian break-up rotation rate. Figure adopted from García Hernández et al. (2015).

It is likely that the similarity between the large separation and the orbital frequency spacings is due to chance. In the remaining objects, the orbital frequency does not have any connection with the large separation.

A further piece of evidence suggesting that the frequencies are separated by the large separation is that they agree with the theoretical models of Suárez et al. (2014) for non-rotating models, as shown in Fig. 1.10. The derived formula for the relation between stellar density and large separation in  $\delta$  Sct stars is:

$$\bar{\rho}/\bar{\rho}_{\odot} = 1.55_{-0.68}^{+1.07}(\Delta\nu/\Delta\nu_{\odot})^{2.035 \pm 0.095}. \quad (1.10)$$

### 1.2.4 Gamma Doradus Stars

Gamma Dor stars have a temperature range of  $6700 \text{ K} < T/T_{\odot} < 7600 \text{ K}$ , which overlaps the  $\delta$  Sct temperature range, although they occupy their own area of the H-R diagram (which is partially outside the classical instability strip, as they are less luminous, as shown in Fig. 1.9). Approximately 12% of the known heartbeat stars are within the  $\gamma$  Dor temperature range. Of these, approximately half pulsate with  $\gamma$  Dor pulsations. Gamma Dor pulsations are low-degree high-order g modes with frequencies on the order of  $1 \text{ d}^{-1}$  (Grigahcène et al., 2010a). These modes penetrate deep into the core of the star and contain information about the central cavity pertaining to the chemical composition and the energy transport mechanism (Guzik et al., 2000).

The driving mechanism for  $\gamma$  Dor stars is called convective blocking (Guzik et al., 2000). Convective blocking occurs at the base of the convection zone where there is an abrupt change from radiative to convective energy transport. At this boundary the radiative luminosity waves are trapped by the steep opacity gradient. As the convective region is unable to adapt to transport the increased number of photons, the outgoing energy is periodically blocked, which drives pulsation. A requirement of this theory is that the convective time scales are longer than, or on the same order as the pulsation periods, which enables the assumption that fluctuations in convection can be approximated to zero during the pulsation cycle. For this mechanism to be effective the star must have a significant convection zone (convection zone base must be  $\sim 0.975 R/R_{\star}$ ); however, for convection zones deeper than 5% the pulsations significantly weaken and the frequency range becomes increasingly narrow (Guzik et al., 2000).

### 1.2.5 Hybrid $\gamma$ Dor– $\delta$ Sct

Hybrid  $\gamma$  Dor– $\delta$  Sct stars, *e.g.* KIC 8569819 (see Chapter 8), were originally identified through the comparison of observations with theoretical models (Bouabid et al.,

2009). However, the *Kepler* data extended our understanding to show that the majority of  $\gamma$  Dor and  $\delta$  Sct stars are hybrids (Grigahcène et al., 2010a). These objects pulsate in both  $\gamma$  Dor modes ( $\nu \approx 1 \text{ d}^{-1}$ ) and  $\delta$  Sct modes ( $\nu$  between  $5 - 50 \text{ d}^{-1}$ ), and make up several hundred of all the observed *Kepler* stars. Recently, Kurtz et al. (2014) identified a  $\gamma$  Dor- $\delta$  Sct hybrid (KIC 11145123) with an extremely rich pulsation spectrum with equally split multiplets in both the p-mode and g-mode regions. Detailed analysis of this object showed that, to first approximation, the object rotates as a solid body. This was determined by considering the splittings of the multiplets: the p-mode multiplets have splittings of  $\sim 0.004 \text{ d}^{-1}$  and the g-mode multiplets have splittings of  $\sim 0.008 \text{ d}^{-1}$ . This factor of two difference between the p and g modes is theoretically predicted for a solid body rotator as:

$$\delta\omega_{n,l,m} = m(1 - C_{nl})\bar{\Omega}_{n,l}. \quad (1.11)$$

where  $\delta\omega_{n,l,m}$  is the frequency perturbation,  $\bar{\Omega}_{n,l}$  is the average stellar rotation rate,  $m$  is the azimuthal order and  $C_{nl}$  is the Ledoux constant, which is  $C_{nl} \approx 0$  for p modes and asymptotically approaches  $C_{nl} = 0.5$  for g modes. Thus from Eqn 1.11 we can conclude that, for KIC 11145123, the surface, which is probed by the p modes, is rotating at the same rate as the core, which is probed by the g modes. Further analysis of this object showed that the slight deviation from a ratio of two provides strong evidence that the surface is rotating slightly faster than the core. This unexpected result could be suggestive that the star has previously undergone mass transfer in a binary system, which caused the envelope to spin-up relative to the core. An alternative hypothesis is that there is an additional unknown angular transport mechanism at work.

Since this interesting discovery, Bedding et al. (2014) have identified 12 stars with rotationally split  $\gamma$  Dor modes. Fig. 1.11 depicts a period-echelle diagram of one of their discoveries, KIC 9244992 (Saio et al., 2015), which clearly shows three ridges for the  $m = -1, 0, +1$  modes. The use of period instead of frequency in the echelle

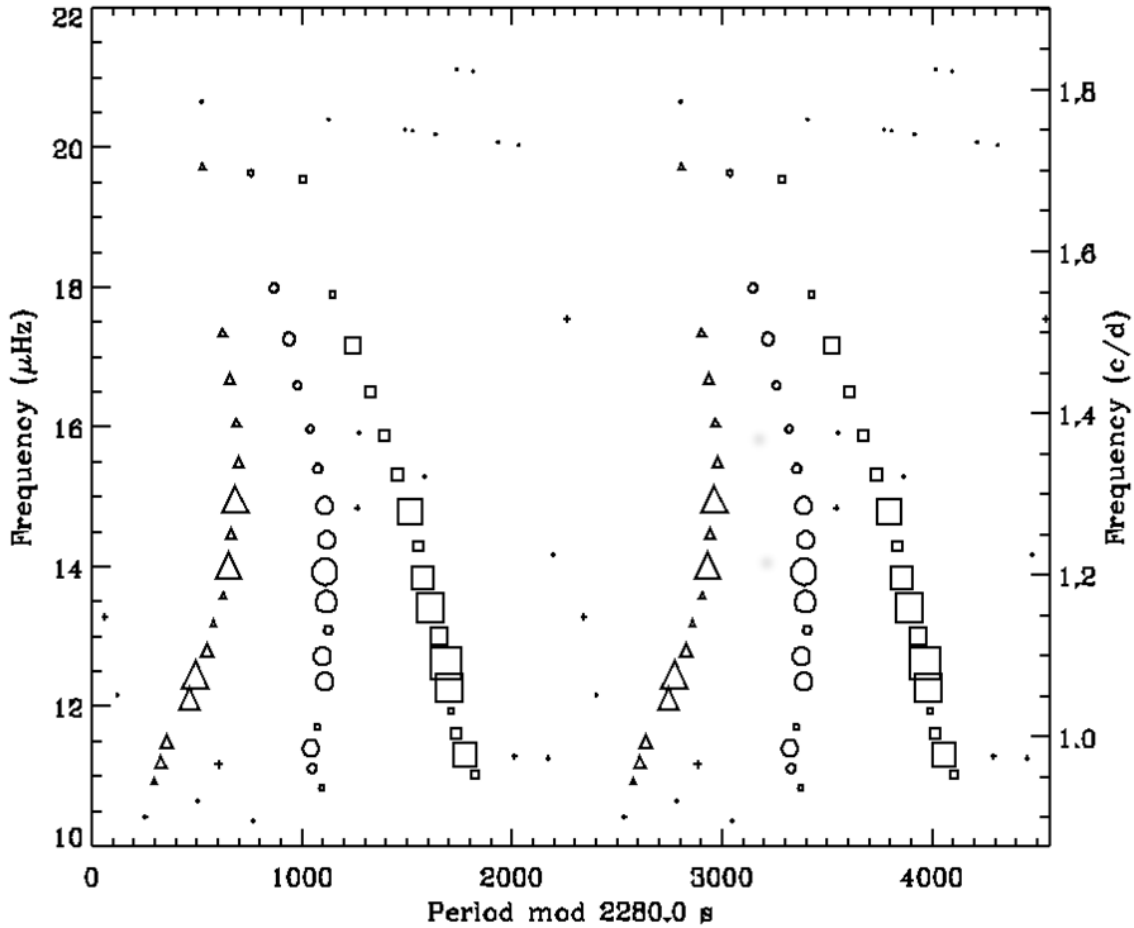


Figure 1.11: Period echelle diagram, plotted twice for clarity for KIC 9244992. Symbol sizes indicate mode amplitudes and symbol shapes indicate different values of azimuthal order  $m$ . Adopted from Bedding et al. (2014).

diagram arises from high order g modes asymptotically tending towards equal period spacing, unlike p modes which asymptotically tend to equal frequency spacing. One of the objects identified by Bedding et al. (2014) was found to have two humps of power in the Fourier transform. Upon creating the period-echelle diagram for each hump, it was found that the regular period spacings,  $\Delta P$ , of the two humps differed by a factor of  $\sqrt{3}$ . This is consistent with the humps containing  $l = 1$  and  $l = 2$  modes as:

$$\Delta P \propto 1/\sqrt{l(l+1)}. \quad (1.12)$$

A further diagnostic tool, proposed by Bouabid et al. (2013), is to plot the period

spacing against the period. Bouabid et al. (2013) predicted that the slope of such a plot depends on the fraction of stellar to critical rotation and  $m$ . Fig. 1.12 depicts the proposed plot for the 12  $\gamma$  Dor stars identified by Bedding et al. (2014). Some of these objects also show departures from equal spacings in the form of “wiggles”. These wiggles were also predicted by Bouabid et al. (2013) and relate to the chemical gradient outside the convective core.

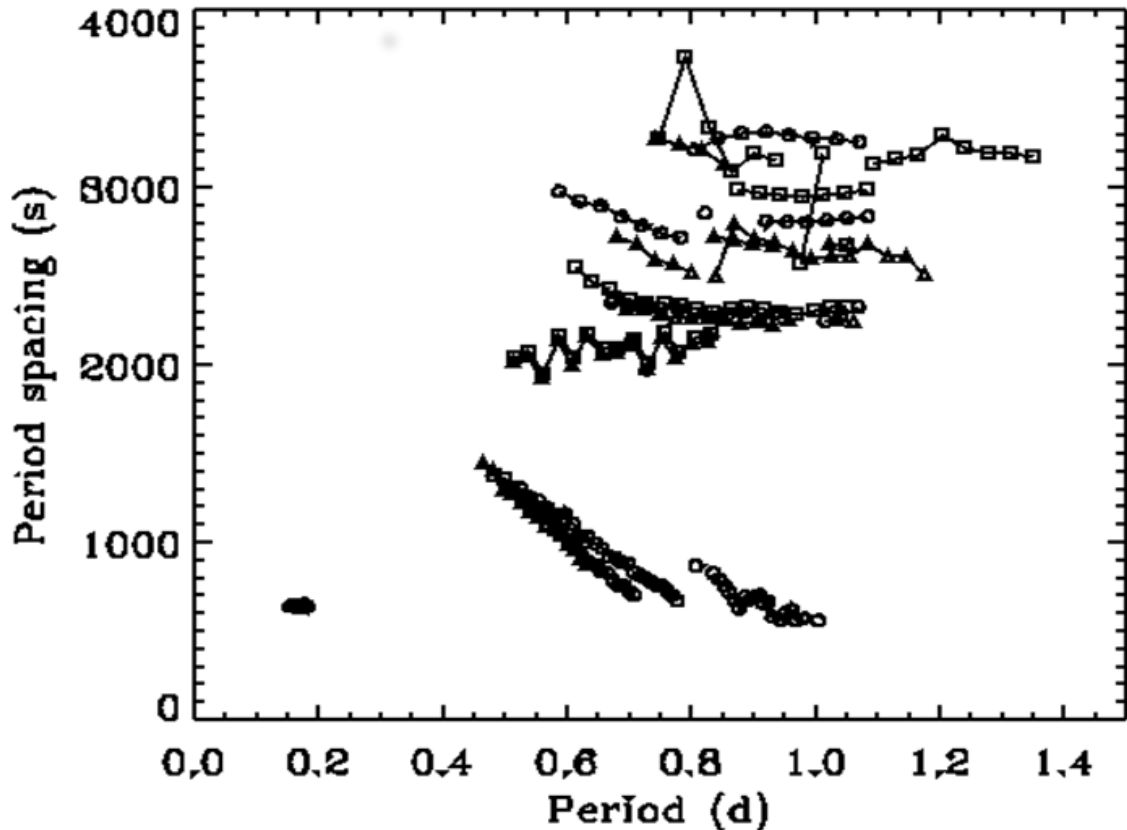


Figure 1.12: Period spacings of  $l = 1$  modes for twelve *Kepler*  $\gamma$  Dor stars. For each star, symbol shapes indicate different values of azimuthal degree  $m$ . Adopted from Bedding et al. (2014).

### 1.2.6 Solar-Like Oscillators

In the *Kepler* sample of heartbeat stars, we have identified 25 stars that pulsate with solar-like oscillations. The study of solar-like oscillations began with the identification (Leighton, 1960) and interpretation (Ulrich, 1970) of p-mode oscillations in the Sun. Unlike pulsating stars along the instability strip, solar-like oscillations

are stochastic pulsations, excited by turbulence in the stellar convective zone. These pulsations have led to several advances in our understanding of the Sun, including its internal rotation profile (Thompson et al., 2003), which provided evidence that the differential rotation of the Sun drives the Sun’s stellar dynamo (Ossendrijver, 2003); and have yielded a test bed for evolutionary models (Bahcall, Basu & Kumar, 1997).

Unlike the Sun, we cannot resolve the disks of other stars and so are only able to study the low degree modes ( $l = 0-3$ ). While this limits the level of detail we can achieve in the models, further theoretical advances, including the echelle diagram, have enabled the translation of these four (or commonly three,  $l = 0-2$ ) available degrees into physical parameters (Grec, Fossat & Pomerantz, 1983). Primarily, the echelle diagram presents the data in such a way that the large and small separations can be identified (see Fig. 1.13).

The large separation,  $\Delta_l$ , is the frequency separation between consecutive orders:

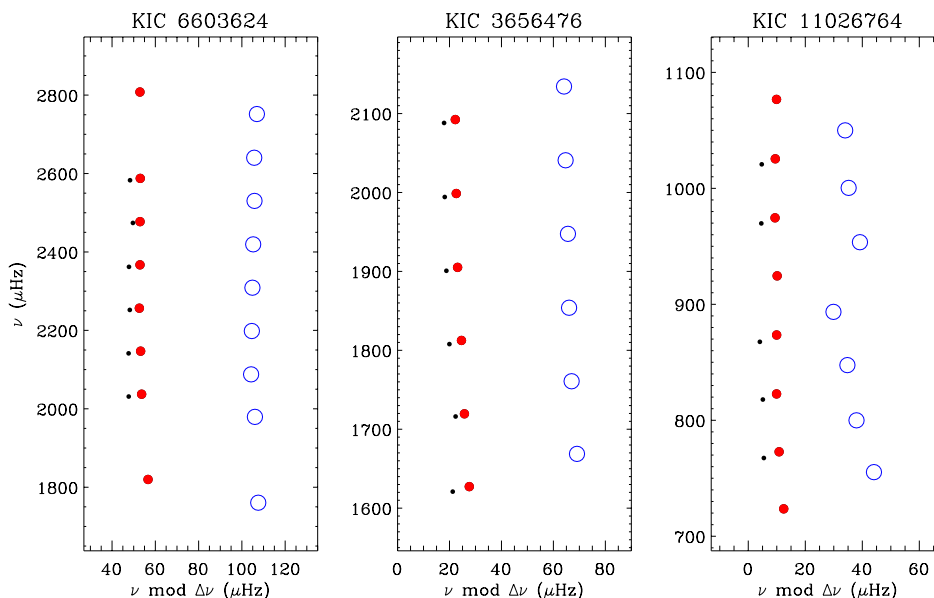


Figure 1.13: Echelle diagrams of three *Kepler* stars (*Kepler* input catalogue number indicated above). The  $l = 0$  modes are indicated by the filled red circles;  $l = 1$  by the open blue circles and  $l = 2$  by the small black points.  $l = 3$  modes are rarely seen from space as the light integrated over the surface does not significantly change, except in the presence of a strong filter such as limb darkening. Figure adopted from Chaplin et al. (2010).

$$\Delta\nu \equiv \nu_{n,l} - \nu_{n-1,l}, \quad (1.13)$$

where  $\nu$  is the mode frequency and the subscripts  $n$  and  $l$  denote the radial order and degree, respectively. Physically  $\Delta_n u$  represents the inverse of the sound travel time from the surface to the core of the star and back again:

$$\Delta\nu = \left[ 2 \int_0^R \frac{dr}{c_s} \right]^{-1}, \quad (1.14)$$

where  $c_s$  is the speed of sound and  $R$  denotes the stellar radius. The small separation,  $\delta\nu_{n,l}$ , is the separation between mode frequencies that have degrees that differ by 2:

$$\delta\nu_{n,l} \equiv \nu_{n,l} - \nu_{n-1,l+2}. \quad (1.15)$$

Otí Floranes, Christensen-Dalsgaard & Thompson (2005) identified the large and small separations as important parameters based on the separation of p modes in the asymptotic regime:

$$\nu_{nl} \approx \frac{n + (1/2)l + \epsilon}{T} + \frac{1}{6}Al(l+1), \quad (1.16)$$

where  $T$  is the sound travel time across the diameter of the star, and  $A$  and  $\epsilon$  are constants. As the second term is small compared to the first, it can be seen that modes of consecutive  $n$  are separated in frequency by  $1/T$  (*i.e.*  $\Delta\nu$ ) and thus are a global measure of the sound travel time and density of the star. Furthermore, modes that are separated by degree  $l+2$  and order  $n-1$  differ by the small quantity  $(2l+3)A/3$ , which is sensitive to the conditions in the stellar core. By plotting these two quantities we create a C-D (Christensen-Dalsgaard) diagram, *e.g.* Fig. 1.14, that is reminiscent of a Hertzsprung-Russell diagram (Christensen-Dalsgaard, 1984). In this C-D diagram, stars evolve by moving down and left, as expected from the



$R$ ; enabling for the first time the determination of stellar masses and radii through asteroseismology:

$$\delta\nu_0 = \left(\frac{M}{M_\odot}\right)^{1/2} \left(\frac{R}{R_\odot}\right)^{-3/2} 134.9 \mu\text{Hz}, \quad (1.17)$$

$$\nu_{\text{max}} \approx \frac{M/M_\odot}{(R/R_\odot)^2 \sqrt{T_{\text{eff}}/5777 \text{ K}}} 3.05 \text{ mHz}. \quad (1.18)$$

By obtaining the temperature of a solar-like oscillator, the mass and radius can be determined through analysis of the pulsations, to first order. Metallicity and rotation are second order effects that have a less significant impact on the determination of the fundamental stellar parameters.

### 1.2.7 Red Giants

As a star ends its hydrogen core burning phase and evolves off the main sequence, it becomes a red giant. When this happens the stellar core contracts and heats, causing the outer envelope to become distended, cool and convective. This convective outer envelope gives rise to solar-like oscillations (Mosser et al., 2011), similar to those of main-sequence solar-like oscillators, although with longer periods due to the red giants' significantly larger envelopes. Of the 25 heartbeat stars found to pulsate with solar-like oscillations, the majority are red giants. This selection bias arises from the fact that the long period oscillations of red giants are visible in the more common 30-min long-cadence data. Chapter 6 details the asteroseismic analysis of 17 red-giant heartbeat stars, one of which is studied in detail. As with main-sequence solar-like oscillators, the mass and radius of a red giant can be determined through asteroseismic scaling relations, *e.g.* Kallinger et al. (2010).

The envelopes of red giants are significantly extended relative to main sequence stars. A consequence of this is that the p modes have lower frequencies, making

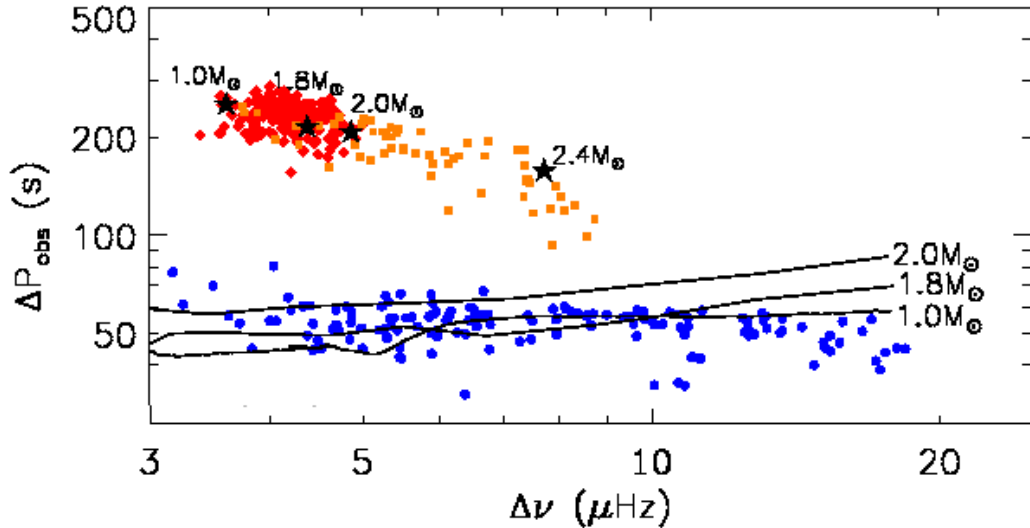


Figure 1.15: The large separation in period space of mixed modes vs. the large frequency separation from p modes for  $\sim 400$  red giants. Two distinct groups can clearly be seen: The helium-core-burning stars (red diamonds and orange squares) and the hydrogen-shell-burning stars (blue circles). The solid lines show average observable period spacings for models of hydrogen-shell-burning giants on the red giant branch as they evolve from right to left. The black stars show theoretical period spacings calculated in the same way, for four models of helium core-burning stars that are midway through that phase (core helium fraction 50%). Caption and figure adopted from Bedding et al. (2011).

them visible in the *Kepler* long cadence ( $\sim 30$  min) data. Furthermore, red giants are described by a polytrope of order 4 rather than a polytrope of order 3, as main sequence stars. For larger polytropic indices the separation between the p mode cavity and g mode cavity (which can be seen in Fig. 1.8 for the Sun) diminishes. This leads to the creation of mixed modes which have properties of both pressure and gravity waves in their respective cavities. Through the study of mixed modes in red giants we can obtain information about the radiative core and convective envelope. This was predicted by Dziembowski et al. (2001) and first observed in KIC 6928997 by (Beck et al., 2012).

As mixed modes are in the asymptotic period regime (Unno et al., 1989), the period spacing of the mixed dipole modes is related to the size of the convective core (Montalbán & Noels, 2013) and can be used to distinguish between Hydrogen shell burning (red giant branch) and Helium core burning (horizontal branch) stars (Bedding et al., 2011). Fig. 1.15 depicts a plot of the mixed-mode period spacings against

p-mode frequency spacings for rotationally split modes in  $\sim 400$  stars. Two distinct groups can clearly be distinguished: the helium-core-burning stars (red diamonds and orange squares) and the hydrogen-shell-burning stars (blue circles).

Mixed modes can also be used to determine the internal and external rotation rates of red giant stars. For an example of this see KIC 5006817, the object under detailed study in Chapter 6. To determine the internal rotation, the level of mixed-mode character is needed, as the size of the mode splitting caused by rotation is dependent on the Ledoux constant, which asymptotically approaches  $C_{n,l} \approx 0.5$  for g modes and  $C_{n,l} \approx 0$  for p modes. This can be estimated by modelling the stellar pulsations using a stellar model and rotational kernels to assess the g- and p-mode contribution for each mode. Fig. 1.16 depicts the contributions to the rotational splitting (as a function of the mass-fraction) to the total rotational splitting, for modes from a representative model of KIC 8366239. The ability to determine the internal rotation rate has led to the understanding that the angular momentum transport between the core and envelope of red giants is very efficient and causes significant slowing down of the core (Marques et al., 2013). Further analysis by Belkacem et al. (2015) showed that the mixed modes indeed contribute to the observed angular momentum transport.

Another interesting outcome arising from rotationally split modes is that the inclination of the star can be determined through consideration of the relative peak amplitudes in a multiplet. First identified by Gizon & Solanki (2003) from observations of the Sun, the visibility of a mode,  $H_{l,m}(i)$  can be described by:

$$H_{l,m}(i) = \frac{(l - |m|)!}{(l + |m|)!} [P_l^{|m|}(\cos i)]^2, \quad (1.19)$$

where  $l$  and  $m$  are the degree and azimuthal order and  $P_l^{|m|}$  are Legendre polynomials (assuming that the energy is equally distributed amongst the multiplet). Subsequently, for dipole modes, which are most common in red giants, edge-on stars

have a significant contribution from  $m = +1, -1$  components and pole-on stars from  $m = 0$  component of a multiplet.

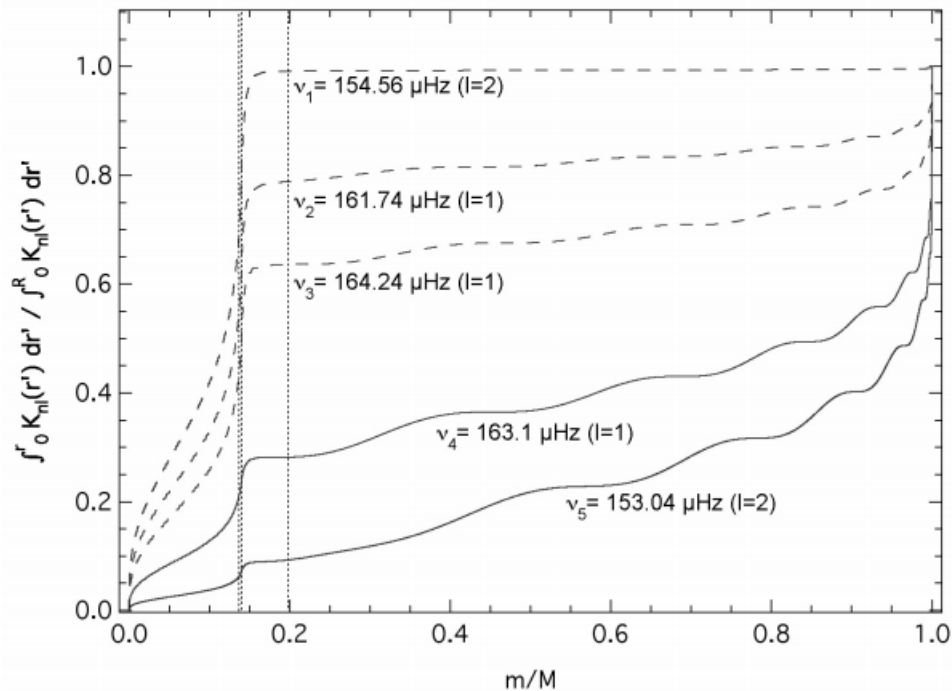


Figure 1.16: Contributions to the total rotational splitting. Partial integrals of normalized rotation kernels, illustrating the contribution from different regions to the rotational splitting for pressure-dominated modes ( $\nu_4, \nu_5$ ; solid lines) and gravity-dominated modes ( $\nu_1, \nu_2, \nu_3$ ; dashed lines), as a function of the mass-fraction for KIC 8366239. The left-most vertical line represents the boundary of the helium burning core and the vertical line at  $m/M \sim 0.2$  represents the end of the hydrogen burning shell and beginning of the convective envelope. Adopted from Beck et al. (2012).

### 1.3 Binary Stars

Fig. 1.17 depicts a sample of binary star light curves taken from the *Kepler* data. Binary stars are key to our understanding of fundamental stellar parameters and orbital dynamics; are important distance indicators; enable the study of stars that are of equal age; and form a test bed for stellar evolution theory. Elegantly, the binary star orbit can be described by the latter two of Kepler's three laws of planetary motion; where Kepler's 2<sup>nd</sup> Law states that the line joining the two orbiting

components must sweep out equal areas in equal time intervals and Kepler's 3<sup>rd</sup> Law states that the masses of the two components,  $M_1$  and  $M_2$ , the semi-major axes of the two components,  $a_1$  and  $a_2$  and the orbital period,  $P$  are related by the following equation:

$$\frac{(a_1 + a_2)^3}{P^2} = \frac{G(M_1 + M_2)}{4\pi^2}. \quad (1.20)$$

The 2<sup>nd</sup> law implies that the connecting line must always pass through the system's center of mass and thus that the orbital periods of the two components must be identical. The 3<sup>rd</sup> law states that through knowledge of the semi-major axes, which can be determined through the radial velocity shifts in the spectra; the inclination, which can be determined through modelling the light curve; and the orbital period, the combined stellar masses can be calculated without any prior assumptions (other than Kepler's 3<sup>rd</sup> Law). Furthermore, by comparing the semi-amplitudes of the two radial velocities, the mass ratio can be determined; when combined with the total mass of the binary system, this gives the individual masses of the stars.

Additional information about the stars and binary orbit can be obtained if the stars are eclipsing. If the components are undergoing partial eclipses, the study of orbital dynamics also enables the identification of tertiary components through eclipse timing variations caused by the gravitational interactions between the three (or more) components. Furthermore, the shape of the eclipses provides information on the inclination of the binary orbit. The configuration from which the most information can be extracted, however, is when the plane of the binary orbit is along the line of sight and the eclipses are total. For this configuration, the components' radii can be calculated using geometric considerations alone and the temperature ratio of the two stars can be determined from the ratio of the eclipse depths (alongside the aforementioned information for partial eclipses). While commonly not eclipsing, the light curves of heartbeat stars contain both orbital and fundamental stellar information as described in Chapter 3. The plethora of information that can be extracted

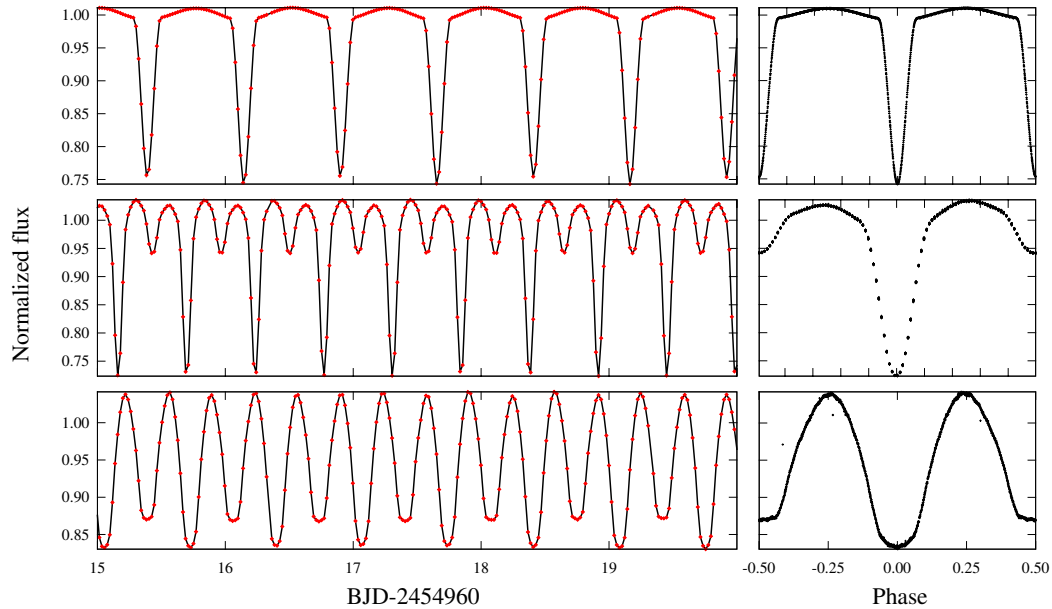


Figure 1.17: Examples of the ultra-high photometric precision and uninterrupted observing mode of *Kepler*. The left panels depict 5-d segments of characteristic *Kepler* light curves in time domain and the right panels show the corresponding phased light curves using all of the Quarter 1 data. Red dots correspond to mid-exposure times of *Kepler*'s 30-min cadence. Top to bottom: a detached eclipsing binary KIC 5513861 ( $P = 1.51012$  d); a semi-detached eclipsing binary KIC 8074045 ( $P = 0.53638$  d); and an over-contact eclipsing binary KIC 3127873 ( $P = 0.67146$  d).

from binary stars is indicative of the importance of these objects, not just for our understanding of stars, but for our understanding of the building blocks that form the Universe.

### 1.3.1 Binary Star Modelling

To determine the properties of the stars in a binary star system, binary star modelling software is used. The primary data inputs are the binary star light and radial velocity curves, although many binary star modelling software packages incorporate additional features that enable the input of multicolour photometry, spectra and polarimetry data, to name but a few. Through the consideration of these inputs and auxiliary information (*e.g.* from spectra), initial estimates of the binary star parameters (*e.g.* inclination and eccentricity) are made. From these initial estimates, two Roche lobes (Avni & Schiller, 1982), which describe the equipotential surfaces of the massless envelopes that encompass the stellar point masses, are created. Within the model, each equipotential surface is covered with a mesh (made of rectangles in

PHOEBE 1.0) and each mesh point contributes to the total flux of the binary system through consideration of many attributes including: the effective temperature of the star, the surface gravity at that point, limb darkening effects and albedo effects. Kepler's laws are then employed to recreate the model at different time points, as the stars orbit each other. At each time point the model flux is summed over the two discrete stellar surfaces (one for a contact binary), taking into consideration the direction of the surface normal vectors and the visibility of each mesh point, relative to the observer. From this information a model light curve is created. At each time point, the radial velocity of each model star, relative to the observer, is also determined using Kepler's laws; these values can be directly compared to the observed radial velocities.

Once an initial model has been created, minimisation techniques, such as Nelder-Mead downhill simplex (Nelder & Mead, 1965), differential corrections (Wilson & Devinney, 1971), or more recently MCMC (Metropolis & Ulam, 1949) are applied to arrive at a best-fit model to the data, where all data are fitted simultaneously. The solution comprises all the fundamental properties of the individual stellar components and the binary star orbit, although the accuracy of these vary, dependent on the nature of the binary star (*e.g.* if both components are visible) and the method of minimization.

PHOEBE (Prša & Zwitter, 2005) is a binary modelling package based on the Wilson-Devinney (hereafter WD) code (Wilson & Devinney, 1971; Wilson & Sofia, 1976; Wilson, 1979; Wilson & Van Hamme, 2004). The first version of the WD code surpassed previous binary modelling codes, such as the Russell model (Russell & Merrill, 1952), by introducing differential corrections for solving the inverse problem. The code was further improved in 1979 to include binary eccentricity, non-synchronous rotation and the ability to fit light and radial velocity curves simultaneously (Wilson, 1979). The recent version of the WD code includes a rigorous treatment of the reflection effect, model atmospheres and an improved approach to third body modelling and spots.

The approach of the WD code and consequently PHOEBE is to combine the flux from discrete surface elements over the distorted stellar surface and compare this value to the observed flux. Limb darkening and gravity darkening are combined with reflection to obtain an accurate representation of the observed flux. In addition, horizon effects, which describe the treatment of the stellar boundary as seen by the observer, and eclipse effects, which describe how this boundary changes during eclipse, are included to obtain the final parameter values for the stellar components (see Chapter 3 for a detailed discussion of modelling aspects relating to heartbeat stars).

PHOEBE incorporates all the functionality of the WD code, but also provides an intuitive graphical user interface alongside many other improvements that make PHOEBE highly applicable to state-of-the-art, precise data. These include: accurate accounting for finite integrations through convolution in Fourier space; the facility to phase-bin the data; updated photometric filters for the various recent space missions, including *Kepler*; an improved treatment of reddening; the ability to work with a up to 100 000 data points (far exceeding 8000 accepted by the WD code); and the ability to interface with PYTHON, which enables user defined functions, *e.g.* the implementation of EMCEE (Foreman-Mackey et al., 2013), a Markov chain Monte Carlo algorithm, which allows uncertainty determination through heuristical scanning.

Currently, the PHOEBE code is undergoing reconstruction to accommodate the precise and high quality data from the *Kepler* (Borucki et al., 2010; Gilliland et al., 2010; Batalha et al., 2010), *MOST* (Walker et al., 2003) and *CoRoT* (Baglin et al., 2006) satellites. These impressive data have challenged the current binary modelling codes and made it necessary to rethink the current assumptions that go into the models. The most fundamental of these are the rasterization of the surface mesh in the numerical models; the use of limb darkening laws; and the treatment of reflection and stellar albedos. Currently, the Wilson-Devinney code uses rectangles to rasterize the stellar surfaces of the numerical models. This produces gaps, which

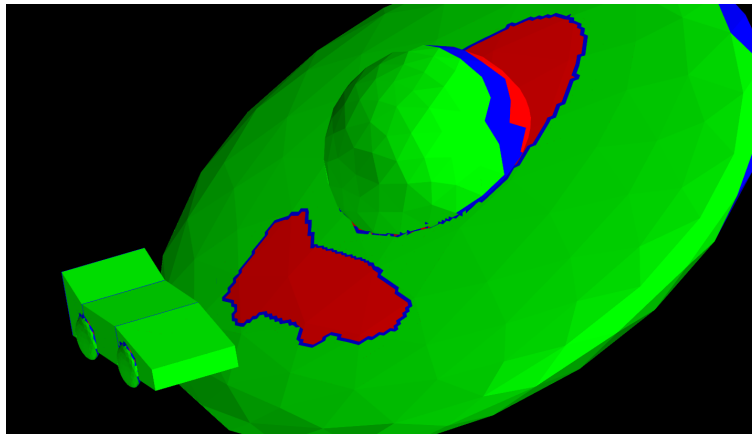


Figure 1.18: Depicted is a PHOEBE 2.0 model of a “Ferrari” orbiting a UFO generated through analytical descriptions of a car and a UFO. The surface is rasterized using a series of triangles. The green triangles are visible, the blue are partially visible and the red are not visible to the observer.

differ in size dependent on the size of the rectangles selected (where smaller rectangles means longer computation times). PHOEBE 2.0 improves on this aspect of the code by introducing triangles instead of rectangles, which are better able to describe an approximately spherical shape. Regarding limb darkening and reflection laws, in PHOEBE 2.0 they are implemented as a function of the surface properties (*e.g.*  $T_{\text{eff}}$  and  $\log g$ ) of each individual surface element, instead of simply applying them as a function of position on the stellar surface. These main improvements will significantly reduce the systematic errors that currently encumber the modelling process. Alongside these important improvements, PHOEBE 2.0 will also be capable of modelling triple and multiple systems; systems with pulsating components; be able to map the surface temperatures of stars and planets; and will be able to simultaneously model magnetic, interferometric, light curve and radial velocity observations. The motto of the PHOEBE team is: “to model anything including a Ferrari eclipsing a UFO”. The result is Fig. 1.18, which is a model generated in PHOEBE using analytical descriptions of a UFO and a car.

### 1.3.2 Doppler Boosting

One addition that I have made to the PHOEBE code using the PYTHON interface, is the addition of Doppler boosting. Doppler boosting (also known as Doppler

beaming) is caused by the radial velocities of the two stars and is the combined effect of shifting the stars' spectral energy distributions with respect to the observed bandpass, aberration and an altered photon arrival rate. The net result of Doppler boosting is an increase in the observed flux from a star when it moves towards the observer, and a decrease when it moves away from the observer. It was predicted to be seen in *Kepler* data by Loeb & Gaudi (2003) and Zucker, Mazeh & Alexander (2007a), and has recently been observed in several systems from ground-based data as well as in *Kepler* and CoRoT light curves (see e.g. Mazeh & Faigler, 2010; van Kerkwijk et al., 2010; Shporer et al., 2010; Bloemen et al., 2011).

Doppler boosting manifests itself in the light curve as an asymmetrical feature that mimics the inverted radial velocity curve of the star from which the signal comes. Due to the high velocities reached by stars in heartbeat systems, it is necessary to account for Doppler boosting when modelling them, especially with high precision photometry such as the *Kepler* data. A full description of Doppler boosting, including an outline of the implementation into the heartbeat star modelling code, can be found in Chapter 3.

### 1.3.3 Apsidal Motion

Apsidal motion is the rotation of the line of apsides about the centre of mass, an attribute commonly found in heartbeat stars. It is primarily caused by the effect of a star's tidal bulge, caused by its companion, on the potential energy distribution within the system, alongside general relativistic effects and rotational perturbations. The observed effect of apsidal motion on a doubly eclipsing binary is that the phases of the eclipses change such that the eclipses appear to move towards and away from each other in a cyclic motion as the orientation of the orbit changes. For heartbeat stars, the shape of the periastron variation changes as a function of the argument of periastron, which cycles with the motion of orbit (see Fig. 1.19). For both types of object, this causes the observer to measure the anomalous period

instead of the real sidereal period. This happens because, as the orbit precesses, we see the eclipses (or periastron brightenings) occur at a slightly different phase in the orbit and consequently the orbital period appears slightly shorter or slightly longer than the sidereal period (depending on the direction of motion with respect to the orbital motion of the stars). As classical apsidal motion occurs at an approximately constant rate, the anomalous period is also almost constant. The equation relating the anomalous period,  $P_a$ , and sidereal period,  $P_s$ , is:

$$P_s = P_a(1 - \omega_1/2\pi), \quad (1.21)$$

where  $\omega_1$  is the variation of the argument of periastron during one orbital cycle (Zasche, 2012).

The rate of apsidal advance is a consequence of the interaction between the stellar components in a binary or multiple system, which is a function of the periastron separation of the stellar components, mass ratio, eccentricity, period, semi-major axis and central density.

Observations of the rate of apsidal advance, whilst taking into account general-relativistic effects where applicable, enable the calculation of the central density parameter  $k_2$ . To obtain the central density parameter of the primary star in a binary system, the non-relativistic formula (Mazeh, 2008) is applied:

$$\frac{P_s}{P_{\text{tidal},1}} \approx k_2 \left( \frac{R_1}{a} \right)^5 \left[ 15f_2(e)q + \left( \frac{\Omega_{1,\text{rot}}}{\omega_{\text{orbit}}} \right)^2 (1 + q) \right], \quad (1.22)$$

where  $P_{\text{tidal},1}$  is the apsidal precession period due to the primary star;  $P_s$  is the orbital period;  $q$  is the mass ratio  $M_2/M_1$  where  $M_1$  is the mass of the primary star and  $M_2$  is the mass of the secondary star;  $\omega_{\text{orbit}} = 2\pi/P_s$ ,  $a$  is the semi-major axis,  $R_1$  is the radius of the primary star;  $\Omega_{1,\text{rot}}$  is the rotational frequency of the primary

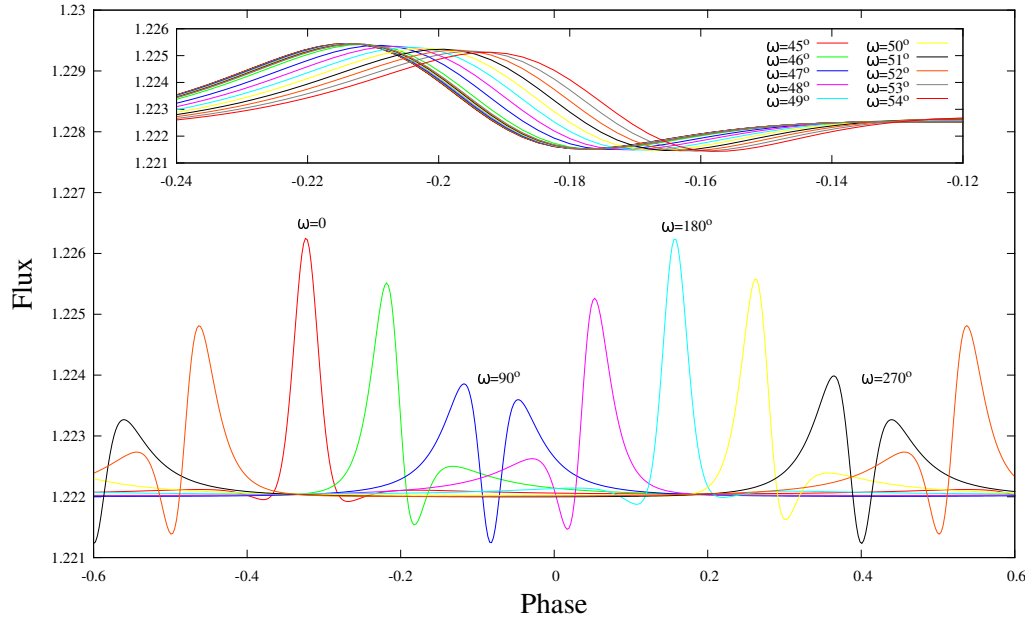


Figure 1.19: The effect of the periastron value,  $\omega$ , on the shape of the periastron brightening for one full cycle of the orbit around the centre of mass. The peaks change both their position *and* their shape drastically as a function of  $\omega$ . The model used in this demonstration is of KIC 3749404, a *Kepler* heartbeat star that exhibits one of the largest periastron advance rates ( $\sim 1^\circ/\text{yr}$ ; Hambleton et al. 2016, in prep.). Depicted in the inset is the light curve variation over 4.5-yrs (slightly longer than the the length of the extended *Kepler* mission).

star and  $f_2(e) \approx (1 + \frac{3}{2}e^2)$  where  $e$  is the eccentricity. For a point mass  $k_2 = 0$  and for a homogeneous sphere  $k_2 = 0.75$ . Typical stellar values of  $k_2$  range from  $\sim 0.001$  for the most centrally condensed stars such as red giants to  $\sim 0.01$  for the younger population of stars.

General relativistic apsidal motion (Mazeh, 2008) must also be accounted for in cases where the binary period is long and/or the masses of the components are large:

$$P_{GR} = 1800(1 - e^2) \left( \frac{P}{\text{day}} \right)^{5/3} \left( \frac{M_1 + M_2}{M_\odot} \right)^{-2/3}, \quad (1.23)$$

where  $P_{GR}$  is the apsidal precession period due to general relativity and is measured in years. To determine the overall rate of apsidal advance,  $P_{tot}$ , we combine these results using the following equation:

$$\frac{1}{P_{tot}} = \frac{1}{P_{GR}} + \frac{1}{P_{tidal,1}}. \quad (1.24)$$

Until recently, there have been discrepancies between the central density derived from apsidal motion observations and those obtained through the theory of stellar evolution (Claret, 1997). In Eqn (1.22) if the rate of apsidal advance is fixed, *i.e.* it is an observed quantity, it can be seen that the central density parameter,  $k_2$ , is highly dependent on the observed value for  $R$  (to the power of 5). The difficulty in determining the radii of stars accurately, alongside difficulties in correctly identifying the stellar temperatures and masses when fitting evolutionary tracks on the Hertzsprung-Russell diagram, has been deemed by Claret & Giménez (2010) to be the main cause of this discrepancy. While this has predominantly been resolved, there are still some objects that demonstrate apsidal motion rates far removed from those theoretically predicted, such as DI Her, AS Cam and V451 Cyg (Claret, 1997). Gies et al. (2012) suggested that discrepancies may hint at the presence of a tertiary component, although Claret & Willems (2003) proposed that deviations from the classical rate may be caused by resonant tides. Furthermore, models created by Claret & Willems (2003) support this prediction and show both positive and negative deviations from the classical apsidal motion rate due to the presence of resonant modes.

KIC 3749404 is a heartbeat star with tidally induced pulsations and rapid apsidal motion (see Chapter 5). The interesting aspect of this object is that the observed apsidal motion is two orders of magnitude larger than the theoretically predicted value. As theorised by Claret & Willems (2003) for binary stars with tidally induced pulsations, we anticipate that this unexpected rate of apsidal advance is due to the presence of tides.

### 1.3.4 Frequency Modulation

The most far-reaching aspect of binary star physics is the ability to determine fundamental stellar parameters through binary star kinematics. Commonly, this is achieved through spectroscopic observations, which are then converted into radial

velocity points by identifying the Doppler shift of each spectrum. An alternative method to this, for stars in binary systems with coherent, stable pulsations, is the frequency modulation (FM) method (Shibahashi & Kurtz, 2012; Shibahashi, Kurtz & Murphy, 2015a).

As stars in binary systems orbit their centre of mass, if one (or both) of the stars is pulsating, the change in radial velocity of a star can be measured by considering the modulation of the pulsation frequency due to the Doppler effect. The FM method is a technique that converts the frequency modulation into orbital parameters through use of the Fourier transform. An alternative method is known as the PM (phase modulation) method (Murphy et al., 2014), which utilizes the phases of pulsations, which also vary due to the light travel time, to determine orbital parameters.

The signature of the FM effect is a multiplet in the Fourier transform, where the peaks are separated by the orbital frequency. The relative amplitudes of the side-lobes to the main peak,  $\alpha$ , is:

$$\alpha = \frac{A_{+1} + A_{-1}}{A_0}, \quad (1.25)$$

where  $A$  is the amplitude and the subscript denotes the sidelobe (0 is the main peak). For the case of  $\alpha \ll 1$ ,  $\alpha$  contains information about the mass function that can be easily extracted:

$$f(m_1, m_2, \sin i) = \alpha^3 \frac{P_{\text{osc}}^3}{P_{\text{orb}}^2} \frac{c^3}{2\pi G}, \quad (1.26)$$

where  $P_{\text{osc}}$  is the period of oscillation of the main peak and  $P_{\text{orb}}$  is the orbital period of the binary star. The semi-major axis of the pulsating component,  $a_1$ , as a function of the inclination,  $i$ , can also be determined, using the following equation:

$$a_1 \sin i = \frac{P_{\text{osc}}}{2\pi} \alpha c. \quad (1.27)$$

It can be seen from Eqn 1.26 that  $\alpha$  depends on the frequency of oscillation and orbital period. Systems with longer orbital periods and larger amplitude pulsations at higher frequencies are thus favourable for FM analysis.

For eccentric systems, while the separation between peaks is still the orbital frequency, the sidelobes now hold information about the argument of periastron:

$$\omega = \frac{\phi_{+1} - \phi_{-1}}{2}, \quad (1.28)$$

where  $\phi$  is the phase of the sidelobe (again, denoted by the subscript), and eccentricity of the system:

$$e \approx \frac{2(A_{+2} + A_{-2})}{A_{+1} + A_{-1}}, \quad (1.29)$$

just as with radial velocities. This method is further described in Chapter 8, which includes the application to the binary system, KIC 8569819.

## 1.4 Conclusion

*Heartbeat* stars and tidally induced pulsations form the main focus of this work. The following chapters contain details of the analyses of a select group of stars demonstrating various effects and discussion of the tools created to analyse them. Primarily, I have endeavoured to model a collection of interesting heartbeat stars using my own codes and augmenting already existing codes (see Chapters 4, 5, 6 and 7). I have used the study of binarity to determine the fundamental stellar parameters and in one case compare the results with those determined through studying the star's solar-like oscillations (see Chapter 6). For another object, the frequency modulation (FM) of the stellar pulsations has also been used to determine the radial velocities of the pulsating component (see Chapter 8). This work marks

the beginning of significant advances in the observational field of heartbeat stars and tidally induced pulsations in binary systems.

## Chapter 2

# The Bayesian Approach to Radial Velocity Determination

Radial velocity determination has long involved a deterministic approach where cross correlation techniques have been used to identify the optimal radial velocities of observed spectra based on template spectra (Tonry & Davis, 1979; Zucker & Mazeh, 1994). While these techniques have proved to be invaluable for the determination of radial velocities in binary stars (for example Mazeh et al. 1995; Torres et al. 1995; Hambleton et al. 2013), the current era of astronomy requires advances in the statistical approach of such methods to enable the determination of radial velocity distributions that include the uncertainty from the input models, and the mean radial velocity and standard deviation based on the peak and spread of the cross correlation peak. By applying Bayesian statistics to the task of radial velocity determination, I was able to produce such distributions while simultaneously generating posteriors for the spectral parameters. This improves our understanding of our data, uncertainties and provides further constraints for the binary system in hand.

In this Chapter the BAYES-TODCOR software is outlined, which combines modern statistics and spectral cross correlation, for the optimal determination of radial

velocities and binary star parameters. In §2.1 Markov Chain Monte Carlo (MCMC) techniques are discussed with special attention to EMCEE (pronounced “M C”), an affine invariant version of MCMC that is used in BAYES-TODCOR; in §2.2 the TODCOR software is described, including a mathematical description of the various steps involved; the BAYES-TODCOR software itself is discussed in §2.3, which includes the results of two versions: the version using CCR (cross correlation), TODCOR’s cross-correlation function, as the log likelihood, and the version using  $\chi^2$ ; and the application to synthetic and observed data is described in detail in §2.4. The code for both versions of BAYES-TODCOR is available in Appendix A.

## 2.1 Markov Chain Monte Carlo Techniques

Monte Carlo simulations are the random sampling of variables to obtain a range of possible results in the form of a distribution. The statistical method was first invented by Stanislaw Ulam in the 1940s (Metropolis & Nicholas, 2011), who developed it for use on nuclear weapons projects (Metropolis & Ulam, 1949). As the method is most useful for solving difficult multi-dimensional problems, it is highly applicable to many problems in mathematics and physics, such as the determination of binary star parameters. The method itself involves: selecting a range of inputs for each variable; drawing from each input range using a predefined distribution, *e.g.* flat or Gaussian; performing a computation on the selected values, such as computing a binary model; combining the results and subsequently making deductions about the input parameters.

The main drawback of the Monte Carlo method is the extensive computation time and large number of processors required to obtain results. This is increasingly true for high dimensional problems. For a single parameter draw, the motion in phase space consists of a vector from the current point in parameter space to the newly drawn point, and as such has two operations. For an N-dimensional parameter

space, the vector is  $N$ -dimensional with each parameter requiring two operations. Thus the computation time scales as  $2^N$ , where  $N$  is the number of parameters. Consequently, the optimization of Monte Carlo simulations was required to make the method more applicable to real-life problems.

A Markov chain is a stochastic chain of events that changes state in discrete steps. A special characteristic of a Markov chain is that the change in state, the transition, only depends on the current state and not on previous states. Markov chains possess the Markov property:

$$p(\theta^{(t+1)}|\theta^{(1)}, \theta^{(2)} \dots \theta^{(t)}) = p(\theta^{(t+1)}|\theta^{(t)}), \quad (2.1)$$

where  $\theta$  is the state space and  $t$  is the iteration. While the steps are random, they are dependent on their transition probability, and consequently, while each individual transition is not predictable, the state of a chain after a large number of transitions can be statistically predicted.

The combination of the Markov chains and Monte Carlo simulations was originally performed by Metropolis et al. (1953) who proposed a “random walk” algorithm. In this algorithm, each particle was moved individually by comparing the result of the next step to the result of the previous step and only accepting results that improve the probability, or, as in his given example, lower the energy state of the system tending to thermodynamic equilibrium.

The present versions of Markov chain Monte Carlo (MCMC) methods are based on one of two algorithms: the Metropolis-Hastings algorithm (Hastings, 1970) and the Gibbs sampler (Turchin, 1971). The main difference between the two is that the conditional distributions,  $Y$  where the posteriors take the form  $p(\theta|Y)$ , of the parameters must be known for the Gibbs sampler; however, this is not necessary for the Metropolis-Hastings algorithm. As we commonly do not know the conditional distributions of the parameters in binary star physics, I elected to use the Metropolis-

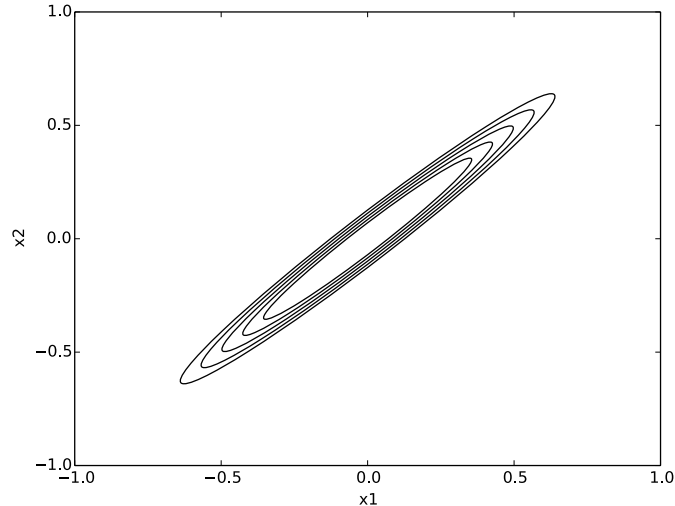


Figure 2.1: The contours of an example of a non-isotropic distribution in phase space, described by Eqn. 2.3.

Hastings algorithm.

For the Metropolis-Hastings algorithm, the process begins with the selection of a arbitrary (random) position in parameter space,  $X$ . The sampler then proposes the next step,  $Y$ , with probability  $q(Y|X)$ . The function that governs the next step,  $g(X \rightarrow Y)$ , is sampler dependent, but is commonly selected to be a Gaussian distribution centred on  $X$  so that  $Y$  is typically close to  $X$ . The ratio between the current probability and the previous probability is then calculated:

$$r = \frac{p(Y)q(X|Y)}{p(X)q(Y|X)}, \quad (2.2)$$

which is reduced to  $r = p(Y)/p(X)$  if the proposed move is symmetric, a requirement for the Metropolis-Hastings algorithm. If  $r \geq 1$  then the probability of  $Y$  is greater than the probability of  $X$  and thus the new step is accepted. If  $r < 1$  then the transition is accepted with probability  $r$ . Consequently, the chain tends to the parameter space with a high probability density and explores the lower probability space less frequently.

EMCEE is an affine invariant implementation of the Metropolis-Hastings MCMC sam-

pler, proposed by Goodman & Weare (2010) and implemented by Foreman-Mackey et al. (2013). While similar to standard implementations of MCMC, EMCEE addresses the problem that arises when sampling a non-isotropic distribution, see Fig. 2.1. In this example, the probability density of  $x$  is:

$$p(x) \propto \exp\left(\frac{-(x_1 - x_2)^2}{2\epsilon} - \frac{(x_1 + x_2)^2}{2}\right). \quad (2.3)$$

For distributions like this, standard MCMC samplers are confined to making steps of size  $\sqrt{\epsilon}$ , which is less than optimal in the direction of (1,1), as shown in Fig. 2.1. The method proposed by Goodman & Weare (2010) involves an affine invariant transformation of the form  $y = Ax + b$  such that  $p(y) \propto p(x)$ . For example, by applying the following transformations:

$$y_1 = \frac{x_1 - x_2}{\sqrt{\epsilon}}, \quad y_2 = x_1 + x_2, \quad (2.4)$$

Eqn. 2.3 becomes the far more tractable:

$$p(y) \propto e^{-0.5(y_1^2 + y_2^2)}, \quad (2.5)$$

which is Gaussian and enables extensive sampling of the phase space in a significantly smaller number of iterations.

Another feature of the method theorised by Goodman & Weare (2010) is the “stretch move”. The stretch move is the proposed affine invariant transition by one walker (Markov chain),  $X_k(t)$  along the line between itself and a second walker,  $X_j$ , in the N-dimensional, parameter space:

$$X_k(t)Y = X_j + Z(X_k(t) - X_j), \quad (2.6)$$

where  $Z$  is a random variable drawn from:

$$g(z) \propto \begin{cases} \frac{1}{\sqrt{z}} & \text{if } z \in [\frac{1}{a}, a] \\ 0 & \text{otherwise} \end{cases}, \quad (2.7)$$

where  $a$  is an adjustable scale parameter that must be greater than one. Goodman & Weare (2010) suggests a value of  $a = 2$ ; however, this value can be adjusted if too few/too many chains are being accepted. This method of selecting the transition proposal is highly effective and has been found to significantly reduce the autocorrelation time. Thus EMCEE is highly applicable and cost efficient for high dimensional problems, such as generating binary star models.

## 2.2 TODCOR

The two dimensional cross-correlation software, TODCOR (Zucker & Mazeh, 1994), takes two template spectra and an observed spectrum, and uses cross correlation techniques to determine the radial velocities of both components in the observed spectrum (assuming the secondary component contributes greater than 3% light). The first astronomical application of the cross correlation technique employed one-dimensional cross correlation to determine the radial velocities and thus redshifts of galaxies (Tonry & Davis, 1979). While this method can also be directly applied to binary star systems, where the cross correlation peaks are well separated in one dimension, when the cross correlation peaks of the primary and secondary components overlap, this renders the secondary peak undetermined and can often skew the results of the primary component.

TODCOR overcomes this shortcoming by assuming that both spectral templates contribute to the observed spectrum and thus determines the cross correlation of both templates simultaneously across an extensive (user defined) range of wavelength shifts. The result is a two-dimensional correlation peak that provides accurate ra-

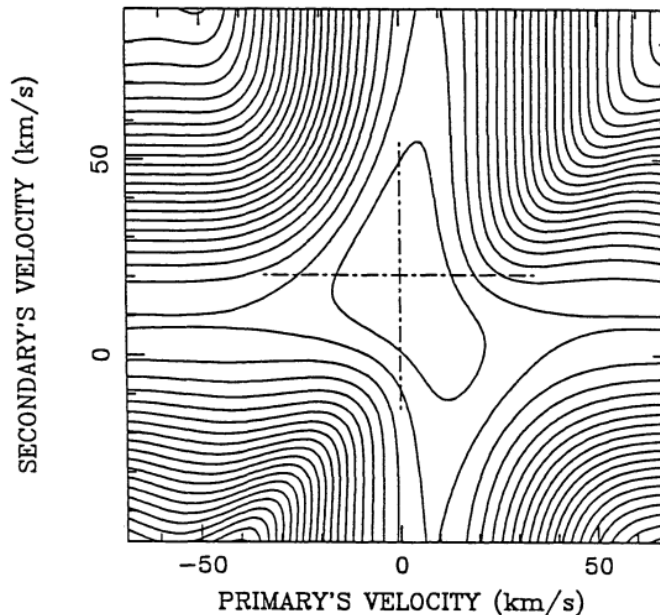


Figure 2.2: A contour plot of the two dimensional correlation function. The dashed lines pass through the maximum and indicates the velocity shift of the primary and secondary components. Figure adapted from Zucker & Mazeh (1994).

dial velocities based on the correlation of both components (see Fig. 2.2). If done directly, two-dimensional cross correlation is computationally expensive. However, Zucker & Mazeh (1994) employed Fast Fourier Transform (FFT) techniques to increase the computation speed from an  $N^2$  computation to an  $N \log N$  computation, thus significantly reducing the computation cost.

Two dimensional cross correlation requires two template spectra,  $g_1(n)$  and  $g_2(n)$ , and an observed spectrum,  $f(n)$ . To utilize FFT techniques, the observed spectrum and template spectra must be in log scale. Consequently, to determine the correlation, the templates are shifted linearly by  $s_1$  and  $s_2$ :

$$g_1(n - s_1) + \alpha g_2(n - s_2), \quad (2.8)$$

where  $\alpha$  is the intensity ratio of the spectra. The correlation function of the two shifts is thus:

$$R_{f,g_1,g_2} = \frac{\sum f(n)g_1(n - s_1) + \alpha \sum f(n)g_2(n - s_2)}{N\sigma_f\sigma_g(s_1, s_2)} \quad (2.9)$$

where  $N$  is the number of overlapping bins between the observations and template spectra,  $\sigma_f$  is the rms noise of the data:

$$\sigma_f^2 = \frac{1}{N} \sum f(n)^2, \quad (2.10)$$

and  $\sigma_g$  is the uncertainty of the shifted template spectra:

$$\sigma_g^2(s_1, s_2) = \frac{1}{N} \sum [g_1(n - s_1) + \alpha g_2(n - s_2)]^2, \quad (2.11)$$

Inserting the full equation for  $\sigma_g^2$  into Eqn. 2.9 we obtain:

$$R_{f,g_1,g_2} = \frac{\sum f(n)g_1(n - s_1) + \alpha \sum f(n)g_2(n - s_2)}{N\sigma_f \sqrt{\sigma_{g_1}^2 + 2\alpha/N \sum g_1(n)g_2[n - (s_2 - s_1)] + \alpha^2\sigma_{g_2}^2}}, \quad (2.12)$$

which contains two correlation computations in the numerator and one in the denominator:

$$C_1(s_1) = \frac{1}{N\sigma_f\sigma_{g_1}} \sum f(n)g_1(n - s_1), \quad (2.13)$$

$$C_2(s_2) = \frac{1}{N\sigma_f\sigma_{g_2}} \sum f(n)g_2(n - s_2), \quad (2.14)$$

$$C_{12}(s_2 - s_1) = \frac{1}{N\sigma_{g_1}\sigma_{g_2}} \sum g_1(n)g_2[n - (s_2 - s_1)]. \quad (2.15)$$

The calculation is thus reduced to:

$$R_{f,g1,g2}(s_1, s_2, \alpha) = \frac{C_1(s_1) + (\sigma_{g2}/\sigma_{g1})\alpha C_2(s_2)}{\sqrt{1 + 2(\sigma_{g2}/\sigma_{g1})\alpha C_{12}(s_2 - s_1) + (\sigma_{g2}/\sigma_{g1})\alpha^2}}. \quad (2.16)$$

The final result contains three cross correlations, one between each template and the observed spectrum, and one between the two templates. All three computations can be performed using FFTs, which leads to a computationally inexpensive and reliable method for obtaining radial velocity information from double lined spectroscopic binary stars.

## 2.3 Bayes' Todcor

When using TODCOR, it is important that the templates selected are representative of the observations. This is often done using a grid of spectra and identifying the best set of templates through trial and error and selecting the best fit based on the highest correlation score. While this technique has been previously adequate, it does not allow for the refinement of the stellar parameters through interpolation of the template spectra, provide posterior probability distributions on the spectral parameters or provide radial velocity distributions based on the variations of possible stellar parameters. For this reason, I have combined TODCOR with EMCEE to determine the radial velocity distributions dependent on the possible range of spectral models. Not only this, but the posteriors on the spectral parameters: the effective temperature,  $\log g$  and  $v \sin i$  of both components, and the combined metallicity of the system are also generated, enabling a more robust uncertainty determination for all parameters involved. This novel technique that I have developed is described in the following section.

### 2.3.1 Parameters

The prominent features of spectra are governed by the following parameters:

- effective temperature,  $T_{\text{eff}}$
- $\log g$
- metallicity
- $v \sin i$

Consequently, these parameters are the constraints on the synthetic spectra and are the parameters from which the MCMC sampler determines the posterior probability distribution functions.

As the metallicity of the majority of stars in binary systems is based on the metallicity of the cloud from which the stars were formed, I elected to make the metallicity a global parameter, i.e. the same for both stars. Within this framework, the optimal solution will contain the metallicity which best fits both components (with more weight to the brighter object). For Am and Ap stars, this assumption does not hold as their metallicity is a result of diffusion. However, the software is easily adaptable to account for this, if necessary.

All other aforementioned parameters are individually allocated to each star. I also made the intensity ratio,  $\alpha$ , a parameter in the model fit. TODCOR offers the option to fit  $\alpha$ ; however, by adding it to our list of parameters, I determine a posterior distribution function for  $\alpha$  and the uncertainty in  $\alpha$  is propagated to the radial velocities and spectral parameters.

### 2.3.2 The Software in a Nutshell

I start off by specifying prior ranges for the  $T_{\text{eff}}$ ,  $\log g$ , metallicity and  $v \sin i$ . The current implementation of the software has the option to specify uniform or Gaussian priors. As further inputs, the program requires the number of chains; a list of the files

with observed spectra; the directory that contains the grid of synthetic spectra (with wavelength for all input files in the same, linear units); the per-point uncertainty of the observed data; the dispersion of the observed spectra; and the name of the output file.

The file names of the synthetic spectra must be in the correct format, *e.g.*:

T07000G40M05.spectra or T07000G40P05.spectra where the temperature of the spectrum must follow “T” (with a leading zero if necessary), the  $\log g$  of the spectrum (in cgs units), multiplied by 10, must be given after the “G”, and the final two digits state the metallicity,  $[\text{Fe}/\text{H}]$ , multiplied by 10, where P indicates positive metallicity and M indicates negative metallicity. This is the standard output when synthesizing spectra using the software SPECTRUM (Gray, 1999). To complement the BAYES-TODCOR software, I have built a parallelized program that creates a grid of spectra from Kurucz model atmospheres (Castelli & Kurucz, 2004) (see §2.4).

Once these variables have been specified, the first part of the software takes the synthetic spectra (from the grid of spectra), which are used as templates, and prepares them for interpolation. Following this, the initial parameter values for each walker are selected at random (from a flat or Gaussian distribution) from the prior ranges and the first iteration begins. For each chain, two synthetic spectra are generated (one for each stellar component) by interpolating the stellar spectra. Following this, checks are in place to ensure that the spectra are within the bounds of the grid. The two spectra are then rotationally broadened, using the values selected by the MCMC sampler, and then instrumentally broadened using functions from PHOEBE 2.0. The spectra are then binned to a dispersion similar to that of the observations (which significantly improves the speed of TODCOR) and written to two files, one for each component, ready for use in TODCOR.

TODCOR is then run from within BAYES-TODCOR to determine the optimal radial velocity shifts of the newly created template spectra against each observed spectrum individually. For each observation, the names of the template files, the observed

spectrum and the intensity ratio (determined by the MCMC sampler), are given as inputs to TODCOR. TODCOR returns the optimal values of the radial velocities and their uncertainties. The templates are then shifted by the TODCOR specified radial velocity, using a PHOEBE 2.0 function, and combined according to the intensity ratio selected by the MCMC sampler. The combined templates are interpolated so that they contain the same wavelength range and number of data points as the observed spectrum. The goodness of fit is then determined using the CCR or  $\chi^2$  test (dependent on the version of BAYES-TODCOR). For each observed spectrum, for each iteration that is accepted by the MCMC sampler, the radial velocities and their uncertainties are stored.

For the CCR version, the log likelihood,  $\ln p$  is determined using:

$$\ln p = -0.5 \left( \frac{1 - \text{CCR}^2}{\sigma^2} \right), \quad (2.17)$$

where CCR is TODCOR's cross correlation function. For the  $\chi^2$  version, I determined  $\ln p$  using:

$$\ln p = -0.5\chi^2. \quad (2.18)$$

I multiply by -0.5 to generate a log likelihood value or log Gaussian distribution. For the  $\chi^2$  version, I chose to keep TODCOR as the method of determining the radial velocity shifts (as opposed to making the velocities priors) as TODCOR is not sensitive to the normalisation of the spectra and thus provides more accurate results. For each chain the sampler receives a log likelihood value and if the log likelihood value is larger (closer to zero) than the previous value, then it will be accepted. If the value is smaller than the previous value, then it may be accepted (to thoroughly explore the parameter space). If a set of parameters is rejected, new parameters are assessed for the same chain until the log likelihood is accepted. Once each chain has

accepted a new log likelihood value, the sampler provides a new set of parameters for each chain, based on a covariance matrix between two chains, and the process is repeated.

The software has the additional feature that it can begin from the posteriors of a previous run. This is convenient if the maximum number of iterations is reached and the program hasn't converged, or if a sub-set of walkers is stuck in a local minimum. This way, the initial distribution for the new run can be sampled from a selection of the posteriors. This can result in multiple walkers having the same parameter values; however, it is preferable, as walkers stuck in a local minimum do not contribute to the improvement of the solution.

### 2.3.3 Posteriors, Distributions and Results

After a period called the burn-in time, during which the various chains are converging to a global minimum, the chains oscillate about the global minimum in a normal distribution (see Fig. 2.3). By sampling the distribution of chains after the burn-in period, the posterior distributions of the spectral parameters can be determined, for example, see Fig. 2.4. From the posteriors it is possible to determine the mean and standard deviation of the parameters, assuming the parameter space is Gaussian, but more importantly, the parameter distributions can be seen, which includes correlations between different parameters, if a parameter value is unique or degenerate, and if there is any information in the data about a given parameter.

For every accepted log likelihood value, the radial velocities and their uncertainties (for both components for each observation) are stored. As I do not provide prior information for the radial velocities, they are not being sampled in the same way as the spectral parameters, but rather being calculated by TODCOR for each model spectrum. To combine the spread of radial velocity values due to the range of possible models with the TODCOR uncertainties, I have built a plotting program that creates normal distributions from the TODCOR values (means and uncertainties). For

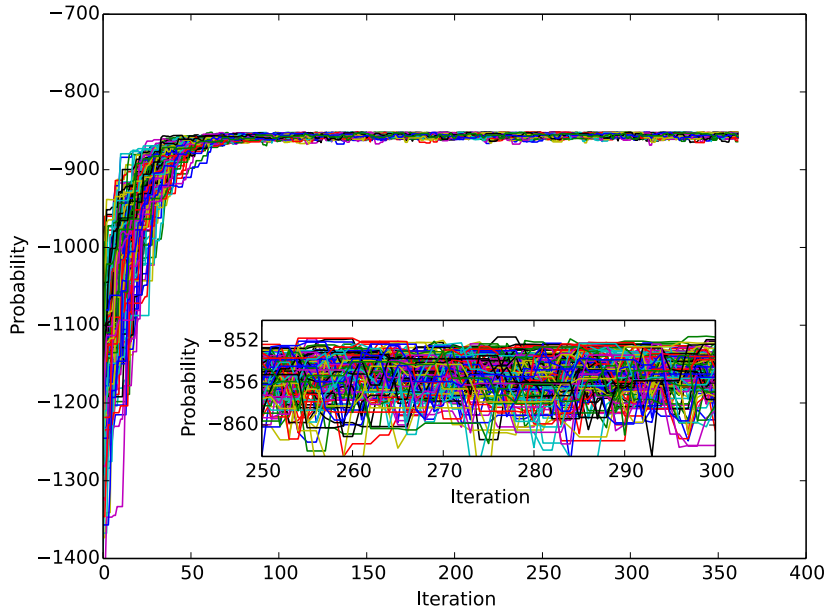


Figure 2.3: The  $\ln p$  as a function of iteration for the  $\chi^2$  version of the BAYES-TODCOR software (when applied to synthetic data), where each colour represents a different chain. As the  $\chi^2$  statistic is not normalised, the value should tend to  $0.5n$ , where  $n$  is the number of data points. This plot is used as a first gauge to determine if the model has converged. From consideration of this plot alone, it appears the burn-in time was approximately  $\sim 100$  iterations, as the probability does not change after this point.

each observation the normal distributions are co-added for each component over all chains and for several iterations (see Fig.2.5). The end product is that for each radial velocity, the mean and standard deviation values are obtained, based the direct uncertainty from TODCOR and the uncertainty propagated from the range of models.

## 2.4 The Application

As I built the BAYES-TODCOR software, I continually tested it on a test suite of simulated observed data see §2.4.1. By doing this I ensured that all individual aspects of the software functioned as expected. Upon the satisfactory completion of the software and tests on simulated data, I applied the software to the observed spectral data of KIC 8164262, a single-lined spectroscopic heartbeat star binary

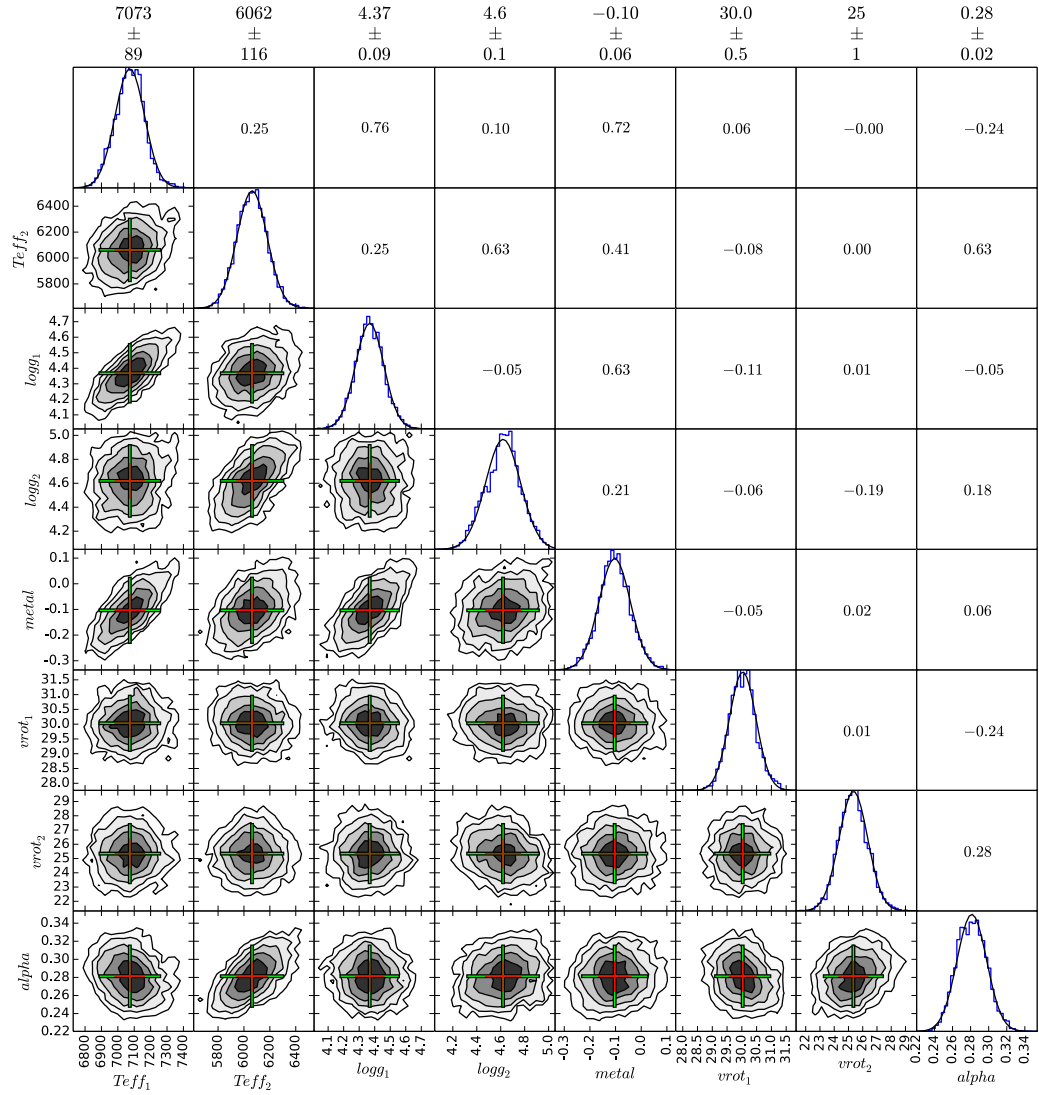


Figure 2.4: Depicted are the posteriors generated using the BAYES-TODCOR program with synthetic data. Lower left sub-plots: two dimensional cross-sections of the posterior probability distribution functions for the effective temperatures  $T_{\text{eff}1}$  and  $T_{\text{eff}2}$ ;  $\log g_1$  and  $\log g_2$ ; the metallicity of both components,  $metal$ ; the stellar rotational velocities  $v_{\text{rot}1}$  and  $v_{\text{rot}2}$ ; and the light ratio,  $alpha$ . The crosses show the  $1\sigma$  (red) and  $2\sigma$  (green) uncertainties, and are centred on the minima. Diagonal sub-plots from top left to bottom right: histograms displaying the probability distribution of each individual parameter. Upper right sub-plots: the correlations for the two-dimensional cross-sections mirrored in the diagonal line where 1 is direct correlation and -1 is a direct anti-correlation. The values above the plot give the mean value and one sigma uncertainty for each parameter, based on the fitted Gaussians.

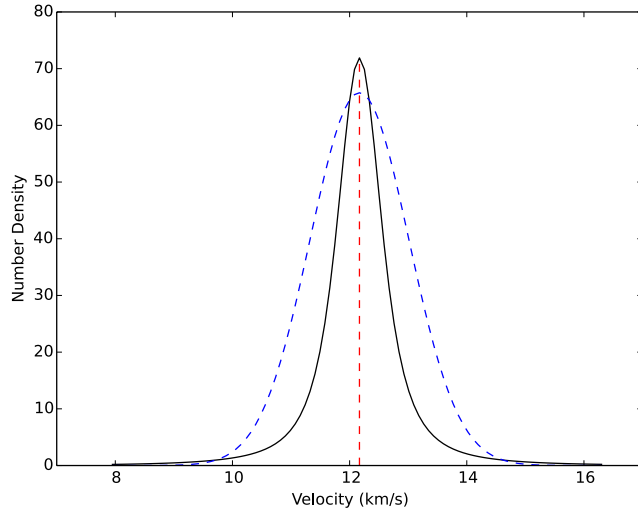


Figure 2.5: Depicted are the normal distributions for the TODCOR mean and average uncertainty (black dashed line) and the combined means and uncertainties determined using the BAYES-TODCOR software (blue line) for KIC 8164262 (see Chapter 4). The red line depicts the weighted mean determined using the BAYES-TODCOR software.

system. Due to the results of the tests, I elected to use the  $\chi^2$  version of the software. The results of this can be found in § 2.4.4.

### Building the Model Spectra

To create the spectral templates and to create synthetic data for testing, it was required that spectra were built from models. I elected to use Castelli-Kurucz ATLAS9 model atmospheres (Castelli & Kurucz, 2004) as they are best in the range 4500 Å and redder (Richard Gray, private communication), which is appropriate for the spectral region of the observed spectra obtained at Kitt Peak Observatory (4600–9050 Å).

SPECTRUM is a spectral synthesis program (Gray, 1999) that takes model atmospheres (that contain information for up to 100 atmospheric layers including layer temperature, electron density, abundances and gas pressure) and converts them into synthetic spectra. To generate a grid of synthetic spectra from models, I have built a program that parallelizes SPECTRUM using MPI (message passing interface). This enables the creation of large numbers of synthetic spectra ( $\sim 3800$ ) in a short amount

of time (dependent on the number of processors and length of the spectra).

The required inputs to the software are the spectral range; the desired dispersion/bin width of the synthetic spectra; the directory of the models; the directory for the newly created synthetic spectra; and the directory of SPECTRUM. As SPECTRUM requires an input file to create each synthetic spectrum, the software reads in the name of each model from the directory of spectral models and generates an input file. The files contain the spectral range, line list, directories of the models and outputs, bin width and the microturbulent velocity. As the object that I was fitting has an approximate spectral type of late A/early F, I specified the microturbulent velocity to be  $\xi_t = 2.0 \text{ km s}^{-1}$  (Gray, Graham & Hoyt, 2001). Following the creation of each input file, the software runs spectrum, which creates a synthetic spectrum.

### 2.4.1 Creation and Application of Synthetic Data

To test the program at its various stages, I created synthetic data where the input quantities were known. The following procedure describes the creation of synthetic data, beginning with synthetic spectra from models and ending with synthetic data that was used as input data for the BAYES-TODCOR software.

First, a model binary star was created using PHOEBE for each synthetic data set (for details of individual models see §2.4.1). Each model was created so that the components were realistic main-sequence stars. Using PHOEBE, radial velocity points were generated for each component.

Synthetic spectra were created for the stars in the models by interpolating the grid of spectra. The spectra were rotationally broadened using a PHOEBE 2.0 function and copies were made so that there was a spectrum for each radial velocity (for each star). Following this, the spectra were shifted (again, using a PHOEBE 2.0 function) according to the radial velocity values from the binary star model. I then combined the shifted spectra for each radial velocity time point. To do this each spectrum

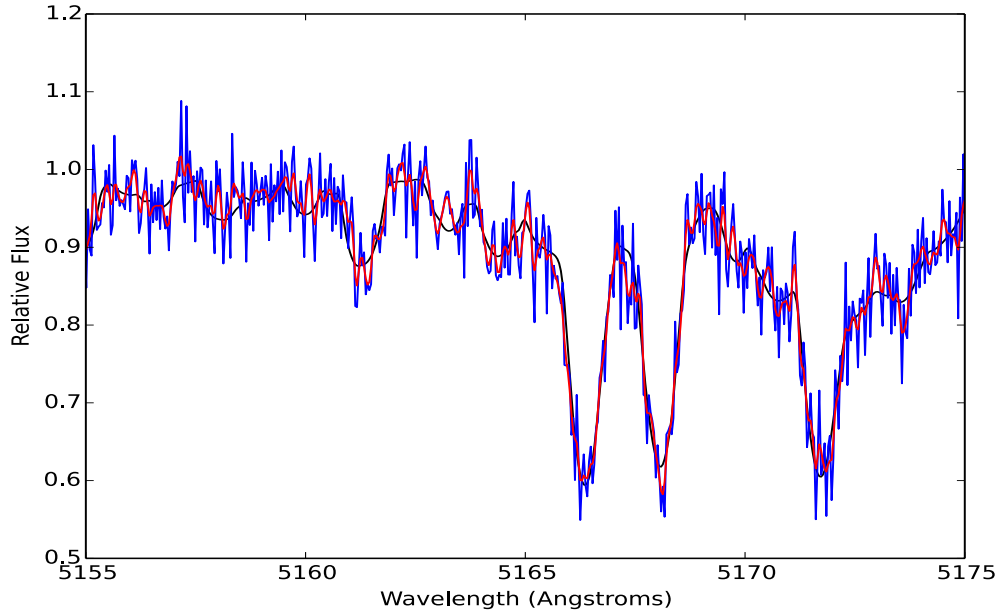


Figure 2.6: A segment of the synthetic observations of *example1* before noise has been added (black line), with Gaussian noise where  $\sigma = 0.04\text{\AA}$  and with noise added (blue line) and subsequent instrumental broadening (red line). A dispersion of  $0.04\text{\AA}$  was applied for the instrumental broadening, mimicking the broadening of the spectrograph on the Kitt Peak 4-m Mayall telescope.

was multiplied by its light fraction and the spectra co-added.

As the PHOEBE 2.0 function for shifting the spectra involves rebinning the data, I found that it was necessary to use a high sampling frequency prior to shifting the spectra, following which I binned the spectra to mimic the dispersion of the observed spectra. Starting with a low sampling frequency led to the spectral profiles changing shape during the rebinning process (as the number of bins is maintained, but the zero point is shifted). After the data had been binned, Gaussian noise was added and the data were instrumentally broadened with a dispersion of  $0.04\text{\AA}$ , equal to the Kitt Peak spectrograph on the 4-m Mayall telescope. Fig. 2.6 depicts a segment of a spectrum with noise added and with subsequent instrumental broadening. Finally, for the purpose of using TODCOR on the data, a line was added to the beginning of each spectrum file denoting the name of the spectrum, date of observation and heliocentric correction.

### Example 1

The first example, *example1*, is an eclipsing binary in a circular orbit that consists of a primary with  $T_{\text{eff}} = 7000 K$  and secondary component with  $T_{\text{eff}} = 6000 K$  in a 10 d orbit. The Gaussian noise added to the spectra has a standard deviation of  $\sigma = 0.04 \text{ \AA}$ . The light and radial velocity curves can be seen in Fig. 2.7. I provide the computed results for both versions of BAYES-TODCOR. Table 2.1 contains the parameters of the model and those determined using BAYES-TODCOR, and Fig. 2.10 depicts the posteriors on the spectral parameters for the CCR version of BAYES-TODCOR. The predefined and computed radial velocities are provided in Table 2.2 and Fig. 2.8 gives the radial velocities and residuals for both versions of BAYES-TODCOR. The radial velocity uncertainties displayed are a combination of the uncertainties provided by TODCOR and the uncertainties from the range of possible spectral models. A section of the fitted spectrum can be seen in Fig. 2.9 for the  $\chi^2$  BAYES-TODCOR software. The red envelope depicts the one sigma range of the model. It can be seen that the black line, the synthetic data without noise, is almost completely encompassed in the red envelope, showing that the model rarely deviates from the “true” values. The posterior distributions of the CCR version of the BAYES-TODCOR software can be seen in Fig. 2.10. All distributions form well defined Gaussians, showing that the results are fully determined.

When comparing the results of the two versions of BAYES-TODCOR for the *example1* binary, which contains two stars that both contribute a significant amount of light, the CCR version produced more accurate and precise radial velocities; however, the  $\chi^2$  version produced more precise and accurate spectral parameters (although the number of parameters is too small to properly discern the overall accuracy). For the CCR version, the distribution of radial velocities with values within  $1\sigma$ , between  $1\sigma$  and  $2\sigma$ , and greater than  $2\sigma$  is as expected for a normal distribution. The  $\chi^2$  version has an excess of radial velocity values that are not in agreement within  $2\sigma$ . This outcome is expected, as the CCR function represents the goodness of fit of the radial

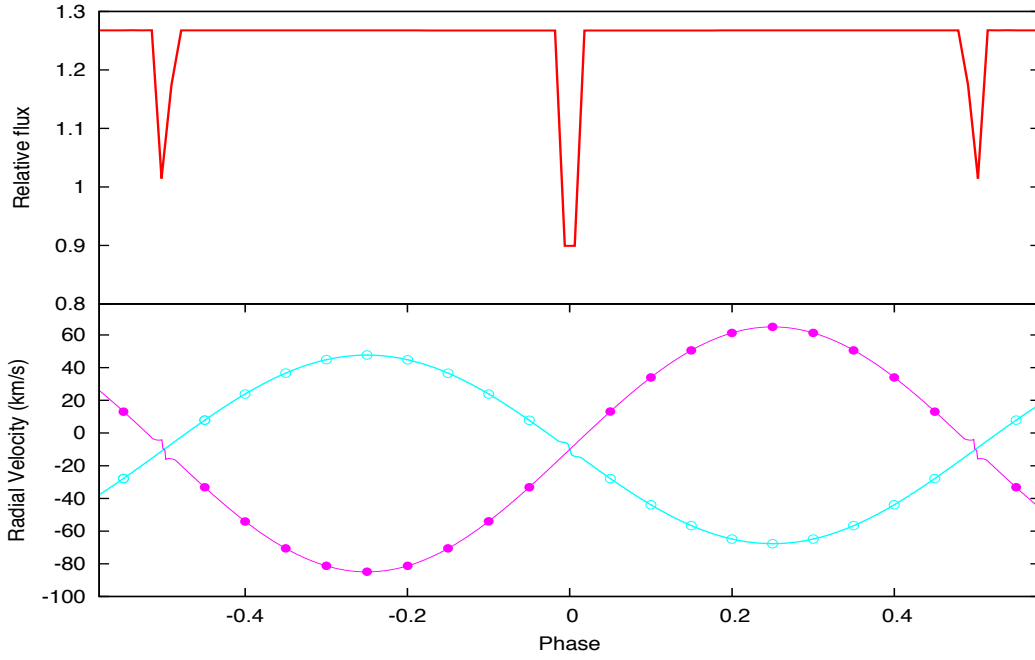


Figure 2.7: The light and radial velocity curve of the *example1* model binary, built to test the BAYES-TODCOR software. The top panel depicts the light curve generated by PHOEBE (red line) and the bottom panel depicts the synthetic radial velocity curves for the primary (blue line) and secondary (pink line) components. The equally spaced radial velocity points depict the phases that synthetic observations were made. Note, synthetic observations were not built during times of eclipse.

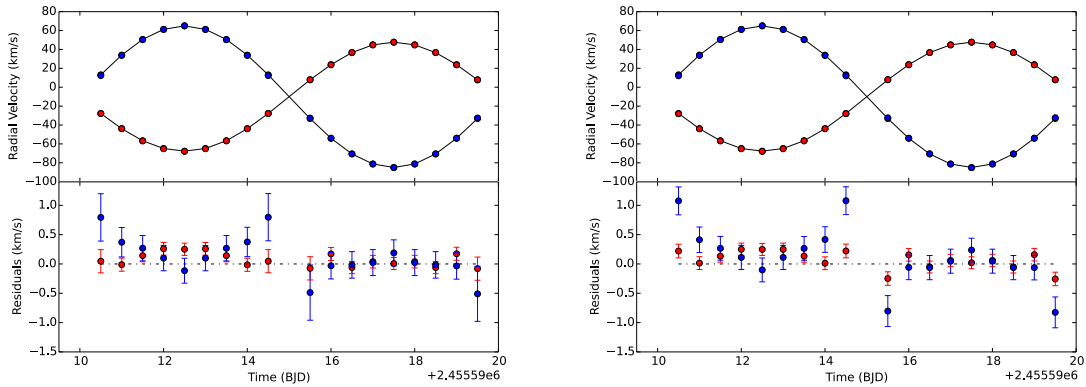


Figure 2.8: The synthetic “observed” and computed radial velocities for the CCR (left panel) and  $\chi^2$  (right panel) versions of the TODCOR software for *example1*. Top panels: the TODCOR computed radial velocity points of the primary (red) and secondary (blue) components. The synthetic “observed” data are denoted by black points and are joined by black lines (the black lines do not represent a model). Lower panels: The residuals of the computed data and their associated one sigma uncertainties.

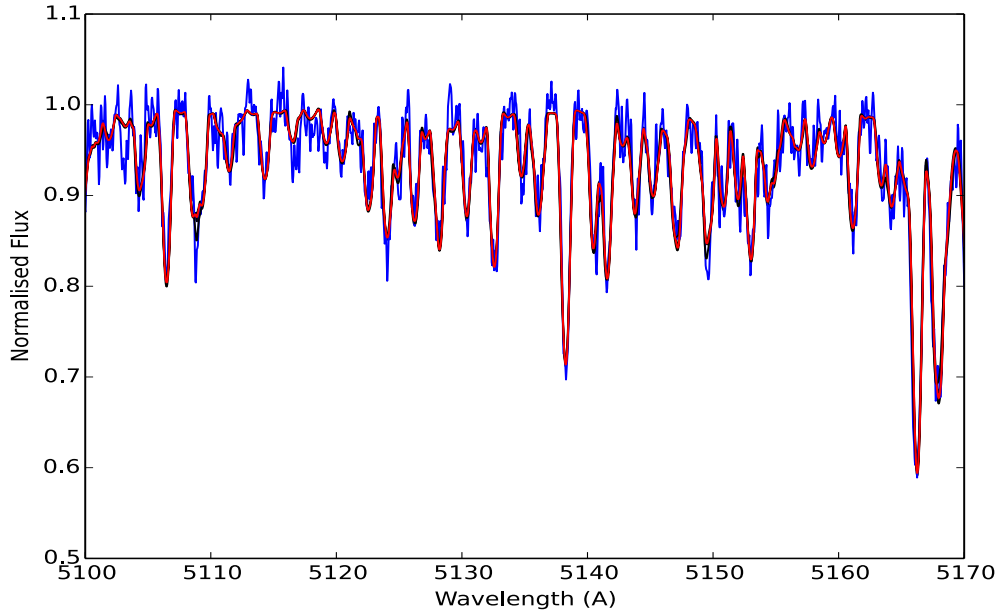


Figure 2.9: A small region of the *example1* synthetic spectral data created for testing (blue). The  $\chi^2$  version of the BAYES-TODCOR best-fit model and one sigma uncertainty (red envelope) are over plotted. The black line depicts the synthetic data without noise. It can be seen that the red envelope almost completely encompasses the black line, showing that this region essentially lies within the one sigma range.

Table 2.1: Parameters of the *example1* synthetic data and corresponding results for the BAYES-TODCOR program using the CCR function and  $\chi^2$ . Alpha denotes the flux ratio. The one sigma uncertainties are given in parentheses. The value highlighted in blue does not agree with the predefined parameter to  $1\sigma$ , but agrees within  $2\sigma$ .

	Input	CCR	$\chi^2$
$T_{\text{eff}1}$	7000	7073(89)	7027(30)
$T_{\text{eff}2}$	6000	6062(116)	5981(32)
$\log g_1$	4.30	4.37(9)	4.32(3)
$\log g_2$	4.43	4.6(1)	4.5(1)
metal	-0.12	-0.10(6)	-0.10(2)
$v \sin i_1$	30	30.0(5)	29.9(1)
$v \sin i_2$	25	25(1)	24.9(3)
alpha	0.28	0.28(2)	0.29(1)

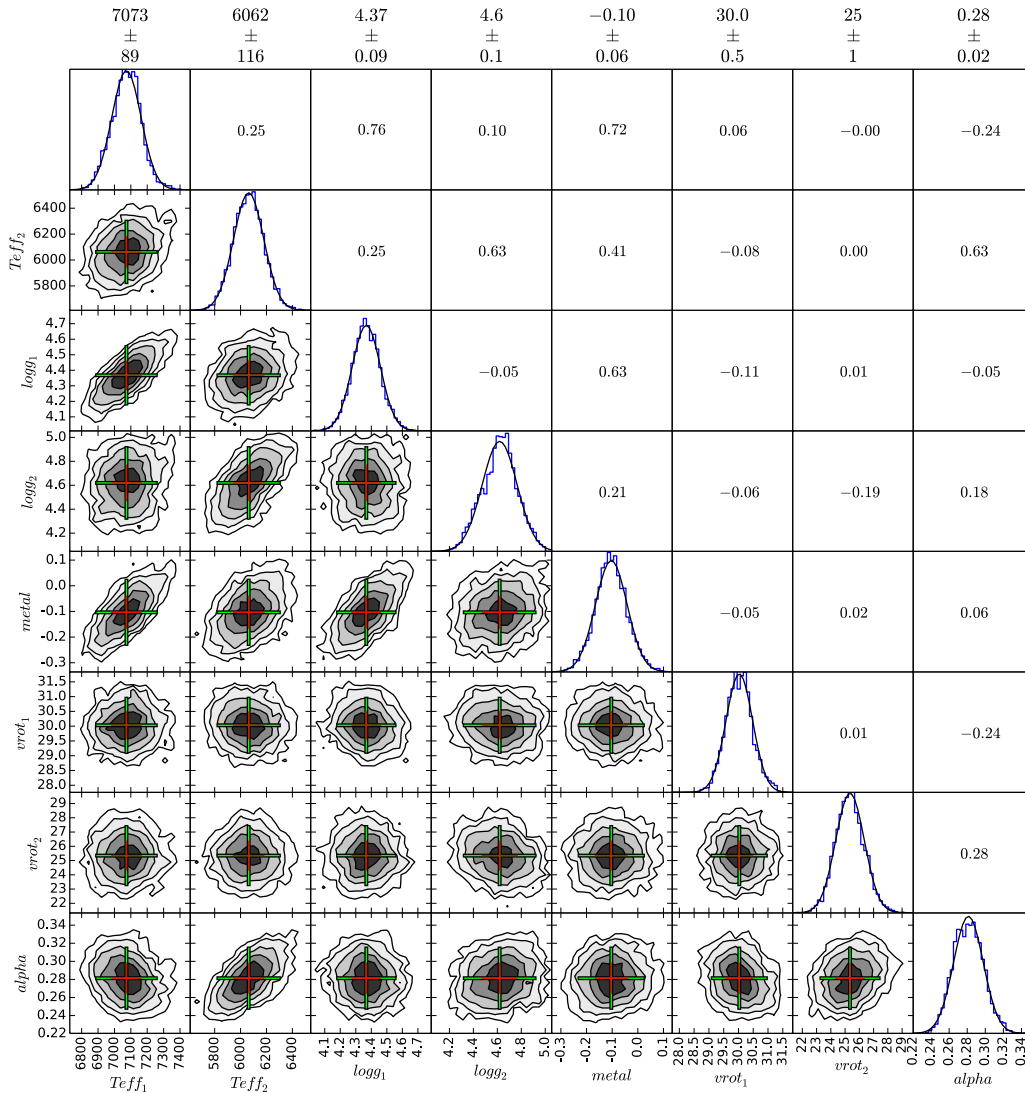


Figure 2.10: The spectral parameter posterior distributions created using the CCR version of the BAYES-TODCOR software for *example1*. Lower left sub-plots: two dimensional cross-sections of the posterior probability distribution functions for the effective temperatures  $T_{\text{eff}1}$  and  $T_{\text{eff}2}$ ;  $\log g_1$  and  $\log g_2$ ; the metallicity of both components, *metal*; the stellar rotational velocities  $v_{\text{rot}1}$  and  $v_{\text{rot}2}$ ; and the light ratio, *alpha*. The crosses show the  $1\sigma$  (red) and  $2\sigma$  (green) uncertainties, and are centred on the minima. Diagonal sub-plots from top left to bottom right: histograms displaying the probability distribution of each individual parameter. Upper right sub-plots: the correlations for the two-dimensional cross-sections mirrored in the diagonal line where 1 is direct correlation and -1 is a direct anti-correlation. The values above the plot give the mean value and one sigma uncertainty for each parameter, based on the fitted Gaussians.

Table 2.2: The radial velocities for the *example1* synthetic data and corresponding results for the BAYES-TODCOR program using the CCR function and  $\chi^2$ . RV1 and RV2 denote the primary and secondary components, respectively. The one sigma uncertainties are given in parentheses. The values highlighted in blue agree with the predefined parameters to  $2\sigma$ , and those highlighted in red do not agree within  $2\sigma$ .

BJD	RV 1			RV 2		
	Synth	CCR	$\chi^2$	Synth	CCR	$\chi^2$
2455600.500050	-27.8	-27.9(2)	-28.0(1)	13.2	12.4(4)	12.0(2)
2455601.000100	-43.9	-43.9(1)	-43.9(1)	34.1	33.7(3)	33.6(2)
2455601.500150	-56.7	-56.8(1)	-56.8(1)	50.6	50.3(2)	50.3(2)
2455602.000200	-64.9	-65.1(1)	-65.1(1)	61.3	61.2(2)	61.1(2)
2455602.500250	-67.7	-67.9(1)	-65.9(1)	64.9	65.0(2)	65.0(2)
2455603.000300	-64.8	-65.1(1)	-65.0(1)	61.2	61.1(2)	61.1(2)
2455603.500350	-56.7	-56.8(1)	-56.8(1)	50.6	50.3(2)	50.3(2)
2455604.000400	-43.9	-43.9(1)	-43.9(1)	34.0	33.6(3)	33.6(2)
2455604.500450	-27.8	-27.9(2)	-28.0(1)	13.1	12.4(4)	12.0(2)
2455605.500550	7.8	7.9(2)	8.1(1)	-33.3	-32.7(5)	-32.4(3)
2455606.000600	23.9	23.7(1)	23.8(1)	-54.1	-54.0(2)	-54.0(2)
2455606.500650	36.7	36.7(1)	36.7(1)	-70.6	-70.6(2)	-70.5(2)
2455607.000700	44.9	44.8(1)	44.8(1)	-81.3	-81.3(2)	-81.3(2)
2455607.500750	47.7	47.7(1)	47.6(1)	-84.9	-85.1(2)	-85.1(2)
2455608.000800	44.8	44.8(1)	44.8(1)	-81.2	-81.3(2)	-81.3(2)
2455608.500850	36.6	36.7(1)	36.7(1)	-70.6	-70.6(2)	-70.5(2)
2455609.000900	23.9	23.7(1)	23.7(1)	-54.0	-54.0(2)	-54.0(2)
2455609.500950	7.8	7.9(2)	8.0(1)	-33.1	-32.6(4)	-32.3(3)

velocities, and is not sensitive to the depths of the lines. Furthermore, the current implementation of the  $\chi^2$  version of BAYES-TODCOR does not take into account the uncertainty of the radial velocities attributed by TODCOR and consequently the results are not expected to be as precise.

### Example 2

The second example, *example2*, is a heartbeat with two components of  $T_{\text{eff}1} = 8000$  K and  $T_{\text{eff}2} = 3500$  K, respectively, in a 30-d orbit. The Gaussian noise added to the spectra has  $\sigma = 0.04$  Å. Table 2.3 contains the parameters of the synthetic data and the corresponding model values determined by both versions of BAYES-TODCOR. The light and radial velocity curves can be seen in Fig. 2.11. The input and computed radial velocities are provided in Table 2.4. A section of the fitted spectrum can be seen in Fig. 2.13 for the  $\chi^2$  BAYES-TODCOR software. The red envelope depicts the one sigma range of the model. It can be seen that the black line, the synthetic data without noise, is completely encompassed in the red envelope, showing that the model fits within the specified errors. The posterior distributions of the CCR version of the BAYES-TODCOR software can be seen in Fig. 2.14. All distributions form well defined Gaussians, showing that the results are fully determined, with the exception of  $\alpha$ , which is very close to zero, as expected.

The comparison of the two versions of software for *example2* produced some slightly unexpected results. While I did not expect that either version would identify the spectral parameters or radial velocities for the secondary component due to its 1% light contribution, for the CCR version, the low light contribution of the secondary component significantly affected the identification of spectral parameters for the primary component. The results suggest that the spectral parameters for both components are unreliable for the CCR version, and conversely, the results for both components are reliable for the  $\chi^2$  version. Interestingly, the determination of  $v \sin i$  is accurate for both methods. Moreover, the radial velocities determined by the CCR

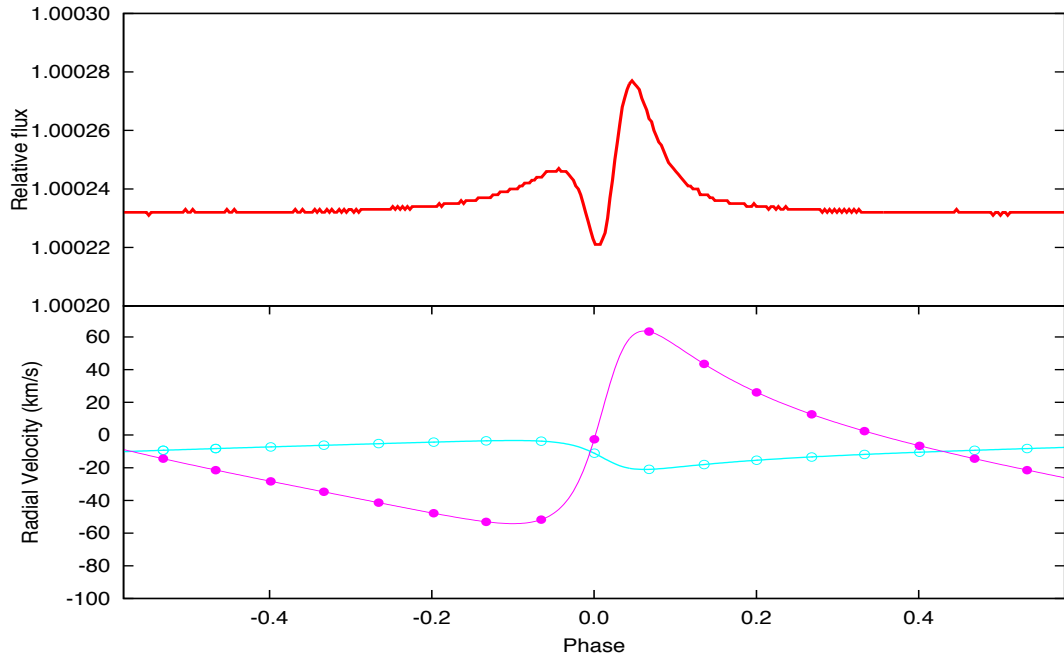


Figure 2.11: The light and radial velocity curve of the *example2* model binary, built to test the BAYES-TODCOR software. The top panel depicts the light curve generated by PHOEBE (red line) and the bottom panel depicts the synthetic radial velocity curves for the primary (blue line) and secondary (pink line) components. The equally spaced radial velocity points depict the phases at which synthetic observations were made.

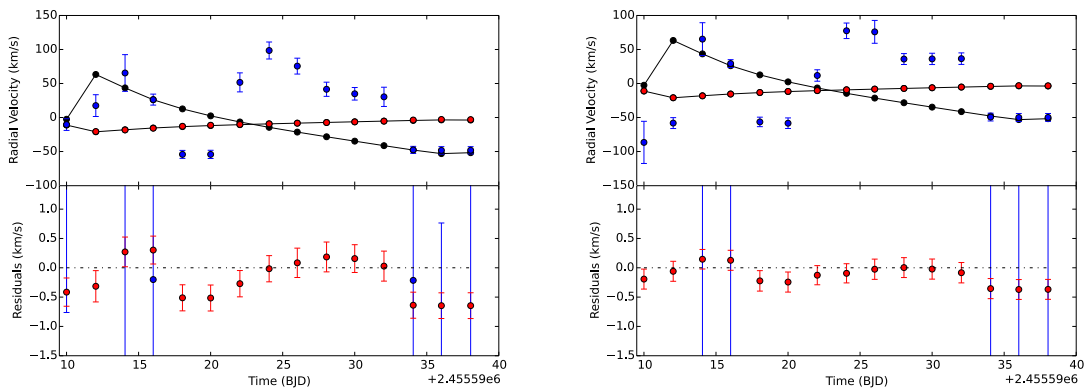


Figure 2.12: The synthetic “observed” and computed radial velocities for the CCR (left panel) and  $\chi^2$  (right panel) versions of the TODCOR software for *example2*. Top panels: the TODCOR computed radial velocity points of the primary (red) and secondary (blue) components. The synthetic “observed” data are denoted by black points and are joined by black lines. Lower panels: The residuals of the computed data and their associated one sigma uncertainties. As expected due to its low light contribution, the secondary component’s radial velocities have not been accurately reproduced.

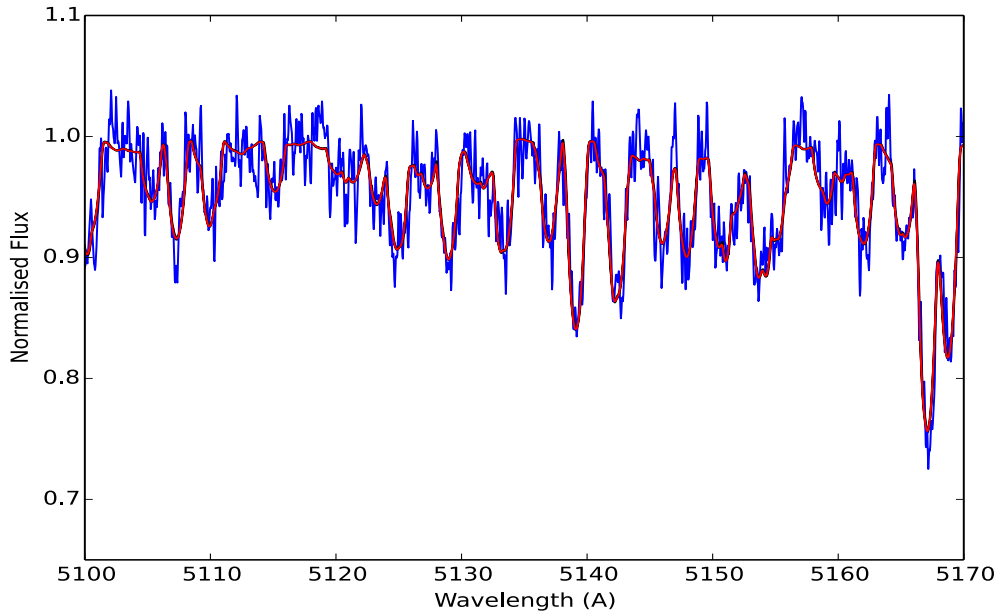


Figure 2.13: A small region of the *example2* synthetic spectrum created for testing (blue). The BAYES-TODCOR best-fit model (red line) and one sigma uncertainty (red envelope, not visible due to small uncertainties) are over plotted. The synthetic data without noise (black line) can barely be seen as black line is completely encompassed by the red envelope, showing that this region completely lies within the one sigma errors. The results from the  $\chi^2$  version of the software were used to create this plot.

Table 2.3: Parameters of the *example2* synthetic data and corresponding results for the BAYES-TODCOR program using the CCR function and  $\chi^2$ . The one sigma uncertainties are given in parentheses. The values highlighted in blue agree with the predefined parameters to  $2\sigma$  precision, and those highlighted in red do not agree within  $2\sigma$ .

	Input	CCR	$\chi^2$
$T_{\text{eff}1}$	8000	7869(61)	7966(31)
$T_{\text{eff}2}$	3500	3892(285)	4014(300)
$\log g_1$	4.29	4.14(7)	4.25(4)
$\log g_2$	4.90	4.3(6)	3.9(6)
metal	+0.3	0.22(4)	0.28(2)
$v \sin i_1$	50	49.8(6)	49.6(4)
$v \sin i_2$	10	8(7)	7(5)
light	0.001	0.003(1)	0.001(1)

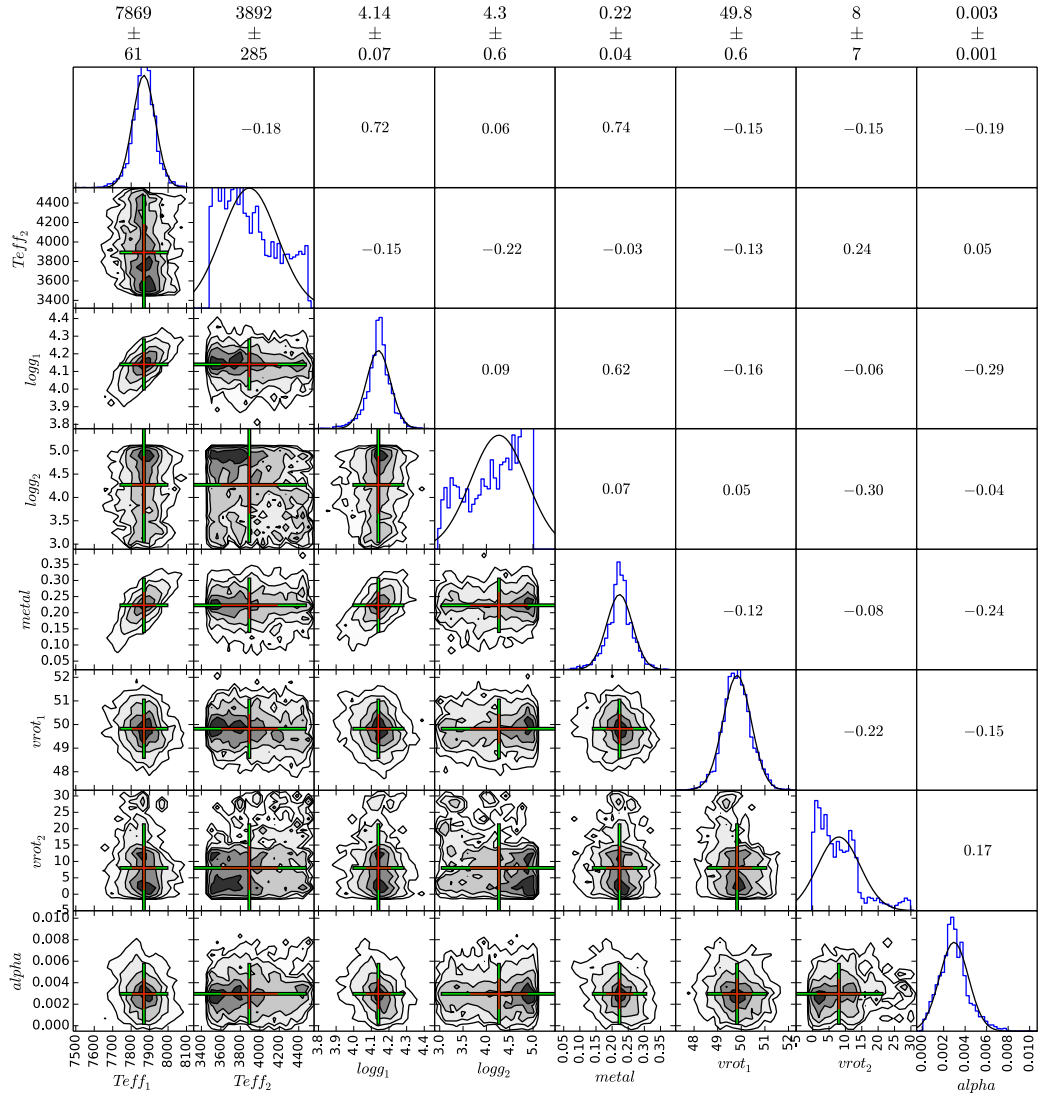


Figure 2.14: The spectral parameter posterior distributions created using the CCR version of the BAYES-TODCOR software for *example2*. Lower left sub-plots: two dimensional cross-sections of the posterior probability distribution functions for the effective temperatures  $T_{\text{eff}1}$  and  $T_{\text{eff}2}$ ;  $\log g_1$  and  $\log g_2$ ; the metallicity of both components, *metal*; the stellar rotational velocities  $v_{\text{rot}1}$  and  $v_{\text{rot}2}$ ; and the light ratio, *alpha*. The crosses show the  $1\sigma$  (red) and  $2\sigma$  (green) uncertainties, and are centred on the minima. Diagonal sub-plots from top left to bottom right: histograms displaying the probability distribution of each individual parameter. Upper right sub-plots: the correlations for the two-dimensional cross-sections mirrored in the diagonal line where 1 is direct correlation and -1 is a direct anti-correlation. The values above the plot give the mean value and one sigma uncertainty for each parameter, based on the fitted Gaussian distributions. As expected, due to the low light contribution of the secondary component, the Gaussian distributions do not fit the histograms for the secondary component parameters.

Table 2.4: The radial velocities for the *example2* synthetic data and corresponding results for the BAYES-TODCOR program using the CCR function and  $\chi^2$ . RV1 and RV2 denote the primary and secondary components, respectively. The one sigma uncertainties are given in parentheses. The values highlighted in blue agree with the predefined parameters to  $2\sigma$  precision, and those highlighted in red do not agree within  $2\sigma$ .

BJD	RV 1			RV 2		
	Synth	CCR	$\chi^2$	Synth	CCR	$\chi^2$
2455600.000000	-11.11	10.7(3)	-10.9(2)	-2.58	-10(9)	-86(31)
2455602.030075	-20.99	-20.6(3)	-20.9(2)	63.29	-2(10)	-58(8)
2455604.060150	-18.03	-18.3(3)	-18.2(2)	43.54	53(20)	65(24)
2455606.015038	-15.42	-15.8(3)	-15.5(2)	26.12	25(9)	29(6)
2455608.045113	-13.40	-12.8(2)	-13.2(2)	12.66	-54(7)	-56(7)
2455610.000000	-11.86	-11.3(2)	-11.6(2)	2.40	-55(6)	-58(8)
2455612.030075	-10.52	-10.2(2)	-10.4(2)	-6.56	27(10)	12(9)
2455614.060150	-9.33	-9.3(2)	-9.2(2)	-14.45	77(13)	77(12)
2455616.015038	-8.28	-8.4(3)	-8.3(2)	-21.43	60(11)	76(17)
2455618.045113	-7.25	-7.5(3)	-7.3(2)	-28.31	36(12)	36(8)
2455620.000000	-6.29	-6.5(3)	-6.3(2)	-34.75	33(11)	36(8)
2455622.030075	-5.29	-5.4(3)	-5.2(2)	-41.37	27(16)	37(8)
2455624.060150	-4.32	-3.6(2)	-4.0(2)	-47.84	-47(6)	-49(6)
2455626.015038	-3.54	-2.9(2)	-3.2(2)	-53.08	-48(6)	-50(6)
2455628.045113	-3.74	-3.1(2)	-3.4(2)	-51.74	-48(6)	-50(6)

version of the program were less accurate and less precise than the  $\chi^2$  version, unlike the results for *example1*. I expect that this is a consequence of the cross correlation of the two model spectra in TODCOR and believe that one dimensional cross correlation would provide better results for these systems. However, this would require removing TODCOR from BAYES-TODCOR and replacing it with a one-dimensional cross correlation program, and consequently is beyond the scope of this work. As the agreement of the radial velocity results follows a normal distribution for the  $\chi^2$  version of the software, the  $\chi^2$  version is deemed more applicable to systems with a dim secondary component. More investigation is required to identify the precise light level where the CCR version of the software is better for radial velocity determination. However, I suspect that the crossover will occur at  $\sim 3\%$  light contribution from the secondary, as this is the specified lower limit for detection of the secondary using TODCOR.

### 2.4.2 Comparison of Uncertainties

To combine the uncertainties from TODCOR with those arising from having a range of possible models, I elected to create a Gaussian for each MCMC chain that comprised the radial velocity measurement (for the primary or secondary component) as the mean and the corresponding TODCOR uncertainty as the standard deviation. Each Gaussian was normalised to 1 and the Gaussian distributions were co-added for each spectrum and each component. On occasion I found that the combination of model and TODCOR uncertainties was smaller than the TODCOR uncertainties alone (see Table 2.5). This is an effect of adding normal distributions. It is expected, however, that BAYES-TODCOR will provide improved uncertainty estimates where the likelihood function is not directly derived from the observed data.

Table 2.5: A comparison of the radial velocity uncertainties between TODCOR and the  $\chi^2$  BAYES-TODCOR software for *example2*. RV1 and RV2 denote the primary and secondary components, respectively. The uncertainty for the primary component is only marginally increased. However, it is anticipated that the difference will be more significant for real objects, where the likelihood function and observed data are less similar. In some cases, the TODCOR uncertainty is greater than the BAYES-TODCOR uncertainty (highlighted in red). This is a consequence of combining Gaussian distributions with similar parameters. The secondary component displays larger differences, which can be attributed to the low contribution of light from the secondary component.

BAYES-TODCOR RV 1	TODCOR RV 1	BAYES-TODCOR RV 2	TODCOR RV 2
0.169	0.161	30.97	5.97
0.170	0.162	8.04	6.69
0.167	0.162	23.96	6.67
0.170	0.162	5.67	6.47
0.173	0.163	6.99	6.60
0.170	0.161	7.83	6.94
0.163	0.160	8.86	4.48
0.163	0.160	11.76	4.54
0.172	0.163	17.18	6.79
0.169	0.171	8.19	7.25
0.170	0.163	8.46	9.15
0.173	0.165	8.64	9.43
0.170	0.160	5.78	5.47
0.168	0.159	5.88	5.79
0.168	0.159	5.78	5.58

### 2.4.3 Spectral Reduction

KIC 8164262 is a single lined spectroscopic binary that is discussed at length in Chapter 4. I obtained two follow-up spectroscopic measurements for this object at Kitt Peak Observatory using the Echelle spectrograph on the 4-m Mayall telescope (for more details on the instrument set-up see Chapter 4). These spectra provided an opportunity to apply the BAYES-TODCOR program to real observations and also provided spectral parameters and radial velocities that were key to generating the binary star model for KIC 8164262. Before I could apply BAYES-TODCOR to these data, I first needed to convert them into a usable format. This was done using IRAF (Tody, 1986).

The first step in reducing the spectra is to debias the images. To debias is to remove the electronic background counts that are inherent to the CCD (and thus not the observations). At the beginning and end of each observing night, bias frames were made, each lasting zero seconds such that only the electron count of the CCD was read out. To remove the average bias from the images, a master bias must be made that contains the median from all the bias frames for each pixel on the CCD. The median is used so that cosmic rays do not affect the master bias. This master bias is then removed from all the science frames and master comparison lamps by subtraction.

We elected to observe two back-to-back science frames of the same object instead of a single science frame of equal exposure time to aid with cosmic ray removal. While this takes longer per object due to read out time, it significantly reduces the time required to manually remove the cosmic rays. When combining the two back-to-back science images, I took the mean, but combined this with one of IRAF's cosmic ray detection algorithms that eliminates the high pixels above a relative threshold. While a few still remain, this significantly reduces the number of cosmic rays in the data.

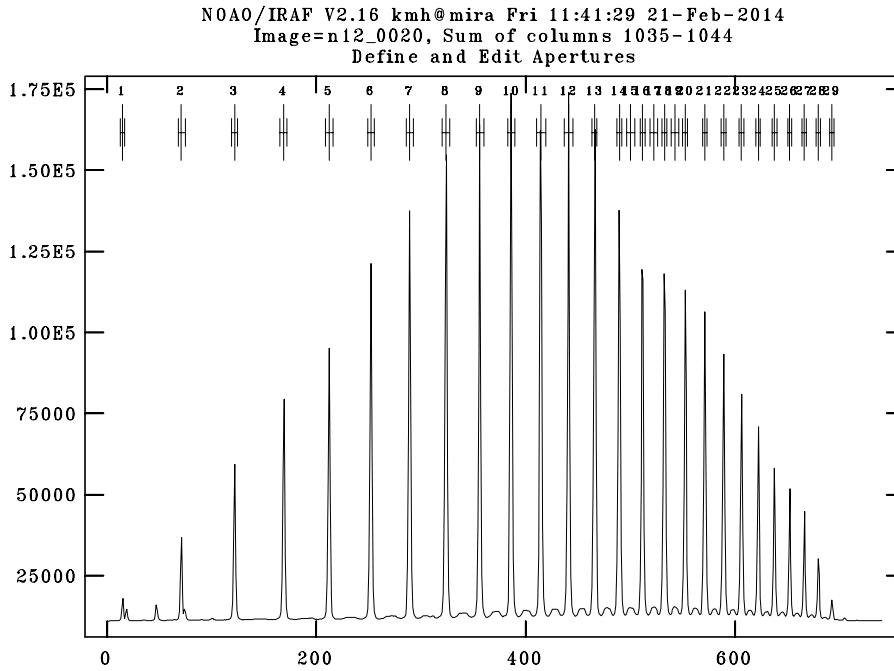


Figure 2.15: An IRAF image of the apertures for KIC 8164262 on night 12. The x-axis is in pixels and the y-axis is in photon counts. The cross hairs and boxes above each aperture are adjusted to select the appropriate centre and width of each aperture.

The next step is to remove the flat field image. A flat field is a representation of the dead pixels and sensitivity variation over the CCD. In our case we elected to make ten 10-s images of the illuminated screen on the dome at the beginning and end of each night (also known as dome flats) and average these to create a master flat-field image. Again, the master flat must also be the median of all the flats taken in one night to avoid cosmic rays. The profile of the blaze function and spectrum shape are then modelled, “flattened”, and removed from the master flat so that only the flat field variations remain. In doing this the spectral image is transformed into one dimension. This is done so that the sharp aperture profiles, low counts between apertures and possible shifts (between the master flat and the science frames) do not affect the flattening of the science frames. The science frame must then be extracted into one dimension and divided by the “flattened” flat.

To generate a one dimensional spectrum, the apertures must be defined, traced and removed from the two dimensional images. The first step is to select the apertures and indicate their centres and widths, as shown in Fig.2.15. Following this the

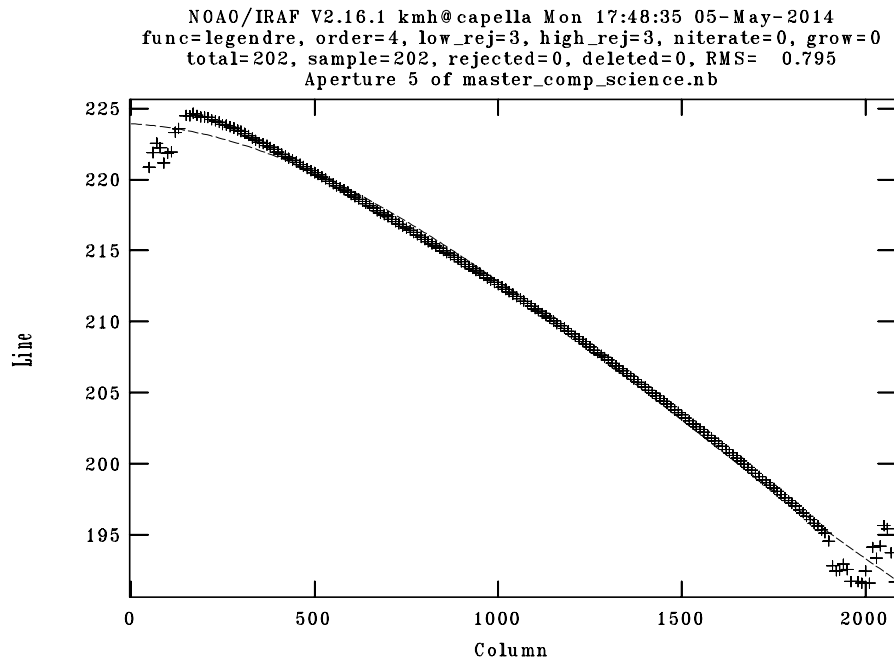


Figure 2.16: Depicted is an IRAF image of the binned photons along one aperture and the polynomial fit (trace) to those photons for a comparison lamp. The points at the ends are excluded to improve the fit.

apertures must be traced by fitting a high order polynomial along each aperture to the points representing binned photons (see Fig. 2.16). This is used to adjust the centres of the apertures at each dispersion point, and must be done to all science images and calibration lamps.

Once the data are in one dimension, the remaining cosmic rays must be extracted. This must be done by hand, although there should not be a significant number remaining due to the merging of back-to-back spectra. The removal only needs to be done for the science frames as the comparison lamps have significantly more counts and consequently cosmic rays rarely interfere with the inherent information. The exposures for comparison lamps are also shorter and so fewer cosmic rays are incident on the CCD during that time.

The spectra are now clean, but still in pixel space. To convert them to wavelength space they must be calibrated using the master lamp - the long exposure lamp taken at the beginning or end of the night, in our case using a ThAr lamp. To

do this several lines on each aperture of the one-dimensional master lamp must be identified by comparing the master lamp to a previously calibrated lamp, preferably from the same instrument. Once a significant number of lines has been identified, IRAF performs a fit to the remaining spectral lines so that the spectrum of the lamp can be displayed in wavelength space. The next step is to use the master lamp to identify the lines in the comparison lamp taken with the instrument pointing at the science object you wish to reduce. This step ensures that the lines, and thus the wavelength scale, do not suffer from shifts due to the motion of the instrument. The comparison lamp is calibrated, as this has known and strong emission lines that are more easily identified than those of an observed spectrum. Once the comparison lamp with the same pointing as the science frame has been calibrated, it can be used to calibrate the science frame.

Finally, to produce a normalised spectrum, a function, usually a Chebyshev polynomial, cubic spline or Legendre polynomial, is fitted to the continuum of each aperture and divided out. The apertures are then in a format that can be merged within IRAF. This provides the final product to which BAYES-TODCOR can be applied.

#### 2.4.4 Application to Observed Data

In §2.4.1 I determined that both versions of BAYES-TODCOR generated acceptable results when tested against synthetic data (where the synthetic spectra and observed spectra were derived from the same models), providing posteriors for the stellar properties with values all within, or close to one sigma of the predefined values. When applying this method to real spectra, however, if the observed spectrum contained lines that weren't in the line list, I found that both the CCR and  $\chi^2$  versions had a bias towards metal poor synthetic spectra. In the CCR version, the reason for this is that cross correlation is far more sensitive to the presence of extra lines than it is to their depths, thus by reducing the metallicity the number of lines was

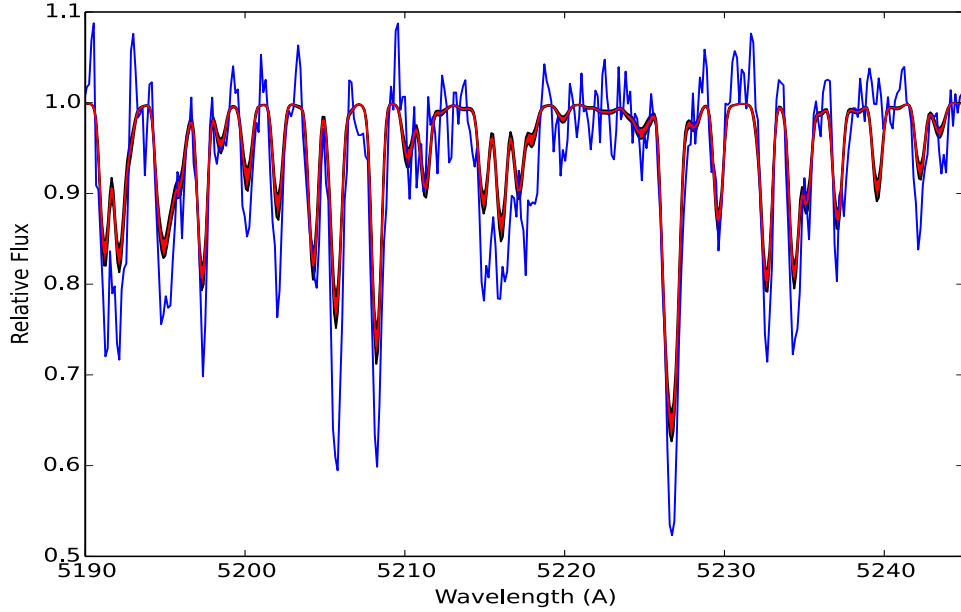


Figure 2.17: Depicted are the observed spectral data of KIC 8164262 (blue), and the fit to the data using BAYES-TODCOR (red). The thickness of the line denotes the one sigma uncertainty. It can be seen that there is a large discrepancy in the depths of the lines, which has been attributed to the use of TODCOR’s cross correlation function as the fitting parameter.

also reduced, allowing for higher correlation scores (see Fig. 2.17). The  $\chi^2$  version was not impacted as badly; however, it still tended towards lower metallicities to find a balance between finding the best fit and accounting for the inadequacy of the likelihood function.

I consequently applied the  $\chi^2$  version of BAYES-TODCOR to the two reduced spectra of KIC 8164262. I elected to fit the spectra by fixing the metallicity to  $[Fe/H] = 0.5$ .

Table 2.6: Parameters and radial velocities of for KIC 8164262 generated using the BAYES-TODCOR  $\chi^2$  software for the fix metallicity of  $[Fe/H] = 0.5$ . When using the  $\log g$  value from the run with free metallicity, the model would not fit the data as the amplitude of the periastron brightening was too large. The one sigma uncertainties are given in parentheses.

$T_{\text{eff}1}$ (K)	6999(83)
$\log g_1$ (dex)	3.9(1)
$v \sin i$ ( $\text{km s}^{-1}$ )	22.9(9)
alpha	0.002

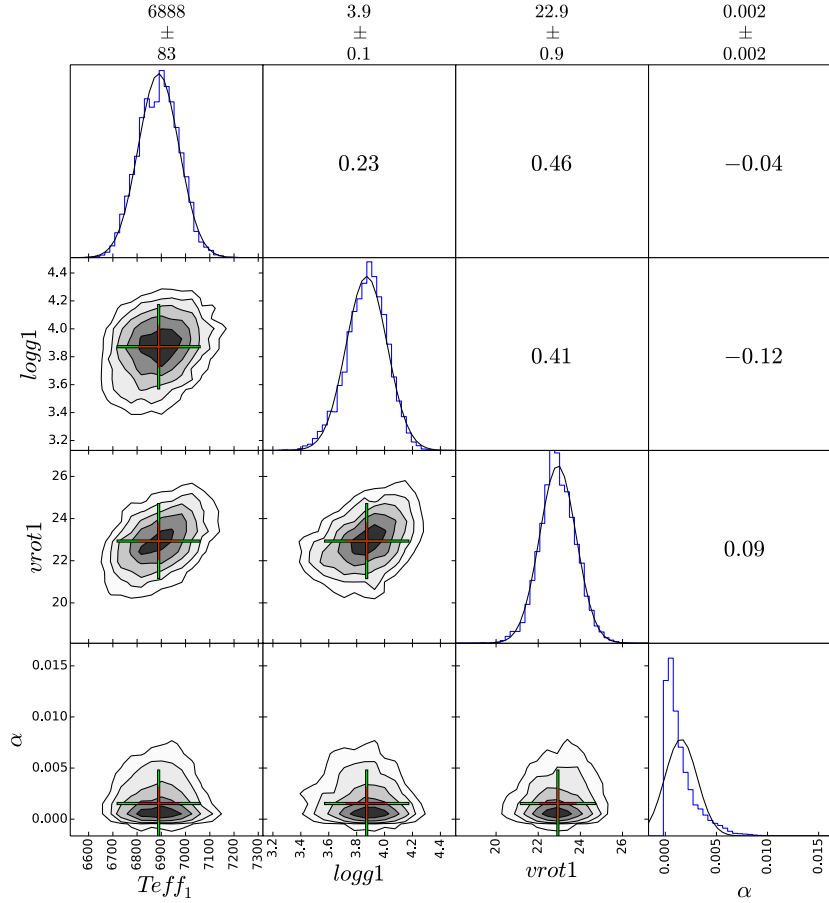


Figure 2.18: Depicted are the posteriors generated using the BAYES-TODCOR program with the two observed spectra of KIC 8164262. I elected to fix the metallicity to  $[Fe/H] = 0.5$  through consideration of the spectra by eye. Lower left sub-plots: two dimensional cross-sections of the posterior probability distribution functions for the primary effective temperature,  $T_{\text{eff}1}$ ; the primary surface gravity,  $\log g_1$ ; the primary stellar rotational velocity  $v_{\text{rot}1}$ ; and  $\alpha$ , the light ratio. The crosses show the  $1\sigma$  (red) and  $2\sigma$  (green) uncertainties, and are centred on the minima. Diagonal sub plots from top left to bottom right: histograms displaying the probability distribution of each individual parameter. Upper right sub-plots: the correlations for the two-dimensional cross-sections mirrored in the diagonal line where 1 is direct correlation and -1 is a direct anti-correlation. The values above the plot give the mean value and one sigma uncertainty for each parameter, based on the fitted Gaussians.

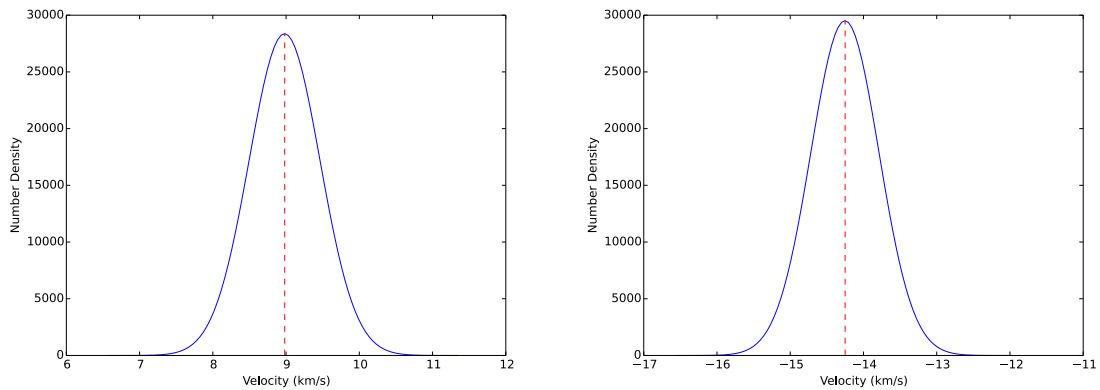


Figure 2.19: Depicted are the distributions of radial velocities of the primary component for the first observed spectrum (left) and second observed spectrum (right) of KIC 8164262. The distributions contain the spread due to the uncertainty in the radial velocity shift and uncertainty in the template spectrum for 100 iterations of BAYES-TODCOR. The dashed red line denotes the mean radial velocity in each case.

I selected  $[Fe/H] = 0.5$ , as when fitted by eye, a high metallicity was required to fit the hydrogen and metal lines simultaneously (spectral fitting by eye was carried out by S. Murphy). When fixing the metallicity to  $[Fe/H] = 0.5$ , the generated parameters allowed for a realistic model that fit the data, unlike the models produced when allowing the metallicity to be a free parameter. The parameters and radial velocities obtained are provided in Table 2.6 and depicted in Figs. 2.18 and 2.19, respectively. When allowing the metallicity to be free (for both versions), the  $\log g$  became too low to appropriately fit the data: the periastron brightening became excessively large in the model. Furthermore, as the primary component is a slowly rotating A star ( $v \sin i = 22.9(9) \text{ km s}^{-1}$ ), the low turbulence enables the diffusion of heavier elements to occur and consequently I expect the metallicity to be greater than solar metallicity.

## 2.5 Conclusion

The BAYES-TODCOR program has been discussed in its current state, including an outline of the testing and application to real data. As it stands, there are two versions, one that uses CCR as the likelihood function and one that uses  $\chi^2$ : both have

pros and cons. The CCR version has been found to be more applicable to determining radial velocities in systems where the secondary component has a significant light contribution, whereas the  $\chi^2$  version is significantly better at determining radial velocities for systems where the secondary component has a low light level. The point at which these two programs cross over has not yet been determined, although I speculate that it occurs when the light contribution of the secondary is  $\sim 3\%$ , when TODCOR is no longer able to detect the secondary component.

I further found that the  $\chi^2$  version is better at determining the spectral parameters for both situations, because  $\chi^2$  is sensitive to all the information in the spectrum, whereas the CCR function is not sensitive to the depth of the lines (but rather the placement of the lines). In both cases the sensitivity is problematic with real spectra. I found that the CCR version tends to lower metallicities to reduce the number of lines in the synthetic spectra, as fewer well-placed lines provide a better correlation score than lines that don't match perfectly (which are expected in real spectra). For the  $\chi^2$  version, the sensitivity of the  $\chi^2$  statistical test to the complete spectrum makes the results very sensitive to the normalisation, and again the number of lines. The ideal statistical test would consider the equivalent width of the lines, as well as the horizontal offset; however, this is beyond the scope of the current work.

The uncertainties provided by BAYES-TODCOR could also be improved by changing the method for combining uncertainties. For example, combining the uncertainties from the range of possible models with the uncertainties from TODCOR using the sum of squares. It has also been suggested by Mazeh (private communication) that when using TODCOR for a single Echelle order it is likely that the uncertainties are generally underestimated, and only by running TODCOR on several apertures separately and combining their uncertainties, can the true uncertainties be ascertained. While this is not implemented in the current version of BAYES-TODCOR to obtain more accurate uncertainty estimates, this would certainly be the next step.

Alongside improvements to the method of combining uncertainties, further tests

on known, well-studied, standard stars should also be undertaken to determine the accuracy that can be expected for real observations and to further discriminate between the uses of the different versions. As TODCOR is not able to fit single-lined spectra adequately, the implementation of one-dimensional cross correlation would likely be a valuable addition. To then finalize the software, all methods should be combined into a single piece of software and a user adjustable input file made, where the user can specify if the object is double or single lined, and the method is then selected on that basis. Other user inputs would include spectral parameter ranges and file names so that the user can fully command the adjustable parameters, and accurately determine the radial velocities and spectral parameters of their binary stars.

# Chapter 3

## The Heartbeat Phenomenon

In close binary systems, tidal interactions between the stellar components cause the stars to become distorted and prolate, with the point of the star extending towards the companion (see Fig. 3.1). Consequently, as the stars progress around the orbit, the stellar profile changes, which creates variations in the observed flux over the orbital period. When combined with the effect of stellar rotation, this phenomenon is known as ellipsoidal variation. In circular systems the light varies periodically, twice per orbit. In eccentric systems, such as heartbeat stars, the same physical principles apply, although due to the varying distance between the stars over the orbit, the stellar shapes are also constantly changing (see Fig. 3.2).

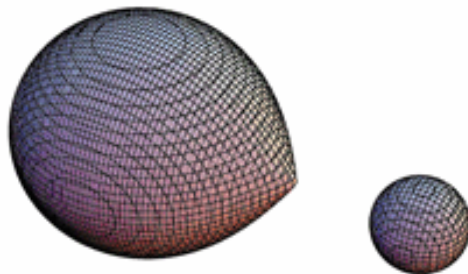


Figure 3.1: An image of a tidally distorted star in a binary system. Due to the gravitational force of the companion, the morphology of the star has become distorted and prolate with the point facing the companion. Although exaggerated in this image, this is one of the two primary effects that give heartbeat star light curves their characteristic shape. Adapted from <http://astro.matf.bg.ac.rs/> (the University of Belgrade)

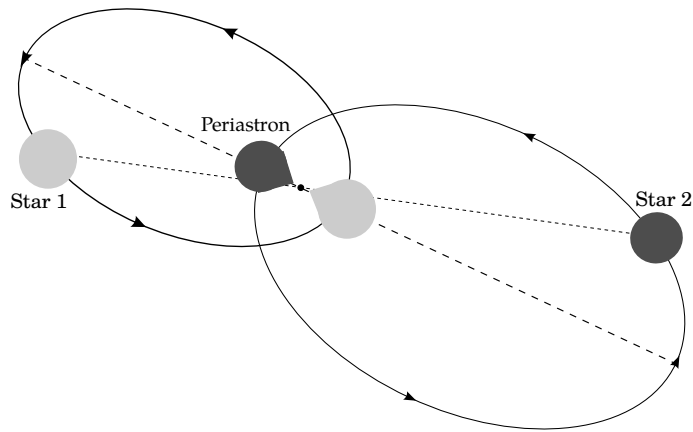


Figure 3.2: A schematic diagram of a heartbeat star orbit depicting the stars at two phases: periastron and a random phase away from periastron. At periastron, due to the gravitational forces of their companions, *star 1* and *star 2* become tidally distorted into a tear drop shape. As heartbeat stars are highly eccentric ( $e = \sim 0.3\text{--}0.9$ ), the tidal distortions are significantly stronger during a small part of the orbit and for the remaining orbit the stars are essentially spherical.

Thus the dominant variation in the light curve, known as the periastron variation or “heartbeat”, occurs once per orbital cycle, at periastron (the time of closest approach).

The first heartbeat star, KOI-54 (depicted in the top panel of Fig. 3.3), was discovered using the *Kepler* satellite (Welsh et al., 2011). Shortly after, many more discoveries were made, including those by: Thompson et al. (2012), who published a catalogue of 17 heartbeat stars from the *Kepler* field; Nicholls & Wood (2012), who identified seven heartbeat stars in the Large Magellanic Cloud using the OGLE survey; one by CoRoT Hareter et al. (2014) using the CoRoT satellite; one by Schmid et al. (2015) using the *Kepler* satellite; and more recently in the *Kepler Binary Star Catalog 3* paper (Kirk et al., 2016), an extensive catalogue of 173 heartbeat stars, observed using the *Kepler* satellite; followed by one analysed by Richardson et al. (2016) using the MOST telescope, which was followed up using the CHARA array. Fig. 3.3 shows a selection of heartbeat stars from the *Kepler* sample. These heartbeat stars were identified through a combined effort from the *Heartbeat* Star Team (including myself), the Planet Hunters, the Eclipsing Binary Working Group and other independent sources, and is the sample upon which this work is based. To ensure each object in this list is a legitimate heartbeat star, I have personally de-

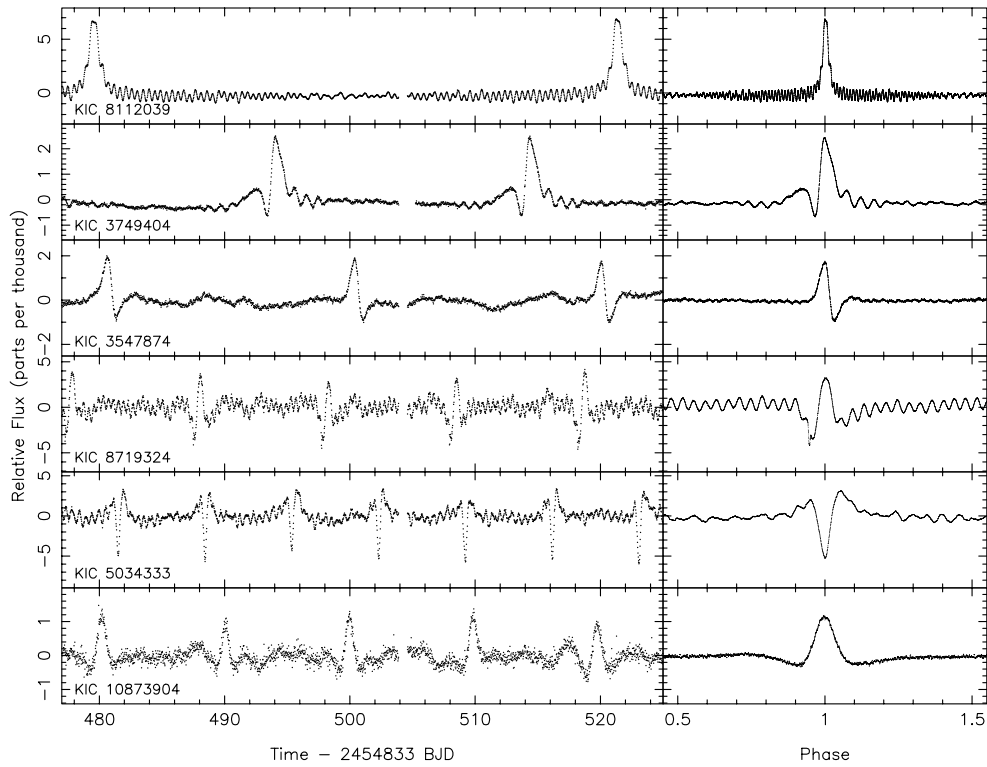


Figure 3.3: A selection of heartbeat stars from the *Kepler* sample. Depicted are the time series (left panel) and phase folded data (right panel). The phase folded data clearly show the pulsations that are integer multiples of the orbital frequency: tidally induced pulsations. KIC 8112039 is KOI-54.

trended the data, determined the period and phase plotted each one using KEPHEM (Prša et al., 2011). I then assessed each phased light curve thoroughly, considering its morphology, amplitude and period, to determine the nature of the variations. If necessary, I then requested a second opinion from other members of the *Heartbeat* Star Team. While radial velocities would provide a definitive answer, this method has so far been successful for our purposes.

Our current sample of 173 heartbeat stars identified in the *Kepler* data<sup>1</sup> primarily contains stars of main sequence spectral type G–A, suggesting that there is a dearth of main sequence heartbeat stars with temperatures less than 5200 K. As demonstrated by Fig. 3.4, all the cool stars in our sample are red giants with  $\log g \leq 3.3$ . Due to the observational bias of *Kepler* towards G-type stars (Borucki et al., 2010), it was expected that our sample would primarily consist of G-type stars. However,

<sup>1</sup>the full list of *Kepler* heartbeat stars is hosted at <http://keplerebs.villanova.edu>

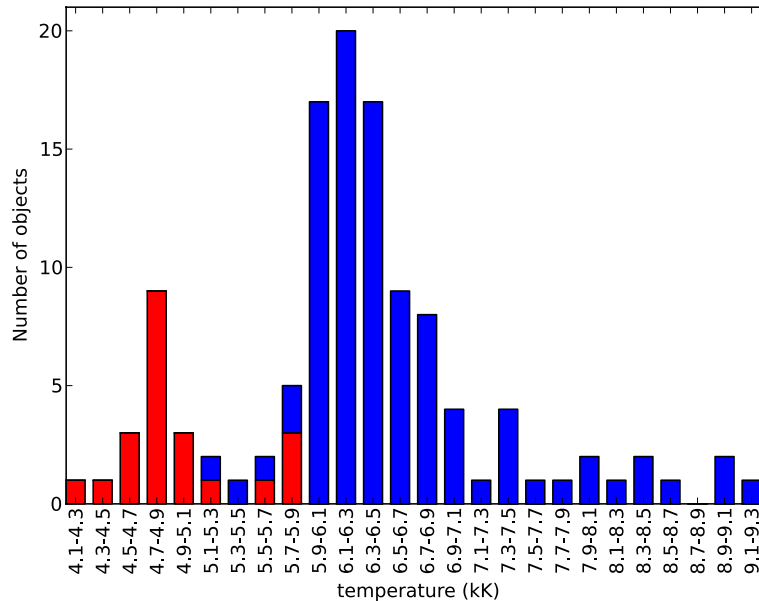


Figure 3.4: A histogram of heartbeat stars as a function of temperature. The red bars mark the red giants with  $\log g \leq 3.3$  and the blue bars mark the main sequence stars. The  $\log g$  values were taken from the *Kepler* Input Catalog.

this is not the case, meaning that there is also a more subtle (real) deficiency of G-type stars, with temperatures less than 6000 K, in our sample. As the transition between convective and radiative outer envelopes occurs at approximately this temperature (Aerts, Christensen-Dalsgaard & Kurtz, 2010) and the time required for circularisation (Zahn, 1977) is shorter for stars with convective outer envelopes (Torres, Andersen & Giménez, 2010), it is possible that the lack of low mass main sequence stars in our sample is a direct consequence of the relationship between stellar structure and tidal evolution.

### 3.1 Tidally Induced Pulsations

When it was first identified in the *Kepler* data, KOI-54 was speculated to be many things, including an star orbiting a black hole. After the units were checked and it was conclusive that the light curve wasn't upside down, *i.e.* magnitudes had not been confused for flux units, the search began for theories of what this object could

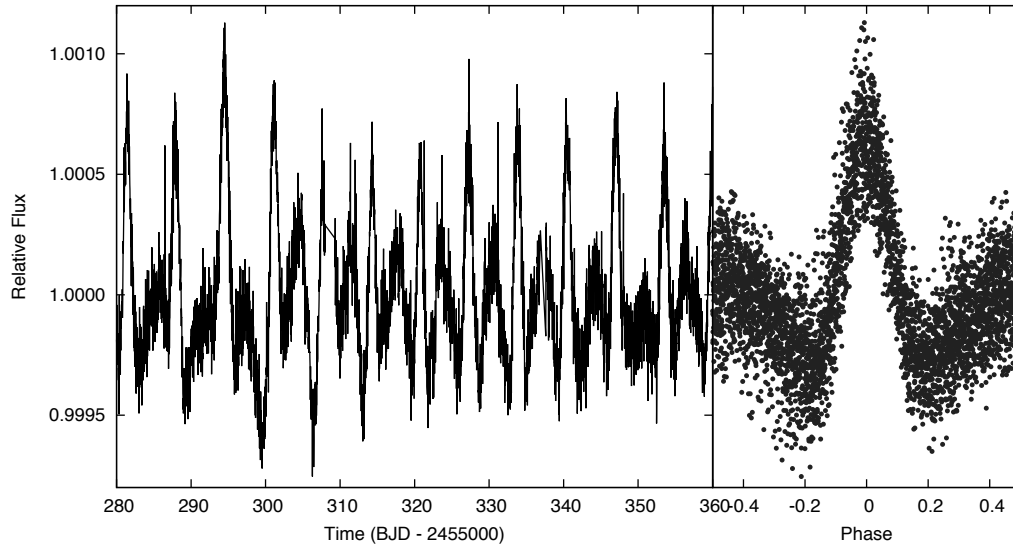


Figure 3.5: The times series (left panel) and phased light curve (right panel) of the Quarter 5 *Kepler* data of KIC 3965556. The non-coherent nature of the light curve is due to the presence of spots on one of the stellar components.

be. When efforts were made to model KOI-54 with the ELC (eclipsing light curve) binary modelling code (Orosz & Hauschildt, 2000), it was found that this interesting light curve was the product of two A stars orbiting each other in a nearly face-on, highly eccentric, non-eclipsing binary system. However, this did not describe all the features - the small scale oscillations ( $\sim 300 \mu\text{mag}$ ) were found to be a prime example of tidally induced pulsations - pulsations driven at multiples of the binary orbital frequency.

Tidally excited modes are stellar oscillations that are driven by the tidal force of the companion star. In a binary system with an eccentric orbit, when a stellar eigenfrequency is close to a multiple of the orbital frequency, the star can act like a forced oscillator, which causes an increase in the oscillation amplitude of the eigenfrequency (relative to non-resonant modes). The signature of tidally excited modes is thus an oscillation frequency at an integer multiple of the orbital frequency.

Tidally induced pulsations have long been theorised (Zahn, 1975; Goldreich & Nicholson, 1989; Witte & Savonije, 2002) as a mechanism for the circularisation of binary star orbits and the spin up of stars. However, until KOI-54, their presence has only

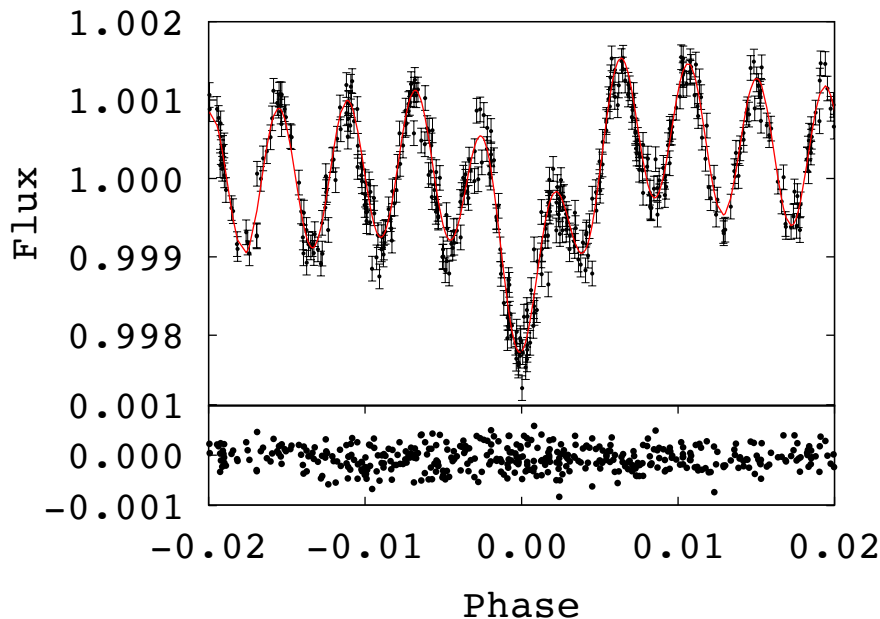


Figure 3.6: Upper panel: A phased light curve (black points) of KIC 8164262, a heartbeat star with a single high amplitude pulsation. The model is overlaid in red and comprises of the binary features and highest amplitude pulsation. The periastron variation, centred on zero, has a similar amplitude to the highest amplitude pulsation. Lower panel: the residuals of the binary model fit to the phased data (black points). Only a fraction of the orbit is shown for clarity.

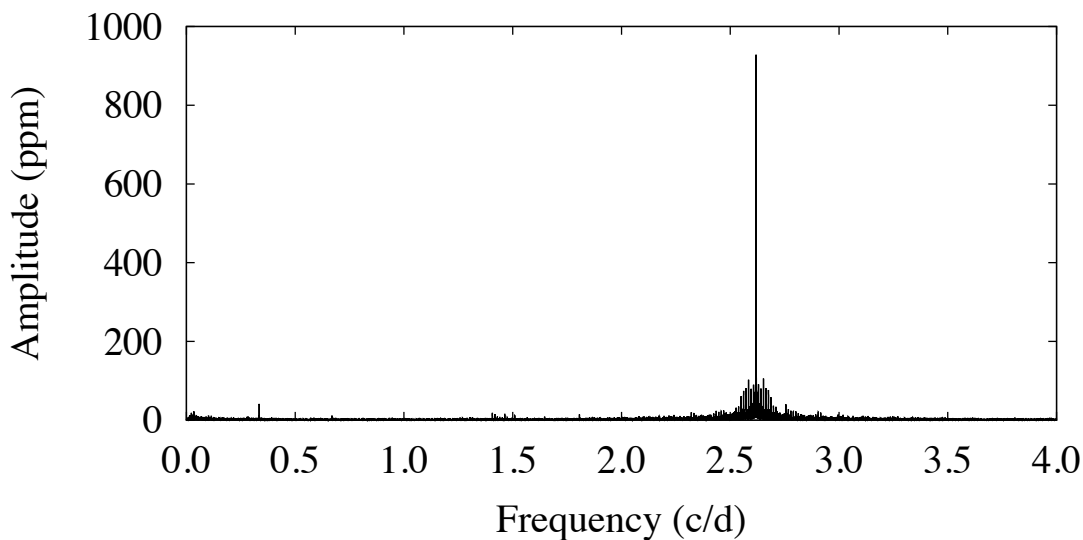


Figure 3.7: Fourier transform of the *Kepler* light curve of KIC 8164262. The data are from Q 1–Q 16. The prominent frequency is the 229<sup>th</sup> harmonic of the orbital frequency. Upon prewhitening of this frequency, the features due to the binary orbit are visible.

been speculated (Maceroni et al., 2009). The unquestionable nature of the tidally induced pulsations in KOI-54 sparked the interest of many theorists and consequently three publications (Fuller & Lai, 2012; Burkart et al., 2012; O’Leary & Burkart, 2014) appeared discussing the physical nature of tidally induced pulsations and the relevance of the 90<sup>th</sup> and 91<sup>st</sup> orbital harmonics - the two prominent pulsation frequencies in KOI-54. Fuller & Lai (2012) proposed that the two highest amplitude tidally induced pulsations were excited through a mechanism called resonant locking (see §3.1.1). Burkart et al. (2012) disputed this on the grounds that the torque produced by the proposed modes was not enough to provide resonant locks and that it is unlikely that two resonant locks would occur simultaneously. Later, O’Leary & Burkart (2014) showed that the 90<sup>th</sup> and 91<sup>st</sup> harmonics were likely  $m = 0$  modes and thus not resonantly locked as suggested by the theory at the time. More recent theory, however, suggests that resonant locks can occur in  $m = 0$  modes (Fuller, in prep.). Another interesting observation by O’Leary & Burkart (2014) was that all of the pulsation modes of KOI-54 are either tidally excited pulsations or their combinations, which was later found to be the case for all the g modes in KIC 4544587 (Hambleton et al., 2013). More commonly, however, I find self-excited g modes, spots and p modes (solar-like oscillations and  $\kappa$ -mechanism pulsations) in heartbeat stars. Fig. 3.5 depicts the times series and phased light curve of a typical heartbeat star with spots.

In our sample approximately 20% of the heartbeat stars demonstrate tidally excited modes, ranging from a single mode to a plethora of oscillations excited by tides. This is commonly the second most dominant feature in the light curve, although there are cases where the resonance is such that the mode amplitude exceeds the amplitude of the ellipsoidal variation caused by the tides. Fig. 3.6 and Fig. 3.7 depict the phased light curve and Fourier transform of KIC 8164262. In both figures a single, dominant frequency (which is the 229th orbital harmonic) is visible.

When considering the Fourier transforms of the light curves in our sample I commonly found a double humped distributions of peaks. I determined that this is a

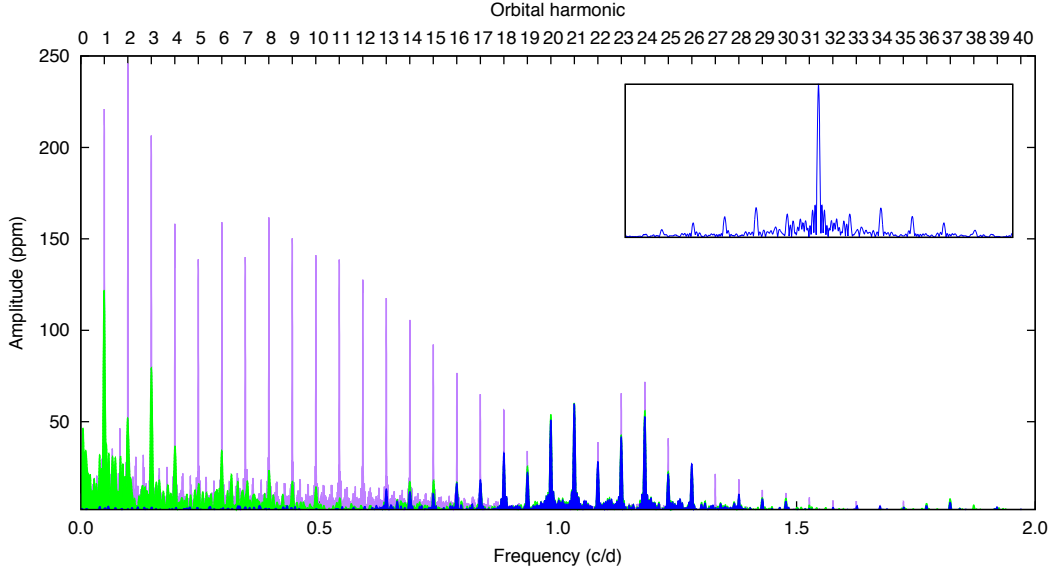


Figure 3.8: A Fourier transform of KIC 3749404 (purple); with the binary model removed (green); and with the binary model and the oscillations below  $0.5 \text{ d}^{-1}$  removed to an amplitude of 1 ppm (blue). The blue Fourier transform depicts the tidally induced pulsations. The sub-plot depicts the window function of each oscillation peak.

consequence of the tidally induced pulsation peaks overlaying the binary star features (as both reside at multiples of the orbital frequency). Fig. 3.8 depicts a Fourier transform with a double humped distribution. The second hump occurs at frequencies where the tidally induced pulsations begin to dominate over the orbital features (in this case starting with  $\nu/\nu_{orb} = 17$ ). In our sample we identified the heartbeat stars that have tidally induced pulsations using an automated pipeline that detects significant changes in the amplitude trends of the orbital harmonic peaks in the Fourier transform. Significant changes were detected by smoothing the points in a frequency-amplitude plot and looking for  $3\sigma$  deviations from the smoothed curve. We found that this method worked successfully the majority of the time ( $\sim 90\%$ ); however, on occasion the program detection was a false positive (if the periastron variation mimicked the signal we were looking for). Systems with eclipses were also problematic for this algorithm as the eclipse feature dominates the Fourier transform and consequently the tidally induced pulsations cannot be detected. I manually studied each phased light curve to improve our detection rate.

When tidally induced mode frequencies overlap the binary harmonic features the

phases of the unresolved peaks are a combination of these two effects, which so far we have been unable to disentangle. For mode frequencies that are well-separated in Fourier space from the binary harmonic frequencies, however, Burkart et al. (2012) showed that, in the majority of cases where the forcing of the orbit is not well tuned to the stellar eigenfrequency, the phase of tidally excited pulsations,  $\delta$  (in fractional period), relative to the phase of periastron,  $\omega_p$ , is directly linked to the azimuthal order of the mode,  $m$ :

$$\delta = \left( \frac{1}{4} + m\phi_0 \right) \pmod{\frac{1}{2}}, \quad (3.1)$$

where:

$$\phi_0 = \frac{1}{4} - \frac{\omega_p}{2\pi} \pmod{1}. \quad (3.2)$$

When  $\delta = 1/4$ , a mode will be observed at maximum amplitude and  $\delta = -1/4$ , the mode will be observed at minimum amplitude at periastron. Therefore, Eqn 3.1 suggests that for  $m = 0$  tidally excited modes, the maximum or minimum should occur at periastron. This not only provides the azimuthal order of the tidally excited modes, but can prove or disprove the tidal nature of an otherwise disputed mode.

While some progress has been made in the field of tidally induced pulsations, there are still many open questions. Observations of heartbeat stars have proved the existence of tidally excited modes, but the direct effect of these modes on the binary star orbital evolution and stellar spin (Zahn, 1975), and rate of apsidal advance (Claret & Willems, 2002) is still unknown, although observational advances are being made (see Chapter 5).

Furthermore, it is still unclear if tidally induced pulsations contain information that can be extracted about internal stellar structure. The reason for the lack of clarity is that the frequency of a tidally excited mode is always a multiple of the orbital

frequency. While it has been suggested that deviations from a precise multiple of the orbital frequency may provide asteroseismic information, the resolution of the *Kepler* data after the four year mission, while excellent, is not good enough to yield such details. Burkart et al. (2012) recently showed that the phases of tidally excited modes are related to the azimuthal order of the pulsation (with a slight dependence on the tuning of the mode), as shown in Eqns 3.1 and 3.2, and that the mode amplitude is believed to be caused by two factors: the closeness to resonance and the ratio of the mode frequency to the orbital frequency. Whether we can utilize our knowledge of the mode amplitudes or the presence of some excited modes and the lack of others to yield fundamental stellar parameters is still unknown.

### 3.1.1 Resonance Locking

The theory of resonantly excited modes – eigenmodes in resonance with the orbit – was studied long before the discovery of heartbeat stars (Witte & Savonije, 1999, 2001; Kumar, Ao & Quataert, 1995). Due to the predicted transient nature of resonant modes, it was not anticipated that they would be observed. However, KOI-54 and KIC 8164262 both have high amplitude modes that are highly stable and cannot be not easily explained by the forcing of the eigenfrequencies alone.

Resonance locking has been proposed as a mechanism that can “lock” a stellar eigenfrequency and the orbit in resonance, thus extending the lifetime of the resonance and making observations of tidal resonance possible.

As two stars in an eccentric configuration orbit each other, the stellar orbit evolves through the transfer of angular momentum, causing the orbit to get smaller and the stars to spin faster. A consequence of the decreasing orbit size is that the orbital period decreases. In parallel, the increase in the stellar rotational velocity causes the stellar eigenfrequencies to change. Resonance locking predicts that, when in resonance, these two effects happen on an equal time scale such that changes in the stellar eigenfrequencies occur simultaneously with changes in the orbital period.

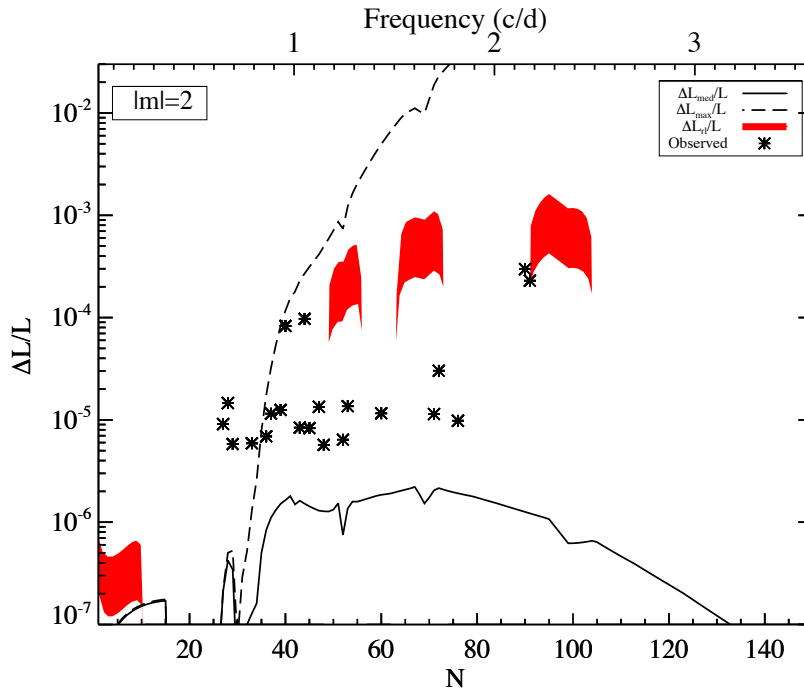


Figure 3.9: Depicted are the identified modes (black stars) of KOI-54 and the model predictions for the average expected amplitude (lower solid line) for forced modes as a function of frequency, the upper bound for tidally excited modes (upper dashed line). The modes present outside the solid line are believed to be travelling waves. The red regions show the model predictions for prograde resonantly locked modes. It can be seen that the 90<sup>th</sup> and 91<sup>st</sup> harmonics are just touching the red region. Figure provided by J. Fuller; private communication.

Thus rather than passing through resonance, the tidally induced pulsations are locked in resonance with the orbit.

Using forced pulsation models we are able to predict the amplitude and frequency of resonantly locked modes for a star with a specific  $T_{\text{eff}}$ , Radius and Mass, combined with the orbital geometry of the binary. For the two stars that we believe to have resonantly locked modes, KOI-54 and KIC 8164262, our current predictions are consistent with the believed resonant modes that we find. Figs 3.9 and 3.10 depict the identified modes (black stars) for KOI-54 and KIC 8164262, respectively. The lower solid line shows the average expected amplitude for forced modes as a function of frequency, and the upper dashed line shows the upper bound for tidally excited modes (that are standing waves). The red regions show the model predictions for prograde resonantly locked modes, and the blue regions show the predictions for retrograde resonantly locked modes. It can be seen that in both cases the high-

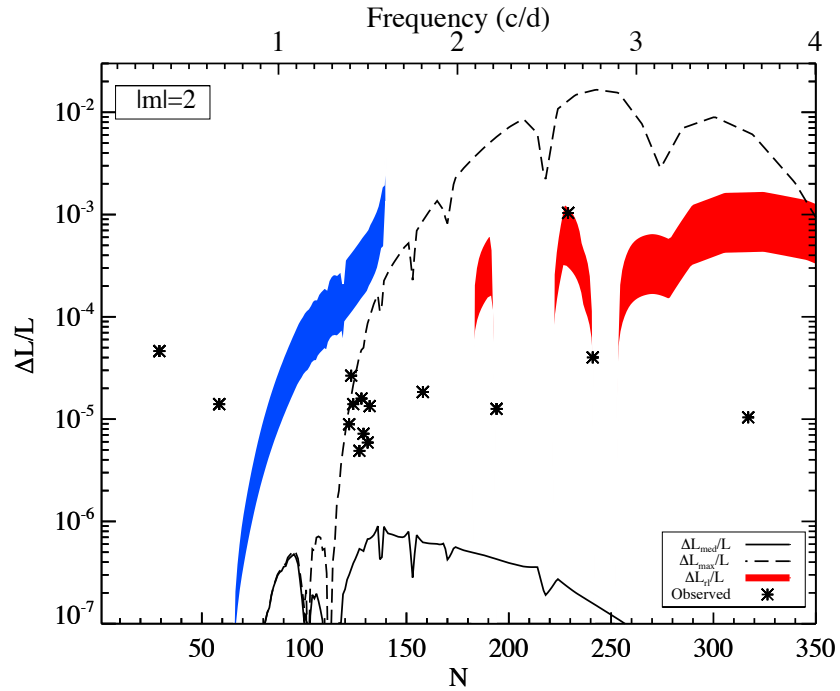


Figure 3.10: Depicted are the identified modes (black stars) of KIC 8164262 and the model predictions for the average expected amplitude (lower solid line) for tidally excited modes as a function of frequency, the upper bound for tidally excited modes (upper dashed line). The two lowest frequency points (black stars) depicted are not orbital harmonics, but are the signature of rotation from spots. The red and blue regions show the model predictions for prograde and retrograde resonantly locked modes, respectively. It can be seen that the highest amplitude harmonic is overlaying the red region. Figure provided by J. Fuller; private communication.

est amplitude modes overlay the red regions suggesting they are resonantly locked prograde modes.

## 3.2 The Bayesian Approach

As the parameter space of binary star systems is highly irregular with many degeneracies and correlations, I elected to use Markov chain Monte Carlo simulations to determine the posterior probability distributions of the parameters that describe the system (see later in this section for a list of parameters). This enables the visualisation of the correlations between different parameters and the uniqueness of the results to be easily assessed, whilst offering robust uncertainty measurements. To accomplish this I combined PHOEBE with the EMCEE, a PYTHON implementation of the affine invariant ensemble sampler for Markov chain Monte Carlo (MCMC) proposed by Goodman & Weare (2010) and written by Foreman-Mackey et al. (2013).

MCMC explores the binary parameter space using a set of Markov chains. In all cases I found 128 chains to be optimal - the minimum requirement is twice the number of parameters, however more chains enable the parameter space to be more thoroughly explored. When running the software, these chains begin with random distributions based only on their prior probability distribution functions and the initial model. They move through the parameter space by assessing their posterior probability distribution function at each point and then selecting a new position based on the position of another chain. The step size is based on the covariance of the two chains. If the move increases the posterior probability distribution function then it is accepted, if the move decreases it, then the move may be accepted (to fully explore the phase space). The acceptance is dependent on the ratio of the old to new probability and the acceptance criteria specified by the user (see Chapter 2 for an extended discussion on Markov chain Monte Carlo techniques). During the initial burn-in time the Markov chains merge towards their equilibrium position. After this

period the chains sample the phase space in terms of their posterior probability distribution functions. The statistics of a large number of iterations provide probability distributions for the model parameters. The number of iterations required depends on the degeneracy of the solution, the number of parameters and the number of data points. When running TODCOR I found that  $\sim 1000$  iterations were necessary, which take approximately 6-24 hr (dependent on the number of spectra and the bin size of the spectra) on 2 processors. When generating a binary model for KIC 3749404 with 7 pulsations I found that  $\sim 100\,000$  iterations were necessary with each iteration taking  $\sim 6$  min on 48 processors. The causes of the long computation times involved in binary star modelling are the incorporation of PHOEBE, and the large number of checks and computations involved alongside the large number of data points and parameters ( $\sim 28$  parameters for KIC 3749404 with 7 pulsations).

Before starting the MCMC computation, an initial binary star model in PHOEBE is required. Once a binary star model that is relatively close to the optimal model has been generated, the important parameters that influence the binary fit must be determined. This can be done by adjusting the parameters and seeing their effect on the light and radial velocity curves. For heartbeat stars the main parameters that are involved in the fitting process for light curves are:

- orbital phase shift: the shift required to keep the zero point in time at zero phase when using phased data;
- eccentricity;
- argument of periastron;
- orbital inclination;
- stellar luminosity ratio;
- effective temperatures;
- stellar potentials or radii;
- gravity darkening exponent,  $\beta$ , for the law  $F \propto g^\beta$ , where  $F$  is the stellar flux and  $g$  is the local gravity (required for both stars if the light from the secondary is significant),

- stellar albedos, which describe the amount of reflected light (both if the light from the secondary is visible);
- the ratio of the stellar rotational to orbital period (both if the light from the secondary is significant);

If eclipses are present, the light curve contains information about the temperature ratio, in which case it is usual to fix the temperature of the primary to that determined through spectral fitting and fit the secondary temperature. If there are no eclipses, unless Doppler boosting (explained in §3.3.2) plays a significant role, it is preferable to fix both temperatures to those determined through spectral fitting. For the latter five parameters listed above, the contribution from the secondary can be ignored if the light of the secondary is not visible (*i.e.*  $L_2 < \sim 3\%$  of the total light and the secondary component is not visible in the spectra or eclipses). For radial velocity curves the following parameters are important:

- orbital phase shift (when the radial velocities are phased);
- eccentricity;
- argument of periastron;
- inclination;
- semi-major axis;
- mass ratio;
- gamma velocity.

Once the parameters that require adjusting have been identified, the ranges of the priors for each of these parameters must be determined. These are the ranges from which the initial guesses of the parameters can be drawn and should be determined by adjusting the parameters until the model becomes obviously wrong (taking into account possible degeneracies). If there is any prior knowledge pertaining to a parameter, *i.e.* temperatures from spectra, then, if fitting temperatures, a Gaussian prior can be selected where the peak of the Gaussian is the previously obtained value, and the previously determined uncertainty equals one sigma for the Gaussian.

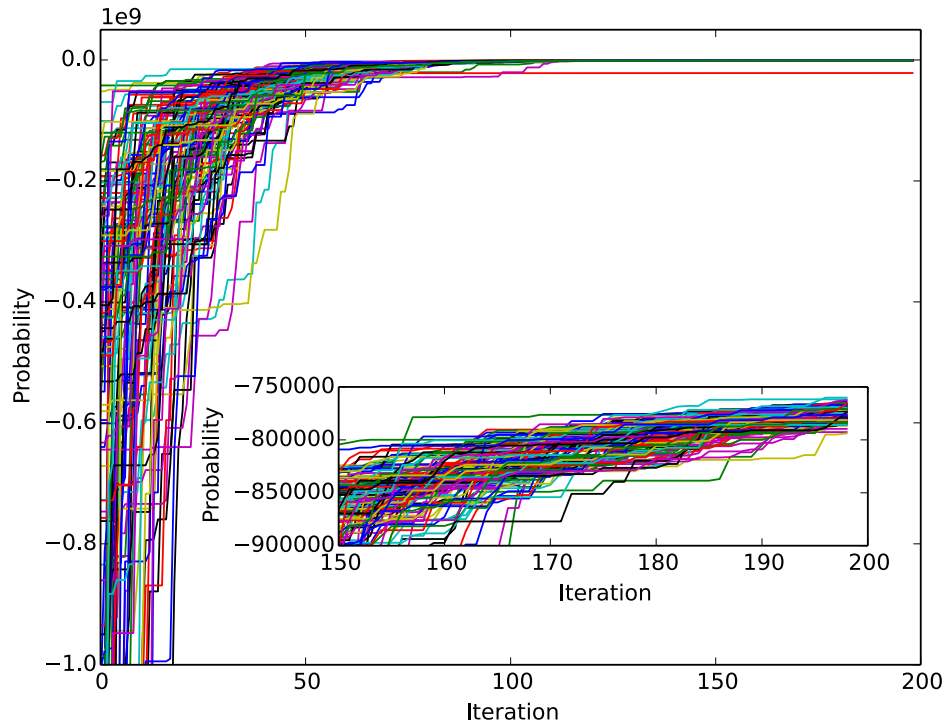


Figure 3.11: The probability as a function of iteration for the model of KIC 8164262, where each colour represents a different chain. This plot is used as a first gauge to determine if the model has converged. From consideration of this plot alone, we can see that the model has not converged as the likelihood value is still rapidly decreasing, as shown in the insert. Furthermore, as we have used the  $\chi^2$  test, we would expect the probability to equal  $-0.5N$  at the time of convergence, which is  $\sim 1000$ . This plot consequently indicates that the number of iterations required to obtain convergence for this model is large, or alternatively, that the uncertainties are underestimated.

Otherwise, a flat uniform prior can be used.

Once the model is running, it is necessary to check if the model has or is still in the process of converging. Fig. 3.11 shows a plot of the likelihood value as a function of iteration, which is very instructive when determining convergence. Initially the distribution of chains is very sporadic as the models have randomly selected parameters based on the prior distributions. As the number of iterations progresses, the chains begin to converge. The first test for model convergence is to see if the likelihood is still increasing with iteration. If the model has converged, the likelihood of the chains will no longer be increasing and will oscillate around a central point with a Gaussian distribution. Once it appears that the likelihood has plateaued, the next test is to look at the variation of parameters as a function of iteration. It is

possible that the parameters are still oscillating between two values or have not yet converged, and that the change in the likelihood is small enough to go undetected in the likelihood plot alone. In this case the model still requires further iterations.

When using the  $\chi^2$  test, the final value of the log likelihood should approximately equal  $-0.5N$  where  $N$  is the number of data points. If not, it is possible that the uncertainty ascribed to the data points is incorrect or the likelihood function is not optimal.

Once the chains have converged and remained that way for  $>150$  iterations, the converged chains can be used to determine the posteriors. The posterior distributions of the parameters can be viewed in two ways: as histograms showing the probability distribution or as two-dimensional cross sections of two parameters. Fig. 3.12 shows the posterior distributions of the binary star KIC 8164262. The posteriors generated through MCMC are well determined, shown by their apparent Gaussian distributions, thus the model is well constrained.

To fully visualise the model, I plot the mean model as a line (overlying the data points), with the one sigma spread from the posteriors plotted as an envelope around the model (see Fig. 3.13). This tool allows the visual inspection of the model and the uncertainties. It is expected that the  $1\sigma$  envelope will overlay the data in places where the mean model does not. If this is not the case it highlights problems with the solution, often suggesting inadequate likelihood function.

### 3.3 Additional Functions for Generating Heartbeat Star Models

For the creation of heartbeat star models, it was necessary to add new functionality to the PHOEBE modelling suite for three reasons: 1) to add new physics not previously available; 2) to add constraints; and 3) to reduce the number of fitted

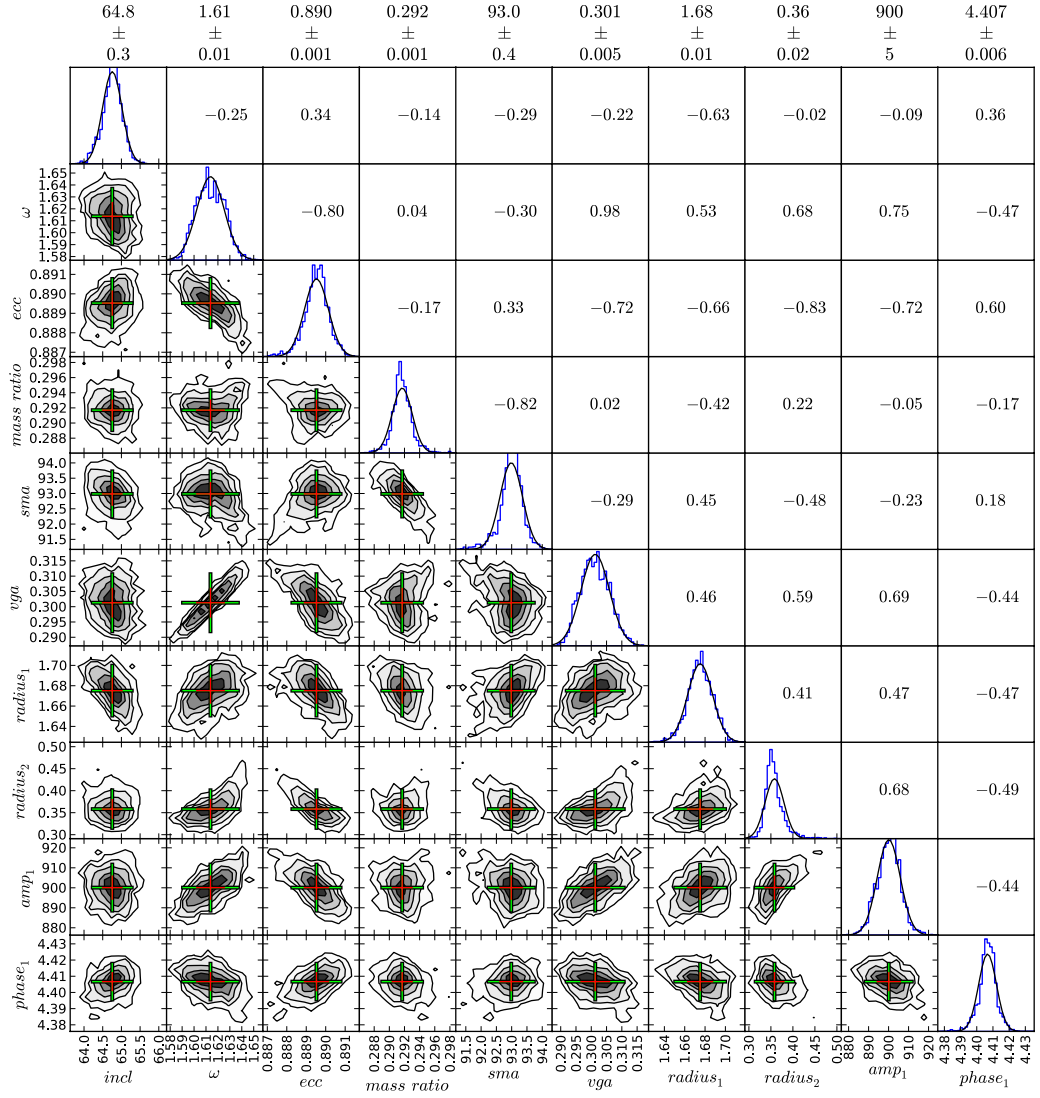


Figure 3.12: Depicted are the posteriors generated using the PHOEBE code combined with MCMC for KIC 8164262. Lower left sub-plots: two dimensional cross-sections of the posterior probability distribution functions for the inclination,  $incl$  ( $^\circ$ ); argument of periastron,  $\omega$  (rad); eccentricity,  $ecc$ ; mass ratio; semi-major axis,  $sma$ ; systemic velocity,  $vga$  ( $\text{km s}^{-1}$ ); primary and secondary radii ( $R_\odot$ ); and the amplitude ( $\mu\text{mag}$ ) and phase (rad) of the primary pulsation. The crosses show the  $1\sigma$  (red) and  $2\sigma$  (green) uncertainties, and are centred on the minima. Diagonal sub-plots from top left to bottom right: histograms displaying the probability distribution of each individual parameter. Upper right sub-plots: the correlations for the two-dimensional cross-sections mirrored in the diagonal line where 1 is direct correlation and -1 is a direct anti-correlation. The values above the plot give the mean value and one sigma uncertainty for each parameter, based on the fitted Gaussians.

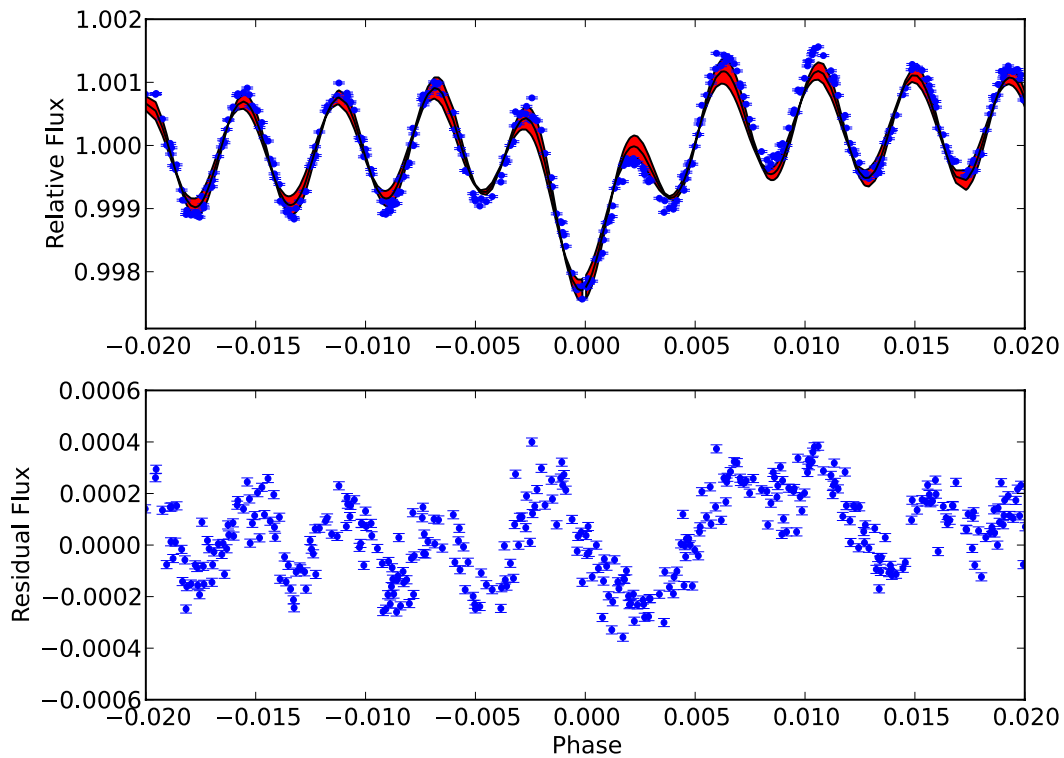


Figure 3.13: Upper panel: a model for KIC 8164262 (black line) with one sigma uncertainty envelope (red) and phased *Kepler* data with per-point uncertainties (blue points). I selected an initial model before full convergence was obtained, as the one sigma envelope is larger during this stage and thus more easily visible. Lower panel: the residuals of the fit to the data.

parameters by calculating parameters. An example of the software that interfaces with the PHOEBE code and includes the additions discussed in this Chapter can be found in Appendix B. Primarily, to fit heartbeat stars accurately, it was necessary to include pulsations in the model. Furthermore, due to the high radial velocities commonly achieved by heartbeat stars, and the high precision of the *Kepler* data, Doppler boosting was also required in the modelling software. When combining MCMC and PHOEBE, the number of parameters that require fitting for each computation is extensive. As the computation time scales linearly with the number of fitted parameters, it is preferable to compute parameters as opposed to fitting them, where possible. Furthermore, when computing parameters a more precise value is obtained and so a function to calculate the luminosity has been added. Finally, as heartbeat stars are generally without eclipses, extra constraints are required to generate a robust fit that combines the information from the Fourier transform and spectroscopy, with the light and radial velocity curve fits. For the purpose of modelling KIC 8164262, I placed constraints on the rotation from the rotational signature in the Fourier transform. For the purpose of modelling all heartbeat stars, I imposed restrictions on the stellar potentials so that they do not overflow their Roche lobes, and added the  $\log g$  value determined through spectroscopy as a known constraint. The details of all the additional functions are listed in this section.

### 3.3.1 The Implementation of Tidally Induced Pulsations

As mentioned earlier in §3.1, tidally induced pulsations are multiples of the orbital frequency. This makes modelling them easier than traditional pulsations for two reasons: it enables the frequency to be defined as a multiple of the orbital frequency, removing the need to fit it; and as the pulsations repeat precisely every orbit, it allows for the model to be generated in phase space which commonly involves less data and consequently shorter computing times. The addition of pulsations into the model has been done by multiplying sine waves, that have defined frequencies of

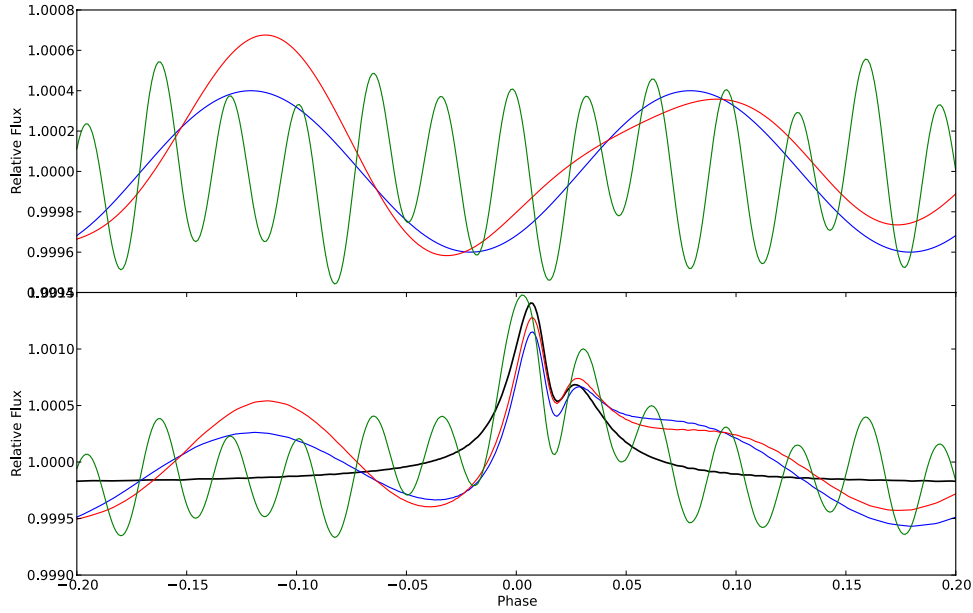


Figure 3.14: Top panel: examples of one (blue) five (red) and three higher frequency (green) sine curves with frequencies that are multiples of the orbital frequency. Bottom panel: the curves from the top panel multiplied with an example heartbeat star model. The colours correspond to the curves in the top panel and the black curve represents the light curve model with no pulsations.

$N \times \nu_{orb}$ , with the light curve model, and fitting the phase and amplitude. Pulsations are a multiplicative feature as they are an intrinsic part of the light curve.

Fig. 3.14 depicts examples of the sine waves generated by the function (top panel) and the same examples multiplied by a model of a heartbeat star (bottom panel). While the addition of sine waves enables the light curve to be modelled successfully and allows the phases and amplitudes of those pulsations to be correctly determined, this is a simple approach to an advanced problem. Since pulsating stars deform and change temperature as they pulsate, the complete treatment of pulsations would include the adjustment of the  $\log g$  and effective temperature of the individual elements on the stellar surface. This, however, is a significantly harder problem for heartbeat stars than for low eccentricity binary stars and single stars, as the tidal deformation of the stellar components at periastron renders spherical harmonics no longer applicable to the problem. As a developer of PHOEBE 2.0 a long term goal is

to add the thorough treatment of pulsations to single and binary star models, and eventually heartbeat stars.

### 3.3.2 Doppler Boosting

Doppler boosting is a phenomenon that comprises three effects:

- The increased arrival rate of the stellar photons as the star moves towards the observer and the decreased arrival rate as the star moves away;
- The Doppler shift of the spectrum as the stars move towards and away from the observer;
- The relativistic beaming or aberration of the photons as the star moves towards the observer.

It was originally suggested by Shakura & Postnov (1987) that Doppler boosting could be visible in binary stars, and that “Different modulation amplitudes of emitted flux should be seen dependent on the geometry of the emitting object”. Loeb & Gaudi (2003) and Zucker, Mazeh & Alexander (2007b) predicted that Doppler boosting would be seen in *Kepler* light curves and as heartbeat stars have high velocities at periastron, it is no surprise that Doppler boosting has been detected in heartbeat stars. Doppler boosting manifests itself in the light curve as an asymmetrical feature that mimics the inverted radial velocity curve of the stellar component from which it comes. If both stars are of similar mass and luminosity, the radial velocity curves are approximately equal, thus the contributions of the two components cancel out. However, if the mass ratio is far from one, the more massive, more luminous star will dominate the effect. To study this effect it is preferable to have a mass ratio small enough that one star dominates the light curve, although large enough that both stars contribute to the light curve, *i.e.*  $\sim 0.5$ . Also, the more the direction of motion is aimed towards the observer, the larger the radial velocity and

thus the larger the amplitude of the effect. Therefore, orbital configurations with inclinations close to  $90^\circ$  produce the largest effects and thus provide more constraints on the model.

For the purpose of modelling, there are two methods that are possible:

- To constrain the mass function or masses of the stellar components using Doppler boosting. This requires knowledge of the sizes and temperatures of the stars.
- To determine the temperatures given the radial velocities and radii of the stars.

In our models, during each MCMC iteration I add the effect of Doppler boosting given the newly determined stellar parameters. Therefore, if the temperatures are fixed, this will help constrain the masses and sizes of the stars, and if the masses are determined by radial velocities, Doppler boosting will help constrain the temperatures. I adjust the model flux based on the following equation adapted from Eqn 2 in Bloemen et al. (2011) to account for Doppler boosting in both components:

$$F_\lambda = F_{0,\lambda} \left( R \left( 1 - B_1 \frac{v_{r,1}}{c} \right) - (1 - R) \left( B_2 \frac{v_{r,2}}{c} \right) \right), \quad (3.3)$$

where  $F_\lambda$  is the observed flux,  $F_{0,\lambda}$  is the emitted flux,  $R$  is the light ratio,  $v_{r,1}$  and  $v_{r,2}$  are the radial velocities of the primary and secondary components.  $B_1$  and  $B_2$  are the passband-weighted boosting factors, where  $B = 5 + d \ln \lambda$  (Loeb & Gaudi, 2003). The boosting factors are determined using look-up tables, which are specific to the *Kepler* passband and are a function of  $T_{\text{eff}}$  and  $\log g$ . Fig. 3.15 depicts a heartbeat star light curve before (black line) and after (red line) the addition of Doppler boosting (top panel), the boosting signal and the primary star's radial velocity curve are shown in the middle panel and lower panel, respectively. As the light from the secondary component is less than 2%, the Doppler boosting follows the inverse profile of the radial velocity curve of the primary component, as expected.

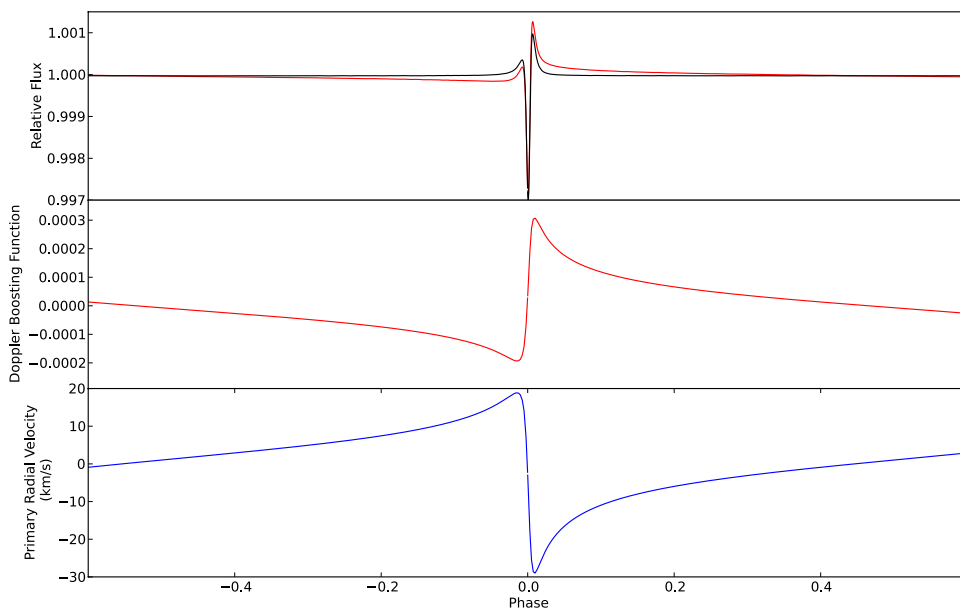


Figure 3.15: Top panel: heartbeat star light curve with (red) and without (black) Doppler boosting. Middle panel: the Doppler boosting signal (red) that has been applied to the light curve in the top panel. Lower panel: the primary star's radial velocity curve. Only the primary component's radial velocity curve is displayed as the light from the secondary is less than 2%, thus the contribution of the secondary component to the Doppler boosting is insignificant.

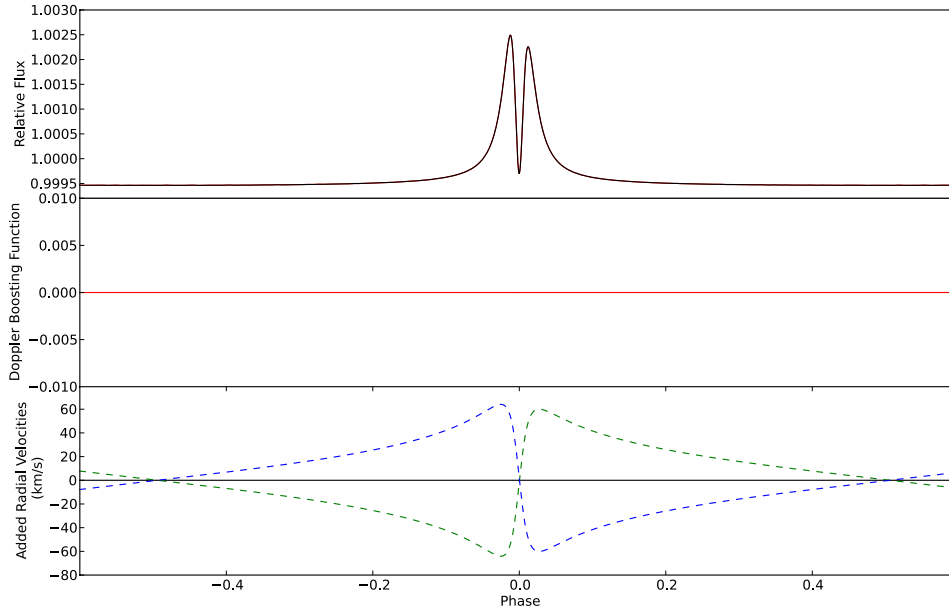


Figure 3.16: Top panel: heartbeat star light curve of two identical components with (red) and without (black) Doppler boosting. Middle panel: the Doppler boosting signal (red) that has been applied to the light curve in the top panel. Lower panel: The radial velocities of the primary and secondary components (blue and green dashed lines), and summed radial velocities of the primary and secondary component (black line) . The identical nature of the primary and secondary components causes the total motion of the two components to be zero and consequently I expect Doppler boosting to have zero contribution to the light curve, as found.

To further test our program I generated a model with two identical stellar components. Fig.3.16 depicts the light curve of the identical components with (red) and without (black) beaming (top panel), the beaming function is depicted in the middle panel and the added radial velocity curves of the primary and secondary components in the bottom panel. By adding the radial velocity curves I show that the total motion of the primary and secondary components cancel. I consequently expect that the contribution of Doppler boosting to be zero, which is shown in the middle and upper panels.

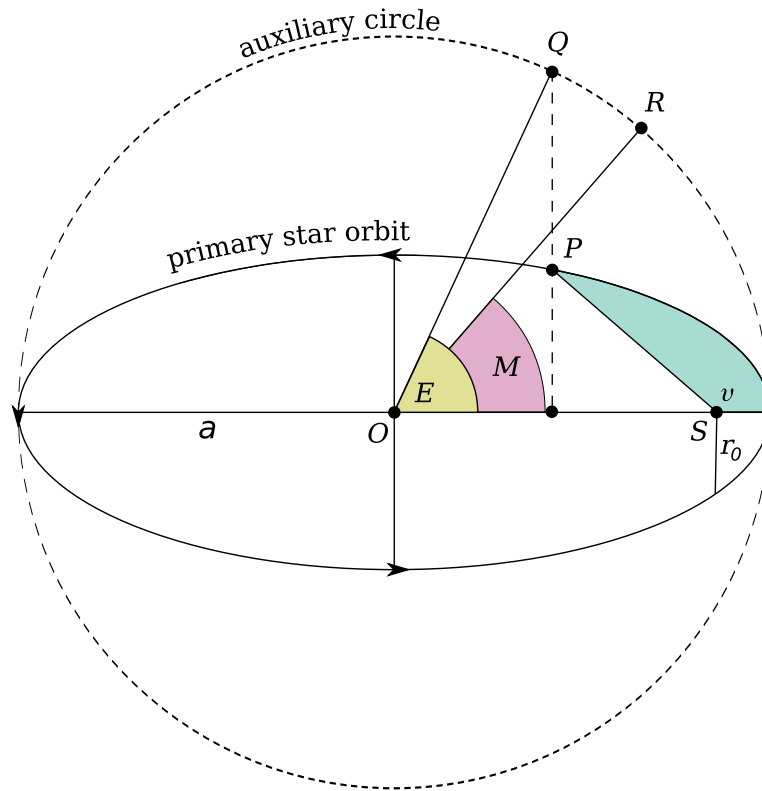


Figure 3.17: A graphical representation of the true anomaly  $v$ , eccentric anomaly  $E$  and the mean anomaly  $M$ . The star is at point  $P$  on the orbit, travelling in a counter-clockwise direction around the focal point  $S$ . Point  $Q$  is the vertical projection of the star's position on the auxiliary circle. The angle  $ROS$  is proportional to the time elapsed since the star's passage through periastron.

### 3.3.3 Phase Shift

In a binary system whose ephemeris is not changing in time due to mass loss or apsidal motion, the two important parameters that define the ephemeris are the zero point in time and binary star period: the sidereal period of the two stellar components. If the data are transformed from the time to the phase domain, an extra parameter needs to be introduced: the phase shift. This convenience parameter is used to horizontally shift the position of a prominent feature, in our case the peak or dip of the ellipsoidal variation, to the location of zero phase. More specifically, when we adjust the argument of periastron and/or eccentricity, the model shifts horizontally such that the peak/dip of the periastron variation is no longer at zero phase. By applying a phase shift to the model, we are then able to align the model with zero phase, and consequently with the data.

With eclipsing binaries, the phase of superior conjunction coincides with the phase of the primary eclipse. Consequently, if the zero point is defined as the time of primary eclipse, the phase shift can be determined using the phase of superior conjunction. To determine the phase of superior conjunction, the first step is to calculate the true anomaly at superior conjunction,  $v_{SC}$ . The true anomaly is the angle between periastron and the location of the star on the orbit, with respect to the focus (closest to the argument of periastron) of the orbital ellipse (see Fig. 3.17). When the star is at superior conjunction this angle is  $v_{SC}$ :

$$v_{SC} = \frac{\pi}{2} - \omega, \quad (3.4)$$

where  $\omega$  is the phase of periastron. If the sign of  $\omega$  is changed, the result is the true anomaly at inferior conjunction.

Using the true anomaly at superior conjunction, we can then determine the eccentric anomaly at superior conjunction,  $E_{SC}$ . The eccentric anomaly is the angle between periastron and point  $Q$  on the auxiliary circle, relative to the center of the ellipse in Fig. 3.17. By incorporating the true anomaly at superior conjunction into our equation, we find the eccentric anomaly at superior conjunction:

$$E_{SC} = 2 \arctan \left( \sqrt{\frac{1-e}{1+e}} \tan \left( \frac{v_{SC}}{2} \right) \right). \quad (3.5)$$

Once the eccentric anomaly at superior conjunction has been calculated, we can determine the mean anomaly at superior conjunction,  $M_{SC}$ . The mean anomaly is the representation of the passage of time as the stars progress around the orbit. It can be visualised by considering a point that is steadily moving around the auxiliary circle, and the angle made between this point, the center of the circle and the point of periastron:

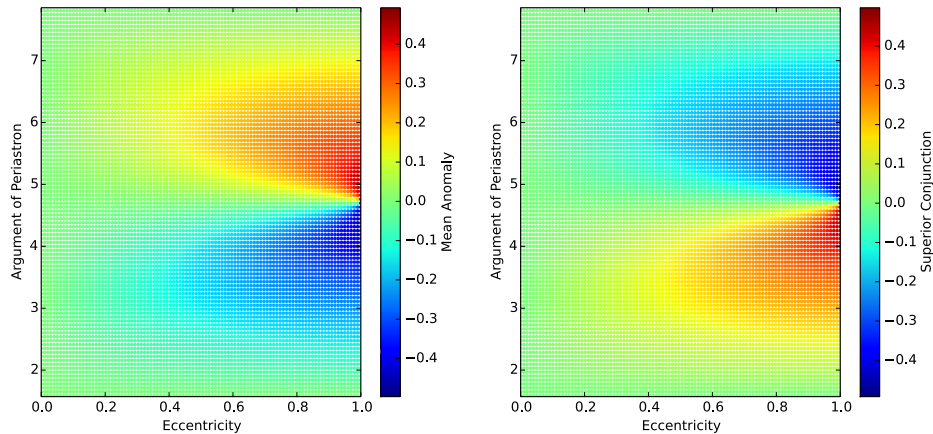


Figure 3.18: Left panel: the computed values of the mean anomaly at superior conjunction as a function of eccentricity and argument of periastron. Right panel: the computed values of the phase of superior conjunction as a function of eccentricity and argument of periastron.

$$M_{SC} = E_{SC} - e \sin(E_{SC}). \quad (3.6)$$

As Kepler's second law predicts, the area swept out by an object moving in an elliptical orbit increases uniformly with time. Thus, using the mean and eccentric anomalies, we can then determine the phase of superior conjunction:

$$\phi_{SC} = \frac{M_{SC} + \omega}{2\pi} - \frac{1}{4} \quad (3.7)$$

Fig. 3.18 depicts the variations of the mean anomaly at superior conjunction and the phase of superior conjunction as a function of eccentricity and argument of periastron. Both the mean anomaly at superior conjunction and the phase of superior conjunction occur at phase zero for low eccentricities and are symmetrical about  $\pi$  rad on the y-axis. However, the mean anomaly at superior conjunction and the phase of superior conjunction are mirrored about  $\pi$  rad on the y-axis.

Initially, I presumed that, as the phase of either inferior or superior conjunction (depending on the object) is closely aligned with the dip of the periastron variation, I would be able to calculate the change in phase of superior/inferior conjunction and

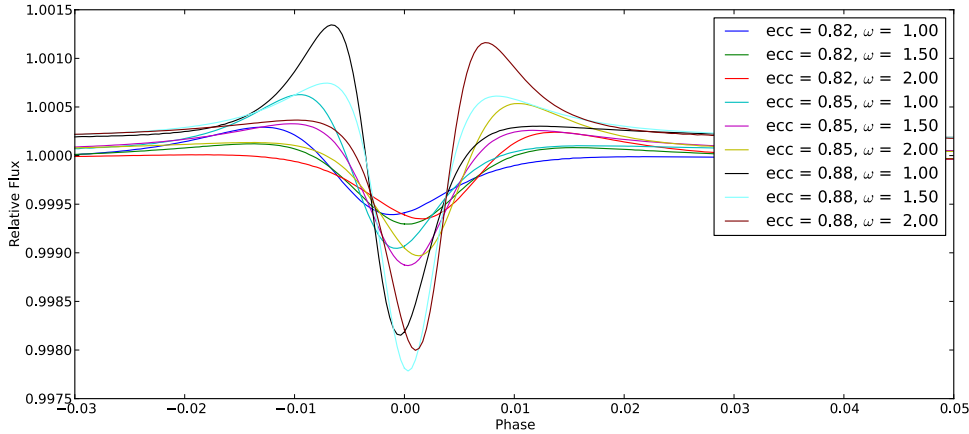


Figure 3.19: Depicted are 9 binary star models with eccentricities between  $ecc = 0.82 - 0.88$  and phase of periastron between  $\omega = 1.0 - 2.0$ . The phase of each model has been calculated by considering the shift of the phase of superior conjunction. If the phase shift of the dip in the periastron variation moved precisely as the phase of superior conjunction, all models would be precisely aligned at zero phase. However, this is not the case and so we are not able to utilize this method for determining the phase shift of heartbeat stars.

apply this change to our model to keep the periastron variation at zero phase. After applying this method to our code, however, and performing extensive tests, I found that, although this is a good approximation, there is a slight deviation between the shift of conjunction and shift of the periastron feature. Consequently, I was unable to utilize this relationship. Fig. 3.19 represents 9 models with eccentricities between  $ecc = 0.82 - 0.88$  and the argument of periastron defined between  $\omega = 1.0 - 2.0$  that have been shifted using the aforementioned method. While the dip of the periastron event is approximately zero for each model, the deviation is too large for the accuracies I require in the modelling process. Consequently, the phase shift is specified as a prior in our models.

### 3.3.4 Passband luminosity

The passband luminosity of the two stellar components determines the the vertical offset of the model from the data. Although PHOEBE accurately calculates the passband luminosity, as I apply additional effects to our models such as Doppler boosting, it is necessary that I calculate the passband luminosity with my own code

after the effects have been added.

At each iteration, the adjustment of parameters changes the luminosity of the stellar components, shifting the model vertically with respect to the data. To re-normalise the model, I use the method of least squares to determine the vertical offset,  $\alpha$ :

$$\alpha = \frac{\sum data \times model}{\sum data^2}, \quad (3.8)$$

The value of alpha (the y-offset) is then combined with the unnormalised primary,  $L_{0,1}$ , and secondary,  $L_{0,2}$ , component luminosities to determine the values of the normalised primary and secondary luminosities:

$$L_2 = \frac{\alpha(L_{0,1} + L_{0,2})}{\frac{L_{0,1}}{L_{0,2}} + 1}, \quad (3.9)$$

$$L_1 = L_2 \frac{L_{0,1}}{L_{0,2}}. \quad (3.10)$$

From these values the luminosity ratio,  $R$ , is then computed, which is required for the computation of Doppler boosting (cf. 3.3.2) and is an informative parameter regarding the system:

$$R = \frac{L_1}{L_1 + L_2}. \quad (3.11)$$

### 3.3.5 The Stellar Equipotential

In 1849 Edouard Albert Roche (1820-1883) provided a formalism that describes equipotential surfaces. This formalism is used to describe stellar geometry, based on the gravitational potentials of the two stellar components and the centrifugal force. The *Principle of Equipotential Surfaces* states that the morphology and character-

istics of both stellar components are defined by the equipotential on the surface. As the Roche geometry is based on this principle, it inherently assumes:

- The stars are point masses surrounded by a massless equipotential envelope;
- The stars act as rigid bodies and any rotation is uniform across the star (*i.e.* no differential rotation);
- Any perturbations, such as stellar pulsations, have negligible periods with respect to the orbital period, *i.e.* the stellar shape is fully defined by the instantaneous force-field.

All of these assumptions are violated by most binary systems, but particularly by heartbeat stars and especially those with strong, long-period pulsations. However, the current state of computing does not allow for the hydrodynamical simulations (or similar) of the individual stars in a binary system. And so, for now, it is necessary to use the assumption of equipotential surfaces.

Kopal (1959) provided the first description of the stellar potential,  $\Omega$ , based on the Roche geometry, also known as the *modified Kopal potential*:

$$\Omega = \frac{1}{\rho} + q \left( \frac{1}{\sqrt{\rho^2 - 2\rho\lambda + 1}} - \rho\lambda \right) + \frac{1}{2}(1 + q)(1 - \nu^2)\rho^2, \quad (3.12)$$

where  $\rho$  is the stellar radius in units of the semi-major axis,  $q$  is the mass ratio and  $\lambda$  and  $\nu$  are the direction trigonometric functions that are from the use of spherical coordinates:  $x = r \sin \theta \cos \phi = \lambda r$  and  $z = r \cos \theta = \nu r$ . In this framework the centre of the co-ordinate system is at the centre of the primary component with the x-axis passing through the centre of the secondary component and the y-axis in the direction of the primary component's pole. This version of the stellar equipotential applies to non-rotating stars in circular orbits. Wilson (1979) later extended Kopal's work to systems with rotating components in eccentric orbits:

$$\Omega = \frac{1}{\rho} + q \left( \frac{1}{\sqrt{\delta^2 + \rho^2 - 2\lambda\delta\rho}} - \frac{\lambda\rho}{\delta^2} \right) + \frac{1}{2}F^2(q+1)\rho^2(1-\nu^2), \quad (3.13)$$

where  $\delta$  is the instantaneous separation between the stellar components in units of the semi-major axis and  $F$  is the spin-to-orbital frequency (also known as the synchronicity parameter). For the equipotential of the secondary component I must change the co-ordinate system so that it is centred on the secondary star. The secondary potential,  $\Omega'$ , is related to the primary star's potential,  $\Omega$  by:

$$\Omega' = \frac{\Omega}{q'} + \frac{q' - 1}{2q'}, \quad (3.14)$$

where  $q' = 1/q$ . In the case of KIC 5006817 (cf. Chapter 6), the primary stellar radius was known through asteroseismology, thus I used it as a constraint for the binary star model. As PHOEBE uses the stellar potential value at periastron as an input, it was necessary to create a function that could read in the stellar potential, eccentricity, synchronicity parameter and mass ratio, and determine the primary star radius in units of the semi-major axis. To do this I selected the Newton-Raphson method, as it is not possible to solve Eqn 3.13 for the radius directly. As the Newton-Raphson method identifies the roots of an equation, I rearranged Eqn 3.13 so that I could determine the value of  $\rho$  for our given potential when  $f(\rho) = 0$ ,  $\rho$ :

$$f(\rho) = -\Omega + \frac{1}{\rho} + q \left( \frac{1}{\sqrt{\delta^2 + \rho^2 - 2\lambda\delta\rho}} - \frac{\lambda\rho}{\delta^2} \right) + \frac{1}{2}F^2(q+1)\rho^2(1-\nu^2). \quad (3.15)$$

The Newton-Raphson method works by selecting an initial guess,  $\rho_0$ , that is relatively close to the actual value of the primary radius; the tangent of the function  $f(\rho_0)$  is then calculated for the estimated value of  $\rho$ ; and a new value for  $\rho$  is found by subtracting the tangent from the initial guess:

$$\rho_{\text{new}} = \rho_0 - \frac{f(\rho_0)}{f'(\rho_0)}. \quad (3.16)$$

This process is then repeated and each time  $\rho_0$  is replaced with the newly obtained value of  $\rho$ . For our purposes I continued the repetitions until a tolerance of  $10^{-6}$  was reached by finding the difference between the current and previous values of  $\rho$ .

To determine the tangent, I require the derivative of the function I am trying to solve:

$$\frac{\partial f(\rho)}{\partial \rho} = -\frac{1}{\rho^2} + q \left( (\lambda\delta - \rho)(\delta^2 + \rho^2 - 2\rho\lambda\delta)^{-3/2} - \frac{\lambda}{\delta^2} \right) + F^2\rho(1+q)(1-\nu^2). \quad (3.17)$$

When testing our methods I inserted the newly determined value of  $\rho$  into Eqn 3.13 to ensure the original potential was returned with the correct level of precision.

For more recent modelling efforts, *i.e.* KIC 3749404 and KIC 8164262 (Chapters 5 and 4, respectively), I elected to create a function that takes the radii as inputs and converts them into stellar potentials, which PHOEBE requires as input, so that our priors are more intuitive. Included in this upgrade is the determination of the critical potential (cf. §3.3.6). Now, the full range of plausible radii, eccentricities, mass ratios and spin-to-orbital period values can be specified without the concern that it will cause the Roche lobe to overflow due a non-ideal combination. The consequence of this is that I can explore more extreme areas of the parameter space that are necessary for heartbeat stars, without causing the PHOEBE software to crash. Fig. 3.20 depicts the values of the stellar potential as a function of radius for given values of  $e$ ,  $q$  and  $F$ , for both the primary and secondary components.

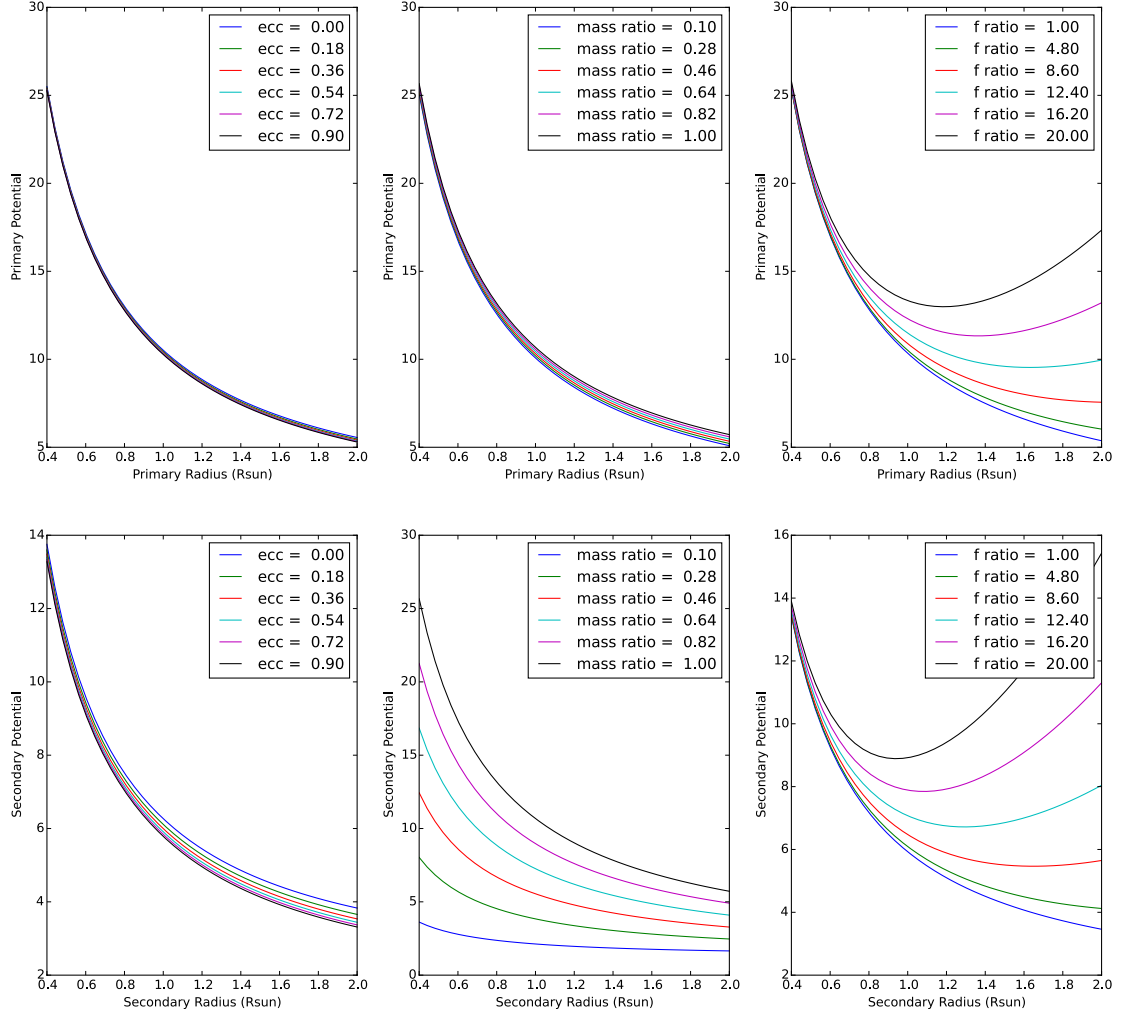


Figure 3.20: The stellar potential as a function of radius for the primary (upper panels) and secondary (lower panels) components. From left to right, the panels depict how varying the eccentricity, mass ratio and spin-to-orbital period affect the relationship between the potential and the stellar radius. In these diagrams the eccentricity, mass ratio and spin-to-orbital period are fixed to 0.5, 0.5 and 1.0 respectively, when they are not a plotted variable. The semi-major axis was set to  $sma = 100 R_{\odot}$  for all plots.

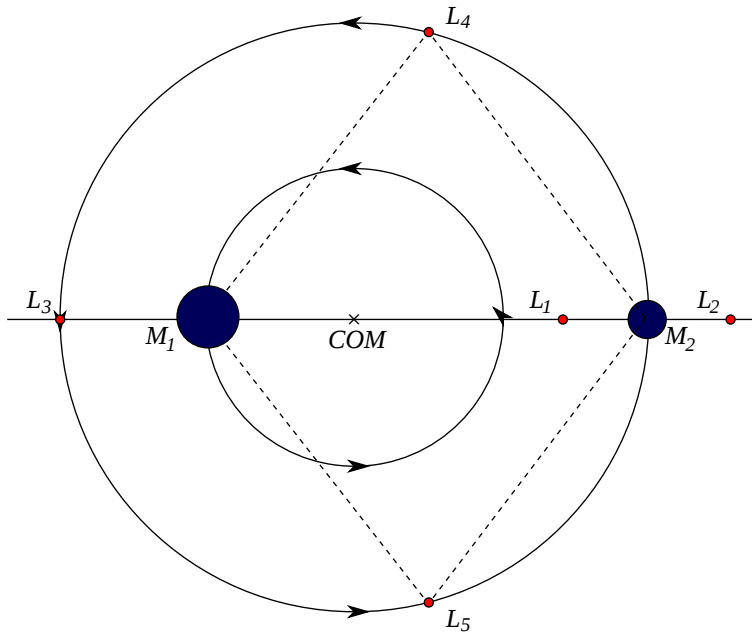


Figure 3.21: A schematic diagram of a circular binary star with the two stars,  $M_1$  and  $M_2$ , the center of mass and the five Lagrangian points clearly marked. Adapted from Prša (2005).

### 3.3.6 The Critical Potential

In any orbital configuration of two bodies there are five points, known as Lagrangian points, at which the net gravitational and centrifugal forces on a test particle is zero (in an accelerated reference frame). In a co-ordinate system that is centred on the primary star, where the x-axis points to the secondary star and the y-axis points from the center to the pole of the primary star, there are three Lagrangian points along the x-axis ( $L_1$ , between the two stars;  $L_2$ , behind the secondary star; and  $L_3$ , behind the primary star) and two points that form equilateral triangles with the two stars ( $L_4$  and  $L_5$ ). Fig. 3.21 depicts a schematic diagram of a circular binary with the five Lagrangian points clearly marked.

If the equipotential of a star equals the potential at  $L_1$ , the consequence is that the star fills its Roche lobe. By the same logic, if the equipotential of a star is smaller than the potential at  $L_1$ , material will flow from the star onto its companion. If the stellar equipotential is smaller than the potential at  $L_2$  (an unphysical case), the secondary star will form a dimple in the back, directed away from its companion. In

all cases the stellar equipotential must be larger than the potential at  $L_2$ , as being smaller creates an unphysical system. Furthermore, if there is no suggestion of mass transfer between the stellar components, for example flickering in the light curve or  $H\alpha$  emission lines in the spectra, and if the object is not overcontact binary, then there is an additional constraint that the equipotential of the star must be larger than the potential at  $L_1$  (which is always larger than  $L_2$ ).

*Heartbeat* stars are extreme systems. Consequently, at periastron, it can happen that one or both of the stars' equipotentials are close to the potential at  $L_1$ . If it is known that an object is not undergoing mass transfer (by studying the spectra), we can apply the constraint that the star's equipotential must be larger than the stellar potential at  $L_1$ . Consequently, this will also mean the stars' potentials is larger than the potential at  $L_2$ , which will prevent the PHOEBE software from crashing.

To compute each of the three Lagrangian points along the x-axis the same methodology is applied; however, three different initial guesses must be used to determine the different roots. First, the force at a given distance,  $x$  (our initial guess), from the central star is calculated. This is equal to the derivative of the potential (Eqn 3.13):

$$\frac{\partial\Omega}{\partial x} = -\frac{x}{(x^2)^{1.5}} - \frac{q(x-d)}{((x-d)^2)^{1.5}} - \frac{q}{d^2} + F^2x(1+q), \quad (3.18)$$

where  $q$  is the mass ratio (with the mass of the star at the center of the co-ordinate system in the denominator),  $F$  is the ratio of the stellar rotational to orbital period and  $d$  is the instantaneous separation of the two stellar components normalised to the semi-major axis. As I am considering the entire orbit, I selected the point where the stellar equipotential is smallest - periastron. Thus  $d = 1 - e$  where  $e$  is the eccentricity and  $d$  is in units of the semi-major axis.

As we cannot solve for  $x$  analytically, again it is necessary to employ a method of minimisation. Furthermore, since we are looking for the value of  $x$  when  $\partial\Omega/\partial x = 0$ , I again selected the Newton-Raphson method, which is applied to functions where

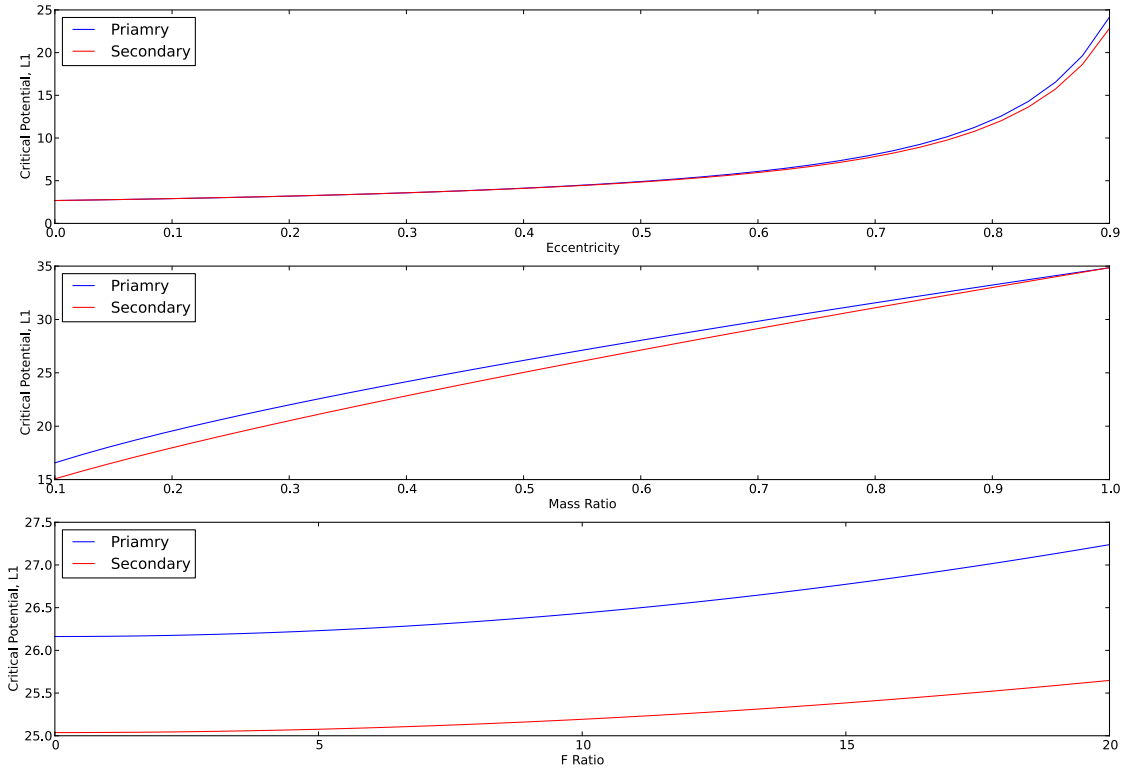


Figure 3.22: The critical potentials of the primary (blue line) and secondary (red line) components at L1 as a function of eccentricity, mass ratio and spin-to-orbital period for  $sma = 100 R_{\odot}$ . When not acting as the independent variable, the parameters  $e$ ,  $q$  and  $F$  are set to 0.5, 0.5 and 1.0 respectively.

the solution to the equation we are solving is a root:  $f(x) = 0$ . I selected a tolerance of  $10^{-6}$  and computed the tangent to the gravitational force using Eqn 3.16. To do this it is required that the root of the partial differential of the gravitational force be calculated:

$$\frac{\partial^2 \Omega}{\partial x^2} = 2x^{-4} + 2q(d-x)^{-4} + F^2(1+q). \quad (3.19)$$

Once the value of  $x$  is determined it is inserted into Eqn 3.13, the potential equation, and the critical potential is determined at the Lagrangian point corresponding to  $x$ . To distinguish between the three Lagrangian points the initial guess is altered. To determine  $x$  at  $L_1$ , an initial guess of  $x_0 = d/2$  (half the distance between the two

stars) is appropriate. Good initial guesses for  $L_2$  and  $L_3$  are dependent on the force function,  $\partial\Omega/\partial x$ , which depends on parameters  $e$ ,  $q$  (the mass ratio) and  $F$ . If the initial guess is far separated from the real value, the solution tends to that for  $L_1$ . If it is necessary to calculate  $L_2$ , for example with contact systems or systems with mass transfer, I determined that starting with a value of  $x$  close to that of  $L_1$  (*i.e.*  $x_{L_1} - 0.05$ ); compared the potential with that at  $L_1$ ; and incrementally decreased the initial value of  $x$  until the minimization outcomes of  $L_1$  and  $L_2$  were no longer identical (to a precision equal to the predefined tolerance); is the best approach.

I tested my approach by comparing our values of  $L_1$ ,  $L_2$  and  $L_3$  with those generated by PHOEBE for a circular orbit with a synchronicity parameter,  $F$ , of 1.0 (more advanced configurations are not calculated by PHOEBE). I found our method to generate the same values as PHOEBE:  $\Omega = 3.75$  for  $L_1$  and  $\Omega = 3.20679$  for  $L_2 = L_3$ . PHOEBE also calculates  $L_1$  for non-circular orbits thus verified our method for multiple combinations including extreme values of  $e$ ,  $q$ , and  $F$ . Fig. 3.22 shows the variation of the critical potentials of the primary and secondary components at  $L_1$  as a function of eccentricity, mass ratio and spin-to-orbital period (where  $sma = 100 R_\odot$ ). It can be seen that the critical potentials of both components increase as  $e \rightarrow 1.0$ , as  $q \rightarrow 1.0$  and as  $F$  increases. Furthermore, the difference between the critical potential of the primary and secondary components increases as  $e \rightarrow 1.0$ , as  $q \rightarrow 0$  and as  $F$  increases (when  $q$  is not equal to 1.0), as expected.

### 3.3.7 The $\log g$ Constraint

Usually, in eclipsing binary stars, the radii and  $\log g$  of the stellar components can be determined through modelling the eclipses. For the majority of heartbeat stars, this is not possible due to a lack of eclipses, and consequently constraints on  $\log g$  must be applied to aid the determination of the fundamental parameters. Furthermore, there exists a degeneracy in the heartbeat star light curve between the mass ratio, stellar potential and gravity darkening. As the values for gravity darkening are

theoretically known, the added constraint of the  $\log g$  value from spectra enables the degeneracy to be broken for single lined spectroscopic heartbeat stars. While this method of determination is significantly less accurate than modelling eclipses, it enables the determination of otherwise unobtainable stellar parameters.

If the  $\log g$  is known, within our software it is specified as a prior (with the range  $\pm 1\sigma$ ) instead of the radius or stellar potential. Within the function the stellar radius is calculated, given the values of the mass ratio,  $q$ , semi-major axis,  $sma$ , and period,  $P$  of the model for a given iteration. To do this, the mass of the stellar component must be determined using a combination of Kepler's Third Law and the mass ratio:

$$m_1 / M_{\odot} = \frac{(P/yr)^2}{1 + q} \frac{1}{(sma/Au)^3}, \quad (3.20)$$

where  $m_1$  is the mass of the primary component and  $q$  is replaced with  $q'$  where  $q' = 1/q$ , to determine the mass of the secondary component,  $m_2$ . The radius,  $r$ , is then computed by combining the prescribed  $\log g$  value with the determined mass,  $m$  (in S.I. units):

$$r = \sqrt{\frac{m}{\log g}}. \quad (3.21)$$

Once the radius has been determined, it is transformed into the stellar potential (see §3.3.5) and added into the PHOEBE code.

### 3.3.8 The Spin-to-Orbital Rotation Frequency

The spin-to-orbital rotation frequency,  $F$ , is a unitless parameter that describes how fast a star is spinning. For heartbeat stars, this parameter is important as the amount of stellar spin contributes to the oblateness of the star, which contributes to the amplitude of the periastron variation in the light curve.

If the  $v \sin i$  value is known from spectra, at each iteration  $F$  can be calculated, given the values of the stellar radius,  $r$ , in kilometres, period,  $P$ , in days, and the inclination,  $i$ , in degrees. First  $v \sin i$  must be converted into  $v$ , the rotational velocity of the star in kilometres per day, using the value of the inclination provided by the MCMC sampler:

$$v = \frac{86400v \sin(i)}{\sin(2\pi i/360)}. \quad (3.22)$$

To then calculate the spin-to-orbital rotational frequency, the radius must be converted from  $R_{\odot}$  to km. The spin-to-orbital rotation frequency,  $F$ , may then be calculated:

$$F = \frac{Pv}{2\pi r}. \quad (3.23)$$

If  $v \sin i$  is not known then a second resort is to assume pseudo-synchronous velocity (Hut, 1981). Pseudo-synchronous velocity occurs when the orbital angular velocity is equal to the rotational angular velocity at periastron (Hut, 1981):

$$F = \sqrt{\frac{1+e}{(1-e)^3}} \quad (3.24)$$

From our detailed studies I have found that some systems, *e.g.* KIC 8164262, are rotating with pseudo-synchronous velocity. Others, however, are far from it, *e.g.* KIC 5006817. Some factors that dictate a system's rotational velocity include third body interactions and recent evolutionary changes – KIC 5006817 is a recently evolved red giant star with an envelope that rotates 13 times slower than the core: neither segment is rotating pseudo-synchronously (see Chapter 6).

## 3.4 Conclusion

The study of heartbeat stars is a new and exciting field, recently propelled by observations from high resolution spacecraft such as *Kepler* and CoRoT. Interesting features of heartbeat stars include tidally induced pulsations, rapid apsidal motion and resonant pulsations and as they are in extreme orbital configurations, they also provide a test bed for binary orbital evolution.

Tidally induced pulsations are pulsations driven by the forcing of the binary star orbit. The signature of tidally induced pulsations are pulsation frequencies at multiples of the orbital frequency. Originally theorised by Zahn (1975), Goldreich & Nicholson (1989) and Witte & Savonije (2002) as a mechanism for the circularisation of the binary star orbit and the spin-up of stars, tidally induced pulsations were conclusively observed for the first time in KOI-54, the iconic heartbeat star, and have been identified in  $\sim 20\%$  of the *Kepler* sample of 173 heartbeat stars. In this work I describe the detailed analysis of KIC 3749404, KIC 8164262 and KIC 4544587 (see Chapters 5, 4 and 7), all of which display tidally induced pulsations.

In this Chapter, I discussed the addition of functionality to the PHOEBE code, necessary for modelling heartbeat stars. This included the addition of sine waves that describe tidally induced pulsations in the light curve. I also incorporated Doppler boosting into my models, alongside functions that calculate the passband luminosity; calculate the stellar potential given the radius; calculate the critical potential to prevent the stars from overflowing their Roche lobes; adding  $\log g$  as a constraint; and calculating the spin-to-orbital rotation frequency, given  $v \sin i$ . I further augmented the PHOEBE code by adding the ability to minimize the residuals using Markov chain Monte Carlo techniques, enabling the creation of parameter posteriors and robust uncertainty estimates.

The addition of the aforementioned functionality to PHOEBE has made it increasingly applicable to modelling heartbeat stars. These additions, while extensive, are

not complete, as a more advanced treatment of tidally induced pulsations, which incorporates adjustments to the binary star model on the level of the stellar mesh as a function of temperature and  $\log g$ , would provide a more thorough treatment of this feature. Furthermore, the application of the Roche potential to heartbeat stars clearly violates the assumptions of the *Principle of Equipotential Surfaces*. It is not clear to what extent this assumption has an affect on the results of binary star modelling; however, to improve this aspect, a complete rewrite of binary modelling codes is required. While these additions would further improve the current modelling approach, the approach outlined here forms the state-of-the-art for the modelling of heartbeat stars, as it currently stands.

# Chapter 4

## KIC 8164262

This chapter features a draft publication of the detailed study of KIC 8164262, a heartbeat star with a single high amplitude ( $\sim 1$  mmag) tidally resonant pulsation and a plethora of tidally induced pulsations. This case study is additionally contextualized by the discussion of heartbeat stars in Chapter 3, which includes a description of tidally induced pulsations and an outline of the program created to model this unusual object.

I led and coordinated the project, which included selection of the star and creating a full, self-consistent binary star model. The Keck spectroscopic observations were co-ordinated by J. Fuller and A. Shporer, and the observations and analysis were undertaken by H. Isaacson and A. Howard. The McDonald observations and analysis were undertaken by M. Endl and W. Cochran. The KPNO observations were undertaken by myself and A. Prša, and I undertook the analysis. I wrote the majority of the publication with the exception of the two paragraphs in Subsection 2.3 describing the Keck and McDonald observations, which were written by H. Isaacson and M. Endl, respectively. J. Fuller also contributed towards the "Discussion and Conclusions" section, Section 5. D. Kurtz and A. Prsa assisted with editing the paper. Finally, D. Kurtz, A. Prsa S. Thompson and J. Fuller contributed extensive and detailed discussion of its content.

# KIC 8164262: a Heartbeat Star Demonstrating Tidally Induced Pulsations with Resonant Locking

K. Hambleton<sup>1,2\*</sup>, J. Fuller<sup>3</sup>, S. Thompson<sup>4</sup>, A. Prša<sup>2</sup>, D. W. Kurtz<sup>1</sup>,  
A. Shporer<sup>5,6</sup>, H. Isaacson<sup>7</sup>, A. Howard<sup>8</sup>, M. Endl<sup>9</sup>, W. Cochran<sup>9</sup>, S. J. Murphy<sup>10</sup>

<sup>1</sup>Jeremiah Horrocks Institute, University of Central Lancashire, Preston, PR1 2HE

<sup>2</sup>Department of Astronomy and Astrophysics, Villanova University, 800 East Lancaster Avenue, Villanova, PA 19085, USA

<sup>3</sup>TAPIR, Walter Burke Institute for Theoretical Physics, Mailcode 350-17 California Institute of Technology, Pasadena, CA 91125

<sup>4</sup>NASA Ames Research Center, Moffett Field, CA 94035, USA

<sup>5</sup>Jet Propulsion Laboratory, California Institute of Technology, 4800 Oak Grove Drive, Pasadena, CA 91109, USA

<sup>6</sup>Sagan Fellow

<sup>7</sup>Astronomy Department, University of California, Berkeley, CA 94720, USA

<sup>8</sup>Institute for Astronomy, University of Hawaii, Honolulu, HI 96822, USA

<sup>9</sup>Department of Astronomy and McDonald Observatory, University of Texas at Austin, 2515 Speedway, Stop C1400, Austin, TX 78712, USA

<sup>10</sup>Stellar Astrophysics Centre, Department of Physics and Astronomy, Aarhus University, DK-8000 Aarhus C, Denmark

In prep.

## ABSTRACT

We present KIC 8164262, a heartbeat star with a prominent ( $\sim 1$  mmag), high-amplitude tidally resonant pulsation and a plethora of tidally induced g-mode pulsations. We obtained follow-up spectroscopic data from three telescopes: Keck, the 4-m Mayall telescope on KPNO and the 2.7-m telescope at McDonald observatory. To determine the spectroscopic parameters, we apply our own software that combines TODCOR with MCMC to the KPNO data. We apply PHOEBE to the *Kepler* light curve and radial velocity data to determine a detailed binary star model, which includes the prominent pulsation and Doppler boosting. The results suggest a slightly evolved F-type primary component with a M-type secondary in a highly eccentric ( $e = 0.886$ ) orbit. In a companion paper (Fuller et al., 2016), we show that the prominent pulsation is held in resonance by a mechanism known as resonant locking.

## 1 INTRODUCTION

Heartbeat stars are eccentric ( $e > 0.3$ ) ellipsoidal variables that undergo strong tidal interactions at the time of periastron. A consequence of these tidal interactions is that (for both components) the stellar cross-section changes shape, and the temperature across the stellar surface varies due to reflection and gravity darkening. These variations appear in the light curve in the form of a tidal pulse, the shape of which is dependant on the eccentricity, argument of periastron and inclination of the object. The first heartbeat star, KOI-54 (Welsh et al. 2011), was discovered using the *Kepler* satellite (Borucki et al. 2010; Gilliland et al. 2010; Batalha et al. 2010). Following this exciting discovery, many new heartbeat stars have been discovered: 17 heartbeat stars identified in the *Kepler* data by Thompson et al. (2012); 7 with the OGLE, the Optical Gravitational Lensing Experiment (Nicholls & Wood 2012); 17 red giant heartbeat stars by Beck et al. (2014); HD 51844 by Hareter et al. (2014) using the CoRoT satellite; KIC 10080943 by Schmid et al. (2015) using the *Kepler* satellite; and more recently a heartbeat star discovered using MOST and followed up with the CHARA array (Richardson et al. 2016). The most up-to-date and extensive list of *Kepler* heartbeat stars, containing 173

objects, has recently been published by Kirk et al. (2016) and can be found at the *Kepler* eclipsing binary website<sup>1</sup>.

Heartbeat stars are a diverse collection of objects, which display interesting characteristics such as solar-like oscillations (Beck et al. 2014), rapid apsidal motion (Hambleton et al. 2013, Hambleton et al. 2016, in prep.) and tidally induced pulsations (Welsh et al. 2011). Tidally induced pulsations, initially theorised by Zahn (1975); Goldreich & Nicholson (1989); Witte & Savonije (2002), are pulsations driven by the the varying tidal forces that occur as the stars orbit each other. They were hypothesised to cause the circularisation of binary star orbits and the spin-up of the stellar components, although, until *Kepler*, their presence had only been identified in HD 174884 (Maceroni et al. 2009). Thanks to *Kepler*, we now have a plethora of objects (173) with tidally induced pulsations. Approximately 20% of the current *Kepler* heartbeat star sample show tidally induced pulsations, providing us with a vast range of frequencies ( $\lesssim 10$  d<sup>-1</sup>) and amplitudes ( $\lesssim 1$  mmag) to investigate. Of these objects, thirteen pulsate with a single dominant, high-amplitude, tidally-excited pulsation, which is in resonance

<sup>1</sup> <http://keplerEBs.villanova.edu>

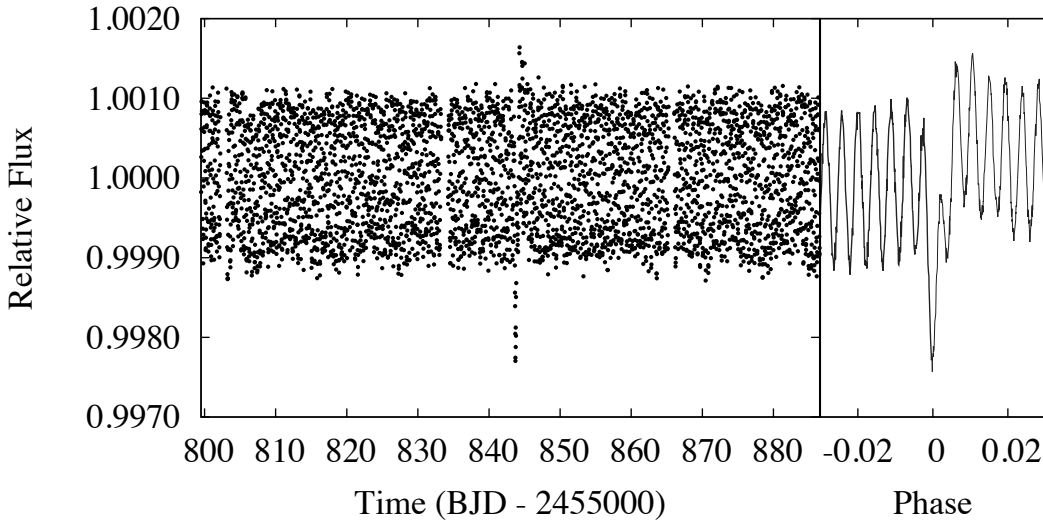


**Figure 1.** Left panel: The observed *Kepler* light curve of KIC 8164262 for a single orbit of 87.45 d during Quarter 9. The time is given in BJD - 2455000. Right panel: a magnified region of the phase-binned *Kepler* light curve from Quarters 0–17, containing the ellipsoidal variation at phase zero.

with the binary star orbit, attested to by the pulsation’s significantly higher amplitude than other modes. KIC 8164262, the focus of this work, is an extreme case with a single, high-amplitude ( $\sim 1$  mmag) tidally induced mode.

Resonant modes were initially theorised by Zahn (1975, 1977). However, due to the evolution of the binary star orbit, it was predicted that resonant pulsations would pass through resonance on a relatively short time scale, making observations extremely rare. This is clearly not the case, shown by the significant number of objects in the *Kepler* data that appear to have resonantly excited pulsations, so a mechanism must be present that maintains resonance. The proposed mechanism of resonance locking, theorised by Witte & Savonije (1999, 2001); Fuller & Lai (2012); Burkart et al. (2012), achieves this by locking the evolution of the binary star orbital period with the evolution of the eigenmodes as the stars spin faster. The theory of resonance locking states that as two stars orbit each other on an eccentric orbit, the orbit evolves via the transfer of angular momentum between the orbit and the stars. This causes the orbit to get smaller, thus the orbital period to get shorter, and the stars to spin faster. In parallel, due to the increase in stellar rotational velocities, the stellar eigenfrequencies change. When in resonance, these two effects happen on equal time scales so that the stellar eigenfrequencies are changing along with the changing orbital period. Consequently, rather than passing through resonance, the tidally induced pulsations are locked in resonance with the orbit.

A more extensive theoretical discussion of resonance locking, both generally and for the case of KIC 8164262, is described in the companion paper Fuller et al. (2016, in prep.; hereafter F16). F16 provides theoretical models showing that the prominent pulsation in KIC 8164262 aligns pre-

**Table 1.** Identifiers and basic data for KIC 8164262.  $K_p$  is the magnitude in the Kepler broadband filter.

Identifiers	
KIC	8164262
KOI	1810
Position and Brightness	
RA	19:24:59.239
Dec	+44:00:01.51
$K_p$	13.36

cisely with the predictions of the resonant locking mechanism, given the fundamental stellar parameters determined in this work. In this work we present the observations of KIC 8164262, a strong candidate for resonant locking. In §2 we describe the ground- and space-based observations; in §3 we outline the detailed binary model of KIC 8164262; in §4 we discuss the pulsations of KIC 8164262; and in §5 we discuss and summarise our findings.

## 2 OBSERVATIONS

KIC 8164262 was initially identified as a heartbeat star by the Kepler Eclipsing Binary Working Group and subsequently added to the Kepler Eclipsing Binary Catalog (Kirk et al. 2016). This object was selected for detailed study primarily due to its high amplitude resonantly excited mode, which makes it a strong candidate for resonant locking. For a list of observable information see Table 1.

## 2.1 Kepler Data

The *Kepler* telescope observed KIC 8164262 nearly continuously for 1470.5 d or 17 Quarters, where a Quarter is defined as a quarter of a complete, 372.5-d, *Kepler* orbit around the Sun (Kjeldsen et al. 2010). The observations of KIC 8164262 were obtained using the long cadence (hear after LC) data mode at a sampling rate of 29.4244 min. For each data point, 270 exposures of 6.02-s were co-added on board (Caldwell et al. 2010), with the remaining time attributed to read-out time. All observations were obtained from the Mikulski Archive for Space Telescopes and were a part of Data Releases 21–23 (Thompson et al. 2013a,b,c).

To create a time series of the relative flux variations of KIC 8164262, we used barycentric times as reported in the TIME column and the fluxes reported in the PDCSAP\_FLUX data column of the *Kepler* data files. These data have been processed through the *Kepler* pipeline (Fanelli et al. 2015), including the PDC (Presearch Data Conditioning) module of the pipeline, which uses a Bayesian, multi-scale principal component analysis to remove common features from the time series (Smith et al. 2012; Stumpe et al. 2012, 2014). We then fitted a low order (<4) polynomial to the times series of each Quarter. Our final light curve is created by dividing by this fit to yield the fractional variation in the flux.

As each *Kepler* pixel is  $4 \times 4$  arcsec, it is possible that some contamination may occur within the photometric mask in the form of light from an additional object. The contamination value for KIC 8164262, is 0.028 for all observed quarters as given in the headers of the downloaded light curve files (Fraquelli & Thompson 2014). Contamination runs from 0 to 1, where 0 implies no contamination and 1 implies complete contamination of the CCD pixels by other stars in the aperture. This contamination value suggests that KIC 8164262 suffers minimally from third light, if at all. To assess the flux incident on each individual pixel we used pyKE (Still & Barclay 2012) to generate the per-pixel light curve plots and examined the flux distribution over the newly defined masks. From this we visually confirmed that no other source is contaminating our observations.

## 2.2 Period Determination

Period analysis was performed to identify the orbital period of the binary system. The analysis was done on all data, Quarters (0–17), using *kephem* (Prša et al. 2011), an interactive package with a graphical user interface that incorporates 3 period finding methods: Lomb-Scargle (LS; Lomb 1976; Scargle 1982), Analysis of Variance (AoV; Schwarzenberg-Czerny 1989), and Box-fitting Least Squares (BLS; Kovács et al. 2002), as implemented in the *vartools* package (Hartman et al. 1998). Using *kephem*, the period and time of the minimum (selected to be the zero point in time) of the ellipsoidal variation were found interactively. The ephemeris was found to be:

$$\text{MinI} = \text{BJD } 2455668.829(3) + 87.4549(6) \times E$$

where the values in the parentheses give the one sigma uncertainties in the last digit. The period uncertainty was obtained by applying an adaptation of the Period Error

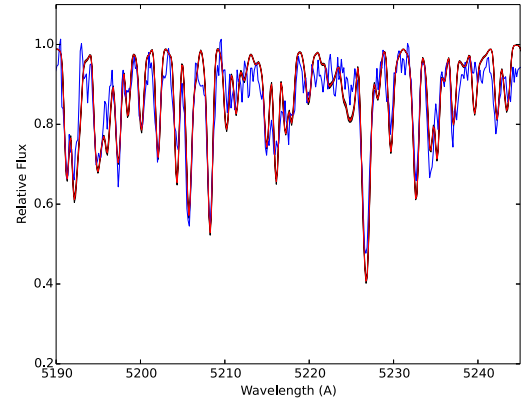


**Figure 2.** A section of the KPNO spectral data from 5190–5245 Å (blue line) with the best fit model (red line) using TODCOR combined with MCMC. The entire fitted region extends from 4800 Å to 6750 Å.

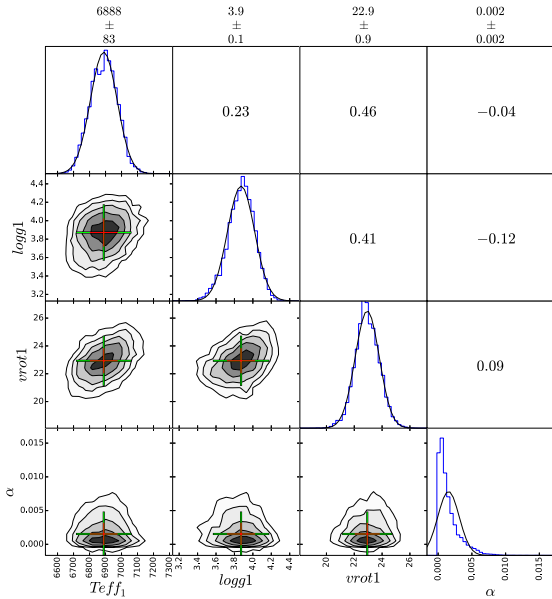
Calculator algorithm of Mighell & Plavchan (2013), as specified in Kirk et al. (2016).

## 2.3 Ground Based Spectroscopy

We obtained three sets of spectra, ten spectra from the HIRES spectrograph on the Keck telescope, Mauna Kea; three spectra using the Tull spectrograph on the 2.7-m telescope at McDonald Observatory; and two spectra using the Echelle Spectrograph on the 4-m Mayall telescope, Kitt Peak National Observatory (KPNO). The object was determined to be an SB1 system. The radial velocities derived from the three sets of observations are reported in Table 2.

Keck observations were taken with the standard setup of the California Planet Search (Howard et al. 2010) over the course of three months, beginning in May of 2015. Exposure times were between 120 and 180 seconds and each spectrum has a SNR of 25 per pixel at 5500 Angstroms with a resolution of 60,000. In order to calculate the systemic radial velocity, we utilize the telluric A and B absorption features that fall on 7594–7621 Å and 6867–6884 Å, respectively. Using the method from Chubak et al. (2012), the positions of the primary star’s spectral lines were measured relative to the telluric features. The positions of the spectral lines were converted into radial velocities and an offset was applied to place the relative radial velocities on the standard scale used by Nidever et al. (2002) and Latham et al. (2002). The errors per measurement are  $\pm 6 \text{ km s}^{-1}$ , owing predominantly to the rapid rotation of the primary star.

We further observed KIC 8164262 with the Tull Coude Spectrograph mounted on the Harlan J. Smith 2.7 m Telescope (Tull et al. 1995) at McDonald Observatory. The Tull spectrograph covers the entire optical spectrum at a resolving power of  $R = 60,000$ . We collected 3 spectra in August 2015. We used exposure times of 600 s (once) and 800 s (twice). The resulting spectra have a SNR ratio from 23 to 26 per resolution element at 5650Å. For each target visit we

4 *Hambleton et al.*

**Figure 3.** Posterior probability distribution functions produced by applying TODCOR combined with MCMC to the spectra obtained using the Mayall telescope at KPNO. Lower left subplots: two dimensional cross-sections of the posterior probability distribution functions. The crosses show the  $1\sigma$  (red) and  $2\sigma$  (green) uncertainties, and are centred on the minima. Diagonal subplots from top left to bottom right: histograms displaying the probability distributions of the effective temperature,  $T_{\text{eff}}$  (K); the surface gravity,  $\log g$  (dex); and the rotational velocity,  $v \sin i$  or  $vrot$  ( $\text{km s}^{-1}$ ); for the primary component, and  $\alpha$ , the fractional light contribution,  $f_2/(f_1 + f_2)$ , where  $f_1$  and  $f_2$  are the light contributions of the primary and secondary, respectively. Upper right subplots: the correlations for the two-dimensional cross-sections mirrored in the diagonal line where 1 is a direct correlation and -1 is a direct anti-correlation. The values above the plot give the mean value and one sigma uncertainty for each parameter, based on the fitted Gaussians.

also obtained a spectrum of HD 182488, the RV standard star, which we used to measure absolute radial velocities by cross-correlating the target star’s spectra with this standard star spectrum.

The KPNO observations were taken in sets of back-to-back exposures on 2013 May 29–30 (900 s each) and 2013 June 17–18 (750 s each). Calibration exposures were taken using a ThAr lamp prior to each exposure. Using the echelle spectrograph, a wavelength coverage of 4600 – 9050 Å was obtained with a resolving power of  $R \sim 20\,000$ . The signal-to-noise ratio obtained was  $\sim 30$  per resolution element. The data were reduced using the IRAF (Image Reduction and Analysis Facility) software package Tody (1986, 1993).

### 2.3.1 Deriving Fundamental Parameters and Radial Velocities from the KPNO Spectra

The radial velocity data from the KPNO observations were generated using the 2-D cross-correlation technique as implemented in TODCOR (Zucker & Mazeh 1994) combined

with the PYTHON implementation of EMCEE, an affine invariant version of Markov chain Monte Carlo (MCMC) method, proposed by Goodman & Weare (2010) and implemented by Foreman-Mackey et al. (2013). By combining these software packages, we were able to simultaneously obtain the posteriors of the fundamental parameters:  $T_{\text{eff}}$ ,  $v \sin i$  and  $\log g$ ; and obtain radial velocity distributions (distributions of possible radial velocities based on the range of possible spectral models and TODCOR uncertainties; Hambleton et al. 2016, in prep.).

MCMC explores the binary parameter space using a set of Markov chains, in this case 128. These chains begin with random distributions based only on their prior probability distribution functions. For both components, we provided uniform priors for  $T_{\text{eff}}$ ,  $v \sin i$  and  $\log g$ : 5000–8500 K, 0–100  $\text{km s}^{-1}$  and 2–5 dex, for the primary component; and 3000–5000 K, 0–100  $\text{km s}^{-1}$  and 4–5 dex for the secondary component. We also fitted the fractional light contribution,  $\alpha$  ( $L_2/(L_1 + L_2)$ ), and provided a prior of 0–0.1. While the results of the secondary component are inconclusive due to the low light contribution ( $< 0.5$  per cent), we marginalized over the secondary star’s atmospheric parameters to avoid biasing our results by selecting a specific spectrum.

At each step two spectra are generated (one for each component), from a grid of templates that are synthesized with SPECTRUM (Gray & Corbally 1994) using Castelli & Kurucz (2004) model atmospheres. The radial velocities of the primary component are then determined by applying TODCOR to the observations using the templates (adjusted to account for their light contributions). The  $\chi^2$  value is determined between the shifted, synthetic spectra and the observed spectra. We specify a global per-point uncertainty for the two spectra of  $\sigma = 0.03$ , which we determined by considering the noise level of the spectra. Each  $\chi^2$  value is then multiplied by -0.5 to obtain the log likelihood for each observed spectrum and the results are summed over all spectra

At each iteration the radial velocities and associated errors produced by TODCOR are also stored. The radial velocity distributions are then determined by combining the TODCOR radial velocity values and errors with the spread caused by the uncertainty in the model spectra. The outcome is a distribution of radial velocities that is marginalized over the model spectra and it includes the uncertainties from TODCOR. During the initial burn-in time, the Markov chains converge towards their maximum likelihood value. The statistics of a large number of iterations ( $\sim 10\,000$  excluding the burn-in time), provide posterior probability distributions for the model parameters. We applied this scheme to the two high resolution KPNO spectra of KIC 8164262 using the spectral range of 4800–6750 Å.

Due to its slow rotation (relative to stars above the Kraft break), we anticipated that KIC 8164262 would be a metal rich star. Consequently, we repeated the aforementioned spectral fitting for a range of metallicities:  $[\text{Fe}/\text{H}] = -0.2$ – $0.5$  in steps of 0.1. By comparing the log likelihoods in each case, we determined that a metallicity of  $[\text{Fe}/\text{H}] = 0.50 \pm 0.05$  provided the best fit (where the Castelli & Kurucz (2004) model libraries have a maximum metallicity of  $[\text{Fe}/\text{H}] = 0.5$ ). Using this method we determined the KPNO radial velocities provided in Table 2 and determined that KIC 8164262 is a single-lined spectroscopic binary with

**Table 2.** Radial velocities and their uncertainties for the primary component of KIC 8164262. The spectral observations were taken using the echelle spectrograph on the 4-m Mayall telescope, NAO, Kitt Peak, the HIRES spectrograph on Keck and Cross-Dispersed Echelle Spectrograph on the 2.7-m telescope at the McDonald Observatory, Fort Davis.

Time (BJD)	RV1 (km s <sup>-1</sup> )
Keck	±6 km s <sup>-1</sup>
2457151.059	26
2457202.893	15
2457228.979	18
2457237.074	28
2457239.988	33
2457241.068	37
2457243.031	15
2457244.791	-10
2457247.027	0
2457255.883	3.
KPNO	
2456442.7814	16.4 ± 2.1
2456461.7050	-2.3 ± 2.0
McDonald	
2457242.6297	29.3 ± 1.3
2457245.6356	14.6 ± 1.3
2457250.8001	1.81 ± 0.94

**Table 3.** Fundamental parameters determined using TODCOR combined with emcee. The software was applied to the spectral range 4800–6750 Å.

Parameters	Values
$T_{\text{eff}}$ (K)	6888 ± 83
$\log g$ (dex)	3.9 ± 0.1
$v \sin i$ (km s <sup>-1</sup> )	23 ± 1

the fundamental parameters listed in Table 3. The best-fit model to a portion of the spectrum is depicted in Fig. 2. The posterior distributions of the spectral parameters are depicted in Fig. 3 and are all Gaussian with the exception of the light ratio, which is consistent with 0, suggesting that the light from the secondary component is negligible. This demonstrates that our model is well constrained.

### 3 BINARY STAR MODEL

#### 3.1 Stellar Rotation

In the Fourier transform of the prewhitened light curve we identified two peaks ( $\nu = 0.3345 \text{ d}^{-1}$  and  $\nu = 0.6690 \text{ d}^{-1}$ ) that are not orbital harmonics. The second peak is the harmonic of the first, which suggests that the peaks are formed by cyclic variations in the light curve due to spots. As the amplitudes of these variations are 0.041(1) mmag and 0.012(1) mmag, respectively, the secondary star, which contributes less than 0.5 per cent of the total light, can be ruled out as the source of these variations. We thus obtain a rotational period for the primary component of 2.98942(6) d.

This is very close to the rotation period obtained by assuming pseudo-synchronous rotation, 3.1(2) d (Hut 1981). In our model we fixed the rotational period of the primary to the value of 2.98942(6) d, which implies  $F = 29.2547(2)$ , where  $F$  is the stellar to orbital rotation rate.

#### 3.2 Binary Model

We applied the binary modelling code PHOEBE (Prša & Zwitter 2005), which is an extension of the Wilson-Devinney code (Wilson & Devinney 1971; Wilson 1979; Wilson & Van Hamme 2004), to the light curve of KIC 8164262. PHOEBE combines the complete treatment of the Roche potential with the detailed treatment of surface and horizon effects such as limb darkening, reflection and gravity brightening to derive an accurate model of the binary star. The current implementation uses the Wilson-Devinney method of summing over the discrete rectangular surface elements that cover the distorted stellar surfaces. An accurate representation of the total observed flux and consequently a complete set of stellar and orbital parameters is then obtained by integrating over the visible elements. PHOEBE incorporates all the functionality of the Wilson-Devinney code, but also provides an intuitive graphical user interface alongside many other improvements, including updated filters and bindings that enable interfacing PHOEBE and PYTHON.

As modelling a large number of data points is computationally expensive, we elected to phase bin the data for the purpose of binary modelling. We argue this is appropriate for KIC 8164262, as the binary features and a tidally induced pulsation both repeat precisely every orbital cycle. Furthermore, KIC 8164262 has no significant temporal variations that would affect the binned light curve, *i.e.* apsidal motion, which would cause a change in the shape of the ellipsoidal variation as a function of time. The absence of apsidal motion is likely due to the long orbital period of KIC 8164262 (87.45 d).

As the information content of the light curve peaks at the time of periastron passage, we did not bin the data between the phases -0.01 and 0.01 and we kept all the data points. At all other phases we binned the data into bins of 100 points, thus significantly reducing the number of data points in these regions. Rather than having discrete segments in the light curve that contain vastly different numbers of data points per unit time, we used a sigmoid function to bridge the number of data points between regions. By using this method, we avoided jumps in the number of data points. Finally, we removed all remaining outliers from the data by eye.

The final binary star model was converged using a combination of PHOEBE and EMCEE. However, to understand our model parameters, we initially created a binary star model using PHOEBE's GUI. For this initial stage we prewhitened the primary pulsation from the light curve. When using the PHOEBE GUI, we identified the parameters that significantly impact the light curve shape of KIC 8164262. As this object is a single-lined non-eclipsing spectroscopic binary, this excludes the majority of parameters that pertain solely to the secondary component, with the exception of the upper limit on the secondary star's relative luminosity.

The parameters that were found to affect the binary star light and radial velocity curves are the eccentricity, in-

6 *Hambleton et al.*

**Table 4.** Fixed parameters and coefficients for the PHOEBE model to the light and radial velocity curves for all available quarters. As the secondary component contributes an insignificant amount of light, the secondary parameters are largely insignificant; however, the parameter values that we selected (based on estimates) are presented here for completeness.

Parameter	Value
Orbital Period (d)	87.4549(3)
Time of primary minimum (BJD)	2455668.829(3)
Primary $T_{\text{eff}}$ (K), $T_1$	6900(100)
Primary synchronicity parameter, $F$	29.2547(2)
Primary Bolometric albedo	0.6
Primary gravity brightening	0.32
Secondary $T_{\text{eff}}$ (K), $T_2$	3500
Secondary radius ( $R_{\odot}$ ), $R_2$	0.5
Secondary synchronicity parameter, $F$	29
Secondary Bolometric albedo	0.6
Secondary gravity brightening	0.32
Third light	0.0

**Table 5.** Adjusted parameters and coefficients of the best-fit model to the light and radial velocity curves for the phased light curve data and all radial velocity measurements. The RV shifts are the vertical shifts applied to radial velocities to account for using different telescopes. The fit was performed using Markov chain Monte Carlo methods and the values in the brackets denote the  $1\sigma$  uncertainties.

Parameter	Value
Mass ratio, $q$	0.2(4)
Primary mass ( $M_{\odot}$ ), $M_1$	1.70(9)
Secondary mass ( $M_{\odot}$ ), $M_2$	0.36(2)
Primary radius ( $R_{\odot}$ ), $R_1$	2.4(1)
Phase shift, $\phi$	0.014(1)
Orbital eccentricity, $e$	0.886(3)
Argument of periastron (rad), $\omega$	1.48(1)
Orbital inclination (degrees), $i$	65(1)
Primary luminosity (%), $L_1$	98.9(2)
Secondary luminosity (%), $L_2$	1.1(1)
Semi-major axis ( $R_{\odot}$ ), $sma$	106(2)
Primary $\log g$ (cgs), $\log g_1$	3.90(3)
KPNO RV shift ( $\text{km s}^{-1}$ ), $shift1$	2.7(1)
McDonald RV shift ( $\text{km s}^{-1}$ ), $shift2$	-2.5(7)

clination, argument of periastron, phase shift, primary radius, primary gravity brightening exponent, luminosity ratio, mass ratio, semi-major axis and systemic velocity, where the phase shift is a convenience parameter that shifts the model horizontally to keep the minimum of the ellipsoidal variation at phase 0.0. As the gravity darkening exponent is completely degenerate with the primary star's radius, we elected to fix the gravity darkening exponent to 0.32, which is the theoretical value for stars with convective outer envelopes (Lucy 1967), even when the envelope is very thin. A list of all the fixed parameters in our binary model can be found in Table 4.

### 3.3 Parameter Space Sampling

To create the final model we combined PHOEBE with MCMC to integrate the power of PHOEBE as a binary modelling code with Bayesian statistics. This was possible due to the recent update of PHOEBE to include python interfacing. We again elected to use EMCEE, an affine invariant version of MCMC, which is discussed in detail in §2.3.1. In addition to the standard functionality of PHOEBE, our models include the ability to fit tidally induced pulsations and Doppler boosting, as prescribed by Bloemen et al. (2011).

For KIC 8164262 we elected to fit the high-amplitude prominent pulsation simultaneously with the binary star features. The signature of a tidally induced pulsation is a pulsation whose frequency is a precise multiple of the orbital frequency. The prominent pulsation in KIC 8164262 is  $228.999(2)\nu_{orb}$  which is consistent with  $229\nu_{orb}$ , given the uncertainty on the orbital period and pulsation frequency. In our model we fixed the frequency of the pulsation to the multiple of the orbital frequency and fitted the phase and amplitude to create an all-encompassing binary star model.

Doppler boosting is proportional to the radial velocity of the two stars and is the combined effect of shifting the stars' spectral energy distributions with respect to the *Kepler* passband, aberration and an altered photon arrival rate. The net result of Doppler boosting is an increase in the observed flux from a star when it moves towards the observer, and a decrease when it moves away from the observer. It was predicted to be seen in the *Kepler* data by Loeb & Gaudi (2003) and Zucker, Mazeh & Alexander (2007), and has been observed in several systems from ground-based data as well as *Kepler* and CoRoT light curves (see e.g. Mazeh & Faigler 2010; van Kerkwijk et al. 2010; Shporer et al. 2010; Bloemen et al. 2011). To determine the Doppler boosting coefficients, we used look-up tables, based on each component's effective temperature and  $\log g$ . These look-up tables take into account the spectrum of the star and the wavelength of the observations, and were computed from Kurucz 2004 model spectra (Castelli & Kurucz 2004) using Eq. (3) of Bloemen et al. (2011). The Doppler boosting contribution was estimated to be  $\sim 300$  ppm. The calculation for Doppler boosting was performed at each iteration.

In our model we restricted the  $\log g$  of the primary component to that determined from spectral fitting,  $\log g_1 = 3.9 \pm 0.1$ . Consequently, at each iteration we calculated the primary star's potential (an input for PHOEBE that is a proxy for the stellar radius), which is a function of the mass ratio, instantaneous separation, spin-to-orbital rotation and  $\log g$ . We also calculated the stellar luminosity, thus reducing the number of fitted parameters to twelve. Of these fitted parameters, eight are binary star parameters: the inclination, eccentricity, argument of periastron, phase shift, mass ratio, semi-major axis, systemic velocity and  $\log g$  of the primary component. Two pulsation parameters are the amplitude and phase of the high-amplitude, tidally-induced pulsation, and two are vertical radial velocity shifts to account for having radial velocity data from three different telescopes. We fixed the pulsation frequency to  $229\nu_{orb}$ , as by definition, tidally induced pulsations are precise multiples of the orbital frequency. Deviations from precise multiples have not been detected, even with the precise, high-resolution *Kepler* data. These parameters were se-

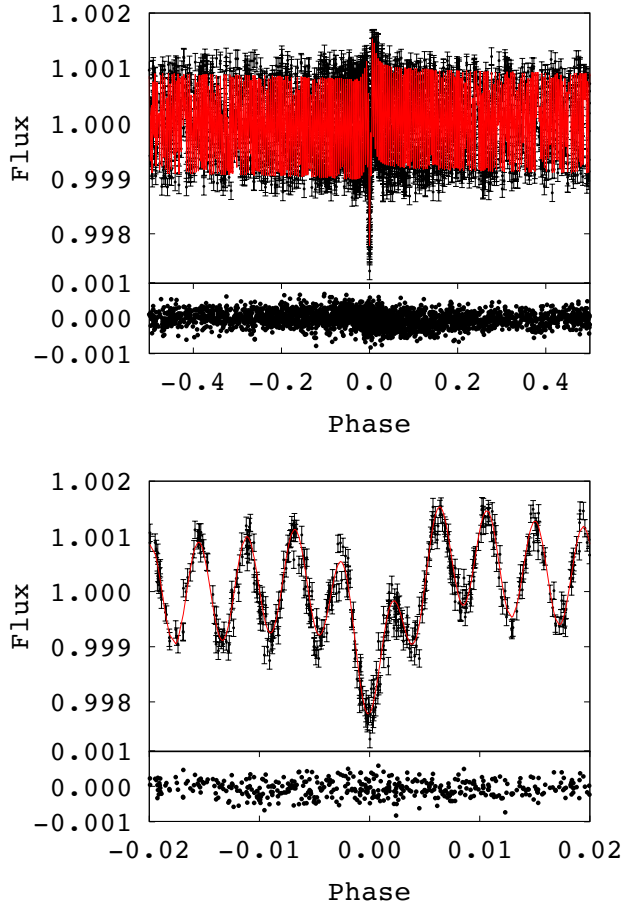


**Figure 4.** Upper panel: The best-fit light curve model (red line) to the *Kepler* data of KIC 8164262 (black). The  $1\sigma$  uncertainties are denoted on the plot. The residuals of the best-fit model are provided below the model. Lower panel: A magnified section of the periastron variation displaying the best-fit model.

lected based on their significant contribution to the light curve. All other parameters do not present a significant contributions and so were excluded from our models, with the exception of the primary effective temperature, which we fixed based on the spectral information; the period and zero point in time, which were fixed based on our period determination; the stellar rotation rate, which we fixed based on the stellar rotation signature in the light curve due to spots; and the aforementioned primary gravity darkening exponent, which we fixed to the observationally determined value of 0.32.

For each parameter we used a flat, uniform prior. The prior ranges were selected to be as large as possible without creating unphysical models, with the exception of  $\log g$ , which we constrained to be within one sigma of the value obtained through spectral fitting and the inclination that was restricted to be below  $90^\circ$ . The likelihood was generated by multiplying the  $\chi^2$  value from the light curve data by -0.5 and summing this with the  $\chi^2$  value from the radial

**Table 6.** Frequencies extracted from the masked light curve of KIC 8164262. The majority of the frequencies extracted are multiples of the orbital frequency, with the exception of the two rotation peaks and three frequencies under  $1\text{ c d}^{-1}$ . The asterisks denotes that the frequency extracted is very close to the large amplitude 229<sup>th</sup> orbital harmonic (such that it  $229\nu_{orb}$ ). Phase 1 is relative to the zero point in time specified in subsection 2.2 and Phase 2 is relative to the time of periastron (2455652.4222(2)). The values in parentheses denote the uncertainty in the last digits of the previous value.

Freq ( $\text{c d}^{-1}$ )	Notes	Amp (ppt)	Phase 1 (rad)	Phase 2 (rad)
2.6184922(3)	$229\nu_{orb}$	1.01(2)	5.19(6)	5.30(6)
0.334512(7)	rotation	0.041(1)	4.06(2)	0.99(2)
2.755699(9)	$241\nu_{orb}$	0.035(1)	0.51(2)	5.46(2)
1.40645(1)	$123\nu_{orb}$	0.023(1)	5.69(4)	5.22(4)
2.61912(2)	$229\nu_{orb}^*$	0.016(2)	1.82(10)	2.01(10)
1.41786(2)	$124\nu_{orb}$	0.015(1)	1.00(6)	5.62(6)
1.80665(2)	$158\nu_{orb}$	0.015(1)	4.10(6)	0.06(6)
1.50933(2)	$132\nu_{orb}$	0.013(1)	0.94(6)	2.43(6)
2.21831(2)	$194\nu_{orb}$	0.012(1)	3.35(7)	0.86(7)
0.66907(2)	rotation	0.012(1)	5.32(7)	5.46(7)
1.46360(3)	$128\nu_{orb}$	0.012(1)	4.56(7)	4.48(7)
2.61832(3)	$229\nu_{orb}^*$	0.011(1)	5.0(1)	5.2(1)
3.62472(3)	$317\nu_{orb}$	0.010(1)	4.88(9)	1.92(9)
1.47501(4)	$129\nu_{orb}$	0.008(1)	1.2(1)	6.2(1)
0.28383(4)	–	0.008(1)	2.3(1)	4.5(1)
0.28033(4)	–	0.008(1)	6.0(1)	2.2(1)
1.42931(4)	$125\nu_{orb}$	0.007(1)	1.4(1)	4.8(1)
0.28504(5)	–	0.007(1)	0.7(1)	2.8(1)
1.56644(4)	$137\nu_{orb}$	0.007(1)	4.2(1)	6.1(1)
2.61901(5)	$229\nu_{orb}^*$	0.006(1)	5.1(2)	5.2(2)
3.01870(6)	$264\nu_{orb}$	0.006(1)	5.5(1)	2.2(1)
0.25121(5)	$22\nu_{orb}$	0.006(1)	6.2(1)	5.4(1)
1.30355(5)	$114\nu_{orb}$	0.006(1)	0.3(1)	4.2(1)

velocity data, again, multiplied by -0.5. Fig. 4 depicts the model fit to the light curve. The light curve fit obtained is well constrained, as shown by the residuals presented in the lower panel. Fig. 5 depicts the radial velocity curve (red line) and data. The blue points are Keck data, the red points are McDonald data and the green points are KPNO data. The lines on the McDonald and KPNO data in the upper panels denote the vertical shift applied due to the difference in the instrumentation (where the horizontal line denotes the original position of the data).

For all parameters, the posteriors shown in Fig. 6, are well approximated by Gaussians. The list of adjustable parameters and their final values from our MCMC model fit are presented in Table 5. The parameters are suggestive of a slightly evolved F star primary component. The light ratio provides an upper estimate of the secondary component's light contribution, which is suggestive of an M-type star. From the parameters obtained, the stars are  $12.1(2)R_\odot$  apart at periastron and  $200(4)R_\odot$  apart at apastron. This significant variation in separation is the driving force of the tidally induced pulsations observed in KIC 8164262.

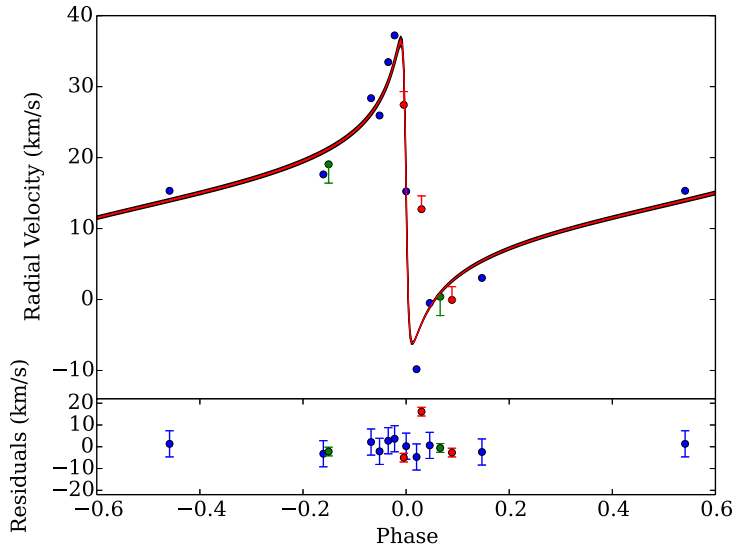


**Figure 5.** Upper panel: The best-fit radial velocity curve (red) to the KPNO radial velocity points (green) Keck radial velocity points (blue) and McDonald radial velocity points (red). The lines on the red and green points denote the vertical shift applied to align the data points, where the horizontal lines denote the original placement of the points. The vertical shifts are attributed to the use of different telescopes and were fitted simultaneously with the binary star model. Bottom panel: the residuals of the best-fit model. The error bars denote the one sigma uncertainty on the radial velocities.

#### 4 PULSATION CHARACTERISTICS

The light curve of KIC 8164262 contains one high-amplitude, tidally-excited mode ( $\nu = 229 \nu_{orb}$ , cf. Fig. 4), which we fitted simultaneously with the binary star model. The amplitude and phase of the  $229^{th}$  orbital harmonic were found to be  $A = 1.01(2)$  mmag and  $\phi = 5.19(6)$  rad (relative to the zero point specified in Subsection 2.2), respectively. Fourier transforms with no peaks removed (top panel), with the binary model and  $229^{th}$  orbital harmonic subtracted (middle panel) and with all the peaks to an amplitude of  $4 \mu\text{mag}$  removed can be seen in Fig. 7. The prominence of the  $229^{th}$  orbital harmonic can clearly be seen in the top panel (note the change of scale for the different panels).

The binary star model, including the high amplitude mode, was then subtracted from the time-series light-curve data and the residuals were analysed. To remove any residual information from the binary star features, the data points were removed from the region between phases  $-0.05$  to  $0.05$ , the phases of the ellipsoidal variation in the original time series. In the Fourier transform, these gaps appear as a window pattern, separated from the main peak by the orbital frequency. However, as the binary orbital period is long compared to the duration of the ellipsoidal variation, the removal of these points did not create a window pattern with a significant amplitude. We applied a Fourier transform to these data and found that the highest amplitude pulsation peak that remained (after the significant high amplitude peak had been removed) had an amplitude of 35 ppm, which is 3.5 per cent of the large amplitude mode fitted simultaneously with the binary features.

We individually extracted each mode from the Fourier transform until we reached an amplitude of  $6 \mu\text{mag}$ . Beyond this point we were unable to distinguish between pulsation frequencies and noise. Table 6 provides a list of the extracted frequencies, amplitudes and phases relative to periastron. We also provide the orbital harmonic number for each pulsation – all peaks are orbital harmonics with the exception of three peaks at  $\nu = 0.28033(4) \text{ d}^{-1}$ ,  $\nu = 0.28383(4) \text{ d}^{-1}$  and  $\nu = 0.28504(5) \text{ d}^{-1}$ , and the two rotational peaks at  $\nu = 0.3345 \text{ d}^{-1}$  and  $\nu = 0.6690 \text{ d}^{-1}$ , discussed in Subsection 3.1. We speculate that the former three pulsations are naturally occurring g mode pulsations as the primary star temperature is consistent with that of a  $\gamma$  Dor pulsator, which pulsates on the order of  $1 \text{ d}^{-1}$  (Grigahcène et al. 2010).

We extended our frequency search beyond the Nyquist frequency to ensure that we had identified all the peaks and that the selected peaks were not reflections of the real peaks about the Nyquist frequency. All peaks beyond the Nyquist frequency showed evidence of super Nyquist aliasing (SNA), aliasing caused by the irregular time sampling of Kepler data due to satellite motion (Murphy, Shibahashi & Kurtz 2013). Thus we conclude that the identified peaks are the real peaks.

#### 5 DISCUSSION AND CONCLUSIONS

KIC 8164262 is an extreme heartbeat star, in that its orbital period and eccentricity are larger than most of the heartbeat stars discovered to date. Its most striking feature is the large

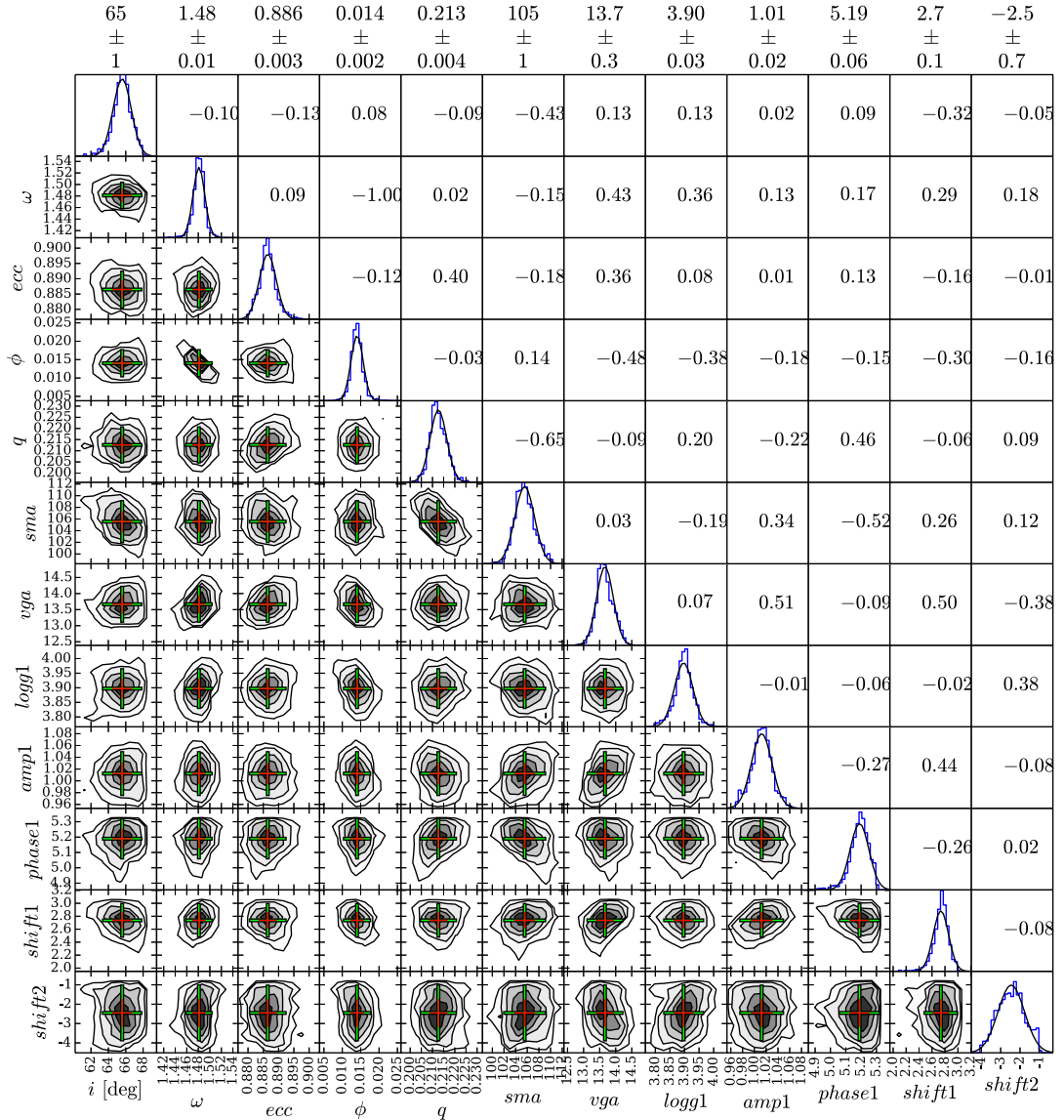


**Figure 6.** Posterior distributions of the binary star parameters for KIC 8164262, where  $incl$  is the inclination of the binary star orbit in degrees;  $\omega$  is the argument of periastron in radians;  $e$  is the eccentricity;  $\phi$  is the orbital phase shift;  $q$  is the mass ratio ( $m_2/m_1$ );  $sma$  is the semi-major axis in  $R_\odot$ ;  $vga$  is the gamma velocity in  $\text{km s}^{-1}$ ;  $logg1$  is the surface gravity in dex;  $amp1$  and  $phase1$  are the amplitude (in mmag) and phase of the high-amplitude pulsation; and  $shift1$  and  $shift2$  are the radial velocity shifts (in  $\text{km s}^{-1}$ ) applied to the KPNO and McDonald radial velocity data sets, respectively. The layout is analogous to that in Fig. 3.

amplitude tidally excited pulsation at  $229 \nu_{\text{orb}}$ , which the largest amplitude tidally excited pulsation observed to date. The frequency of this pulsation is not unusual (frequencies of  $0.5 \text{ d}^{-1} \lesssim \nu_{\text{orb}} \lesssim 3 \text{ d}^{-1}$  are common in heartbeat stars), it simply occurs at a large orbital harmonic because of the small orbital frequency. However, the amplitude of the pulsation is exceptional, as it is over twenty times larger than

any other pulsation in KIC 8164262, and roughly four times larger than any pulsations in KOI-54.

We have presented the light and radial velocity data of KIC 8164262, a heartbeat star with tidally induced pulsations, one of which is extremely prominent. The LC *Kepler* data of Quarters 0–17 and radial velocities from three different telescopes (Keck, the 4-m Mayall telescope at KPNO and the 2.7 m telescope on the McDonald Observatory) were

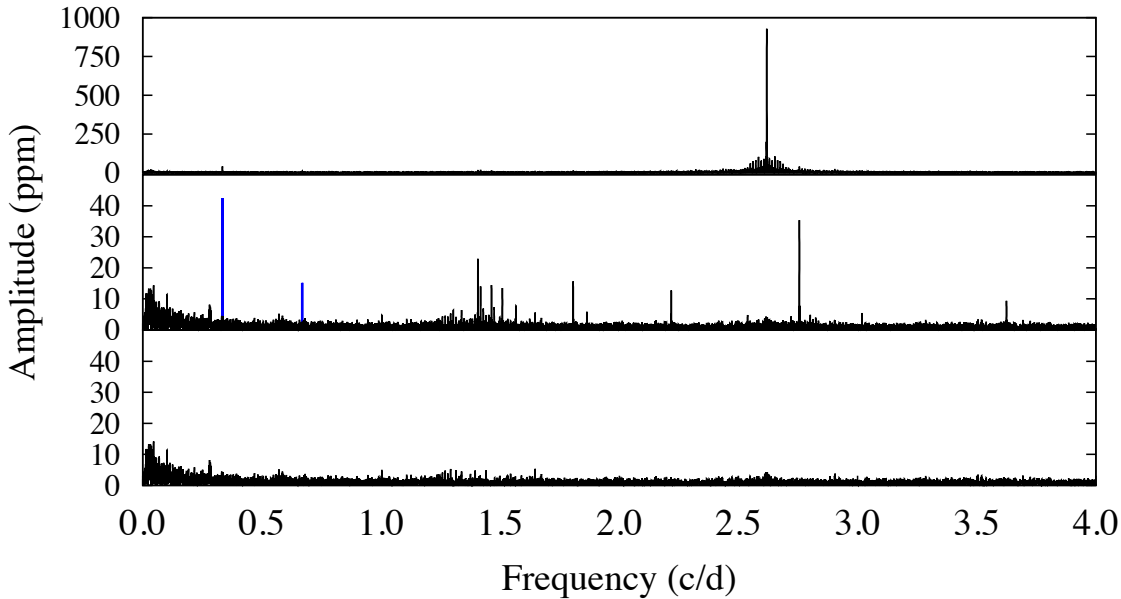


**Figure 7.** Fourier transforms showing the frequency spectrum at different stages. Starting from the top, depicted are the Fourier transforms with: no peaks removed (note the single prominent peak at  $2.6 \text{ d}^{-1}$ , the  $229^{\text{th}}$  orbital harmonic); the binary model and primary pulsation subtracted (note the change of scale), where the two rotation peaks at  $0.3345 \text{ d}^{-1}$  and  $0.6690 \text{ d}^{-1}$  are highlighted in blue; all peaks removed to an amplitude of  $4 \mu\text{mag}$ .

modelled using PHOEBE combined with EMCEE, an affine invariant version of MCMC. We further augmented the software to include the ability to model tidally induced pulsations, which we used to model the prominent tidally induced pulsation at  $229 \nu_{orb}$ , and to model Doppler boosting. The results of the spectral analysis on the KPNO spectra, specifically the effective temperature and  $\log g$  of the primary component, were also incorporated into the modelling effort to fully constrain the fundamental parameters. Using these combined software packages, we determined that KIC 8164262 contains a slightly evolved F-type star, which is producing the tidally induced pulsations, and a M-type star.

Such a large amplitude mode requires explanation and may yield clues to tidal dissipation processes in binary star systems. In a companion paper, F16, we calculate the expected frequencies and amplitudes of tidally excited pulsations from theoretical considerations. We find that an extremely finely tuned resonance is required to tidally excite a mode to the observed amplitude, and such a resonance is unlikely to occur by chance. Instead, we find that the pulsation is well explained (in both frequency and amplitude) as a resonantly locked mode. In this scenario, the combined effects of stellar evolution and spin-down are balanced by ongoing tidal circularization and synchronization in a self-regulating process such that the frequency of a single pulsation mode is held at resonance with the tidal forcing. The result is an increased rate of tidal dissipation compared to conventional expectations (see Zahn (2008) for a review).

For A–F stars, tidal interactions are expected to be weak due to the absence of a thick convective envelope and the presence of only a small convective core, entailing an effective tidal quality factor (which measures the efficiency of tidal dissipation) of  $Q > 10^5$ . However, for KIC 8164262 we calculate the effective tidal quality factor to be  $Q \sim 10^4$  while the resonance lock is active, corresponding to an orbital circularization timescale of  $\sim 1 \text{ Gyr}$ . This is suggestive of the importance of resonance locking for the acceleration of orbital circularization. Further details are presented in F16.

We performed pulsational analysis on the *Kepler* light curve of Quarters 0–17 with the binary star model removed. We found that all the identified peaks, with the exception of five, were multiples of the orbital frequency, thus we conclude that these are all tidally induced pulsations. Of the remaining 5 we identified three peaks at  $\nu = 0.28033(4) \text{ d}^{-1}$ ,  $\nu = 0.28383(4) \text{ d}^{-1}$  and  $\nu = 0.28504(5) \text{ d}^{-1}$ , which are likely g-mode pulsations originating from the primary component. The remaining two peaks have frequencies at  $\nu = 0.3345 \text{ d}^{-1}$  and  $\nu = 0.6690 \text{ d}^{-1}$ , where the latter is the harmonic of the former. This is suggestive of cyclical variation due to spots. Using the frequencies of these peaks we calculated the rotational period of the primary component to be  $2.98942(6) \text{ d}$ . Interestingly, this agrees with the theoretically predicted period for pseudo-synchronous rotation,  $3.1(2) \text{ d}$ . Considering this rotation period combined with the primary star radius determined in § 3.2 ( $R_1 = 2.4(1) R_\odot$ ) and  $v \sin i$  determined through spectra ( $v \sin i = 23(1) \text{ km s}^{-1}$ ) we infer that the

inclination of the star is  $i_{star} = 35(3)^\circ$ , suggesting that the primary star is miss-aligned with the binary star orbit by  $30(3)^\circ$ . Similar misalignment has been observed in objects such as DI Her, which is also a detached, eccentric ( $e = 0.489$ ) binary system (Albrecht et al. 2009). If the star is miss-aligned, it is likely that the misalignment occurred during early binary formation (Albrecht et al. 2011).

## 6 ACKNOWLEDGEMENTS

The authors express their sincere thanks to NASA and the *Kepler* team for allowing them to work with and analyse the *Kepler* data making this work possible. The *Kepler* mission is funded by NASA's Science Mission Directorate. This work was also supported by the STFC (Science and Technology Funding Council). KH, ST and JF acknowledge support through NASA K2 GO grant (11-KEPLER11-0056). We would like to thank the RAS for providing grants which enabled KH's attendance to conferences and thus enabled the development of collaborations and the successful completion of this work. AP acknowledges support through NASA K2 GO grant (NASA 14-K2GO1\_2-0057). We acknowledge the observations taken using the 4-m Mayall telescope, KPNO; the Keck telescope, Mauna Kea; and the 2.7-m telescope at the McDonald Observatory.

## REFERENCES

- Albrecht S., Reffert S., Snellen I. A. G., Winn J. N., 2009, *Nature*, 461, 373
- Albrecht S., Winn J. N., Carter J. A., Snellen I. A. G., de Mooij E. J. W., 2011, *ApJ*, 726, 68
- Batalha N. M. et al., 2010, *ApJ*, 713, L109
- Beck P. G. et al., 2014, *A&A*, 564, A36
- Bloemen S. et al., 2011, *MNRAS*, 410, 1787
- Borucki W. J., Koch D., Basri G., Batalha N., Brown T., Caldwell D., et al., 2010, *Science*, 327, 977
- Burkart J., Quataert E., Arras P., Weinberg N. N., 2012, *MNRAS*, 421, 983
- Caldwell D. A., Kolodziejczak J. J., Van Cleve J. E., Jenkins J. M., Gazis P. R., Argabright V. S., et al., 2010, *ApJ*, 713, L92
- Castelli F., Kurucz R. L., 2004, *ArXiv Astrophysics e-prints*
- Chubak C., Marcy G., Fischer D. A., Howard A. W., Isaacson H., Johnson J. A., Wright J. T., 2012, *ArXiv e-prints*
- Fanelli M. N., Jenkins J. M., Bryson S. T., Quintana E. V., Twicken J. D., Wu H. W., Tenenbaum P., Allen C. L., 2015, *Kepler Data Processing Handbook*
- Foreman-Mackey D., Hogg D. W., Lang D., Goodman J., 2013, *PASP*, 125, 306
- Fraquelli D., Thompson S. E., 2014, "Kepler Archive Manual"
- Fuller J., Lai D., 2012, *MNRAS*, 420, 3126
- Gilliland R. L., Brown T. M., Christensen-Dalsgaard J., Kjeldsen H., Aerts C., et al., 2010, *PASP*, 122, 131
- Goldreich P., Nicholson P. D., 1989, *ApJ*, 342, 1079
- Goodman J., Weare J., 2010, *Com. App. Math. Comp. Sci.*, 5, 65
- Gray R. O., Corbally C. J., 1994, *AJ*, 107, 742
- Grigahcène A. et al., 2010, *ApJ*, 713, L192
- Hambleton K. M. et al., 2013, *MNRAS*, 434, 925
- Hareter M. et al., 2014, *A&A*, 567, A124
- Hartmann E., 1998, *CAGD*, 15, 377
- Howard A. W. et al., 2010, *ApJ*, 721, 1467
- Hut P., 1981, *A&A*, 99, 126
- Kirk B. et al., 2016, *AJ*, 151, 68
- Kjeldsen H., Christensen-Dalsgaard J., Handberg R., Brown T. M., Gilliland R. L., Borucki W. J., Koch D., 2010, *Astronomische Nachrichten*, 331, 966
- Kovács G., Zucker S., Mazeh T., 2002, *A&A*, 391, 369
- Latham D. W., Stefanik R. P., Torres G., Davis R. J., Mazeh T., Carney B. W., Laird J. B., Morse J. A., 2002, *AJ*, 124, 1144
- Loeb A., Gaudi B. S., 2003, *ApJ*, 588, L117
- Lomb N. R., 1976, *Ap&SS*, 39, 447
- Lucy L. B., 1967, *ZEASAJ*, 65, 89
- Maceroni C. et al., 2009, *A&A*, 508, 1375
- Mazeh T., Faigler S., 2010, *A&A*, 521, L59+
- Mighell K. J., Plavchan P., 2013, *AJ*, 145, 148
- Murphy S. J., Shibahashi H., Kurtz D. W., 2013, *MNRAS*, 430, 2986
- Nicholls C. P., Wood P. R., 2012, *MNRAS*, 421, 2616
- Nidever D. L., Marcy G. W., Butler R. P., Fischer D. A., Vogt S. S., 2002, *ApJS*, 141, 503
- Prša A. et al., 2011, *AJ*, 141, 83
- Prša A., Zwitter T., 2005, *ApJ*, 628, 426
- Richardson N. D. et al., 2016, *MNRAS*, 455, 244
- Scargle J. D., 1982, *ApJ*, 263, 835
- Schmid V. S. et al., 2015, *A&A*, 584, A35
- Schwarzenberg-Czerny A., 1989, *MNRAS*, 241, 153
- Shporer A., Kaplan D. L., Steinfeldt J. D. R., Bildsten L., Howell S. B., Mazeh T., 2010, *ApJ*, 725, L200
- Smith J. C. et al., 2012, *PASP*, 124, 1000
- Still M., Barclay T., 2012, *PyKE: Reduction and analysis of Kepler Simple Aperture Photometry data. Astrophysics Source Code Library*
- Stumpe M. C., Smith J. C., Catanzarite J. H., Van Cleve J. E., Jenkins J. M., Twicken J. D., Girouard F. R., 2014, *PASP*, 126, 100
- Stumpe M. C. et al., 2012, *PASP*, 124, 985
- Thompson S. E. et al., 2013a, *Kepler Data Release 21 Notes*
- Thompson S. E. et al., 2013b, *Kepler Data Release 22 Notes*
- Thompson S. E. et al., 2013c, *Kepler Data Release 23 Notes*
- Thompson S. E. et al., 2012, *ApJ*, 753, 86
- Tody D., 1986, in *Proceedings of the International Society for Optical Engineering*, Vol. 627, *Instrumentation in astronomy VI*, Crawford D. L., ed., p. 733
- Tody D., 1993, in *Astronomical Society of the Pacific Conference Series*, Vol. 52, *Astronomical Data Analysis Software and Systems II*, Hanisch R. J., Brissenden R. J. V., Barnes J., eds., p. 173
- Tull R. G., MacQueen P. J., Sneden C., Lambert D. L., 1995, *PASP*, 107, 251
- van Kerkwijk M. H., Rappaport S. A., Breton R. P., Justham S., Podsiadlowski P., Han Z., 2010, *ApJ*, 715, 51
- Welsh W. F. et al., 2011, *ApJS*, 197, 4
- Wilson R. E., 1979, *ApJ*, 234, 1054
- Wilson R. E., Devinney E. J., 1971, *ApJ*, 166, 605
- Wilson R. E., Van Hamme W., 2004, *Computing Binary Star Observables (in Reference Manual to the Wilson-*

12 *Hambleton et al.*

Devinney Program)

Witte M. G., Savonije G. J., 1999, *A&A*, 350, 129

Witte M. G., Savonije G. J., 2001, *A&A*, 366, 840

Witte M. G., Savonije G. J., 2002, *A&A*, 386, 222

Zahn J.-P., 1975, *A&A*, 41, 329

Zahn J.-P., 1977, *A&A*, 57, 383

Zahn J.-P., 2008, in *EAS Publications Series*, Vol. 29, *EAS Publications Series*, Goupil M.-J., Zahn J.-P., eds., pp. 67–90

Zucker S., Mazeh T., 1994, *ApJ*, 420, 806

Zucker S., Mazeh T., Alexander T., 2007, *ApJ*, 670, 1326

# Chapter 5

## KIC 3749404

This chapter features a draft publication of the detailed study of KIC 3749404, a heartbeat star with tidally induced pulsations and rapid apsidal motion. This case study is additionally contextualized by the discussion of heartbeat stars in Chapter 3, which includes a description of tidally induced pulsations and an outline of the program created to model this interesting object.

I led and coordinated the project, which included selection of the star and creating a full, self-consistent binary star model. I further determined of the rate of apsidal motion and compared it with theoretical values. I wrote the majority of the publication with the exception of subsection 2.2, entitled “Ground-based spectroscopy”, which was co-written by S. Quinn and S. Murphy. The spectroscopic analysis was led by S. Quinn and D. Latham. S. Murphy provided additional spectroscopic analysis. D. Kurtz assisted with editing the paper, and he, A. Prša, S. Thompson and J. Fuller contributed extensive, detailed discussion of its content.

# KIC 3749404: A Heartbeat Star with Rapid Apsidal Advance Indicative of a Tertiary Component

K. Hambleton<sup>1,2\*</sup>, D. W. Kurtz<sup>2</sup>, A. Prša<sup>2</sup>, S. N. Quinn<sup>3</sup>, J. Fuller<sup>4</sup>, S. J. Murphy<sup>5</sup>, S. Thompson<sup>6</sup>, D. W. Latham<sup>7</sup>, A. Shporer<sup>8†</sup>

<sup>1</sup>Department of Astronomy and Astrophysics, Villanova University, 800 East Lancaster Avenue, Villanova, PA 19085, USA

<sup>2</sup>Jeremiah Horrocks Institute, University of Central Lancashire, Preston, PR1 2HE, UK

<sup>3</sup>Department of Physics & Astronomy, Georgia State University, 25 Park Place Suite 605, Atlanta, GA 30302, USA

<sup>4</sup>TAPIR, Walter Burke Institute for Theoretical Physics, Mailcode 350-17

<sup>5</sup>Stellar Astrophysics Centre, Department of Physics and Astronomy, Aarhus University, DK-8000 Aarhus C, Denmark

<sup>6</sup>NASA Ames Research Center, Moffett Field, CA 94035, USA

California Institute of Technology, Pasadena, CA 91125, USA

<sup>7</sup>Harvard-Smithsonian Center for Astrophysics, 60 Garden St, Cambridge, MA 02138, USA

<sup>8</sup>Jet Propulsion Laboratory, California Institute of Technology, 4800 Oak Grove Drive, Pasadena, CA 91109, USA

In prep.

## ABSTRACT

Heartbeat stars are eccentric ( $e > 0.2$ ) ellipsoidal variables whose light curves resemble a cardiogram. We present the observations and corresponding model of KIC 3749404, a highly eccentric ( $e = 0.66$ ), short period ( $P = 20.3$  d) heartbeat star with tidally induced pulsations. A binary star model was created using PHOEBE, which we modified to include tidally induced pulsations and Doppler boosting. The morphology of the photometric periastron variation (heartbeat) depends strongly on the eccentricity, inclination and argument of periastron. We show that the inclusion of tidally induced pulsations in the model significantly changes the parameter values, specifically the inclination and those parameters dependent on it. Furthermore, we determine the rate of apsidal advance by modelling the periastron variation at the beginning and end of the 4-yr *Kepler* data set and dividing by the elapsed time. We compare the model with the theoretical expectations for classical and general relativistic apsidal motion and find the observed rate to be two orders of magnitude greater than the theoretical rate. We find that the observed rate cannot be explained by tidally induced pulsations alone and consequently hypothesise the presence of a third body in the system.

**Key words:** stars: binaries: eclipsing – stars: binaries: tidal – stars: oscillations – stars: individual: KIC 3749404 – variable:  $\gamma$  Dor

## 1 INTRODUCTION

Heartbeat stars are an interesting class of eccentric ellipsoidal variables introduced by Thompson et al. (2012). The study of heartbeat stars was initiated with the discovery of KIC 8112039 (also known as KOI-54, where KOI stands for *Kepler* Object of Interest; Welsh et al. 2011) and subsequent theoretical papers on this iconic object (Fuller & Lai 2012; Burkart et al. 2012; O’Leary & Burkart 2014). The most prominent feature in the light curve of KOI-54, and all heartbeat stars, is the variation in brightness at periastron, which is a consequence of stellar deformation caused by tides

and mutual irradiation. The morphology of this feature primarily depends on the argument of periastron, eccentricity and inclination of the object, as described by Kumar, Ao & Quataert (1995). For most heartbeat stars, irradiation is a second-order effect in the light curve; however, for KOI-54 and other objects with components of similar size and with a small periastron distance, irradiation can also be dominant in the light curve (e.g., it is about 50 per cent of the heartbeat amplitude of KOI-54). The amplitude of the periastron variation also depends on the periastron distance, mutual irradiation and effects such as gravity darkening, making detailed models necessary.

With the advent of highly precise observations from satellites such as *Kepler* (Borucki et al. 2010; Gilliland et al. 2010; Batalha et al. 2010), *MOST* (Walker et al. 2003) and

\* Email: kmhambleton@uclan.ac.uk

† Sagan Fellow

*CoRoT* (Baglin et al. 2006), it is obvious that these objects are not as rare as previously thought. To date, with the help of Planet Hunters, the *Kepler* Eclipsing Binary Working Group and the *Kepler* Science Office, we (the Heartbeat stars team) have identified 173 heartbeat stars in the *Kepler* data. An up-to-date list of *Kepler* heartbeat stars can be found at the *Kepler* Eclipsing Binary web page<sup>1</sup> (Kirk et al. 2016). Heartbeat stars have also been observed using other projects, including two by the CoRoT mission (Maceroni et al. 2009; Hareter et al. 2014), and eight by the ground-based Optical Gravitational Lensing Experiment, OGLE (Nicholls & Wood 2012). For details of heartbeat stars observed using the *Kepler* satellite, see Welsh et al. (2011); Thompson et al. (2012); Hambleton et al. (2013); Beck et al. (2014); Schmid et al. (2015); Smullen & Kobulnicky (2015).

Due to the strong and variable gravitational interactions between stellar components, a subset of these objects exhibit tidally excited modes. These occur when the forcing frequency of the tide is close to a stellar eigenfrequency, significantly increasing the amplitude of the mode. Caused by resonances with dynamical tides, these modes were hypothesised by Cowling (1941) and Zahn (1975) to be the mechanism for orbital circularisation. Prior to the launch of *Kepler*, tidally excited modes had only been identified in a handful of objects (e.g., HD177863; Willems & Aerts 2002). However, in the *Kepler* data alone, we have identified 24 objects showing obvious, high amplitude tidally induced pulsations, and following closer inspection estimate that  $\sim 20$  per cent of our sample pulsate with tidally excited modes.

KIC 3749404 is a binary star system containing an A and an F star in a close ( $P = 20.3$  d), highly eccentric ( $e \sim 0.66$ ) orbit. The work of Smullen & Kobulnicky (2015) contains a catalog of heartbeat star radial velocities and their corresponding models for 7 objects including KIC 3749404. We expand on this work by providing a complete model of the *Kepler* light curve and radial velocity data. A list of identifiers and basic data for KIC 3749404 can be found in Table 1. KIC 3749404 was selected for detailed study due to its interesting light curve morphology and prominent tidally excited pulsations, which can be seen in Fig. 1. The signature of tidally excited modes are frequencies that are precise integer multiples of the orbital frequency. This feature is obvious in KIC 3749404, as the phased data clearly show the pulsations – this only occurs when the number of pulsations per orbit is very close to an integer.

Apsidal motion is the rotation of the line of apsides about the binary centre of mass, which, in heartbeat stars, is seen as a change in the shape of the ellipsoidal variation (heartbeat) over time. Classical apsidal motion occurs when gravitational interactions generate a tidal bulge on the surface of a star or stellar rotation causes a star to become oblate. This deviation from stellar point masses causes the orbit to precess about the center of mass. Apsidal motion is additionally caused by General Relativity. KIC 3749404 demonstrates rapid apsidal motion. This is an interesting feature, as a discrepancy has been found in several objects between the central density parameter ( $k_2$ ) determined through apsidal advance and that predicted by models, e.g.

**Table 1.** Identifiers and basic data for KIC 3749404. The *Kepler* magnitude specified is derived from the *Kepler* broadband filter.

Identifiers	
KIC	3749404
TYC	3134-165-1
GSC	03134-00165
2MASS	J19281908+3850135
Position and magnitudes	
RA (J2000)	19:28:19.0894
Dec (J2000)	+38:50:13.603
<i>V</i>	10.6
<i>B</i>	10.9
Kp	10.6

see Gimenez & Garcia-Pelayo (1982). While many of these cases can be attributed to the inadequate treatment of stellar rotation, or imprecise stellar radii (as the theoretical rate of classical apsidal advance scales with  $R^{-5}$ ), as shown by Claret & Gimenez (1993), there are some cases where theory and observation do not agree, e.g. Guinan & Maloney (1985). One reason for this discrepancy could be the presence of tidally induced pulsations. Papaloizou & Pringle (1980) theorised that tidally induced pulsations could alter the rate of apsidal advance, and Claret & Willems (2003) further showed that the degree of the discrepancy is likely associated with the phase of the resonance relative to the orbit. For KIC 3749404, we find that the level of discrepancy is, however, unlikely to be a consequence of tidally induced pulsations alone. We thus hypothesise that the rapid apsidal motion is a consequence of a tertiary component in the system.

## 2 OBSERVATIONS

### 2.1 *Kepler* photometry

The observations of KIC 3749404 consist of both long cadence (LC) data, during Quarters 0–17, and short cadence (SC) data, during Quarters 3.3 and 11–17. *Kepler* Quarters are variable in time span, but typically are about 93 d, or one quarter of a complete 372.5-d orbit around the Sun (Kjeldsen et al. 2010). LC data correspond to a sampling rate of 29.4244 min and SC data to a sampling rate of 58.8488 s. The *Kepler* photometric observations that have been analysed for KIC 3749404 span from 2009 May – 2013 May. All observations were obtained from the Mikulski Archive for Space Telescopes and were a part of Data Releases 21–23 (Thompson et al. 2013a,b,c). We used the long cadence data to obtain a model of the binary features and the g-mode frequencies, and to determine the rate of apsidal advance. We used the SC data of Quarters 11–17 to look for the presence of pressure modes (p modes). We identified possible signatures of low-amplitude unresolved p modes at  $\sim 31$  d<sup>-1</sup>. However, as these are in the region of 4 known artifacts, 31.00 d<sup>-1</sup>, 31.10 d<sup>-1</sup>, 31.35 d<sup>-1</sup>, 31.61 d<sup>-1</sup> (Christiansen et al. 2013) and because we do not see them reflected about the Nyquist frequency in the long-cadence data, we

<sup>1</sup> <http://keplerebs.villanova.edu>

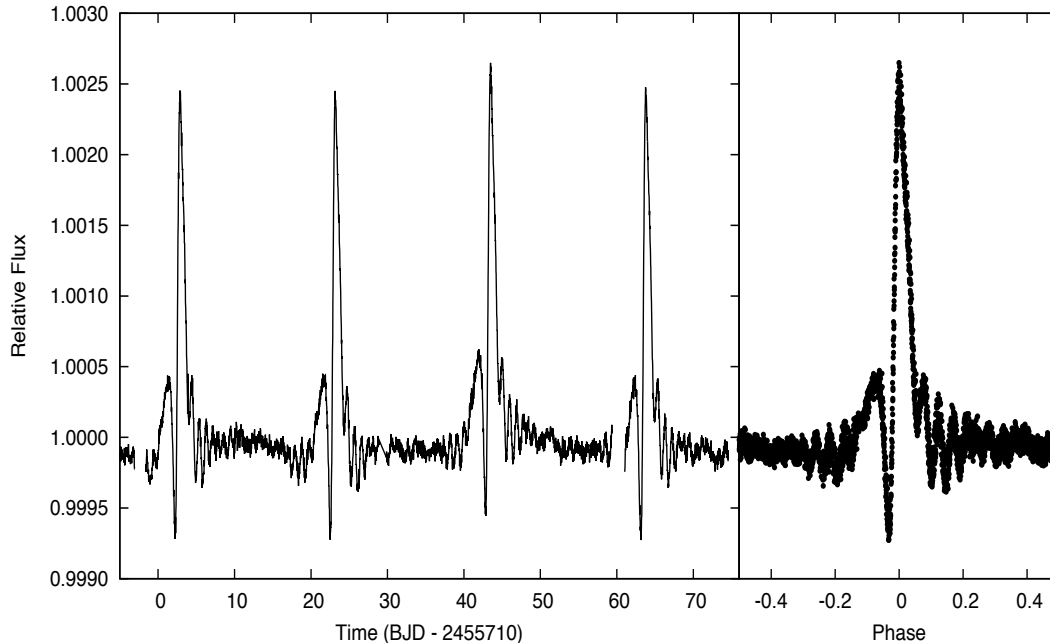


**Figure 1.** *Kepler* long-cadence (Quarters 9–10) time series (left) and the phase folded light curve (right) of KIC 3749404. The dominant feature of the light curve, repeating once per orbital cycle (20.3 d), is the variability due to tidal deformation. Tidally excited modes, the smaller variations, are also clearly visible in the phase folded light curve due to their commensurability with the orbital period.

conclude that there are no p modes in the short cadence light curve of KIC 3749404.

The photometric observations were made using the *Kepler* broadband filter, which is essentially a white light filter. When selecting the type of *Kepler* product to use we noted that the msMAP version of the PDC (pre-search data conditioning) *Kepler* pipeline does not preserve periodicities greater than  $\sim 20$  d (Christiansen et al. 2013). As the orbital period of KIC 3749404 is  $\sim 20$  d, we elected to use the simple aperture photometry data (instead of PDC) to ensure that no information had been removed by the *Kepler* pipeline, which is fine-tuned for transiting planet detection.

As each *Kepler* pixel is  $4 \times 4$  arcsec, it is possible that some contamination will occur within the photometric field. The contamination value for KIC 3749404, specified by the Kepler Asteroseismic Science Operations Centre (KASOC), is estimated to be 0.011, where 0 implies no contamination and 1 implies complete contamination of the CCD pixels. This contamination value suggests that KIC 3749404 suffers minimally from third light, if at all. We applied the *pyKE* tools (Still & Barclay 2012) to the target pixel files to assess the flux incident on each individual pixel. From this we determined that the contamination level for KIC 3749404 is negligible.

The data were detrended using third order polynomials that were applied between breaks in the data, using the *kephem* software. *Kephem* (Prša et al. 2011), an interactive graphical user interface package that enables the detrending of data using Legendre polynomials and further incorporates 3 methods of period analysis: Lomb-Scargle

(LS; Lomb 1976; Scargle 1982), Analysis of Variance (AoV; Schwarzenberg-Czerny 1989), and Box-fitting Least Squares (BLS; Kovács et al. 2002), as implemented in the *vartools* package (Hartman et al. 2008).

We further cleaned the data by removing obvious outliers. For the determination of the binary and pulsation parameters we used Quarters 8–10. We did not use the total data set as the periastron variation is changing in time due to apsidal motion, which causes smearing of the periastron variation. We chose to use Quarters 8–10 as these data were observed simultaneously with the spectral observations and three Quarters provide an acceptable balance between the number of orbits and the smearing of the periastron variation in the phase folded light curve due to apsidal motion.

Due to computational costs, the total number of data points was then reduced from 12 361 to 1 436. To effect the reduction, we assigned each data point with a random number from 0 to 1, and removed all points above a specified threshold: 0.25 for the periastron variation and 0.12 for all other points. To avoid having discrete jumps in the number of data points at the transition regions, we applied sigmoid functions so that the number of data points was gradually increased/decreased. We elected to use random selection over binning the data to avoid weighting the data towards spurious trends. We determined the per-point uncertainty to be  $\sigma = 8.2$  ppm by finding the standard deviation of segments of the data (away from the periastron variation) with the initial model and harmonics of the orbital frequency removed. This was repeated for 10 segments and the results averaged.

**Table 2.** Radial velocities of the two components of KIC 3749404, determined using TODCOR. The spectra were observed using the Tillinghast Reflector Echelle Spectrograph on the 1.5-m telescope at the Fred L. Whipple Observatory between UT 2011 May 10 and 2011 Jun 23. The uncertainties on the primary and secondary radial velocities are  $\sigma = 1.0 \text{ km s}^{-1}$  for all measurements.

BJD 2450000.0 +	Primary $\text{km s}^{-1}$	Secondary $\text{km s}^{-1}$
5691.9395	-41.0	19.8
5692.9411	-89.3	84.8
5693.9409	-71.0	60.3
5694.8716	-55.2	38.0
5695.9629	-42.6	21.0
5696.8644	-34.1	10.6
5697.8724	-26.6	1.2
5698.9011	-19.9	-10.1
5699.7996	-15.7	-15.0
5701.8281	-6.6	-26.0
5704.8259	4.9	-42.6
5705.8248	8.6	-47.9
5727.8552	14.2	-55.0
5728.9439	17.6	-58.6
5729.8041	18.8	-62.1
5731.9046	0.3	-36.6
5732.8222	-64.9	50.5
5733.7524	-86.9	80.2
5734.9330	-63.9	49.8
5735.7603	-52.0	33.1

## 2.2 Binary Orbital Period Determination

Using *kephem* (as described in §2.1), period analysis was performed on all the LC data (Quarters 0–17) to determine the period of the binary orbit and BJD<sub>0</sub>, the zero point in time (the maximum of the periastron variation). Due to the apsidal motion in the system, it is important to note that the period is the anomalous period and not the sidereal period. The ephemeris was found to be:

$$\text{MinI} = \text{BJD } 2455611.342(3) + 20.30635(8) \times E$$

where MinI is the orbital ephemeris and the values in the parentheses give the one sigma uncertainties in the last digit. The period uncertainty was obtained by applying an adaptation of the Period Error Calculator algorithm of Mighell & Plavchan (2013), as specified in Kirk et al. (2016).

## 2.3 Ground-based spectroscopy

We followed-up KIC 3749404 spectroscopically to measure the radial velocities of the two components and to characterize the stellar atmospheres. A total of 20 observations were collected with the Tillinghast Reflector Echelle Spectrograph (TRES; Fűrész 2008) on the 1.5-m telescope at the Fred L. Whipple Observatory between UT 2011 May 10 and 2011 June 23. The spectra cover the wavelength between  $\sim 3900$  and  $9000 \text{ \AA}$  at a resolving power of  $R \approx 44000$ . We extracted the spectra following the procedures outlined by Buchhave et al. (2010).

We derived the radial velocities for both stars from the

TRES spectra using the two-dimensional cross-correlation technique TODCOR (Zucker & Mazeh 1994), with synthetic spectral templates generated from Kurucz model atmospheres. TODCOR uses two dimensional cross-correlation to identify the optimal radial velocities of the two input model spectra with respect to the observed data. We used one echelle order of about  $100 \text{ \AA}$  centered on  $5190 \text{ \AA}$ , which includes the gravity-sensitive Mg I b triplet. The radial velocities are reported in Table 2. For discussion on the determination of the spectroscopic parameters and the case for the Am nature of the primary star, see §3.4.

## 3 BINARY MODELLING

### 3.1 Tidally Excited Modes

Stellar pulsation modes may be tidally excited when a multiple of the binary orbital frequency is close to a stellar eigenfrequency. The signature of a tidally excited mode is a pulsation frequency that is a precise multiple of the orbital frequency. In the initial analysis of KIC 3749404 we identified 7 pulsations that are multiples of the orbital frequency with amplitudes greater than  $20 \mu\text{mag}$ . The nature of tidally excited pulsations makes them intrinsically difficult to extract: their frequencies are multiples of the orbital frequency and hence they overlap with orbital harmonics created by the Fourier decomposition of the near-periastron heartbeat signal. This is especially problematic for relatively low-frequency tidally excited modes, which are common. For this reason we added the capability to PHOEBE to model the binary features and pulsations simultaneously by combining the binary star model with sine waves at frequencies that are multiples of the orbital frequency. To our knowledge, this is the first time that pulsations have been modelled simultaneously with light curve and radial velocity data. We further incorporated Markov chain Monte Carlo methods to fit our model to the data.

Prior to fitting the binary star features and pulsation parameters simultaneously, we identified the prominent pulsations in the light curve. To do this, we generated the residuals to the initial binary fit; masked the region of the periastron variation (between phases -0.19–0.12) to reduce the impact of an imperfect model/over-fitting the pulsations; and applied a Fourier transform to the residual data.

The Fourier transform of the original, detrended data contains a double peaked distribution of frequencies where all the frequencies are multiples of the orbital frequency (cf. Fig. 2). The first peaked distribution of frequencies describe the binary star features in the light curve, including the periastron variation, and the second is caused by tidally induced pulsations. To further analyse the pulsations, we removed an initial binary model from the data and prewhitened any remaining frequencies below  $0.5 \text{ d}^{-1}$ , most of which are instrumental in nature, to an amplitude of  $4 \mu\text{mag}$ . From the Fourier transform of the residual data, with the low frequency peaks removed, we identified all remaining significant harmonics from the data (down to  $20 \mu\text{mag}$ ) and fitted them simultaneously using linear least-squares. In order of amplitude, the identified frequencies are: (21, 24, 20, 23, 22, 25, 18)  $\times \nu_{orb}$ . For a more detailed discussion of the tidally induced pulsations, including the final pulsation parameters from the binary star model, see §3.1.

**Table 3.** Fixed parameters and coefficients for the PHOEBE best-fit model to the *Kepler* light curve for Quarters 8–10. The values in the parentheses specify the one sigma uncertainties in the previous digit. The effective temperatures were determined using the spectral analysis performed in §3.4. The binning undertaken with this analysis did not preserve  $v \sin i$ . We therefore used the  $v \sin i$  measurements obtained from our TODCOR analysis in §2.3.

Parameter	Values
Primary $T_{\text{eff}}$ (K)	8000(300)
Secondary $T_{\text{eff}}$ (K)	6900(300)
Primary $v \sin i$ ( $\text{km s}^{-1}$ )	29(2)
Secondary $v \sin i$ ( $\text{km s}^{-1}$ )	9(2)
Orbital Period (d)	20.30635(15)
Time of primary minimum (BJD)	2455611.342(3)
Primary Bolometric albedo	1.0
Secondary Bolometric albedo	0.6
Third light	0.000(6)

The majority of heartbeat stars, including KIC 3749404, do not have eclipses. We see a dip in the light curve of KIC 3749404 because at that phase the stars are tidally distorted due to gravitational affects and we are viewing both stars with a smaller and cicker surface area relative to their surface area during the rest of the orbit. As there are no eclipses present in the light curve of KIC 3749404, we are unable to determine from which component the tidally induced pulsations originate. However, as they form a single peaked distribution in the Fourier transform, we conclude that they originate in one star, although which star is currently not known.

### 3.2 Simultaneous Binary and Pulsation Modelling

We applied the binary modelling code PHOEBE (Prša & Zwitter 2005), which is an extension of the Wilson-Devinney code (Wilson & Devinney 1971; Wilson 1979; Wilson & Van Hamme 2004), to the light curve of KIC 3749404. PHOEBE combines the complete treatment of the Roche potential with the detailed treatment of surface and horizon effects such as limb darkening, reflection and gravity brightening to derive an accurate model of the binary parameters. The current implementation uses the Wilson-Devinney method of summing over the discrete rectangular surface elements, which cover the distorted stellar surfaces, to determine an accurate representation of the total observed flux and consequently a complete set of stellar and orbital parameters. PHOEBE incorporates all the functionality of the Wilson-Devinney code, but also provides an intuitive graphical user interface alongside many other improvements, including updated filters and bindings that enable interfacing between PHOEBE and PYTHON (see §3.3).

We calculated the value of  $F$  for each component, where  $F$  is the ratio of the rotational to orbital period. This was done for each component at each iteration by combining the spectroscopically determined  $v \sin i$  values ( $v_1 \sin i = 29 \pm 2 \text{ km s}^{-1}$  and  $v_2 \sin i = 9 \pm 2 \text{ km s}^{-1}$ ) with the model-determined values of the inclination and radii. We further fixed the stellar albedos to  $A_1 = 1.0$  and  $A_2 = 0.6$ , which are theoretically predicted for stars with radiative and convective outer envelopes, respectively (Ruciński 1969a,b). We

**Table 4.** Mean values of the fitted and calculated parameters determined using PHOEBE with EMCEE for 0 and 7 pulsations. The values are derived from Gaussian fits to the posterior distributions. The rotation rate refers to the number of rotations per orbit and the primary fractional luminosity is  $L_1/(L_1 + L_2)$ . The values in parentheses give the uncertainty in the previous digit.

Parameter	Number of pulsations	
	0	7
Fitted		
Orbital inclination (degrees)	60.2(1)	62(1)
Argument of periastron (rad)	2.14(2)	2.15(3)
Eccentricity	0.633(3)	0.658(5)
Primary gravity brightening	0.95(3)	0.96(2)
Secondary gravity brightening	0.29(2)	0.52(5)
Primary polar radius ( $R_{\odot}$ )	1.9(1)	1.98(4)
Secondary polar radius ( $R_{\odot}$ )	1.1(1)	1.20(3)
Mass ratio	0.73(1)	0.738(8)
Phase shift	-0.110(3)	-0.109(4)
Gamma velocity ( $\text{km s}^{-1}$ )	-14(2)	-15(7)
Semi-major axis ( $R_{\odot}$ )	43(1)	45.7(5)
Calculated		
Primary mass ( $M_{\odot}$ )	1.5(1)	1.78(6)
Secondary mass ( $M_{\odot}$ )	1.1(1)	1.32(4)
Primary fractional luminosity	0.85(4)	0.82(2)
Primary rotation rate	7.1(3)	7.1(2)
Secondary rotation rate	4.0(1)	4.0(1)

elected to fix the period and zero point in time (time of photometric maximum) to the values determined using *kephem* (see Table 3), as the Lomb-Scargle method is more accurate than PHOEBE for ephemeris determination.

Following the work of Diaz-Cordoves & Gimenez (1992) and van Hamme (1993), who showed that the square-root and logarithmic limb darkening laws are preferable for objects that radiate towards the IR and UV, respectively, we elected to use the logarithmic limb darkening law, as within PHOEBE this is a system-wide parameter, and the primary star contributes the larger fraction of light to the system.

### 3.3 Posterior Determination of the Binary Star Parameters

To determine the posteriors of the binary and pulsational parameters, we combined PHOEBE with EMCEE, a PYTHON implementation of the affine invariant ensemble sampler for Markov chain Monte Carlo (MCMC) proposed by Goodman & Weare (2010) and implemented by Foreman-Mackey et al. (2013).

MCMC explores the binary parameter space using a set of Markov chains, in this case 128. These chains begin with random distributions of each parameter based only on the prior probability distributions. They move through parameter space by assessing their posteriors at each point and then selecting a new position based on the position of another chain. The step size is based on the covariance of the two chains. If the move increases the a posterior likelihood then it is accepted; if the move decreases it then it may be accepted with a certain probability. During the initial burn-in time the Markov chains are merging towards their max-

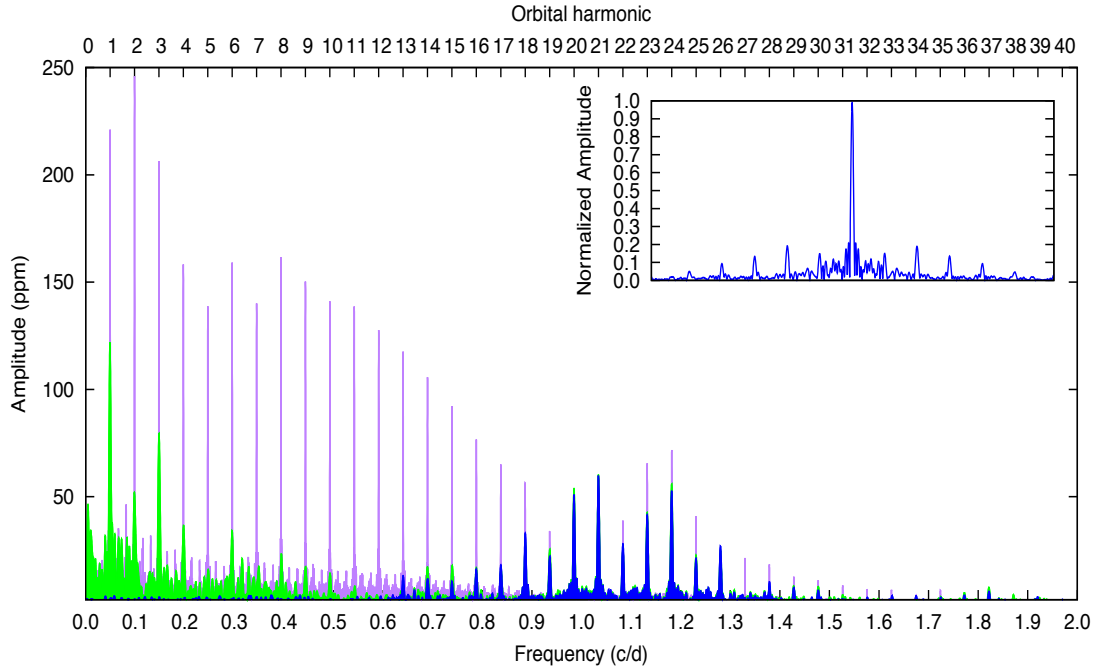


**Figure 2.** A Fourier transform of the original detrended data (purple); data with the initial binary star model removed (green); and with the initial binary star model and frequencies less than  $0.5 \text{ d}^{-1}$  (down to an amplitude of  $4 \mu\text{mag}$ ) removed (blue). The latter, blue Fourier transform contains tidally induced pulsations only. The insert depicts the window pattern of the highest amplitude peak ( $21 \nu_{orb}$ ). All the peaks are at precise multiples of the orbital frequency.

imum likelihood position. The statistics of a large number of iterations provide posterior distributions for the model parameters.

We generated two models for KIC 3749404, one containing the most significant pulsations, and one without pulsations (to see the effect of pulsations on the binary star parameters). The model without pulsations comprises 10 binary star parameters. From the residuals of this model, we identified seven pulsations with amplitudes greater than  $20 \mu\text{mag}$ , thus the second model contains 7 pulsations and comprises 24 parameters: 10 binary star parameters and an amplitude and phase parameter for each pulsation. As the fitted pulsations are tidally induced, we fixed each pulsation frequency to a multiple of the orbital frequency (as determined from our frequency analysis). The pulsations were modelled by simultaneously fitting sine waves with the binary star model.

The binary parameters were selected based on their contribution to the observed flux variation to KIC 3749404. For the results of the best-fit models, see Table 4 for a list of fundamental parameters and Table 5 for a list of the pulsation parameters from the model with 7 pulsations. For the binary star model, the inclination, eccentricity, argument of periastron, phase shift, primary and secondary radii, and primary and secondary gravity darkening exponents were sampled using MCMC. The phase shift is the horizontal offset required to keep the model's periastron variation centred at phase 0.0 when changing the argument of periastron and eccentricity in the phase folded data.

For each model iteration the limb darkening exponents were calculated; the luminosity was fitted using least-squares; and the effect of Doppler boosting was added to the light curve for each component. Doppler boosting is caused by the radial motion of the two stars and is the combined effect of the Doppler shifting of the stars' spectral energy distributions, aberration and an altered photon arrival rate. The net result of Doppler boosting is an increase in the observed flux from a star when it moves towards the observer, and a decrease when it moves away. It was predicted by Loeb & Gaudi (2003) and Zucker, Mazeh & Alexander (2007), and has recently been observed in several systems from ground-based data as well as *Kepler* and *CoRoT* light curves (see e.g. Mazeh & Faigler 2010; van Kerkwijk et al. 2010; Shporer et al. 2010; Bloemen et al. 2011). To model the Doppler boosting signal, Eqn 2 in Bloemen et al. (2011) provides a function that can easily be applied to the binary star model:

$$F_{\lambda} = F_{0,\lambda} \left[ R \left( 1 - B_1 \frac{v_{r,1}}{c} \right) - (1 - R) \left( B_2 \frac{v_{r,2}}{c} \right) \right], \quad (1)$$

where  $F_{\lambda}$  is the observed flux,  $F_{0,\lambda}$  is the emitted flux,  $R$  is the light ratio,  $v_{r,1}$  and  $v_{r,2}$  are the radial velocities of the primary and secondary components,  $B_1$  and  $B_2$  are the passband-weighted boosting factors, where  $B = 5 + d \ln F_{\lambda} / d \ln \lambda$  (Loeb & Gaudi 2003).

For each parameter we used a flat, uniform prior. The prior ranges were selected to encompass all physical models given the spectroscopic information. We restricted the

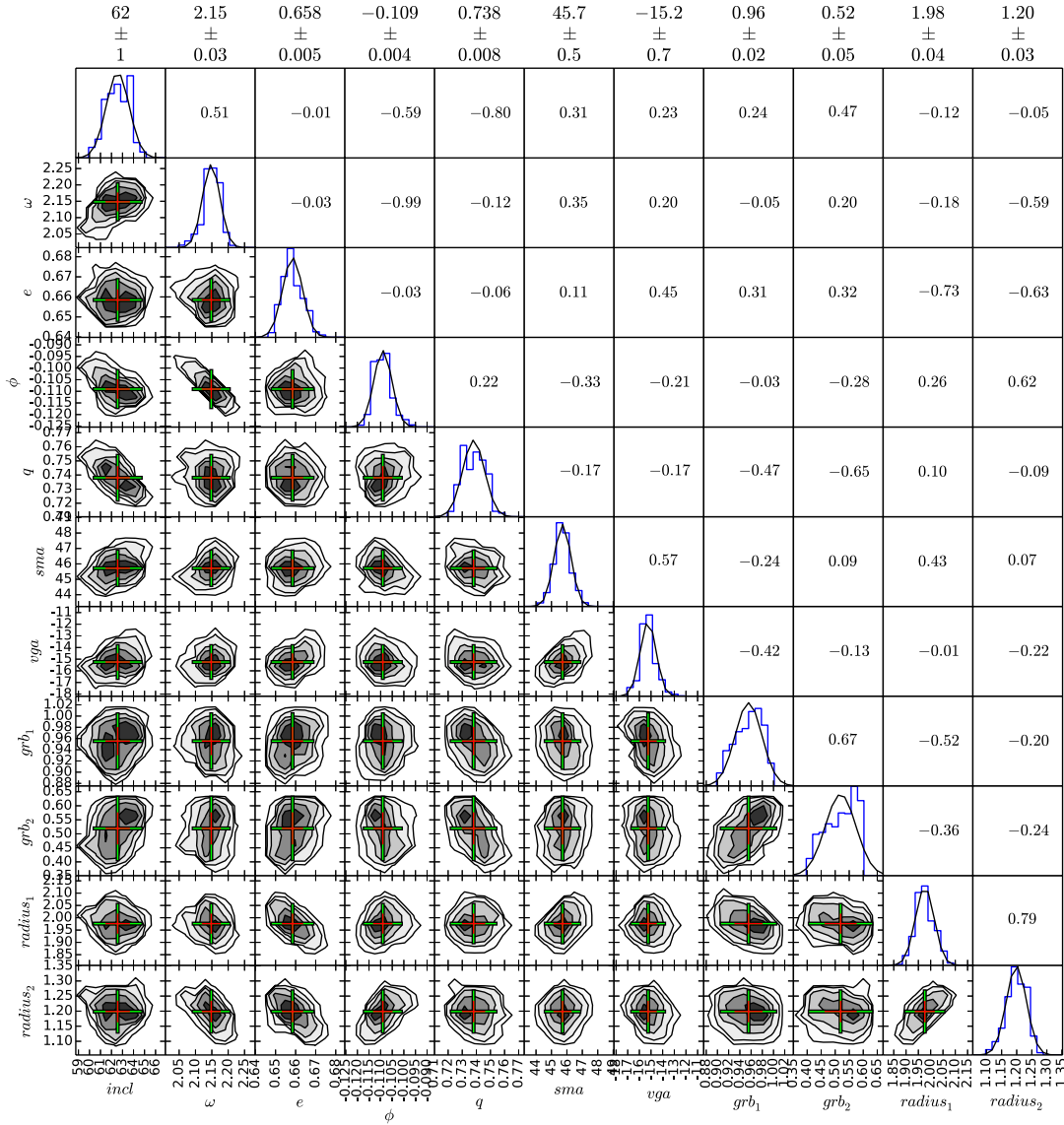


**Figure 3.** The posterior distributions of the binary star parameters for the model with seven pulsations, where  $incl$  is the inclination of the binary star orbit in degrees;  $\omega$  is the argument of periastron in radians;  $e$  is the eccentricity;  $\phi$  is the phase shift;  $q$  is the mass ratio ( $m_2/m_1$ );  $sma$  is the semi-major axis in  $R_\odot$ ;  $vga$  is the gamma velocity in  $\text{km s}^{-1}$ ;  $grb_1$  and  $grb_2$  are the gravity brightening exponents of the primary and secondary components, respectively; and  $radius_1$  and  $radius_2$  are the primary and secondary polar radii in  $R_\odot$ , respectively. We elected to calculate the polar radii since they are more constant throughout the orbit (as opposed to the point radii). Lower left sub-plots: two dimensional cross sections of the posteriors. The crosses show the one sigma (red) and two sigma (green) uncertainties, and are centred on the minima. Diagonal sub-plots from top left to bottom right: histograms displaying the posterior distribution of each individual parameter. Upper right values: the correlations for the two-dimensional cross sections mirrored along the diagonal, where 1 is complete correlation, -1 is a complete anti-correlation and 0 is no correlation. The values above the plot give the mean value and one sigma uncertainty for each parameter, based on the fitted Gaussians.

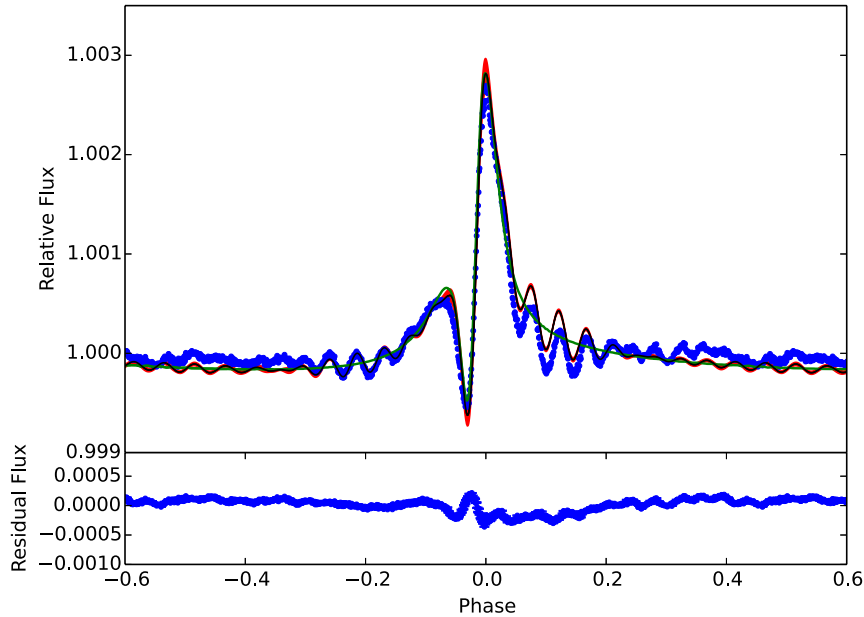


**Figure 4.** Upper panel: Best-fit PHOEBE model without pulsations (green line) and including 7 pulsations (black line). The observed light curve (blue points) was prepared as specified in §3.2. The red envelope depicts the  $1\sigma$  spread of the final 128 models determined using MCMC for the model with 7 pulsations. Lower panel: the residuals (blue points) of the best-fit model. The uncertainties are depicted on the residual points, although they are not visible on the scale provided.

prior on the inclination to be below  $90^\circ$  to avoid obtaining a double peaked distribution reflected about  $90^\circ$ . We also restricted the gravity darkening exponents to the ranges  $0.8 - 1.0$  for the primary and  $0.2 - 0.6$  for the secondary component, where the gravity darkening exponents are predicted to be 1.0 and 0.32 for stars with radiative (von Zeipel 1924) and convective (Lucy 1968) envelopes, respectively.

In our model we assumed that the noise is Gaussian, which does not take into account correlated noise contributions (see, e.g., Barclay et al. 2015). Consequently, it is likely our uncertainties are underestimated. Fig. 3 shows the posterior distributions of the best-fit model. It can be seen that all the parameter histograms (top left to bottom right diagonal plots) are normal distributions, with the exception of the secondary gravity brightening exponent, which shows a slightly skewed distribution. The upper panel of Fig. 4 shows the best-fit PHOEBE model with 7 pulsations (black with red,  $1\sigma$  envelope) and the best-fit PHOEBE model with no pulsations included (green). The lower panel shows the residuals from the model including pulsations. Both models are the average of 128 models, one from each Markov chain. The envelope denotes the  $1\sigma$  spread of results determined by finding the standard deviation of the models. Fig. 5 depicts the best-fit model to the radial velocity data for the PHOEBE model with 7 pulsations, which was fitted simultaneously with the light curve.

In the light curve, it can be seen that there is a significant deviation of the model from the data in the phases

following the periastron variation and in the regions that are flatter, relative to the periastron variation. The cause of this may lie in detrending, as heartbeat star light curves often do not have an obvious baseline. All remaining features in the observed data are fit adequately by the model. The more pronounced red regions near the peak and trough of the periastron variation show that the models are sampling a wider distribution in these areas, which are encapsulated in the uncertainties.

When comparing the two models, the most striking differences stem from different inclinations of the two models:  $i = 60.2 \pm 1.0^\circ$  and  $i = 63 \pm 1.0^\circ$  for the models with zero and seven pulsations, respectively. These differences (although only at the  $2\sigma$  level) translate to a significantly larger semi-major axis in the model with pulsations ( $2.7 R_\odot$  larger), and larger masses ( $0.28 M_\odot$  for the primary and  $0.12 M_\odot$  for the secondary; see Table 4), with the pulsation model favouring the more massive stars. Finally, the radii of both components are larger for the model with pulsations. These differences convey the importance of modelling pulsations simultaneously with the light curve. It is also important to note that the argument of periastron is identical for both models, conveying the robustness of our determined value.

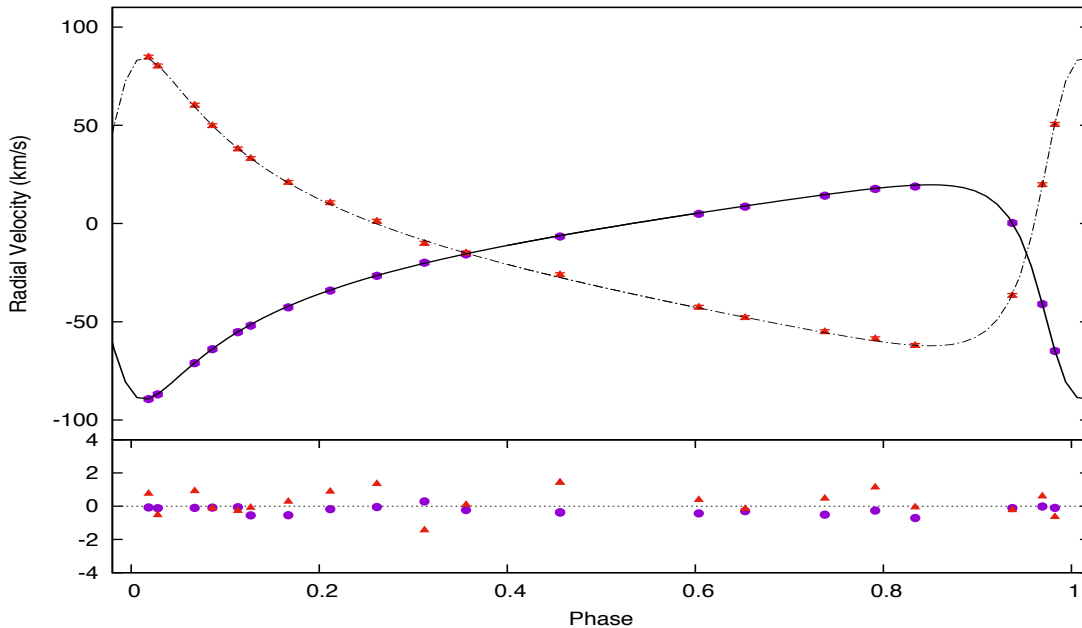


**Figure 5.** Upper panel: the observed radial velocities of KIC 3749404 for the primary (purple circles) and secondary component (red triangles). The uncertainties are plotted but barely visible in comparison with the point sizes. The best-fit model (where the light curve model includes 7 pulsations) is shown for the primary component (solid line) and secondary component (dashed line). Lower panel: the residuals to the best fit model. A dotted horizontal line is placed at zero for clarity. See §3 for details of the binary star model. The spectra from which these radial velocities were derived were observed between UT 2011 May 10 and 2011 Jun 23, using the Tillinghast Reflector Echelle Spectrograph (TRES) mounted on the 1.5-m Tillinghast Reflector at the Fred L. Whipple Observatory on Mt. Hopkins, AZ.

**Table 5.** The pulsation amplitude and phase values for the binary model combined with tidally induced pulsations. The frequencies were fixed to precise multiples (harmonics) of the orbital frequency. The phase is relative to the binary model zero point in time.

Multiple of $\nu_{orb}$	Frequency $\text{d}^{-1}$	Amplitude ppm	phase rad
18	0.8864(6)	18(2)	5.0(1)
20	0.9849(7)	39(4)	3.05(9)
21	1.0341(7)	52(8)	2.50(7)
22	1.0834(7)	22(5)	2.4(1)
23	1.1326(7)	36(7)	1.06(8)
24	1.1818(7)	60(5)	0.90(8)
25	1.2311(8)	15(6)	0.90(8)

### 3.4 Spectroscopic analysis and the case for the Am nature of the primary component

To determine the spectroscopic stellar parameters, we performed an analysis similar to those used to characterize the stars of the circumbinary planet-hosting binary systems Kepler-34, Kepler-35, and KOI-2939 (Welsh et al. 2012; Kostov et al. 2015), though the properties of KIC 3749404 necessitated a few changes. Blended lines can prevent accurate classifications, so we included in this analysis only

the 14 TRES spectra that have a velocity separation greater than  $40 \text{ km s}^{-1}$  between the two stars. We began by cross-correlating the TRES spectra against a five-dimensional grid of synthetic composite spectra. The grid we used for KIC 3749404 contains every combination of stellar parameters in the ranges  $T_1 = [5500, 8500]$ ,  $T_2 = [5500, 8500]$ ,  $\log g_1 = [2.5, 5.0]$ ,  $\log g_2 = [3.0, 5.0]$ , and  $[M/H] = [-1.0, +0.5]$ , with grid spacings of 250 K in  $T$ , and 0.5 dex in  $\log g$  and in  $[M/H]$  (20,280 total grid points).<sup>2</sup> At each step in the grid, TODCOR was run in order to determine the radial velocities of the two stars and the light ratio that produces the best-fit set of 14 synthetic composite spectra, and we saved the resulting mean correlation peak height from these 14 correlations. Finally, we interpolated along the grid surface defined by these peak heights to arrive at the best-fit combination of stellar parameters.

The spectroscopic analysis was limited by the degeneracy among the parameters (i.e., a nearly equally good fit was obtained by slightly increasing or decreasing  $T$ ,  $\log g$ , and

<sup>2</sup> We ran a separate TODCOR grid solely to determine the  $v \sin i$  values, which we left fixed in the larger grid. This is justified because the magnitude of the covariance between  $v \sin i$  and the other parameters is small. This simplification reduces computation time by almost two orders of magnitude. The final  $v \sin i$  values are  $v_1 \sin i = 29(2) \text{ km s}^{-1}$  and  $v_2 \sin i = 9(2) \text{ km s}^{-1}$ .

[M/H] in tandem), but the light curve model provided independently determined surface gravities (see §3.2) that were partially able to lift the degeneracy. We thus included these gravities in our analysis, and found that the best fit occurred for a very high metallicity ([M/H] > +0.5); however the resulting parameters and light ratio of the spectral templates were inconsistent with the binary model. The expected flux ratio can be approximated by assuming black body radiation and integrating Planck's law across the TODCOR bandpass:

$$\frac{F_2}{F_1} = \left(\frac{R_2}{R_1}\right)^2 \int_{\lambda_i}^{\lambda_f} \frac{e^{hc/(\lambda k_B T_1)} - 1}{e^{hc/(\lambda k_B T_2)} - 1} d\lambda. \quad (2)$$

Recognizing that the combination of surface gravities with the mass ratio from the radial velocities can yield the area ratio, the above equation can be rewritten solely in terms of the spectroscopic observables:

$$\frac{F_2}{F_1} = q \left(10^{\log g_1 - \log g_2}\right) \int_{\lambda_i}^{\lambda_f} \frac{e^{hc/(\lambda k_B T_1)} - 1}{e^{hc/(\lambda k_B T_2)} - 1} d\lambda, \quad (3)$$

where  $q$  is the mass ratio,  $M_2/M_1$ . For our best-fit templates, the measured and expected light ratios differed by more than a factor of 2, at high significance.

These inconsistencies in the light ratio and the temperatures indicated that the spectroscopic model was not yet sufficient. Given that the primary is an A star and the best fit occurred for high metallicities, we next explored the possibility that the two stars have different apparent metallicities. If the primary is an Am star, displaying photospheric enrichment in metallic lines, we would expect the spectra for the primary and secondary to be fit by templates of different metallicity even though they presumably formed with identical compositions.

We first tested this by running new grids of TODCOR correlations that include a sixth dimension, along which lies the metallicity of the secondary. This improved the agreement between the spectral templates and binary star model, including the light ratios, which were then within 25% of each other. The newly determined metallicities of the primary and secondary components were  $[m_1/H] > +0.50$  and  $[m_2/H] = 0.00$ , respectively. While we are only able to report lower limits for the primary because our library of synthetic spectra only includes metallicities up to  $[m/H] = +0.5$ , these results suggest that the primary may be an Am star (and that the secondary is not).

Consequently, we examined spectra taken at quadrature for the chemical abundance anomalies seen in Am stars. The observed spectrum was compared with the synthesized binary spectra using the algorithm developed and described by Murphy et al. (2015). Suitable atmospheric parameters for the components of the binary system were chosen such that the synthetic hydrogen line profiles matched the observed profiles. A satisfactory match was obtained with  $T_1 = 8000(300)$  K,  $T_2 = 6900(300)$  K,  $\log g_1 = 3.8(3)$ ,  $\log g_2 = 4.0(3)$ ,  $v_1 \sin i = 30(5)$  km s<sup>-1</sup> and  $v_2 \sin i = 10(5)$  km s<sup>-1</sup>, using  $[\text{Fe}/\text{H}] = 0.0$  for both components. This configuration leads to a mass ratio of  $M_2/M_1 = 0.74$  and a light ratio of  $L_1/(L_1 + L_2) = 0.80$ . The synthetic and observed spectra were smoothed to classification resolution (2.5 Å per 2 pixel) to reduce the effects of noise and additional sources of spectral line broadening that are hard to quantify (Murphy et al. 2016). It is worth noting that, due to the applied smoothing, the  $v \sin i$  values of the initial analysis are more

reliable ( $v_1 \sin i = 29(2)$  km s<sup>-1</sup> and  $v_2 \sin i = 9(2)$  km s<sup>-1</sup>). With these parameters, the observed metal line profiles were much stronger than the synthetic ones. By increasing the global metallicity of the primary component, the fit to the metal lines improved at the expense of the fit to the hydrogen lines; increasing by +0.5 dex, the fit to the hydrogen line profiles worsened considerably, with substantial further improvement to the metal lines required.

For the primary component, agreement with the hydrogen line profiles could have been restored with small changes to  $T_1$  and  $\log g_1$ , but the morphology of the metal lines could not be improved with further changes to the global metallicity, alone. Already at +0.2 dex, the synthetic Ca II K line was stronger than the observed spectrum, while the Fe, Sr and Ti lines remained poorly matched. Increasing the metallicity to +0.5 dex resulted in discrepant Ca II K and hydrogen lines, and substantial further enhancement of the synthetic Sr and Fe lines was still required. Thus the observations show selective metal enrichment of the photosphere, which match the abundance patterns of Am stars (see, e.g. Murphy et al. 2012).

A-type stars in close binary systems commonly show Am peculiarities (Abt 1967; see Murphy 2014 for a review). The fact that the primary is an Am star is therefore expected. The secondary star is an early F star for which Am-type peculiarity is less common (Wolff 1983), presumably due to the increase in convective mixing. The derivation of abundances for a chemically peculiar star in a double-lined spectroscopic binary system is a state-of-the-art challenge beyond the scope of this paper. For the purpose of this work, our current analysis suggests that the appearance of the spectra is consistent with the light curve model, which we described in detail in §3.2.

#### 4 APSIDAL MOTION

Apsidal motion is the rotation of the elliptical orbit about the centre of mass. The rate of classical apsidal advance is determined by the non-spherical mass distribution within the stars due to tidal distortions and rotation. General relativity produces additional apsidal motion. The net apsidal motion depends on the component's masses, radii, rotation rates, and density profiles, in addition the orbital semi-major axis and eccentricity.

When initially phasing the 4-yr light curve of KIC 3749404, it was clear, due to the significant smearing of the periastron variation, that KIC 3749404 is undergoing rapid apsidal motion. Fig. 6 depicts several models showing the change of the periastron variation of KIC 3749404 as a function of the argument of periastron for a complete cycle about the centre of mass. The insert shows a model depicting the apsidal advance over the 4 yr data set.

To determine the rate of periastron advance, we fitted  $\omega$  at the beginning (Quarters 1 and 2, LC data) and end (Quarters 15 and 16, LC data) of our data set (Quarters 0 and 17 are short Quarters that did not contain any periastron variations and thus were not used). As our aim was to determine the change in the argument of periastron, we fixed all parameters except the argument of periastron and phase shift, to those determined for the best-fit model of Quarters 8–10 (including pulsations). We also included a global pulsa-

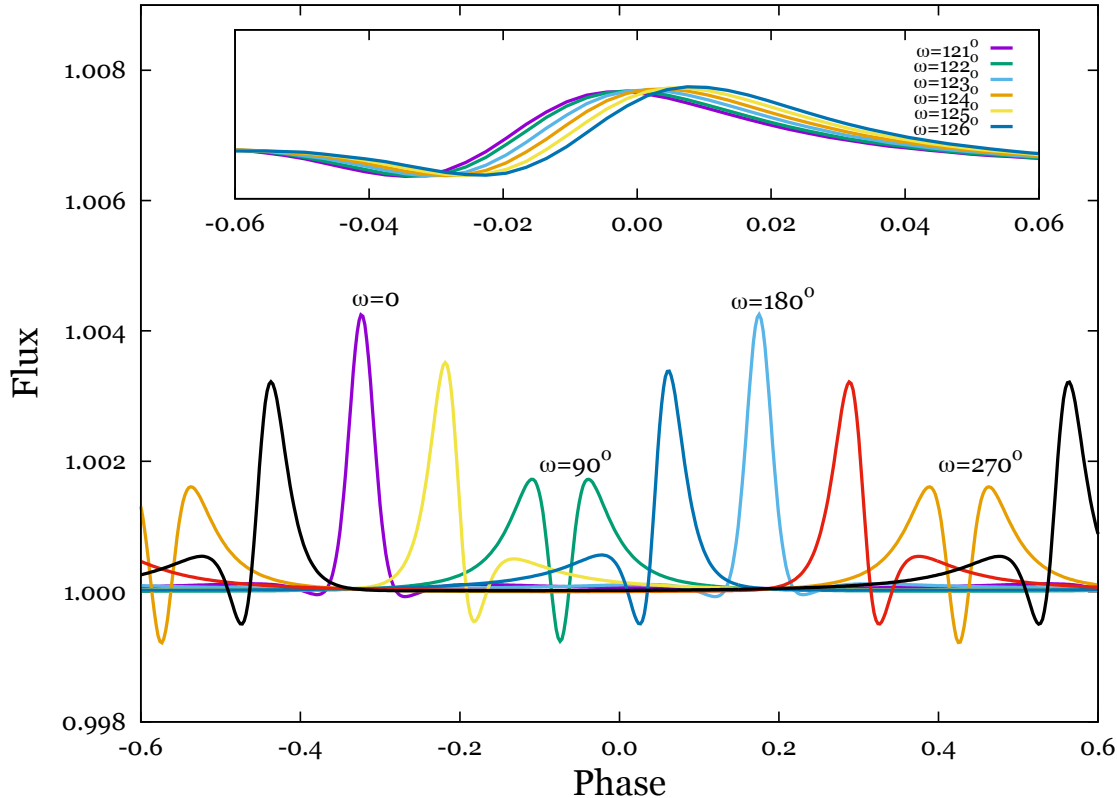


**Figure 6.** Models of KIC 3749404 with different values of  $\omega$ , the argument of periastron. The figure highlights the effect of the periastron value on the shape of the periastron variation for one full orbital cycle about the centre of mass. The periastron variation drastically changes both its position in phase space and its shape (width and amplitude) with the changing values of  $\omega$ . The inset shows the measured effect on the light curve shape over the 4-yr length of the Kepler data set used.

tion phase-shift (which shifts all the pulsations by the same amount), as the phases of the pulsations were observed to shift by a different amount than the longitude of periastron. Since the pulsation phases depends on the azimuthal numbers of the tidally excited modes, measuring this phase shift can help identify them.

We selected the initial and final data sets so that they contained five orbits. Using this method we determined the initial and final values for the argument of periastron to be 2.122(2) and 2.195(1), respectively (see Figs 7 and 8 for the model fits and posteriors, respectively). For the two data sets we selected the peak of the periastron variation in the middle of the data set as the zero point in time for that section of data. To obtain the rate of periastron advance we divided the change in the argument of periastron by the difference in time between the two data sets (1309.773(4) d). We determined the rate of apsidal advance to be 1.166(1) $^\circ$ /year.

To compare our observed value for the rate of apsidal advance with the predicted rate, we then used the tables of Claret (1997) to obtain the apsidal motion constants (Love numbers) of the primary and secondary components to be  $k_{2,1} = 0.0036(5)$  and  $k_{2,2} = 0.0042(4)$ , for models similar to the stars in KIC 3749404 (where  $k_2 = 0$  for a point mass

and  $k_2 = 0.75$  for a homogeneous sphere). We assumed that both components of KIC 3749404 are main-sequence stars and used the fundamental parameters from the model with pulsations. Using these values we calculated the classical theoretical rate of apsidal advance (Cowling 1938; Sterne 1939; Kopal 1959) using:

$$\begin{aligned} \dot{\omega}_{CL}^{theor} (deg/yr) = & 365.25 \left( \frac{360}{P} \right) \left\{ k_{2,1} r_1^5 \left[ 15 f_2(e) (M_2/M_1) \right. \right. \\ & \left. \left. + \left( \frac{\tilde{\omega}_{r,1}}{\tilde{\omega}_k} \right)^2 \left( \frac{1 + M_2/M_1}{(1 - e^2)^2} \right) \right] \right. \\ & \left. + k_{2,2} r_2^5 \left[ 15 f_2(e) (M_1/M_2) \right. \right. \\ & \left. \left. + \left( \frac{\tilde{\omega}_{r,2}}{\tilde{\omega}_k} \right)^2 \left( \frac{1 + M_1/M_2}{(1 - e^2)^2} \right) \right] \right\}, \end{aligned} \quad (4)$$

where  $P$  is the orbital period,  $k_{2,1}$  and  $k_{2,2}$  are the apsidal motion constants for the primary and secondary components, respectively,  $f_2(e) = (1 + 3/2e^2 + 1/8e^4)(1 - e^2)^{-5}$  where  $e$  is the eccentricity,  $M_1$  and  $M_2$  are the masses of the primary and secondary components in solar mass units,  $r_1$

and  $r_2$  are the radii of the primary and secondary component in terms of the semi-major axis,  $\tilde{\omega}_{r,1}$  and  $\tilde{\omega}_{r,2}$  are the angular axial rotational speeds of the primary and secondary stars, and  $\tilde{\omega}_k = 2\pi/P$ . For the classical rate of apsidal advance we obtained  $\dot{\omega}_{CL}^{theor} = 0.002(7)^\circ/\text{yr}$ . As KIC 3749404 has a large eccentricity and relatively short orbital period, the general relativistic contribution is significant. Thus we calculated the general relativistic apsidal motion term (Levici 1937; Kopal 1959):

$$\dot{\omega}_{GR}^{theor} (\text{deg/yr}) = 9.2872 \times 10^{-3} \frac{(M_1 + M_2)^{2/3}}{(P/2\pi)^{5/3}(1 - e^2)} (\text{deg/yr}). \quad (5)$$

We obtained the general relativistic contribution to be  $\dot{\omega}_{GR}^{theor} = 0.005(1)^\circ/\text{yr}$  giving a combined value of  $\dot{\omega}_{CL+GR}^{theor} = 0.007(6)^\circ/\text{yr}$ .

The observed rate of apsidal advance of  $1.166(1)^\circ/\text{yr}$  determined through light curve modelling is two orders of magnitude larger than the theoretically predicted rate of  $0.007(6)^\circ/\text{yr}$ . We are aware that the classical, theoretical rate of apsidal advance is strongly dependent on the stellar radii (to the 5<sup>th</sup> power) and that, as the light curve of KIC 3749404 does not contain eclipses, our radii determination is based on the Roche lobe geometry (which is not as accurate as direct detection through eclipse modelling). However, the difference between the theoretical and predicted rates is highly significant and, consequently, there is no way that the apsidal motion rate of KIC 3749404 could be reduced to the theoretical rate through tweaking assumptions or inflating uncertainties. We hypothesise that the rapid rate of apsidal advance of KIC 3749404 is due to a tertiary component in the system.

#### 4.1 Precession from Tidally Induced Pulsations

In addition to apsidal motion produced by the rotational and equilibrium tidal distortion of the stars, the dynamical tidal distortion (i.e., tidally induced pulsations) can produce significant orbital precession. Tidally induced pulsations are typically produced by gravity modes within the stellar components, which create oscillations in the gravitational fields of the stars, in addition to the luminosity variations seen in Fig. 4. The aspherically distorted gravitational field (averaged over an orbital cycle) can produce significant orbital precession, depending on the amplitude to which the gravity modes are excited.

The effect of dynamical tides on apsidal motion has previously been investigated in Smeyers & Willems (2001); Willems & Aerts (2002); Claret & Willems (2002) for binaries of various stellar masses, orbital periods, and eccentricities. These authors found that the contribution of dynamical tides to orbital precession is generally small (especially at orbital periods exceeding 5 days), except when very near resonance with stellar oscillation modes. Even in this case, the precession rate is typically only altered at a level of order unity, and it cannot be enhanced by a factor of  $\sim 100$  as is required to explain the apsidal motion in KIC 3749404. Moreover, non of the tidally excited gravity modes in the components of KIC 3749404 are particularly close to resonance. We infer this from comparison with other heartbeat stars that have pulsations near resonance (e.g., KOI-54, Welsh et al.

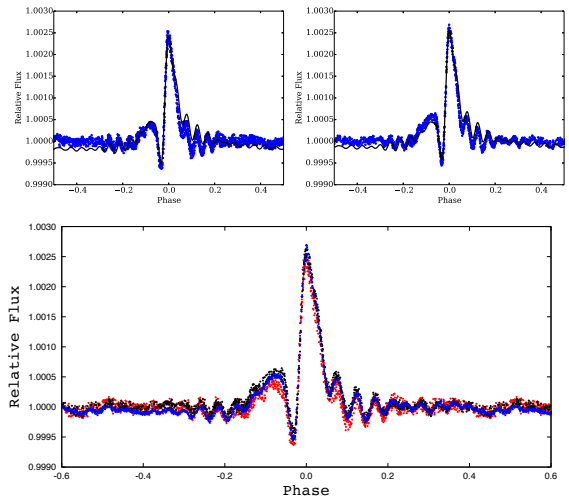


**Figure 7.** Top panel: the best-fit models (black lines) for the initial segment of data (left panel) of Quarters 1 and 2 (blue dots), and the final segment of data (right panel) for Quarters 15 and 16 (blue dots). To perform the fit, the parameters from the model with pulsations were fixed, with the exception of the argument of periastron, phase shift and a global pulsation phase shift parameter, which were fitted. Bottom panel: The phase folded *Kepler* data of Quarters 1 and 2 (red); Quarters 8, 9 and 10 (blue); and Quarters 15 and 16 (black). The data clearly demonstrate the changing shape of the light curve due to the advance of periastron.

(2011); KIC 8164262, Hambleton et al., in prep) where the pulsations close to resonance have significantly larger amplitudes than other pulsations in the system. Therefore, we find it unlikely that tidally induced pulsations can produce the rapid apsidal motion of KIC 3749404.

#### 4.2 Precession from a Third Body

One possibility is that the rapid apsidal motion in KIC 3749404 is caused by the gravitational influence of an external perturber. To order of magnitude, the precession rate due to an external third body is (Eggleton & Kiseleva-Eggleton 2001):

$$\dot{\omega}_{3B} \approx \frac{M_3}{M_1 + M_2 + M_3} \frac{1}{(1 - e_{in}^2)^{1/2}(1 - e_{out}^2)^{3/2}} \frac{\Omega_{out}}{\Omega_{in}} \Omega_{out}. \quad (6)$$

Here,  $M_3$  is the mass of the third body, while  $e_{in}$  and  $e_{out}$  refer to the eccentricities of the inner and outer orbits, and  $\Omega_{in}$  and  $\Omega_{out}$  refer to their orbital angular frequencies. The precise precession rate depends on the relative inclination of the systems which is not constrained.

We expect the third body to have  $M_3 < M_1, M_2$  because it is not visible in the spectra, and orbital stability requires  $\Omega_{out} \ll \Omega_{in}$ . Making the simplifying assumption of  $e_{out} = 0$ , and using the measured values of  $e_{in}$  and  $\Omega_{in}$  yields

$$\dot{\omega}_{3B} \sim \frac{M_3}{M_1 + M_2 + M_3} \left( \frac{P_{in}}{P_{out}} \right)^2 10^4 \text{ deg/yr}. \quad (7)$$

Equating this with the observed rate of precession of  $\dot{\omega}_{obs} \simeq$

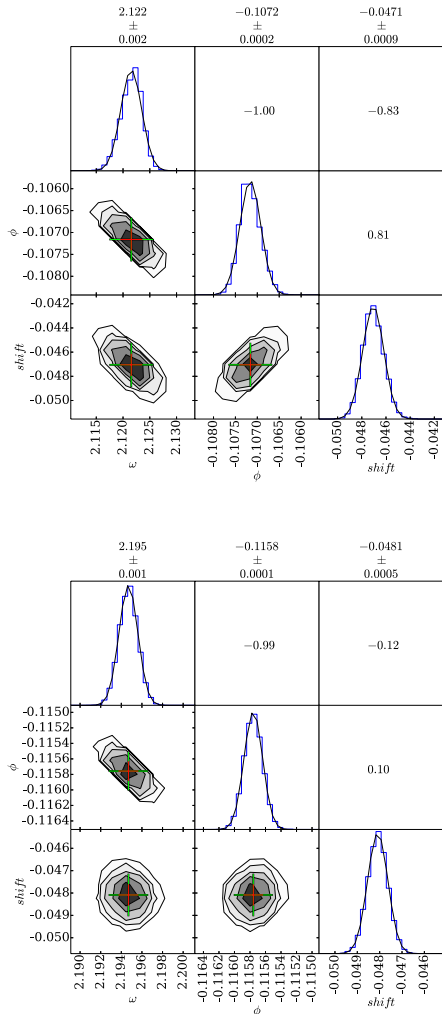


**Figure 8.** Posterior distributions of the apsidal motion parameters for the model of the first section (top panel) and last section (bottom panel) of *Kepler* data. Here  $\omega$  is the argument of periastron;  $\phi$  is the light curve phase shift, which is required to keep the periastron variation centred when changing the argument of periastron; and *shift* represents the amount by which all the pulsation phases are shifted with respect to their values for the original model with 7 pulsations. The layout is analogous to that of Fig. 3.

1 deg/yr yields the requirement

$$\frac{M_3}{M_1 + M_2 + M_3} \left( \frac{P_{\text{in}}}{P_{\text{out}}} \right)^2 \sim 10^{-4}. \quad (8)$$

A typical low-mass companion of  $M_3 \sim 0.5 M_\odot$  would then require  $P_{\text{out}} \sim 2$  yr. Of course, different companion masses, eccentricities, and inclinations would change the required orbital period of the third body, but we expect this period to be on the order of years to produce the observed apsidal motion. A third body at this orbital separation, in-

clination and eccentricity would have a semi-amplitude of  $\sim 5 \text{ km s}^{-1}$  and could likely be detected through long term RV variations of the primary binary, or possibly via an infrared excess in the spectrum. We encourage follow-up observations of KIC 3749404 to constrain the nature of a putative third body and determine whether the observed precession is driven by three-body processes or tidal interactions.

Dependent on the inclination of the tertiary component's orbit, it is also possible that nodal precession could occur. Given a long enough time base, this could also be detected in the orbit as a change in the radial velocity amplitude due to the motion of the inner binaries center of mass (see *e.g.* Mayor & Mazeh (1987)). Furthermore, in heartbeat stars, this could be observed as a change in the morphology of the periastron variation due to a change in the inner binaries inclination. During the analysis of KIC 3749404 we did not detect a clear signature of nodal precession in the light curve given our uncertainties.

### 4.3 Stellar Components

As predicted by theory, the gravity brightening exponent for the radiative, primary component, determined through our models, is  $\sim 1$  (von Zeipel 1924). For the secondary component the posterior distribution is a slightly skewed normal distribution. By considering the peak of the skewed distribution (not the Gaussian fit to the posterior distribution) we find the gravity brightening exponent to be  $\beta = 0.59 \pm 0.08$ . While this is not in agreement with the value of  $\beta = 0.32$ , suggested by Lucy (1967), we find our value in close agreement ( $\sim 2\sigma$ ) with that of Claret & Bloemen (2011), who computed  $\beta = 0.48$  for comparable models. This value was computed using ATLAS models (Castelli & Kurucz 2004) and the *Kepler* bandpass, and taking into account local gravity and convection. It is also likely that the tidal distortion affects the gravity darkening exponent, as discussed by Espinosa Lara & Rieutord (2012).

In our binary models we fixed the primary and secondary rotation rates to those obtained through spectral fitting,  $v \sin i_1 = 29(2) \text{ km s}^{-1}$  and  $v \sin i_2 = 9(2) \text{ km s}^{-1}$ . Combining these values with our model-determined inclination and radii, for the model with pulsations, we obtained  $F_1 = 7.1(2)$  and  $F_2 = 4.0(1)$ , where  $F$  is the ratio of the stellar rotational to orbital period and the subscript denotes the primary and secondary components, respectively. For both models, the one with, and the one without pulsations, we obtained the same values with slightly different uncertainties (see Table 4). Interestingly, the primary component is rotating slightly faster than the predicted pseudo-synchronous rotation rate (Hut 1981), the stellar rotation synchronous with the orbital velocity at periastron, which was calculated to be  $F = 5.34$  for both components; while the secondary component is rotating slightly slower.

## 5 SUMMARY AND CONCLUSIONS

We have modelled the heartbeat star binary system KIC 3749404 by combining a comprehensive assortment of tools including the binary modelling software, PHOEBE; EMCEE, a python implementation of the affine invariant Markov chain Monte Carlo techniques; and our own software to

fit pulsations and Doppler boosting. With these tools we were able to obtain two successful fits to the heartbeat star light and radial velocity curves simultaneously: one without pulsations and one with all the tidally induced pulsations greater than  $20 \mu\text{mag}$  (7 pulsations). From these fits we obtained the fundamental parameters of the binary system (see Table 3). The difference between the results of these two models hinges on the different inclination values:  $60.2(1)^\circ$  without pulsations and  $62(1)^\circ$  with pulsations. This 2 sigma difference subsequently produced a larger semi-major axis and masses in the model with pulsations ( $3(1) R_\odot$  larger for the semi-major axis, and  $0.3(1) M_\odot$  and  $0.1(1) M_\odot$  larger for the primary and secondary component, respectively).

Analysis of the stellar spectra highlighted a mismatch between the spectral templates and observations for the primary component. Increasing the metallicity improved the general fit to the metal lines; however, worsened the fit to the Ca II K lines and the hydrogen lines, which are important temperature indicators in A stars. This selective enrichment of the photosphere matches the abundance patterns of Am stars. The presence of Am stars in binaries is common, due to the slow rotation (compared to single A stars) and increased convective mixing. Thus we conclude that the primary component of KIC 3749404 is an Am star.

As there is significant smearing of the periastron variation in the phased *Kepler* light curve, which is indicative of apsidal motion, we elected to model the rate of apsidal advance. This was done by fitting two new models, one to the beginning (Quarters 1 and 2) and one to the end (Quarters 15 and 16) of our data set. For the new models, all the values were fixed to those previously determined for the model with pulsations, except for the argument of periastron and phase shift, which were fitted, along with an additional parameter to shift all the pulsation phases by a fixed amount. The difference between the argument of periastron at the beginning and end of our data set, divided by the duration of the data set gave us an estimate of the rate of apsidal advance ( $\dot{\omega}_{obs} = 1.166(1)^\circ/\text{yr}$ ). Comparing this value to the theoretical rate of apsidal advance, accounting for both classical and general relativistic effects ( $\dot{\omega}_{theo} = 0.007(6)^\circ/\text{yr}$ ), we found that the orbit of KIC 3749404 is precessing faster than predicted by two orders of magnitude. While we accept that the lack of eclipses in our light curve limits the determination of the stellar radii and rate of apsidal advance, the extreme disagreement between theory and observation is unlikely a consequence of our chosen methods, even when considering that the rate of classical apsidal advance scales as  $R^{-5}$ . After eliminating tidally induced pulsations as the sole cause of rapid apsidal motion, we hypothesise that it is due to the presence of a tertiary component in the system.

## 6 ACKNOWLEDGEMENTS

The authors express their sincere thanks to NASA and the *Kepler* team for allowing them to work with and analyse the *Kepler* data making this work possible. The *Kepler* mission is funded by NASA's Science Mission Directorate. KH and AP acknowledge support from the NSF grant #1517460. This work was also supported by the STFC (Science and Technology Funding Council). The authors would like to thank Ed Guinan for the enlightening discussion on apsi-

dal motion. KH, ST and JF acknowledge support through NASA K2 GO grant (11-KEPLER11-0056). We would like to thank the RAS for providing grants which enabled KH's attendance to conferences and thus enabled the development of collaborations and the successful completion of this work. AP acknowledges support through NASA K2 GO grant (NASA 14-K2GO1-2-0057). We acknowledge the observations taken using the 1.5-m telescope at the Fred L. Whipple Observatory.

## REFERENCES

- Abt H. A., 1967, in *Magnetic and Related Stars*, R. C. Cameron, ed., pp. 173–+
- Baglin A. et al., 2006, in *COSPAR, Plenary Meeting*, Vol. 36, 36th COSPAR Scientific Assembly, pp. 3749–+
- Barclay T., Endl M., Huber D., Foreman-Mackey D., Cochran W. D., MacQueen P. J., Rowe J. F., Quintana E. V., 2015, *ApJ*, 800, 46
- Batalha N. M. et al., 2010, *ApJ*, 713, L109
- Beck P. G. et al., 2014, *A&A*, 564, A36
- Bloemen S. et al., 2011, *MNRAS*, 410, 1787
- Borucki W. J., Koch D., Basri G., Batalha N., Brown T., Caldwell D., et al., 2010, *Science*, 327, 977
- Buchhave L. A. et al., 2010, *ApJ*, 720, 1118
- Burkert J., Quataert E., Arras P., Weinberg N. N., 2012, *MNRAS*, 421, 983
- Castelli F., Kurucz R. L., 2004, *ArXiv Astrophysics e-prints*
- Christiansen J. L. et al., 2013, *Kepler Data Characteristics Handbook*
- Claret A., 1997, *A&A*, 327, 11
- Claret A., Bloemen S., 2011, *A&A*, 529, A75
- Claret A., Gimenez A., 1993, *A&A*, 277, 487
- Claret A., Willems B., 2002, *A&A*, 388, 518
- Claret A., Willems B., 2003, *A&A*, 410, 289
- Cowling T. G., 1938, *MNRAS*, 98, 734
- Cowling T. G., 1941, *MNRAS*, 101, 367
- Diaz-Cordoves J., Gimenez A., 1992, *A&A*, 259, 227
- Eggleton P. P., Kiseleva-Eggleton L., 2001, *ApJ*, 562, 1012
- Espinosa Lara F., Rieutord M., 2012, *A&A*, 547, A32
- Fűrész G., 2008, PhD thesis, University of Szeged, Hungary
- Foreman-Mackey D., Hogg D. W., Lang D., Goodman J., 2013, *PASP*, 125, 306
- Fuller J., Lai D., 2012, *MNRAS*, 420, 3126
- Gilliland R. L., Brown T. M., Christensen-Dalsgaard J., Kjeldsen H., Aerts C., et al., 2010, *PASP*, 122, 131
- Gimenez A., Garcia-Pelayo J. M., 1982, in *Astrophysics and Space Science Library*, Vol. 98, IAU Colloq. 69: Binary and Multiple Stars as Tracers of Stellar Evolution, Kopal Z., Rahe J., eds., pp. 37–46
- Goodman J., Weare J., 2010, *Com. App. Math. Comp. Sci.*, 5, 65
- Guinan E. F., Maloney F. P., 1985, *AJ*, 90, 1519
- Hambleton K. M. et al., 2013, *MNRAS*, 434, 925
- Hareter M. et al., 2014, *A&A*, 567, A124
- Hartmann E., 1998, *CAGD*, 15, 377
- Hut P., 1981, *A&A*, 99, 126
- Kirk B. et al., 2016, *AJ*, 151, 68

# Chapter 6

## KIC 5006817

This chapter features the published asteroseismic case study of 18 red-giant heartbeat stars, including the detailed study of KIC 5006817. This work is contextualized by Chapter 1 which includes detailed discussion on solar-like oscillations and red giants, and Chapter 3, which provides an introduction to heartbeat stars.

I am the second author of this publication and personally led the binary star modelling effort. This included creating a full, self-consistent binary star model and writing Sections 6 and 7, entitled “Binary parameters of KIC 5006817” and “Combined asteroseismic and binary interpretation”, respectively. This publication was led by P. Beck, who undertook most of the writing, and the asteroseismic analysis and interpretation. The majority of the spectral observations were obtained by S. Bloemen. J. Vos created the evolutionary model of KIC 5006817, which he wrote about in Section 8, entitled “Impact of stellar evolution on eccentric binary systems”. The remaining authors listed on the publication contributed discussion and comments.

# Pulsating red giant stars in eccentric binary systems discovered from *Kepler* space-based photometry

## A sample study and the analysis of KIC 5006817

P. G. Beck<sup>1</sup>, K. Hambleton<sup>2,1</sup>, J. Vos<sup>1</sup>, T. Kallinger<sup>3</sup>, S. Bloemen<sup>1</sup>, A. Tkachenko<sup>1</sup>, R. A. García<sup>4</sup>, R. H. Østensen<sup>1</sup>, C. Aerts<sup>1,5</sup>, D. W. Kurtz<sup>2</sup>, J. De Ridder<sup>1</sup>, S. Hekker<sup>6</sup>, K. Pavlovski<sup>7</sup>, S. Mathur<sup>8</sup>, K. De Smedt<sup>1</sup>, A. Derekas<sup>9</sup>, E. Corsaro<sup>1</sup>, B. Mosser<sup>10</sup>, H. Van Winckel<sup>1</sup>, D. Huber<sup>11</sup>, P. Degroote<sup>1</sup>, G. R. Davies<sup>12</sup>, A. Prša<sup>13</sup>, J. Debosscher<sup>1</sup>, Y. Elsworth<sup>12</sup>, P. Nemeth<sup>1</sup>, L. Siess<sup>14</sup>, V. S. Schmid<sup>1</sup>, P. I. Pápics<sup>1</sup>, B. L. de Vries<sup>1</sup>, A. J. van Marle<sup>1</sup>, P. Marcos-Arenal<sup>1</sup>, and A. Lobel<sup>15</sup>

<sup>1</sup> Instituut voor Sterrenkunde, KU Leuven, 3001 Leuven, Belgium  
e-mail: paul.beck@ster.kuleuven.be

<sup>2</sup> Jeremiah Horrocks Institute, University of Central Lancashire, Preston PR1 2HE, UK

<sup>3</sup> Institut für Astronomie der Universität Wien, Türkenschanzstr. 17, 1180 Wien, Austria

<sup>4</sup> Laboratoire AIM, CEA/DSM-CNRS – Université Denis Diderot-IRFU/Sap, 91191 Gif-sur-Yvette Cedex, France

<sup>5</sup> Department of Astrophysics, IMAPP, University of Nijmegen, PO Box 9010, 6500 GL Nijmegen, The Netherlands

<sup>6</sup> Astronomical Institute Anton Pannekoek, University of Amsterdam, Science Park 904, 1098 XH Amsterdam, The Netherlands

<sup>7</sup> Department of Physics, Faculty of Science, University of Zagreb, 10000 Zagreb, Croatia

<sup>8</sup> Space Science Institute, 4750 Walnut street Suite #205, Boulder CO 80301, USA

<sup>9</sup> Konkoly Observ., Research Centre f. Astronomy and Earth Sciences, Hungarian Academy of Sciences, 1121 Budapest, Hungary

<sup>10</sup> LESIA, CNRS, Université Pierre et Marie Curie, Université Denis Diderot, Observatoire de Paris, 92195 Meudon Cedex, France

<sup>11</sup> NASA Ames Research Center, Moffett Field CA 94035, USA

<sup>12</sup> School of Physics and Astronomy, University of Birmingham, Edgbaston, Birmingham B13 2TT, UK

<sup>13</sup> Department of Astronomy and Astrophysics, Villanova University, 800 East Lancaster avenue, Villanova PA 19085, USA

<sup>14</sup> Institut d'Astronomie et d'Astrophysique, Univ. Libre de Bruxelles, CP226, boulevard du Triomphe, 1050 Brussels, Belgium

<sup>15</sup> Royal Observatory of Belgium, Ringlaan 3, 1180 Brussels, Belgium

Received 12 August 2013 / Accepted 16 December 2013

### ABSTRACT

**Context.** The unparalleled photometric data obtained by NASA's *Kepler* Space Telescope has led to improved understanding of red giant stars and binary stars. Seismology allows us to constrain the properties of red giants. In addition to eclipsing binaries, eccentric non-eclipsing binaries that exhibit ellipsoidal modulations have been detected with *Kepler*.

**Aims.** We aim to study the properties of eccentric binary systems containing a red giant star and to derive the parameters of the primary giant component.

**Methods.** We applied asteroseismic techniques to determine the masses and radii of the primary component of each system. For a selected target, light and radial velocity curve modelling techniques were applied to extract the parameters of the system and its primary component. Stellar evolution and its effects on the evolution of the binary system were studied from theoretical models.

**Results.** The paper presents the asteroseismic analysis of 18 pulsating red giants in eccentric binary systems, for which masses and radii were constrained. The orbital periods of these systems range from 20 to 440 days. The results of our ongoing radial velocity monitoring programme with the Hermes spectrograph reveal an eccentricity range of  $e = 0.2$  to  $0.76$ . As a case study we present a detailed analysis of KIC 5006817, whose rich oscillation spectrum allows for detailed seismic analysis. From seismology we constrain the rotational period of the envelope to be at least 165 d, which is roughly twice the orbital period. The stellar core rotates 13 times faster than the surface. From the spectrum and radial velocities we expect that the Doppler beaming signal should have a maximum amplitude of 300 ppm in the light curve. Fixing the mass and radius to the asteroseismically determined values, we find from our binary modelling a value of the gravity darkening exponent that is significantly larger than expected. Through binary modelling, we determine the mass of the secondary component to be  $0.29 \pm 0.03 M_{\odot}$ .

**Conclusions.** For KIC 5006817 we exclude pseudo-synchronous rotation of the red giant with the orbit. The comparison of the results from seismology and modelling of the light curve shows a possible alignment of the rotational and orbital axis at the  $2\sigma$  level. Red giant eccentric systems could be progenitors of cataclysmic variables and hot subdwarf B stars.

**Key words.** stars: solar-type – binaries: general – stars: rotation – Sun: oscillations – stars: individual: KIC5006817 – asteroseismology

## 1. Introduction

The NASA *Kepler* space telescope (Borucki et al. 2010) has been delivering unprecedented photometric data for more than 150 000 stars. These nearly continuous observations that now cover more than 1000 d have allowed major advances in our

understanding of stellar structure of single stars and of multiple-star systems. The asteroseismic investigation of red giant stars has become one of *Kepler*'s success stories.

Red giants are evolved stars that have ceased hydrogen burning in the core and left the main sequence. This late phase of stellar evolution splits into several episodes, which are associated

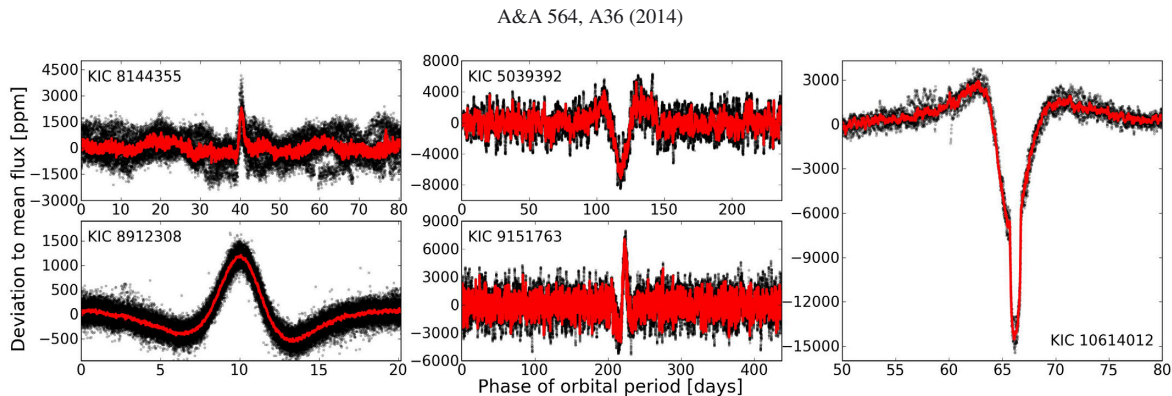


**Fig. 1.** Five examples of *Kepler* light curves of red giant heartbeat stars from our sample. Black dots and red line show the corrected and rebinned (30 min) light curves, respectively. KIC 8144355 is the star with the highest eccentricity, KIC 5039392 is the most luminous star, and KIC 9151763 is the star with the longest orbital period. The low-luminosity RGB star KIC 8912308 has the shortest orbital period in our sample. The *right panel* shows a zoom on the partial eclipse during the heartbeat event of KIC 10614012.

with subsequent modifications of the stellar structure. As the helium core contracts, the energy generation rate in the hydrogen-burning shell that surrounds the core increases the luminosity causing an increase in the stellar radius. The core's mass and density keep growing until the core is hot enough to ignite helium, as the helium settles from the burning hydrogen shell. For stars with birth masses below approximately  $2.3 M_{\odot}$ , the helium core fusion starts with a helium flash in a series of off-centre thermal subflashes (e.g. Bildsten et al. 2012) that result in a thermal runaway. At this point the core expands by two orders of magnitude, reducing the temperature of the overlying hydrogen-burning shell. The luminosity of the star drops, the radius contracts and the red giant settles onto the horizontal branch, where metal-rich stars are concentrated in the red clump.

A large portion (in radius) of the red giant's envelope is convective, and oscillations are excited stochastically in a part of that envelope. These solar-like oscillations correspond to pressure modes (p modes), and their frequencies follow a characteristic comb-like pattern (Tassoul 1980). The mode amplitudes range from a few tens to a few hundred parts per million (ppm) in observed flux, or of the order of  $10 \text{ m s}^{-1}$  or less in radial velocity (Frandsen et al. 2002; De Ridder et al. 2006), which is barely detectable from ground-based observations. In the era before high-precision photometric space missions, solar-like oscillations of red giants were only confirmed in a handful of bright stars from extensive single- and multisite campaigns of high-precision spectroscopy. Examples are  $\xi$  Hya (Frandsen et al. 2002),  $\varepsilon$  Oph (De Ridder et al. 2006), and  $\eta$  Ser (Hekker et al. 2006). Photometric measurements from space have substantially increased the number of red giants with detected oscillation signals. The detection of nonradial modes in a multitude of red giants observed with the CoRoT satellite was a major milestone towards an improved understanding of red giants, since it allowed for more sophisticated asteroseismic analyses (De Ridder et al. 2009).

Pressure modes have their largest amplitude in the convective envelope, while gravity modes (g modes) have their largest amplitude in the deep interior. At some stages of stellar evolution, p modes and g modes can couple and become a mixed mode. The firm identification of such mixed modes in *Kepler* and CoRoT data by Beck et al. (2011), Bedding et al. (2011), and Mosser et al. (2011a) extended the sensitivity of the seismic analysis towards the core regions of red giant stars (Dupret et al. 2009, and references therein). The analysis of mixed modes allows us to determine the evolutionary

state (Bedding et al. 2011; Mosser et al. 2011a) and constrain the core rotation of red giants (Beck et al. 2012; Deheuvels et al. 2012).

The seismology of red giants is largely built on scaling relations for pressure modes that have already been described by Kjeldsen & Bedding (1995). These relations have been applied in numerous papers since then (e.g. Kallinger et al. 2010b; Huber et al. 2011; Corsaro et al. 2013). Results from scaling relations have recently been compared with results of independent methods. Huber et al. (2012) found a good agreement within the observational uncertainties for evolved stars. From comparing results for the eclipsing binary KIC 8410637 from binary modelling and seismology, Frandsen et al. (2013) found an excellent agreement for the surface gravity. But, the masses determined by the two methods deviated slightly. Additionally, a large set of red giants in eclipsing binaries was recently reported by Gaulme et al. (2013) which will allow for new sample studies.

The *Kepler* mission has also recently discovered the existence of a new class of eccentric ellipsoidal binary stars for which the binary characteristics can be determined over the complete range of inclinations and as such are not limited to the narrow range of eclipsing systems. These so-called *Heartbeat* stars (Welsh et al. 2011; Thompson et al. 2012) are defined as eccentric, detached binary systems that undergo strong gravitational distortions and heating during periastron passage, which are clearly depicted in their light curves (e.g. Fig. 1). Kumar et al. (1995) developed a theory of such objects and demonstrated how the morphology of the light curve is defined by the eccentricity, argument of periastron and inclination. Furthermore, the amplitude of the periastron variation is determined by the periastron separation, masses and structure of the stellar components. Consequently, these parameters can in principle be gauged through consideration of the light and radial velocity curves. The first such object discovered to confirm the theory was KOI 54 (HD 187091, Welsh et al. 2011). Subsequently, more tidally interacting eccentric binary systems have been discovered in the *Kepler* field as well as in the Magellanic clouds from OGLE observations by Thompson et al. (2012), Hambleton et al. (2013) and Nicholls & Wood (2012), respectively. Only observations from *Kepler* provide the temporal resolution to allow for a dedicated seismic analysis for these stars. Table 1 lists several newly-found heartbeat stars in the *Kepler* field of view with a component exhibiting solar-like oscillations.

The seismic study of a sample of 18 eccentric systems (Fig. 2) is presented in Sect. 3. For a detailed seismic study,

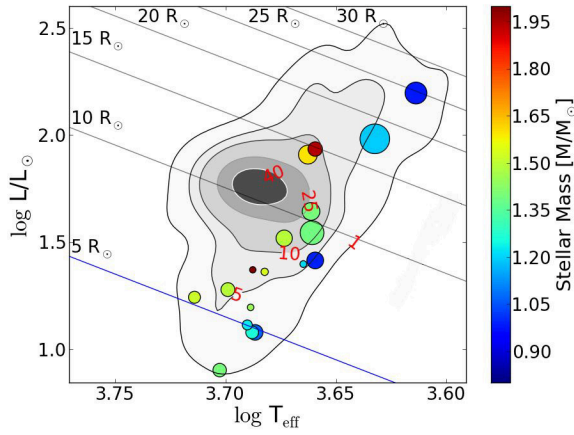


**Fig. 2.** Position of the 18 red giant heartbeat stars from Tables 1 and 2 in the HR diagram, where the colour shows the mass of the red giant, derived from seismology. The size of the dots represents the orbital period, ranging between 20 and 438 d. The contour surfaces reflect the density distribution of 1000 pulsating red giants. The darkest areas mark the position of the densely populated red clump. Numbers in red indicate the star count per bin, for which the contour surfaces have been drawn. Lines of equal radii in the HR diagram have been drawn for selected stellar radii between 5 and  $30 R_{\odot}$ .

a large number of oscillation modes is needed to allow for an optimal comparison with theoretical models. The star with the richest power density spectrum is KIC 5006817. Sections 4–6 describe the seismic, spectroscopic and binary analyses of this system. The results of these different analyses are compared in Sect. 7. In Sect. 8 we reflect upon the possibility that heartbeat stars are potential subdwarf B (sdB) and cataclysmic variables (CV) progenitors.

## 2. Observations

The *Kepler* datasets used in this study cover a time base up to 1300 d (Quarters Q0–Q14) in the long cadence observing mode of *Kepler*. In this mode, integrations of 6.04 s are taken every 6.54 s and 270 such integrations are co-added for transmission to Earth to give an integration time of 29.43 min, leading a Nyquist frequency of  $283.4 \mu\text{Hz}$ . For one target a month of short cadence data was available. In this observing mode, the individual integrations are stacked to exposures of 58.8 s, which leads to a Nyquist frequency of  $8495 \mu\text{Hz}$  (Fig. 3). To produce light curves which are robust against long period instrumental drifts, we extracted the photometric flux from the pixel data following the methods described by Bloemen (2013). The light curves were corrected following García et al. (2011). The target pixel data were also used to inspect whether the light curve was contaminated by neighbouring field stars. In all cases a significant contamination is unlikely.

Red giant heartbeat candidates were selected by inspecting the light curves. Also the subsequent versions of the *Kepler* eclipsing binary catalogue (Prša et al. 2011; Slawson et al. 2011; Matijević et al. 2012) were searched for candidates among the stars classified as red giants.

The light curves of red giant stars are dominated by the low frequency signals of the granulation background and of the solar-like oscillations (Fig. 4), which hamper a determination of the precise value of the orbital period from the reoccurring

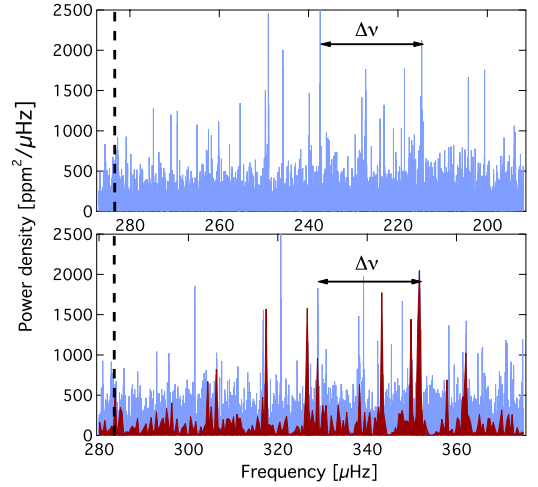


**Fig. 3.** Power density spectra of KIC 8803882 from 1250 d of long and 30 d of short cadence data are shown in blue and red, respectively. The formal Nyquist frequency (dashed line) separates the reflected oscillation power (top panel, sub-Nyquist frequency range) and the original power excess (bottom panel, super-Nyquist frequency range).

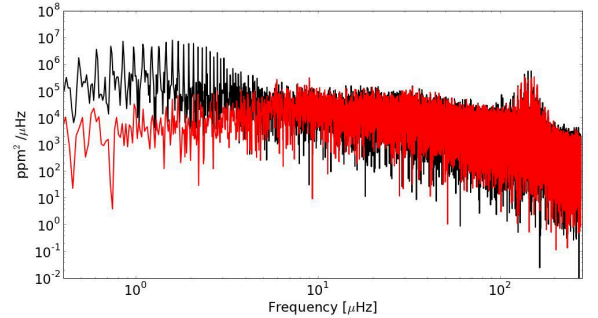


**Fig. 4.** Power density spectrum (PDS) of the light curve of KIC 5006817. The black PDS was calculated from the original light curve. The red PDS originates from a high-passband filtered light curve, corrected for the mean flux variation during the periastron passage. A zoom into the power excess is shown in Fig. 5.

flux modulation at periastron (hereafter referred to as *heartbeat event*). Therefore, the light curves were smoothed with a boxcar with a width of a few days and analyzed using the phase dispersion minimisation technique (Stellingwerf 1978). By testing for strictly periodic recurrences, confusion with other variability sources, such as stellar activity or instrumental artefacts is excluded.

For an independent confirmation of the binary nature of the discovered heartbeat systems, we searched for radial velocity variations from spectra obtained with the Hermes spectrograph (Raskin et al. 2011), mounted on the 1.2 m *Mercator* Telescope at La Palma, Canary Islands, Spain. This highly efficient échelle spectrograph has a resolving power of  $R = 86\,000$ . The raw spectra were reduced with the instrument-specific pipeline. The radial velocities were derived through weighted cross-correlation of the wavelength range between 478 and 653 nm of each spectrum with an Arcturus template (Raskin et al. 2011). For our prime target, KIC 5006817, two orbital cycles were monitored

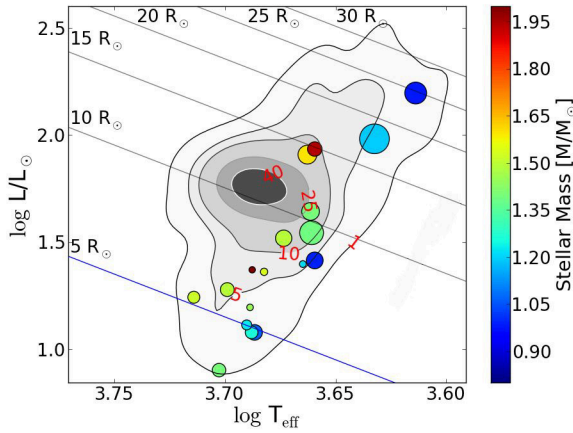


**Fig. 2.** Position of the 18 red giant heartbeat stars from Tables 1 and 2 in the HR diagram, where the colour shows the mass of the red giant, derived from seismology. The size of the dots represents the orbital period, ranging between 20 and 438 d. The contour surfaces reflect the density distribution of 1000 pulsating red giants. The darkest areas mark the position of the densely populated red clump. Numbers in red indicate the star count per bin, for which the contour surfaces have been drawn. Lines of equal radii in the HR diagram have been drawn for selected stellar radii between 5 and  $30 R_{\odot}$ .

a large number of oscillation modes is needed to allow for an optimal comparison with theoretical models. The star with the richest power density spectrum is KIC 5006817. Sections 4–6 describe the seismic, spectroscopic and binary analyses of this system. The results of these different analyses are compared in Sect. 7. In Sect. 8 we reflect upon the possibility that heartbeat stars are potential subdwarf B (sdB) and cataclysmic variables (CV) progenitors.

## 2. Observations

The *Kepler* datasets used in this study cover a time base up to 1300 d (Quarters Q0–Q14) in the long cadence observing mode of *Kepler*. In this mode, integrations of 6.04 s are taken every 6.54 s and 270 such integrations are co-added for transmission to Earth to give an integration time of 29.43 min, leading a Nyquist frequency of  $283.4 \mu\text{Hz}$ . For one target a month of short cadence data was available. In this observing mode, the individual integrations are stacked to exposures of 58.8 s, which leads to a Nyquist frequency of  $8495 \mu\text{Hz}$  (Fig. 3). To produce light curves which are robust against long period instrumental drifts, we extracted the photometric flux from the pixel data following the methods described by Bloemen (2013). The light curves were corrected following García et al. (2011). The target pixel data were also used to inspect whether the light curve was contaminated by neighbouring field stars. In all cases a significant contamination is unlikely.

Red giant heartbeat candidates were selected by inspecting the light curves. Also the subsequent versions of the *Kepler* eclipsing binary catalogue (Prša et al. 2011; Slawson et al. 2011; Matijević et al. 2012) were searched for candidates among the stars classified as red giants.

The light curves of red giant stars are dominated by the low frequency signals of the granulation background and of the solar-like oscillations (Fig. 4), which hamper a determination of the precise value of the orbital period from the reoccurring

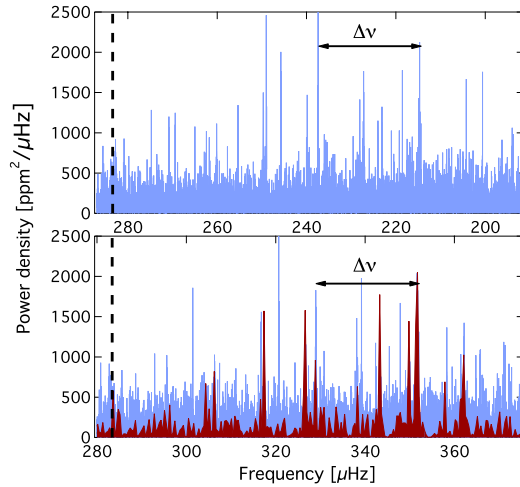


**Fig. 3.** Power density spectra of KIC 8803882 from 1250 d of long and 30 d of short cadence data are shown in blue and red, respectively. The formal Nyquist frequency (dashed line) separates the reflected oscillation power (*top panel*, sub-Nyquist frequency range) and the original power excess (*bottom panel*, super-Nyquist frequency range).

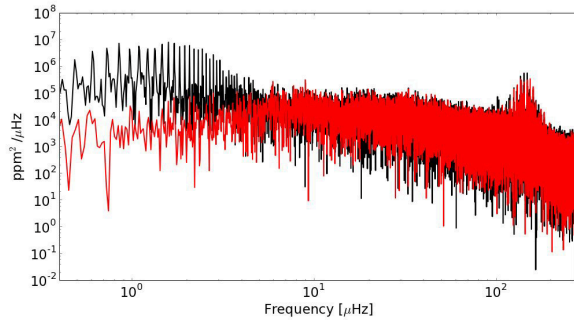


**Fig. 4.** Power density spectrum (PDS) of the light curve of KIC 5006817. The black PDS was calculated from the original light curve. The red PDS originates from a high-passband filtered light curve, corrected for the mean flux variation during the periastron passage. A zoom into the power excess is shown in Fig. 5.

flux modulation at periastron (hereafter referred to as *heartbeat event*). Therefore, the light curves were smoothed with a boxcar with a width of a few days and analyzed using the phase dispersion minimisation technique (Stellingwerf 1978). By testing for strictly periodic recurrences, confusion with other variability sources, such as stellar activity or instrumental artefacts is excluded.

For an independent confirmation of the binary nature of the discovered heartbeat systems, we searched for radial velocity variations from spectra obtained with the Hermes spectrograph (Raskin et al. 2011), mounted on the 1.2 m *Mercator* Telescope at La Palma, Canary Islands, Spain. This highly efficient échelle spectrograph has a resolving power of  $R = 86\,000$ . The raw spectra were reduced with the instrument-specific pipeline. The radial velocities were derived through weighted cross-correlation of the wavelength range between 478 and 653 nm of each spectrum with an Arcturus template (Raskin et al. 2011). For our prime target, KIC 5006817, two orbital cycles were monitored

**Table 1.** Seismic and fundamental parameters for 14 oscillating red giant heartbeat stars, ordered by descending orbital period.

Star KIC	$\nu_{\max}$ [ $\mu\text{Hz}$ ]	$\Delta\nu$ [ $\mu\text{Hz}$ ]	$\Delta\Pi_1$ [sec]	$\delta f_{\max}$ [nHz]	Evol. phase	$R$ [ $R_{\odot}$ ]	$M$ [ $M_{\odot}$ ]	$\log g$ [dex]	$L$ [ $L_{\odot}$ ]	$T_{\text{eff}}$ [K]	$P_{\text{orbit}}$ [d]	$A$ [ppt]	$ \Delta RV $ [ $\text{km s}^{-1}$ ]
9151763	$13.8 \pm 0.2$	$1.98 \pm 0.01$	–	–	RGB?	$17.6 \pm 0.4$	$1.19 \pm 0.08$	2.01	$96 \pm 16$	4290	437.5	+7.1	32.2
7431665	$54.0 \pm 0.7$	$5.46 \pm 0.02$	$\sim 67$	–	RGB	$9.4 \pm 0.1$	$1.39 \pm 0.05$	2.62	$35 \pm 2$	4580	281.4	–3.0	[37.8]
5039392	$6.2 \pm 0.1$	$1.13 \pm 0.01$	–	–	RGB	$24.0 \pm 0.7$	$0.98 \pm 0.07$	1.67	$157 \pm 24$	4110	236.7	–6.0	42.3
9540226*	$27.4 \pm 0.4$	$3.18 \pm 0.01$	–	–	RGB	$14.1 \pm 0.3$	$1.6 \pm 0.1$	2.37	$81 \pm 13$	4600	175.4	–7	45.3
8210370	$44.1 \pm 0.8$	$4.69 \pm 0.02$	–	–	RGB?	$10.5 \pm 0.2$	$1.40 \pm 0.08$	2.54	$44 \pm 4$	4585	153.5	–5.3	22.1
11044668	$50.2 \pm 0.2$	$5.65 \pm 0.01$	$\sim 60$	83(?)	RGB	$8.18 \pm 0.09$	$0.99 \pm 0.03$	2.59	$26 \pm 3$	4565	139.5	–3.8	[43.0]
10614012*	$70.2 \pm 0.9$	$6.54 \pm 0.02$	–	–	RGB	$8.6 \pm 0.2$	$1.49 \pm 0.08$	2.74	$33 \pm 4$	4715	132.1	–4.7	49.3
9163796	$153.2 \pm 0.7$	$13.53 \pm 0.04$	–	–	RGB	$4.46 \pm 0.03$	$0.89 \pm 0.01$	3.09	$12 \pm 1$	4820	121.3	$\pm 0.5$	70.1
2444348	$30.5 \pm 0.3$	$3.26 \pm 0.01$	–	–	RGB	$14.9 \pm 0.3$	$1.94 \pm 0.11$	2.38	$86 \pm 14$	4565	103.5	–1.7	7.7
<b>5006817</b>	$145.9 \pm 0.5$	$11.64 \pm 0.01$	78	450	RGB	$5.84 \pm 0.09$	$1.49 \pm 0.06$	3.08	$19 \pm 3$	5000	94.8	–1.7	23.5
8803882	$347 \pm 3$	$22.6 \pm 0.4$	–	500(?)	RGB	$3.68 \pm 0.1$	$1.4 \pm 0.1$	3.45	$8 \pm 1$	5043	89.7	+0.5	[1.9]
8144355	$179 \pm 2$	$13.95 \pm 0.04$	$\sim 78$	210(?)	RGB	$4.90 \pm 0.09$	$1.26 \pm 0.08$	3.16	$12 \pm 2$	4875	80.6	+2.1	18.9
9408183	$164.8 \pm 0.2$	$13.29 \pm 0.02$	$\sim 93$	450	RGB	$5.02 \pm 0.07$	$1.23 \pm 0.05$	3.12	$13 \pm 1$	4900	49.7	+1.5	64.4
2720096	$110.1 \pm 0.7$	$9.17 \pm 0.01$	–	–	RGB	$6.98 \pm 0.08$	$1.54 \pm 0.06$	2.95	$23 \pm 2$	4812	26.7	+1.0	4.0
8095275	$69.3 \pm 0.3$	$6.81 \pm 0.01$	–	–	RGB	$7.78 \pm 0.08$	$1.21 \pm 0.05$	2.74	$25 \pm 3$	4622	23.0	–6.0	20.6

**Notes.** The star's identifier in the *Kepler* Input Catalogue (KIC) is given. Eclipsing systems are marked with an asterisk. The columns  $\nu_{\max}$  and  $\Delta\nu$  report the frequency of the oscillation power excess and the large frequency separation between radial modes for a given star.  $\Delta\Pi_1$  quantifies the true period spacing of dipole modes. The maximum value of the detected rotational splitting  $\delta f$  is listed. The evolutionary phase RGB describes H-shell burning red giant. Ambiguous values are marked with “?”. The columns  $R$ ,  $M$ ,  $L$ , and  $\log g$  report the stellar radius, mass, luminosity, effective temperature and surface gravity from scaling relations, respectively.  $T_{\text{eff}}$  was adopted from the KIC. The uncertainties of  $\log g$  are on the order of 0.01 dex and for the temperature typically smaller than 150 K.  $P_{\text{orbit}}$  gives the orbital period from photometry. The column  $A$  lists the maximum amplitude of the heartbeat in a rebinned phase diagram. The error estimate for  $P_{\text{orbit}}$  and  $A$  from the PDM is not reliable due to the remaining contamination of the solar-like oscillations and therefore not given.  $|\Delta RV|$  reports the maximum difference in radial velocity. Square brackets mark systems for which the orbital parameters could not yet be determined from radial velocities.

**Table 2.** Low-luminosity red giants with  $\nu_{\max}$  higher than  $283 \mu\text{Hz}$  from long cadence data.

Star KIC	$f_{\max}$ [ $\mu\text{Hz}$ ]	$(\nu_{\max})$ [ $\mu\text{Hz}$ ]	$\Delta\nu$ [ $\mu\text{Hz}$ ]	$R$ [ $R_{\odot}$ ]	$M$ [ $M_{\odot}$ ]	$\log g$ [dex]	$L$ [ $L_{\odot}$ ]	$T_{\text{eff}}$ [K]	$P_{\text{orbit}}$ [d]	$A$ [ppt]	$ \Delta RV $ [ $\text{km s}^{-1}$ ]
7799540	$220 \pm 5$	(347.2)	24.0	3.64	1.52	3.50	17.5	5177	71.8	+0.5	[31.8]
2697935*	$161 \pm 3$	(405.6)	$\sim 28$	3.26	1.45	3.574	15.7	4883	21.5	$\pm 1.3$	52.1
8912308	$217 \pm 9$	(350.2)	22.7	4.20	2.02	3.50	23.5	4872	20.2	+1.2	61.4

**Notes.** The definition of columns KIC,  $\Delta\nu$ ,  $M$ ,  $R$ ,  $\log g$ ,  $L$ ,  $P_{\text{orbit}}$ ,  $A$  and  $|\Delta RV|$  is the same as in Table 1.  $f_{\max}$  and  $(\nu_{\max})$  indicate the frequency of the maximum oscillation power, reflected at the Nyquist frequency and reconstructed power excess, respectively.  $T_{\text{eff}}$  was adopted from the KIC parameters. The uncertainties of  $M$ ,  $R$ ,  $\log g$  and  $L$  are better than 2, 5, 1, and 15 per cent, respectively.

**Table 3.** Orbital parameters for systems for which the periastron has been monitored with the Hermes spectrograph.

Star KIC	$n_{\text{RV}}$	$P_{\text{orbit}}$ [d]	$e$	$\Omega$ [rad]	$K$ [ $\text{km s}^{-1}$ ]	$\gamma$ [ $\text{km s}^{-1}$ ]	$T_0$ [HJD]	Eclipse duration
9151763	24	$437.51 \pm 0.03$	$0.73 \pm 0.01$	$3.03 \pm 0.01$	$16.20 \pm 0.04$	$-92.89 \pm 0.03$	$2455949.64 \pm 0.06$	
5039392	13	$236.70 \pm 0.02$	$0.44 \pm 0.01$	$4.96 \pm 0.01$	$22.6 \pm 0.2$	$-14.96 \pm 0.05$	$2454874.2 \pm 0.27$	
9540226*	31	$175.43 \pm 0.01$	$0.39 \pm 0.01$	$0.07 \pm 0.01$	$23.32 \pm 0.04$	$-12.37 \pm 0.02$	$2456425.89 \pm 0.09$	P: 4 d; S: 3 d
8210370	16	$153.50 \pm 0.01$	$0.70 \pm 0.01$	$1.17 \pm 0.01$	$12.96 \pm 0.36$	$-0.76 \pm 0.08$	$2454937.35 \pm 0.01$	
10614012*	22	$132.13 \pm 0.01$	$0.71 \pm 0.01$	$1.23 \pm 0.01$	$24.68 \pm 0.03$	$-0.92 \pm 0.02$	$2454990.48 \pm 0.01$	1 d
9163796	17	$121.30 \pm 0.01$	$0.69 \pm 0.01$	$0.00 \pm 0.01$	$35.64 \pm 0.01$	$-11.05 \pm 0.01$	$2456409.60 \pm 0.01$	
2444348	17	$103.50 \pm 0.01$	$0.48 \pm 0.01$	$4.30 \pm 0.01$	$4.76 \pm 0.02$	$14.47 \pm 0.01$	$2454947.74 \pm 0.09$	
<b>5006817</b>	70	$94.812 \pm 0.002$	$0.7069 \pm 0.0002$	$4.0220 \pm 0.0005$	$11.709 \pm 0.005$	$-14.021 \pm 0.002$	$2456155.924 \pm 0.002$	
8144355	19	$80.55 \pm 0.01$	$0.76 \pm 0.01$	$2.79 \pm 0.01$	$9.44 \pm 0.04$	$0.02 \pm 0.03$	$2455914.43 \pm 0.02$	
9408183	7	$49.70 \pm 0.01$	$0.42 \pm 0.01$	$0.17 \pm 0.01$	$37.17 \pm 0.04$	$-14.37 \pm 0.01$	$2454989.80 \pm 0.01$	
2720096	13	$26.70 \pm 0.01$	$0.49 \pm 0.01$	$6.11 \pm 0.01$	$2.28 \pm 0.03$	$9.92 \pm 0.01$	$2454990.67 \pm 0.05$	
8095275	25	$23.00 \pm 0.01$	$0.32 \pm 0.01$	$2.19 \pm 0.01$	$10.50 \pm 0.06$	$-8.58 \pm 0.03$	$2454971.02 \pm 0.03$	
2697935*	27	$21.50 \pm 0.01$	$0.41 \pm 0.02$	$2.33 \pm 0.06$	$26.5 \pm 0.6$	$-74.4 \pm 0.4$	$2454990.9 \pm 0.1$	0.1 d
8912308	28	$20.17 \pm 0.01$	$0.23 \pm 0.01$	$3.34 \pm 0.01$	$30.78 \pm 0.02$	$-52.69 \pm 0.01$	$2454994.06 \pm 0.01$	

**Notes.** Number of radial velocity measurements,  $n_{\text{RV}}$ ; orbital period  $P_{\text{orbit}}$ ; eccentricity  $e$ ; argument of periastron  $\Omega$ ; radial velocity amplitude  $K$ ; velocity of the system  $\gamma$ ; and zero point  $T_0$ . The duration of the eclipse is given. P and S indicate the primary and secondary eclipses, respectively.

**Table 4.** Inclination values for individual pressure-dominated modes.

$m = 0$	Inclination
137.02	$70.2 \pm 5$
137.93	$76.3 \pm 5$
148.29	$82.9 \pm 4$
149.19	$80.2 \pm 4$
mean	$77 \pm 9$

**Notes.** Individual inclinations for the pressure-dominated dipole modes, centred on the  $m = 0$  component, in the range between 130 and 155  $\mu\text{Hz}$  (Fig. 7).

**Table 5.** Fundamental parameters of the red giant KIC 5006817.

$T_{\text{eff}}$ [K]	$\log g$ [dex]	[Fe/H] [dex]	$v_{\text{micro}}$ [km s $^{-1}$ ]	$LB$ [km s $^{-1}$ ]
$5000 \pm 250$	$3.0 \pm 0.5$	$-0.06 \pm 0.12$	$3.0 \pm 0.5$	$8 \pm 1$

**Notes.** Results for the effective temperature  $T_{\text{eff}}$ , surface gravity  $\log g$ , and microturbulence  $v_{\text{micro}}$  of the red giant component. The last column gives the total line broadening as defined in Sect. 5.1.

in 2012 as well as in 2013. Radial velocity monitoring for the other stars listed in Table 1 is ongoing. Tables 1 to 3 report the first orbital results for stars in our sample.

### 3. Eccentric red giant systems in the *Kepler* data

In total, we found 18 red giant stars in eccentric binary systems that show the characteristic gravitational distortion of heartbeat stars. These stars were found in a sample of *Kepler* red giants that encompass about 16 000 stars. All stars show the clear signature of solar-like oscillations (Tables 1 and 2). Figure 1 shows phase diagrams of five selected stars.

The global seismic analysis of red giant stars enables us to accurately constrain the fundamental parameters of the main component of the binary system. The characteristic comb-like structure of solar-like oscillations originates from p modes and therefore depends on the sound speed in the acoustic cavity. The main characteristics of the power excess (central frequency of the oscillation power excess,  $\nu_{\text{max}}$ , and the large frequency separation between consecutive radial modes,  $\Delta\nu$ ) scale well with the mass and radius, and to a lesser extent with effective temperature (e.g. Kjeldsen & Bedding 1995; Mosser et al. 2013). Following the approach of Kallinger et al. (2010b) we estimated the radius, mass, luminosity,  $\log g$  and effective temperature of our sample stars (Tables 1 and 2) and place the red giant components of the binaries in the Hertzsprung-Russell (HR) diagram shown in Fig. 2. All stars except two have masses between 1 and 1.5  $M_{\odot}$ . The majority of the *Kepler* red giants are located in this mass range.

#### 3.1. Evolutionary status of red giant heartbeat stars

Seismic information can reveal the evolutionary status of the star. Stars with a large frequency separation  $\Delta\nu \gtrsim 9 \mu\text{Hz}$  (i.e.  $R_{\text{RG}} \lesssim 7 R_{\odot}$ ) are located well below the red clump (Fig. 2) and therefore can only be in the hydrogen shell burning phase. A value of  $\Delta\nu \lesssim 3 \mu\text{Hz}$  (i.e.  $R_{\text{RG}} \gtrsim 13 R_{\odot}$ ) occurs for stars located above the red clump. Such stars are likely to be H-shell burning stars, high up on the RGB, although in principle they also could be stars on the low asymptotic giant branch (AGB). Stars with frequency separation  $3 \lesssim \Delta\nu \lesssim 9 \mu\text{Hz}$  can also be in the helium core burning phase (Bedding et al. 2011; Mosser et al. 2012b).

Therefore, a further criterion to determine the evolutionary state of stars with radii larger than  $7 R_{\odot}$  is needed.

The period separation of mixed dipole modes is a powerful diagnostic to distinguish between hydrogen shell and helium core burning stars (cf. Bedding et al. 2011; Mosser et al. 2011b). The true period spacing  $\Delta\Pi_1$  describes the constant period spacing of pure dipole g modes, which cannot be observed directly. However, one can determine the value of  $\Delta\Pi_1$  by fitting a theoretical mixed mode pattern to the actually observed modes in the power spectrum (Mosser et al. 2012a). Stars which exhibit a value of  $\Delta\Pi_1 \lesssim 100$  s are burning hydrogen in a shell around the inert helium core, while stars with a larger  $\Delta\Pi_1$  value belong to stars on the AGB or RC. The estimated values of the true period spacing  $\Delta\Pi_1$  for the pulsators are given in Table 1.

Several stars do not or barely show dipole mixed modes and it is impossible to recover their mixed mode pattern. For these stars we did not determine the evolutionary state from the period spacing but used the phase shift ( $\epsilon_c$ ) of the central radial mode as an indicator. Kallinger et al. (2012) have shown that in a diagram of  $\epsilon_c$  versus the large separation  $\Delta\nu$ , the stars fall into groups which can be identified as H-shell burning, He-core burning and AGB stars. For most stars, the identification of the evolutionary stage from  $\epsilon_c$  and the observed period spacing are in agreement. Therefore we are also able to estimate the evolutionary state of stars which did not show a clear forest of dipole modes.

For nearly all heartbeat red giants we could constrain them to be in the state of H-shell burning. The remaining stars are also likely to be in the same evolutionary state but we cannot rule out more evolved phases. Among our sample there are 5 stars in a  $\Delta\nu$  range where the stars can either be an RGB or RC star. Statistically there is a chance of about 70 per cent that a given red giant in this range burns He in its core (Kallinger et al. 2012). Even though the number statistics are still poor we find clear preference for RGB primaries in heartbeat stars. In Sect. 8, we discuss that this could be a result of binary evolution.

#### 3.2. Giants with power excess above the formal Nyquist frequency

In the power density spectrum of KIC 8803882, we find a reverse combination of  $l = 2$  and 0 modes with respect to the known comb-like structure between 200  $\mu\text{Hz}$  and the LC-Nyquist frequency of 283  $\mu\text{Hz}$  with an apparent large separation of  $\Delta\nu = 22.7 \mu\text{Hz}$  (Fig. 3). Stars which show similar structures in their power spectra are KIC 8912308, KIC 2697935 and KIC 7799540 (cf. Table 2).

As the dataset of KIC 8803882 contained a month of short cadence observations (Q14.1), we could compare the analysis of the super Nyquist frequency range from long cadence data with the same, well resolved frequency range from short cadence data. This comparison, depicted in Fig. 3, allows us to explore the frequency range above the formal Nyquist frequency,  $\nu_{\text{Nyquist}} = 283 \mu\text{Hz}$  for long cadence data (Murphy et al. 2013). We determined the large separation  $\Delta\nu$  through manual peakbagging of the long cadence data to be 22.7  $\mu\text{Hz}$ , which is in perfect agreement with the large separation of 22.65  $\mu\text{Hz}$  from short cadence data. The standard approach to determine the frequency of the power excess (e.g. Kallinger et al. 2010b) uses a simultaneous fit of the Gaussian envelope, multiple power laws for the background and a white noise component. In the super Nyquist frequency domain, we find an artificial background with increasing power density towards higher frequencies as the signal of the low frequency domain is mirrored. Therefore, we determined the position of  $\nu_{\text{max}}$  by fitting a broad Gaussian to the reflected signal

and calculated the true frequency of the power excess,

$$\nu_{\max}^{\text{true}} = 2 \cdot \nu_{\text{Nyquist}} - \nu_{\max}^{\text{reflected}}. \quad (1)$$

From the values obtained for KIC 8803882, KIC 8912308, KIC 2697935, and KIC 7799540 (cf. Tables 1 and 2) we conclude that they are low-luminosity red giants.

#### 4. Case study of KIC 5006817

While ensemble asteroseismology allows the easy characterisation of large samples of red giant stars (e.g. Huber et al. 2011; Hekker et al. 2011; Kallinger et al. 2010b; Mosser et al. 2012a), studies of individual stars in a close binary grant us additional insight into the structure of the primary as well as the interaction between the binary system components. As a proof-of-concept of what such objects have to offer compared to single pulsators, we organised a spectroscopic campaign on the heartbeat star with the richest oscillation pattern, KIC 5006817.

The power density spectrum of the *Kepler* observations of KIC 5006817 is shown in Fig. 4. It contains power excess centred around  $146 \mu\text{Hz}$ . Apart from the typical granulation signal and a series of low frequency peaks ( $<10 \mu\text{Hz}$ ) originating from the heartbeat event, no other significant frequencies are present (Fig. 4). The oscillation power excess itself is typical for a red giant primary. The frequency range of the excited oscillation modes is shown in Fig. 5. For a detailed asteroseismic analysis, only modes with a signal of at least 8 times the background level were extracted. The frequencies of the individual modes were extracted as the centroid of the power density in narrow predefined windows, which we checked for consistency by fitting Lorentzian profiles to a number of modes.

KIC 5006817's seismic mass and radius estimates are  $1.49 \pm 0.06 M_{\odot}$  and  $5.84 \pm 0.09 R_{\odot}$ , respectively (Table 1). The true period spacing of 78 s indicates that the star is in the phase of H-shell burning (Bedding et al. 2011; Mosser et al. 2012b). In the HR Diagram shown in Fig. 2, this star is located well below the red clump.

##### 4.1. Seismic information on the stellar rotation

The power density spectra of many red giants contain clear signatures of the rotational splitting of nonradial modes, which enables us to learn more about the internal rotation of those stars. This effect arises as rotation breaks the degeneracy of nonradial modes by shifting the mode frequencies of the components with azimuthal order  $m \neq 0$  away from the central multiplet frequency ( $m = 0$ ):

$$f_{n,\ell,m} = f_{n,\ell,0} + \delta f_{n,\ell,m}, \quad (2)$$

with the rotational splitting  $\delta f_{n,\ell,m}$  given by

$$\delta f_{n,\ell,m} = m \cdot \frac{\Omega}{2\pi} \cdot (1 - C_{nl}), \quad (3)$$

where  $\Omega$  is the average rotation frequency in the cavity in which a given mode propagates and  $C_{nl}$  is the Ledoux constant (Ledoux 1951). The values of the rotational splittings reported in this work are taken to be equal to the frequency separation between two consecutive multiplet components (i.e.  $|\Delta m| = 1$ ). If no central peak ( $m = 0$ ) is detected, we take half the value of the frequency difference between outer dipole components. We refer to such values as the normalised rotational splitting. In the power density spectrum of KIC 5006817, we find rotationally

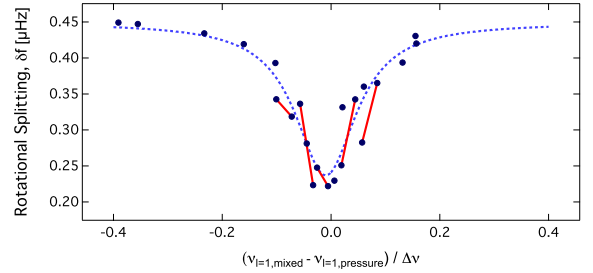


**Fig. 6.** Splitting-échelle diagram of rotationally affected dipole modes in KIC 5006817. Measured rotational splittings are shown as dots. Solid lines connect two splittings originating from the same dipole mode triplet. The  $x$ -axis gives the position of a rotationally split dipole mode  $\nu_{l=1,\text{mixed}}$  with respect to the pure pressure dipole mode  $\nu_{l=1,\text{pressure}}$  and as fraction of the large frequency separation  $\Delta\nu$ . The dashed line describes the modulation of the rotational splitting through a Lorentzian profile (Mosser et al. 2012a).

split modes of the spherical degree  $\ell = 1$ . The multiplet structure in  $\ell = 2$  can originate from splitting or mixed modes. In principle, also  $\ell = 3$  modes should be split. However, we have no clear identification of them as in this star  $\ell = 3$  modes have amplitudes close to the significance limit.

As g-dominated and p-dominated modes are sensitive to the rotation in the central and outer regions of the star, respectively, they can be used to probe the internal rotation gradient. Beck et al. (2012) showed that larger splitting of g-dominated than of p-dominated dipole modes, as found in KIC 5006817 (Figs. 6 and 7) reveals that its interior, rotates multiple times faster than its envelope.

For some dipole multiplets the presence of a significant central peak ( $m = 0$ ) allowed us to measure the individual splittings for the  $m = -1$  and  $+1$  components, revealing asymmetries. Such pairs of splittings are connected with a solid line in Fig. 6. As rotation shifts the frequency of modes, each mode within a triplet has a slightly different oscillation cavity, which also modifies its mixed character in terms of p- and g-mode components. The asymmetries are mirrored around the pure p mode and follow the Lorentzian description (Fig. 6).

The smallest measured rotational splitting of dipole modes is about  $0.21 \mu\text{Hz}$  and was measured in two asymmetric p-mode dominated mixed modes. This is about 2.25 times smaller than the largest splitting  $\delta f_{\max}$  of  $0.45 \mu\text{Hz}$  found for g-mode dominated dipole modes. The largest splitting values ( $\delta f_{\max}$ ) originating from the g-mode dominated dipole modes are consistent with those measured for large samples of single pulsating red giants (e.g. Beck et al. 2012; Mosser et al. 2012a).

The extracted rotational splitting of dipole modes (Fig. 6), shows the expected modulation as a function of the degree of mixed character (Mosser et al. 2012b,a). The mode identification from the universal red giant oscillation pattern for pressure modes (Mosser et al. 2012a), and from asymptotic expansion for mixed modes and the rotational splittings (Mosser et al. 2012a,b) is indicated with vertical bars in Fig. 5. We note that a perfect fit is not needed to identify the modes.

##### 4.2. Testing of the rotational profile from forward modelling

Because of the conservation of angular momentum, one expects the core of a red giant to rotate significantly faster than its surface. Previous analyses (Beck et al. 2012; Deheuvels et al. 2012; Mosser et al. 2012a) only revealed the ratio of the

P. G. Beck et al.: Pulsating red giant stars in eccentric binaries

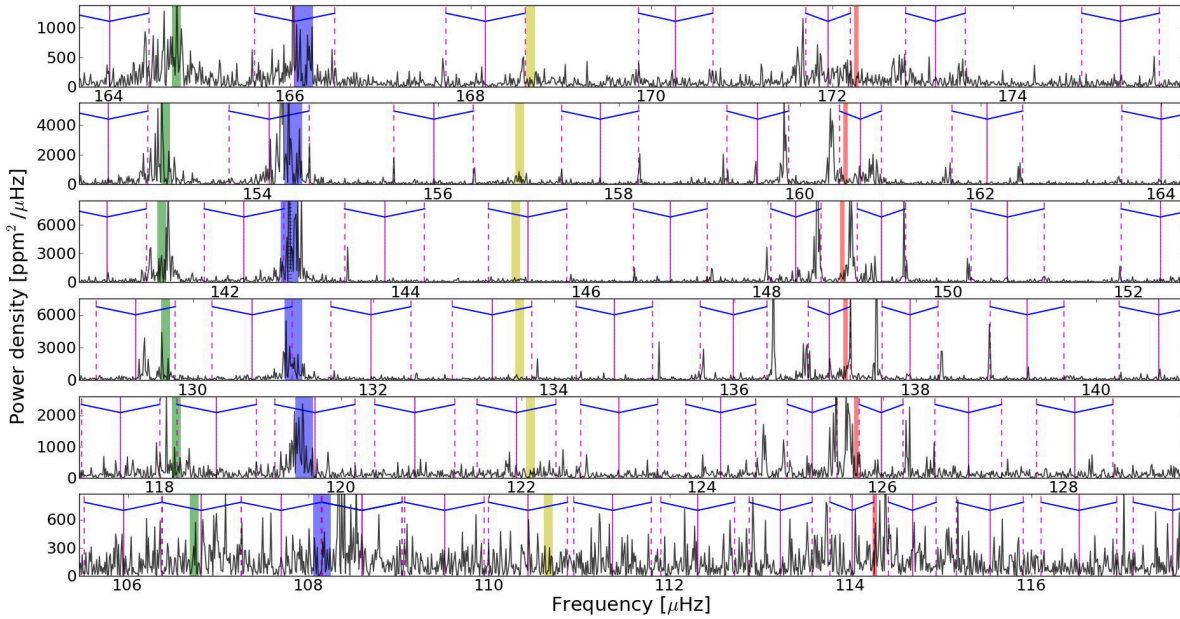


**Fig. 5.** Power density spectrum (PDS) of KIC 5006817 (Q0–Q13). Each panel contains one radial order. Mode identifications of the pure p modes come from the universal frequency pattern (Mosser et al. 2011b) for  $\ell = 0, 1, 2$  and 3 and are indicated with blue, red, green and yellow vertical bars, respectively. The effects of rotation are visible as the splitting of dipole modes, located in the centre of each panel. The observed PDS is overlaid with the theoretical frequencies of mixed dipole modes ( $m = 0$ , solid thin lines) and the theoretical frequencies of the rotationally split components ( $m = \pm 1$ , dashed thin lines) which have been calculated using methods described by Mosser et al. (2012a,b). The components belonging to one rotationally split multiplet are indicated through V-markers at the top of each panel.

core-to-surface rotation rate, rather than the shape of the rotational gradient in the transition region between the faster rotating core and the slower rotating envelope. Goupil et al. (2013) propose a way to infer directly the ratio of the average envelope to core rotation rates from the observations. In this paper, we take a different approach by using forward modelling.

In principle, the number of rotationally split modes in KIC 5006817 and their different degree of mixed character (and therefore different “sensitivity” to internal layers of the star) should enable us to probe the rotation rate at different depths of the star, i.e. to resolve the rotational gradient to more than a ratio between the core and surface value. The radial structure of a red giant is dominated by a helium core and an extended convective envelope. To mimic this structure we considered models consisting of consecutive shells, which are each assumed to rotate rigidly, but with different angular velocities.

We computed such a representative  $1.5 M_{\odot}$  model using the Yale Stellar Evolution Code (YREC; Demarque et al. 2008; Guenther et al. 1992). The model was selected to approximately reproduce the observed radial modes and true dipole period spacing of KIC 5006817, where we note that no “exact” match is necessary as the mode eigenfunctions (and therefore the rotational kernels) of similar models are almost identical (see also Deheuvels et al. 2012). Our representative model was computed for near solar composition ( $Z = 0.02$ ,  $Y = 0.28$ ) assuming the solar mixture by Grevesse et al. (1996) and a mixing length parameter ( $\alpha_{\text{MLT}} = 1.8$ ). The model has a radius, effective temperature, age, and inert He core mass fraction of about  $5.8 R_{\odot}$ , 4855 K, 2.8 Gyr, and 0.14, respectively. More details about the input physics of the model are given in Kallinger et al. (2010a).

We focussed on the two radial orders (i.e. the frequency range of  $\sim 130$  to  $\sim 155 \mu\text{Hz}$ ), in which 9 rotationally split dipole

modes with good signal-to-noise were extracted. Additionally, we tested if rotational splittings from two  $\ell = 2$  modes can be measured. In Fig. 7 we show the power density spectrum of the two radial orders of KIC 5006817 along with the mode inertia of the  $\ell = 0$  to 3 modes computed for our representative model, in the adiabatic approximation.

In order to determine which layers dominate the rotational splitting of a given mode, we computed the adiabatic eigenfunctions for the 9 dipole and 2 quadrupole modes (using the non-radial nonadiabatic stellar pulsation code by Guenther 1994) as well as their rotational kernels. The integrated and normalised kernels are shown as a function of the fractional radius in Fig. 8, illustrating that all dipole modes contain a significant contribution from the fast rotating core region, even the most p-mode dominated ones (indicated as d3 and d7). The kernels are almost flat in the radiative region of the envelope (between the two dashed vertical lines). This is in agreement with the analysis of the kernels for KIC 8366239 (Beck et al. 2012). The dipole splittings provide an upper limit for the surface rotation rate. More promising are the  $\ell = 2$  kernels, but even those contain significant contributions from the core and from the inner part of the convective envelope.

For a better quantitative result, we deduce the rotation profile  $\Omega(r)$  such that

$$\delta f_{n,\ell} = \frac{1}{2\pi I_{n,\ell}} \int_{r=0}^R K_{n,\ell}(r) \Omega(r) dr, \quad (4)$$

is satisfied for the measured splittings. Here  $I_{n,\ell}$  and  $K_{n,\ell}$  are the mode inertia and the rotational kernel of a given mode, respectively, and  $R$  is the radius of the model. To solve this equation, several inversion techniques have been developed in the past

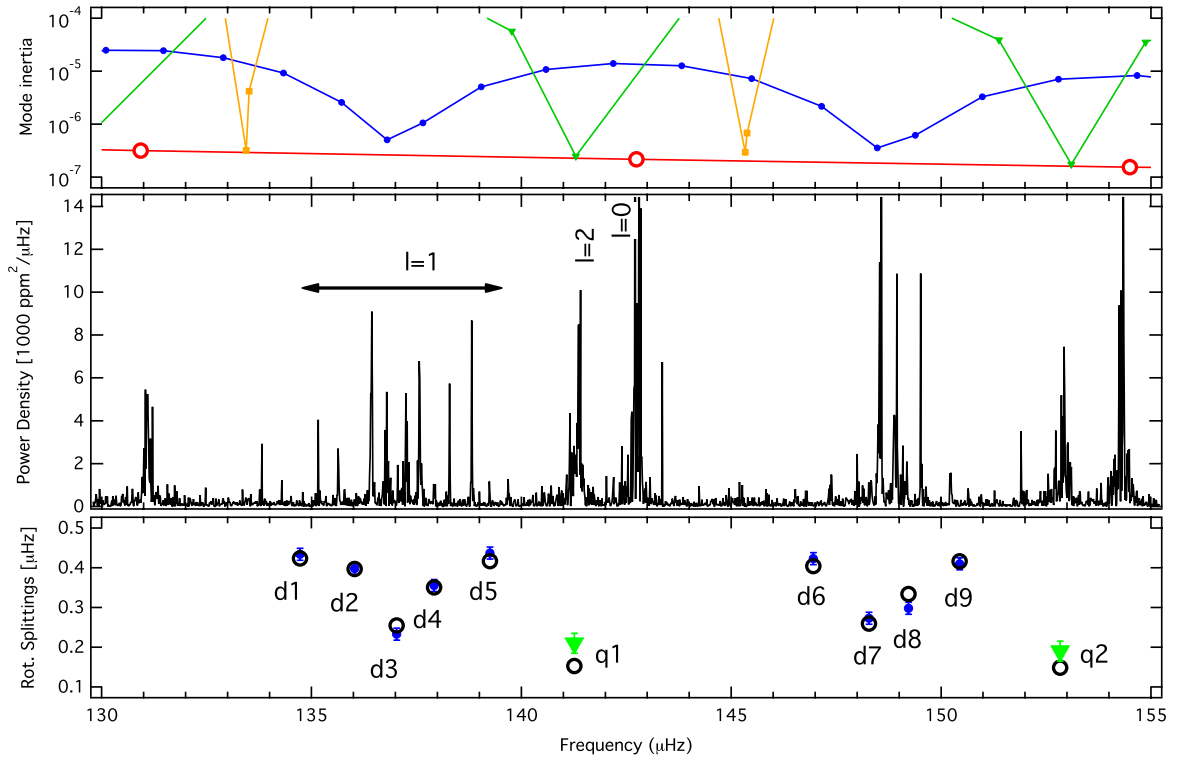


**Fig. 7.** Frequencies for the two central radial orders of KIC 5006817. *Top panel:* the coloured dots connected with line segments indicate the inertia (right axis with arbitrary scale) of the  $m = 0$  adiabatic modes computed for a representative model for KIC 5006817 (red circles, blue filled dots, green triangles, and yellow squares correspond to  $\ell = 0, 1, 2$  and  $3$  modes, respectively). *The middle panel* provides a zoom on the frequencies in the range of the two central radial orders. *Bottom panel:* measured rotational splittings for  $\ell = 1$  (blue dots) and  $2$  (green triangles) modes. Open black circles indicate the splittings that result from our best-fit 2-zone model. Dipole modes are labelled with  $d$ , quadrupole modes with  $q$ .

with the aim to determine the internal rotation profile of the Sun. A summary how to apply them to an evolved star is available in [Deheuvels et al. \(2012\)](#).

The inversion of the integral in Eq. (4) is a highly ill-conditioned problem and either requires numerical regularisation or localised averages of the true rotation profile in different regions of the star. We used both, adopting the regularised least squares method (RLS; e.g. [Christensen-Dalsgaard et al. 1990](#)) and the subtractive optimally localised averages technique (SOLA; e.g. [Schou et al. 1998](#)). In doing so, we can determine the core to surface rotation rate. However, as soon as we increased the number of shells, aiming to locate where the transition between fast rotating core and the slowly rotating envelope is taking place, both methods failed. Either the results became numerically unstable or it was impossible to evaluate the reliability of the result.

We therefore chose to apply a Bayesian forward modelling approach. We computed synthetic rotational splittings for a model (using Eq. (4)), which was first divided into several solidly rotating shells, where the rotation rate of each shell was treated as a free parameter. To fit the synthetic splittings to the measured ones, we used a Bayesian nested sampling algorithm called MULTINEST ([Feroz et al. 2009](#)) that provides a probability density distribution (PDD) for each fitted parameter, from which we assessed the best-fit values and their uncertainties. The PDDs allowed us to test the reliability of a specific model, e.g. a flat PDD for a specific shell implies that the measured rotational

splittings do not contain information about the rotation rate in this specific region of the star. Additionally, MULTINEST provides the model evidence, which allows us to compare different assumptions for the rotation rates in the shells and evaluate which one reproduces the observations best. We tested different numbers and combinations of shells and found that a 2-zone model (core and envelope) is better by several orders of magnitude. Even introducing regularisation priors (e.g. a smooth gradient between consecutive shells) did not improve the description of  $\Omega(r)$ .

#### 4.3. Core and surface rotation

The final model we adopted is a 2-zone one with a core (inner 1 per cent in radius or 14 per cent in mass) and an envelope zone, where we found that the placement of the exact position of the border between the two zones only marginally influences the result. Our best fit constrained the rotation frequency (or period) for the core and the envelope to be  $0.93 \pm 0.02 \mu\text{Hz}$  ( $\sim 12.5$  d) and  $0.07 \pm 0.02 \mu\text{Hz}$  ( $\sim 165$  d), respectively. This corresponds to a core-to-surface rotation rate of about 13. The envelope rotation rate is an average value for 99 per cent of the radius of the star and very likely overestimates the true surface rotation. This asteroseismic result points towards a surface rotation velocity of  $1.9 \text{ km s}^{-1}$ .

Including the two  $\ell = 2$  modes only marginally affects the rotation rate but increases the uncertainty, which is why they

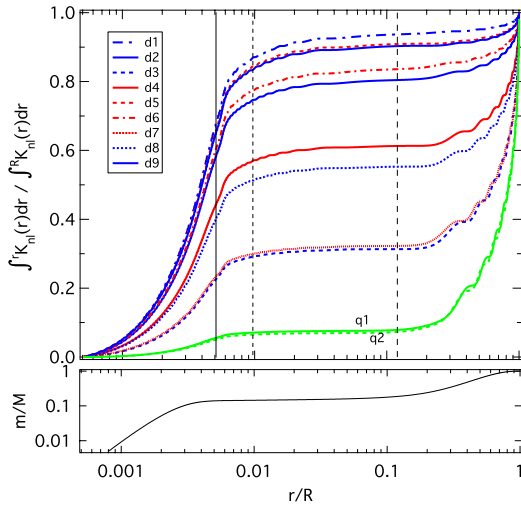


**Fig. 8.** Normalised integrated rotation kernels of the dipole  $\ell = 1$  (blue and red) and quadrupole  $\ell = 2$  modes (green) for the two central radial orders as a function of fractional radius. The kernel labels refer to modes in Fig. 7. The vertical lines indicate from left to right the border of the He core (solid line), the H-burning shell (short-dashed line), and the base of the convective envelope (long-dashed line). *Bottom panel:* the model's fractional mass as a function of the fractional radius. The labels (not the colours) of dipole and quadrupole modes are consistent with Fig. 7.

were not taken into account for the final result. We conclude that the currently available observations do not allow us to assess the detailed rotational gradient in the envelope of KIC 5006817, as it was possible for the Sun. We are limited to describing the rotational profile of red giants with a step function.

#### 4.4. Inclination of the axis of rotation and pulsation

The inclination angle of the rotation axis towards the observer can be deduced from the rotational splittings. For solar-like oscillators, the excitation of all  $2\cdot\ell+1$  components and the equipartition of energy is assumed if the time base of the observations resolves the lifetime effects of a mode.

For dipole modes, the inclination is determined by the height of the  $m = 0$  and  $m = \pm 1$  modes, provided that all components with the same  $|m|$  are excited such that they have the same height in power density (Gizon & Solanki 2003; Ballot et al. 2006). We have also shown that each component of a split multiplet has a slightly different cavity which should result in slightly different heights and lifetimes, an effect absent in the Sun as it has no mixed modes. To compensate for these differences, we do not fit the heights of the  $m = \pm 1$  in a given mode individually, but force the heights of the fit to be equal.

Simultaneously fitting all dipole modes in at least one radial order compensates in principle the effects of a changing level of mixed character between p and g modes. This transition is symmetrically mirrored around the pure dipole pressure mode. We tested this approach for the radial orders around 135 and 150  $\mu\text{Hz}$ , resulting in inclination values of  $i_{\text{rot}} = 73^\circ \pm 3^\circ$  and  $i_{\text{rot}} = 80^\circ \pm 3^\circ$  respectively. A global fit of both radial orders lead to  $i_{\text{rot}}^{\text{global}} = 76^\circ \pm 4^\circ$ , assuming alignment of the rotation and pulsation axis. We compare these values to the mean inclination of  $i_{\text{rot}}^{\text{mean}} = 77^\circ \pm 9^\circ$ , obtained from the individual rotational split

multiplets of the pressure-dominated modes in this frequency range (Table 4). These modes have the highest signal and the shortest lifetimes, and therefore are closest to the assumption of equipartition of mode energy. The uncertainty is an underestimate as it was computed adopting the assumptions mentioned above.

## 5. Spectroscopy of KIC 5006817

To obtain an independent estimate of the eccentricity of the system, KIC 5006817 has been monitored spectroscopically with the Hermes spectrograph (cf. Sect. 2) in 2012 and 2013. The 60 observations span about 160 d, during which the periastron passages were monitored with several observations a night. The radial velocities derived from these spectra are shown in the top panel of Fig. 9.

### 5.1. Fundamental parameters

The first 44 individual spectra were shifted by the derived radial velocity value and averaged to produce a high signal-to-noise ratio (S/N) spectrum to determine the stellar atmospheric parameters like effective temperature,  $T_{\text{eff}}$ , surface gravity  $\log g$ , microturbulence  $v_{\text{micro}}$  and the total line broadening from rotation and macroturbulence ( $v \sin i + v_{\text{macro}}$ ).

Given the seismic estimate of rotation and inclination, the total line broadening is dominated by macroturbulence. We used the combination of local thermal equilibrium (LTE) Kurucz-Castelli atmosphere models (Castelli & Kurucz 2004) with the LTE abundance calculation routine MOOG by Sneden (1973). A detailed description of all steps needed to derive the atmospheric parameters can be found in, e.g., De Smedt et al. (2012).

The determination of the atmospheric parameters was based upon Fe I and Fe II lines which are abundantly present in red giants spectra. The Fe lines used were taken from VALD line lists (Kupka et al. 2000). We first calculated in MOOG the theoretical equivalent width (EW) of all available Fe I and Fe II in a wavelength range between 400 and 700 nm for a grid, centred on the seismic parameters found (Table 1). The equivalent widths (EW) of lines were measured via direct integration, the abundance of the line was then computed by an iterative process where theoretically calculated EWs were matched to the observed EW. If the calculated EW deviated from the theoretical EW by a factor of 10, the line was rejected due to possible blends. The stellar parameters are listed in Table 5 and are based on the results from 52 Fe I and 32 Fe II lines.

### 5.2. Spectral disentangling

In order to look for signatures of a companion in our spectra, we used the spectral disentangling (SPD) method as implemented in the FDBINARY code (Ilijic et al. 2004). Being applied in Fourier space, the method provides a self-consistent and fast solution for the individual spectra of stellar components of a multiple system and a set of orbital parameters simultaneously (Hadrava 1995). The SPD method usually requires a time-series of spectra with good, homogeneous orbital phase coverage and delivers high S/N mean spectra of individual components.

We used the highest S/N spectra to perform the spectral disentangling in a wide wavelength range from 480 to 580 nm. The spectra were split into smaller chunks, typically 5 nm wide, to avoid strong undulations in the continuum of the resulting decomposed spectra from which the Fourier-based SPD

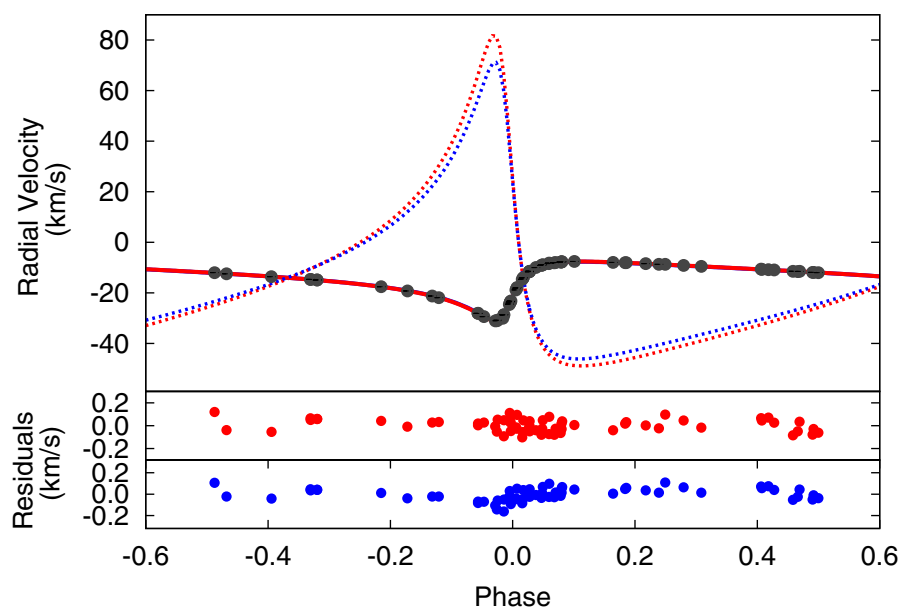


**Fig. 9.** Radial velocity observations (gray points) with the best-fit model without beaming (solid red line) and with beaming (solid blue line – not visible) phased over 94.82 d. The uncertainty in the radial velocity is smaller than the size of the points. The model with beaming cannot be seen on this scale due to the overlap of the model without beaming. The model of the secondary component is presented for both the beaming (dashed blue line) and non-beaming (dashed red line) best-fit models. *Middle panel:* best-fit residuals of the binary model without beaming (red points). *Lower panel:* residuals of the best-fit binary model with beaming (blue points).

method is known to suffer (see, e.g. [Hadrava 1995](#); [Ilijic et al. 2004](#)). Besides the above mentioned metal lines region that also contains the  $H_{\beta}$  spectral line, we also focussed on a few other regions centred at some helium lines (He I 447, 492, and 502 nm, and He II 469, 541, and 656 nm,) as well as the  $H_{\alpha}$  line. This was done to verify whether the companion could be a white dwarf showing only helium and/or hydrogen lines. In neither of these regions could we detect the lines of the secondary. We estimate the detection limit of the order of 3 percent of the continuum, which means that any contribution below this level would not be detectable in our rather low S/N spectra ( $\approx 20$ – $30$  in Johnson V).

We also attempted to go beyond our actual detection limit of 3 percent, by applying the least-squares deconvolution (LSD) method ([Donati et al. 1997](#)) to the 44 individual spectra. This method is based on the two fundamental assumptions of self-similarity of all spectral lines and linear addition of blends, and enables the computation of a high-quality average line profile, which is formally characterised by a very high S/N. The first assumption requires hydrogen and helium lines as well as the metal lines with pronounced damping wings to be excluded from the calculations. Moreover, for slowly rotating stars (the case of KIC 5006817), where the rotation is not the dominant source of the line broadening, the self-similarity is only applicable to the lines of (nearly) the same strengths. To account for this, we introduced a multiprofile technique as described by [Kochukhov et al. \(2010\)](#), which enables the computation of several average profiles simultaneously for several sets of spectral lines grouped, e.g. according to their relative strengths. The model is then represented as a convolution of the computed mean profiles with the *line mask* which contains information about the position of individual lines as well as their relative strengths.

Furthermore, part of the lines in the spectrum (e.g. those with overlapping absorption coefficients) add up non-linearly which

requires a revision of the second fundamental assumption of the technique. In order to account for the model imperfections due to non-linear blending of the lines, we additionally fitted strengths of the individual lines from the mask to match the observations. This improved procedure (for more details, see [Tkachenko et al. 2013](#)) provided us with high S/N (of the order of 450–500) LSD model spectra which we then used for the SPD in three metal lines regions. Similar to our previous experience with the original spectra, we got a null result, in the sense that no signature of the secondary has been detected, this time, in the high S/N composite spectra. In this case, our detection limit is estimated to be of the order of 1 percent of the continuum, which is mainly due to the imperfect continuum normalisation rather than the observational noise. We thus conclude that KIC 5006817 is a single-lined spectroscopic binary.

## 6. Binary parameters of KIC 5006817

The morphology of the photometric light curve is a consequence of ellipsoidal modulation in an eccentric system. The shape of the “heartbeat” feature in the light curve is a function of the inclination, which dictates the peak to dip ratio; the eccentricity, which affects the relative width of the feature; and the argument of periastron which affects the symmetry of the feature. The magnitude of the heartbeat feature is dependent on the radii of the components, their masses and gravity darkening exponents, and the orbital inclination.

To study the binary properties of KIC 5006817, we simultaneously modelled the photometric and radial velocity data of KIC 5006817 using the modelling code, PHOEBE ([Prša & Zwitter 2005](#)). This code is an extension of the Wilson-Devinney code ([Wilson & Devinney 1971](#); [Wilson 1979](#); [Wilson & Van Hamme 2004](#)) and combines the complete treatment of the Roche

potential with a detailed treatment of surface and horizon effects such as limb darkening, gravity darkening, ellipsoidal modulation and reflection effects to arrive at a comprehensive set of stellar and orbital parameters.

The orbital period of the binary is close to the length of one *Kepler* quarter ( $\sim 3$  months), which is the typical time scale of long term instrumental trends in *Kepler* data. Consequently, in the case of KIC 5006817, accurate detrending of the light curve is a challenge. We have therefore manually extracted each light curve, on a quarter-by-quarter basis, from pixel level data to create the best behaved light curve possible. We then fitted and divided out a linear trend from each Quarter to detrend and normalise the data. We selected a linear trend to avoid removing the beaming information from the light curve.

### 6.1. Orbital ephemeris

From the long cadence *Kepler* photometry of KIC 5006817 (Quarters 0–12) we determined the zero point in the data (the time of the periastron minimum) to be  $2455\,019.221 \pm 0.008$  using the KEPHEM software package (Prša et al. 2011). Combining this with the spectroscopically determined period ( $94.812 \pm 0.002$  d) we obtained the following ephemeris in the Barycentric Julian date:

$$\text{Min } I = 2455\,019.221 \pm 0.008 + 94.812 \pm 0.002 \text{ d} \times E,$$

where  $E$  is the number of orbits.

### 6.2. Input parameters

In our fits, we have fixed the effective temperature of the primary component to the spectroscopic value:  $T_{\text{eff},1} = 5000$  K (Table 5).

Assuming the secondary component is a main sequence star (from its lack of visibility in the spectra), we can place an upper limit of  $\sim 5400$  K on its effective temperature by assuming that it contributes 1 per cent of the total flux (the lower limit for spectral disentangling). This temperature is an upper limit and is likely an overestimate, given the mass determined from the binary model ( $\sim 0.3 M_{\odot}$ , see Sect. 6.5 and Table 6). Due to the evolutionary state of the primary and low mass of the secondary, we assumed that both components have substantial convective outer envelopes and consequently adopted the standard albedo value of 0.6 (Ruciński 1969a,b). As both objects radiate towards the infrared end of the optical spectrum, as suggested by Diaz-Cordoves & Gimenez (1992) and van Hamme (1993), we have selected the square-root limb darkening law (Eq. (6) in Diaz-Cordoves & Gimenez 1992).

### 6.3. Fitting procedure

After manually tweaking the initial parameters until an approximate fit to the photometric data and the spectroscopic radial velocities was accomplished, we applied differential corrections (Wilson & Sofia 1976) to optimise the parameters.

The binary model created has the mass and radius of the primary component fixed to the asteroseismic value. Using differential corrections we simultaneously fitted the eccentricity and argument of periastron to the radial velocity and light curves; fitted the semi-major axis and gamma velocity to the radial velocity curve and fitted only the remaining parameters to the light curve. The fitted and fixed parameters of the best-fit model are listed in Table 6, Figs. 9 and 10 show the phase binned light curve and radial velocity data with the best-fit model (red line)

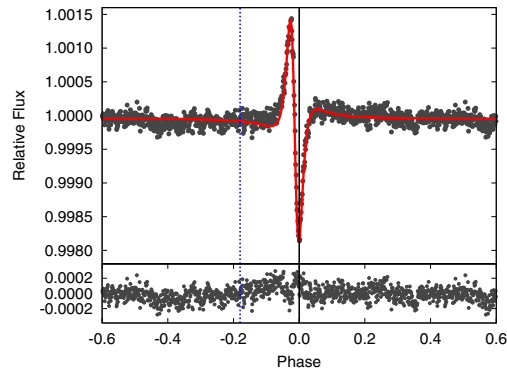


**Fig. 10.** Theoretical PHOEBE model without beaming (red line) and observed light curve (black points) of the phased (94.82 d), binned *Kepler* long-cadence data of Quarters 0–12. Lower panel: residuals of the best-fit model. The dashed and solid lines are centred on the times of superior and inferior conjunction respectively.

**Table 6.** Parameters and coefficients for the PHOEBE best-fit model to the *Kepler* light curve for Quarters 0–12 long cadence data for the non-beaming and beaming cases.

Parameter	Non-beaming	Beaming
Mass ratio, $q$	$0.199 \pm 0.001$	$0.20 \pm 0.03$
Secondary mass ( $M_{\odot}$ ), $M_2$	$0.30 \pm 0.01$	$0.29 \pm 0.03$
Semi-major axis ( $R_{\odot}$ ), $a$	$106.1 \pm 0.5$	$105.6 \pm 0.9$
Orbital eccentricity, $e$	$0.71 \pm 0.01$	$0.71 \pm 0.02$
Argument of periastron (rad), $\omega$	$4.0 \pm 0.1$	$4.01 \pm 0.06$
Orbital inclination ( $^{\circ}$ ), $i$	$62 \pm 4$	$61 \pm 6$
Primary potential, $\Omega_1$	$16.7 \pm 0.2$	$16.2 \pm 0.2$
Gamma velocity ( $\text{km s}^{-1}$ ), $\gamma$	$-14.01 \pm 0.01$	$-14.43 \pm 0.08$
Primary $\log g$ (cgs), $\log g_1$	$3.078 \pm 0.007$	$3.022 \pm 0.007$
Gravity darkening exponent, $GRD$	$1.00 \pm 0.03$	$1.07 \pm 0.03$
Primary fractional point radius	0.0644	0.0679
Primary fractional pole radius	0.0637	0.0676
Phase of periastron	0.0121	0.0094
Primary $x_1$ coeff.	0.718	0.717
Primary $y_1$ coeff.	0.716	0.714
Fixed Parameters	Values: both Cases	
Primary $T_{\text{eff}}$ (K)	5000 $\pm$ 250	
Third light	0.0	
Orbital period (d)	94.812 $\pm$ 0.002	
Time of primary minimum (BJD)	245 019.221 $\pm$ 0.008	
Primary bolometric albedo	0.6	

**Notes.** The secondary component’s potential, radius and  $\log g$  are not noted as these parameters have no signature in the light curve and radial velocity data. The fractional radii quoted are the radii relative to the semi-major axis. For the mass and radius of the primary component, see Table 1. The limb darkening coefficients ( $x_1$  and  $y_1$ ) are for the square root limb darkening law and were taken from the PHOEBE limb darkening tables (Prša et al. 2011). For the beaming case we assumed 100% of the flux comes from the primary component.

in the upper panel and the corresponding residuals in the lower panel.

### 6.4. The puzzling absence of a Doppler beaming signal

So far, we have not taken into account the effect of Doppler beaming on the light curve. Doppler beaming is caused by the radial velocity of the two stars and is the combined effect of shifting the stars’ spectral energy distributions with respect to

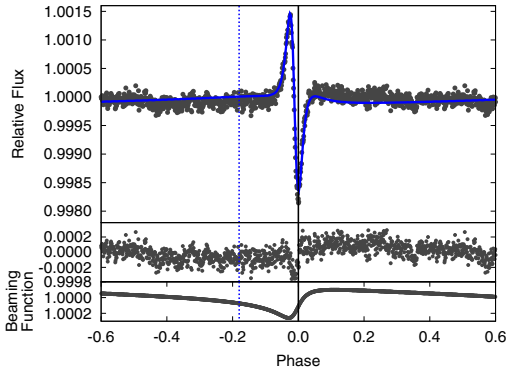


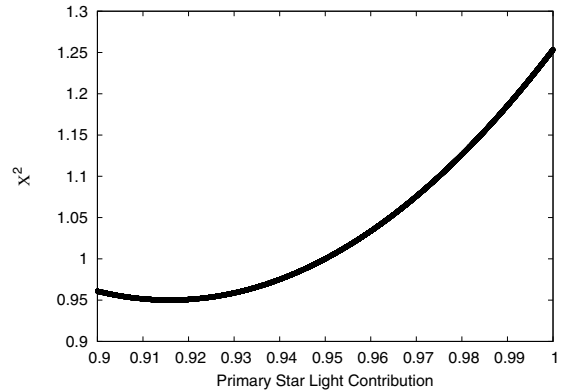
**Fig. 11.** Theoretical PHOEBE model similar to Fig. 10, but including beaming (blue line). The dotted and dashed lines are centered on the times of superior and inferior conjunction, respectively. *Middle panel:* residuals of the best-fit beaming model. *Lower panel:* Doppler beaming function that has been added to the model to incorporate beaming. The axis is inverted for comparison with the residuals.

the *Kepler* bandpass, aberration and an altered photon arrival rate. The net result of Doppler beaming is an increase in the observed flux from a star when it moves towards the observer, and a decrease when it moves away from the observer. It was predicted to be seen in *Kepler* data by Loeb & Gaudi (2003) and Zucker et al. (2007), and has recently been observed in several systems from ground-based data as well as *Kepler* and CoRoT light curves (see e.g. Mazeh & Faigler 2010; van Kerkwijk et al. 2010; Shporer et al. 2010; Bloemen et al. 2011).

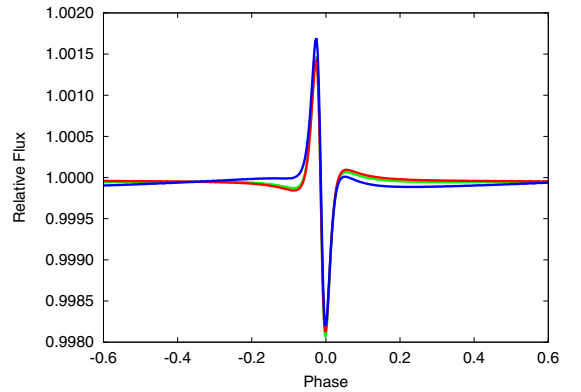
Based on the radial velocity measurements of the primary star (semi-amplitude,  $K = 11.78 \text{ km s}^{-1}$  – see Table 3), we estimate that Doppler beaming should have a significant contribution in the light from the red giant in KIC 5006817, of the order of  $\sim 300$  ppm. Since spectroscopy indicates that the secondary component in the binary has an insignificant luminosity compared to the primary, we looked into the effect of Doppler beaming assuming that all the observed flux is emitted by the red giant primary component. The Doppler beaming signal was modelled following Eq. (2) in Bloemen et al. (2011). The Doppler beaming coefficient of the red giant primary, which takes into account the spectrum of the star and the wavelength of the observations, was computed using Eq. (3) of Bloemen et al. (2011) to be  $\langle B_1 \rangle = 4.59 \pm 0.21$  from Kurucz 2004 model spectra (Castelli & Kurucz 2004).

Figure 11 depicts the phase-folded light curve and best-fit model including beaming for KIC 5006817. The residuals of this model, however, contain a significant sinusoidal wave, similar in nature to that of the beaming function. The beaming signal thus seems to be invisible in the observed light curve. At phase zero the beaming signal has been fitted by adjusting the inclination of the model, however, the fit is still less adequate in this region than for the non-beaming case.

Possible reasons for the absence of a beaming signal in the data are a very high third light contamination which reduces the observed amplitude of the effect; a significant beaming signal from the secondary that partly or fully cancels out the beaming signal of the primary; or that the inherent long period instrumental trends in the *Kepler* data are concealing the beaming signal. The first possibility can be ruled out, since no bright source of third light is seen close to the target and no contaminating light was found in the spectra. To evaluate the second possibility – that



**Fig. 12.** The  $\chi^2$  goodness of fit to the continuum light curve (light curve with the periastron variation removed) as a function of the fraction of light contributed by the primary component, for multiple models. For each model the fraction of light was randomised (90–100 per cent for the primary component) and the beaming function was calculated for both the primary and secondary components. The goodness of fit was then assessed away from the periastron variation as only the beaming has an effect on this section of the light curve.



**Fig. 13.** Best-fit model to the phased light curve data (red), the same model with beaming and 100 per cent light contribution from the primary component (blue), and with beaming and 91.5 per cent light contribution from the primary component (green) – the best fit model when allowing the flux ratio to be fitted.

the beaming signal from the secondary is cancelling out the primary beaming signal, we scanned the parameter space to find the light ratio (with beaming from both components) that best fitted the data. We only fitted the continuum section of the light curve, since the beaming effect can be compensated for at the phase of the periastron variation by adjusting the inclination. When including Doppler beaming for the secondary component, we assumed that it is a main sequence object with a mass of  $0.3 M_{\odot}$ , giving a Doppler beaming coefficient of  $\langle B_2 \rangle \approx 6.5$ .

Figure 12 shows the  $\chi^2$  value as a function of primary light contribution. We find a clear preference for a contribution of 91.5 per cent from the primary component and 8.5 per cent from the secondary component. As shown in Fig. 13, the modelled light curve for the preferred light ratio (green line) is approximately equal to the light curve excluding beaming, suggesting that the preferred configuration leads to the secondary essentially cancelling out the beaming from the primary component. If the

secondary is a  $0.3 M_{\odot}$  main sequence star, it can not, however, contribute on the order of 8 per cent of the light in the system, and furthermore, a main sequence star this bright would have been easily detected in our spectroscopic data. We also considered the option that the secondary is a continuum white dwarf as this would not necessarily show up in the spectra. However, we can rule out this possibility as the temperature would need to be greater than 40 000 K for it to contribute 8.5 per cent of the flux and as such the light curve would show an extreme reflection effect (the white dwarf reflecting off the red giant), which we do not observe. We would also see evidence for such a white dwarf in the spectroscopic data, as continuum white dwarfs (which do not have a signal in spectroscopic data) have effective temperatures  $\lesssim 12\,000$  K. Furthermore, a hot star would have a lower beaming factor and thus require a greater flux contribution from the secondary component.

Other than missing or incomplete physics in the binary models, the final possibility that we have postulated is that the *Kepler* satellite is not stable enough on longer timescales to preserve the beaming signal in the data. While this seems like a more convincing option, given that the trends in the *Kepler* light curves have a larger amplitude than the beaming signal, and that the timescales of the orbital period and a *Kepler* quarter are similar, we find it surprising that we are unable to detect any signature of the beaming signal given that we used a minimally evasive detrending method. We also note that the beaming signal was still missing when using a higher order Legendre polynomial in place of the linear trend.

The slope of the beaming signal is largest at the phase of the periastron brightening, and therefore significantly influences the optimal set of parameters found when fitting the heartbeat. Since we do not understand the absence of the beaming signal, we present the results of the fits to the data both including beaming, assuming 100 per cent light contribution from the primary, and without beaming. The optimal parameter values for both cases are listed in Table 6.

### 6.5. Mass ratio, primary potential and gravity darkening degeneracies

When fitting the binary characteristics, we found that the mass ratio, primary potential (which is essentially the inverse of the primary radius) and gravity darkening exponent are degenerate with each other. To assess the level of degeneracy between the potential and the gravity darkening exponent, a scan of the parameter space was undertaken whereby the primary gravity darkening exponent was randomly adjusted following which the primary potential and light factor were fitted to the light curve using differential corrections. Figure 14 shows the gravity darkening value and corresponding potentials for multiple models. The points are coloured with respect to their  $\chi^2$  value to show the goodness of fit for each individual model. The results show a complete degeneracy between the primary potential and primary gravity darkening exponent. Repeating this experiment for the primary potential and mass ratio, we again found a complete degeneracy. For this reason we elected to fix the primary mass and radius to the asteroseismically determined values,  $1.49 \pm 0.06 M_{\odot}$  and  $5.84 \pm 0.08 R_{\odot}$ , respectively.

Keeping the gravity darkening exponent as a free parameter, we found a best binary model fit to the gravity darkening coefficient to be  $1.00 \pm 0.03$  and  $1.07 \pm 0.03$  for the beaming and non-beaming cases, respectively. These values are not in agreement with the accepted value of  $GRD = 0.32$  for a star with a convective envelope (Lucy 1967), although this is an empirically

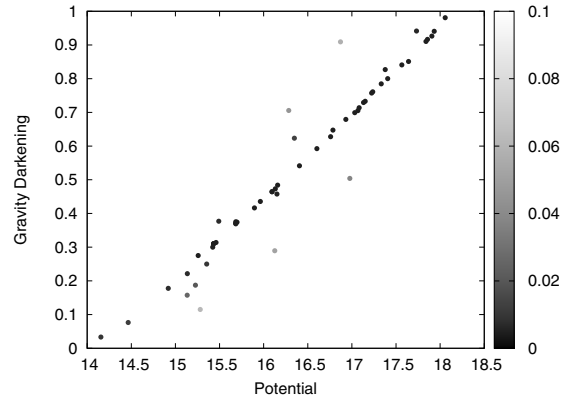


**Fig. 14.** Gravity darkening value as a function of the primary potential, where each point represents an individual binary model. For each model the gravity darkening exponent was determined randomly (between 0.0 and 1.0) and a model generated by fitting the light factor and potential, whilst keeping all other parameters fixed. The points are coloured by the  $\chi^2$  goodness of fit to demonstrate that the outliers are a consequence of an inadequate fit (the lower  $\chi^2$  values denote the better models, here depicted in black).

determined value for main sequence objects. More recent literature suggests an increased value of  $\sim 0.5$  based on computations of atmosphere models (Claret & Bloemen 2011). In this case the value is specific for stars with an effective temperature and surface gravity close to that of the red giant in KIC 5006817. While this value is closer to that determined, there is still a large discrepancy between the observed and theoretical values. A possibility is that the uncertainties of the asteroseismic mass and radius are underestimated. However, a closer look suggests that the radius would have to increase by three sigma and the mass decrease by three sigma to reach the gravity darkening exponent suggested by Claret & Bloemen (2011). While a three sigma limit may be plausible, the change in values would require the density – the most constrained asteroseismic value – to deviate significantly from that determined, which is unlikely. The most likely explanation is that the accepted gravity darkening exponent needs to be revised or completely mitigated from the models (Espinosa Lara & Rieutord 2012).

### 6.6. Uncertainty determination

The uncertainties of the parameters were determined using two methods: through standard errors and their propagation, and through Monte Carlo heuristic scanning. A scan of the parameter space was undertaken for the most correlated (but not completely degenerate) parameters, which were determined by applying the correlation matrix function in PHOEBE. With a fixed mass ratio and gravity darkening, the most correlated parameters were determined to be the inclination, eccentricity and argument of periastron. The magnitude of the periastron brightening was not found to be significantly correlated with these parameters, which determine the shape of the periastron brightening.

We applied Monte Carlo simulations to perturb the solutions of the eccentricity, argument of periastron and inclination. The applied method required the computation of the potential and phase shift, and the iterative randomisation of the eccentricity and argument of periastron by 10 per cent, and the inclination by 20 per cent. At each iteration a comparison between

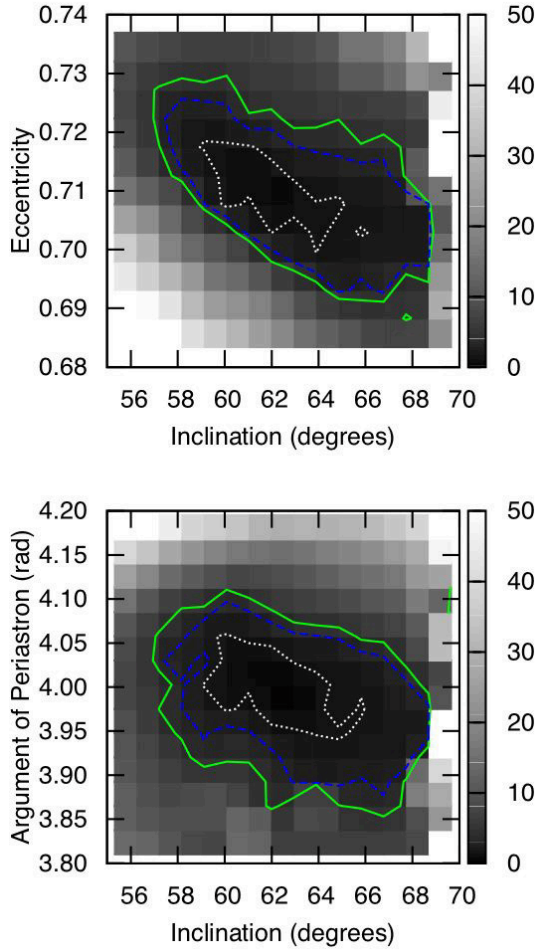


**Fig. 15.** Density maps of the Monte Carlo simulations of the inclination vs. eccentricity (*upper panel*) and the inclination vs. argument of periastron (*lower panel*) for the non-beaming case. The grey scale depicts the  $\chi^2$  values mapped across the grid. The colour bar depicts the grey scale pertaining to the different values of  $\chi^2$ . The contours (from inner to outer) denote the  $1\sigma$  (dotted white line),  $2\sigma$  (dashed blue line) and  $3\sigma$  (solid green line) confidence intervals. The uncertainties for the inclination, argument of periastron and eccentricity were determined using the  $1\sigma$  confidence contours displayed.

the model and phased data was made using the  $\chi^2$  statistical test. The  $\chi^2$  values for each solution were then mapped out across a parameter grid with confidence intervals, which serve as uncertainty estimates (cf. Fig. 15). The optimum combination of the displayed parameters can be identified from the density maps, where the  $1\sigma$ ,  $2\sigma$  and  $3\sigma$  uncertainty values are presented as contours.

## 7. Combined asteroseismic and binary interpretation

Assuming the equilibrium tide model (Zahn 1966, 1989; Remus et al. 2012), which applies to stars with convective outer envelopes, we calculated approximate timescales for the synchronisation and circularisation of KIC 5006817, using the work of

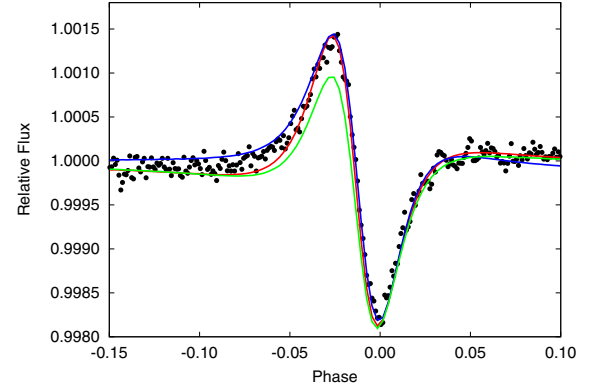


**Fig. 16.** Comparison between the data (grey points), the best-fit light curve model without beaming (dotted red line), the best-fit model with beaming (dashed blue line), and the best-fit model for an imposed orbital inclination of  $76^\circ$ , as determined through asteroseismology (solid green line). A change in the inclination changes the ratio between the maximum and minimum of the periastron variation (also known as the heartbeat event).

Zahn (1977). The synchronisation timescale denotes the amount of time needed for the star's rotational angular velocity to equal its orbital angular velocity at periastron (pseudo-synchronous rotation) and for the stars' axes to become perpendicular to the orbit. The circularisation time scale is the maximum time the orbit will take to circularise. Applying Eq. (6.1) of Zahn (1977) we determined the synchronisation timescale due to gravitational interactions to be  $2 \times 10^{12}$  yr, which is prohibitively large.

To determine whether KIC 5006817 is synchronised we compared the inclination of the orbit and the rotational axis, and considered the rotation rate of the red giant. The inclination measured from rotational splitting is sensitive to the orientation of the rotational axis of the primary pulsator, while the inclination determined from the shape of the heartbeat event describes the orientation of the orbital plane. In the case of KIC 5006817, these two inclination angles were found to agree within  $2\sigma$ :  $i_{\text{rot}} = 77^\circ \pm 9^\circ$  versus  $i_{\text{orbit}} = 62^\circ \pm 4^\circ$  ( $61^\circ \pm 6^\circ$  for the beaming case).

To assess this difference graphically, Fig. 16 compares the best-fit binary model without beaming (red) and with beaming (blue) and with the orbital model with an imposed orbital inclinations of  $76^\circ$  (green) taken from asteroseismology. It is clear that the maximum in the light curve is not well approximated with such a high orbital inclination. On the other hand, the very low visibility of the zonal modes ( $|m| = 0$ ) in the centre of the rotationally split triplets, under the assumption of equal intrinsic amplitudes, definitely excludes inclinations below  $70^\circ$ .

If the system were rotating pseudo-synchronously, following Eq. (44) of Hut (1981), using the observationally derived eccentricity and orbital period, one would expect a rotation period of about 11 d for KIC 5006817. Such rapid surface rotation is immediately ruled out from the width of the absorption lines in the spectrum of the primary. Moreover, the splitting of the  $l = 1$  modes points towards a rotation period of at least 165 d, which is more than 1.7 times the orbital period. Thus we conclude that, as expected, KIC 5006817 is not in a synchronised orbit.

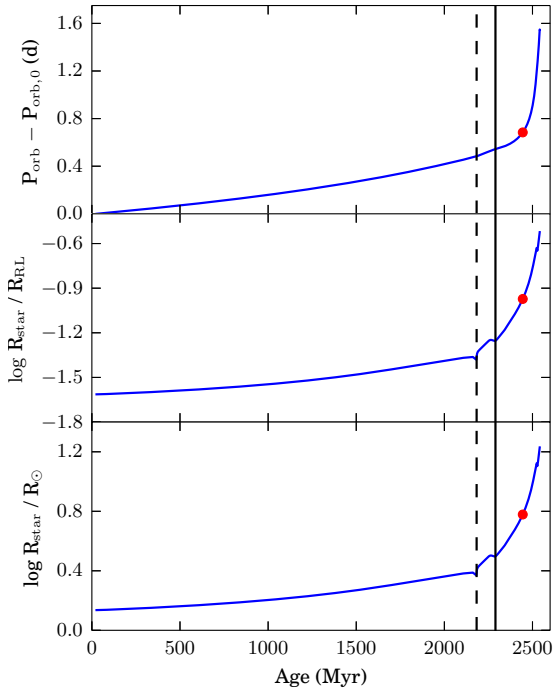


**Fig. 17.** Modelling the orbital period (*top panel*), Roche lobe filling factor (*middle panel*) and radius of the red giant main component (*lower panel*) of binary system with MESA with the approximated values of KIC 5006817. The models start at the zero age main sequence (ZAMS) and stop with the onset of the RLOF. The dashed line marks the end of the hydrogen core burning (TAMS). The solid line marks the bottom of the RGB. The position of a model with the radius of  $6 R_{\odot}$ , which equals the current state of KIC 5006817 is shown as a red dot.

## 8. Impact of stellar evolution on eccentric binary systems

Most hot subdwarf B (sdB) stars and cataclysmic variables (CV) are supposed to be produced from binaries that have undergone mass transfer and drastic mass loss during either a common envelope (CE) phase or a phase of stable Roche lobe overflow while on the RGB (Han et al. 2002, 2003; Nelemans & Tout 2005). Several unsolved questions remain regarding the exact sdB-progenitors and the details of the mass loss mechanism (Hu et al. 2008; Østensen 2009; Heber 2009).

### 8.1. Modelling the binary evolution of KIC 5006817

Currently, the binary system KIC 5006817 is dynamically stable on timescales shorter than the evolutionary timescales of the red giant component. The system parameters, determined in the previous sections show that in its current configuration the orbit is wide compared to the Roche radii of the components. The low mass of the secondary component suggests that this star is most likely an M dwarf, which will stay on the main sequence for the remaining lifetime of the red giant companion. The evolution of the system will therefore mainly depend on the evolution of the red giant component (Fig. 17).

MESA<sup>1</sup> (Paxton et al. 2010, 2011, 2013) is a one dimensional stellar evolution code originally designed for single star evolution. The code is adapted to handle binary systems by letting them evolve one step at a time, after which the orbital evolution is updated as well. The standard binary evolution that is included in MESA (version: November 2012) only handles the evolution of circular binaries. To check the evolution of an eccentric binary in which one of the components is a red giant, we implemented the equations derived by Verbunt & Phinney (1995) to account for tidal interactions. The evolution of the eccentricity is governed by,

$$\frac{d \ln e}{dt} = -1.7 f \left( \frac{T_{\text{eff}}}{4500 \text{ K}} \right)^{\frac{4}{3}} \left( \frac{M_{\text{env}}}{M_{\odot}} \right)^{\frac{2}{3}} \frac{M_{\odot}}{M} \frac{M_2}{M} \frac{M + M_2}{M} \left( \frac{R}{a} \right)^8 \frac{1}{\text{yr}} \quad (5)$$

where  $M_{\text{env}}$  is the mass of the convective envelope of the RG star.  $M_2$  is the mass of the companion and  $a$  refers the semi-major axis of the orbit. The factor  $f$  is calculated based on the mixing length parameter  $\alpha$ ,

$$f = 1.01 \left( \frac{\alpha}{2} \right)^{(4/3)}. \quad (6)$$

At every time step of MESA,  $M_{\text{env}}$  and  $T_{\text{eff}}$  are obtained from the stellar structure model. The start of the Roche lobe overflow (RLOF) is calculated based on the Roche-Lobe calculated at periastron passage.

To study the changes of eccentricity, period and the radius of the Roche lobe on such an eccentric binary system caused by the red giant evolution, we created an approximate model of the system KIC 5006817, using the starting masses  $M_{\text{RG}} = 1.5 M_{\odot}$  and  $M_{\text{MS}} = 0.3 M_{\odot}$ , an initial orbital period  $P_{\text{orbit},0} = 94.0 \text{ d}$  and eccentricity to  $e = 0.70$ . On the red giant branch a Reimers wind (Kudritzki & Reimers 1978) was assumed, with  $\eta = 0.5$ .

When we let this binary model evolve, we find that the orbital period slowly increases during the main sequence evolution (Fig. 17, top panel); the rate of increase will accelerate as the star starts to ascend the red giant branch, mainly caused by mass loss due to the stellar wind on the RGB (Hurley et al. 2002). The eccentricity remains stable. Only when the red giant is close to filling its Roche lobe, the system will circularise on the order of a few 10 000 years.

The middle panel of Fig. 17 depicts how the expanding radius of the red giant component gradually grows to fill its Roche lobe ( $R_{\text{star}}/R_{\text{Roche Lobe}} < 1$ ). From the bottom panel of Fig. 17, it becomes obvious that the onset of RLOF at periastron passages will happen well below the tip of the RGB. From MESA single models, we find that a giant of  $1.5 M_{\odot}$  will have a maximum radius of about  $140 R_{\odot}$  before igniting helium. Exactly how the orbital period will change during this process depends on how much of the transferred mass is accreted by the companion, and how much escapes the system.

The periastron distance is  $32 \pm 1 R_{\odot}$ , which corresponds to  $\sim 4$  times the current radius of the red giant. When exceeding a radius, larger than the current semi-major axis of  $106 R_{\odot}$  (Table 6), the red giant will completely engulf its companion in all phases of the orbit, leading to a CE phase while it is ascending the RGB. The interaction between two components during the CE phase for a rather similar system has been studied by Han et al. (2002), showing that the secondary component

<sup>1</sup> Modules for Experiments in Stellar Astrophysics, see <http://mesa.sourceforge.net>

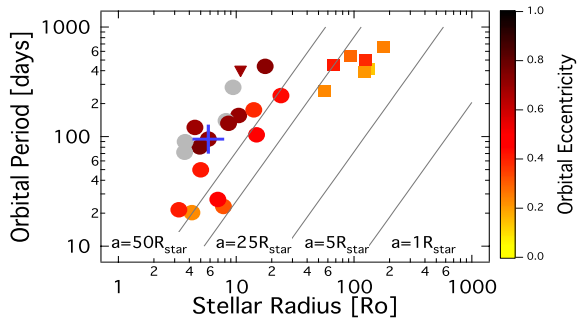


**Fig. 18.** Stellar radius of the main component versus the orbital period of the binary system. Colour indicates the eccentricity of the systems (Table 3). Stars from our sample (Tables 1 and 2) are plotted as filled dots. KIC 5006817 is marked with a cross. The eclipsing red giant KIC 8410637 (Hekker et al. 2010; Frandsen et al. 2013) is shown as a triangle. The stars found in the LMC (Nicholls & Wood 2012) are shown as squares. Solid lines show the period of a system with a total mass of  $1.8 M_{\odot}$  and a semi-major axis, which is a multiple of the stellar radius.

will spiral down inside the red giant primary. This phase happens rapidly compared to the evolutionary time scale of the red giant. A critical point is reached when the companion arrives at the bottom of the convective envelope and penetrates the initially radiative zone below it. The dynamical instability that follows will eject the envelope unless the companion is disrupted first (Han et al. 2002).

Once the red giant ejects its envelope, we are left with the “naked” stellar core. If the red giant enters a CE-phase near the tip of the RGB, we would find a helium core which will become sdB stars. Otherwise, the system is likely to become a CV. Currently a majority of the observed long period sdB binaries have an eccentric orbit (Vos et al. 2013), indicating that their progenitor must have had a high eccentricity as well, as is the case with heartbeat stars. We therefore expect to find nearly exclusively stars in the H-shell burning phase in these eccentric systems and hardly any stars which have experienced He-core ignition and now settled on the red clump. The latter is only expected if the system’s separation is large enough.

### 8.2. Comparison to other known red giant stars in eccentric binary systems

As a consequence of the expanding radius of the red giant, a relation between the radius of the primary and the orbital period for such interacting systems is expected, since only binaries with large enough periastron distances can stably exist. From seismology, we obtained the radii of a sample of red giant stars, located in such eccentric systems that are undergoing gravitational distortion, to a range between 2 and  $24 R_{\odot}$ , as given in Table 1. Nicholls & Wood (2012) reported seven similar systems from OGLE observations of the Large Magellanic Cloud (LMC). Although the OGLE light curves are not suitable for seismic investigations, they can constrain the fundamental parameters of the stars from modelling the phase diagram and photometric calibrations. The red giant systems found in the LMC are higher up in the HR Diagram than the stars in our sample and also have in general longer orbital periods (260–660 d). Figure 18, in which the stellar radii and orbital periods of the stars in the LMC and *Kepler* sample are compared, shows that systems hosting bigger

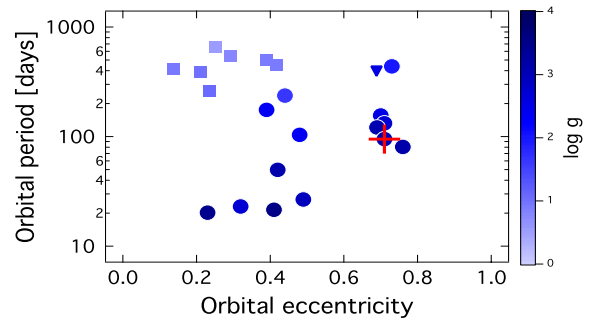


**Fig. 19.** Comparing the eccentricities of known eccentric systems with ellipsoidal modulation. Colour indicates the  $\log g$  of the red giant component. Dots represent the stars from our sample for which we could derive the eccentricities from radial velocities. KIC 5006817 and KIC 8410637 are shown as a cross and triangle, respectively. Squares show the derived eccentricities of the stars in the LMC.

stars tend to have longer periods and ellipsoidal variation occurs for a specific combination of stellar radius and orbital period. We note that our sample is biased due to the selection of stars which show the heartbeat effect. However, as shorter periods lead to smaller systems, which cannot stay stable for a long time. These stars show a minimum orbital periods. In systems with shorter period mass transfer should eventually occur.

In our ongoing spectroscopic campaign we have currently obtained enough radial velocity measurements for 14 systems in our sample to derive their orbital parameters. The full orbital parameters of these systems are given in Table 3. Fig. 19 depicts the eccentricities of the red giant heartbeat stars on the lower RGB found with *Kepler* from our sample with the eccentricities of those close to the tip of the RGB (Nicholls & Wood 2012). The majority of the systems in Table 1 for which we have RV data have eccentricities between  $0.23 < e < 0.5$ , which is compatible with the range of eccentricities reported by Thompson et al. (2012) for their objects. Also, the 4 stars with periods shorter than 30 d belong to the least eccentric in our sample. Among the long periodic systems, 5 exhibit eccentricities larger than 0.7. Our most eccentric system is KIC 8144355 ( $P_{\text{Orbit}} = 80.6$  d,  $e = 0.76 \pm 0.01$ ).

The systems found in the LMC so far have eccentricities that range between  $0.15 < e < 0.45$ , which suggests that the stars might have experienced some circularisation. It is not yet clear if mass transfer has already started in these systems or if the circularisation is forced by tidal interaction. Yet the two samples are too small to draw a firm conclusion. In subsequent work, we will further investigate the distribution of eccentricities in the *Kepler* red giant heartbeat stars from photometric and radial velocity data on larger datasets.

Finally, we note that KIC 8410637, an eclipsing binary with a 408 d period (Hekker et al. 2010; Frandsen et al. 2013) has a period and a high eccentricity ( $e \sim 0.7$ ), compatible with the other red giant heartbeat stars (Figs. 18 & 19) but no heartbeat events are visible.

## 9. Conclusions

In this work we have studied a sample of 18 red giant stars in eccentric binary systems, detected with the *Kepler* satellite, that exhibit flux modulation as a result of binary interaction during their periastron passage. All giants in the systems in our sample

exhibit solar-like oscillations, so we applied asteroseismic techniques to determine their global properties, as well as their evolutionary states. As shown in the analysis of one selected system, the approach of combining asteroseismic and binary modelling analyses is very powerful.

For KIC 5006817, this new approach revealed a low mass companion with a mass of  $M_2 = 0.29 \pm 0.03 M_\odot$  (where the uncertainty encompasses both the beaming and non-beaming cases). Estimates based on the radial velocity curve and the optical spectrum revealed that Doppler beaming should be contributing 300 ppm to the light curve although the light curve modelling did not support this. This is possibly a consequence of the long term trends in the *Kepler* data, given that the period of KIC 5006817 is  $\sim 95$  d, which is very close to the length of a *Kepler* quarter (90 d).

Through modelling the binary characteristics, while fixing the primary mass and radius to the asteroseismically determined values, the gravity darkening value was determined to be  $GRD = 1.0 \pm 0.03$  for the non-beaming case and  $GRD = 1.07 \pm 0.03$  for the beaming case. These values are inconsistent with the empirical value determined by *Lucy* (1967),  $GRD = 0.32$ , and the more recent model dependent value determined by *Claret & Bloemen* (2011),  $GRD = 0.5$ . To obtain a binary model with values closer to those predicted by theory, the density of the primary component would need to deviate significantly from the well constrained asteroseismic value. For this reason we speculate that the gravity darkening values require further revision.

From modelling the binary evolution of an approximate binary system, we conclude that the system is in fact too young to be synchronised. When comparing the properties of the full sample (Table 1), we found a correlation between the radius of the primary red giant component and the orbital period. Furthermore, all stars show seismic characteristics of stars in the state of H-shell burning. For a few, we cannot rule out a membership of the red clump or AGB. We argue that this is an effect of stellar evolution as the red giant's radius along the red giant branch will increase until the helium core ignites. If a system gets too close, it can undergo a common envelope phase which could lead to the ejection of the convective envelope of the red giant. This scenario is a potential evolutionary channel for the formation of cataclysmic variables and sdB stars.

Our sample is an interesting class of ellipsoidal variables which offers unique conditions to study interactions in and the evolution of eccentric binary systems. Optimal cases are systems which show the heartbeat effect and exhibit primary and secondary eclipses or are double lined spectroscopic binaries, as for such systems also for the secondary component independent fundamental parameters can be derived. The ensemble of stars presented here allows us to study the binary interaction and the future fate of such eccentric systems in a new way, to help unravel common-envelope physics.

*Acknowledgements.* We acknowledge the work of the team behind *Kepler*. Funding for the *Kepler* Mission is provided by NASA's Science Mission Directorate. The ground-based follow-up observations are based on spectroscopy made with the *Mercator* Telescope, operated on the island of La Palma by the Flemish Community, at the Spanish Observatorio del Roque de los Muchachos of the Instituto de Astrofísica de Canarias. This work partially used data analyzed under the NASA grant NNX12AE17G. This research is (partially) funded by the Research Council of the KU Leuven under grant agreement GOA/2013/012. The research leading to these results has received funding from the European Research Council under the European Community's Seventh Framework Programme (FP7/2007–2013)/ERC grant agreement n°227224 (PROSPERITY). The research leading to these results has received funding from the European Community's Seventh Framework Programme FP7-SPACE-2011-1, project number 312844 (SPACEINN). K.H. was supported by a UK STFC PhD grant. J.D.R., T.K. and E.C. acknowledge

the support of the FWO-Flanders under project O6260 – G.0728.11. T.K. also acknowledges financial support from the Austrian Science Fund (FWF P23608). A.T. was supported by the Fund for Scientific Research. S.H. was supported by the Netherlands Organisation for Scientific Research (NWO). V.S.S. is an Aspirant Ph.D. Fellow of the FWO, Belgium. A.D. is supported by a János Bolyai Research Scholarship of the Hungarian Academy of Sciences. This project has been supported by the Hungarian OTKA Grants K76816, K83790, MB08C 81013 and KTIA URKUT\_10-1-2011-0019 grant and the “Lendület-2009” Young Researchers Programme of the Hungarian Academy of Sciences. P.G.B thanks Nick Cox for observational work.

## References

- Ballot, J., García, R. A., & Lambert, P. 2006, *MNRAS*, 369, 1281  
 Beck, P. G., Bedding, T. R., Mosser, B., et al. 2011, *Science*, 332, 205  
 Beck, P. G., Montalbán, J., Kallinger, T., et al. 2012, *Nature*, 481, 55  
 Bedding, T. R., Mosser, B., Huber, D., et al. 2011, *Nature*, 471, 608  
 Bildsten, L., Paxton, B., Moore, K., & Macias, P. J. 2012, *ApJ*, 744, L6  
 Bloemen, S. 2013, Ph.D. Thesis, University of Leuven, Belgium  
 Bloemen, S., Marsh, T. R., Østensen, R. H., & et al. 2011, *MNRAS*, 410, 1787  
 Borucki, W. J., Koch, D., Basri, G., et al. 2010, *Science*, 327, 977  
 Castellí, F., & Kurucz, R. L. 2004, *IAU Symp.*, 210, poster A20  
 Christensen-Dalsgaard, J., Schou, J., & Thompson, M. J. 1990, *MNRAS*, 242, 353  
 Claret, A., & Bloemen, S. 2011, *A&A*, 529, A75  
 Corsaro, E., Fröhlich, H.-E., Bonanno, A., et al. 2013, *MNRAS*, 430, 2313  
 De Ridder, J., Barban, C., Carrier, F., et al. 2006, *A&A*, 448, 689  
 De Ridder, J., Barban, C., Baudin, F., et al. 2009, *Nature*, 459, 398  
 De Smedt, K., Van Winckel, H., Karakas, A. I., et al. 2012, *A&A*, 541, A67  
 Deheuvels, S., García, R. A., Chaplin, W. J., et al. 2012, *ApJ*, 756, 19  
 Demarque, P., Guenther, D. B., Li, L. H., Mazumdar, A., & Straka, C. W. 2008, *ApSS*, 316, 31  
 Diaz-Cordoves, J., & Gimenez, A. 1992, *A&A*, 259, 227  
 Donati, J.-F., Semel, M., Carter, B. D., Rees, D. E., & Collier Cameron, A. 1997, *MNRAS*, 291, 658  
 Dupret, M.-A., Belkacem, K., Samadi, R., et al. 2009, *A&A*, 506, 57  
 Espinosa Lara, F., & Rieutord, M. 2012, *A&A*, 547, A32  
 Feroz, F., Hobson, M. P., & Bridges, M. 2009, *MNRAS*, 398, 1601  
 Frandsen, S., Carrier, F., Aerts, C., et al. 2002, *A&A*, 394, L5  
 Frandsen, S., Lehmann, H., Hekker, S., et al. 2013, *A&A*, 556, A138  
 García, R. A., Hekker, S., Stello, D., et al. 2011, *MNRAS*, 414, L6  
 Gaulme, P., McKeever, J., Rawls, M. L., et al. 2013, *ApJ*, 767, 82  
 Gizou, L., & Solanki, S. K. 2003, *ApJ*, 589, 1009  
 Goupil, M. J., Mosser, B., Marques, J. P., et al. 2013, *A&A*, 549, A75  
 Grevesse, N., Noels, A., & Sauval, A. J. 1996, in *Cosmic Abundances*, eds. S. S. Holt, & G. Sonneborn, *ASP Conf. Ser.*, 99, 117  
 Guenther, D. B. 1994, *ApJ*, 422, 400  
 Guenther, D. B., Demarque, P., Kim, Y.-C., & Pinsonneault, M. H. 1992, *ApJ*, 387, 372  
 Hadrava, P. 1995, *A&AS*, 114, 393  
 Hambleton, K. M., Kurtz, D. W., Prša, A., et al. 2013, *MNRAS*, 434, 925  
 Han, Z., Podsiadlowski, P., Maxted, P. F. L., Marsh, T. R., & Ivanova, N. 2002, *MNRAS*, 336, 449  
 Han, Z., Podsiadlowski, P., Maxted, P. F. L., & Marsh, T. R. 2003, *MNRAS*, 341, 669  
 Heber, U. 2009, *Ann. Rev. Astron. Astrophys.*, 47, 211  
 Hekker, S., Aerts, C., De Ridder, J., & Carrier, F. 2006, *A&A*, 458, 931  
 Hekker, S., Debosscher, J., Huber, D., et al. 2010, *ApJ*, 713, L187  
 Hekker, S., Elsworth, Y., De Ridder, J., et al. 2011, *A&A*, 525, A131  
 Hu, H., Dupret, M.-A., Aerts, C., et al. 2008, *A&A*, 490, 243  
 Huber, D., Bedding, T. R., Stello, D., et al. 2011, *ApJ*, 743, 143  
 Huber, D., Ireland, M. J., Bedding, T. R., et al. 2012, *ApJ*, 760, 32  
 Hurley, J. R., Tout, C. A., & Pols, O. R. 2002, *MNRAS*, 329, 897  
 Hut, P. 1981, *A&A*, 99, 126  
 Ilijic, S., Hensberge, H., Pavlovski, K., & Freyhammer, L. M. 2004, in *Spectroscopically and Spatially Resolving the Components of the Close Binary Stars*, eds. R. W. Hilditch, H. Hensberge, & K. Pavlovski, *ASP Conf. Ser.*, 318, 111  
 Kallinger, T., Gruberbauer, M., Guenther, D. B., Fossati, L., & Weiss, W. W. 2010a, *A&A*, 510, A106  
 Kallinger, T., Mosser, B., Hekker, S., et al. 2010b, *A&A*, 522, A1  
 Kallinger, T., Hekker, S., Mosser, B., et al. 2012, *A&A*, 541, A51  
 Kjeldsen, H., & Bedding, T. R. 1995, *A&A*, 293, 87  
 Kochukhov, O., Makaganiuk, V., & Piskunov, N. 2010, *A&A*, 524, A5  
 Kudritzki, R. P., & Reimers, D. 1978, *A&A*, 70, 227  
 Kumar, P., Ao, C. O., & Quataert, E. J. 1995, *ApJ*, 449, 294

- Kupka, F. G., Ryabchikova, T. A., Piskunov, N. E., Stempels, H. C., & Weiss, W. W. 2000, *Baltic Astron.*, 9, 590
- Ledoux, P. 1951, *ApJ*, 114, 373
- Loeb, A., & Gaudi, B. S. 2003, *ApJ*, 588, L117
- Lucy, L. B. 1967, *ZAp*, 65, 89
- Matijević, G., Prša, A., Orosz, J. A., et al. 2012, *AJ*, 143, 123
- Mazeh, T., & Faigler, S. 2010, *A&A*, 521, L59
- Mosser, B., Barban, C., Montalbán, J., et al. 2011a, *A&A*, 532, A86
- Mosser, B., Belkacem, K., Goupil, M. J., et al. 2011b, *A&A*, 525, L9
- Mosser, B., Goupil, M. J., Belkacem, K., et al. 2012a, *A&A*, 548, A10
- Mosser, B., Goupil, M. J., Belkacem, K., et al. 2012b, *A&A*, 540, A143
- Mosser, B., Michel, E., Belkacem, K., et al. 2013, *A&A*, 550, A126
- Murphy, S. J., Shibahashi, H., & Kurtz, D. W. 2013, *MNRAS*, 430, 2986
- Nelemans, G., & Tout, C. A. 2005, *MNRAS*, 356, 753
- Nicholls, C. P., & Wood, P. R. 2012, *MNRAS*, 421, 2616
- Østensen, R. H. 2009, *Commun. Asteroseismol.*, 159, 75
- Paxton, B., Bildsten, L., Dotter, A., et al. 2010, *Astrophysics Source Code Library*, ascl: 1010.083
- Paxton, B., Bildsten, L., Dotter, A., et al. 2011, *ApJS*, 192, 3
- Paxton, B., Cantiello, M., Arras, P., et al. 2013, *ApJS*, 208, 4
- Prša, A., & Zwitter, T. 2005, *ApJ*, 628, 426
- Prša, A., Batalha, N., Slawson, R. W., et al. 2011, *AJ*, 141, 83
- Raskin, G., van Winckel, H., Hensberge, H., et al. 2011, *A&A*, 526, A69
- Remus, F., Mathis, S., & Zahn, J.-P. 2012, *A&A*, 544, A132
- Ruciński, S. M. 1969a, *Acta Astron.*, 19, 125
- Ruciński, S. M. 1969b, *Acta Astron.*, 19, 245
- Schou, J., Antia, H. M., Basu, S., et al. 1998, *ApJ*, 505, 390
- Shporer, A., Kaplan, D. L., Steinfadt, J. D. R., et al. 2010, *ApJ*, 725, L200
- Slawson, R. W., Prša, A., Welsh, W. F., et al. 2011, *AJ*, 142, 160
- Snedden, C. A. 1973, Ph.D. Thesis, The University of Texas at Austin, USA
- Stellingwerf, R. F. 1978, *ApJ*, 224, 953
- Tassoul, M. 1980, *ApJS*, 43, 469
- Thompson, S. E., Everett, M., Mullally, F., et al. 2012, *ApJ*, 753, 86
- Tkachenko, A., Van Reeth, T., Tsymbal, V., et al. 2013, *A&A*, 560, A37
- van Hamme, W. 1993, *AJ*, 106, 2096
- van Kerkwijk, M. H., Rappaport, S. A., Breton, R. P., et al. 2010, *ApJ*, 715, 51
- Verbunt, F., & Phinney, E. S. 1995, *A&A*, 296, 709
- Vos, J., Østensen, R. H., Németh, P., et al. 2013, *A&A*, 559, A54
- Welsh, W. F., Orosz, J. A., Aerts, C., et al. 2011, *ApJS*, 197, 4
- Wilson, R. E. 1979, *ApJ*, 234, 1054
- Wilson, R. E., & Devinney, E. J. 1971, *ApJ*, 166, 605
- Wilson, R. E., & Sofia, S. 1976, *ApJ*, 203, 182
- Wilson, R. E., & Van Hamme, W. 2004, *Computing Binary Star Observables (in Reference Manual to the Wilson-Devinney Program)*
- Zahn, J. P. 1966, *Ann. d'Astrophys.*, 29, 489
- Zahn, J.-P. 1977, *A&A*, 57, 383
- Zahn, J.-P. 1989, *A&A*, 220, 112
- Zucker, S., Mazeh, T., & Alexander, T. 2007, *ApJ*, 670, 1326

# Chapter 7

## KIC 4544587

This chapter features the published case study of KIC 4544587, a heartbeat star with tidally induced gravity modes, tidally influenced pressure modes and rapid apsidal motion. This work is contextualized by Chapter 3, which provides an introduction to heartbeat stars and tidally induced pulsations.

This work was completed in part for my MSc work; however, further work was undertaken during the course of my PhD studies. Prior to the commencement of my PhD studies, a binary model of KIC 4544587 had been created; however, only formal uncertainties had been ascertained. The spectra had been acquired (by J. Southworth), converted into radial velocities (by S. Bloemen) and included in the binary star model. During my PhD studies I determined full statistical uncertainties on the most correlated binary star parameters; further spectra were obtained and converted to radial velocities by A. Prša and subsection 2.2, entitled “Ground-based spectroscopy” was co-written by S. Bloemen and A. Prša; K. Pavlovski and I worked on spectral disentangling, which is described in Sections 3 and 4, entitled “Spectral Disentangling: Orbit” and “Atmospheric Parameters”, respectively (written by K. Pavlovski). Further pulsational analysis was performed by myself and D. Kurtz, which led to Subsection 7.1, entitled “Tidal interactions and combination frequencies”, which contains a footnote about the gravity modes written

---

by J. Fuller. D. Kurtz applied the frequency modulation technique to KIC 4544587 and wrote subsection 7.2, entitled “Pulsation frequency modulation: the FM effect”. And J. Guzik performed pulsational modelling, which she wrote about in subsection 7.3, entitled “Stellar evolution and pulsation models”. I wrote the majority of the publication with the exception of the parts explicitly stated above. D. Kurtz and A. Prša contributed detailed discussion and guidance in the completion of this work.



## KIC 4544587: an eccentric, short-period binary system with $\delta$ Sct pulsations and tidally excited modes

K. M. Hambleton,<sup>1,2,3\*</sup> D. W. Kurtz,<sup>1</sup> A. Prša,<sup>3</sup> J. A. Guzik,<sup>4</sup> K. Pavlovski,<sup>5</sup>  
S. Bloemen,<sup>2</sup> J. Southworth,<sup>6</sup> K. Conroy,<sup>7</sup> S. P. Littlefair<sup>8</sup> and J. Fuller<sup>9</sup>

<sup>1</sup>Jeremiah Horrocks Institute, University of Central Lancashire, Preston PR1 2HE, UK

<sup>2</sup>Instituut voor Sterrenkunde, KU Leuven, Celestijnenlaan 200D, B-3001 Leuven, Belgium

<sup>3</sup>Department of Astronomy and Astrophysics, Villanova University, 800 East Lancaster Avenue, Villanova, PA 19085, USA

<sup>4</sup>Los Alamos National Laboratory, XTD-2 MS T-086, Los Alamos, NM 87545-2345, USA

<sup>5</sup>Department of Physics, Faculty of Science, University of Zagreb, Croatia

<sup>6</sup>Astrophysics Group, Keele University, Staffordshire ST5 5BG, UK

<sup>7</sup>Department of Physics and Astronomy, Vanderbilt University, Nashville, TN 37235, USA

<sup>8</sup>Department of Physics and Astronomy, University of Sheffield, Sheffield S3 7RH, UK

<sup>9</sup>Center for Space Research, Department of Astronomy, Cornell University, Ithaca, NY 14853, USA

Accepted 2013 May 17. Received 2013 May 15; in original form 2012 September 3

### ABSTRACT

We present *Kepler* photometry and ground-based spectroscopy of KIC 4544587, a short-period eccentric eclipsing binary system with self-excited pressure and gravity modes, tidally excited modes, tidally influenced p modes and rapid apsidal motion of 182 yr per cycle. The primary and secondary components of KIC 4544587 reside within the  $\delta$  Scuti and  $\gamma$  Dor instability region of the Hertzsprung–Russell diagram, respectively. By applying the binary modelling software PHOEBE to prewhitened *Kepler* photometric data and radial velocity data obtained using the William Herschel Telescope and 4-m Mayall telescope at Kitt Peak Northern Observatory (KPNO), the fundamental parameters of this important system have been determined, including the stellar masses,  $1.98 \pm 0.07$  and  $1.60 \pm 0.06 M_{\odot}$ , and radii,  $1.76 \pm 0.03$  and  $1.42 \pm 0.02 R_{\odot}$ , for the primary and secondary components, respectively. Frequency analysis of the residual data revealed 31 modes, 14 in the gravity mode region and 17 in the pressure mode region. Of the 14 gravity modes, 8 are orbital harmonics: a signature of tidal resonance. While the measured amplitude of these modes may be partially attributed to residual signal from binary model subtraction, we demonstrate through consideration of the folded light curve that these frequencies do in fact correspond to tidally excited pulsations. Furthermore, we present an echelle diagram of the pressure mode frequency region (modulo the orbital frequency) and demonstrate that the tides are also influencing the p modes. A first look at asteroseismology hints that the secondary component is responsible for the p modes, which is contrary to our expectation that the hotter star should pulsate in higher radial overtone, higher frequency p modes.

**Key words:** binaries: eclipsing – stars: individual: KIC 4544587 – stars: oscillations – stars: variables:  $\delta$  Scuti.

### 1 INTRODUCTION

The  $\delta$  Scuti stars form an integral part of the instability strip, spanning a 2-mag range of evolutionary stages, from pre-main sequence to the terminal-age main sequence (Rodríguez & Breger 2001). Their luminosities are in the range  $0.6 \leq \log(L/L_{\odot}) \leq 2.0$  and their effective temperatures in the range  $6300 \leq T_{\text{eff}} \leq 9000$  K (Buzasi et al. 2005). They oscillate in radial and non-radial pressure modes (p modes) and low-order gravity modes (g modes) with observed

periods ranging from approximately 18 min to 8 h (Pamyatnykh 2000; Amado et al. 2004; Grigahcène et al. 2010a).

The  $\kappa$ -mechanism is the primary driving mechanism of  $\delta$  Scuti pulsations, although Antoci et al. (2011) suggested that one  $\delta$  Scuti star may pulsate with stochastically excited modes similar to those seen in the Sun and solar-like pulsators.  $\delta$  Scuti stars have a mass range between 1.5 and 2.5  $M_{\odot}$  (Lefèvre et al. 2009). At approximately 2  $M_{\odot}$  there is a transitional phase where the size of the convective outer envelope becomes negligible for higher mass stars and their outer envelopes become dominated by radiative energy transport; at approximately 1.5  $M_{\odot}$ , stars of higher mass develop

\* E-mail: kmhambleton@uclan.ac.uk

a convective core (Aerts, Christensen-Dalsgaard & Kurtz 2010). As this critical transition in the convective envelope occurs within the range of masses encompassed by  $\delta$  Scuti stars, the asteroseismic investigation of  $\delta$  Scuti stars may eventually unveil fundamental information pertaining to the physical processes that govern this transition.

$\gamma$  Dor stars are main-sequence stars in the temperature range  $6800 \leq T_{\text{eff}} \leq 7600$  K that pulsate in high-order gravity modes driven by convective blocking (Guzik et al. 2000) with pulsation periods typically of the order of 1 d (Grigahcène et al. 2010b). As  $\gamma$  Dor stars are a relatively new class of stars (Balona, Kriscunas & Cousins 1994), until recently their recorded numbers were low and consequently  $\delta$  Scuti stars were believed to dominate the classical pulsators on the main sequence (Breger 2000). However, with the implementation of advanced instruments such as *Kepler* (Borucki et al. 2010; Batalha et al. 2010; Gilliland et al. 2010), *MOST* (Walker et al. 2003) and *CoRoT* (Baglin et al. 2006), many stars demonstrating both  $\delta$  Scuti and  $\gamma$  Dor characteristics have been observed; thus, new classification criteria, containing  $\gamma$  Dor– $\delta$  Scuti and  $\delta$  Sct– $\gamma$  Dor hybrid stars, have been introduced (Grigahcène et al. 2010a). Following this revision, through the characterization of 750 A–F type main-sequence stars, the percentage of  $\delta$  Scuti stars on the main sequence is now estimated to be 27 per cent,  $\gamma$  Dor stars accounting for 13 per cent, hybrids accounting for 23 per cent and the remaining stars being classified as other types of variables, e.g. spotted stars showing rotational variations (Uytterhoeven et al. 2011).

In a study of 119 A0–A9 stars,  $35 \pm 5$  per cent were found to be in multiple systems (Abt 2009). However, only 22 per cent of the  $\delta$  Scuti stars catalogued are known to be multiple stars (Rodríguez & Breger 2001). In binary systems the rotational velocity of each stellar component tends towards a velocity that is synchronous with the orbital period as the orbit evolves. As synchronous velocity depends linearly on radius and scales with orbital period (to the power of 2/3), it generally implies an equatorial velocity less than of  $120 \text{ km s}^{-1}$  (Abt 2009), while most  $\delta$  Scuti stars are found to have velocities greater than  $120 \text{ km s}^{-1}$ . Below this value the turbulence in the outer stellar envelope only enables a negligible amount of meridional mixing to occur. This allows for diffusion to take place, which prevents pulsation through the settling of helium out of the He II ionization zone (Breger 1970). Thus, it has previously been assumed that multiplicity indirectly inhibits pulsation. However, there are many cases, including HD 174884 (Maceroni et al. 2009), HD 177863 (Willems & Aerts 2002) and the newly identified class of eccentric ellipsoidal variables known as *heartbeat* stars (Thompson et al. 2012) – including the iconic KOI-54 (Welsh et al. 2011; Burkart et al. 2012; Fuller & Lai 2012) – that demonstrate how, in some circumstances, multiplicity can not only alter but also increase pulsation amplitudes through the tidal excitation of eigenmodes. It is worthy of note, however, that the existence of tidally driven modes in binary star systems does not invalidate the theory that binarity also indirectly suppresses self-excited modes.

Through the use of binary modelling techniques, direct measurements of stellar masses, radii and distances are possible. Asteroseismic modelling of the identified modes can provide information pertaining to the internal stellar structure and rotation of the pulsating component, making multiple systems with  $\delta$  Scuti components extremely valuable. Currently, the thorough asteroseismic analysis of  $\delta$  Scuti stars is rarely achieved due to our current inability to model a large number of oscillatory modes excited via the  $\kappa$ -mechanism. However, with the advent of cutting-edge observations from instruments such as *Kepler* and *CoRoT* and new methodologies such as those used by García Hernández et al. (2009) on

**Table 1.** Other identifiers and basic data for KIC 4544587. The  $Kp$  passband specified is derived from the *Kepler* broad-band filter.

Identifiers	
TYC	3124-1348-1
GSC	03124-01348
2MASS	J19033272+3941003
Position and brightness	
RA (J2000)	19:03:32.7274
Dec. (J2000)	+39:41:00.314
$V$	10.8
$B$	10.9
$Kp$	10.8

HD 174936, it is expected that an increasing number of these intriguing objects will be solved in the foreseeable future.

The *Kepler* satellite, with its highly precise photometry, is generating observations unparalleled in precision and subsequently giving greater insight into the study of stellar structure through the use of asteroseismology. The primary objective of the *Kepler* mission is the identification and classification of planets through the transit method. However, the instrumentation required for such observations is highly applicable to the field of asteroseismology (Gilliland et al. 2010). Attributes, such as a stable platform, that enable extended observations, and a precision as good as a few parts per million, make the *Kepler* observations quintessential for the advancement of asteroseismology. A dynamic range of over 10 mag, in addition to a  $105 \text{ deg}^2$  field of view, gives *Kepler* an unprecedented advantage for obtaining high-quality asteroseismic data. Moreover, the ability to generate short-cadence data of  $\sim 1$  min time resolution allows for detailed photometric analyses of pulsating stars across the Hertzsprung–Russell (H-R) diagram.

KIC 4544587 (where KIC is an acronym for ‘*Kepler* Input Catalogue’) is an eccentric ( $e = 0.28$ ), short-period ( $P = 2.1891$  d) binary system that contains at least one pulsating component (cf. Table 1 for a list of observable information and identifiers). It was initially identified as a binary by Prša et al. (2011) as part of the first release of the *Kepler* Eclipsing Binary Catalog (<http://keplerebs.villanova.edu>). The temperature of the primary component is equivalent to a late A-type star that is within the  $\delta$  Scuti instability strip and the secondary component’s temperature is indicative of an early F star, which is likely to be a  $\gamma$  Dor variable.

Primarily this object was selected as a likely candidate for tidally induced pulsations due to the close proximity of the components at periastron,  $\sim 4 R_{\odot}$  surface to surface. KIC 4544587 also has interesting orbital characteristics including a brightening at periastron in the *Kepler* photometric light curve due to the combination of tidal distortion and substellar heating. Such a feature is indicative of an eccentric binary with its components in close proximity (Maceroni et al. 2009; Thompson et al. 2012).

In this paper, information obtained from modelling the binary features of the photometric and radial velocity (RV) curves of KIC 4544587, and the results of the pulsational frequency analysis are presented. In Section 2, the observations are discussed, including adjustments to the original data set. Sections 3 and 4 describe the spectral disentangling and the atmospheric parameters determined from the disentangled spectra. In Section 5, the determination of the orbital period is detailed. In Section 6, the binary light-curve modelling method is discussed, which focuses on the use of the binary modelling software, PHOEBE (Prša & Zwitter 2005). Section 7

**Table 2.** The number of data points and duty cycle acquired for each individual *Kepler* quarter. The LC data correspond to a sampling rate of 29.4244 min and SC data to a sampling rate of 58.8488 s.

Quarter	Cadence	Number of data points	Duty cycle (per cent)
0	LC	476	99.5
1	LC	1639	98.1
3.2	SC	44 000	98.5
6	LC	4397	97.2
7	SC	128 830	98.1
8	SC	98 190	94.3

contains the frequency analysis and includes discussion of the evidence for resonance effects. A summary of this paper, with concluding remarks, is given in Section 8.

## 2 OBSERVATIONS

### 2.1 *Kepler* photometry

The *Kepler* photometric observations of KIC 4544587 consist of both long-cadence (hereafter LC) data, during Quarters 0–11, and short-cadence (hereafter SC) data during Quarters 3.2, 7, 8, 9 and 10. For our purposes we used a subset of these data up to and including Quarter 8 (see Table 2 and Fig. 1), which were available at the time of analysis. A quarter is defined as a quarter of a complete, 372.5-d, *Kepler* orbit around the Sun (Kjeldsen et al. 2010). LC data correspond to a sampling rate of 29.4244 min and SC data to a sampling rate of 58.8488 s. For both formats 6.02-s exposures are co-added on board; this occurs 270 times to form an LC and 9 times to form an SC data point (Caldwell et al. 2010), with any remaining time attributed to readout time. The data are time-stamped with truncated Barycentric Julian Date (Gilliland et al. 2010), which is Barycentric Julian Date minus 2400000. The total

*Kepler* photometric observations that have been analysed span from 2009 May to 2011 March and comprise 277 514 data points.

The photometric observations were made using the *Kepler* broadband filter, which is similar to Cousins *Rc*. It is advised in the data release notes that accompany the *Kepler* data that the corrections made in the pipeline can have adverse effects on the binary signal in the data. For this reason the simple aperture photometry light curves were used instead of those created by the photometer performance assessment portion of the pipeline (Li et al. 2010).

From the total data set, 9471 points were removed as outliers, of which 661 data points were removed from Quarter 3.2, 2448 from Quarter 7 and 5597 from Quarter 8. These outliers were selected by eye as the intrinsic variations in the data significantly reduce the effectiveness of automated sigma clipping. Cosmic rays and other noise sources are the dominant causes of outliers, and small gaps in the data are also present due to safe-mode events, spacecraft rolls and brightening events known as Argabrightening, named after the discoverer, V. Argabright (Van Cleve 2009). These gaps, however, are minimal, which can be seen by the high duty cycle that was obtained for each quarter independently, with the exception of the safe-mode event at the beginning of Quarter 8.

The SC data have the advantage of increased time resolution, which enables the identification of the p-mode pulsations present in this object (see Fig. 2). Consequently, Quarters 7 and 8 were used for the binary modelling and mode identification of KIC 4544587 (with the exception of modelling the rate of apsidal advance where all LC data were used). A customized target mask was constructed for Quarters 7 and 8 so that the average flux level was consistent over the two quarters. This is important for asteroseismic analysis as quarter-to-quarter flux variations can cause instrumental amplitude modulation in the data. `PYKE` software (provided by the *Kepler* Guest Observer office: <http://keplergo.arc.nasa.gov/>) was used to define the mask, generate the new data files and convert the data from FITS to ASCII format. We detrended and normalized each month of data individually by fitting a first- or second-order Legendre

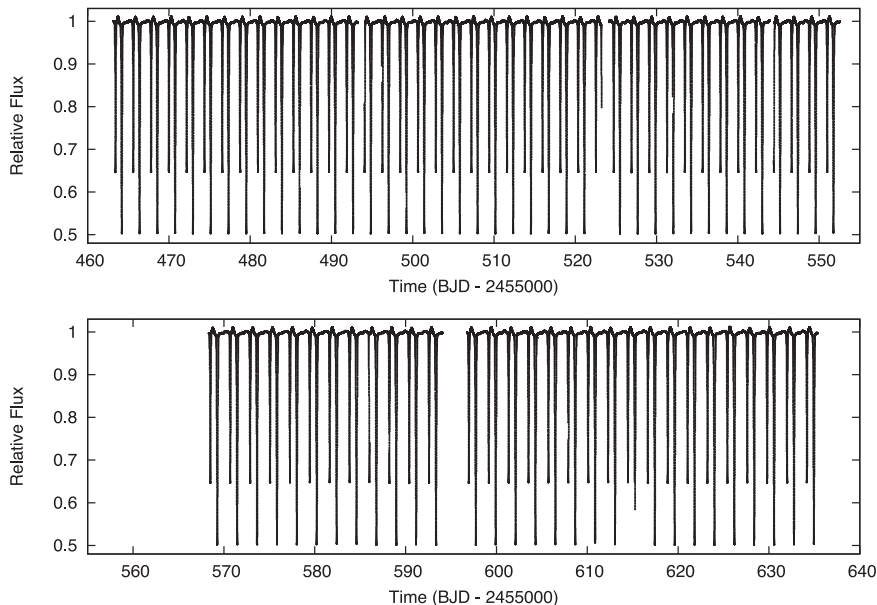


**Figure 1.** The observed *Kepler* SC light curve of KIC 4544587 for Quarters 7 (upper panel) and 8 (lower panel). Data are missing from the beginning of Quarter 8 due to a safe-mode event. The time is in BJD.

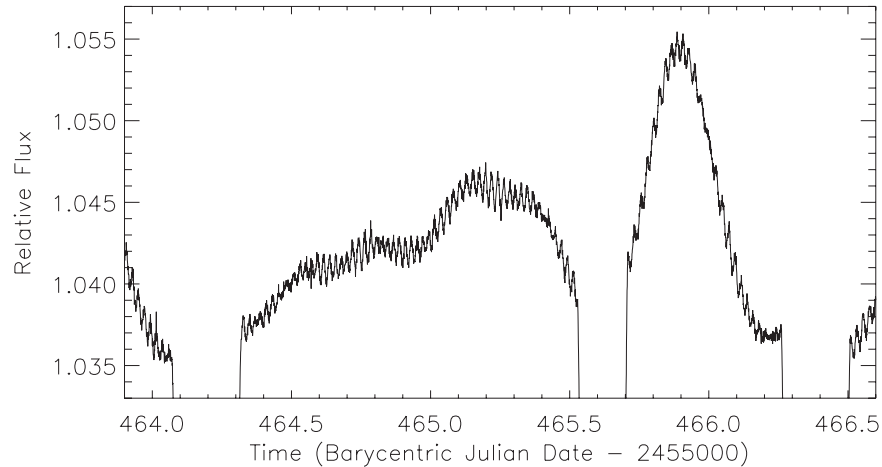


**Figure 2.** An amplified image of the out-of-eclipse phase of the *Kepler* Quarter 7 SC light curve. Here the both the p-mode (periods in the range 30 min–1 h) and the g-mode pulsations ( $\sim 1$  d) are clearly visible. The pronounced periastron brightening can also be seen at approximately BJD 245 5466.

polynomial to segments of data separated by gaps (i.e. caused by spacecraft rolls and safe-mode events). As the eclipses affect the detrending process, we elected to fit the polynomials to the out-of-eclipse envelope only. The out-of-eclipse envelope was identified by sigma clipping the data. Using this method we (temporarily) removed all data points  $5\sigma$  above and  $0.05\sigma$  below the light curve. The long-term trends in the out-of-eclipse envelope were then fitted and the trends removed from the original data. Finally, we applied a Fourier transform to the polynomials and found that all significant peaks were  $\nu < 0.03$  d $^{-1}$ , showing that we did not remove any information intrinsic to the system through this method.

As each *Kepler* pixel is  $4 \times 4$  arcsec, it is expected that some contamination may occur within the photometric mask. The contamination value for KIC 4544587, specified by the Kepler Asteroseismic Science Operations Center, is estimated to be 0.019, where 0 implies no contamination and 1 implies complete contamination of the CCD pixels. This contamination value suggests that KIC 4544587 suffers minimally from third light, if at all. We applied the `PYKE` software to the target pixel files to assess the flux incident on each individual pixel. Light curves for each pixel were generated and the flux distribution over the newly defined masks was examined. From this we determined that the contamination level for KIC 4544587 is negligible.

## 2.2 Ground-based spectroscopy

38 spectra were obtained using the Intermediate dispersion Spectrograph and Imaging System (ISIS) on the William Herschel Telescope (WHT). The spectra were taken on 2011 June 18–21 and 2012 June 7–14 with resolving powers of  $R \sim 17\,000$  and  $\sim 22\,000$ , respectively. Calibration exposures using CuAr and CuNe lamps were taken prior to each 300-s exposure of KIC 4544587. Blue and red spectra were obtained using wavelength coverages of 4200–4550 and 6100–6730 Å, respectively. The gratings H2400B (blue arm) and R1200R (red arm) were used. A 0.5-arcsec slit was used to give Nyquist sampling on the CCD and to limit RV errors due to the positioning of the star within the slit. The signal-to-noise ( $S/N$ ) obtained was  $\sim 100$  per resolution element. The data were reduced using optimal extraction techniques as implemented in the `PAMELA` package (Marsh 1989).

The initial RV curves were determined using the 2D cross-correlation technique as implemented in TODCOR (Two-dimensional Correlation Technique, Zucker & Mazeh 1994) on the red and blue spectra together. The templates for the primary and the secondary components were taken from Castelli & Kurucz (2004) model atmospheres, using  $T_1 = 8250$  K,  $\log g_1 = 4.0$ ,  $[M/H]_1 = 0.0$  and  $T_2 = 8000$  K,  $\log g_2 = 4.0$ ,  $[M/H]_2 = 0.0$ , respectively. Of the 38 spectra taken, cross-correlation failed to produce a good RV fit for one spectrum. Subsequent improvement to the RV curves was done by revising the templates according to the best-fitting photometric model and applying them to both blue and red ends:  $T_1 = 8600$  K,  $\log g_1 = 4.24$  and  $T_2 = 7750$  K,  $\log g_2 = 4.33$ , respectively. A systematic offset slightly larger than  $1\sigma$  was found between the RVs of the red arm and the blue arm. As there is no obvious cause for this discrepancy, each simultaneous exposure was averaged over the two arms and the discrepancy included in the uncertainty of the RV measurements. The final RV data have a typical  $1\sigma$  uncertainty of  $\sim 7.3$  km s $^{-1}$  and are listed in Table 3 and depicted in Fig. 3 with the best-fitting RV model folded on the period and zero-point obtained from the light curve.

Subsequently, five high-resolution spectra were taken using the echelle spectrograph on the 4-m Mayall telescope at KPNO with  $R \sim 20\,000$  and a wavelength range of 4500–9000 Å. The data were wavelength-calibrated and flux-normalized as depicted in Fig. 4, where Doppler splitting is clearly visible. As the per-wavelength  $S/N$  ratio of the KPNO spectra is notably lower than the WHT spectra, the 2D cross-correlation technique, TODCOR, gave significantly larger uncertainties. We consequently used the broadening function technique (Rucinski 1992) to determine the RVs for KPNO spectra. The broadening functions are rotational broadening kernels, where the centroid of the peak yields the Doppler shift and where the width of the peak is a measure of the rotational broadening. For the template we used the RV standard HD 182488, with  $v_{\text{rot}} = -21.508$  km s $^{-1}$ .

## 3 SPECTRAL DISENTANGLING: ORBIT

We applied the technique of spectral disentangling (hereafter SPD) to isolate spectra for the two binary components individually (Simon & Sturm 1994). Through this technique we determined the effective

**Table 3.** RV data of the primary (RV1) and secondary (RV2) components and their respective uncertainties (standard deviation) for 38 spectra obtained with the WHT and 5 spectra from the 4-m Mayall telescope. The ISIS was used in conjunction with the WHT to obtain simulations red-band (6100–6730 Å) and the blue-band (4200–4550 Å) spectra. The average RV for each given time is specified. The echelle spectrograph was used on the 4-m Mayall telescope.

Time (BJD)	RV1 (km s <sup>-1</sup> )	RV2 (km s <sup>-1</sup> )
WHT		
245 5730.621 52	71.9 ± 5.2	-133.8 ± 6.5
245 5730.657 50	91.2 ± 4.7	-154.5 ± 5.8
245 5730.699 32	102.2 ± 4.1	-177.3 ± 5.3
245 5731.556 25	-52.2 ± 5.3	30.9 ± 5.7
245 5731.601 21	-62.3 ± 5.3	37.8 ± 5.7
245 5731.646 68	-69.4 ± 5.0	43.8 ± 5.5
245 5731.701 16	-77.3 ± 4.8	50.4 ± 5.9
245 5732.439 58	-79.5 ± 4.9	54.9 ± 5.8
245 5732.485 00	-67.9 ± 4.7	46.0 ± 5.3
245 5732.525 38	-54.9 ± 4.7	36.8 ± 5.9
245 5732.577 57	-38.0 ± 5.0	16.1 ± 8.7
245 5732.622 38	-25.4 ± 3.8	5.3 ± 9.3
245 5732.657 37	-12.2 ± 4.3	19 ± 12
245 5732.692 00	13.9 ± 9.6	-52 ± 39
245 5732.726 88	29.2 ± 3.5	-103.1 ± 9.2
245 5733.411 85	46.1 ± 7.3	-74.6 ± 5.0
245 5733.459 56	-2 ± 22	-55.3 ± 5.5
245 5733.504 35	-23.6 ± 9.7	-42.6 ± 5.2
245 5733.540 24	-31.4 ± 5.3	-22.6 ± 5.9
245 5733.576 12	-32.5 ± 9.7	-4.6 ± 9.5
245 5733.667 81	-41 ± 17	14 ± 14
245 5734.031 82	-73 ± 14	51 ± 20
245 5734.434 76	-108.0 ± 7.2	79.0 ± 7.4
245 5734.515 79	-100.0 ± 6.8	72.8 ± 8.0
245 5734.559 67	-99.2 ± 9.0	66.5 ± 8.7
245 5734.602 65	-94.6 ± 9.0	53.4 ± 8.9
245 6086.653 88	-108.1 ± 4.2	82.3 ± 5.1
245 6087.475 73	82.3 ± 4.5	-146.8 ± 5.5
245 6087.579 88	119.9 ± 4.2	-193.3 ± 5.3
245 6087.671 36	123.6 ± 4.2	-198.0 ± 5.1
245 6087.734 10	113.4 ± 4.0	-184.5 ± 5.0
245 6088.612 05	-91.0 ± 4.2	59.7 ± 4.9
245 6089.573 01	37.8 ± 3.8	-105.8 ± 6.5
245 6089.678 23	88.0 ± 4.1	-155.9 ± 4.9
245 6089.732 87	109.0 ± 4.7	-181.1 ± 5.6
245 6090.717 62	-79.3 ± 4.4	49.7 ± 5.1
245 6091.496 76	-71.9 ± 5.4	39.4 ± 6.3
245 6092.449 32	37 ± 15	-64.9 ± 7.1
KPNO		
245 6085.684 47	79.6 ± 2.9	-138.4 ± 0.8
245 6087.662 30	127.4 ± 2.9	-198.0 ± 0.7
245 6087.959 06	45.6 ± 2.3	-100.9 ± 1.8
245 6088.704 13	-95.7 ± 3.5	75.1 ± 1.9
245 6091.959 50	126.3 ± 5.0	-191.4 ± 1.2

temperatures of the two components using the Balmer lines. The medium-resolution ISIS/WHT spectra, described in Section 2.2, contain H $\gamma$  and H $\alpha$  lines, and the medium-resolution echelle KPNO spectra contain H $\beta$  and H $\alpha$  lines. The `FDBINARY`<sup>1</sup> code (Ilijic et al.

<sup>1</sup> <http://sail.zpf.fer.hr/fdbinary>

2004), which is based on a Fourier variant of SPD (Hadrava 1995), was first applied to the time series of ISIS/WHT spectra since they are more numerous than the KPNO spectra. Since some of the eclipse spectra are affected by the Rossiter–McLaughlin effect, and the line profiles are disturbed, only out-of-eclipse spectra were used. This substantially reduced the number of spectra available for SPD, but the phase coverage was still adequate to suppress the undulations in the disentangled spectra of the components (Hensberge, Ilijic & Torres 2008). The absence of in-eclipse spectra resulted in an ambiguity in the placement of the continuum of the disentangled spectra. Therefore, we performed SPD in separation mode, and then corrected the separated spectra for line blocking and light dilution using the procedure described in Pavlovski & Hensberge (2005).

In SPD individual component spectra are calculated simultaneously and are self-consistently optimized with the orbital parameters, whereby the determination of RVs is bypassed (Simon & Sturm 1994; Hadrava 1995). In this sense, each individual RV exposure is not optimized and as such no comparison can be made with measured RVs (Pavlovski & Hensberge 2010). The orbital parameters calculated by SPD are given in Table 4 and represent the mean values calculated through disentangling five short spectral regions from the ISIS/WHT blue spectra, which cover the spectral interval from 4200 to 4600 Å. Telluric lines affect the ISIS/WHT red spectra, which are centred on the H $\alpha$  line; thus, we removed them manually before the application of SPD. Since only five spectra were available in the region of the H $\beta$  line, when using SPD, we fixed all the orbital parameters with the exception of the time of periastron.

An important outcome of SPD is an enhancement of the S/N ratio in the disentangled spectra, as the spectra are co-added during the SPD process. Due to the significant number of WHT/ISIS blue and red spectra, the S/N has vastly improved. However, for the KPNO spectra the gain is small due to the limited number of spectra available for analysis. The effect of disentangling on the S/N ratio, for different numbers of input spectra (as well as their original S/N), is clearly depicted in Fig. 5.

#### 4 ATMOSPHERIC PARAMETERS

Once separated, the spectra remain in the common continuum of the binary system, diluted by their companion’s contribution to the total light of the system. The light ratio between the components is derived from the light-curve solution and makes renormalization of the individual component spectra straightforward. We further computed the light ratio for the Johnson *U* (0.685), *B* (0.697) and *V* (0.667) passbands, whilst keeping all other parameters fixed, to determine the deviation of the light ratio as a function of wavelength. We note that the value derived from the light curve using the *Kepler* passband (0.670) is approximately equal to that of the Johnson *V* band, so we expected that the H $\gamma$  line is most affected by our selection as its wavelength is furthest from the Johnson *V* band. Consequently, with the surface gravities of the components known from the complementary light and RV curve solutions, the degeneracy between the effective temperature and the surface gravity can be broken. We determined the components’ effective temperatures by fitting the renormalized individual spectra with the synthetic theoretical spectra (Tamajo, Pavlovski & Southworth 2011).

The genetic algorithm, as implemented in `PIKAIA` (Charbonneau 1990), was used in the global optimization of the code `STARFIT` (Pavlovski et al., in preparation). A grid of local thermodynamic

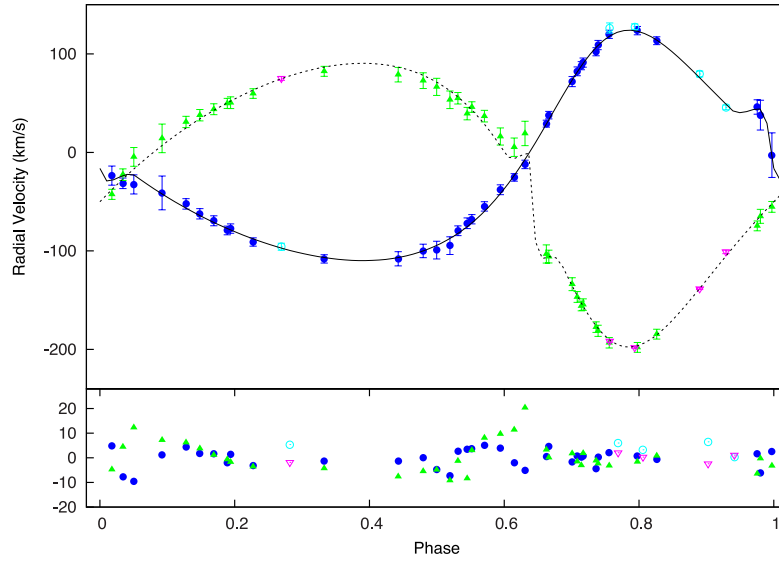


**Figure 3.** Top panel: RV curve generated from 38 spectra obtained using ISIS on the WHT and 5 spectra obtained using the echelle spectrograph on the 4-m Mayall telescope at KPNO, folded over the orbital period. The blue solid circles and light blue open circles represent the primary component from the WHT and KPNO data, respectively, the green solid triangles and the pink open triangles represent the secondary component from the WHT and KPNO data, respectively, and the solid and dashed lines represent the primary and secondary components. The errors bars show the uncertainties in the RV measurements. Bottom panel: the residuals from the best fit to the RV data.

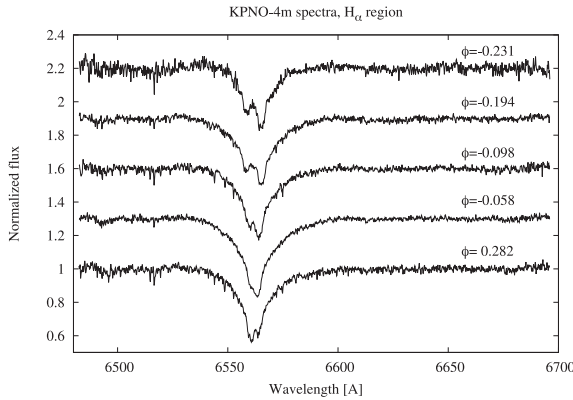


**Figure 4.** The  $H\alpha$  region of the five echelle spectra acquired by the 4-m Mayall telescope at Kitt Peak with  $R \sim 20000$  and the wavelength span 4500–9000 Å. The components are clearly resolved in the five spectra.

**Table 4.** The orbital elements of the binary system KIC 4544587 derived by SPD of time series ISIS/WHT blue spectra.

Parameter	SPD
Orbital period $P$ (d)	2.189 094 (fixed)
Time of periastron passage, $T_0$ (BJD)	245 5461.450(1)
Eccentricity, $e$	0.288(26)
Longitude of periastron, $\omega$	328.5(22)
Velocity semi-amplitude $K_A$ ( $\text{km s}^{-1}$ )	117.8(9)
Velocity semi-amplitude $K_B$ ( $\text{km s}^{-1}$ )	145.8(10)
Mass ratio $q$	0.808(8)

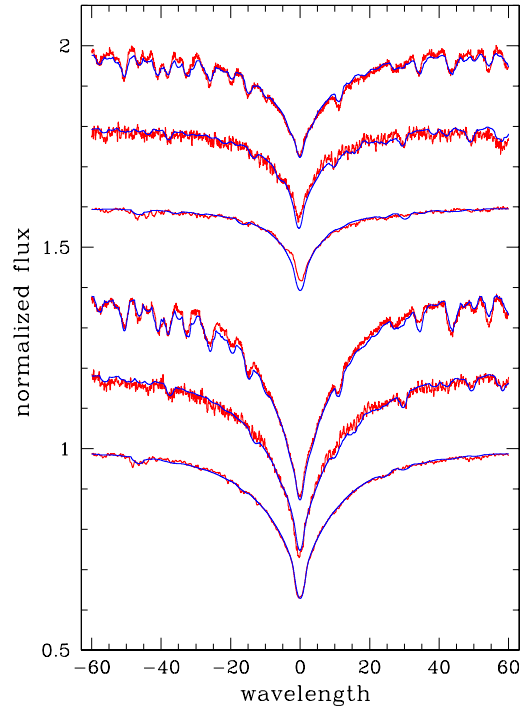


**Figure 5.** Comparison between disentangled spectra in the common continuum of the binary system (red lines, differentiable also by the noise) and best-fitting theoretical spectra (blue lines) for the secondary component (upper three spectra) and primary component (lower three spectra). The  $H\alpha$ ,  $H\beta$  and  $H\gamma$  lines are depicted in ascending order and have been offset by 0.1 for clarity.

**Table 5.** Atmospheric parameters for the components of KIC 4544587, derived from a constrained optimal fit of the disentangled spectra with the light factor as a fixed (upper section) and free (middle section) parameter. For both the fixed and free case, the projected rotational velocities (lower section) are fixed to the values derived by the optimal fitting of the metallic lines in the disentangled ISIS/WHT blue spectra.

Parameter	Primary	Secondary
$T_{\text{eff}}$ (K)	8090(90)	7620(135)
$\log g$ (cgs)	4.22 (fixed)	4.23 (fixed)
Light factor	0.670 (fixed)	0.330 (fixed)
$T_{\text{eff}}$ (K)	8600(100)	7750(180)
$\log g$ (cgs)	4.12(2)	4.31(2)
Light factor	0.634/0.646/0.670	0.366/0.354/0.330
$v \sin i$ (km s <sup>-1</sup> )	86.5(13)	75.8(15)

equilibrium synthetic spectra was calculated using the `UCLSYN`<sup>2</sup> code (Smalley, Smith & Dzwretsky 2001) and `ATLAS9` model atmospheres for solar metallicity  $[M/H] = 0$  (Castelli, Gratton & Kurucz 1997). The grid covers  $T_{\text{eff}}$  from 6000 to 10 000 K in steps of 250 K, and  $\log g$  from 3.50 to 4.50 in steps of 0.5 dex.

The projected rotational velocities of the components were also optimized. However, as convolution with the rotational kernel has little influence on the broad Balmer lines, we avoided simultaneous determination of the  $T_{\text{eff}}$  and  $v \sin i$ . Instead, we determined the  $v \sin i$  of the components by fitting the least blended metal lines. The results are given in Table 5. As  $v \sin i = 86 \pm 13 \text{ km s}^{-1}$ , KIC 4544587 has an equatorial velocity of  $v_{\text{eq}} < 120 \text{ km s}^{-1}$ , below which diffusion can occur. Thus, it is likely that the primary component is a metallic-lined Am star (Abt 2009).

Alongside the optimal fitting of the renormalized disentangled spectra of H $\gamma$ , H $\beta$  and H $\alpha$  lines separately (with the surface gravities and projected rotational velocities held fixed), we have also derived optimal atmospheric parameters in the constrained mode (Tamajo et al. 2011). In constrained mode, the light ratio between the components is a free parameter when fitting for the effective temperatures. Also, the surface gravities were left to be free parameters. In the search for the optimal set of parameters, we also adjusted for the velocity shift between disentangled and theoretical spectra, to enable a slight adjustment of the continua of the disentangled spectra. Disentangling the Balmer lines is a difficult task due to their broadening, which is much larger than their Doppler shift. Moreover, when determining the effective temperature, the correct continuum placement is difficult because the Balmer lines of the primary extend over a considerable number of echelle orders, making the correction of the blaze and order merging somewhat uncertain. The optimal set of the parameters obtained when performing constrained fitting, with the light factor as both a free and fixed parameter, is given in Table 5.

## 5 PERIOD DETERMINATION

Period analysis was performed to identify the orbital period of the binary system. An initial estimate was obtained by applying `PERIOD04` (Lenz & Breger 2004) to the SC data from Quarter 3.2 only. `PERIOD04` applies a Fourier transform to the data and uses a least-squares fit to optimize the amplitudes and phases. Further analysis was then performed on all the SC data (Quarters 3.2, 7 and 8) using `KEPHEM`

(Prša et al. 2011), an interactive package with a graphical user interface (GUI) that incorporates three methods: Lomb–Scargle (Lomb 1976; Scargle 1982), analysis of variance (Schwarzenberg-Czerny 1989) and box-fitting least squares (Kovács, Zucker & Mazeh 2002), as implemented in the `VARTOOLS` package (Hartmann 1998). Using `KEPHEM`, the period and time of primary minimum were found interactively. The period was determined by dragging the mouse over a periodogram in the lower panel of the GUI to see how it affected the alignment of the phased data presented in the upper panel of the GUI. To determine an accurate period, the zoom tool was utilized on both the periodogram and phased data. The zero-point was then selected by dragging the primary eclipse in the top panel containing the phased data and align it with zero phase. The ephemeris was found to be  $\text{Min } I = \text{BJD } 245\,5462.006\,137(9) + 2.189\,094(5) \times E$ ,

where the values in the parentheses give the uncertainty in the previous digits. The uncertainties were obtained by identifying the range of values that would yield a visibly indistinguishable result; beyond this uncertainty range the discrepancy is notably increased. Due to apsidal motion, the relative separation of the eclipses changes as a function of the rotation of the orbit. Consequently, the period specified is the anomalous period, which is the period measured by phasing the data on one eclipse (primary eclipse), leaving the other eclipse (secondary eclipse) smeared. Although this is a small effect, the smearing could be seen over the duration of the data used in this analysis. See Section 6.2 for further discussion on the apsidal motion of KIC 4544587.

## 6 BINARY MODELLING

### 6.1 PHOEBE

`PHOEBE` (Prša & Zwitter 2005) is a binary modelling package based on the Wilson–Devinney (hereafter WD) code (Wilson & Devinney 1971; Wilson 1979; Wilson & Van Hamme 2004). `PHOEBE` incorporates all the functionality of the WD code but also provides an intuitive GUI alongside many other improvements that make `PHOEBE` highly applicable to the precise *Kepler* data. These include: uncertainty calculations through heuristical scanning algorithms (which scan parameter space by generating results from multiple starting points to determine the mean and standard deviation); the facility to phase bin the data; updated filters for the various recent space missions including *Kepler*; the correct treatment of reddening and the ability to work with a large number of data points.

When modelling the data, the initial inputs were a combination of the effective temperatures and  $\log g$  values identified through fitting the disentangled spectra with the light factors as a free parameter,  $8600 \pm 100 \text{ K}$ ,  $7750 \pm 180 \text{ K}$ , 4.12 and 4.31, for the primary and secondary, respectively. We elected to use the results from this mode as a single light factor does not account for the change in each component’s relative light contribution for the different spectral ranges. For the initial investigation, a model light curve was generated from the observationally constrained and estimated input parameters. First, the passband luminosity of the model was computed so that the out-of-eclipse flux levels were correctly positioned with respect to the observed light-curve data. Following this the eccentricity ( $e$ ) and argument of periastron ( $\omega$ ) were adjusted until the separation between the primary and secondary eclipses, which is proportional to  $e \cos \omega$ , was equal to that of the observed data. This also involved adjusting the phase shift to retain the position of the model’s eclipses. Once the separation was tightly constrained, the phase shift,  $e$  and  $\omega$  were further adjusted, whilst maintaining the value for  $e \cos \omega$ , to obtain the relative widths of the primary

<sup>2</sup> <http://www.astro.keele.ac.uk/~bs/pubs/uclsyn.pdf>

**Table 6.** Adjusted parameters and coefficients of the best-fitting model to the *Kepler* light curve for Quarters 7 and 8. The limb darkening coefficients correspond to the logarithmic limb darkening law. The uncertainties were determined through modelling and Monte Carlo methods, and concur with those obtained through fitting the disentangled spectra. The limb darkening coefficients were taken from the PHOEBE limb darkening tables (Prša et al. 2011).

Parameter	Values
Mass ratio	0.810(12)
Primary mass ( $M_{\odot}$ ), $M_1$	1.98(7)
Secondary mass ( $M_{\odot}$ ), $M_2$	1.61(6)
Primary radius ( $R_{\odot}$ ), $R_1$	1.82(3)
Secondary radius ( $R_{\odot}$ ), $R_2$	1.58(3)
Phase shift	0.0831(3)
Semimajor axis ( $R_{\odot}$ ), $a$	10.855(46)
Orbital eccentricity, $e$	0.275(4)
Argument of periastron (rad), $\omega$	5.74(3)
Orbital inclination (degrees), $i$	87.9(3)
Primary $T_{\text{eff}}$ (K), $T_1$	8600(100)
Secondary $T_{\text{eff}}$ (K), $T_2$	7750(180)
Primary potential, $\Omega_1$	7.09(10)
Secondary potential, $\Omega_2$	7.12(10)
Gamma velocity ( $\text{km s}^{-1}$ )	-20.13(7)
Apsidal advance (yr per cycle)	182(5)
Sidereal period (d)	2.189 0951(7)
Primary relative luminosity	0.668(2)
Secondary relative luminosity	0.332(1)
Primary $\log g$ (cgs), $\log g_1$	4.241(9)
Secondary $\log g$ (cgs), $\log g_2$	4.33(1)
Primary linear limb darkening coeff.	0.634
Secondary linear limb darkening coeff.	0.664
Primary logarithmic limb darkening coeff.	0.282
Secondary logarithmic limb darkening coeff.	0.268

and secondary eclipses, which are proportional to  $e \sin \omega$ . The combined depths and widths of the eclipses were then adjusted by altering the inclination and stellar potentials, respectively.

Once an initial model had been generated, the differential corrections algorithm was applied in an iterative process to obtain an accurate fit to the light-curve data. Once the model was tightly constrained, the RV curves were incorporated to fit the mass ratio, gamma velocity and the projected semimajor axis. As the photometric light curve contains essentially no information about these parameters for a detached system, the fit was performed on the RV curves independently. This avoids improper weighting due to the vastly different number of data points between the different types of curves. Once the best-fitting solution had been achieved for these parameters, the differential corrections algorithm was applied to the light curve for all other parameters specified in Table 6.

When generating the model we assumed pseudo-synchronous stellar rotation after Hut (1981), which was determined to be 1.87 times the orbital period. Pseudo-synchronous rotation is indicative of the rotational velocity of the stellar components at periastron. We also fixed the orbital period since *KEPHEM* is more appropriate for period determination than the differential corrections algorithm. Due to the low contamination and following the analysis of the pixel level data, we assumed no third light in the system.

When modelling a binary system with one or more pulsating components (where the pulsations occur on the time-scale of the orbit), multiple iterations are required so that the data are thoroughly prewhitened, leaving only the binary signature. This enables the orbital characteristics to be modelled correctly without interference

**Table 7.** Fixed parameters and coefficients for the PHOEBE best-fitting model to the *Kepler* light curve for Quarter 7. The rotation is specified as a ratio of stellar to orbital rotation, and the fine grid raster is the number of surface elements per quarter of the star at the equator and coarse grid raster is used to determine whether the stars are eclipsing at a given phase.

Parameter	Values
Third light	0.0
Orbital period (d)	2.189 094(5)
Time of primary minimum (BJD)	245 5462.006 137(9)
Primary rotation	1.83
Secondary rotation	1.83
Primary bolometric albedo	1.0
Secondary bolometric albedo	1.0
Primary gravity brightening	1.0
Secondary gravity brightening	1.0
Primary fine grid raster	90
Secondary fine grid raster	90
Primary coarse grid raster	60
Secondary coarse grid raster	60

from the stellar pulsations. The method used involved subtracting the computed orbital model from the original observed data, subsequent frequency analysis on the residual data, and finally, the removal of the identified pulsations from the original data. This method is only viable when the pulsations can be considered as perturbations, which is the case for KIC 4544587. What remains is a light curve predominantly free of pulsations for subsequent binary modelling. Three iterations were required when modelling KIC 4544587, with subsequent iterations having negligible effect. The fitted and fixed parameters, and their corresponding values for our best-fitting model, can be found in Tables 6 and 7, respectively.

The model obtained for KIC 4544587, as seen in Fig. 6, still shows some systematic discrepancies in the residuals during primary and secondary eclipses. These discrepancies arise from a combination of (1) the existence of pulsations that are commensurate with the orbital period and (2) the precise nature of the *Kepler* data. As some of the pulsations are commensurate with the orbital period, they occur at precisely the same time each orbit. During eclipse phase, however, the relative flux from the pulsating component either increases or decreases, dependent on which star is being eclipsed. This introduces a change in the amplitude of the pulsation during eclipse phase that manifests itself in the residuals of the model. Additionally, the highly precise *Kepler* data have highlighted the inadequate treatment of parameters such as limb darkening, stellar albedo and the incomplete treatment of surface discretization (Prša & Zwitter 2005), which have previously been considered satisfactory. Currently efforts are being made towards improving the models to account for the physics that has previously been omitted (Prša et al., in preparation). However, until this major task, which is outside the scope of this paper, is completed, these systematics are unavoidable when generating a binary model of the *Kepler* data and thus are accounted for in the uncertainties attributed to the fitted parameters.

Uncertainty estimates were obtained using a combination of formal errors, generated by fitting all the parameters simultaneously using PHOEBE, and those determined through Monte Carlo heuristic scanning. A scan of the parameter space was undertaken for the most correlated parameters using Monte Carlo methods. The results of the Monte Carlo simulations can be found in Figs 7 and 8. The Monte Carlo simulations perturbed the solutions of the best-fitting model by a predefined amount (5 per cent) in order to identify the

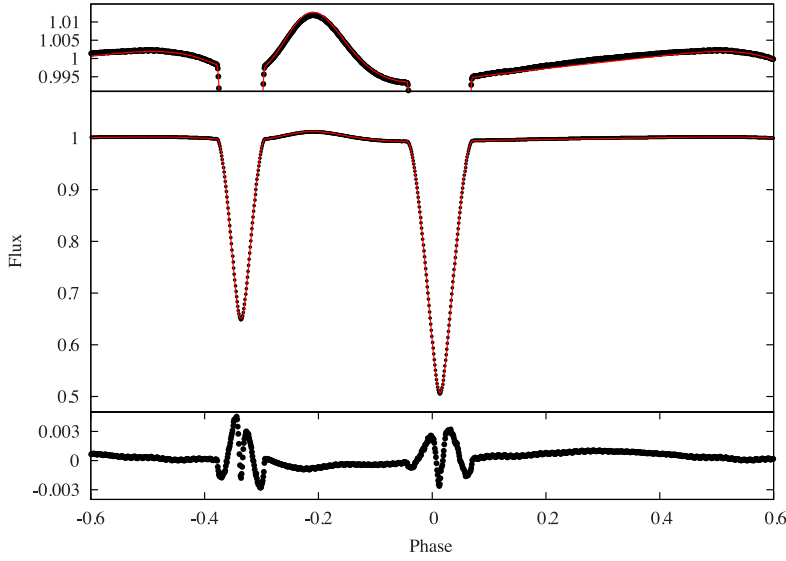


**Figure 6.** Middle panel: theoretical PHOEBE model (red line) and observed light curve, prewhitened with the pulsation frequencies displayed in Section 7 (black points) for the SC data of Quarters 7 and 8. Lower panel: the residuals (black points) of the best-fitting model. Upper panel: a magnified image of the out-of-eclipse data and PHOEBE model fit.

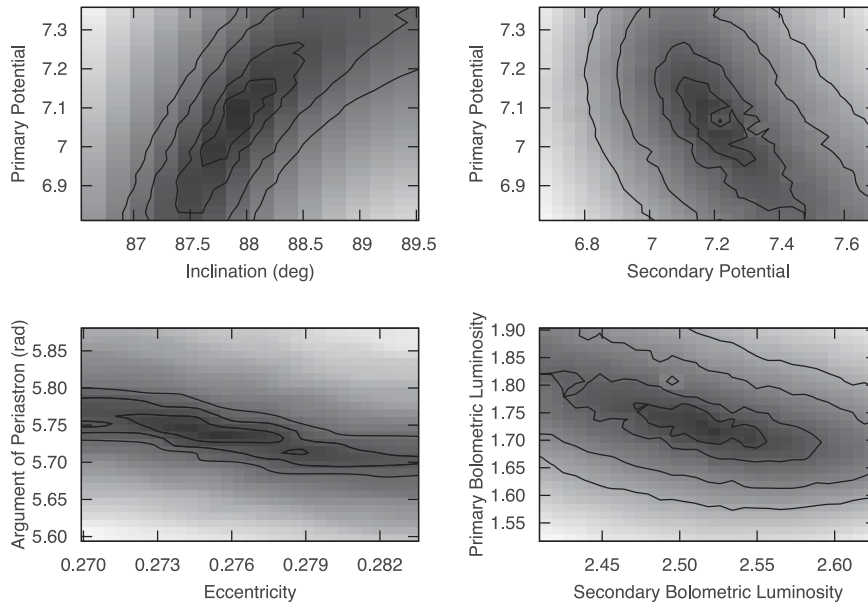


**Figure 7.** Density maps showing the distribution of results from the Monte Carlo simulations for the most correlated parameters: potential of the primary versus inclination (top left), primary versus secondary potential (top right), argument of periastron versus eccentricity (bottom left) and the luminosity of the primary versus the luminosity of the secondary (bottom right). The contours represent the uncertainty in terms of standard deviation, with the innermost contour representing the  $1\sigma$  uncertainty and subsequent contours representing increments of  $1\sigma$ .

spread of possible results and their corresponding  $\chi^2$  values. The  $\chi^2$  values for each solution were then mapped out into confidence intervals which serve as the uncertainty estimates. From the density maps, the optimum values of the correlated parameters displayed on the axes can be seen by identifying the combination with the lowest  $\chi^2$  value. The  $1\sigma$  uncertainty values are determined by considering the spread of the innermost contour.

## 6.2 Orbital evolution

Apsidal motion is the rotation of the elliptical orbit about the centre of mass (Claret & Gimenez 1993), which can be caused by the presence of a tertiary component or through the gravitational interactions occurring between the binary components. Using PHOEBE we determined the rate of apsidal advance for KIC 4544587 to

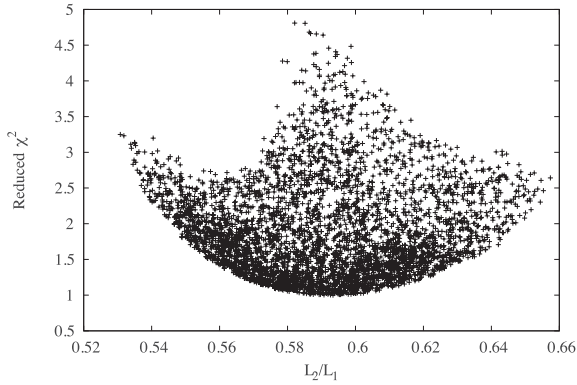


**Figure 8.** A scatter plot showing the spread of results obtained from the Monte Carlo simulation for the luminosity ratio as a function of  $\chi^2$ . A clear boundary with a definite minimum can be seen, which signifies that the luminosity ratio is unambiguous.

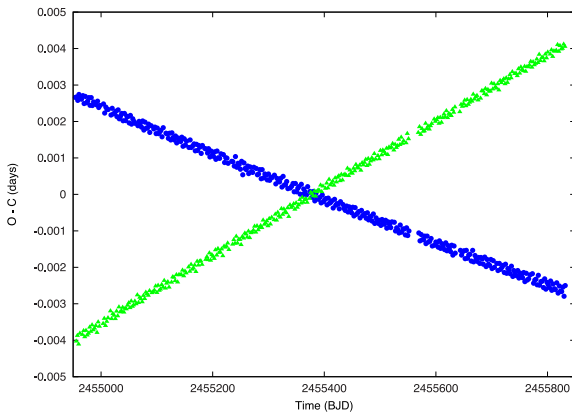


**Figure 9.** Depicted are the eclipse timing variations, which demonstrate the deviation of the observed primary (blue circles) and secondary (green triangles) eclipses from the model as a function of time. The average period was selected for the standard model and thus it can be seen that both eclipses deviate from each other. The opposing direction of the primary and secondary eclipses is suggestive of classical apsidal motion. With a longer time base it is expected that the trend would appear more sinusoidal. The standard model was generated using four polynomials of order 10, which was found to be the optimal order to reduce the scatter.

be  $0.04306(2) \text{ rad yr}^{-1}$ . This equates to a full rotation of the orbit in  $182(5) \text{ yr}$ . Fig. 9 shows the eclipse timing variations of KIC 4544587, and depicts the primary and secondary eclipses moving linearly in opposite directions, which is suggestive of classical apsidal advance caused by tidal distortions. Gies et al. (2012) modelled the eclipse timing variations of 41 eclipsing binaries, including KIC 4544587, and concluded that these variations are a combination of apsidal motion and tidal interactions.

The parameters determined by PHOEBE are indicative of an eccentric short-period system with two components in close proximity ( $\sim 4.4 R_{\odot}$  surface to surface, at periastron). Although the periastron distance is small, we still do not expect any mass transfer as the potentials of the two components far exceed the potential at L1 ( $\sim 4.8$ ), as specified by PHOEBE.

Eccentric short-period binary systems are uncommon due to the rapid rate of circularization ( $10^7 \text{ yr}$ ) compared with the time-scale of stellar evolution. Zahn (1975) theorized that orbital circularization

occurs due to the radiative damping of tidally excited oscillations in the stellar outer envelope. For this reason, the eccentric short-period nature of KIC 4544587 is either the result of tidal capture, recent formation of the system, the presence of a tertiary component or a consequence of its resonant pulsations. As the *Kepler* field does not contain any prominent star-forming regions, it is not expected that KIC 4544587 is a newly formed binary system. Furthermore, as the system is formed from two intermediate-mass main-sequence stars, it is also unlikely that the system has undergone tidal capture. Thus, the eccentric nature of KIC 4544587 is likely a consequence of either a third body or the system’s extreme tidal interactions (see Section 7.1 for a discussion of tidal resonance).

## 7 PULSATION CHARACTERISTICS

The light curve of KIC 4544587 demonstrates clear pulsations in two regions of the frequency spectrum: with periods of the order of days and periods of the order of 30 min, both of which can be seen in the light curve. We used PERIOD04 and our own codes to generate a frequency spectrum of the residual data (the detrended data with the orbital fit subtracted), which can be seen in Fig. 10. We also performed eclipse masking by removing the data points occurring during eclipse phases to remove any residual binary information from the light curve. In the Fourier transform, the gaps created in the data manifest themselves in the window pattern, with peaks separated from the real peak by the orbital frequency. Although this is not ideal, masking is highly important for the identification of resonantly excited modes, which is a crucial aspect of the analysis of KIC 4544587. Without removing the aforementioned points, the systematics would have presented themselves as frequencies at multiples of the orbital frequency, identical to the signature of tidally excited modes; thus, masking was required to differentiate between these two possibilities.

PERIOD04 incorporates a least-squares fitting technique to simultaneously generate amplitudes and phases for all the identified frequencies. For an assumed background level of  $40 \mu\text{mag}$ , we report the frequencies with amplitudes of  $3\sigma$  or more. The prominent frequency peaks were identified in two regions,  $0\text{--}5$  and  $30\text{--}50 \text{ d}^{-1}$ , which correspond to g modes and p modes, respectively, although the lowest frequency peak [ $f_{24} = 0.04089(6) \text{ d}^{-1}$ ] is possibly due to remaining instrumental effects.

The high-frequency, high-overtone p-mode frequencies are typical for a  $\delta$  Scuti star of temperature similar to that of the primary star, which is towards the hotter, blue edge of the instability strip. An estimate of the radial overtones of the modes can be made from the pulsation constant,  $Q$ , defined by the period–density relation:

$$P \sqrt{\frac{\rho}{\rho_{\odot}}} = Q, \quad (1)$$

which can be rewritten in the form

$$\log Q = -6.454 + \log P + 0.5 \log g + 0.1 M_{\text{bol}} + \log T_{\text{eff}}. \quad (2)$$

From the latter relation and the fundamental parameters given in Table 6, we find for the frequency range  $30\text{--}50 \text{ d}^{-1}$  for the primary star  $0.017 > Q > 0.012$ , and for the secondary star  $0.021 > Q > 0.015$ . These are indicative of radial overtones in the range  $3 \leq n \leq 5$  (Stellingwerf 1979). Pulsation in higher radial overtone p modes such as these (as opposed to pulsation in the fundamental and first overtone modes) is more typical of hotter  $\delta$  Sct stars, and hence suggests that the p modes arise in the primary star.

We applied a Fourier transform up to the SC Nyquist frequency but did not find any peaks beyond  $48.04449(19) \text{ d}^{-1}$ . Once the

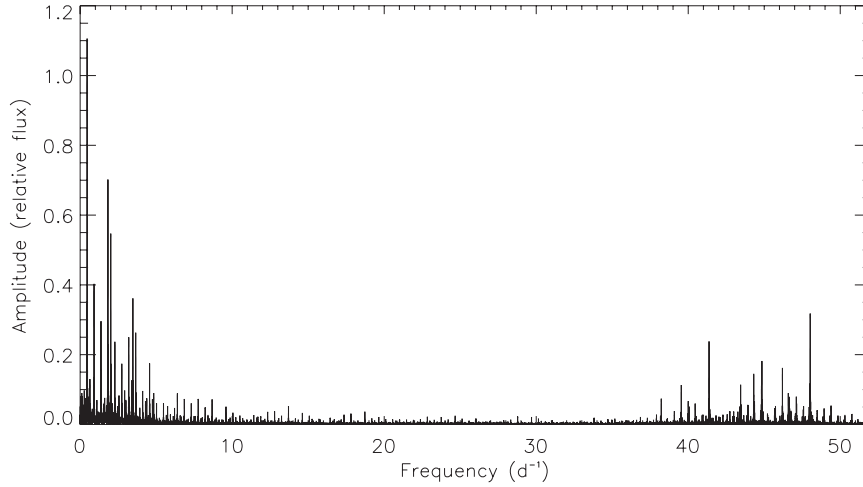


**Figure 10.** An amplitude spectrum of the residual, eclipse-masked data for the SC data of Quarters 7 and 8. Here the high-frequency p-mode regime is clearly separated from the lower frequency g-mode regime.

frequencies specified in Table 8 had been prewhitened, an amplitude excess still remained in both the p-mode and g-mode regions. However, as we could not be certain that further detections were real, we did not continue to extract modes beyond this point.

We identified 31 frequencies, 14 in the lower frequency g-mode region and 17 p-mode region, in the frequency spectrum between 0.1 and 49  $\text{d}^{-1}$  (see Table 8). Of the 14 g-mode frequencies, we identified 8 that are multiples of the orbital frequency (see Section 7.1).

The remaining g modes are either  $\gamma$  Dor pulsations, most likely from the secondary component, which is in the  $\gamma$  Dor instability strip, or non-resonant tidally driven modes, as predicted by Weinberg et al. (2012). Currently we are unable to differentiate as both outcomes have identical signatures, although as the secondary is in the  $\gamma$  Dor instability strip we would expect it to pulsate with intrinsically excited g modes.

### 7.1 Tidal interactions and combination frequencies

Tidally excited modes are stellar pulsations that have been excited by the tidal forces of the companion star. A prime example of this is KOI-54 (Welsh et al. 2011). In a binary system with an eccentric orbit, when a stellar eigenfrequency is close to a multiple of the orbital frequency, a near-resonance occurs that causes an increase in oscillation amplitude (relative to non-resonant modes). The signature of a tidally excited mode is an oscillation frequency at a multiple of the orbital frequency. We identified eight frequencies in the g-mode region that are multiples of the orbital frequency. We expect that these are tidally excited  $l = 2$  modes; however, as the eclipses are only partial, we are unable to use the in-eclipse data to determine mode angular degrees or which modes belong to which star.

Previously believed to be short-lived, Witte & Savonije (1999) demonstrated that the duration of tidal resonance can be prolonged through resonant locking. Resonant locking is a result of the change in stellar spin, due to the exchange of angular momentum in the system as the orbit evolves, causing variations in the eigenfrequencies of the stellar components. This, combined with the change in the orbital period of the system, causes a coupling between the newly

**Table 8.** The identified pulsation frequencies and their corresponding amplitudes and phases. The values in parentheses give the  $1\sigma$  uncertainty in the previous digit. The uncertainty in the amplitude is  $0.004 \times 10^{-3}$  relative flux units.

Designation	Frequency ( $\text{d}^{-1}$ )	Amplitude (flux $\times 10^{-3}$ )	Phase (rad)
$f_1 = \nu_{\text{orb}}$	0.456 81(1)	1.001	0.746(3)
$f_2 = 4\nu_{\text{orb}}$	1.827 10(1)	0.593	0.3822(4)
$f_3$	2.011 24(1)	0.561	0.0758(5)
$f_4 = 3\nu_{\text{orb}}$	1.370 41(1)	0.520	0.3514(5)
$f_5$	3.468 22(1)	0.373	0.9864(7)
$f_6$	48.022 31(4)	0.329	0.547(2)
$f_7 = 7\nu_{\text{orb}}$	3.197 60(2)	0.244	0.301(1)
$f_8$	41.370 20(5)	0.236	0.892(3)
$f_9$	44.846 95(6)	0.181	0.780(3)
$f_{10}$	0.125 46(3)	0.164	0.996(2)
$f_{11}$	46.196 62(8)	0.152	0.990(4)
$f_{12}$	0.127 21(4)	0.140	0.396(2)
$f_{13} = 97\nu_{\text{orb}}$	44.309 82(9)	0.134	0.776(4)
$f_{14} = 2\nu_{\text{orb}}$	0.913 88(4)	0.133	0.026(2)
$f_{15}$	48.044 49(19)	0.122	0.331(9)
$f_{16} = 10\nu_{\text{orb}}$	4.567 92(4)	0.116	0.532(2)
$f_{17} = 8\nu_{\text{orb}}$	3.6545(5)	0.106	0.055(2)
$f_{18}$	39.542 80(11)	0.106	0.984(6)
$f_{19}$	1.611 86(5)	0.103	0.897(3)
$f_{20}$	43.447 56(12)	0.101	0.733(6)
$f_{21}$	44.817 96(12)	0.099	0.088(6)
$f_{22} = 9\nu_{\text{orb}}$	4.111 22(6)	0.093	0.813(3)
$f_{23}$	46.583 40(13)	0.092	0.056(7)
$f_{24}$	0.040 89(6)	0.091	0.829(3)
$f_{25}$	1.585 41(7)	0.078	0.545(3)
$f_{26}$	38.226 68(16)	0.076	0.109(8)
$f_{27}$	44.299 02(21)	0.054	0.80(1)
$f_{28}$	44.361 18(29)	0.052	0.70(1)
$f_{29}$	40.053 72(23)	0.051	0.30(1)
$f_{30}$	46.674 01(23)	0.051	0.10(1)
$f_{31}$	44.756 38(24)	0.049	0.68(1)
$f_{32}$	47.953 73(26)	0.045	0.69(1)

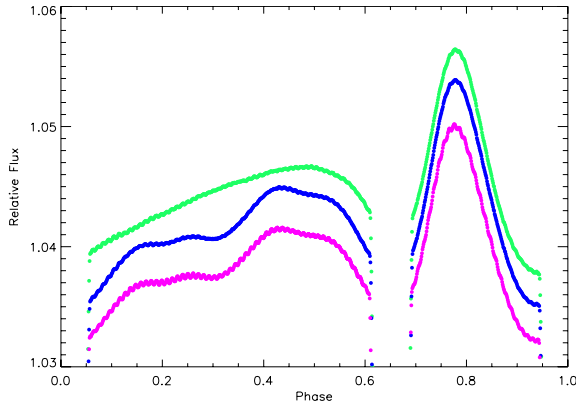


**Figure 11.** A magnified image of the phase-binned *Kepler* photometric SC light curve of Quarters 7 and 8 with no frequencies prewhitened (pink, bottom curve), all the frequencies *except* those that are harmonics prewhitened (blue, middle curve) and *all* the frequencies prewhitened (green, top curve). The blue and pink light curves only demonstrate a minimal difference as all non-commensurate pulsations are cancelled out when the data are phase binned. The only explanation for the remaining variation in the blue and pink light curves is that they are tidally excited pulsations. The light curves have been offset by 0.03 relative flux units for clarity.

resonant eigenfrequency and the orbital frequency, which increases the probability of observing this intriguing phenomenon significantly.

During the identification of the frequencies the data were masked so that the Fourier transform was only applied to the out-of-eclipse data. Consequently, it is unlikely that the presence of these frequencies in the Fourier transform can be completely attributed to an inadequate orbital solution. More convincingly, Fig. 11 shows a magnified image of the out-of-eclipse phase-binned data of Quarters 7 and 8 with no frequencies removed (pink, bottom curve), all the identified frequencies *except* the orbital harmonics removed (blue, middle curve) and *all* the identified frequencies removed (green, top curve). The pink light curve is visibly thicker than the blue light curve because the non-commensurate pulsations are still present, although have essentially cancelled out. We have no explanation for the prominent variations in the out-of-eclipse section of the light curve other than that they are tidally excited modes. We have also ruled out spots as the cause of the light-curve variations as spots are commensurate with the rotational frequency of the star and not the orbital frequency – our rotational velocity measurements are consistent with a pseudo-synchronous velocity; thus, we would expect peaks in the Fourier transform at multiples of 1.87 times the orbital frequency if the variations were caused by spots.

The p modes were analysed using the unmasked residual data from Quarters 7 and 8. To look for regular spacings we generated a diagram similar to an echelle diagram (Grec, Fossat & Pomerantz 1983), but modulo the orbital frequency (cf. Fig. 12). We prewhitened all g modes prior to the identification of the p modes to avoid any crosstalk from the window pattern. In Fig. 12 the filled circles represent the frequencies in Table 8 and the open circles represent frequencies with amplitudes in the region  $0.02\text{--}0.04 \times 10^{-3}$  relative flux units. The latter are not reported in our table as they are below our predefined confidence limit, although here they highlight the vertical groupings which indicate that many of the p-mode frequencies are multiplets split by the orbital frequency. Our working hypothesis is that the highest amplitude peak in a ver-

tical group is the self-excited p mode and the remaining p modes in that group are the product of non-linear coupling between the self-excited p modes and tidally induced g modes. To our knowledge this effect has not previously been observed and is considered an important tool for identifying g modes in the Sun (Chapellier et al. 2012). In our case, this deduction suggests that one of the stars is pulsating in both p modes and g modes, information that we could not have determined otherwise. An alternative hypothesis, suggested by Weinberg, Arras & Burkart (2013), states that through non-resonant three wave interactions the dynamical tide can excite daughter p-mode and g-mode waves; however, we refrain from discussing the physical nature of these modes at this time.<sup>3</sup>

Combination modes created from the same type of mode, however, have been observed in numerous stars including the  $\delta$  Scuti stars FG Virginis (Breger et al. 2005) and KIC 11754974 (Murphy, 2012 submitted), and the white dwarf star GD 358 (Winget et al. 1994). Brickhill (1983) determined that the likely cause of combination frequencies is non-linear interactions related to convective turn-over time-scales. Changes in the convective zone during the pulsation cycle cause a change in the amount of flux attenuation. This distorts the stellar shape and causes the pulsations to deviate from pure sinusoids generating combination frequencies in the Fourier transform.

Wu & Goldreich (2001) demonstrated that non-linear interactions could help with mode identification because non-linear mode coupling will only occur between specific modes and different modes generate different amplitude combinations, e.g.  $l = 2$  modes generate larger amplitude combination frequencies than  $l = 1$  modes. One of the most challenging requirements of modelling  $\delta$  Sct stars is mode identification; thus, combination frequencies could be key identifiers to obtaining a true asteroseismic model of the multitude of modes presented by this fascinating object.

## 7.2 Pulsation frequency modulation: the FM effect

Recently Shibahashi & Kurtz (2012) have shown that pulsating stars in binary orbits have frequency multiplets split by the orbital frequency in their amplitude spectra. This is a simple consequence of the light travel time effect causing the pulsation phases to be

<sup>3</sup> After this paper was submitted, we realized that the g modes whose frequencies are not multiples of the orbital harmonics (i.e.  $f_3, f_5, f_{19}$  and  $f_{25}$  from Table 8) are also indicative of non-linear tidal processes. Specifically, rather than having frequencies at orbital harmonics, these g modes have frequencies that *sum* to orbital harmonics. Note that  $f_3 + f_5 = 12v_{\text{orb}}$  and  $f_{19} + f_{25} = 7v_{\text{orb}}$ . These combination frequencies suggest that these modes are excited by parametric three-mode resonance, as detailed in Weinberg et al. (2012) and by Papaloizou & Pringle (1981). However, the non-linear driving mechanisms may be different for the two pairs of modes listed above. In the language of Weinberg et al. (2012), the excitation of  $f_{19}$  and  $f_{25}$  may be due to non-linear driving by the dynamical tide. Essentially, this is the standard three-mode coupling in which a parent mode non-linearly drives a pair of daughter modes whose frequencies sum to that of the parent mode, as observed in the KOI-54 system (Burkart et al. 2012; Fuller & Lai 2012). In this case, the parent mode is the dynamical tide at  $f_7 = 7v_{\text{orb}}$ , which is dominated by a nearly resonant g mode. The origin of  $f_3$  and  $f_5$  likely cannot be explained by this mechanism because there is no visible parent mode at  $f_3 + f_5 = 12v_{\text{orb}}$ . Instead, these modes are likely excited via non-linear driving by the equilibrium tide. In this case, the ‘parent’ mode is the component of the equilibrium tide that oscillates at 12 times the orbital frequency (which is dominated by the f mode rather than a g mode). These findings further substantiate our pulsational models which show that we do not expect to see  $\gamma$  Dor modes in either component.

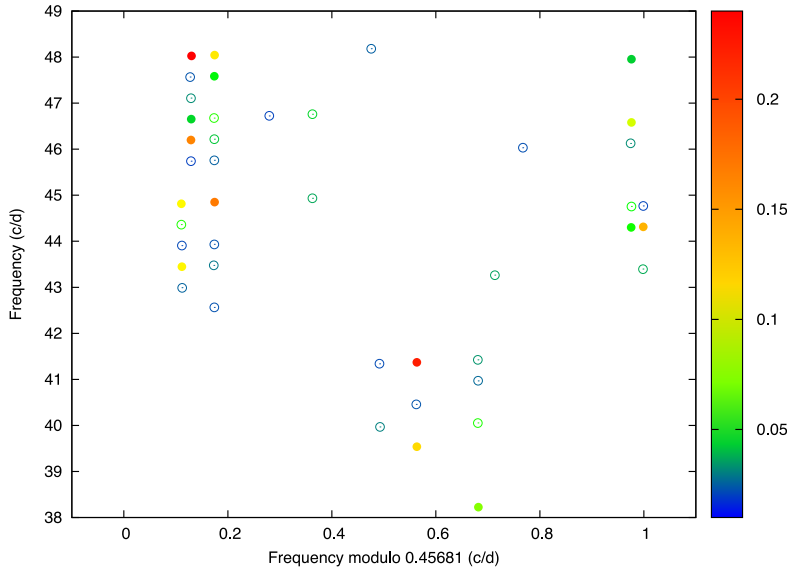


**Figure 12.** An echelle diagram of the p-mode frequencies modulo the orbital frequency using the SC *Kepler* data of Quarters 7 and 8. The points are coloured in terms of their amplitude in units of relative flux  $\times 10^{-3}$  (see the key at the right of the figure). The filled circles denote p-mode values taken from Table 8 and the open circles represent frequencies with amplitudes in the region  $0.02\text{--}0.04 \times 10^{-3}$  relative flux units, which are below our predefined confidence limit of  $3\sigma$ . The uncertainty in the frequencies is smaller than the points, thus not depicted. A high-pass filter was applied to the g-mode region prior to the identification of the p modes to remove any possible window pattern. The data was not masked.

periodically modulated by the orbital motion as seen by the observer. When the effect is large enough to be measured, RVs can be measured directly from the light curve without the need for spectroscopic RVs. Shibahashi & Kurtz (2012) demonstrate this by deriving the mass function from photometric data alone for the K-K binary and A star in the complex multiple system KIC 4150611 to better precision than has been possible with spectroscopic RVs.

In the case of KIC 4544587 this effect is not measurable, even at the extremely high precision of the *Kepler* data. Consequently, we are not able to complement our spectrally defined RV points with a photometrically defined RV curve. However, we are able to conclude that the frequency modulation (FM) signature is not present in our frequency spectrum and thus does not interfere with our frequency analysis. Shibahashi & Kurtz (2012) characterize the phase modulation with a parameter,  $\alpha$ , given by

$$\alpha = \frac{(2\pi GM_{\odot})^{1/3}}{c} \left( \frac{m_1}{M_{\odot}} \right)^{1/3} q(1+q)^{-2/3} \frac{P_{\text{orb}}^{2/3}}{P_{\text{osc}}} \sin i, \quad (3)$$

where  $P_{\text{osc}}$  is the pulsation period,  $P_{\text{orb}}$  is the orbital period,  $m_1$  is the mass of the primary star and  $q = m_1/m_2$  is the mass ratio. For KIC 4544587 the exact value of  $\alpha$  depends on which star is considered to be pulsating, which is not yet known, but  $\alpha \sim 0.04$ , in either case, since  $q \sim 1$ . For a value of  $\alpha$  this low, Shibahashi & Kurtz (2012) show that, to first order, a frequency triplet split by the orbital frequency is expected for each pulsation frequency, where the amplitude ratio of the side peaks to the central peak is given by

$$\frac{A_{+1} + A_{-1}}{A_n} \approx \alpha, \quad (4)$$

where  $A_{+1}$ ,  $A_{-1}$  and  $A_n$  represent the amplitudes of the peaks at  $f_n + \nu_{\text{orb}}$ ,  $f_n - \nu_{\text{orb}}$  and  $f_n$ , respectively, where  $\nu_{\text{orb}} = 1/P_{\text{orb}}$  is the orbital frequency. In addition, for this low value of  $\alpha$ , the side peaks have essentially the same amplitude.

Table 8 shows that the highest amplitude p mode in KIC 4544587,  $f_6 = 48.0240 \text{ d}^{-1}$ , has an amplitude of  $329 \mu\text{mag}$ . Therefore, we expect the orbital sidelobes generated by the light travel time effect to have amplitudes for this best case of about  $7 \mu\text{mag}$ , which is below the limit of detection in our data, but may ultimately be detectable with a more extensive *Kepler* data set.

### 7.3 Stellar evolution and pulsation models

To estimate the frequency content expected for stars similar to KIC 4544587, we calculated stellar evolution and pulsation models for single spherically symmetric non-rotating stars using the mass, radius and effective temperature constraints obtained from binary modelling and spectroscopic analysis. The models use the stellar evolution and pulsation codes described in Guzik et al. (2000), including an updated version of the Iben (1963, 1965) stellar evolution code with OPAL (Iglesias & Rogers 1996) opacities, Alexander & Ferguson (1994) low-temperature opacities, the Grevesse & Noels (1993) solar mixture and the Pesnell (1990) linear non-adiabatic stellar pulsation codes. We did not include diffusive helium, element settling or convective overshooting.

We do not know the interior abundances or ages of these stars. However, we attempted to find evolved models of the same initial composition and age that matched the constraints of the two stars in KIC 4544587. The models that were the closest to satisfying these criteria have helium abundance  $Y = 0.27$ , metallicity  $Z = 0.017$  and mixing length/pressure scaleheight 1.90, very near to the values calibrated for the Sun for these evolution and pulsation codes, and the Grevesse–Noels solar abundance mixture (see, e.g., Guzik & Mussack 2010). The age of the models is approximately 235 Myr. The observational constraints, plus the model parameters for two sets of models, are given in Table 9.

**Table 9.** Stellar properties derived from observations and stellar evolution models.  $Y$  and  $Z$  are initial helium and element mass fractions, respectively. The first set of models (column 3) has the same age and composition, while column 4 shows parameters for the best-fitting models that do not have the same age and abundances.

Parameters	Observations	Coeval models	Single best-fitting models
Primary			
Mass ( $M_{\odot}$ )	1.98(7)	1.95	1.98
Radius ( $R_{\odot}$ )	1.76(3)	1.73	1.76
$T_{\text{eff}}$ (K)	8600(100)	8774	8604
$Y$		0.27	0.28
$Z$		0.017	0.023
Age (Myr)		235	171
Secondary			
Mass ( $M_{\odot}$ )	1.60(6)	1.57	1.60
Radius ( $R_{\odot}$ )	1.43(2)	1.48	1.43
$T_{\text{eff}}$ (K)	7750(180)	7543	7813
$Y$		0.27	0.27
$Z$		0.017	0.016
Age (Myr)		235	0 (ZAMS)

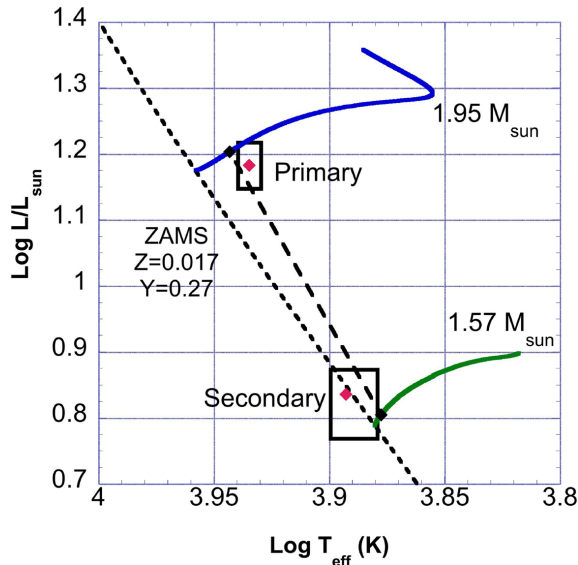


**Figure 13.** An H-R diagram for the models of Table 9. The boxes outline the parameter space for the observationally derived primary and secondary components. The short-dashed line is zero-age main-sequence position for stellar models with  $Z = 0.017$ ,  $Y = 0.27$ . Also shown are evolutionary tracks for a  $1.95\text{-}M_{\odot}$  (blue) and  $1.57\text{-}M_{\odot}$  (green) model. The two models with the same age and composition (column 3 of Table 9) closest to the observational constraints are connected by the long-dashed line. The red diamonds mark the best-fitting models for each star (column 4 of Table 9) that do not have exactly the same age and composition.

Fig. 13 shows the evolution tracks for stars of these masses and the observational constraints. The two coeval models miss the observational constraints by a small amount: it is difficult to find a secondary with a small enough radius, and a primary that is cool enough, for the same age. To gauge the magnitude of the problem, we also searched for single-star best-fitting models. We found

that we could fit the primary parameters exactly using a model with a higher metallicity (0.023), with age 171 Myr; the higher metallicity allowed a slightly higher mass and produced the desired lower effective temperature. For the secondary, we needed to reduce the metallicity to 0.016 to reduce the radius; the desired radius of  $1.43 R_{\odot}$  is reached at the zero-age main sequence (ZAMS).

We calculated the  $l = 0, 1$  and  $2$  non-adiabatic pulsation frequencies for the models in Table 9. For the models with age 235 Myr, we find that the  $1.95\text{-}M_{\odot}$  model is predicted to have only one unstable  $\delta$  Sct-type frequency for  $l = 0$  (7th overtone,  $59.4 \text{ d}^{-1}$ ),  $l = 1$  ( $56.3 \text{ d}^{-1}$ ) and  $l = 2$  ( $58.9 \text{ d}^{-1}$ ). The  $1.57\text{-}M_{\odot}$  model for the secondary is predicted to have unstable  $\delta$  Sct-type frequencies in a very wide range,  $21\text{--}90 \text{ d}^{-1}$  for the  $l = 0$  (radial) modes (fundamental through 10th overtones),  $21\text{--}93 \text{ d}^{-1}$  for the  $l = 1$  and  $22\text{--}96 \text{ d}^{-1}$  for the  $l = 2$  modes. Overall, the p-mode frequency content of KIC 4544587 seems to correspond better to that of the secondary, contrary to the findings of the  $Q$ -value equation, but these calculations do not rule out tidal excitation of modes in the primary.

The predicted unstable frequency content for the best-fitting non-coeval models in column 4 of Table 9 is similar, with the primary showing just a few p modes for each degree  $l = 0, 1$  and  $2$  between  $46$  and  $61 \text{ d}^{-1}$ , a little higher but overlapping the p-mode frequency range observed in KIC 4544587. For the  $1.60\text{-}M_{\odot}$  secondary, the range of unstable p modes is a little smaller than for the  $1.57\text{-}M_{\odot}$  higher metallicity model in column 3 of Table 9, and shows eight unstable modes between  $22$  and  $75 \text{ d}^{-1}$  for each degree  $l = 0, 1$  and  $2$ .

We also examined the possibility of unstable g-mode frequencies for these models in the observed range of  $1.5\text{--}3.5 \text{ d}^{-1}$ . While we can find many g modes for either  $l = 1$  or  $l = 2$  in this frequency range, all of the modes are stable. The models have envelope convection zones that are quite shallow, with a temperature at the base of  $50\,000\text{--}60\,000 \text{ K}$ , near or a little hotter than the region of second helium ionization. At this location, the convective time-scale at the convection zone base is shorter than the pulsation period, so  $\gamma$  Dor g modes are not expected to be pulsationally unstable via the convective blocking mechanism. Verification of this conclusion using a pulsation code with a time-dependent convection treatment would be worthwhile. On the other hand, in either star, g modes consistent with those observed could be tidally or stochastically excited.

While they are useful to guide expectations for intrinsic pulsation frequencies, these single-star non-rotating pulsation and evolution models are not adequate for an asteroseismic analysis. Tidal effects and rotation will distort the stars, and so the pulsation modes observed will not correspond to those calculated assuming spherical symmetry. Mode coupling will alter the observed frequencies. The surfaces of these stars are separated by only  $4.3 R_{\odot}$  at periastron. It is unlikely, but possible, that mass transfer occurred during an earlier evolution stage. In addition, tidal forces can cause mixing of hydrogen into the stellar core that would slow the evolution compared to that of single stars and alter the internal structure (Liakos et al. 2012).

## 8 SUMMARY AND CONCLUSIONS

We have presented the *Kepler* photometric and ground-based spectroscopic model of KIC 4544587, a detached eclipsing binary system with p-mode and g-mode pulsations, apsidal motion, tidally excited modes and combination frequencies. The SC data of Quarters 7 and 8 were used in the binary modelling and pulsation analysis

of KIC 4544587 with the exception of modelling the apsidal motion and eclipse timing variations where all available quarters were used. RV curves have been incorporated into the binary model, which were generated from 38 spectra obtained using ISIS on the WHT and five spectra using the echelle spectrograph on the 4-m Mayall telescope at KPNO.

The binary model was created using PHOEBE in an iterative process where the pulsations were identified in the residuals of the orbital fit and subsequently prewhitened to leave only the binary signature for modelling purposes. We were able to obtain a reasonable, but not completely ideal, binary model fit. Primarily this is due to the resonant pulsations in KIC 4544587, which have periods commensurate with the orbital period and do not diminish when phasing the data. However, it is also because of the inadequate treatment of certain physical parameters (most prominently gravity brightening, limb darkening and albedo) in the binary modelling process, highlighted by the precise nature of the *Kepler* data. Addressing this deficiency is a work in progress (Degroote et al., in preparation; Prša et al., in preparation).

A best-fitting model was obtained and uncertainty estimates were determined using a combination of formal errors and Monte Carlo simulations, which were used to determine uncertainties for parameters that are highly correlated. The distributions obtained in these simulations demonstrated minimal degeneracy, attesting to the uniqueness of the obtained binary solution. From the binary model fit, we determined the fundamental parameters of the stellar components. These include the mass and radius of the primary  $\delta$  Scuti component,  $1.98 \pm 0.07 M_{\odot}$  and  $1.82 \pm 0.03 R_{\odot}$  and the mass and radius of the secondary component,  $1.61 \pm 0.06 M_{\odot}$  and  $1.58 \pm 0.03 R_{\odot}$ . We also determined that the system has rapid apsidal motion,  $182 \pm 5$  yr per cycle, which may be partially attributable to the resonant pulsations.

The binary characteristics were subsequently separated from the inherent pulsations and 31 modes were identified, 14 in the g-mode region and 17 in the p-mode region. Of the 14 g-mode pulsations, 8 were found to have frequencies that are multiples of the orbital frequency; therefore, we conclude that the majority of these are tidally excited pulsations. 17 p-mode frequencies were identified in the residuals, many of which demonstrate separations that are multiples of the orbital frequency. Our current hypothesis is that these are combination modes, formed through the non-linear interactions between p modes and g modes. The stellar pulsation models predict many more unstable p modes for the secondary component than the primary, so it is possible that these p modes originate in the secondary component; however, the secondary could also have a few unstable p modes. The pulsation models show that neither star has a convection zone deep enough to produce unstable g modes, at least via the convective blocking mechanism. The g modes, however, could also be tidally driven and originate with either the primary or secondary. Further investigation into the non-linear mode interactions and tidal excitation of the pulsation modes will require modelling of pulsations in tidally distorted rotating stars, and is beyond the scope of this paper.

## ACKNOWLEDGEMENTS

We express our sincere thanks to NASA and the *Kepler* team for allowing us to work with and analyse the *Kepler* data, making this work possible. The *Kepler* mission is funded by NASA's Science Mission Directorate. This work was also supported by the Science and Technology Funding Council (STFC). We would also like to thank the RAS for providing grants which enabled KH's atten-

dance at conferences and thus enabled the development of collaborations and the successful completion of this work. AP acknowledges support through NASA Kepler PSP grant NNX12AD20G. The research leading to these results has received funding from the European Research Council under the European Community's Seventh Framework Programme (FP7/2007–2013)/ERC grant agreement no. 227224 (PROSPERITY), as well as from the Research Council of KU Leuven grant agreement GOA/2008/04. We acknowledge the observations taken using the 4-m Mayall telescope at the NOAO, survey number #11A-0022 and the Isaac Newton Group of Telescopes for the use of the William Herschel Telescope (WHT). The WHT is operated on the island of La Palma by the Isaac Newton Group in the Spanish Observatorio del Roque de los Muchachos of the Instituto de Astrofísica de Canarias. We would also like to thank Susan Thompson and William Welsh for their comments and suggestions.

## REFERENCES

- Abt H. A., 2009, *AJ*, 138, 28
- Aerts C., Christensen-Dalsgaard J., Kurtz D., 2010, *Astroseismology*. Springer, Berlin
- Alexander D. R., Ferguson J. W., 1994, *ApJ*, 437, 879
- Amado P. J., Moya A., Suárez J. C., Martín-Ruiz S., Garrido R., Rodríguez E., Catala C., Goupil M. J., 2004, *MNRAS*, 352, L11
- Antoci V. et al., 2011, *Nat*, 477, 570
- Baglin A. et al., 2006, in 36th COSPAR Scientific Assembly Vol. 36 of COSPAR, Plenary Meeting, CoRoT: A High Precision Photometer for Stellar Evolution and Exoplanet Finding. p. 3749
- Balona L. A., Krisciunas K., Cousins A. W. J., 1994, *MNRAS*, 270, 905
- Batalha N. M. et al., 2010, *ApJ*, 713, L109
- Borucki W. J. et al., 2010, *Sci*, 327, 977
- Breger M., 1970, *BAAS*, 2, 298
- Breger M., 2000, in Breger M., Montgomery M., eds, *ASP Conf. Ser. Vol. 210, Delta Scuti and Related Stars*. Astron. Soc. Pac., San Francisco, p. 3
- Breger M. et al., 2005, *A&A*, 435, 955
- Brickhill A. J., 1983, *MNRAS*, 204, 537
- Burkart J., Quataert E., Arras P., Weinberg N. N., 2012, *MNRAS*, 421, 983
- Buzasi D. L. et al., 2005, *ApJ*, 619, 1072
- Caldwell D. A. et al., 2010, *ApJ*, 713, L92
- Castelli F., Kurucz R. L., 2004, arXiv:preprints
- Castelli F., Gratton R. G., Kurucz R. L., 1997, *A&A*, 318, 841
- Chapellier E., Mathias P., Weiss W. W., Le Contel D., Debosscher J., 2012, *A&A*, 540, A117
- Charbonneau P., 1990, PhD thesis, Univ. Montreal, Canada
- Claret A., Gimenez A., 1993, *A&A*, 277, 487
- Fuller J., Lai D., 2012, *MNRAS*, 420, 3126
- García Hernández A., Moya A., Michel E., Garrido R., Suárez J. C., Rodríguez E., Amado P. J., Martín-Ruiz S., 2009, *A&A*, 506, 79
- Gies D. R., Williams S. J., Matson R. A., Guo Z., Thomas S. M., Orosz J. A., Peters G. J., 2012, *AJ*, 143, 137
- Gilliland R. L. et al., 2010, *PASP*, 122, 131
- Grec G., Fossat E., Pomerantz M. A., 1983, *Sol. Phys.*, 82, 55
- Grevesse N., Noels A., 1993, in Prantzos N., Vangioni-Flam E., Casse M., eds, *Origin and Evolution of the Elements*. Cambridge Univ. Press, Cambridge, p. 15
- Grigahcène A. et al., 2010a, *Astron. Nachr.*, 331, 989
- Grigahcène A. et al., 2010b, *ApJ*, 713, L192
- Guzik J. A., Mussack K., 2010, *ApJ*, 713, 1108
- Guzik J. A., Kaye A. B., Bradley P. A., Cox A. N., Neuforge C., 2000, *ApJ*, 542, L57
- Hadrava P., 1995, *A&AS*, 114, 393
- Hartmann E., 1998, *Comput.-Aided Geom. Des.*, 15, 377
- Hensberge H., Ilijic S., Torres K. B. V., 2008, *A&A*, 482, 1031
- Hut P., 1981, *A&A*, 99, 126

- Iben I., Jr, 1963, *ApJ*, 138, 452  
 Iben I., Jr, 1965, *ApJ*, 141, 993  
 Iglesias C. A., Rogers F. J., 1996, *ApJ*, 464, 943  
 Ilijic S., Hensberge H., Pavlovski K., Freyhammer L. M., 2004, in Hilditch R. W., Hensberge H., Pavlovski K., eds, *ASP Conf. Ser. Vol. 318, Obtaining Normalised Component Spectra with FDBinary*. Astron. Soc. Pac., San Francisco, p. 111  
 Kjeldsen H., Christensen-Dalsgaard J., Handberg R., Brown T. M., Gilliland R. L., Borucki W. J., Koch D., 2010, *Astron. Nachr.*, 331, 966  
 Kovács G., Zucker S., Mazeh T., 2002, *A&A*, 391, 369  
 Lefèvre L. et al., 2009, *Commun. Asteroseismol.*, 158, 189  
 Lenz P., Breger M., 2004, in Zverko J., Ziznovsky J., Adelman S. J., Weiss W. W., eds, *Proc. IAU Symp. 224, The A-Star Puzzle*. Cambridge Univ. Press, Cambridge, p. 786  
 Li J. et al., 2010, in Radziwill N. M., Bridger A., eds, *Proc. SPIE Conf. Ser. Vol. 7740, Photometer Performance Assessment in Kepler Science Data Processing*. SPIE, Bellingham, p. 11  
 Liakos A., Niarchos P., Soydugan E., Zasche P., 2012, *MNRAS*, 422, 1250  
 Lomb N. R., 1976, *Ap&SS*, 39, 447  
 Maceroni C. et al., 2009, *A&A*, 508, 1375  
 Marsh T. R., 1989, *PASP*, 101, 1032  
 Pamyatnykh A. A., 2000, in Breger M., Montgomery M., eds, *ASP Conf. Ser. Vol. 210, Delta Scuti and Related Stars*. Astron. Soc. Pac., San Francisco, p. 215  
 Papaloizou J., Pringle J. E., 1981, *MNRAS*, 196, 371  
 Pavlovski K., Hensberge H., 2005, *A&A*, 439, 309  
 Pavlovski K., Hensberge H., 2010, in Prša A., Zejda M., eds, *ASP Conf. Ser. Vol. 435, Binaries – Key to Comprehension of the Universe*. Astron. Soc. Pac., San Francisco, p. 207  
 Pesnell W. D., 1990, *ApJ*, 363, 227  
 Prša A., Zwitter T., 2005, *ApJ*, 628, 426  
 Prša A. et al., 2011, *AJ*, 141, 83  
 Rodríguez E., Breger M., 2001, *A&A*, 366, 178  
 Rucinski S. M., 1992, *AJ*, 104, 1968  
 Scargle J. D., 1982, *ApJ*, 263, 835  
 Schwarzenberg-Czerny A., 1989, *MNRAS*, 241, 153  
 Shibahashi H., Kurtz D. W., 2012, *MNRAS*, 422, 738  
 Simon K. P., Sturm E., 1994, *A&A*, 281, 286  
 Smalley B., Smith K. C., Dowretsky M. M., 2001  
 Stellingwerf R. F., 1979, *ApJ*, 227, 935  
 Tamajo E., Pavlovski K., Southworth J., 2011, *A&A*, 526, A76  
 Thompson S. E. et al., 2012, *ApJ*, 753, 86  
 Uytterhoeven K. et al., 2011, *A&A*, 534, A125  
 Van Cleve J. E., 2009, *Kepler Data Release 6 Notes (KSCI-19046-001)*, NASA Ames Research Center, Moffett Field, CA, USA  
 Walker G. et al., 2003, *PASP*, 115, 1023  
 Weinberg N. N., Arras P., Quataert E., Burkart J., 2012, *ApJ*, 751, 136  
 Weinberg N. N., Arras P., Burkart J., 2013, *arXiv:e-prints*  
 Welsh W. F. et al., 2011, *ApJS*, 197, 4  
 Willems B., Aerts C., 2002, in Aerts C., Bedding T. R., Christensen-Dalsgaard J., eds, *ASP Conf. Ser. Vol. 259, IAU Colloq. 185: Radial and Nonradial Pulsations as Probes of Stellar Physics*. Astron. Soc. Pac., San Francisco, p. 76  
 Wilson R. E., 1979, *ApJ*, 234, 1054  
 Wilson R. E., Devinney E. J., 1971, *ApJ*, 166, 605  
 Wilson R. E., Van Hamme W., 2004, *Computing Binary Star Observables (in Reference Manual to the Wilson-Devinney Program)*, Univ. Florida, Gainesville  
 Winget D. E. et al., 1994, *ApJ*, 430, 839  
 Witte M. G., Savonije G. J., 1999, *A&A*, 350, 129  
 Wu Y., Goldreich P., 2001, *ApJ*, 546, 469  
 Zahn J.-P., 1975, *A&A*, 41, 329  
 Zucker S., Mazeh T., 1994, *ApJ*, 420, 806

This paper has been typeset from a  $\text{\TeX}/\text{\LaTeX}$  file prepared by the author.

# Chapter 8

## KIC 8569819

This chapter features a published case study of the detailed study of KIC 8569819, a binary star with high-amplitude pulsations that enabled the clear application of the FM (frequency modulation) method. This case study, while not of a heartbeat star, utilizes the program created to model heartbeat stars, discussed in Chapter 3.

I am the second author of this publication and personally led the binary star modelling effort. This included creating a full, self-consistent binary star model and writing §4 entitled “Binary Modelling”. D. Kurtz led the project and wrote the majority of the publication. H. Shibahashi and S. Murphy contributed to the theoretical aspect including discussion and editing of the publication. A. Prša analysed the eclipse timing variations, discussed in subsection 3.2 entitled “Further FM of  $\nu_1$ : a cautionary tale”.

# Validation of the frequency modulation technique applied to the pulsating $\delta$ Sct– $\gamma$ Dor eclipsing binary star KIC 8569819

Donald W. Kurtz,<sup>1</sup>★ Kelly M. Hambleton,<sup>1,2</sup> Hiromoto Shibahashi,<sup>3</sup>  
Simon J. Murphy<sup>1,4</sup> and Andrej Prša<sup>2,1</sup>

<sup>1</sup>Jeremiah Horrocks Institute, University of Central Lancashire, Preston PR1 2HE, UK

<sup>2</sup>Department of Astrophysics and Planetary Science, Villanova University, Villanova 19087, USA

<sup>3</sup>Department of Astronomy, The University of Tokyo, Bunkyo-ku, Tokyo 113-0033, Japan

<sup>4</sup>Sydney Institute for Astronomy, School of Physics, Department of Astronomy, The University of Sydney, NSW 2006, Australia

Accepted 2014 October 1. Received 2014 September 29; in original form 2014 August 17

## ABSTRACT

KIC 8569819 is an eclipsing binary star with an early F primary and G secondary in a 20.85-d eccentric orbit. The primary is a  $\delta$  Sct– $\gamma$  Dor star pulsating in both p modes and g modes. Using four years of *Kepler* Mission photometric data, we independently model the light curve using the traditional technique with the modelling code PHOEBE, and we study the orbital characteristics using the new frequency modulation technique. We show that both methods provide the equivalent orbital period, eccentricity and argument of periastron, thus illustrating and validating the FM technique. In the amplitude spectrum of the p-mode pulsations, we also discovered an FM signal compatible with a third body in the system, a low-mass M dwarf in an 861-d orbit around the primary pair. However, the eclipses show no timing variations, indicating that the FM signal is a consequence of the *intrinsic* change in pulsation frequency, thus providing a cautionary tale. Our analysis shows the potential of the FM technique using *Kepler* data, and we discuss the prospects to detect planets and brown dwarfs in *Kepler* data for A and F stars even in the absence of transits and with no spectroscopic radial velocity curves. This opens the possibility of finding planets orbiting hotter stars that cannot be found by traditional techniques.

**Key words:** techniques: radial velocities – stars: individual: KIC 8569819 – stars: oscillations – stars: variables:  $\delta$  Scuti.

## 1 INTRODUCTION

Binary stars are a primary source of fundamental information about stars, particularly their masses and radii. For asteroseismology, modelling of stellar pulsations depends on external determinations of effective temperature and surface gravity, usually from spectroscopy. For heat-driven pulsators where masses and radii cannot be derived from the pulsation frequency spectrum, independent information from eclipsing binary modelling provides important constraints that narrow the range of possible asteroseismic models. Where pulsating stars are found in binaries, the synergy of the independent techniques from asteroseismology and from the physics of the binary orbit greatly improves our astrophysical inferences about the stars and our confidence in the models that describe them.

The *Kepler* Space Mission collected time series light curves of over 190 000 stars over its four-year main mission lifetime from 2009 to 2013. *Kepler* has an orbital period about the Sun of

372.4536 d; during the main mission, the satellite performed four quarterly rolls (quarters are just over 93 d) per orbit of the Sun. It acquired data of the same field with a  $\sim 92$  per cent duty cycle. Its mission is to find extrasolar planets, with emphasis on Earth-like planets and planets in the habitable zone. Its planet candidate list has 4234 entries<sup>1</sup> as of 2014 August, nearly 1000 of which have been confirmed; in time, 95 per cent are expected to be confirmed. It also has a list of 2645 EB stars.<sup>2</sup> More than 500 main-sequence and subgiant solar-like pulsators have been studied asteroseismically with fundamental parameters derived (Chaplin et al. 2014). These are critical for the characterization of extrasolar planets orbiting those stars, so that the asteroseismology and planet studies are synergistic. About 13 000 red giant stars have been studied asteroseismically (Mosser, Belkacem & Vrard 2013; Stello et al. 2013), leading to a better understanding of the stellar structure of giants, and even allowing the determination of core and surface rotation rates

\*E-mail: [dwkurtz@uclan.ac.uk](mailto:dwkurtz@uclan.ac.uk)

<sup>1</sup> <http://kepler.nasa.gov/Mission/discoveries/candidates/>

<sup>2</sup> <http://keplerebs.villanova.edu>

(Beck et al. 2012), initiating *observational* studies of angular momentum transport in stars with stellar evolution. With *Kepler* data, there has now even been an asteroseismic determination of core-to-surface rotation in a main-sequence star (Kurtz et al. 2014).

The emphasis of the *Kepler* search for habitable planets has been on cool stars, where transits are easier to detect because of the larger planet-to-star size ratio and the proximity of the habitable zones to the host star, hence the shorter orbital periods. The pulsations in cooler stars are stochastically excited by energy in the atmospheric convection zone. The stars show high radial overtone pulsations that are asymptotically nearly equally spaced in frequency, allowing mode identification, and ultimately the extraction of stellar mass, radius and age (Aerts, Christensen-Dalsgaard & Kurtz 2010). The best-calibrated cases, such as  $\alpha$  Cen (see chapter 7.2.3 of Aerts et al. 2010), allow mass and radius to be determined independently from astrometry and from interferometry. Comparison of the fundamental techniques with the asteroseismic results suggests that asteroseismic masses and radii are as accurate as 2 per cent in the best cases.

Hotter stars in *Kepler* data are studied less. This is particularly true for the  $\delta$  Sct and  $\gamma$  Dor stars, where matching models to the observed frequency spectra remains a challenge. Compared with cooler stars, hot stars are not well suited for planetary searches either, for two principal reasons: (i) the transits across the much brighter discs are smaller and more difficult to detect, and can be hidden in the much larger amplitude pulsational variations of most A stars; and (ii) ground-based radial velocity studies to determine the masses of companion exoplanets are more difficult because of the higher masses of the hotter main-sequence stars and because of the rotationally broadened spectral lines compared to cooler stars below the Kraft (rotational) break near mid-F spectral type. The first example of a transiting exoplanet orbiting a pulsating  $\delta$  Sct star is WASP-33b (HD 15082), where  $\delta$  Sct pulsations of amplitude about 1 mmag were found subsequent to the transit discovery (Herrero et al. 2011). This star has generated considerable interest with further infrared (Deming et al. 2012) and optical studies and models (Kovács et al. 2013; von Essen et al. 2014). The interest is primarily in the use of pulsation characteristics as probes of interactions between the planet and the star. The extrasolar planets encyclopedia<sup>3</sup> lists only a handful of planets around A stars, the most notable being Fomalhaut b (Kalas et al. 2013), the four planets orbiting the  $\gamma$  Dor star HR 8799 (Marley et al. 2012), and V342 Peg (Esposito et al. 2013), which have been directly imaged. In consequence, the prevalence of exoplanets orbiting upper main-sequence stars is essentially unknown.

Shibahashi & Kurtz (2012) developed a new technique for determining orbital parameters of binaries that is based on frequency modulation. This dramatically extends our ability to study binary stars in the *Kepler* data set by providing a method that yields traditional ‘spectroscopic’ orbital parameters from photometry alone. Many of the thousands of  $\delta$  Sct stars in the *Kepler* data set have stable pulsation frequencies. For those stars that are in binary systems, the pulsation frequency is modulated by the orbital motion, producing equally split frequency multiplets in the amplitude spectrum that can be unambiguously identified. Shibahashi & Kurtz (2012) show how these multiplets can be used to determine the orbital frequency, the mass function (as in a spectroscopic single-lined binary star),  $a \sin i$  for the pulsating primary star and the eccentricity. More recently, Shibahashi, Kurtz & Murphy (in preparation) have extended the technique to include the determination of the argument

of periastron. These are all parameters that in the past required a large spectroscopic data set to determine radial velocities. Recently, Murphy et al. (2014) developed an analogous technique based on phase modulation (PM). This technique is equivalent to FM, and is more easily automated.

In this paper, we focus on KIC 8569819, an EB in an eccentric orbit with a primary star that is a pulsating  $\delta$  Sct- $\gamma$  Dor star. We derive orbital parameters independently from both the EB light curve fitting, and from the FM technique.

## 2 KIC 8569819: AN ECLIPSING BINARY FM STAR

KIC 8569819 is a  $Kp = 13.0$  eclipsing binary with  $T_{\text{eff}} = 7100$  K and  $\log g = 4.0$  (cgs units) in the *Kepler* Input Catalogue (KIC; see Huber et al. 2014 for a discussion of errors in the KIC; at this temperature and surface gravity, they are about  $\pm 250$  K in  $T_{\text{eff}}$  and  $\pm 0.2$  in  $\log g$ ). The contamination parameter is 0.237, but a visual check of the pixel-level data shows that the mask used in the reductions does not include the nearest possible contaminating star.

The data used for the analysis in this paper are *Kepler* quarters 0 to 17 (Q0–Q17) long cadence (LC) data with 29.4-min integration times. We used the multiscale, maximum a posteriori (msMAP) pipeline data; information on the reduction pipeline can be found in the *Kepler* data release notes<sup>4</sup> 21. Fig. 1 depicts a light curve for KIC 8569819 for a section of the LC msMAP data where we can see both primary and secondary eclipses. The separation between the eclipses is close to 0.5, but closer examination shows that primary eclipse lasts for about 13 h, and secondary for 6.5 h, requiring a high eccentricity of  $e \approx 0.4$ , detailed in Section 4. The eclipses are flat-bottomed (total), therefore  $i \approx 90^\circ$ . The primary eclipse takes longer: it occurs near apastron, with the cooler companion being in front.

The FM analysis of KIC 8569819 is presented in Section 3 and the EB light curve analysis in Section 4. These two analyses were performed independently for objective comparison of the results.

## 3 FM ANALYSIS OF KIC 8569819

### 3.1 FM of $\nu_1$ : the 20.85-d binary

For the analysis of the pulsation frequencies, we have masked out the eclipses from the light curve. This is necessary because of the high-amplitude peaks they generate at low frequency in the amplitude spectrum; these have spectral window patterns that extend out to the  $\delta$  Sct range of the pulsation frequencies. The pulsation amplitudes also change during eclipses because of the changing background light level, and because of the partial obscuration of the pulsating star during ingress and egress of the primary eclipse. That generates amplitude modulation sidelobes to the pulsation peaks separated by exactly the orbital frequency, hence overlapping with the FM signal that we are studying. Unless the binary star model encompasses a full description of the pulsations, masking the data set is preferred to subtracting a binary model fit alone.

Fig. 2 shows the amplitude spectrum out to nearly the Nyquist frequency ( $\sim 24.5 \text{ d}^{-1}$ ) for KIC 8569819 for the masked Q0–17 LC data. There are pulsations in both the g-mode and p-mode frequency regions. Since the relative amplitude of the FM sidelobes to the amplitude of the central peak, i.e. the detectability of the FM signal,

<sup>3</sup> <http://exoplanet.eu>

<sup>4</sup> [https://archive.stsci.edu/kepler/data\\_release.html](https://archive.stsci.edu/kepler/data_release.html)

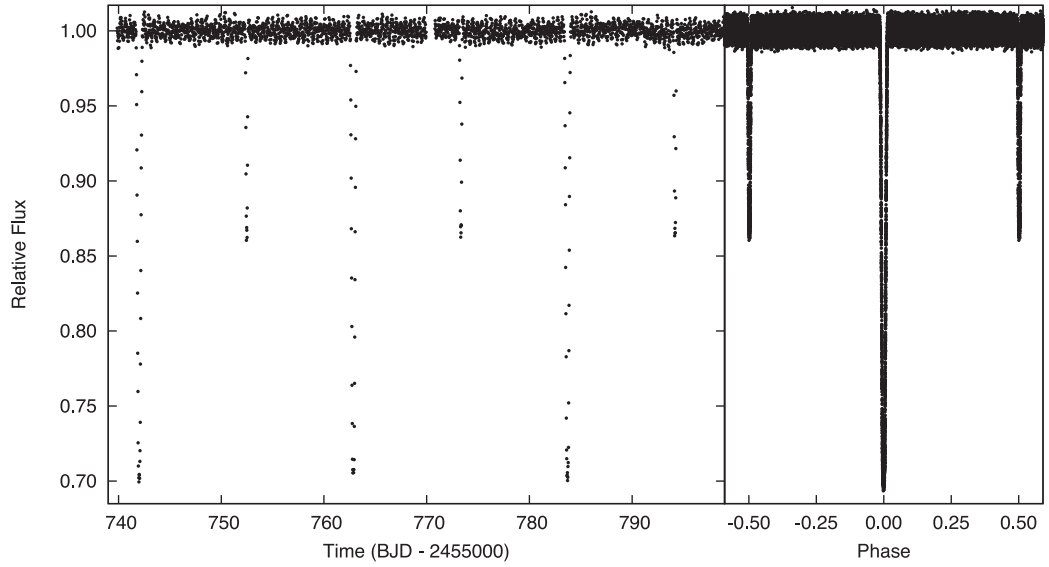


**Figure 1.** A phased light curve of KIC 8569819 for the Q0–17 msMAP LC data with no further processing. The left-hand panel shows three cycles of the 20.84-d binary orbit with primary and secondary eclipses. The right-hand panel shows the full Q0–17 LC data set phased on the orbital period.

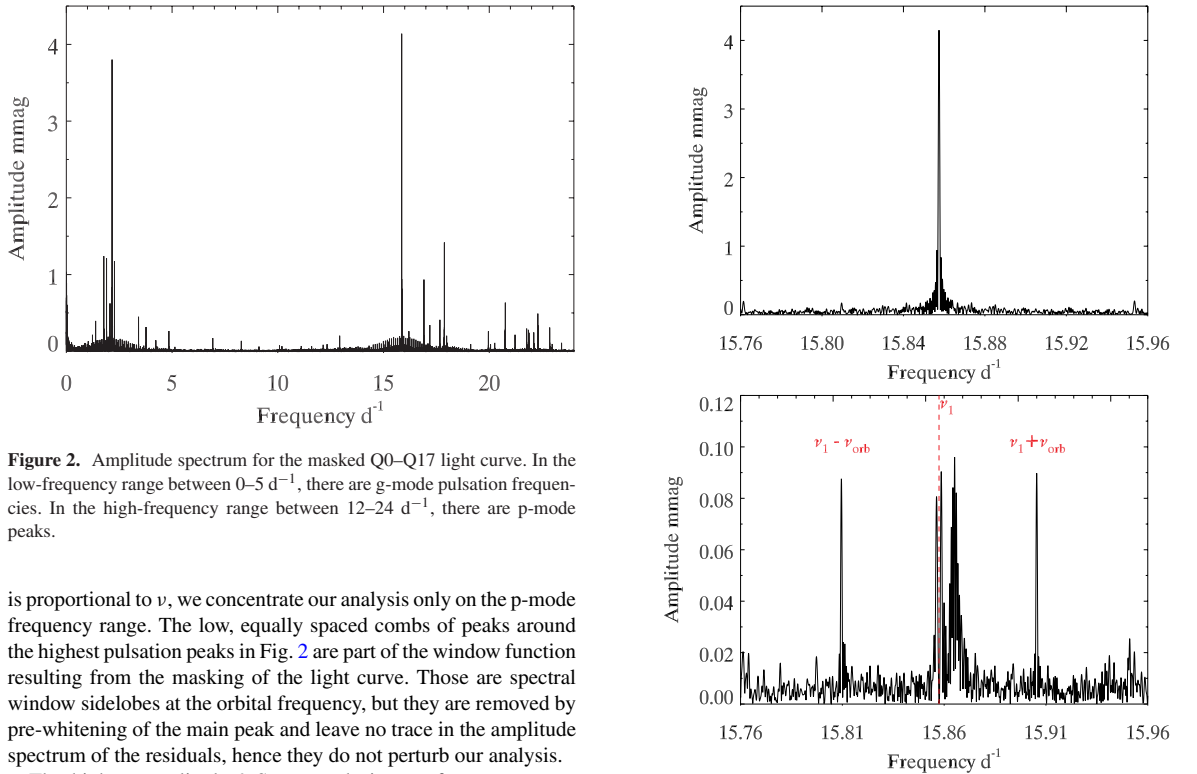


**Figure 2.** Amplitude spectrum for the masked Q0–Q17 light curve. In the low-frequency range between 0–5  $\text{d}^{-1}$ , there are g-mode pulsation frequencies. In the high-frequency range between 12–24  $\text{d}^{-1}$ , there are p-mode peaks.

is proportional to  $\nu$ , we concentrate our analysis only on the p-mode frequency range. The low, equally spaced combs of peaks around the highest pulsation peaks in Fig. 2 are part of the window function resulting from the masking of the light curve. Those are spectral window sidelobes at the orbital frequency, but they are removed by pre-whitening of the main peak and leave no trace in the amplitude spectrum of the residuals, hence they do not perturb our analysis.

The highest amplitude  $\delta$  Sct p mode is at a frequency  $\nu_1 = 15.8574687(5) \text{ d}^{-1}$  and is shown in the top panel of Fig. 3. For an estimate of the p-mode radial overtone, it is useful to calculate the  $Q$  value for  $\nu_1$ . This is defined to be

$$Q = P_{\text{osc}} \sqrt{\frac{\rho}{\rho_{\odot}}}, \quad (1)$$

**Figure 3.** Top: an amplitude spectrum for the masked Q0–Q17 light curve in the  $\delta$  Sct frequency range of the highest amplitude p mode. Bottom: after pre-whitening  $\nu_1$ . There are important peaks on either side of  $\nu_1$  that are discussed in the text. Here, note the equally spaced sidelobes near  $\nu = 15.81 \text{ d}^{-1}$  and  $15.91 \text{ d}^{-1}$  that are separated from  $\nu_1$  by  $\nu_{\text{orb}}$ . These are the FM first sidelobes. There is some visual indication of the presence of the second sidelobes.

**Table 1.** A non-linear least-squares fit of the highest amplitude frequency seen in Fig. 3 and its first orbital FM sidelobes to the Q0–Q17 LC masked *Kepler* data for KIC 8569819. The frequencies are separated by  $\nu_{\text{orb}} = 0.047964 \pm 0.000014 \text{ d}^{-1}$ . The zero-point in time for the phase is BJD 245 5672.2.

	Frequency ( $\text{d}^{-1}$ )	Amplitude (mmag)	Phase (rad)
$\nu_1 - \nu_{\text{orb}}$	$15.8095167 \pm 0.0000211$	$0.089 \pm 0.005$	$2.9067 \pm 0.0561$
$\nu_1$	$15.8574721 \pm 0.0000005$	$4.150 \pm 0.005$	$2.4425 \pm 0.0012$
$\nu_1 + \nu_{\text{orb}}$	$15.9054555 \pm 0.0000197$	$0.096 \pm 0.005$	$-1.2593 \pm 0.0524$
$\nu_{\text{orb}1} = \nu_1 - (\nu_1 - \nu_{\text{orb}})$	$0.047955 \pm 0.000021$		
$\nu_{\text{orb}2} = (\nu_1 + \nu_{\text{orb}}) - \nu_1$	$0.047973 \pm 0.000020$		
$\nu_{\text{orb}1} - \nu_{\text{orb}2}$	$0.000018 \pm 0.000029$		
$\nu_{\text{orb}} \equiv \langle \nu_{\text{orb}1}, \nu_{\text{orb}2} \rangle$	$0.047964 \pm 0.000014$		
$P_{\text{orb}} \text{ (d)}$	$20.849 \pm 0.006$		

where  $P_{\text{osc}}$  is the pulsation period and  $\bar{\rho}$  is the mean density.  $Q$  is known as the ‘pulsation constant’. Using the definition of mean density as  $\bar{\rho} = \frac{M}{\frac{4}{3}\pi R^3}$ , surface gravity as  $g = \frac{GM}{R^2}$ , absolute luminosity as  $L = 4\pi R^2 \sigma T_{\text{eff}}^4$  and absolute magnitude as  $M_{\text{bol}} = -2.5 \log L + \text{constant}$ , equation (1) can be rewritten as

$$\log Q = -6.454 + \log P_{\text{osc}} + \frac{1}{2} \log g + \frac{1}{10} M_{\text{bol}} + \log T_{\text{eff}}, \quad (2)$$

where  $P_{\text{osc}}$  is given in d,  $\log g$  is in cgs units and  $T_{\text{eff}}$  is in K. Using the KIC values of  $T_{\text{eff}} = 7100 \text{ K}$  and  $\log g = 4.0$ , and estimating the bolometric magnitude to be 2.8, we obtain  $Q = 0.030$ , typical of fundamental to first overtone pulsation in  $\delta$  Sct stars (Stellingwerf 1979). We thus conclude that the p-mode frequencies are likely to be due to low overtone modes. Pre-whitening the data by  $\nu_1$  gives the amplitude spectrum of the residuals depicted in the bottom panel of Fig. 3, where the first FM orbital sidelobes are annotated.

Table 1 shows the non-linear least-squares fit of  $\nu_1$  and its first FM orbital sidelobes. The formal errors from the least-squares fit include all of the variance in the data, which (as can be seen in Fig. 2) includes astrophysical variance due to all pulsation frequencies in both the g-mode and p-mode regions. To estimate the intrinsic scatter, we focused on a featureless section of the amplitude spectrum in the range 9–10  $\text{d}^{-1}$ . The highest peaks in that region have amplitudes of  $\sim 20 \mu\text{mag}$ . For an amplitude spectrum with this density of frequencies, even for normally distributed data we expect numerous peaks with amplitudes greater than  $3\sigma$ , and in practice we find that the highest amplitude peaks have amplitudes about four times the formal amplitude error for the least-squares fit. We therefore estimate the amplitude error to be  $0.005 \text{ mmag}$  ( $20 \mu\text{mag}/4$ ). Since phase and frequency errors scale with amplitude error (Montgomery & O’Donoghue 1999), we scale the formal errors for frequency and phase in Table 1 by the same factor as the revised error in amplitude.

The frequency triplet in Table 1 is equally split; the two splittings agree to  $0.6\sigma$ , suggesting that our reduced errors are conservative. The average of the two splittings is the orbital frequency,  $\nu_{\text{orb}} = 0.047964 \pm 0.000014 \text{ d}^{-1}$ . This differs by  $0.14\sigma$  from  $\nu_{\text{orb}} = 0.047962 \text{ d}^{-1}$  obtained by phase-folding the eclipses (cf. Fig. 1). Phase-folding provides a more precise orbital frequency than the FM signal because of the much higher signal-to-noise ratio for the eclipses compared to the orbital pulsational frequency shifts. The agreement between the two methods is excellent.

Next, we re-fit the frequency multiplet by forcing the splitting to be exactly equal. There is no significant difference to the result whether the orbital period is chosen from the frequency splitting or from phase-folding, so to keep the FM analysis independent, we

**Table 2.** A least-squares fit of the frequency quintuplet for the highest amplitude mode to the Q0–Q17 LC *Kepler* data for KIC 8569819. The frequencies of the multiplet are separated by the orbital frequency,  $\nu_{\text{orb}} = 0.047964 \pm 0.000014 \text{ d}^{-1}$  ( $P_{\text{orb}} = 20.849 \pm 0.006 \text{ d}$ ). The zero-point for the phases has been chosen to be a time when the phases of the first sidelobes to the highest amplitude frequency are equal,  $t_0 = \text{BJD } 245\,5679.120\,90$ . It can be seen that the phases of the first sidelobes differ from that of the phase of  $\nu_1$  by  $-1.62 \pm 0.06 \text{ rad}$ , which is equal to  $\pi/2$  as required by the theory (Shibahashi & Kurtz 2012). The mass function and orbital eccentricity are derived from the sidelobes’ amplitudes.

	Frequency ( $\text{d}^{-1}$ )	Amplitude (mmag)	Phase (rad)
$\nu_1 - 2\nu_{\text{orb}}$	15.761 5434	$0.014 \pm 0.005$	$-3.0812 \pm 0.2775$
$\nu_1 - \nu_{\text{orb}}$	15.809 5077	$0.089 \pm 0.005$	$-0.7630 \pm 0.0561$
$\nu_1$	15.857 4721	$4.148 \pm 0.005$	$0.8593 \pm 0.0012$
$\nu_1 + \nu_{\text{orb}}$	15.905 4365	$0.096 \pm 0.005$	$-0.7630 \pm 0.0541$
$\nu_1 + 2\nu_{\text{orb}}$	15.953 4009	$0.022 \pm 0.005$	$2.9350 \pm 0.2029$

use the value from Table 1. For the study of orbital characteristics using the FM technique (Shibahashi & Kurtz 2012), it is important that the splittings are exactly equal; we are then able to use the phase information, since frequency and phase are coupled in the Fourier sinusoidal description.

This coupling between frequency and phase is easy to see. The function we fit to our data has the form  $\cos(\omega t + \phi)$ , where  $\omega = 2\pi\nu$  is the angular frequency. If we imagine a change to the angular frequency such that  $\omega' = \omega + \delta\omega$ , then we can write the argument of the cosine function to be  $\omega't + \phi = (\omega + \delta\omega)t + \phi = \omega t + (\phi + \delta\omega t) = \omega t + (\phi + \delta\phi) = \omega t + \phi'$  where  $\phi' = \phi + \delta\omega t$ . It is not possible to distinguish between a change  $\delta\omega$  to the frequency or a change  $\delta\phi$  to the phase without an external constraint.

Table 2 lists the results of fitting the equally spaced quintuplet for the highest amplitude  $\delta$  Sct mode to the data. The zero-point in time, BJD 245 5679.120 90  $\pm 0.26$ , has been chosen to set the phases of the first FM sidelobes equal; the error in the zero-point is derived from  $1\sigma$  in the difference between the sidelobe phases. This zero-point corresponds to the time when the motion of the stars is perpendicular to the line of sight. Thus, by measuring the difference between the zero-point time and the time of superior conjunction, we can derive the argument of periastron. The time difference can be converted to a phase difference, and the phase difference, via mean and eccentric anomaly, converted to true anomaly. The true anomaly is a measure of the angle between the point of the orbit where

$v_r = 0$  and superior conjunction; a simple Keplerian integrator can be employed to solve this for the argument of periastron, which yields  $\omega = 4.59 \pm 0.16$  rad.

The difference between the first sidelobe phases and the central peak phase is  $-1.62 \pm 0.06$  rad, which is equal to  $-\pi/2$  within the errors, as expected from the FM theory. The minus sign indicates that the line-of-sight crossing of the pulsating star occurs on the far side of the orbit for the chosen time zero-point,  $t_0$ . This phase relationship demonstrates that the frequency triplet describes pure frequency modulation, as expected for FM.

Shibahashi & Kurtz (2012) define a parameter  $\alpha$  that measures the amplitude of the phase modulation when the pulsation frequency is treated as fixed (equation 4 therein). When  $\alpha \ll 1$ , it is given by

$$\alpha = \frac{A_{+1} + A_{-1}}{A_0}, \quad (3)$$

where  $A_{+1}$  and  $A_{-1}$  are the observed amplitudes of the first FM sidelobes, and  $A_0$  is the observed amplitude of the central peak of the FM multiplet. From Table 2, we then find for KIC 8569819 that  $\alpha = 0.0444 \pm 0.0017$ . From this amplitude ratio, the pulsation period and the orbital period, the mass function can be derived:

$$f(m_1, m_2, \sin i) \equiv \frac{(m_2 \sin i)^3}{(m_1 + m_2)^2} = \alpha^3 \frac{P_{\text{osc}}^3}{P_{\text{orb}}^2} \frac{c^3}{2\pi G}. \quad (4)$$

Using the data in Table 2, we find  $f(m_1, m_2, \sin i) = 0.141 \pm 0.016 M_\odot$ . Adopting a typical mass of  $m_1 = 1.7 M_\odot$  for the primary and  $i \approx 90^\circ$ , a secondary mass is  $m_2 = 1 M_\odot$ , hence the companion to the  $\delta$  Sct star is probably a solar-like main-sequence star.

We can also derive the semimajor axis of the primary star about the barycentre. That is given by

$$a_1 \sin i = \frac{P_{\text{osc}}}{2\pi} \alpha c, \quad (5)$$

from which we find  $a_1 \sin i = 0.0772 \pm 0.0030$  au.

To derive the eccentricity of the system, we have fitted a frequency quintuplet split by the orbital frequency about  $\nu_1$  to the Q0–17 LC data as shown in Table 2. While the second FM sidelobes in Fig. 3 are only marginally visible, the least-squares fit shows them to be significant to  $2.8\sigma$  and  $4.4\sigma$ . The false alarm probability of finding peaks of this significance at *particular* frequencies (i.e. the second FM sidelobes) is  $F = \exp(-z)$  (Horne & Baliunas 1986), where  $z$  is the power signal-to-noise ratio. Taking an average amplitude signal-to-noise ratio of 3.6 for our second FM sidelobes gives  $z = 12.96$  and  $F = 2.4 \times 10^{-6}$ . Hence, we can use the FM sidelobes to derive the eccentricity:

$$e = \frac{2(A_{+2} + A_{-2})}{(A_{+1} + A_{-1})} = 0.39 \pm 0.08, \quad (6)$$

where  $A_{+2}$  and  $A_{-2}$  are the observed amplitudes of the second FM sidelobes. While the phases of the second sidelobes contain information about the argument of periastron, the errors are too large to use them in this case.

### 3.2 Further FM of $\nu_1$ : a cautionary tale

We now return to the peaks in the immediate vicinity of  $\nu_1$  (cf. bottom panel of Fig. 3, and the zoomed pre-whitened region in Fig. 4). A multiplet of peaks and a doublet can be seen in the amplitude spectrum after  $\nu_1$  has been pre-whitened. The multiplet on the right consists of several unresolved peaks that are likely caused by a low amplitude ( $\sim 10 \mu\text{mag}$ ) independent pulsation mode that is amplitude-modulated on a time-scale longer than the 4-yr data

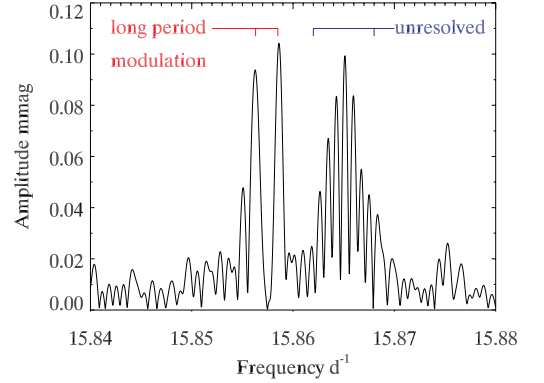


**Figure 4.** A zoomed-in region around  $\nu_1$  after pre-whitening. The multiplet of peaks to the right is most likely the result of a low, amplitude-independent pulsation mode that is modulated on a time-scale longer than the data span, since the sidelobes are not fully resolved. The other two central peaks are equally spaced about  $\nu_1$  and are caused by pure frequency modulation with a period of 861 d.

set. This kind of amplitude modulation is commonly seen for  $\delta$  Sct stars in the *Kepler* data (see e.g. Bowman & Kurtz 2014), hence we discuss these frequencies no further here.

On the other hand, the doublet seen in Fig. 4 is fully resolved from  $\nu_1$  and equally spaced on either side. By repeating the phase relationship exercise done on the outer set of sidelobes, we find that the peaks are caused by pure frequency modulation with a modulation period of 861 d. It is tempting to conclude that these peaks are the FM sidelobes caused by a third companion orbiting the binary. Tables 3 and 4 show the fit of the inner sidelobes to  $\nu_1$ . The modulation period is derived to be  $861 \pm 11$  d. If we assumed that this frequency modulation is caused by a third body, then from the amplitudes of the orbital sidelobes given in Table 4 it would follow that  $\alpha = 0.0441 \pm 0.0017$ , from equation (5)  $a \sin i = 38$  light-seconds, and from equation (4) the mass function is  $f(m_1 + m_2, m_3, \sin i) = 0.000119 \pm 0.000012 M_\odot$ . Using the derived mass of the binary,  $m_1 + m_2 = 2.7 M_\odot$  and  $i \sim 90^\circ$ , we would obtain a tertiary mass of  $m_3 = 0.098 \pm 0.003 M_\odot$ , i.e. a low-mass main-sequence M dwarf star. We examine this proposition now, and show it to be incorrect.

Many  $\delta$  Sct stars show pulsation modes that are amplitude-modulated, but modes can also be intrinsically frequency-modulated (e.g. Breger 2000; Bowman & Kurtz 2014). Thus, another interpretation of the close frequency sidelobes to  $\nu_1$  is that they represent *intrinsic* (i.e. non-dynamical) frequency modulation of that pulsation mode on a time-scale of 861 d. A test to discriminate between intrinsic and dynamical frequency modulation is to look for the sidelobes in *several* pulsation frequencies. In the case of dynamical frequency modulation (third body), all pulsation frequencies must show the same FM signature, akin to that in Fig. 3. In the case of intrinsic frequency modulation, different frequencies will have different sidelobes, corresponding to different pulsation cavities in the star.

Unfortunately, all other p-mode amplitudes are at least a factor of 4 or more smaller than the amplitude of  $\nu_1$  (cf. Fig. 2), hence we do not have sufficient signal in other frequencies to test for the very low amplitudes of closely spaced FM sidelobes expected for an 861-d orbital period. While asteroseismology might not provide a definitive answer, we do have another test: eclipse timing variations (ETVs; Conroy et al. 2014). When a binary star is in a gravitationally

**Table 3.** A non-linear least-squares fit of the highest amplitude frequency seen in Fig. 3 and its first closely spaced FM sidelobes seen in Fig. 4 to the Q0–Q17 LC masked *Kepler* data for KIC 8569819. The frequencies are separated by  $\nu_{\text{mod}} = 0.001161 \pm 0.000015 \text{ d}^{-1}$ , giving a modulation period of  $861 \pm 11 \text{ d}$ . The zero-point in time for the phase is BJD 245 5679.129 20.

	Frequency ( $\text{d}^{-1}$ )	Amplitude (mmag)	Phase (rad)
$\nu_1 - \nu_{\text{mod}}$	$15.8562606 \pm 0.0000216$	$0.089 \pm 0.005$	$-1.5634 \pm 0.0570$
$\nu_1$	$15.8574741 \pm 0.0000005$	$4.152 \pm 0.005$	$0.0284 \pm 0.0016$
$\nu_1 + \nu_{\text{mod}}$	$15.8585831 \pm 0.0000204$	$0.096 \pm 0.005$	$-1.2470 \pm 0.0529$
$\nu_{\text{mod}_1}$	$0.001214 \pm 0.000022$		
$\nu_{\text{mod}_2}$	$0.001109 \pm 0.000020$		
$\nu_{\text{mod}_1} - \nu_{\text{mod}_2}$	$0.00006 \pm 0.00003$		
$\nu_{\text{mod}} \equiv (\nu_{\text{mod}_1}, \nu_{\text{mod}_2})$	$0.001161 \pm 0.000015$		
$P_{\text{mod}} \text{ (d)}$	$861 \pm 11$		

**Table 4.** A linear least-squares fit of the close frequency triplet for the highest amplitude mode to the Q0–Q17 LC *Kepler* data for KIC 8569819 with exactly equal splitting. The frequencies of the triplet are separated by the modulation frequency,  $\nu_{\text{mod}} = 0.001157 \pm 0.000014 \text{ d}^{-1}$  ( $P_{\text{mod}} = 861 \pm 11 \text{ d}$ ). The zero-point for the phases has been chosen to be a time when the phases of the first sidelobes to the highest amplitude frequency are equal,  $t_0 = \text{BJD } 245\,5347.567\,63$ . It can be seen that the phases of the first sidelobes differ from that of the phase of  $\nu_1$  by  $-1.56 \pm 0.03 \text{ rad}$ , which is equal to  $-\pi/2$ , proving pure FM.

	Frequency ( $\text{d}^{-1}$ )	Amplitude (mmag)	Phase (rad)
$\nu_1 - \nu_{\text{mod}}$	15.856313	$0.088 \pm 0.005$	$1.8345 \pm 0.0560$
$\nu_1$	15.857474	$4.149 \pm 0.005$	$-2.8897 \pm 0.0012$
$\nu_1 + \nu_{\text{mod}}$	15.858635	$0.095 \pm 0.005$	$1.8344 \pm 0.0522$

bound system with another body, its centre of mass will move around the system’s barycenter. Because of the light time travel effect, the time of eclipses depends on the binary star’s position on the outer orbit. If a third body were present in the system, then the eclipsing binary would be separated by  $a \sin i = 38 \text{ light-seconds}$  from the barycenter, hence we would see a clear signal of that amplitude in eclipse timings. We measure eclipse times by first finding a polynomial chain that fits the entire phased light curve, and then we fit the same chain to each successive eclipse, allowing for the temporal shift. The best-attained precision of ETVs in *Kepler* data is  $\sim 6 \text{ s}$  (Conroy et al. 2014), but this is heavily degraded in the case of KIC 8569819 by intrinsic variability that causes variations in eclipse shapes. Nevertheless, variations of a  $\sim 76 \text{ s}$  peak-to-peak amplitude would be easily detected. Fig. 5 depicts the ETV curve and no signal at or around  $861 \text{ d}$  is detected.

Another technique can independently verify the orbital period of the binary, and evaluate the possibility of a third body in a wider orbit: phase modulation (Murphy et al. 2014). The method involves precise determination of the pulsation frequencies of the highest amplitude peaks in the Fourier transform of the stellar light curve, using a non-linear least-squares fit to the Q0–Q17 data with the eclipses masked, and subsequent subdivision of the light curve into smaller segments for analysis. The phase of each peak in each segment is determined, and converted into a light arrival time delay (‘time delay’, hereafter). The binary motion of the pulsating star should cause an identical signature on each pulsation frequency, with a period equal to the binary orbital period, and an amplitude equal to the light travel time across the projected semimajor axis. Details can be found in Murphy et al. (2014).

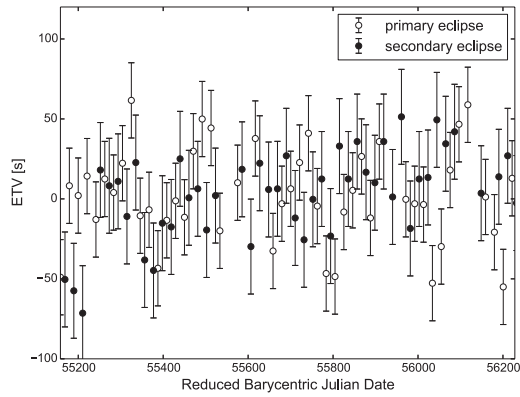


**Figure 5.** ETVs for KIC 8569819. Eclipse times are measured by fitting a polynomial chain to the entire phased light curve, and using that function to fit the time offset of each successive eclipse (Conroy et al. 2014). Primary ETVs are depicted with open circles and secondary ETVs are depicted with filled circles.

We chose a segment size of  $5 \text{ d}$  so that the A star–G star orbit is well sampled, and we investigated the four highest peaks from Fig. 2. The Fourier transform of the time delays of each peak is shown in the upper panel of Fig. 6, where the agreement on the known  $20.85\text{-d}$  period of the A star–G star pair is good. The lower panel of Fig. 6 is the Fourier transform of the weighted average time delay – the mean time delay of the four individual peaks, weighted by the phase uncertainties. This shows the orbital frequency of  $0.048 \text{ d}^{-1}$  (giving  $P_{\text{orb}} = 20.85 \pm 0.01 \text{ d}$ ), but also shows some variability near  $0.001 \text{ d}^{-1}$ . It can be seen in the upper panel that this arises from non-equal contributions from the individual time delays. This illustrates that the long-period variability is not of a binary origin, else each pulsation frequency would respond identically, as in the case for the  $20.85\text{-d}$  orbit.

These lines of evidence lead us to conclude that the closely spaced sidelobes to  $\nu_1$  represent an intrinsic frequency modulation that is *not* dynamical. The nature of frequency and amplitude modulation in  $\delta \text{ Sct}$  stars is not well understood; this is a topic of current research with the  $4\text{-yr Kepler}$  data sets for thousands of  $\delta \text{ Sct}$  stars (Bowman & Kurtz 2014). Importantly, any finding of frequency modulation of pulsation frequencies in pulsating stars must be studied in multiple frequencies for the same star to distinguish between intrinsic and dynamical frequency modulation.

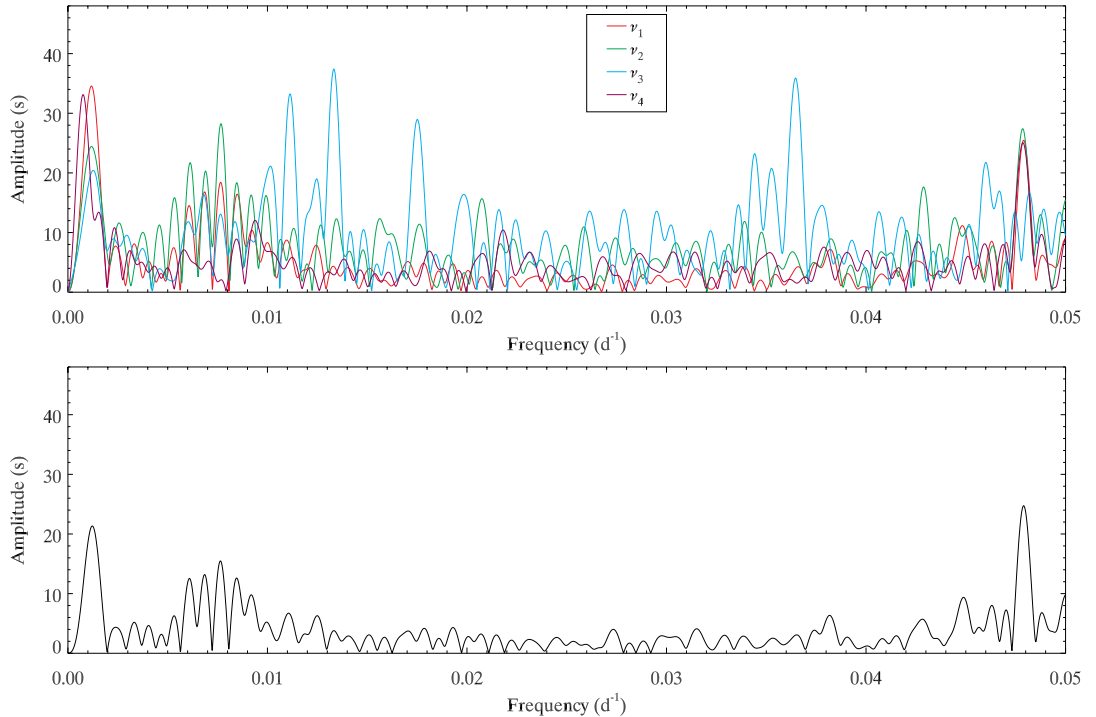


**Figure 6.** Top: the Fourier transform of the light arrival time delays for the four highest amplitude peaks from Fig. 2. Bottom: the average time delay, weighted by the observed phase uncertainties. The time delays for each of these four peaks agree well on an orbital period of  $20.85 \pm 0.01$  d, as indicated by the peak at  $0.048 \text{ d}^{-1}$  in the lower panel. However, the lower panel also shows some power at  $0.001 \text{ d}^{-1}$ , originating from the four individual peaks in differing amounts, implicating FM as the cause. Further discussion is provided in the text.

We should stress, however, that if the close sidelobes given in Table 4 and shown in Fig. 4 had had amplitudes of only  $0.020 \text{ mmag}$ , which would be a  $4\sigma$  signal, and if they had been dynamical, then the mass function would have given a mass for the third body of about  $17 M_{\text{Jupiter}}$ . This shows that the FM technique is capable of finding brown dwarfs and gas giant planets in long-period orbits around  $\delta$  Sct A stars. Other standard techniques cannot find such objects. A-type stars are too bright for transit detections of small companions; the pulsations mask shallow transits; and such stars are too massive for ground-based radial velocity techniques. The FM technique (Shibahashi & Kurtz 2012) and the PM technique (Murphy et al. 2014) with  $\delta$  Sct stars observed by *Kepler* have the potential to explore this parameter space for exoplanets.

#### 4 BINARY MODELLING

In this section, we present our modelling of the eclipsing binary light curve. This was done independently of the FM analysis presented in the last section, except for the use of the mass function. We do not have a spectroscopic radial velocity curve for this star, hence we use the photometric equivalent of a radial velocity curve, i.e. the FM mass function.

##### 4.1 Period analysis

We performed a period analysis on all the available Q0–17 LC data using the computer package *KEPHEM* (Prša et al. 2011). *KEPHEM* is an interactive graphical user interface package that incorporates

three methods of period analysis: Lomb-Scargle (Lomb 1976; Scargle 1982), Analysis of Variance (Schwarzenberg-Czerny 1989) and Box-fitting Least-Squares (Kovács, Zucker & Mazeh 2002), as implemented in the *VARTOOLS* package (Hartman 1998). Using *KEPHEM*, the period and  $\text{BJD}_0$  (the time of primary minimum) were found, giving an ephemeris:

$$\text{MinI} = \text{BJD } 245\,4970.56(1) + 20.84993(3)\text{d} \times E. \quad (7)$$

As can be seen by comparing with the FM analysis in the last section, the light curve fitting of the eclipses gives a more accurate determination of the orbital period.

##### 4.2 Determination of the eccentricity and argument of periastron through binary star analysis

To demonstrate the validity of the FM method, we generated a binary model to determine the eccentricity and argument of periastron of this system. In our model, we assumed the mass of the primary star to be  $m_1 = 1.7 M_{\odot}$ , estimated from the primary star’s effective temperature. Consequently, from the mass function determined through FM, we arrived at a mass for the secondary component of  $m_2 \sim 1.0 M_{\odot}$  (as the system is equator-on). While these assumptions disable the full determination of the binary star parameters, they are adequate to solve robustly for the eccentricity and argument of periastron to validate the FM method.

We applied the binary modelling code *PHOEBE* (Prša & Zwitter 2005), which is an extension of the Wilson–Devinney code

(Wilson & Devinney 1971; Wilson 1979),<sup>5</sup> to the light curve of KIC 8569819. PHOEBE combines the complete treatment of the Roche potential with the detailed treatment of surface and horizon effects such as limb darkening, reflection and gravity brightening to derive an accurate model of the binary parameters. The current implementation uses the Wilson–Devinney method of summing over the discrete rectangular surface elements, which cover the distorted stellar surfaces, to determine an accurate representation of the total observed flux and consequently a complete set of stellar and orbital parameters. PHOEBE incorporates all the functionality of the Wilson–Devinney code, but also provides an intuitive graphical user interface alongside many other improvements, including updated filters and bindings that enable interfacing between PHOEBE and PYTHON (see Section 4.2.1 below).

The data were detrended using second-order polynomials that were applied between breaks in the *Kepler* data, using the KEPHEM software. We further cleaned the data by removing all spurious points by eye. To reduce the number of data points, for the purpose of modelling, we assigned each data point with a random number from 0 to 1, and removed all points with random numbers above a specified threshold – 0.5 during the eclipse phases and 0.01 away from eclipse. This way we retained 50 per cent of the data points during eclipse and 1 per cent of the points away from eclipse. We used a sigmoid function to bridge the number of data points between regions so that discrete changes in the number of data points were avoided. The number of data points was reduced from 60 554 to 4390. The per-point uncertainty was determined using the standard deviation of the residuals (data minus model) in the out-of-eclipse regions.

Our initial binary model inputs consisted of the effective temperature from the KIC, which we prescribed for the temperature of the primary component ( $T_{\text{eff}} = 7100$  K); an estimate of the secondary component’s temperature ( $T_{\text{eff}} \sim 6100$  K) from consideration of the depths of the eclipses; and the surface gravity value from the KIC  $\log g = 4.0$  (cgs units). As the eclipses are separated by  $\sim 0.5$  in phase, we initially assumed an eccentricity of  $e = 0.0$ . However, analysis of the relative widths of the eclipses showed that the eccentricity is closer to  $e = 0.4$ , with an argument of periastron of  $\omega \approx 3\pi/2$  implying that we are looking down the line of apsides.

We assumed pseudo-synchronous rotation, which is stellar rotation synchronous with the orbital velocity at periastron (Hut 1981), and determined the rotation of the components to be  $F = 2.715$  rotations per orbit. We assessed the impact of the stellar rotation on the light curve and found an adjustment from  $F = 1.0$  to  $F = 5.0$  generates a model difference of 0.05 per cent, which is insignificant. As the Lomb-Scargle method is more accurate than PHOEBE for ephemeris determination, the period and zero-point in time were fixed to the values determined using KEPHEM.

When considering the stellar surfaces, we assumed that the primary component has a radiative surface, thus an albedo of  $A = 1.0$ , and a gravity-darkening exponent,  $\beta$ , of  $\beta = 1.0$  (von Zeipel 1924). For the secondary component, we assigned the value of  $A = 0.6$  for the albedo and  $\beta = 0.32$  for the gravity-darkening exponent (Lucy 1967). Recent updates in the theory of gravity darkening suggest that this value is dependent on temperature (Claret & Bloemen 2011) and/or level of stellar distortion (Espinosa Lara & Rieutord 2012). However, for this system, the gravity-darkening value has a negligible effect (0.03 per cent model difference from  $\beta = 0$  to 1, hence the value prescribed by Lucy 1967 was deemed acceptable).

**Table 5.** Adjusted parameters and coefficients of the best-fitting model to the *Kepler* light curve for Q0–17. The uncertainties were determined through MCMC methods. The linear and logarithmic limb darkening coefficients are the terms that describe the limb darkening of each component. The limb-darkening coefficients were taken from the PHOEBE limb-darkening tables (Prša et al. 2011).

Parameter	Values
Phase shift, $\phi$	0.001 515(9)
Orbital eccentricity, $e$	0.366(1)
Argument of periastron (rad), $\omega$	4.722 31(8)
Orbital inclination (degrees), $i$	89.91(6)
$T_{\text{eff}}$ ratio (K), $T_2/T_1$	0.8517(5)
Primary relative luminosity, $L_1$	0.873(4)
Secondary relative luminosity, $L_2$	0.1275(6)
Primary linear limb-darkening coefficient	0.6169
Secondary linear limb-darkening coefficient	0.6382
Primary logarithmic limb-darkening coefficient	0.2495
Secondary logarithmic limb-darkening coefficient	0.2002

Table 5 provides a complete list of the fixed parameters and their assumed values.

#### 4.2.1 Posterior determination of the orbital parameters

To determine the posterior probability distribution functions of the binary parameters (cf. Fig. 7), we combined PHOEBE with the EMCEE, a PYTHON implementation of the affine invariant ensemble sampler for Markov chain Monte Carlo (MCMC) proposed by Goodman & Weare (2010) and written by Foreman-Mackey et al. (2013).

MCMC explores the binary parameter space using a set of Markov chains, in this case 128. These chains begin with random distributions based only on the prior probability distribution functions and the initial model. They move through parameter space by assessing their posterior probability distribution function at each point and then selecting a new position based on the position of another chain. The step size is based on the covariance of the two chains. If the move increases the posterior probability distribution function then it is accepted, if the move decreases the probability then it may be accepted (to fully explore the phase space). During the initial burn-in time, the Markov chains merge towards their equilibrium position. After this period, the chains sample the phase space in terms of their posterior probability distribution functions. The statistics of a large number of iterations ( $\sim 150\,000$  excluding the burn-in time), provide probability distributions for the model parameters.

We sampled seven parameters in our multidimensional parameter space, based on their contribution to the observed flux variation of this system. As only the ratio of the temperatures can be determined from light-curve analysis, the effective temperature of the secondary was sampled, whilst keeping the primary temperature fixed. We selected the secondary temperature, since the KIC temperature provides a constraint for the primary effective temperature. The inclination, eccentricity, argument of periastron, primary and secondary potentials (potentials of the Roche lobe – a proxy for the inverse radius) and luminosity were also sampled using MCMC methods. At each iteration, we calculated the phase shift using the new values of eccentricity and argument of periastron. All other parameters in our models were either well determined (period and zero-point in time), theoretically determined (albedo and gravity darkening) or insignificant for this system (stellar rotational velocity and gravity darkening).

<sup>5</sup> A manual for the Wilson–Devinney code is available on-line <ftp://ftp.astro.ufl.edu/pub/wilson/>

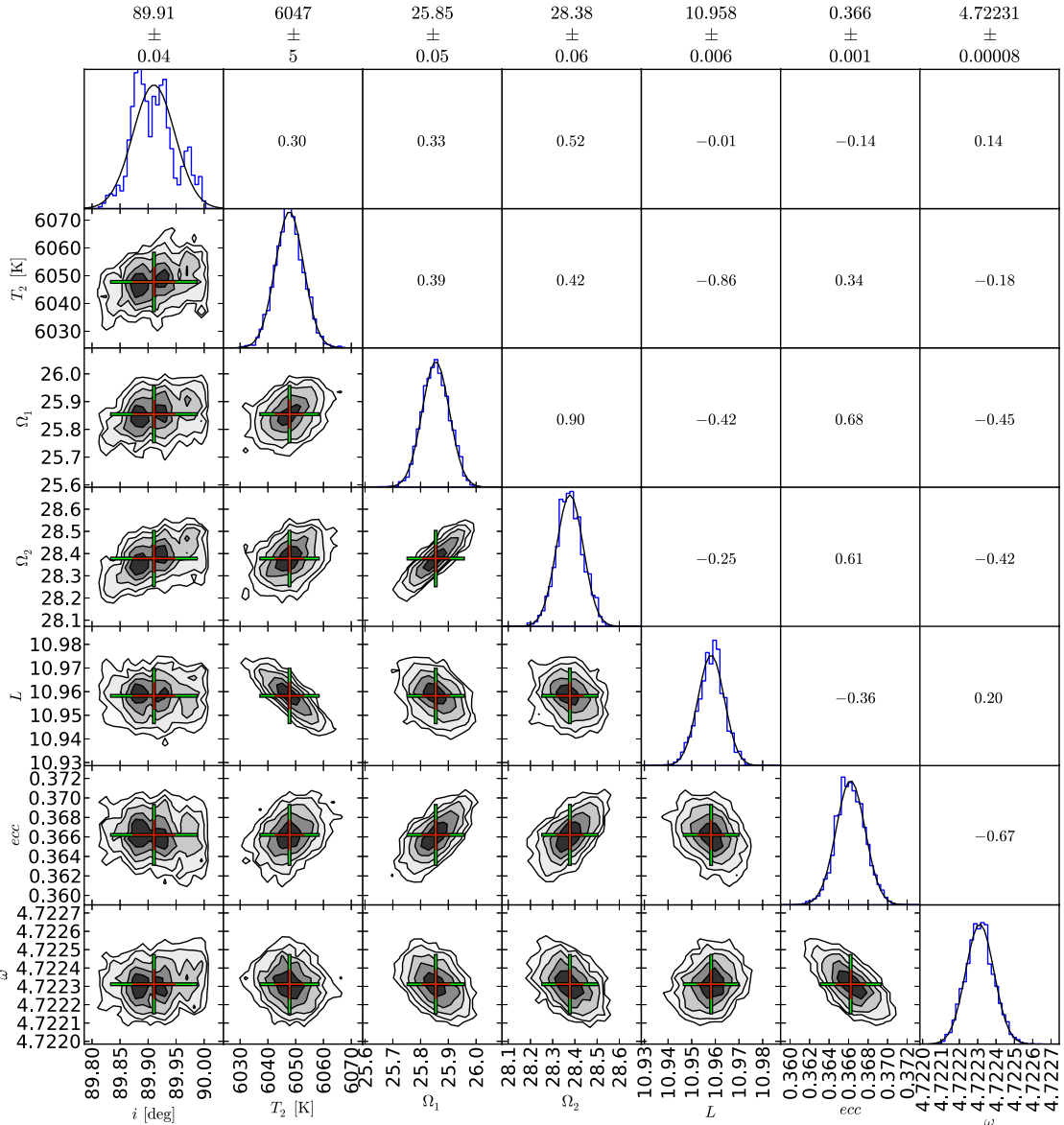


**Figure 7.** Lower-left subplots: two-dimensional cross-sections of the posterior probability distribution functions. The crosses show the  $1\sigma$  (red) and  $2\sigma$  (green) uncertainties, and are centred on the minima. Diagonal subplots from top left to bottom right: histograms displaying the probability distribution of each individual parameter. Upper-right subplots: the correlations for the two-dimensional cross-sections mirrored in the diagonal line where 1 is direct correlation and  $-1$  is a direct anticorrelation. The values above the plot give the mean value and  $1\sigma$  uncertainty for each parameter, based on the fitted Gaussians.

For each parameter, we used a flat, uniform prior. The prior ranges were selected to be as large as possible without creating unphysical models. We restricted the prior on the inclination to be contained below  $90^\circ$  to avoid obtaining a double-peaked distribution reflected about  $90^\circ$ . The likelihood function was generated by computing the  $\chi^2$  difference between the initial model and data. Fig. 8 shows the average of the last 1024 models generated using MCMC (eight from each Markov chain). The thickness of the line denotes the spread of the last 1024 models. The lower panel shows the residuals to the best-fitting model. Error bars on the residuals show the per-point standard deviation for the last 1024 models.

The posteriors generated through MCMC are well determined, thus the model is well constrained. For all parameters except the inclination, the Gaussian fit to each posterior, shown in Fig. 7, is excellent and provides a robust error estimate. The inclination, however, presents an apparent multimodal distribution, which is a consequence of a small star passing over a large disc. Here, the information regarding the points of ingress and egress is limited, yet constrained to a very small range of inclinations. To account for the inexact fit of the Gaussian, we have increased the uncertainty of the inclination from that determined through Gaussian fitting, 0:04 to 0:06.

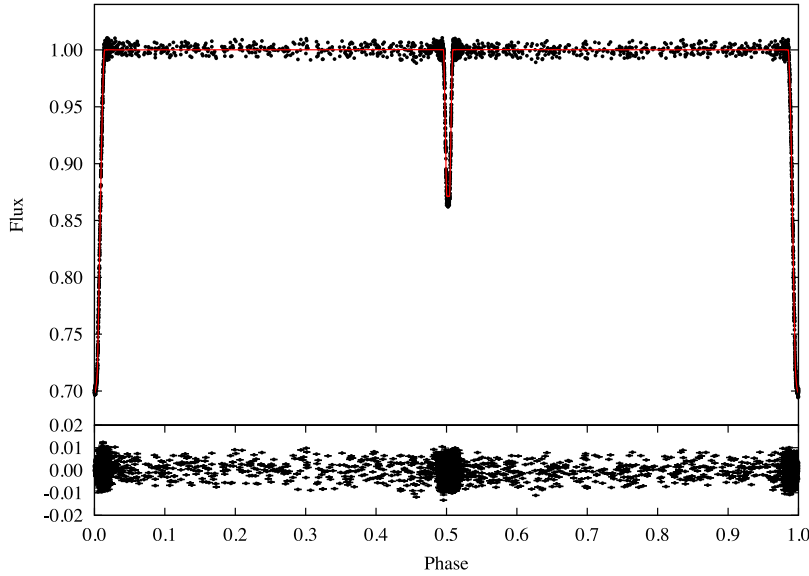


**Figure 8.** Upper panel: theoretical PHOEBE model (red line) and observed light curve (black points), prepared as specified in Section 4.2. The width of the line depicts the spread of the final 1048 models determined using MCMC. Lower panel: the residuals (black points) of the best-fitting model. The per-point uncertainty in the model is displayed as error bars.

**Table 6.** Fixed parameters and coefficients for the PHOEBE best-fitting model to the *Kepler* light curve for Q0–17. The rotation is specified as a ratio of the stellar rotational to orbital velocity. The mass ratio and semimajor axis were fixed to generate a model with a primary mass of  $m_1 = 1.7 M_\odot$  and a secondary mass of  $m_2 = 1.0 M_\odot$ , in line with the mass function determined through the FM method. The fine grid raster is the number of surface elements per quarter of the star at the equator and coarse grid raster is used to determine whether the stars are eclipsing at a given phase.

Parameter	Values
Orbital Period (d)	20.849 93(3)
Time of primary minimum BJD <sub>0</sub>	2454 970.56(1)
Primary $T_{\text{eff}}$ (K), $T_1$	7100(250)
Mass ratio, $q$	0.588
Semimajor axis ( $R_\odot$ ), $a$	44.6
Third light, $l_3$	0.0
Primary rotation, $f_1$	2.715
Secondary rotation, $f_2$	2.715
Primary bolometric albedo, $A_1$	1.0
Secondary bolometric albedo, $A_2$	0.6
Primary gravity brightening, $\beta_1$	1.0
Secondary gravity brightening, $\beta_2$	0.32
Primary fine grid raster	90
Secondary fine grid raster	90
Primary coarse grid raster	60
Secondary coarse grid raster	60

The stellar potentials and radii are highly dependent on the mass ratio, and thus by assuming the masses we were unable to obtain accurate values. To determine the extent of our assumptions, we perturbed the mass ratio by 10 per cent and assessed the impact this had on the model. When both increasing and decreasing the mass ratio by 10 per cent (whilst calculating the potentials to keep the

**Table 7.** Comparison of results from traditional eclipsing binary star light-curve modelling and the FM technique. The agreement validates the FM method for those who are more accustomed to traditional eclipsing binary light-curve modelling.

	PHOEBE	FM
Orbital period (d)	$20.849\,93 \pm 0.000\,03$	$20.849 \pm 0.006$
Eccentricity	$0.366 \pm 0.001$	$0.39 \pm 0.08$
Argument of periastron (rad)	$4.722\,31 \pm 0.000\,08$	$4.59 \pm 0.16$

radii fixed), we found a model difference of 0.6 per cent. As the noise in our data is  $\sim 2$  per cent, this difference is not significant. Thus, we find that the values reported in Table 6 are independent of assumption that the mass ratio is  $q = 0.588$ .

## 5 CONCLUSIONS

We have demonstrated the validity of the FM technique (Shibahashi & Kurtz 2012) by showing the consistent results obtained from it when compared to a traditional eclipsing binary light-curve analysis. We derived the mass function from the FM technique of Shibahashi & Kurtz (2012). That additional constraint was then used in the light-curve modelling by traditional methods. The orbital period, eccentricity and argument of periastron derived independently from both the FM method and light-curve modelling are in good agreement, as is shown in Table 7. This was the primary goal of this paper for readers who are familiar with traditional binary star light-curve modelling, but not yet with the FM technique.

While light-curve modelling produces higher accuracy for orbital period and eccentricity in the case of KIC 8569819, that is only true for EB stars. For non-eclipsing systems, the FM technique is still applicable, whereas traditional techniques work less well for ellipsoidal variables, and not at all for non-distorted, longer orbital period systems. We also have presented a cautionary note in the use of FM in the discovery of additional pure FM in KIC 8569819 that is

not the result of orbital motion, but is intrinsic to the pulsation cavity of the highest amplitude mode in the star. Thus, our message is that FM is a powerful technique, but at least two pulsation frequencies in a star must give consistent results to conclude a dynamical origin of the FM.

#### ACKNOWLEDGEMENTS

The authors express their sincere thanks to NASA and the *Kepler* team for allowing them to work with and analyse the *Kepler* data, making this work possible. The *Kepler* mission is funded by NASA's Science Mission Directorate. This work was also supported by the STFC (Science and Technology Funding Council). SJM was supported by the Australian Research Council.

#### REFERENCES

- Aerts C., Christensen-Dalsgaard J., Kurtz D. W., 2010, *Asteroseismology*. Springer-Verlag, Berlin
- Beck P. G. et al., 2012, *Nature*, 481, 55
- Bowman D. M., Kurtz D. W., 2014, *MNRAS*, 444, 1909
- Breger M., 2000, *MNRAS*, 313, 129
- Chaplin W. J. et al., 2014, *ApJS*, 210, 1
- Claret A., Bloemen S., 2011, *A&A*, 529, A75
- Conroy K. E., Prša A., Stassun K. G., Orosz J. A., Fabrycky D. C., Welsh W. F., 2014, *AJ*, 147, 45
- Deming D. et al., 2012, *ApJ*, 754, 106
- Espinosa Lara F., Rieutord M., 2012, *A&A*, 547, A32
- Esposito S. et al., 2013, *A&A*, 549, A52
- Foreman-Mackey D., Hogg D. W., Lang D., Goodman J., 2013, *PASP*, 125, 306
- Goodman J., Weare J., 2010, *Comments Appl. Math. Comput. Sci.*, 5, 65
- Hartmann E., 1998, *Computer-Aided Geometric Design*, 15, 377
- Herrero E., Morales J. C., Ribas I., Naves R., 2011, *A&A*, 526, L10
- Horne J. H., Baliunas S. L., 1986, *ApJ*, 302, 757
- Huber D. et al., 2014, *ApJS*, 211, 2
- Hut P., 1981, *A&A*, 99, 126
- Kalas P., Graham J. R., Fitzgerald M. P., Clampin M., 2013, *ApJ*, 775, 56
- Kovács G., Zucker S., Mazeh T., 2002, *A&A*, 391, 369
- Kovács G. et al., 2013, *A&A*, 553, A44
- Kurtz D. W., Saio H., Takata M., Shibahashi H., Murphy S. J., Sekii T., 2014, *MNRAS*, 444, 102
- Lomb N. R., 1976, *Ap&SS*, 39, 447
- Lucy L. B., 1967, *Z. Astrophys.*, 65, 89
- Marley M. S., Saumon D., Cushing M., Ackerman A. S., Fortney J. J., Freedman R., 2012, *ApJ*, 754, 135
- Montgomery M. H., O'Donoghue D., 1999, *Delta Scuti Star Newsl.*, 13, 28
- Mosser B., Belkacem K., Vradar M., 2013, *EAS Publ. Ser.*, 63, 137
- Murphy S. J., Bedding T. R., Shibahashi H., Kurtz D. W., Kjeldsen H., 2014, *MNRAS*, 441, 2515
- Prša A., Zwitter T., 2005, *ApJ*, 628, 426
- Prša A. et al., 2011, *AJ*, 141, 83
- Scargle J. D., 1982, *ApJ*, 263, 835
- Schwarzenberg-Czerny A., 1989, *MNRAS*, 241, 153
- Shibahashi H., Kurtz D. W., 2012, *MNRAS*, 422, 738
- Stellingwerf R. F., 1979, *ApJ*, 227, 935
- Stello D. et al., 2013, *ApJ*, 765, L41
- von Essen C. et al., 2014, *A&A*, 561, A48
- von Zeipel H., 1924, *MNRAS*, 84, 702
- Wilson R. E., 1979, *ApJ*, 234, 1054
- Wilson R. E., Devinney E. J., 1971, *ApJ*, 166, 605

This paper has been typeset from a  $\text{\TeX}/\text{\LaTeX}$  file prepared by the author.

# Chapter 9

## Conclusions and Future Work

### 9.1 Conclusion

With more precision comes more questions: this is certainly true of the *Kepler* mission. Before the *Kepler* mission, objects such as heartbeat stars had only been theorised. Kumar, Ao & Quataert (1995) suggested that we would see light curves with strange configurations if we observe binary stars with compact components, such as neutron stars. Little did we know, that with enough precision in our data, all combinations of objects could produce the interesting shapes we now know to be heartbeat star light curves.

Currently we have a database of 173 heartbeat stars that have been identified in the *Kepler* data<sup>1</sup>. However, heartbeat stars have also been observed by other missions: 7 with the Optical Gravitational lensing experiment, OGLE (Nicholls & Wood, 2012); 1 by Hareter et al. (2014) using the CoRoT satellite and more recently a heartbeat star was discovered using MOST and followed up with the CHARA array (Richardson et al., 2016). The large number of heartbeat stars now known is a testament to the scientific advances that can be made through space-based technologies. Furthermore, the interesting features of many of the heartbeat stars have made them exceedingly

---

<sup>1</sup>the full list of *Kepler* heartbeat stars is hosted at <http://keplerebs.villanova.edu>

interesting to study. These include heartbeat stars with tidally induced pulsations, which have provided irrefutable evidence that pulsations provide a mechanism for energy dissipation, as theorised by Zahn (1975); heartbeat stars with components displaying solar-like oscillations, which have allowed complementary techniques to provide an extensive overview of interesting systems; heartbeat stars with rapid apsidal motion, which have provided evidence that tidally induced pulsations affect the rate of apsidal advance (see Chapter 5); and those with large-amplitude pulsations that have enabled the study of tidal resonance (see Chapter 4) and furthermore allow the application of the frequency modulation and/or phase modulation technique, thus allowing for the independent generation of radial velocity curves for the pulsating components (see Chapter 8).

When observing new phenomena, the first step is to look to the literature to see if the concept had previously been thought of. In the case of heartbeat stars, the theories of both the static tide or ellipsoidal variation and the dynamical tide or tidally induced pulsations had both been published, with special attention to the theory of tidally induced pulsations. The concept of tidally induced pulsations was originally theorised by Zahn (1975), Goldreich & Nicholson (1989) and Witte & Savonije (2002). It is only in the past few years, however, with the advent of high-precision space-based missions, that we have finally achieved the detail required in the observations to verify that tidally induced pulsations exist.

The basis of this work was the initial investigation of heartbeat stars with a focus on tidally induced pulsations. This included building tools to better enable the analysis of these intricate objects. The BAYES-TODCOR software was created to improve our radial velocity determination, which is critical for the precise modelling of heartbeat stars (see Chapter 2). The software is a combination of Bayesian statistics (through the PYTHON implementation of an affine-invariant version of MCMC (Foreman-Mackey et al., 2013)) with the widely used TODCOR (Zucker & Mazeh, 1994) radial velocity software. An advantage of the BAYES-TODCOR software is that the fundamental parameters for the best-fit spectral models are output as poste-

rior distributions, enabling the correlations between parameters to be explored and providing more robust uncertainty estimates. The BAYES-TODCOR program has primarily been applied to synthetic spectra, although has also been used to determine the radial velocities derived from the Kitt Peak spectra of KIC 8164262 (see Chapter 4). The BAYES-TODCOR software played a fundamental role in the analysis of KIC 8164262 as it provided posterior distributions for the fundamental parameters and radial velocities for the primary component. Of specific importance for this object was the determination of the posterior for the primary star's  $\log g$ , as this was used to constrain the photometric model and allowed a self-consistent solution to be reached.

To model the photometric and radial velocity curves of heartbeat stars the binary modelling software, PHOEBE, was used. To make this extensive and intricate code applicable to the unusual light curves of heartbeat stars, it was required that the code be augmented. Additions to the code included the ability to model tidally induced pulsations by adding sine waves to the light curve model. As the frequencies of tidally induced pulsations are known to a high precision and are multiples of the orbital frequency, we elected to fix the frequencies and fit the phases and amplitudes of the sine waves.

Another addition was the ability to model Doppler boosting. The function, taken from Eqn 2 of Bloemen et al. (2011) and extended to account for beaming in both components, requires the effective temperature,  $\log g$  and radial velocities of each star, and the relative luminosity of the stars. Look-up tables are also used to determine the passband-weighted boosting factors, which are dependent on the wavelength range of the observations. Doppler boosting provides an extra constraint on otherwise degenerate parameters such as the stellar radius and the mass ratio.

A third important addition was the implementation of Markov chain Monte Carlo techniques to arrive at a best-fit solution. EMCEE, a python implementation of the affine-invariant version of MCMC (Goodman & Weare, 2010), was combined with

PHOEBE to enable an improved statistical approach to fitting the model parameters. The outcome of the new models is a set of posterior probability distributions that provide robust uncertainties and display the correlations between parameters. Other updates to the code include the ability to set priors on the stellar radii instead of the potential; the implementation of the critical-potential boundaries, which stop stars from overflowing their Roche lobes; and the ability to calculate (instead of fit) the relative luminosity, reducing the number of fitted parameters by one. These updates were implemented by interfacing between PYTHON and PHOEBE, and provide adequate improvements that enable the PHOEBE code to effectively model heartbeat stars.

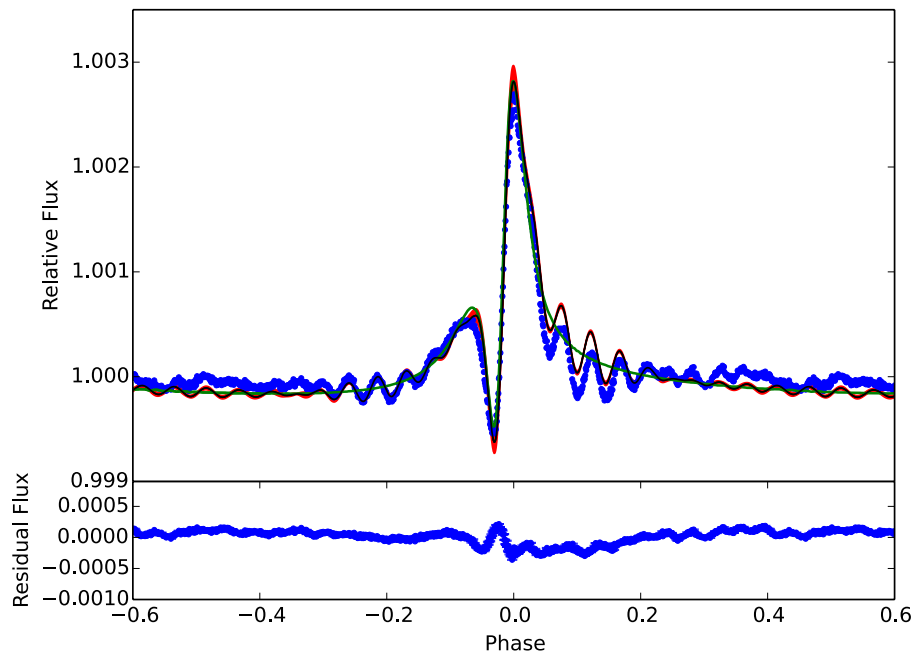


Figure 9.1: Upper panel: Best-fit PHOEBE model without pulsations (green line) and including 7 pulsations (black line), and the phased *Kepler* light curve (blue points) of KIC 3749404. The red envelope depicts the  $1\sigma$  spread of the final 128 models determined using MCMC for the model with 7 pulsations. Lower panel: the residuals (blue points) of the best-fit model. The uncertainties are depicted on the residual points, although they are not visible on the scale provided.

The augmented version of the PHOEBE binary modelling software was applied to a selection of objects, including KIC 3749404 (see Fig. 9.1), the heartbeat star with rapid apsidal motion. First, a general binary star model was generated, which was

a combined solution of the light and radial velocity curves. This demonstrated that KIC 3749404 contains an A and an F star in a close orbit with a period of  $p=20.3$  d and an eccentricity of  $e=0.66$ . The separation of the two components at periastron is  $\sim 16 R_{\odot}$ . We then used the light curve solution to determine the rate of apsidal advance. To do this, two sections of the light curve, one at the beginning and one at the end of the *Kepler* data set (which spans Quarters 0–17) were modelled to determine the change in the argument of periastron. The majority of parameters were fixed to those determined for the general model and only the phase shift, argument of periastron and a pulsation shift were fitted. It was determined that KIC 3749404 has an apsidal motion rate of  $\dot{\omega}_{obs} = 1.166(1)^{\circ}/\text{yr}$ . The theoretical rate for the classical and general relativistic apsidal motion was found to be  $\dot{\omega}_{theor}^{CL+GR} = 0.007(6)^{\circ}/\text{yr}$ . We attribute this significant difference in values to the tidally induced pulsations present in KIC 3749404, as predicted by Claret & Willems (2002).

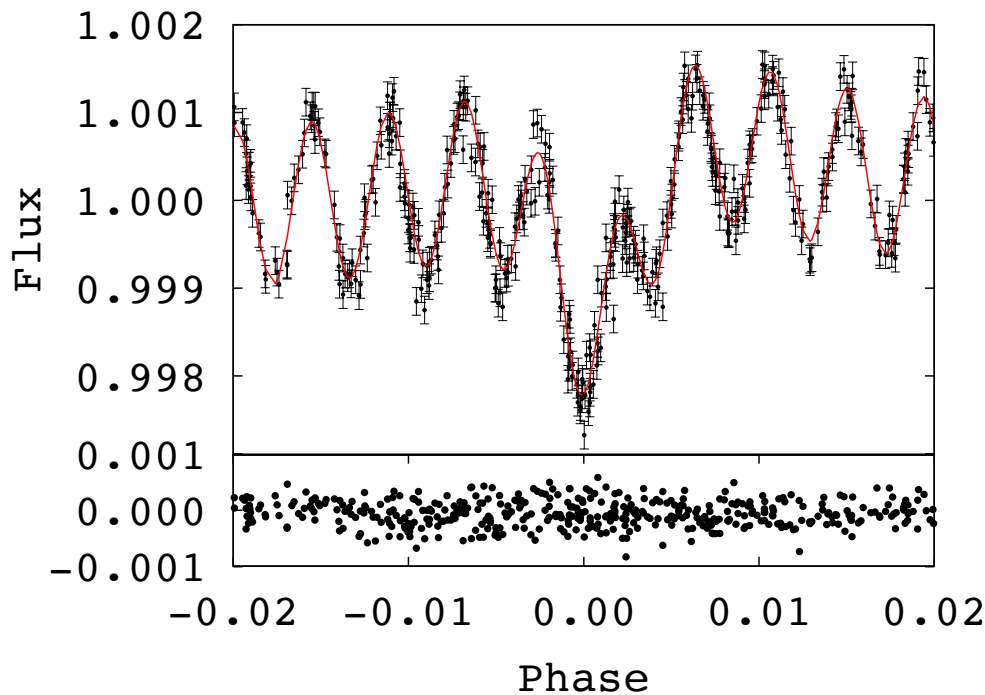


Figure 9.2: Upper panel: A magnified region of the best-fit light curve model (red line) to the phased *Kepler* data of KIC 8164262 (black), focused on the ellipsoidal variation. one sigma uncertainties are displayed on the data points. Lower panel: The corresponding residuals of the best-fit model.

---

Another object we elected to study in detail is KIC 8164262. KIC 8164262 contains a slightly evolved A star and an M star in a highly eccentric ( $e=0.882$ ) orbit. This object piqued our interest as it presented one high-amplitude ( $\sim 1$  mmag) pulsation peak (see Fig. 9.2), which made it a candidate for the resonant locking mechanism. Resonant locking was proposed by Witte & Savonije (1999), Witte & Savonije (2001), Fuller & Lai (2012) and Burkart et al. (2012) to be the mechanism that enables a stellar pulsation to remain in resonance with the binary orbit. Without any mechanism, due to the evolution of the binary star orbit, the pulsation would pass through resonance on a short time-scale, thus it would be unlikely that we would observe objects with resonantly excited pulsations. In the *Kepler* data alone, however, we have identified thirteen candidates, suggesting that there is a mechanism that prolongs resonance.

As two stars orbit each other, assuming the orbit is eccentric, the orbit evolves via the transfer of angular momentum. This causes the orbit to circularise and get smaller, thus the orbital period to get shorter, and the stars to spin faster. In parallel, due to the increase in the stellar rotational velocities, the stellar eigenfrequencies change. The theory of resonance locking states that, when in resonance, these two effects happen on equal time scales, such that the stellar eigenfrequencies are changing simultaneously with the changing orbital period. Consequently, rather than passing through resonance, the tidally induced pulsations are locked in resonance with the orbit. Our contribution to this problem was to provide the fundamental stellar and pulsational properties of KIC 8164262. Now we are working alongside theorists to determine whether the high-amplitude pulsation is indeed in resonance and furthermore, if it is resonantly locked.

We studied a sample of 18 red-giant heartbeat stars to assess their properties as solar-like oscillators. We selected one of the 18 objects, KIC 5006817, to study in detail (see Fig. 9.3). The purpose of this study was to incorporate the results of the solar-like oscillation analysis to constrain the results of the binary star analysis. This was especially useful in the case of KIC 5006817 as the secondary component is

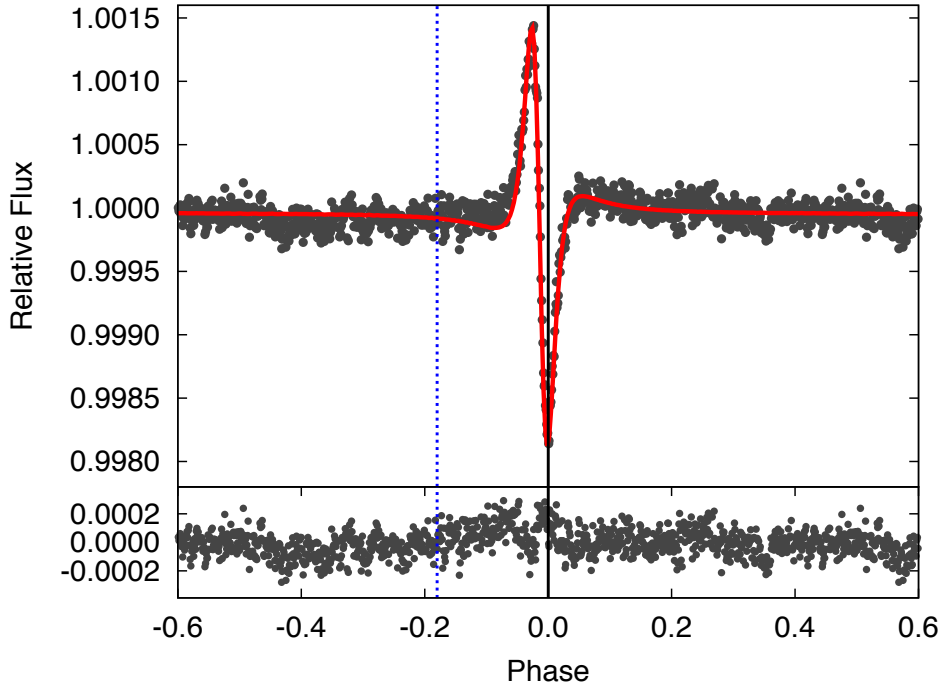


Figure 9.3: Theoretical PHOEBE model without beaming (red line) and observed light curve (black points) of the phased (94.82 d), binned Kepler long cadence data of Quarters 0–12 for KIC 5006817. Lower panel: the residuals of the best-fit model. The dashed and solid lines are centred on the times of superior and inferior conjunction respectively. Our analysis showed that the long term Doppler boosting component was not present in the data. We expect that this is a consequence of the *Kepler* processing pipeline and our own detrending.

a low mass ( $M = 0.3 M_{\odot}$ ), main-sequence star, and consequently has an insignificant flux contribution to the light curve and spectra. The modelling was done both with and without the addition of Doppler boosting due to the apparent absence of the signature in the light curve away from the periastron variation. It is likely that the long term component of the Doppler boosting signal was missing from the light curve due to the long orbital period ( $\sim 90$  d) of the binary: the *Kepler* satellite is not stable enough to preserve signals over long time scales. Furthermore, the closeness of the orbital period to a single *Kepler* Quarter also make it difficult to extract signals that are cyclic over a complete orbit. Another interesting result from KIC 5006817 is that, given the mass and radius determined through asteroseismology, the gravity darkening exponent ( $\beta \approx 1$ ) did not agree with theoretical values:  $\beta = 0.32$  (Lucy, 1967) and  $\beta = 0.5$  (Claret & Bloemen, 2011)). We expect that this is a consequence of the tidal distortion of the object at periastron, as suggested by Espinosa Lara &

Rieutord (2012).

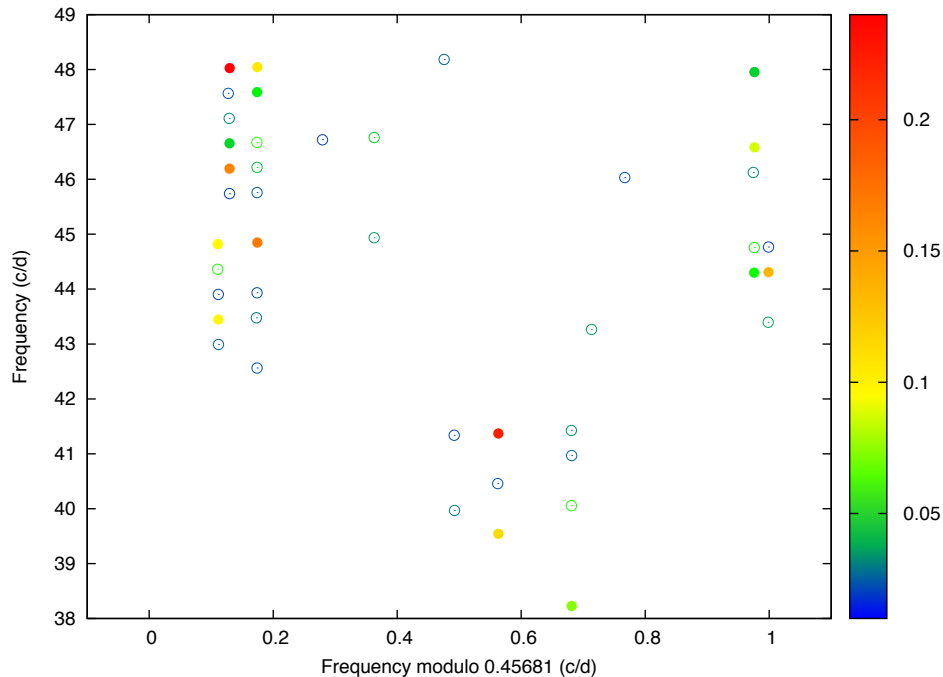


Figure 9.4: An echelle diagram of the p-mode frequencies modulo the orbital frequency using the short cadence *Kepler* data of Quarters 7 and 8 for KIC 4544587. The points are coloured in terms of their amplitude in units of relative flux  $\times 10^{-3}$  (see the key at the right of the figure). The filled circles are the identified p-mode values and the open circles represent further frequencies with amplitudes in the region  $0.02 - 0.04 \times 10^{-3}$  relative flux units, which are below our predefined confidence limit of  $3\sigma$ . The uncertainty in the frequencies is smaller than the points, thus not depicted. A high pass filter was applied to the g-mode region prior to the identification of the p-modes to remove any possible window pattern.

KIC 4544587 is a short-period ( $P = 2.189$  d), eccentric ( $e = 0.275$ ), doubly-eclipsing binary star with tidally induced g-modes, mode coupling and tidally influenced p-modes. This interesting object was modelled using PHOEBE, following which, the uncertainties for the most correlated parameters were determined using Monte Carlo simulations. The results of the light and radial velocity curve fit showed that the system contains a late A and early F star in a detached system. The purpose of modelling this object was to determine the binary and fundamental parameters and prove that it was pulsating with tidally induced pulsations. During the analysis, by creating an echelle-like diagram (modulo the orbital period), we found that many of the p-modes were separated by, but not multiples of, the orbital frequency (see Fig.9.4). Our current theory is that these multiplets are a consequence of non-linear coupling between a single p mode and the tidally induced g (gravity) modes.

Finally, we found that the g modes that are not multiples of the orbital frequency are all combination modes excited by parametric three mode resonance, which is in line with our asteroseismic models that suggest neither star should pulsate with g modes.

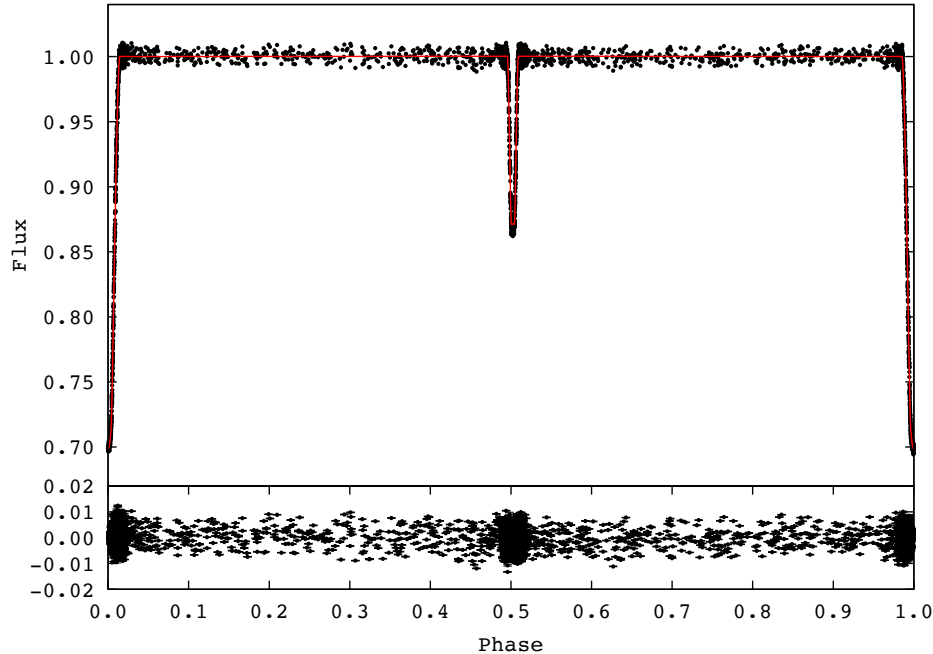


Figure 9.5: Upper panel: theoretical PHOEBE model (red line) and observed *Kepler* light curve (black points) for KIC 8569819. The width of the line depicts the spread of the final 1048 models determined using MCMC. Lower panel: the residuals (black points) of the best-fit model. The per-point uncertainty in the model is displayed as error bars.

While not a heartbeat star, the tools developed for the analysis of heartbeat stars were applied to KIC 8569819, a double eclipsing binary star with a strong FM (frequency modulation) signal (see Fig 9.5). In a binary star, stable pulsation frequencies are modulated by the motion of the star as it orbits its companion. The FM signature is displayed as a main peak with sidelobes that are all separated by the orbital frequency. The phases of the sidelobes must also be equal to each other, but be  $\pi/2$  rad different from the main peak. The analysis of these sidelobes provides the orbital period, mass function and eccentricity of the binary (Shibahashi & Kurtz, 2012), and the argument of periastron (Shibahashi, Kurtz & Murphy, 2015b). The purpose of this work was to provide an obvious observational case of FM, with a binary star model that corroborates the results of the FM analysis (the period and

eccentricity - the theory for the argument of periastron had not been developed at this point). An interesting outcome of this analysis is that a second set of peaks was found that suggested a tertiary component. However, the eclipses showed no evidence of eclipse timing variations, showing that the peaks were not the consequence of a third component. This result further highlighted the need for more than one set of sidelobes to ensure a reliable result.

## 9.2 Future Work

While working on heartbeat stars I have come across many interesting objects, and choosing which to study in detail is a task in itself. Below is the description of a couple of objects that I feel have significant merit that make them worthy of detailed study, although there is a plethora of interesting objects that, given enough time and (wo)man power, could lead to some very interesting results:

KIC 5733154 was identified by Simon Murphy, through the application of the PM (phase modulation) method, to be a heartbeat star that is a black hole candidate. The PM method is a different approach to extracting the same physics as the FM method. Initial analysis has been able to eliminate the possibility that the mass ratio ( $1.3 \pm 0.3$ ) is due to an A-type main-sequence or evolved companion to the pulsating  $\delta$  Sct star (assuming the pulsating component is the less massive component) and further data collection (in the form of spectra) and analysis (specifically binary star modelling) will help distinguish between a neutron star, a smaller companion to the  $\delta$  Sct star and a black hole. If the analysis supports the hypothesis that this object is a black hole, it will be the closest known black hole to the Earth.

KIC 5034333 is a short period ( $P = 6.9$  d) eccentric binary system with a heartbeat star light curve (cf. Fig. 9.6). The combination of the pulsations and the FM signature suggest that the secondary component is a  $\delta$  Sct star and the primary component is  $\sim 3 M_{\odot}$ . The most interesting feature of KIC 5034333 is that it has

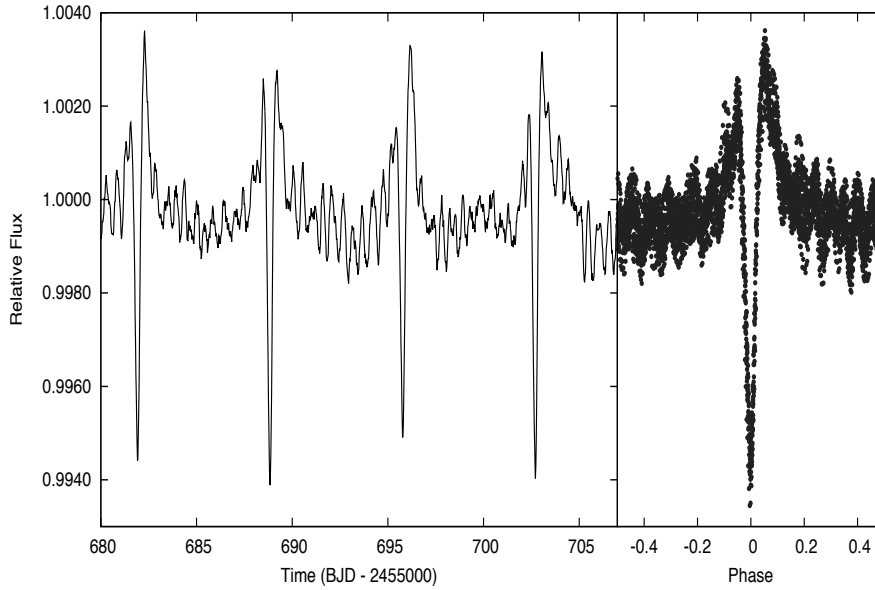


Figure 9.6: The *Kepler* long-cadence time series (left) and phased light curve (right) of KIC 5034333 for Quarter 9. The phased data clearly depict the presence of tidally driven modes as the pulsations are commensurate with the orbital period. This object does not appear to have any eclipses, although the shape of the light curve is rich in information about the fundamental parameters due to the tidal distortions of the stellar components and as such will be an ideal object to model.

one tidally excited mode at  $9.5 \text{ c d}^{-1}$ , making it the first tidally excited pressure (p) mode. Other interesting features include a strong FM signature; naturally occurring p modes that allow for pulsational modelling; and an interesting triplet at  $53.3 \text{ c d}^{-1}$  that has a splitting of twice the orbital period, specifically the frequencies are 8, 8.5 and 9 times the orbital frequency. Nine spectra have been taken at Kitt Peak National Observatory, by both myself and my collaborators, and also a single high quality spectrum has been acquired at Calar Alto. These data will be incorporated into the subsequent analysis of KIC 5034333.

Finally, the heartbeat star group, including myself, has recently obtained radial velocities for 42 objects ranging from 2 to 13 radial velocities per object. The aim of this work is to determine statistical properties of heartbeat stars, especially those with tidally induced pulsations. The sample of stars includes all those known to have tidally induced pulsations, those with rotational peaks in the Fourier transform and those with naturally occurring pulsations (where tidally induced pulsations are the highest priority). The next step in this work will be to fit the radial velocity data to

determine orbital information and in the case of double-lined spectroscopic binaries, the masses. Furthermore, if we employ the BAYES-TODCOR software, we will also obtain the  $T_{eff}$ ,  $\log g$  and rotational rates of the stars. We then intend to build a pipeline that will model the light curves of heartbeat stars and provide a full complement of parameters for each object. The scientific intention of this work is to better understand the mechanism that excites tidally driven pulsations by studying the correlations between the presence of tidally induced pulsations and the fundamental stellar parameters, including temperature, mass, periastron distance and stellar structure, to name but a few. We anticipate that the energy transfer process in the stellar envelopes (thus effective temperatures of the stars), stellar masses, eccentricities and periastron distances will all play an important role in determining the presence and amplitudes of tidally induced pulsations. We anticipate that the analysis of our current data set will bring us closer to understanding heartbeat stars and the ringing of tidally induced pulsations.

# Appendix A

## The BayesTodcor Software: the $\chi^2$ version and the *CCR* version

This appendix contains the PYTHON code for the BAYES-TODCOR program. It is divided into two sections, one containing the code for the  $\chi^2$  version and one containing the *CCR* version, as described in Chapter 2.

### A.1 The $\chi^2$ version

---

```
#!/usr/bin/python
```

```
"""
```

```
19/06/14: This program uses TODCOR, a two dimensional cross correlation  
program to determine the velocities by finding the best templates. It  
also generates posteriors for teff, logg, metallicity and vrot of two  
objects in a binary system and the light ratio.
```

```
You must run this program in the TODCOR directory. This program will  
store an interpolated spectrum for each processor in a directory  
called interp_spec. Each time you run this program it will delete the
```

directory containing spectra from the previous run.

You must specify directories with a trailing / in all cases.

In TAPE1 you must specify all the inputs as usual, EXCEPT the request must be set to "U" for the file names of the synthetic spectra and the observed spectrum so that they will be requested interactively. Do not leave any empty lines in TODCOR's TAPE1 as this will cause a malfunction.

There may be some inf's in the output file (<star name>.posteriors.dat). This is the value returned if the values are out of bounds, unphysical yet in bounds, or if TODCOR does not produce a value for the given parameters. The mcmc chains will move away from these parameters in time.

The velocities are now outputted in "blobs" which means that they are selected when the lnprob is selected by the sampler. The velocities are not posteriors, they are distributions based on the output of TODCOR.

To Start, adjust all the values in the INPUT box. You will need a folder that contains a set of synthetic spectra. Your prior ranges must be within the range of spectra that you have, ie. if your synthetic spectra have Teff's starting at 5000 K, your priors must not go below 5000 K.

```
"""
```

```
import emcee  
from emcee.utils import MPIPool
```

```
import re
import numpy as np
import pylab as pyl
import os
import logging
import shutil
from subprocess import Popen, PIPE
from phoebe.algorithms import interp_nDgrid
from phoebe.parameters import tools
from phoebe.atmospheres.tools import broadening_rotational
import phoebe.atmospheres.tools as atm
from interp import interp
import pickle
import sys
from mpi4py import MPI
import random
from phoebe.atmospheres.tools import broadening_instrumental
import matplotlib.pyplot as pl

#####
#####INPUTS#####
#n_walkers: number of walkers, must be even and can be too
#small. Usually 128 will suffice
n_walkers = 128

#iters: number of iterations for each walker
iters = 1000000

# state: set to None to start MCMC from scratch or to a
# file name that contains your last <n_walkers> posteriors
# to start from the end of your last run
```

```
state = "priors.dat"

#spec_dir: the directory containing the synthetic spectra
spec_dir = "../data/bin0.04/"

#todcor_dir: the name of the directory where you run this
#program /and/ where TODCOR is contained.
todcor_dir = "/home/kmh/Stars/tools/todcor/mcmc/"

#obs_spec: list of the observed spectra
ex_dir = str(1)
ex = str(2)
sd = "../ex/ex"+ex_dir+"/prep/"

obs_spec = [sd+"prep_noise_ex"+ex+"_0.dat",sd+"prep_noise_ex"+ex+"_1.dat",
sd+"prep_noise_ex"+ex+"_2.dat",sd+"prep_noise_ex"+ex+"_3.dat",
sd+"prep_noise_ex"+ex+"_4.dat",sd+"prep_noise_ex"+ex+"_5.dat",
sd+"prep_noise_ex"+ex+"_6.dat",sd+"prep_noise_ex"+ex+"_7.dat",
sd+"prep_noise_ex"+ex+"_8.dat",sd+"prep_noise_ex"+ex+"_9.dat",
sd+"prep_noise_ex"+ex+"_10.dat",sd+"prep_noise_ex"+ex+"_11.dat",
sd+"prep_noise_ex"+ex+"_12.dat",sd+"prep_noise_ex"+ex+"_13.dat",
sd+"prep_noise_ex"+ex+"_14.dat",sd+"prep_noise_ex"+ex+"_15.dat",
sd+"prep_noise_ex"+ex+"_16.dat",sd+"prep_noise_ex"+ex+"_17.dat"]

#obj_name: the name of the object to be added as a prefix
#to the results file
obj_name = '../ex/ex'+ex_dir+'/output/chi2_CCR_ex'+ex_dir

#sigma: uncertainty in the data
sigma = 0.08
```

```
#disp: dispersion or bin width of the observed data
disp = 0.04

#State the prior ranges (min and max vals) on the temp1, temp2, logg1,
#logg2, metal, vrot1, vrot2 and alpha (the light ratio). In this program
    the stars are assumed to
#have the same metallicity.
prior_boxes = [(6000.,8000.), (5000.,7000.), (3.,5.), (3.,5.), (-0.5,0.5),
               (0.,50.), (0.,30.), (0,1.0)]

#####
#####

n_blobs = [0. for i in range(len(obs_spec)*4)]

def group(x, nr_elements):
    # Cut of the last elements so that x contains an exact
    # multiple of nr_elements
    x_cut = x[:nr_elements*(len(x)/nr_elements)]
    #print x_cut
    # reshape the array so that it is grouped in groups on nr_element
    x_2D = x_cut.reshape((len(x_cut)/nr_elements, nr_elements))
    #print x_2D
    # average the groups with nr_elements
    x_new = np.average(x_2D, axis=1)
    return x_new

def unique(myset):
    d = dict()
    for elem in myset:
        d[elem] = 1.
```

```

    return d.keys()

def rpars(pars):
    #return [random.gauss(p[0],p[1]) for p in pars]
    return [np.random.rand() * (p[1]-p[0]) + p[0] for p in pars]

def save_pickle(data, fn):
    f = open(fn, 'w')
    pickle.dump(data, f)
    f.close()

def get_vals():

    res = open("TAPE7", "r")
    ccr    = 0.0
    vel1   = -1000.
    vel1_u = -1.
    vel2   = -1000.
    vel2_u = -1.

    for line in res:
        if re.match("(.)BOUNDARY(.)", line):
            print "WARNING: INCREASE SEARCH AREA"
            return ccr,vel1,vel1_u,vel2,vel2_u
        if re.match("(.)1\\)(.)",line):
            if line[18] != "*" and line[5] != "*":
                vel1 = float(line[3:11])
                vel1_u = float(line[16:])
                if np.isnan(vel1_u) == True:
                    return 0.0, -1000, -1, -1000, -1
            else:

```

```
        return 0.0, -1000, -1, -1000, -1
elif re.match("(.)2\)(.*)",line):
    if line[18] != "*" and line[5] != "*":
        vel2 = float(line[3:11])
        vel2_u = float(line[16:])
        if np.isnan(vel2_u) == True:
            return 0.0, -1000, -1, -1000, -1
        else:
            return 0.0, -1000, -1, -1000, -1
elif re.match("(.)CORRELATION SCORE(.)", line):
    if line[43] != "*":
        ccr = float(line[41:49])
        if (ccr < 0):
            print "Correlation less than 0"
            return 0.0, -1000, -1, -1000, -1
        else:
            return 0.0, -1000, -1, -1000, -1
return ccr,vel1,vel1_u,vel2,vel2_u
```

#### #MPI settings

```
comm = MPI.COMM_WORLD
myrank = comm.Get_rank()
nprocs = comm.Get_size()
TAG_REQ = 11
TAG_CONTINUE = 22
```

```
if myrank == 0:
```

```
    node = comm.recv(source=MPI.ANY_SOURCE,tag=TAG_REQ)
```

```

#Make a directory to keep all the interpolated spectra
os.system("rm -r interp_spec/")
os.mkdir("%s" % ("interp_spec/"))
packet = {}
packet['continue'] = True
for node in range(1,nprocs):
    comm.send(packet,node,tag=TAG_CONTINUE)

else:
    while True:
        comm.send(myrank,0,tag=TAG_REQ)
        packet = comm.recv(source=0,tag=TAG_CONTINUE)

        if packet['continue'] == True:
            break

#Load the wavelengths (same for all synthetic spectra)
lambd=np.loadtxt(spec_dir+str([fname for fname in
    os.listdir(spec_dir)][0])).T[:1]

#Make empty lists for the parameter names and values
temp = []
logg = []
metal = []
temp_val = []
logg_val = []
met_val = []
new_file = []

#Read in the file names of the spectra

```

```

files = os.listdir(spec_dir)

#Create lists of parameter names from the file names
for file_name in files:
    temp.append(file_name[0:6])
    logg.append(file_name[6:9])
    metal.append(file_name[9:12])

#Identify all unique parameters
temps = unique(temp)
loggs = unique(logg)
metals = unique(metal)

#Sort parameter names (metals are more complicated)
temps.sort()
loggs.sort()

#Make lists of values (for axes)
i=0
for i,t in enumerate(temps,0):
    temp_val.append(float(t[1:]))

i=0
for i,l in enumerate(loggs,0):
    logg_val.append(float(l[1:])*0.1)

#Separate positive and negative metals
i=0
for i,m in enumerate(metals,0):
    if m[0] == "M":
        met_val.append((float(m[1:])*-1.))

```

```

else:
    met_val.append(float(m[1:]))

met_val.sort()

i=0
for i,m in enumerate(met_val,0):
    if (m < 0):
        metals[i]="M"+str(m*-1)
    else:
        metals[i] = "P"+str(m)
    if (len(metals[i]) < 5):
        metals[i] = metals[i][:1]+"0"+metals[i][1:-2]
    else:
        metals[i] = metals[i][::-2]
    met_val[i] = met_val[i]*0.1

#Make a list of inf's, the same length as the spectra files
empty = np.ones(len(lambd[0]))*np.inf

#Create a list of empty lists for each parameter
temp_e = [[empty]]*len(temps)
logg_e = [[empty]]*len(loggs)
met_e = [[empty]]*len(metals)

#Create a grid of empty lists
template_ = np.asarray([empty for x in temp_e for y in logg_e for z in
    met_e])

```

```
#Reshape the grid
template = np.reshape(template_,(len(temp_e),len(logg_e),len(met_e),-1))

#Populate the grid with flux for combinations with spectra
i,j,k=0,0,0
for i,t in enumerate(temps,0):
    for j,l in enumerate(loggs,0):
        for k,m in enumerate(metals,0):

            for f in files:
                if f == (t+l+m+".spectrum"):
                    template[i][j][k] = np.loadtxt(spec_dir+f).T[-1:]

#Create grid axes
axes = (np.array(temp_val), np.array(logg_val), np.array(met_val))
print "axes = ", axes

#Bin the synthetic wavelength data so that it is the same length as the
    observed
lambd_obs, flux_obs = np.loadtxt(obs_spec[0],skiprows=1,unpack=True)
print "len_obs = ", len(lambd_obs)
lambd_new = [i for i in lambd[0] if (i < lambd_obs[-1] and i >
    lambd_obs[0])]
print "lambd new = ", len(lambd_new)
bin_size = round(float(len(lambd_new))/float(len(lambd_obs)))
print "bin_size = ", bin_size
bin_lambd = group(lambd[0], bin_size)

def lnprob(x,prior_boxes,lambd,ndim):
    i=0
```

```

#Set the limits of the parameters
for i in range(0,ndim):
    if x[i] < prior_boxes[i][0] or x[i] > prior_boxes[i][1]:
        print "Value out of bounds",x[i], prior_boxes[i][0],
            prior_boxes[i][1]
        return -1.*np.inf,n_blobs

print "pars = ", x[0],x[1],x[2],x[3],x[4],x[5],x[6]

pars = np.array([[x[0], x[2], x[4]], [x[1], x[3], x[4]]])

spectra = interp(pars,axes,template)
if np.isnan(spectra[0][0]) == True or np.isnan(spectra[1][0]) == True:
    print "Unphysical parameters: ", pars
    return -1.*np.inf,n_blobs

spec1_b = broadening_rotational(lambd, spectra[0], x[5])
spec2_b = broadening_rotational(lambd, spectra[1], x[6])

#Instrumentally broaden spectra
spec1_inst =
    broadening_instrumental(lambd,spec1_b,disp,width_type='sigma')
spec2_inst =
    broadening_instrumental(lambd,spec2_b,disp,width_type='sigma')

bin_flux1 = group(spec1_inst, bin_size)
bin_flux2 = group(spec2_inst, bin_size)

#Make a new spectrum file for each synthetic spectrum
#the same two spectra are used for all observations
#(one for each star)

```

```
f1 = open('%sstar1synth%d.dat' % ("interp_spec/",myrank), "w")
f1.write("%2.1f %2.1f %2.1f %s\n" % (0.0, 0.0, 0.0, "spec1"))
f2 = open('%sstar2synth%d.dat' % ("interp_spec/",myrank), "w")
f2.write("%2.1f %2.1f %2.1f %s\n" % (0.0, 0.0, 0.0, "spec2"))

for i in range (len(bin_lambd)):
    f1.write("%7.2f %9.8f\n" % (bin_lambd[i], bin_flux1[i]))
    f2.write("%7.2f %9.8f\n" % (bin_lambd[i], bin_flux2[i]))
f1.close()
f2.close()

i=0.
blobs = []
ccr_func = 0.
alpha = x[7]
L2 = alpha/(1. + alpha)
L1 = 1. - L2

chi2_tot = 0.
for i in range(0,len(obs_spec)):
    process = Popen("./todcor", shell=False, stdin=PIPE, stdout=PIPE)
    process.communicate('%s\n%sstar1synth%d.dat\n%sstar2synth%d.dat\n%f\n'
        %
            (obs_spec[i], "interp_spec/",myrank, "interp_spec/",myrank,alpha))

    #Get the values from TAPE7 (the output from
    #TODCOR that contains the results)

    c,v1,v1_u,v2,v2_u = get_vals()
    blobs.append(v1)
```

```

blobs.append(v1_u)
blobs.append(v2)
blobs.append(v2_u)

if v1 == -1000 or v2 == -1000 or c == 0.0:
    print "TODCOR didn't converge: ",v1,v2
    return -1*np.inf,n_blobs

# shift the interpolated spectra according to the values from
# TODCOR

sh1 = np.array(atm.doppler_shift(lambd, v1, flux=spec1_inst))
sh2 = np.array(atm.doppler_shift(lambd, v2, flux=spec2_inst))

# interpolate the spectra so that model and obs have equal points
# for the chi2 calculation

lambd_obs, flux_obs =
    np.loadtxt(obs_spec[i],skiprows=1,unpack=True)
spec1_interp = pyl.interp(lambd_obs,lambd,sh1,left=None,
    right=None)
spec2_interp = pyl.interp(lambd_obs,lambd,sh2,left=None,
    right=None)

chi2 = 0
for j in range(len(lambd_obs)):
    chi2+=((flux_obs[j]-(spec1_interp[j]*L1 +
        spec2_interp[j]*L2))**2)/
        (sigma*sigma)*(1./v1_u**2)*(1./v2_u**2)
    chi2_tot +=chi2
lnp = -0.5*chi2_tot

```

```
print "chi2_tot = ", -0.5*chi2_tot

return lnp, blobs

def run(prior_boxes, state, n_walkers, iters, partial_save=True):

    #specify the number of dimensions
    ndim = 8

    #load new priors or start from the beginning
    if state is not None:
        p0 = np.loadtxt(state)[: , 1:-1]
    else:
        p0 = np.array([rpars(prior_boxes) for i in xrange(n_walkers)])

    pool = MPIPool()
    if not pool.is_master():

        pool.wait()
        sys.exit(0)

    #Generate the samples
    sampler = emcee.EnsembleSampler(n_walkers, ndim, lnprob, pool=pool,
        args=[prior_boxes, lambda[0], ndim])

    #partial save if specified
    if not partial_save:
        pos, prob, state, bl = sampler.run_mcmc(p0, 2)
        pool.close()
```

```

save_pickle([pos, bl, prob, sampler.chain],
            obj_name+'mcmc_run.dat')

#Extract the values from the sampler and save in multiple files
else:
    f = open(obj_name+'.posteriors.dat', "w")
    f2 = open(obj_name+'.vels.dat',"w")
    f3 = open(obj_name+'.all.dat',"w")
    f.close()
    f2.close()
    f3.close()

for result in sampler.sample(p0, iterations=iters,
                             storechain=False):

    position = result[0]
    blob = result[3]

    f = open(obj_name+'.posteriors.dat',"a")
    f2 = open(obj_name+'.vels.dat',"a")
    f3 = open(obj_name+'.all.dat',"a")

    #Write out all the information to the files
    for k in range(position.shape[0]):
        f.write("%d %s %f \n" %
                (k, " ".join(['%.10f' % i for i in position[k]]),
                 result[1][k]))

        f2.write("%d %s %f \n" %
                (k, " ".join(['%.10f' % l for l in blob[k]]),
                 result[1][k]))

```

```
f3.write("%d %s %s %f \n" %
        (k, " ".join(['%.10f' % i for i in position[k]]),
          " ".join(['%.7f' % l for l in blob[k]]),
          result[1][k]))

f.close()
f2.close()
f3.close()

pool.close()
save_pickle([result, 0, sampler.chain], obj_name+'.mcmc_run.dat')
```

```
run(prior_boxes, state, n_walkers, iters, True)
```

---

## A.2 The *CCR* version

---

```
#!/usr/bin/python
```

```
"""
```

```
19/06/14: This program uses TODCOR, a two dimensional cross correlation
program to determine the velocities by finding the best templates. It
also generates posteriors for teff, logg, metallicity and vrot of two
objects in a binary system and light ratio.
```

```
You must run this program in the TODCOR directory. This program will
store an interpolated spectrum for each processor in a directory
called interp_spec. Each time you run this program it will delete the
directory containing spectra from the previous run.
```

```
You must specify directories with a trailing / in all cases.
```

```
In TAPE1 you must specify all the inputs as usual, EXCEPT the request
must be set to "U" for the file names of the synthetic spectra and
the observed spectrum so that they will be requested interactively.
Do not leave any empty lines in TODCOR's TAPE1 as this will cause a
malfunction.
```

```
There may be some inf's in the output file (<star name>.posteriors.dat).
This is the value returned if the values are out of bounds,
unphysical yet in bounds, or if TODCOR does not produce a value for
the given parameters. The mcmc chains will move away from these
parameters in time.
```

```
The velocities are outputted in "blobs" which means that they are
selected when the lnprob is selected by the sampler. The velocities
```

are not posteriors, they are distributions based on the output of TODCOR.

To Start, adjust all the values in the INPUT box. You will need a folder that contains a set of synthetic spectra. Your prior ranges must be within the range of spectra that you have, ie. if your synthetic spectra have Teff's starting at 5000 K, your priors must not go below 5000 K.

```
"""
```

```
import emcee
from emcee.utils import MPIPool
import re
import numpy as np
import os
import logging
import shutil
from subprocess import Popen, PIPE
from phoebe.algorithms import interp_nDgrid
from phoebe.parameters import tools
from phoebe.atmospheres.tools import broadening_rotational
from interp import interp
import pickle
import sys
from mpi4py import MPI
import random
from phoebe.atmospheres.tools import broadening_instrumental
```

```

#####
#####INPUTS#####
#n_walkers: number of walkers, must be even and can be too
#small. Usually 128 will suffice
n_walkers = 128

#iters: number of iterations for each walker
iters = 10000000

#example number for test purposes
ex = str(2)
ex_dir = str(2)

# state: set to None to start MCMC from scratch or to a
# file name that contains your last <n_walkers> posteriors
# to start from the end of your last run
state = None

#spec_dir: the directory containing the synthetic spectra
spec_dir = "../data/bin0.04/"

#todcor_dir: the name of the directory where you run this
#program /and/ where TODCOR is contained.
todcor_dir = "/home/kmh/Stars/tools/todcor/mcmc/"

#obs_spec: list of the observed spectra

sd = "../ex/ex"+ex_dir+"/prep/"

obs_spec = [sd+"prep_noise_ex"+ex+"_0.dat",sd+"prep_noise_ex"+ex+"_1.dat",
sd+"prep_noise_ex"+ex+"_2.dat",sd+"prep_noise_ex"+ex+"_3.dat",
sd+"prep_noise_ex"+ex+"_4.dat",sd+"prep_noise_ex"+ex+"_5.dat",

```

```
sd+"prep_noise_ex"+ex+"_6.dat",sd+"prep_noise_ex"+ex+"_7.dat",
sd+"prep_noise_ex"+ex+"_8.dat",sd+"prep_noise_ex"+ex+"_9.dat",
sd+"prep_noise_ex"+ex+"_10.dat",sd+"prep_noise_ex"+ex+"_11.dat",
sd+"prep_noise_ex"+ex+"_12.dat",sd+"prep_noise_ex"+ex+"_13.dat",
sd+"prep_noise_ex"+ex+"_14.dat"]

#obj_name: the name of the object to be added as a prefix
#to the results file
obj_name = '../ex/ex'+ex_dir+'/output/CCR_ex'+ex_dir

#sigma: uncertainty in the method/data
sigma = 0.04

disp = 0.04 #the same as bin width, but can be more accurate for
    broadening

#State the prior ranges (min and max vals) on the temp1, temp2, logg1,
#logg2, metal, vrot1, vrot2 and alpha (the light ratio). In this program
    the stars are assumed to
#have the same metallicity.
prior_boxes = [(7500.,8500.), (3500.,4500.), (3.,5.), (3.,5.), (0.0,0.5),
    (0.,70.), (0.,30.), (0,1.0)]

#####
#####

n_blobs = [0. for i in range(len(obs_spec)*4)]

def group(x, nr_elements):
    # Cut of the last elements so that x contains an exact
    # multiple of nr_elements
```

```

x_cut = x[:nr_elements*(len(x)/nr_elements)]
#print x_cut
# reshape the array so that it is grouped in groups on nr_element
x_2D = x_cut.reshape((len(x_cut)/nr_elements, nr_elements))
#print x_2D
# average the groups with nr_elements
x_new = np.average(x_2D, axis=1)
return x_new

def unique(myset):
    d = dict()
    for elem in myset:
        d[elem] = 1.
    return d.keys()

def rpars(pars):
    #return [random.gauss(p[0],p[1]) for p in pars]
    return [np.random.rand() * (p[1]-p[0]) + p[0] for p in pars]

def save_pickle(data, fn):
    f = open(fn, 'w')
    pickle.dump(data, f)
    f.close()

def get_vals():
    res = open("TAPE7", "r")
    ccr = 0.0
    vel1 = -1000.
    vel1_u = -1.
    vel2 = -1000.

```

```
vel2_u = -1.

for line in res:
    if re.match("(.)BOUNDARY(.)", line):
        print "WARNING: INCREASE SEARCH AREA"
        return ccr,vel1,vel1_u,vel2,vel2_u
    if re.match("(.)1\\)(.)",line):
        if line[18] != "*" and line[5] != "*":
            vel1 = float(line[3:11])
            vel1_u = float(line[16:])
            if np.isnan(vel1_u) == True:
                return 0.0, -1000, -1, -1000, -1
            else:
                return 0.0, -1000, -1, -1000, -1
    elif re.match("(.)2\\)(.)",line):
        if line[18] != "*" and line[5] != "*":
            vel2 = float(line[3:11])
            vel2_u = float(line[16:])
            if np.isnan(vel2_u) == True:
                return 0.0, -1000, -1, -1000, -1
            else:
                return 0.0, -1000, -1, -1000, -1
    elif re.match("(.)CORRELATION SCORE(.)", line):
        if line[43] != "*":
            ccr = float(line[41:49])
            if (ccr < 0):
                print "Correlation less than 0"
                return 0.0, -1000, -1, -1000, -1
            else:
                return 0.0, -1000, -1, -1000, -1
return ccr,vel1,vel1_u,vel2,vel2_u
```

```
#MPI settings

comm = MPI.COMM_WORLD

myrank = comm.Get_rank()

nprocs = comm.Get_size()

TAG_REQ = 11

TAG_CONTINUE = 22

if myrank == 0:

    node = comm.recv(source=MPI.ANY_SOURCE,tag=TAG_REQ)

    #Make a directory to keep all the interpolated spectra

    os.system("rm -r interp_spec/")

    os.mkdir("%s" % ("interp_spec/"))

    packet = {}

    packet['continue'] = True

    for node in range(1,nprocs):

        comm.send(packet,node,tag=TAG_CONTINUE)

else:

    while True:

        comm.send(myrank,0,tag=TAG_REQ)

        packet = comm.recv(source=0,tag=TAG_CONTINUE)

        if packet['continue'] == True:

            break

#Load the wavelengths (same for all synthetic spectra)
```

```
lambda=np.loadtxt(spec_dir+str([fname for fname in
    os.listdir(spec_dir)][0])).T[:1]

#Make empty lists for the parameter names and values
temp = []
logg = []
metal = []
temp_val = []
logg_val = []
met_val = []
new_file = []

#Read in the file names of the spectra
files = os.listdir(spec_dir)

#Create lists of parameter names from the file names
for file_name in files:
    temp.append(file_name[0:6])
    logg.append(file_name[6:9])
    metal.append(file_name[9:12])

#Identify all unique parameters
temps = unique(temp)
loggs = unique(logg)
metals = unique(metal)

#Sort parameter names (metals are more complicated)
temps.sort()
loggs.sort()
```

```

#Make lists of values (for axes)

i=0
for i,t in enumerate(temps,0):
    temp_val.append(float(t[1:]))

i=0
for i,l in enumerate(loggs,0):
    logg_val.append(float(l[1:])*0.1)

#Separate positive and negative metals

i=0
for i,m in enumerate(metals,0):
    if m[0] == "M":
        met_val.append((float(m[1:])*-1.))

    else:
        met_val.append(float(m[1:]))

met_val.sort()

i=0
for i,m in enumerate(met_val,0):
    if (m < 0):
        metals[i]="M"+str(m*-1)
    else:
        metals[i] = "P"+str(m)
    if (len(metals[i]) < 5):
        metals[i] = metals[i][:1]+"0"+metals[i][1:-2]
    else:
        metals[i] = metals[i][::-2]

```

```
met_val[i] = met_val[i]*0.1

#Make a list of inf's, the same length as the spectra files
empty = np.ones(len(lambd[0]))*np.inf

#Create a list of empty lists for each parameter
temp_e = [[empty]]*len(temps)
logg_e = [[empty]]*len(loggs)
met_e = [[empty]]*len(metals)

#Create a grid of empty lists
template_ = np.asarray([empty for x in temp_e for y in logg_e for z in
    met_e])

#Reshape the grid
template = np.reshape(template_, (len(temp_e), len(logg_e), len(met_e), -1))

#Populate the grid with flux for combinations with spectra
i,j,k=0,0,0
for i,t in enumerate(temps,0):
    for j,l in enumerate(loggs,0):
        for k,m in enumerate(metals,0):

            for f in files:
                if f == (t+l+m+".spectrum"):
                    template[i][j][k] = np.loadtxt(spec_dir+f).T[-1:]

#Create grid axes
axes = (np.array(temp_val), np.array(logg_val), np.array(met_val))
print "axes = ", axes
```

---

```

#bin the synthetic wavelength data so that it is the same length as the
    observed

len_obs = len(np.loadtxt(obs_spec[0],skiprows=1))
print "len_obs = ", len_obs
print "len lambda = ", len(lambda[0])
bin_size = int(len(lambda[0])/len_obs)
bin_lambda = group(lambda[0], bin_size)

def lnprob(x,prior_boxes,lambda,ndim):
    i=0
    #Set the limits of the Gaussian
    for i in range(0,ndim):
        if x[i] < prior_boxes[i][0] or x[i] > prior_boxes[i][1]:
            print "Value out of bounds",x[i], prior_boxes[i][0],
                prior_boxes[i][1]
            return -1.*np.inf,n_blobs

print "pars = ", x[0],x[1],x[2],x[3],x[4],x[5],x[6]

pars = np.array([[x[0], x[2], x[4]], [x[1], x[3], x[4]]])
spectra = interp(pars,axes,template)
if np.isnan(spectra[0][0]) == True or np.isnan(spectra[1][0]) == True:
    print "Unphysical parameters: ", pars
    return -1.*np.inf,n_blobs

#rotationally broaden the spectra
spec1_b = broadening_rotational(lambda, spectra[0], x[5])
spec2_b = broadening_rotational(lambda, spectra[1], x[6])

#instrumentally broaden spectra

```

```
spec1_inst =
    broadening_instrumental(lambd,spec1_b,disp,width_type='sigma')
spec2_inst =
    broadening_instrumental(lambd,spec2_b,disp,width_type='sigma')

bin_flux1 = group(spec1_inst, bin_size)
bin_flux2 = group(spec2_inst, bin_size)

#make a new spectrum file for each synthetic spectrum
#the same two spectra are used for all observations
#(one for each star)
f1 = open('%sstar1synth%d.dat' % ("interp_spec/",myrank), "w")
f1.write("%2.1f %2.1f %2.1f %s\n" % (0.0, 0.0, 0.0, "spec1"))
f2 = open('%sstar2synth%d.dat' % ("interp_spec/",myrank), "w")
f2.write("%2.1f %2.1f %2.1f %s\n" % (0.0, 0.0, 0.0, "spec2"))

for i in range (len(bin_lambd)):
    f1.write("%7.2f %9.8f\n" % (bin_lambd[i], bin_flux1[i]))
    f2.write("%7.2f %9.8f\n" % (bin_lambd[i], bin_flux2[i]))
f1.close()
f2.close()

i=0.
blobs = []
ccr_func = 0.
alpha = x[7]

for i in range(0,len(obs_spec)):
    process = Popen("./todcor", shell=False, stdin=PIPE, stdout=PIPE)
    process.communicate('%s\n%sstar1synth%d.dat\n%sstar2synth%d.dat\n%f\n'
```

```

%
(obs_spec[i], "interp_spec/", myrank, "interp_spec/", myrank, alpha))

#Get the values from TAPE7 (the output from
#TODCOR that contains the results)

c, v1, v1_u, v2, v2_u = get_vals()
blobs.append(v1)
blobs.append(v1_u)
blobs.append(v2)
blobs.append(v2_u)

if v1 == -1000 or v2 == -1000 or c == 0.0:
    print "TODCOR didn't converge: ", v1, v2
    return -1*np.inf, n_blobs
ccr_func += -0.5*((1-c*c)/(sigma*sigma))

return ccr_func, blobs

def run(prior_boxes, state, n_walkers, iters, partial_save=True):

#specify the number of parameters with priors (excluding blobs)
ndim = 8

#load new priors or start from the beginning
if state is not None:
    p0 = np.loadtxt(state)[: , 1:-1]
else:
    p0 = np.array([rpars(prior_boxes) for i in xrange(n_walkers)])

```

```
pool = MPIPool()
if not pool.is_master():

    pool.wait()
    sys.exit(0)

#Generate the samples
sampler = emcee.EnsembleSampler(n_walkers, ndim, lnprob, pool=pool,
                               args=[prior_boxes, lambda[0], ndim])

#partial save if specified
if not partial_save:
    pos, prob, state, bl = sampler.run_mcmc(p0, 2)
    pool.close()
    save_pickle([pos, bl, prob, sampler.chain],
               obj_name+'mcmc_run.dat')

#Extract the values from the sampler and save in multiple files
else:
    f = open(obj_name+'.posteriors.dat', "w")
    f2 = open(obj_name+'.vels.dat', "w")
    f3 = open(obj_name+'.all.dat', "w")
    f.close()
    f2.close()
    f3.close()

    for result in sampler.sample(p0, iterations=iters,
                                storechain=False):

        position = result[0]
        blob = result[3]
```

```
f = open(obj_name+'.posteriors.dat','a')
f2 = open(obj_name+'.vels.dat','a')
f3 = open(obj_name+'.all.dat','a')

#Write out all the information to the files
for k in range(position.shape[0]):
    f.write("%d %s %f \n" %
            (k, " ".join(['%.10f' % i for i in position[k]]),
             result[1][k]))

    f2.write("%d %s %f \n" %
            (k, " ".join(['%.10f' % l for l in blob[k]]),
             result[1][k]))

    f3.write("%d %s %s %f \n" %
            (k, " ".join(['%.10f' % i for i in position[k]]),
             " ".join(['%.7f' % l for l in blob[k]]),
             result[1][k]))

f.close()
f2.close()
f3.close()

pool.close()
save_pickle([result, 0, sampler.chain], obj_name+'.mcmc_run.dat')

run(prior_boxes, state, n_walkers, iters, True)
```

---

# Appendix B

## The heartbeat Star Modelling Software

This appendix contains the PYTHON code for the heartbeat star modelling software. This software incorporates Markov chain Monte Carlo methods and interfaces with the binary modelling software, PHOEBE, to generate posteriors for the binary model parameters of heartbeatstars, as detailed in Chapter 3.

---

```
#!/usr/bin/python

import emcee
from emcee.utils import MPIPool
import numpy as np
import phoebeBackend as phb
import pickle
import sys

from phoebe.algorithms import interp_nDgrid
from phoebe.dynamics import keplerorbit
```

---

```

#####
#####CHANGE THIS SECTION#####
#####

ph_pars = ['phoebe_incl', 'phoebe_perr0', 'phoebe_ecc',
           'phoebe_pshift', 'phoebe_rm', 'phoebe_sma', 'phoebe_vga',
           'phoebe_grb1', 'phoebe_grb2', 'phoebe_radius1',
           'phoebe_radius2']#radii must go last in list

ph_prior_boxes = [(60.,6.), (1.9, 0.4), (0.6,0.1), (-0.2,0.2),
                  (0.72,0.04), (43.,5.), (-17.,5.), (0.8,0.2),
                  (0.3,0.5), (1.6,1.), (1.1,0.35)]

puls_pars = ['amp1', 'phase1', 'amp2', 'phase2', 'amp3', 'phase3', 'amp4',
            'phase4', 'amp5', 'phase5', 'amp6', 'phase6', 'amp7', 'phase7']

puls_prior_boxes
    =[(3e-5,5e-5), (2.3,0.4), (2e-5,7e-5), (0.75,0.4), (1e-5,5e-5),
      (2.8,0.7), (1e-5,9e-5), (0.8,0.7), (1e-5,3e-5), (1.8,0.8),
      (0.5e-6,8e-5), (0.7,0.4), (5e-6,5e-5), (4.2,1.0)]

freq_multi = [21,24,20,23,22,25,18]
phoebe_file = '../param/3749_mcmc.ph'
lc_file = "../data/3749_binned-cleaned.dat"
rv1_file = '../data/K03749404_RV1.dvel'
rv2_file = '../data/K03749404_RV2.dvel'
n_pulse = str(7)
state = 'priors.dat' #set to None to start MCMC from scratch
nwalkers = 128 #Must be at least twice the number of parameters and even
niter = 10000
ztime = 55611.3423 #Tzero in param
period = 20.30635

```

```
vsini1 = 29.2 #In km/s
vsini2 = 9.2

#####

#####

#####

c = 2.99792458e5 #Speed of light in km/s

table = np.loadtxt('/home/users/kmhambleton/pulse/tables/BF_grid.dat').T

axval, pgrid = interp_nDgrid.create_pixeltypgrid(table[:2], table[-1:])

rv_time=np.linspace(0.,1.,100)

rv1_time,rv1_data,rv1_sigma=np.loadtxt(rv1_file,unpack=True)
rv2_time,rv2_data,rv2_sigma=np.loadtxt(rv2_file,unpack=True)

rv_phase = (np.array((rv1_time)-ztime)%period)/period

time, flux, sigma = np.loadtxt(lc_file, unpack=True)

def save_pickle(data, fn):
    #Save file as a pickel
    f = open(fn, 'w')
    pickle.dump(data, f)
    f.close()
```

---

```

def get_conjunction_phase (conj_o,phase_o):
    #This function is related to the phase shift, but calculating the
    #phase shift for heartbeat stars didn't seem to work so well.
    ecc      = phb.getpar("phoebe_ecc")
    omega    = phb.getpar("phoebe_perr0")
    ups_c    = np.pi/2. - omega #('+'=inferior, '-'=superior)
    E_c      = 2. * np.arctan ( np.sqrt ((1.-ecc)/(1.+ecc)) * np.tan
        (ups_c/2.) )
    M_c      = E_c - ecc * np.sin (E_c)
    conj_n   = (M_c + omega) / 2. / np.pi - 0.25
    if (conj_o == 100):
        #For the first time just determine the phase of conjunction.
        return conj_n
    else:
        phase = phase_o + (conj_o - conj_n)
        #Set phase to new value in phoebe
        if (phase < -0.5):
            phase = phase + 1.0
        elif (phase > 0.5):
            phase = phase - 1.0
        phb.setpar("phoebe_pshift",phase,0)
        return phase

def get_lum(model):
    #Calculates the luminosity and shifts the model vertically
    hla     = phb.getpar("phoebe_hla",0)
    cla     = phb.getpar("phoebe_cla",0)
    if (cla <= 0.):
        return False, False

```

```
alpha = 0
sum_model = 0.
for i in range(len(model)):
    alpha += model[i]*flux[i]*sigma[i]*sigma[i]
    sum_model += model[i]*model[i]*sigma[i]*sigma[i]
alpha = alpha/sum_model
model = alpha*model
#Calculate new light fractions using alpha
z = (hla+cla)/(4.*np.pi)
y = hla/cla

cla = z*4.*np.pi*alpha/(y+1.)
hla = y*cla
light = hla/(hla + cla)
if (light <=0 or cla <= 0):
    return False, False
return light, model

def interp_beaming(teff, logg):
    #Interpolates the beaming tables (you need the tables for
    #this to work)
    B = interp_nDgrid.interpolate([[teff], [logg]], axval, pgrid)
    return B[0][0]

def add_boosting(light,model_rv,model_rv2,model):
    #Adds Doppler boosting to the model
    vga = phb.getpar("phoebe_vga")
    teff1 = phb.getpar("phoebe_teff1")
    teff2 = phb.getpar("phoebe_teff2")
```

---

```

logg1 = phb.getpar("phoebe_logg1")
logg2 = phb.getpar("phoebe_logg2")
if (logg2 >= 5.0):
    logg2 = 4.999
if (logg1 >= 5.0):
    logg1 = 4.999
if (teff2 < 3500.):
    teff2 = 3500.
if (teff1 < 3500.):
    teff1 = 3500.

B = interp_beaming(teff1, logg1)
B2 = interp_beaming(teff2, logg2)
func1 = light*B*(model_rv-vga)/c
func2 = (1-light) * B2*(model_rv2-vga)/c
return model*(1.- func1 - func2)

```

```

def get_potential(radius,val):
    #I found it easier to work with radii instead of potentials. This
    #function converts to potentials from the inputted radii

    sma = phb.getpar("phoebe_sma")
    rad = radius/sma
    delta = 1. + phb.getpar("phoebe_ecc")
    lamda = 1.
    nu = 0.
    if val == 1:
        f = phb.getpar("phoebe_f1")
        rm = phb.getpar("phoebe_rm")
        return 1./rad + rm*(1./np.sqrt(delta**2 + rad**2 - \
            2.*rad*lamda*delta) - rad*lamda/delta**2) + \
            0.5*f**2*(1. + rm)*rad**2*(1. - nu**2)

```

```
else:
    f    = phb.getpar("phoebe_f2")
    rm   = 1./phb.getpar("phoebe_rm")
    pot  = 1./rad + rm*(1./np.sqrt(delta**2 + rad**2 - \
        2.*rad*lamda*delta) - rad*lamda/delta**2) + \
        0.5*f**2*(1. + rm)*rad**2*(1. - nu**2)
    return pot/rm + 0.5*(rm-1)/rm

def check_pars(x):
    #For all the parameters set the new values and check that they are
    #in bounds. If they are out of bounds then the log probability
    #(chi2) will be reduced to -np.inf
    for i in range(len(ph_pars)):
        #Convert from radius to potential:
        if ph_pars[i] == "phoebe_radius1" :
            if x[i] < ph_prior_boxes[i][0] or x[i] > (ph_prior_boxes[i][1]
                + ph_prior_boxes[i][0]):
                print "radius 1 is out of range", x[i]
                return False,False
            f1_val = set_f_ratio(x[i],1)
            phb.setpar("phoebe_pot1",get_potential(x[i],1),0)
        elif ph_pars[i] == "phoebe_radius2" :
            if x[i] < ph_prior_boxes[i][0] or x[i] > (ph_prior_boxes[i][1]
                + ph_prior_boxes[i][0]):
                print "radius 2 is out of range", x[i]
                return False,False
            f2_val = set_f_ratio(x[i],2)
            phb.setpar("phoebe_pot2",get_potential(x[i],2),0)
        else:
            phb.setpar(ph_pars[i], x[i], 0)
    return f1_val,f2_val
```

---

```

def crit_pot():
    #My program was crashing due to phoebe overflowing the critical
    #potential. This function checks to see if the potential is smaller
    #than the critical potential.
    q = phb.getpar("phoebe_rm")
    pot1 = phb.getpar("phoebe_pot1")
    pot2 = phb.getpar("phoebe_pot2")
    d = 1. - phb.getpar("phoebe_ecc")
    new_x1 = d/2.
    f = phb.getpar("phoebe_f1")
    pot_l1_1 = get_lagrange(q,f,d,new_x1)
    if (pot1 < pot_l1_1):
        print "pot 1 less than crit pot", pot_l1_1, pot1
        return False
    f = phb.getpar("phoebe_f2")
    q = 1./q
    pot_l1_2 = get_lagrange(q,f,d,new_x1)/q + 0.5*(q-1)/q
    if (pot2 < pot_l1_2):
        print "pot 2 less than crit pot", pot_l1_2, pot2
        return False
    return True

def get_lagrange(q,f,d,new_x):
    #This function gets the lagrangian points do determine the
    #critical potential
    x = -1e50
    while (np.abs(x-new_x) > 0.0000000001):
        x = new_x

```

```
y = -x*(x*x)**-1.5 -q*(x-d)*((x-d)*(x-d))**-1.5 -q/d/d +
    f*f*(1+q)*x
d_y = (2*x*x)/(x*x)**2.5 + q*(2*(x-d)*(x-d))/((x-d)*(x-d))**2.5 +\
    f*f*(1+q)
new_x = x - y/d_y

pot = 1.0/np.sqrt(new_x*new_x) +
    q*(1.0/np.sqrt((new_x-d)*(new_x-d))-new_x/d/d) +
    0.5*f*f*(1+q)*(new_x*new_x)

return pot

def test_logg():
    #This function checks phoebe's log g is within range. This is
    #different from the logg used in this
    #program, due to the different orbital point at which the radius is
    #defined.
    logg1 = phb.getpar("phoebe_logg1")
    logg2 = phb.getpar("phoebe_logg2")
    if (logg1 <= 1.0 or logg1 >= 5.0):
        print "log g 1 is out of bounds ", logg1
        return False
    if (logg2 <= 1.0 or logg2 >= 5.0):
        print "log g 2 is out of bounds ", logg2
        return False
    return True

def make_cos (time,freq,amp,phi):
    #This function makes the sine that is applied to the light curve
```

---

```

return tuple(amp*np.cos(2*np.pi*(np.array(time))
                *freq+phi))

def add_sines(time,x,freq_multi,numb_sine,puls_prior_boxes):
    #Create a list of sine curves, each with the
    #new values for amp, and phase.
    amp = 0.
    phi = 0.
    k = 0.
    y_tot = np.zeros([len(time)])

    #Sum up the sine waves
    for k in range(numb_sine):
        amp = x[len(ph_pars)+2*k]
        phi = x[len(ph_pars)+1+2*k]
        if amp < puls_prior_boxes[2*k][0] or amp >
            (puls_prior_boxes[2*k][1] + puls_prior_boxes[2*k][0]):
            return False, []
        if phi < puls_prior_boxes[1+2*k][0] or phi >
            (puls_prior_boxes[1+2*k][1] + puls_prior_boxes[1+2*k][0]):
            return False, []

        y_tot += (make_cos(time,freq_multi[k],amp,phi))

        if amp < 1e-6 or phi < 0. or phi > 6.2831853071:
            return False, []
    y_tot += 1.

    #Combine the pulsations and binary model
    return True, y_tot

```

```
def get_chi2_lc(data,model,error):
    j = 0
    #Includes the sqrt(flux) to accuount for the increase
    #in noise when less photons are being received
    chi2 = 0
    for j in range (len(data)):
        chi2+=((data[j]-model[j])**2)/(error[j]*error
            [j]*np.sqrt(data[j]))
    return chi2

def get_chi2_rv(rv_phase,rv1_data,rv1_sigma,rv2_data,rv2_sigma):
    model_rv1_chi2 = np.array(phb.rv1(tuple(rv_phase),0))
    model_rv2_chi2 = np.array(phb.rv2(tuple(rv_phase),0))
    k=0
    chi2_rv1 = 0
    chi2_rv2 = 0
    for k in range (len(rv1_data)):
        chi2_rv1+=((rv1_data[k]-model_rv1_chi2[k])**2)/(rv1_sigma[k]**2)
        chi2_rv2+=((rv2_data[k]-model_rv2_chi2[k])**2)/(rv2_sigma[k]**2)
    return chi2_rv1 + chi2_rv2

def rpars(pars):
    return [np.random.rand() * p[1] + p[0] for p in pars]

def r_from_logg(x,ph_pars):
    for i in range(len(ph_pars)):
        #Convert from radius to potential:
        if ph_pars[i] == "phoebe_logg1" :
            logg1 = x[i]
```

---

```

        g = 10**(logg1)/100. #g in m/s**2
    if ph_pars[i] == "phoebe_rm":
        rm = x[i]
    if ph_pars[i] == "phoebe_sma":
        sma = x[i]*0.0046491 #sma in Au
p = period/365.242 #period in years
m1m2 = sma**3/p**2
m1 = m1m2/(1.+rm)
m = m1*1.9891e30
return m1, (np.sqrt(6.67e-11*m/g))/6.955e8

def set_f_ratio(radius,val):
    #Calculate the rotation parameter
    incl = phb.getpar("phoebe_incl")
    if (val == 1):
        vrot = vsini1
    else:
        vrot = vsini2

    vrot_day = vrot*24*60*60/np.sin(incl/360.*np.pi*2.)
    radius_km = radius*695500

    fval = period/(2.*np.pi*radius_km/vrot_day)
    if (val == 1):
        phb.setpar("phoebe_f1",fval, 0)
        return fval
    else:
        phb.setpar("phoebe_f2",fval, 0)
        return fval

#####

```

```
#####
```

```
def lnprob(x, prior_boxes, time, flux, sigma, ph_pars, numb_sine, nu_orb,
          freq_multi):
    #Determine the posterior probabilities

    blobs = []

    #Check all the phoebe parameters are in bounds
    #and convert radii to potentials
    fval_1, fval_2 = check_pars(x)
    if (fval_1 == False):
        return -np.inf, [0.0,0.0]

    #Determine if the potentials are less than the
    #critical potentials
    if (crit_pot() == False):
        return -np.inf, [0.0,0.0,0.0]

    #Update the limb darkening coefficents (create a model
    #first to update the logg)
    model_test = (phb.lc((0.0,),0))

    #Test logg values are in bounds
    if (test_logg() == False):
        return -1.*np.inf, [0.0,0.0,0.0]

    #Update limb darkening values
    phb.updateLD()

    #Generate a model of lcs and rvs
    model = np.array(phb.lc(tuple(time),0))
```

---

```

#Make rv models

#rv_time is an array of 100 phase points.
model_rv_ = np.array(phb.rv1(tuple(rv_time),0))
model_rv2_ = np.array(phb.rv2(tuple(rv_time),1))

#Interpolate the rvs (faster) to get same number of points
#as lc data
model_rv = np.interp(time,rv_time,np.array(model_rv_))
model_rv2 = np.interp(time,rv_time,np.array(model_rv2_))

#Calculate light levels
light, model = get_lum(model)
if (light == False):
    return -np.inf, [0.0,0.0,0.0]

#Calculate boosting
b_model = add_boosting(light,model_rv,model_rv2,model)

#Re-calculate light levels
light_n, b_model = get_lum(b_model)
if (light_n == False):
    return -np.inf, [0.0,0.0,0.0]

sine_val, sines =
    add_sines(time,x,freq_multi,numb_sine,puls_prior_boxes)
if (sine_val == False):
    return -np.inf, [0.0,0.0,0.0]
tot_model = sines*tuple(b_model)

#Make blobs from calculated data

```

```
blobs.append(light_n)
blobs.append(fval_1)
blobs.append(fval_2)

#Calculate chi2 for light curve
chi2 = get_chi2_lc(flux,tot_model,sigma)

#Calculate chi2 for rv1 and rv2
chi2_rv = get_chi2_rv(rv_phase,rv1_data,rv1_sigma,rv2_data,rv2_sigma)

#Calculate the log probability and check to see if
lnp = -0.5 * (chi2 + chi2_rv)

#Write out the parameter values and the log probability
sys.stderr.write("% 9.4f " * len(x) % tuple(x))
sys.stderr.write("% 12.6f\n" % lnp)

#Return the log probability
return lnp, blobs

#####
#####

def run(phoebe_file, ph_pars, puls_pars, ph_prior_boxes, puls_prior_boxes,
        state, nwalkers, niter, freq_multi, partial_save=False):
    phb.init()
    phb.configure()
    phb.open(phoebe_file)

    numb_sine = len(puls_pars)/2
```

---

```

priors = ph_prior_boxes + puls_prior_boxes
ndim = len(puls_pars+ph_pars)
nu_orb  = 1./float(phb.getpar("phoebe_period"))

#Set penalties for an out-of-bounds situation:
for i, par in enumerate(ph_pars):
    phb.setlim(par, ph_prior_boxes[i][0],
               ph_prior_boxes[i][0] + ph_prior_boxes[i][1])

#Load from previous mcmc run if option is not None
if state is not None:
    p0 = np.loadtxt(state)[: , 1:-1]
else:
    p0 = np.array([rpars(priors) for i in xrange(nwalkers)])

#Tests to see if nodes are available for MPI
pool = MPIPool()
if not pool.is_master():
    pool.wait()
    sys.exit(0)

#Generate the emcee sampler with given inputs
sampler = emcee.EnsembleSampler(nwalkers, ndim, lnprob,
                                args=[priors,time,flux,sigma,ph_pars,numb_sine,
                                       nu_orb, freq_multi],
                                pool=pool)

if not partial_save:
    pos, prob, state, blob = sampler.run_mcmc(p0, 2)
    pool.close()
    save_pickle([pos, blob, prob, sampler.chain], phoebe_file +

```

```
        '.7.mcmc_run.dat')

else:
    f = open(phoebe_file + '.7.mcmc_chain.dat', "w")
    f.close()

    for result in sampler.sample(p0, iterations=niter,
                                storechain=False):
        position = result[0]
        blobs    = result[3]
        f = open(phoebe_file + '.7.mcmc_chain.dat', "a")
        for k in range(position.shape[0]):
            f.write("%d %s %s %f\n"
                    % (k, " ".join(['%.10f' % i for i in
                                     position[k]]), " ".join(['%.10f' % j for j
                                                                in blobs[k]]), result[1][k]))
        f.close()

    pool.close()
    save_pickle([result, 0, sampler.chain], phoebe_file +
                '.7.mcmc_run.dat')

phb.quit()

#####
if __name__ == "__main__":

    run(phoebe_file, ph_pars, puls_pars, ph_prior_boxes,
        puls_prior_boxes, state, nwalkers, niter, freq_multi, True)
```

---

# Bibliography

- Aerts C., Christensen-Dalsgaard J., Kurtz D., 2010, *Astroseismology*. Springer
- Alexander M. E., 1973, *Ap&SS*, 23, 459
- Antoci V. et al., 2014, *ApJ*, 796, 118
- Antoci V. et al., 2011, *Nature*, 477, 570
- Avni Y., Schiller N., 1982, *ApJ*, 257, 703
- Baglin A. et al., 2006, in *COSPAR, Plenary Meeting, Vol. 36, 36th COSPAR Scientific Assembly*, pp. 3749–+
- Bahcall J. N., Basu S., Kumar P., 1997, *ApJ*, 485, L91
- Batalha N. M. et al., 2010, *ApJ*, 713, L109
- Beck P. G. et al., 2014, *A&A*, 564, A36
- Beck P. G. et al., 2012, *Nature*, 481, 55
- Bedding T. R. et al., 2011, *Nature*, 471, 608
- Bedding T. R., Murphy S. J., Colman I. L., Kurtz D. W., 2014, *ArXiv e-prints*
- Belkacem K. et al., 2015, *A&A*, 579, A30
- Bloemen S. et al., 2011, *MNRAS*, 410, 1787
- Borucki W. J., Koch D., Basri G., Batalha N., Brown T., Caldwell D., et al., 2010, *Science*, 327, 977

- Bouabid M.-P., Dupret M.-A., Salmon S., Montalbán J., Miglio A., Noels A., 2013, MNRAS, 429, 2500
- Bouabid M.-P., Montalbán J., Miglio A., Dupret M.-A., Grigahcène A., Noels A., 2009, in American Institute of Physics Conference Series, Vol. 1170, American Institute of Physics Conference Series, Guzik J. A., Bradley P. A., eds., pp. 477–479
- Breger M., Lenz P., Pamyatnykh A. A., 2008, Communications in Asteroseismology, 157, 56
- Breger M., Pamyatnykh A. A., Pikall H., Garrido R., 1999, A&A, 341, 151
- Burkart J., Quataert E., Arras P., Weinberg N. N., 2012, MNRAS, 421, 983
- Buzasi D. L. et al., 2005, ApJ, 619, 1072
- Castelli F., Kurucz R. L., 2004, ArXiv Astrophysics e-prints
- Chaplin W. J. et al., 2010, ApJ, 713, L169
- Christensen-Dalsgaard J., 1984, in Space Research in Stellar Activity and Variability, Mangeney A., Praderie F., eds., p. 11
- Claret A., 1997, A&A, 327, 11
- Claret A., Bloemen S., 2011, A&A, 529, A75
- Claret A., Giménez A., 2010, A&A, 519, A57
- Claret A., Willems B., 2002, A&A, 388, 518
- Claret A., Willems B., 2003, A&A, 410, 289
- Conroy K. E. et al., 2014, PASP, 126, 914
- Cowling T. G., 1941, MNRAS, 101, 367
- Cunha M. S. et al., 2007, A&AR, 14, 217

- Darwin G. H., 1879, *The Observatory*, 3, 79
- Derekas A. et al., 2011, *Science*, 332, 216
- Dziembowski W. A., Gough D. O., Houdek G., Sienkiewicz R., 2001, *MNRAS*, 328, 601
- Espinosa Lara F., Rieutord M., 2012, *A&A*, 547, A32
- Foreman-Mackey D., Hogg D. W., Lang D., Goodman J., 2013, *PASP*, 125, 306
- Fuller J., Lai D., 2012, *MNRAS*, 420, 3126
- García Hernández A., Martín-Ruiz S., Monteiro M. J. P. F. G., Suárez J. C., Reese D. R., Pascual-Granado J., Garrido R., 2015, *ArXiv e-prints*
- García Hernández A., Moya A., Michel E., Garrido R., Suárez J. C., Rodríguez E., Amado P. J., Martín-Ruiz S., 2009, *A&A*, 506, 79
- García Hernández A. et al., 2013, *A&A*, 559, A63
- Gies D. R., Williams S. J., Matson R. A., Guo Z., Thomas S. M., Orosz J. A., Peters G. J., 2012, *AJ*, 143, 137
- Gilliland R. L., Brown T. M., Christensen-Dalsgaard J., Kjeldsen H., Aerts C., et al., 2010, *PASP*, 122, 131
- Gizon L., Solanki S. K., 2003, *ApJ*, 589, 1009
- Goldreich P., Nicholson P. D., 1989, *ApJ*, 342, 1079
- Goodman J., Weare J., 2010, *Com. App. Math. Comp. Sci.*, 5, 65
- Gray R. O., 1999, *SPECTRUM: A stellar spectral synthesis program*. *Astrophysics Source Code Library*
- Gray R. O., Graham P. W., Hoyt S. R., 2001, *AJ*, 121, 2159
- Grec G., Fossat E., Pomerantz M. A., 1983, *Sol. Phys*, 82, 55

- Grigahcène A. et al., 2010a, *ApJ*, 713, L192
- Grigahcène A. et al., 2010b, *Astronomische Nachrichten*, 331, 989
- Guzik J. A., Kaye A. B., Bradley P. A., Cox A. N., Neuforge C., 2000, *ApJ*, 542, L57
- Haghighipour N., Orosz J., Welsh W., 2014, in *AAS/Division for Planetary Sciences Meeting Abstracts*, Vol. 46, *AAS/Division for Planetary Sciences Meeting Abstracts*, p. 301.08
- Hambleton K. M. et al., 2013, *MNRAS*, 434, 925
- Handler G., Kanaan A., Montgomery M. H., 1997, *A&A*, 326, 692
- Hareter M. et al., 2014, *A&A*, 567, A124
- Hastings W. K., 1970, *Biometrika*, 57, 97
- Huber D. et al., 2010, *ApJ*, 723, 1607
- Hut P., 1980, *A&A*, 92, 167
- Hut P., 1981, *A&A*, 99, 126
- Kallinger T. et al., 2010, *A&A*, 522, A1
- Khaliullin K. F., Khaliullina A. I., 2010, *MNRAS*, 401, 257
- Kirk B. et al., 2016, *AJ*, 151, 68
- Kjeldsen H., Bedding T. R., 1995, *A&A*, 293, 87
- Kopal Z., 1959, *Close binary systems*
- Kumar P., Ao C. O., Quataert E. J., 1995, *ApJ*, 449, 294
- Kurtz D. W., Saio H., Takata M., Shibahashi H., Murphy S. J., Sekii T., 2014, *MNRAS*, 444, 102

- Lamb H., 1909, Proc. London Math Soc., 7, 122
- Leighton R. B., 1960, in IAU Symposium, Vol. 12, Aerodynamic Phenomena in Stellar Atmospheres, Thomas R. N., ed., pp. 321–325
- Loeb A., Gaudi B. S., 2003, ApJ, 588, L117
- Lucy L. B., 1967, ZEASAJ, 65, 89
- Maceroni C. et al., 2009, A&A, 508, 1375
- Marques J. P. et al., 2013, A&A, 549, A74
- Mazeh T., 2008, in EAS Publications Series, Vol. 29, EAS Publications Series, Goupil M.-J., Zahn J.-P., eds., pp. 1–65
- Mazeh T., Faigler S., 2010, A&A, 521, L59+
- Mazeh T., Zucker S., Goldberg D., Latham D. W., Stefanik R. P., Carney B. W., 1995, ApJ, 449, 909
- Metropolis, Nicholas, 2011, Los Alamos Science
- Metropolis M., Ulam S., 1949, Journal of the American Statistical Association, 44, 335341
- Metropolis N., Rosenbluth A., Rosenbluth M., Teller A., E. T., 1953, J. Chem. Phys., 21, 10871092
- Montalbán J., Noels A., 2013, in European Physical Journal Web of Conferences, Vol. 43, European Physical Journal Web of Conferences, p. 3002
- Mosser B. et al., 2011, A&A, 532, A86
- Murphy S. J., Bedding T. R., Shibahashi H., Kurtz D. W., Kjeldsen H., 2014, MNRAS, 441, 2515
- Nelder J. A., Mead R., 1965, Computer Journal, 7, 308

- Nicholls C. P., Wood P. R., 2012, MNRAS, 421, 2616
- O’Leary R. M., Burkart J., 2014, MNRAS, 440, 3036
- Orosz J. A., 2015, in Astronomical Society of the Pacific Conference Series, Vol. 496, Astronomical Society of the Pacific Conference Series, Rucinski S. M., Torres G., Zejda M., eds., p. 55
- Orosz J. A., Hauschildt P. H., 2000, A&A, 364, 265
- Ossendrijver M., 2003, A&AR, 11, 287
- Otí Floranes H., Christensen-Dalsgaard J., Thompson M. J., 2005, MNRAS, 356, 671
- Prša A., 2005, PhD thesis, University of Ljubljana
- Prša A. et al., 2011, AJ, 141, 83
- Prša A., Zwitter T., 2005, ApJ, 628, 426
- Reese D., Lignières F., Rieutord M., 2008, A&A, 481, 449
- Richardson N. D. et al., 2016, MNRAS, 455, 244
- Russell H. N., Merrill J. E., 1952, The determination of the elements of eclipsing binaries
- Saio H., Kurtz D. W., Takata M., Shibahashi H., Murphy S. J., Sekii T., Bedding T. R., 2015, MNRAS, 447, 3264
- Schmid V. S. et al., 2015, A&A, 584, A35
- Shakura N. I., Postnov K. A., 1987, A&A, 183, L21
- Shibahashi H., Kurtz D. W., 2012, MNRAS, 422, 738
- Shibahashi H., Kurtz D. W., Murphy S. J., 2015a, MNRAS, 450, 3999
- Shibahashi H., Kurtz D. W., Murphy S. J., 2015b, MNRAS, 450, 3999

- Shporer A., Kaplan D. L., Steinfadt J. D. R., Bildsten L., Howell S. B., Mazeh T., 2010, *ApJ*, 725, L200
- Smullen R. A., Kobulnicky H. A., 2015, *ApJ*, 808, 166
- Suárez J. C., García Hernández A., Moya A., Rodrigo C., Solano E., Garrido R., Rodón J. R., 2014, *A&A*, 563, A7
- Tassoul M., 1980, *ApJS*, 43, 469
- Thompson M. J., Christensen-Dalsgaard J., Miesch M. S., Toomre J., 2003, *ARAA*, 41, 599
- Thompson S. E. et al., 2012, *ApJ*, 753, 86
- Tody D., 1986, in *Proceedings of the International Society for Optical Engineering*, Vol. 627, *Instrumentation in astronomy VI*, Crawford D. L., ed., p. 733
- Tonry J., Davis M., 1979, *AJ*, 84, 1511
- Torres G., Andersen J., Giménez A., 2010, *A&AR*, 18, 67
- Torres G., Stefanik R. P., Latham D. W., Mazeh T., 1995, *ApJ*, 452, 870
- Turchin V. F., 1971, *Theory of Probability and its Applications*, 16, 720
- Ulrich R. K., 1970, *ApJ*, 162, 993
- Unno W., Osaki Y., Ando H., Saio H., Shibahashi H., 1989, *Nonradial oscillations of stars*
- van Kerkwijk M. H., Rappaport S. A., Breton R. P., Justham S., Podsiadlowski P., Han Z., 2010, *ApJ*, 715, 51
- Walker G. et al., 2003, *PASP*, 115, 1023
- Welsh W. F. et al., 2011, *ApJS*, 197, 4
- Welsh W. F. et al., 2012, *Nature*, 481, 475

- White T. R., Bedding T. R., Stello D., Christensen-Dalsgaard J., Huber D., Kjeldsen H., 2011, *ApJ*, 743, 161
- Wilson R. E., 1979, *ApJ*, 234, 1054
- Wilson R. E., Devinney E. J., 1971, *ApJ*, 166, 605
- Wilson R. E., Sofia S., 1976, *ApJ*, 203, 182
- Wilson R. E., Van Hamme W., 2004, Computing Binary Star Observables (in Reference Manual to the Wilson-Devinney Program)
- Witte M. G., Savonije G. J., 1999, *A&A*, 350, 129
- Witte M. G., Savonije G. J., 2001, *A&A*, 366, 840
- Witte M. G., Savonije G. J., 2002, *A&A*, 386, 222
- Zahn J.-P., 1975, *A&A*, 41, 329
- Zahn J.-P., 1977, *A&A*, 57, 383
- Zasche P., 2012, *AcA*, 62, 97
- Zimmerman M., Thompson S. E., Hambleton K., Fuller J., Shporer A., Isaacson H. T., Howard A., Kurtz D., 2016, in American Astronomical Society Meeting Abstracts, Vol. 227, American Astronomical Society Meeting Abstracts, p. 344.09
- Zucker S., Mazeh T., 1994, *ApJ*, 420, 806
- Zucker S., Mazeh T., Alexander T., 2007a, *ApJ*, 670, 1326
- Zucker S., Mazeh T., Alexander T., 2007b, *ApJ*, 670, 1326